ANNUAL REPORT

University Research Initiative

Contract No.: N00014-92-J-1808

March 1992 - April 1993

The Processing and Mechanical Properties of High Temperature/ High Performance Composites

by

A.G. Evans & F. Leckie
University of California,
Santa Barbara

University of Pennsylvania
Harvard University
Washington State University
Carnegie Mellon University
University of Virginia

Book 2 of 5:

CONSTITUENT PROPERTIES AND MACROSCOPIC PERFORMANCE: CMCs

SUMMARY

OF

TABLE OF CONTENTS

BOOK 2

CONSTITUENT PROPERTIES AND MACROSCOPIC PERFORMANCE: CMCs

26.	On the Flexural Properties of Brittle Multilayer Materials	C.A. Folsom F.W. Zok F.F. Lange
27.	The Creep Behavior of CAS/Nicalon Continuous-Fiber Composites	C.H. Weber J.P.A. Löfvander A.G. Evans
28.	Stress Corrosion and Fatigue Cracking in a Unidirectional Ceramic-Matrix Composite	S.M. Spearing F.W. Zok A.G. Evans
29.	Tensile and Flexural Ultimate Strength of Fiber-Reinforced Ceramic-Matrix Composites	F. Hild J.-M. Domergue F.A. Leckie A.G. Evans
30.	Fracture Resistance Characteristics of a Metal-Toughened Ceramic	B.D. Flinn C.S. Lo F.W. Zok A.G. Evans
31.	On the Strength of Ductile Particle Reinforced Brittle Matrix Composites	G. Bao F.W. Zok
32.	SiC/CAS: A Notch Insensitive Ceramic Matrix Composite	C. Cady T.J. Mackin A.G. Evans
33.	Notch Sensitivity and Stress Redistribution in CMCs	T.J. Mackin T.E. Purcell M.Y. He A.G. Evans

EXECUTIVE SUMMARY

1. GENERAL STRATEGY

The overall program embraces property profiles, manufacturing, design and sensor development (Fig. 1) consistent with a concurrent engineering philosophy. For this purpose, the program has created networks with the other composites activities. *Manufacturing* research on MMCs is strongly coupled with the 3M Model Factory and with the DARPA consolidation team. Major links with Corning and SEP are being established for CMC manufacturing. *Design Team* activities are coordinated by exchange visits, in February/March, to Pratt and Whitney, General Electric, McDonnell Douglas and Corning. Other visits and exchanges are being discussed. These visits serve both as a critique of the research plan and as a means of disseminating the knowledge acquired in 1992.

The program strategy concerned with design attempts to provide a balance of effort between *properties* and *design* by having studies of mechanisms and property profiles, which intersect with a focused activity devoted to design problems (Fig. 2). The latter includes two foci, one on MMCs and one on CMCs. Each focus reflects differences in the property emphases required for design. The intersections with the mechanism studies ensure that commonalties in behavior continue to be identified, and also facilitate the efficient transfer of models between MMCs and CMCs.

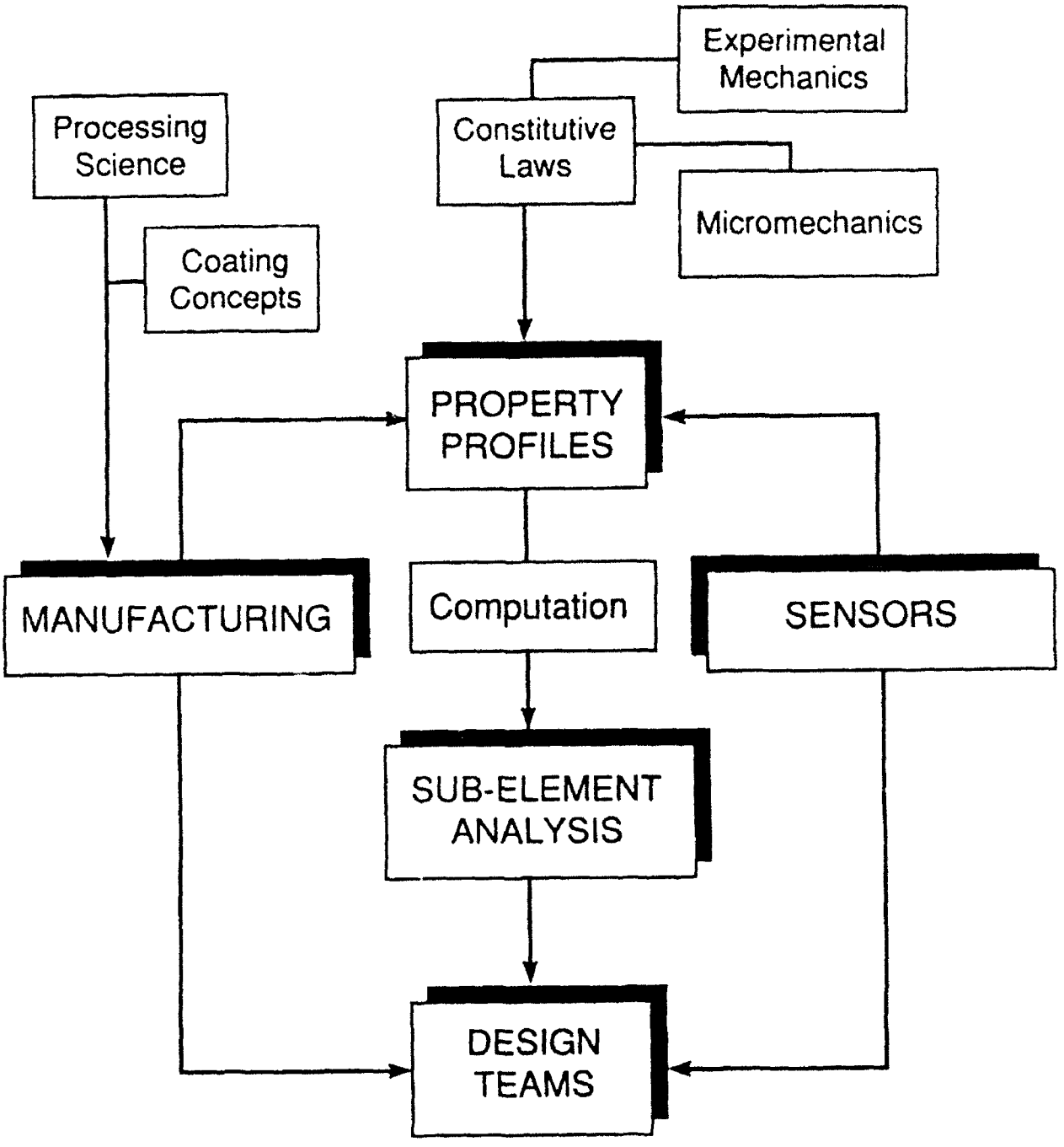

Fig. 1 The Concurrent Engineering Approach

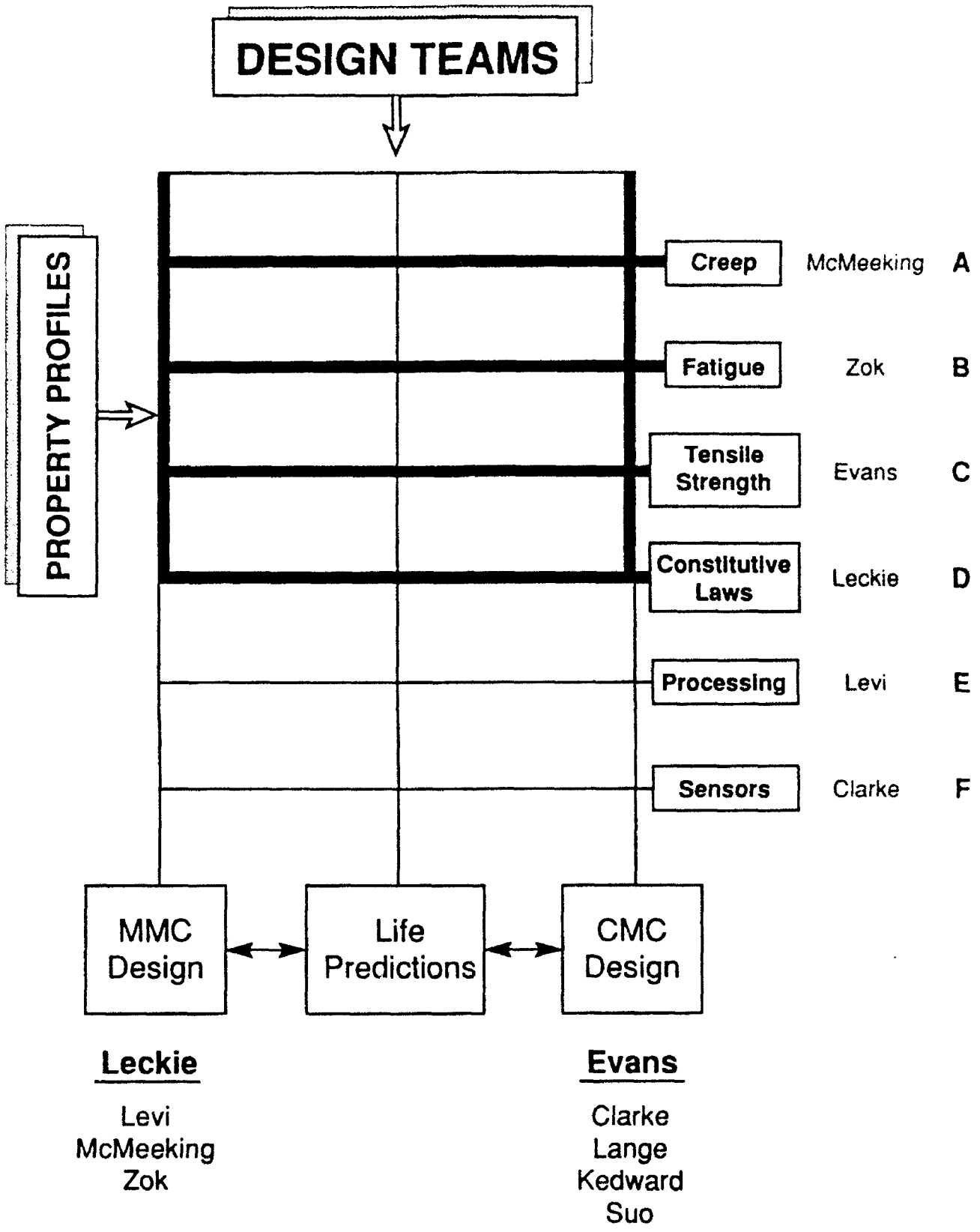

Fig. 2

Matrix Structure of Program

2. PROPERTY PROFILES

Each research activity concerned with properties begins with experiments that identify the principal property-controlling phenomena. Models are then developed that relate the physical response to constituent properties. These models, when validated, provide the constitutive laws required for calculating stress redistribution, failure and damage progression. They also provide a solid physics and mechanics understanding, which can be used to judge the effectiveness of the simplified procedures needed for design purposes.

2.1 Fatigue

Studies of the propagation of dominant mode I fatigue cracks from notches in MMCs, including the role of fiber bridging and fiber failure, have been comprehensively addressed (Zok, McMeeking). Software programs that include these effects have been developed. These are being transferred to Pratt and Whitney and KAMAN Sciences. The effects of thermal cycling on crack growth in MMCs have also been modelled (McMeeking). The results highlight the opposing effects of cycling on matrix crack growth and fiber failure (the fatigue threshold), when thermal cycles are superposed onto load cycles. Notably, matrix crack growth is enhanced by out-of-phase thermomechanical cycling, but fiber failure is suppressed (and vice versa for in-phase cycling). Experimental studies that examine these predictions are planned (Zok).

Studies have also been conducted on systems that exhibit *multiple* matrix cracking (Zok). The tensile stress-strain behavior of composites containing such cracks is analogous to the behavior of unidirectional CMCs

under monotonic tensile loading. As a result, models developed to describe the tensile response of the CMCs have found utility in describing the MMCs. However, two important differences in the two classes of composite have been identified and are presently being addressed. The first deals with the nature of the crack patterns. In the CMCs, the cracks are more or less uniformly spaced and generally span across the entire composite section. In contrast, the MMCs exhibit a broader distribution of crack sizes, many of which are short compared with the specimen dimensions. Methodologies for measurement and interpretation of crack densities in MMCs are being developed. The second problem deals with degradation in the interfacial sliding properties with cyclic sliding in the MMCs. Such degradation is presently being studied using fiber push-out tests in fatigued specimens.

Thermal fatigue studies on MMCs subject to transverse loading have been performed and have established the conditions that allow shakedown (Leckie). The shakedown range is found to be strongly influenced by the extent of matrix creep, which defines a temperature limitation on the use of the material. The eventual outcome of this activity would be the specification of parameters that ensure shakedown and avoid ratcheting.

The next challenge for MMCs concern the quantification of transitions in fatigue behavior, especially those found at higher temperatures. These include multiple matrix cracking and shear band formation. Experimental studies are in progress which will be used to establish a mechanism map. The map, when developed, would explicitly identify the transitions (Zok). The analogous behavior found in CMCs will facilitate this development. Other high temperature phenomena to be explored include changes in the interfacial sliding behavior due to both relaxations in the thermal residual stresses and the growth of reaction products near the fiber-matrix interface.

Fatigue damage studies on 2-D CMCs will focus on interface and fiber degradation phenomena, especially at elevated temperatures (Evans, Zok). Cyclic loading into the stress range at which matrix cracks exist is known to modify the interface sliding stress and may weaken the fibers. These degradation effects can be distinguished, because they change the hysteresis loop and reduce the UTS, respectively. Experiments that probe these material responses are planned. In addition, models that include the influence of cyclic fiber failure and pull-out on fatigue damage will be developed (Suo).

2.2 Matrix Cracking

Models of the plastic strain and modulus changes caused by various modes of matrix cracking have been developed. These solutions have provided a rationale for experimental studies on the tensile and shear behavior of CMCs and on the fatigue of MMCs (Hutchinson, Zok, Evans, Suo, Budiansky, McMeeking). The information has been used in two distinct ways. (i) Test methodologies have been devised that relate stress/displacement measurements to constituent properties (Table I). (ii) Stress/strain curves and matrix crack evolution have been simulated for specific combinations of constituent properties.

The development of the procedures and their implementation are still in progress. Independent solutions have been established for matrix cracks in 0° plies and 90° plies upon tensile loading. The former has been experimentally validated on 1-D materials (SiC/SiC and SiC/CAS). Measurements of plastic strain, hysteresis loops and crack densities have been checked a inst the models for consistency.

TABLE I

Relevant Constituent Properties and Measurement Methods

CONSTITUENT PROPERTY	MEASUREMENT
Sliding Stress, τ	• Pull-Out Length, $\bar{h}$ • Saturation Crack Spacing, $\bar{l}_s$ • Hysteresis Loop, $\delta\varepsilon_{1/2}$ • Unloading Modulus, $\bar{E}_L$
Characteristic Strength, S_c, m	• Fracture Mirrors • Ultimate Strength, S
Misfit Strain, Ω (q)	• Bilayer Distortion • Permanent Strain, ε_p • Residual Crack Opening
Matrix Fracture Energy, Γ_m	• Monolithic Material • Saturation Crack Spacing, $\bar{l}_s$ • Matrix Cracking Stress, $\bar{\sigma}_{mc}$
Debond Energy, Γ_i	• Permanent Strain, ε_p • Residual Crack Opening

The next challenge is to couple the models together in order to simulate the evolution of matrix cracks in 2-D materials, subject to tensile loading (Hutchinson, Budiansky). Related effects on the ultimate tensile strength caused by stress concentrations in the fibers in the presence of matrix cracks, would also be evaluated. Experimental measurements of stress/strain behavior in 2-D CMCs, with concurrent observations of matrix crack evolution, would be used to guide and validate such models (Evans, Kedward).

2.3 Constitutive Equations

Constitutive equations provide the link between material behavior at the meso-scale and the performance of engineering components. The equations can be established from the results of uniaxial and transverse tensile tests together with in-plane shear loading. For a complete formulation, which describes accurately the growth of failure mechanisms and the conditions of failure at the meso-scale, it is also necessary to perform calculations which are valid at the micro-scale.

These procedures have been completed for metal-matrix composites (Jansson, Leckie), and the resulting constitutive equations are operational in the ABAQUS finite element code. The behavior of simple panels penetrated by circular holes have been studied and the results await comparison with experiments which are planned for the coming year. The constitutive equations are formulated in terms of state variables which include the hardening tensors and damage state variables which describe debonding at the interface and void growth in the matrix. The format is sufficiently general to allow the inclusion of failure mechanisms such as environmental attack as the appropriate understanding is available. For

example, the effect of matrix and fiber creep mechanisms (Aravas) have also been introduced into ABAQUS, and it is proposed to extend the creep conditions to include the effects of variable loading and temperature.

A similar approach has been taken towards the modulus of CMCs. In this case, efforts have been made to include the influence of matrix cracking, in-plane shearing and fiber breakage. The latter consideration is based on the global load sharing model (Hayhurst). The equations are also available in ABAQUS. At present, matrix cracking is introduced by assuming a matrix stress accompanied by an increase of strain. However, based on the more recent understanding of the growth of matrix cracks (above) it is intended to introduce these mechanisms into the constitutive equations for CMCs.

2.4 Creep

The emphases of the creep investigations have been on the anisotropic characteristics of unidirectional layers in which the fibers are elastic, but the matrix creeps. Experiments and models of the longitudinal creep properties of such materials have been initiated (McMeeking, Leckie, Evans, Zok, Aravas). The critical issues in this orientation concern the incidence of fiber failure and the subsequent sliding response of the interface. A modelling effort has established an approach that allows the stochastic evolution of fiber failure to occur as stress is transferred onto the fibers by matrix creep (McMeeking). This approach leads to creep rates with a large power law exponent. Various attempts are underway to incorporate the interface sliding initiated by fiber breaks and to introduce sliding into the creep rate formulation. Experiments being performed on unidirectional Ti matrix materials are examining the incidence of fiber failures on the creep

deformation (Evans, Leckie, Zok). These results will guide the modelling effort concerned with interface sliding effects. Insight will also be gained about fiber failure stochastics during creep, especially differences from room temperature behavior.

The transverse creep properties are expected to have direct analogies with composite deformation for a power law hardening matrix (Section 2.3). In particular, the same effects of debonding and matrix damages arise and can be incorporated in an equivalent manner (Leckie, Aravas). Testing is being performed on Ti MMCs and on SiC/CAS to validate the models.

Experiments on Ti-matrix 0°/90° cross-ply composites are planned. Creep models appropriate to cross-ply materials will be developed by combining those corresponding to the unidirectional materials in the longitudinal and transverse orientations, using a rule-of-mixtures approach. Such an approach is expected to be adequate for loadings in which the principal stresses coincide with the fiber axes. Alternate approaches will be sought to describe the material response in other orientations.

Some CMCs contain fibers that creep more extensively than the matrix. This creep deformation has been found to elevate the stress in the matrix and cause time dependent evolution of matrix cracks. This coupled process results in continuous creep deformation with relatively low creep ductility. Experiments on such materials are continuing (Evans, Leckie) and a modelling effort will be initiated (Suo). The models would include load transfer into the matrix by creeping fibers, with sliding interfaces, leading to enhanced matrix cracking.

2.5 Tensile Strength

The ultimate strength (UTS) of both CMCs and MMCs (as well as fatigue and creep thresholds) is dominated by fiber failure. With the global load sharing (GLS) concept of fiber failure now well established, the recent emphasis has been on defining the constituent properties needed to ensure GLS. The approach has been to perform local load sharing calculations and then compare experimental UTS data with the GLS predictions (Curtin, Evans, Leckie). The situation is unresolved. However, initial calculations on CMCs (Curtin) and MMCs (Evans) have provided some insight. Two key remaining issues concern the magnitude of the stress concentration in intact fibers caused by matrix cracks and the role of fiber pull-out in alleviating those stresses. Calculations of these effects are planned (Budiansky, Suo).

Degradation of the fiber strength upon either high temperature (creep) testing, atmospheric exposure, or fatigue are other topics of interest. Rupture testing performed under these conditions will be assessed in terms of degradation in fiber properties.

3. DESIGN TEAMS

3.1 The Approach

The overall philosophy of the design effort is to eventually combine *material models*, with a *materials selector*, and a *data base*, within a unified software package (Prinz). One example of a composites data base is that developed for MMCs by KAMAN Sciences, which forms the basis for a potential collaboration. The materials selector has already been developed

for monolithic materials (Ashby) and is available for purchase. This selector requires expansion to incorporate phenomena that have special significance for high temperature composites, including creep and thermal fatigue. These new features will be developed and included in the advanced selector software (Ashby).

The modelling approach is illustrated in Table II. Failure mechanisms and their effect on material behavior have been introduced into constitutive equations. The stress, strain and damage fields which develop in components during the cycles of loading and temperature can then be computed. Experiments shall be performed on simple components such as holes in plates, and comparison made with the computational predictions. Since constitutive equations are modeled using the results of coupon tests, it is likely that additional failure modes shall come to light during component testing. These mechanisms shall be studied and the appropriate mechanics developed so that their influence is correctly factored into the constitutive equations. In this way, increased confidence in the reliability of the constitutive equations can be established in a systematic way.

In practice, it is most probable that the constitutive equations are too complex for application at the creative level of the design process. It is then that simple but reliable procedures are of greater use. Some success has been achieved in this regard for MMCs subjected to cyclic mechanical and thermal loading (Jansson, Ponter, Leckie), as well as for strength calculations of CMC panels penetrated by holes (Suo) and the fatigue of MMCs (Zok, McMeeking). In all cases simplifications are introduced after a complete and reliable analysis has been completed which provides a standard against which the effects of simplification can be assessed.

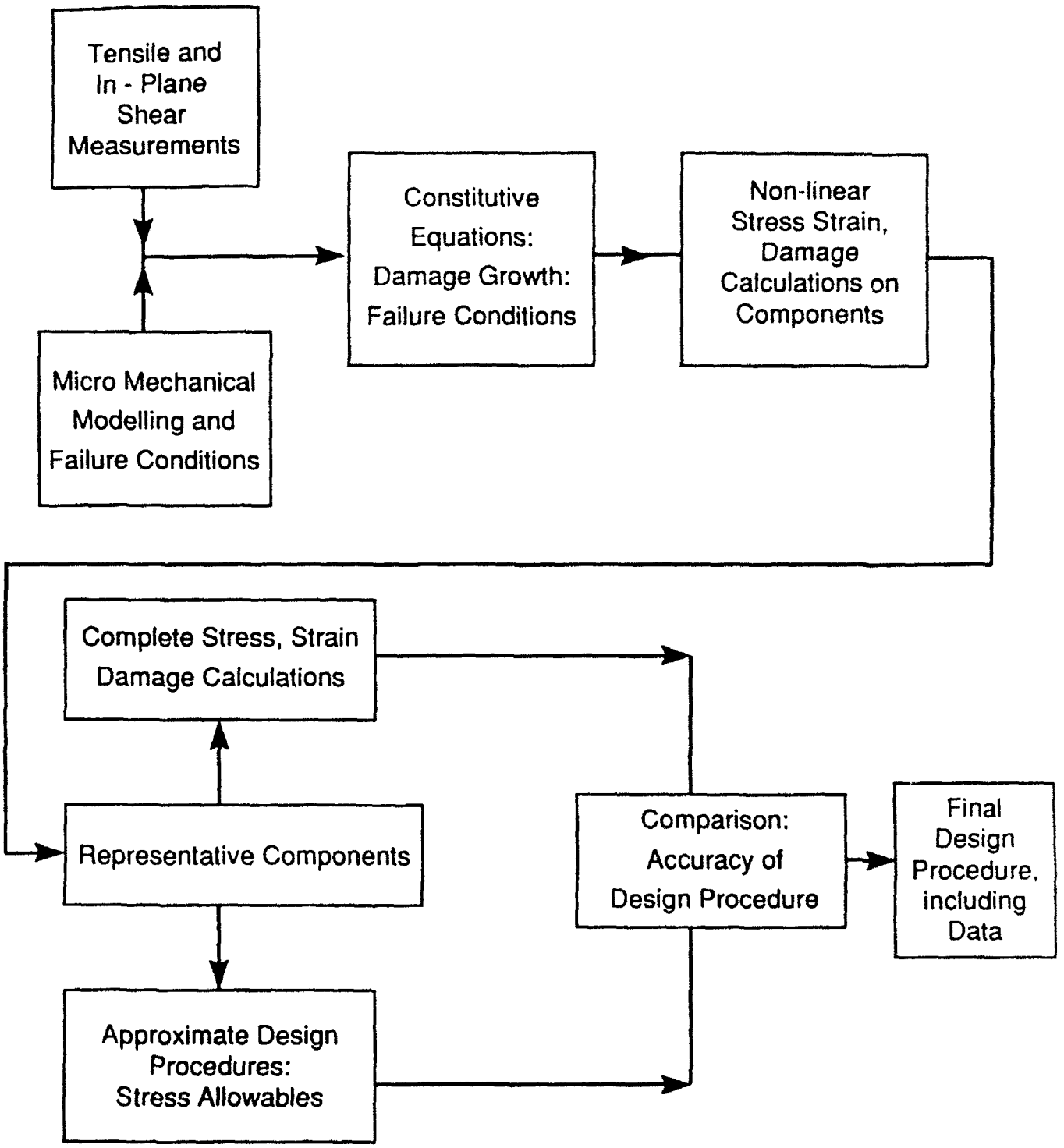

Table II

The Modelling Approach

3.2 Ceramic Matrix Composite Design

The design effort on CMCs will have its major focus on pin-loaded holes used for attachments (Fig. 3). A smaller activity, expected to expand in 1994, will address delamination cracking. The hole design includes several related topics. Each topic is concerned with aspects of constitutive law development (Table III), highlighted during the study group. Combined experimental and modelling efforts on the *tensile properties* of CMCs have established that the plastic strains are dominated by matrix cracks in the 0° plies. The matrix cracking models developed in the program demonstrate that these strains are governed by four independent constituent properties [(Table I) τ, Γ_i, Ω and Γ_m] which combine and interrelate through five non-dimensional parameters (Table IV). This modelling background suggests a concept for using model-based knowledge to develop constitutive laws. The following steps are involved (Table III). (i) A model-based methodology for inferring the constituent properties of unidirectional CMCs from macroscopic stress/strain behavior has been devised and is being experimentally tested on a range of materials (Evans). (ii) Upon validation, the models would allow stress/strain curves to be simulated (Hutchinson). This capability would facilitate a sensitivity study to be performed, in order to determine the minimum number of independent parameters that adequately represent the constitutive law. A strictly empirical law would require 3 parameters (yield strength, hardening rate and unloading modulus). Consequently, the objective might be to seek 3 combinations of the 4 constituent properties. (iii) Experiments would be performed and models developed that establish the matrix cracking sequence in 2-D materials (Hutchinson, Evans, Kedward). These would be conducted on

DESIGN PROBLEM IN CMC's

Design of Holes in Nozzles / Combustors

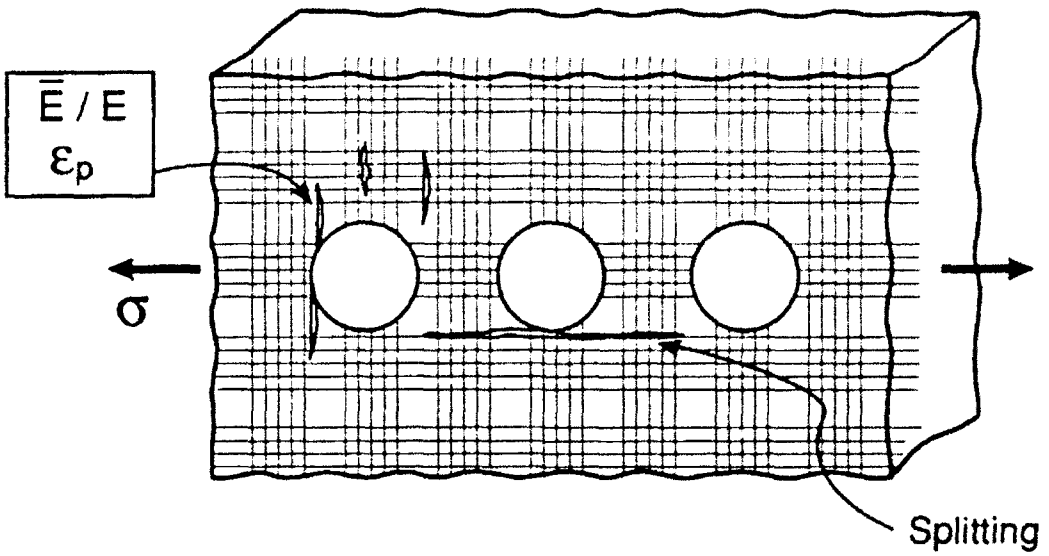

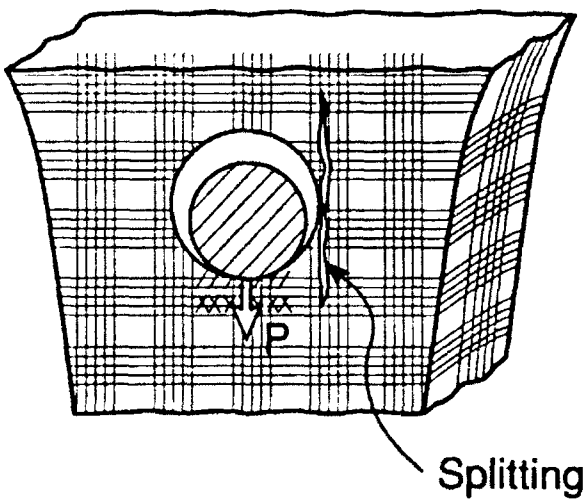

Issues

Tensile Rupture
Crushing
Splitting

Design Variables

Hole Size
Hole Spacing
Fiber Architecture
Material Choice
New Concepts

Fig. 3

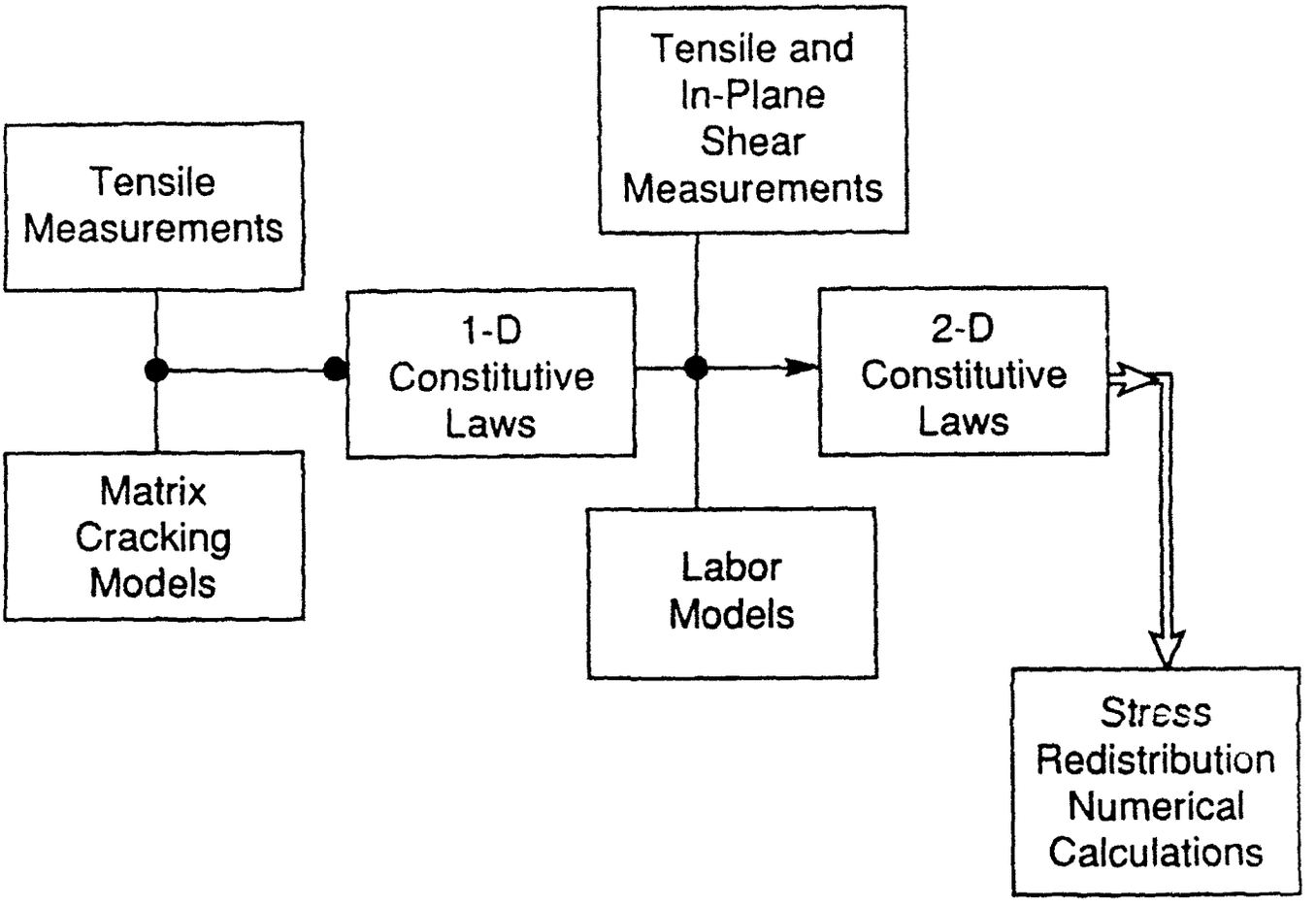

Table III

Design Strategy for CMCs

TABLE IV

Summary of Non-Dimensional Coefficients

$\mathcal{A}_b = [f/(1-f)]^2 \left(E_f E_L / E_m^2\right)(a_o \tau / R S_u)$, Flaw Index for Bridging

$\mathcal{A}_p = \left(a_o / \bar{h}\right)\left(S_p / E_L\right)$, Flaw Index for Pull-Out

$\mathcal{D} = \Gamma_m (1-f)^2 E_f E_m / f \tau^2 E_L R$, Crack Spacing Index

$\mathcal{H} = b_2 (1-a_1 f)^2 R \bar{\sigma}_p^2 / 4 \bar{d} \tau E_m f^2$, Hysteresis Index

$I = \bar{\sigma}_p / E_m \Omega$, Misfit Index

$\mathcal{M} = 6\tau \Gamma_m f^2 E_f / (1-f) E_m^2 R E_L$, Matrix Cracking Index

$Q = E_p f \Omega / E_L (1-\nu)$, Residual Stress Index

$\Delta_1 = (1/c_1 \Omega)\sqrt{\Gamma_i / E_m R}$, Debond Index

CMCs with a range of different constituent properties and fiber architectures. The plastic strains would be related to constituent properties by adapting the 1-D models.

The in-plane shear behavior will be characterized by performing experiments and developing models of matrix cracking that govern the plastic *shear strain* in 2-D CMC (Evans, Hutchinson, Bao). The information will be used to establish the constitutive laws for in-plane shear, as well as interlaminar shear. For continuity of interpolation between tension and shear, the shear models will include the same constituent properties as those used to represent the tensile behavior.

The model-based constitutive laws, based on matrix damage, will be built into a CDM (continuum damage mechanics) formulation, compatible with finite element codes (Hayhurst). Computations will be performed to explore *stress redistribution* around holes and other strain concentration sites. The calculations will establish visualizations of stress evolution that can be compared with experimental measurements performed using the SPATE method, as well as by Moiré interferometry (Mackin, Evans). These experiments will be on specimens with notches and holes, loaded in tension. The comparisons between the measured and calculated stress patterns will represent the ultimate validation of the constitutive law. The composite codes, when validated, will be made available to industry.

Some preliminary experimental work will be performed on pin-loaded holes. Damage patterns will be monitored and stress redistribution effects assessed using SPATE (Kedward, Evans, Mackin). These experiments will be conducted on SiC/CAS and SiC/C. The results will provide the focus for future CDM computations, based on the constitutive law for the material.

Smaller scale activities will involve basic aspects of stress redistribution around holes caused by fatigue and creep *damage*, using the experience gained from the matrix cracking studies. Some experimental measurements of these effects will be performed using SPATE (Zok, Evans).

Some delamination crack growth measurements and calculations are also envisaged (Ashby, Kedward, Hutchinson). Cantilever beam and C-specimens will be used for this purpose (Fig. 4). During such tests, crack growth, multiple cracking and stiffness changes will be addressed. Models of bridging by inclined fibers will be developed (Ashby) and used for interpretation.

3.3 Metal Matrix Composite Design

The 3D constitutive equations for MMCs are now available for use in the ABAQUS finite element code, and the immediate task is to use these equations to predict the behavior of representative components (Leckie). One such system is a ring-type structure which is being studied together with Pratt and Whitney. Clearly no experimental verification is possible with a component of this scale, but the experience of Pratt and Whitney shall provide invaluable input on the effectiveness of the calculations. A component sufficiently simple to be tested is the panel penetrated by holes. The holes shall be both unloaded and loaded (Jansson), and it is expected to include the effects of cyclic mechanical and thermal loading.

It is proposed to develop simplified procedures which are based on shakedown procedures (Jansson, Leckie). Demonstrations have already been made of the effectiveness of the Gohfeld method (which uses only simple calculations) in representing the behavior of MMCs subjected to cyclic thermal loading.

TRANSVERSE CRACKING OF CMC

CONVENTIONAL COUPON TESTS

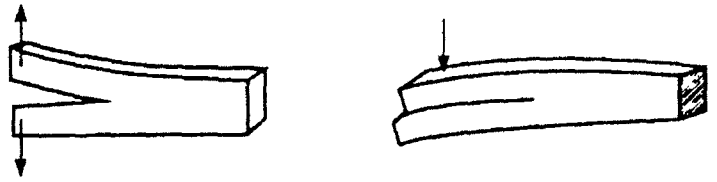

- Fiber Bridging Problem ($\mathcal{G} >> \Gamma_T$)

IMPROVED TESTS

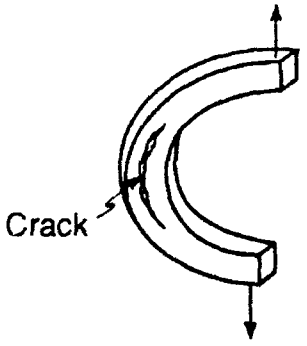

da/dN vs. $\mathcal{G}$

SUB - ELEMENT TEST

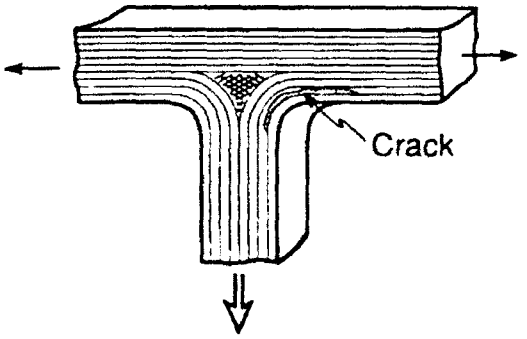

DESIGN PROBLEM

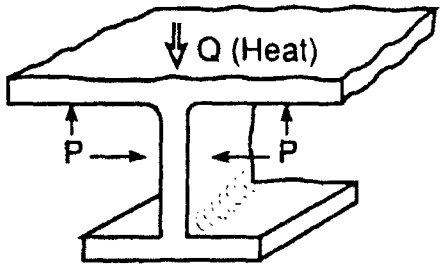

- Thermal Conductivity
- Fiber Architecture
- Matrix Toughness

Fig. 4

During the complex histories of stress and temperature, it is known that the matrix-fiber interface properties change. Fatigue loading (Zok) is know to decrease the interface sliding stress. Transverse creep appears to cause matrix-fiber debonding (Jansson), which might result in loss of the ability to transfer stress between matrix and fiber. It is intended to study this effect of transverse creep on the integrity of the longitudinal strength of the material by performing tests on panels which shall allow rotation of the stress fields. A good understanding now exists of the fatigue properties of MMCs (Zok). It is intended to extend the ideas developed from earlier theoretical studies (McMeeking, Evans) to include cyclic thermal effects and experimental programs on holes in plates.

4. MANUFACTURING

The activities in processing and manufacturing have had the following foci:

- Matrix development to address specific requirements identified by the design problems, particularly first matrix cracking in CMCs (Lange) and creep strengthening in MMC/IMCs (Levi, Lucas).
- Hybrid architectures which offer possible solutions to environmental degradation and thermal shock problems (Evans, Lange, Leckie, Levi, Yang, Zok).
- Software development that predicts and controls fiber damage and interface properties during densification (Wadley).
- Processing techniques to generate model MMC sub-elements (Leckie, Levi, Yang).

4.1 Metal Matrix Composites

Work on MMC matrix development has focused on dispersion strengthening approaches to increase the *transverse* tensile and creep strength of 1-D and 2-D fiber architectures. The initial work has emphasized a model system, Cu/Al_2O_3, wherein dispersoids are produced by internal oxidation of a dilute Cu-Al alloy deposited by PVD onto sapphire fibers. These are subsequently consolidated by HIP'ing. Specimens with fiber volume fractions of $0.3 \leq f \leq 0.5$ and 2-3% γ-Al_2O_3 dispersoids (~ 20 nm in size) have been produced in this manner and will be tested to assess their transverse creep behavior. The new emphasis will be on higher temperature matrices based on TiB dispersoids in Ti-(Cr/Mo)-B alloys (Levi). Initial solidification studies have demonstrated the potential of these materials as *in-situ* composites. Efforts are underway to develop sputtering capabilities to implement this concept.

Fiber damage during densification of composite prepregs generated by plasma-spray (GE) and PVD (3M) have also been emphasized (Wadley). Interdiffusion studies coupled with push-out tests have been used to study the evolution of reaction layers in Ti/SiC composites and their effect on the relevant interfacial properties as a function of process parameters. Additional efforts under other programs have focused on developing predictive models for fiber breakage during densification. The interdiffusion and breakage models are being incorporated into software that predicts pressure-temperature paths, which simultaneously minimize fiber damage and control the interface properties.

The feasibility of producing MMC sub-elements consisting of fiber reinforced rings (1-D) and tubes (2-D) has been demonstrated by using

liquid metal infiltration of Al alloy matrices (Levi). These are presently undergoing testing in combined tension/torsion modes. Future efforts will be directed toward extending the technique to other shapes (e.g., plates with reinforced holes), as well as devising methods to modify the (currently strong) interfaces. The identification of methods that provide the appropriate interfacial debonding/sliding characteristics should enable the use of these composites as *model systems* for higher temperature MMCs, such as Ti.

4.2 Intermetallic Matrix Composites

The focus of the IMC processing activities has been on the synthesis of $MoSi_2/\beta$-SiC_p composites by solidification processing. These materials are of interest as potential matrices for fiber composites. Significant progress was made in the elucidation of the relevant Mo-Si-C phase equilibria, the growth mechanisms of SiC from the melt and their impact on reinforcement morphology, as well as the orientation relationships between matrix and reinforcements, and the interfacial structure. An amorphous C layer, ≤5 nm thick, was found at the $MoSi_2$/SiC interface in the as cast condition, and persisted after 12 h heat treatments at 1500°C. This interfacial layer has been reproduced in α-SiC_p/($MoSi_2$ + C) composites produced by powder metallurgy techniques and was found to exhibit promising debonding and pull-out behavior during fracture (Levi). Future efforts are aimed at implementing this *in-situ coating* concept in α-SiC fiber composites.

4.3 Ceramic Matrix Composites

The processing issues for creating CMCs with high *matrix strength* continue to be explored (Lange, Evans). The basic concept is to create a strong ceramic matrix framework within a fiber preform, by means of slurry

infiltration followed by heat treatment. This strong framework would then be infiltrated by a polymer precursor and pyrolyzed to further densify the matrix. It has been demonstrated that strong matrices of Si_3N_4 can be produced using this approach (Lange). Further work will address relationships between matrix strength and microstructure (Lange, Evans).

4.4 Hybrids

These activities cover materials consisting of thin monolithic ceramic layers alternating with layers containing high strength fibers bonded by a glass or metallic binder. The primary motivation behind this concept is the potential for manufacturing shapes that have a high resistance to environmental degradation and also have good thermal shock resistance. The concept has been demonstrated using alumina plates and graphite reinforced polymer prepregs (Lange). The availability of glass-ceramic bonded SiC_f prepregs and tape-cast SiC plates has facilitated the extension of this technique to high temperature systems (Lange). Future assessment will address new crack control concepts. These concepts would prevent damage from propagating into the fiber reinforced layers, especially upon thermal loading (Zok, Lange). If successful, this concept would allow the development of hybrid CMCs which impart resistance to environmental degradation, as well as high thermal strain tolerance.

Preliminary work has been performed on laminates consisting of alumina plates and sapphire-fiber reinforced Cu monotapes (Levi). The latter are produced by deposition of Cu on individual fibers which are subsequently aligned and bonded by hot pressing between two Cu foils. After suitable surface preparation, the alumina/monotape assemblies are

bonded by hot pressing. Future work is aimed at implementing the concept with Ni based alloys.

5. SENSORS

The principal challenge being addressed is the non-destructive and non-evasive measurement of stresses in composites (Clarke, Wadley). The motivation is to make detailed measurements of stresses in components for incorporation into evolving design models, as well as validation of the stress distributions computed by finite element methods. A major emphasis has been placed on measuring the residual stresses in sapphire fibers in various matrices, using the recently developed technique of optical fluorescence spectroscopy. These measurements have provided data on the distribution of residual thermal stresses in the fiber reinforcement, as a function of depth below the surface. This approach will be extended, in conjunction with finite element modelling (Hutchinson), to measure the stresses during the process of fiber pull-out from a variety of metal and ceramic matrices. Initial experiments indicate that such in-situ measurements are feasible.

The technique will also be applied to the measurement of the stresses in sapphire fibers located in the vicinity of pin-loaded holes in order to understand the manner in which the stresses redistribute during loading. It is anticipated that this measurement will provide information about the detailed fiber loadings and also about the stresses that cause debonding of the fibers from the matrix. Moreover, in support of the activities on thermal ratcheting, the redistribution of stresses with thermal cycling will be established. This will be accomplished by using the fluorescence technique as well as Moiré interferometry, based on lithographically defined features.

MATERIALS

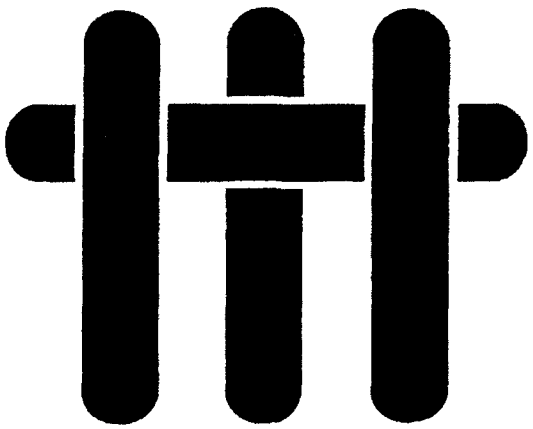

A METHODOLOGY FOR RELATING THE TENSILE CONSTITUTIVE BEHAVIOR OF CERAMIC MATRIX COMPOSITES TO CONSTITUENT PROPERTIES

by

A.G. Evans, J.M. Domergue and E. Vagaggini
Materials Department
College of Engineering
University of California
Santa Barbara, California 93106–5050

KJS 3/16/93

NOMENCLATURE

a_i parameters found in the paper by Hutchinson and Jensen[21]
a_o length of unbridged matrix crack
b_i parameters found in the paper by Hutchinson and Jensen[21]
c_i parameters found in the paper by Hutchinson and Jensen[21]
f fiber volume fraction
f_ℓ fiber volume fraction in loading direction
$\bar{h}$ mean fiber pull-out length
ℓ_p plastic zone size
$\bar{\ell}$ mean matrix crack spacing
$\bar{\ell}_s$ mean saturation crack spacing
m shape parameter for fiber strength distribution
q residual stress in matrix in axial orientation
t ply thickness
2w plate width
E Young's modulus of composite
E_* Young's modulus of material with matrix cracks
E_f Young's modulus of fiber
E_L ply modulus in longitudinal orientation
E_m Young's modulus of matrix
E_L ply modulus in longitudinal orientation
E_s secant modulus
E_T ply modulus in transverse orientation
$\bar{E}_L$ unloading modulus
$\bar{E}_t$ tangent modulus
L mean crack spacing in 90° plies
L_g gauge length
L_o reference length
R fiber radius
S tensile strength
S_c characteristic fiber strength
S_o scale factor for fiber strength
S_p pull-out 'strength'
S_u UTS subject to global load sharing
S_* tensile strength in presence of a flaw or notch

T shear strength

α compliance coefficient
β residual stress coefficient
γ shear strain
δ displacement
δ_c characteristic length
$\delta\varepsilon$ hysteresis loop width
ε strain
ε_e elastic strain
ε_p permanent strain
ε^* contribution to permanent strain caused by matrix cracks
ν Poisson's ratio (assumed to be the same for fiber and matrix)
λ pull-out coefficient
σ stress
σ_R residual stress in 0/90 material along fiber axis
σ_τ lower bound stress for tunnel cracking
$\bar{\sigma}_i$ debond stress
$\bar{\sigma}_{mc}$ matrix cracking stress
$\bar{\sigma}_o$ stress acting on 0° plies in a 2-D material
$\bar{\sigma}_p$ peak stress
$\bar{\sigma}_s$ saturation stress
$\bar{\sigma}_T$ misfit stress
τ interface sliding resistance
χ matrix cracking coefficient
Γ fracture energy
Γ_i interface debond energy
Γ_o dissipation associated with traction law
Γ_m matrix fracture energy
Ω misfit strain

ABSTRACT

A methodology for the straightforward and consistent evaluation of the constituent properties of CMCs is summarized, based on analyses from the literature. The results provide a constitutive law capable of simulating the stress/strain behavior of these materials. The approach is illustrated using data for two CMCs: SiC/CAS and SiC/SiC. The constituent properties are also used as input to mechanics procedures that characterize stress redistribution and predict the effect of strain concentrations on macroscopic performance.

1. INTRODUCTION

For the structural application of ceramic matrix composites (CMCs), it is necessary to have a methodology that prescribes the influence of strain concentrations, such as notches, on tensile properties. Ideally, this methodology should have explicit connections to the constituent properties (fibers, matrix, interface), such that efficient design procedures can be implemented. This article contributes toward this objective by surveying the tensile properties of CMCs and the mechanisms that govern their properties, in a manner that leads to a methodology for relating macroscopic behavior to constituent properties. A mechanics approach that addresses the influence of strain concentrations is then summarized and compared with preliminary experimental results.

CMCs usually have substantially lower notch sensitivity than monolithic brittle materials[1-4] and, in several cases, exhibit notch insensitive behavior.[5-7] This desirable characteristic of CMCs arises because the material may *redistribute stresses* around strain concentration sites. There are two fundamental mechanisms of stress redistribution:[8-12] (i) distributed *matrix cracking* and (ii) fiber failure involving *pull-out*. An understanding of these effects provides a basis for devising a methodology to characterize and predict properties. In most CMCs, the Linear Elastic Fracture Mechanics (LEFM) methodology successfully devised for metals cannot be used,[2,8,12-14] because failure does not occur by the propagation of a dominant mode I crack. Alternative mechanics are needed, based on the actual mechanisms of failure. A more relevant mechanics is that based on the Large-Scale Bridging of matrix cracks by fibers[8,13-15] (LSBM). However, even LSBM is inadequate. It must be augmented by Continuum Damage Mechanics (CDM)[16] in order to establish a rigorous methodology.

The basic approach has the following features. An informed background needed for progress is provided by experimental results used in conjunction with models of

matrix cracking and fiber failure. The matrix cracking and fiber failure observations are conducted on 2-D materials in tension and shear. Large-Scale Bridging Mechanics are used to rationalize the observed damage mechanisms. The tensile properties measured in the presence of holes and notches, when combined with damage observations, establish the mechanics approach needed to rationalize the influence of strain concentrations.

The strategy is facilitated by devising *mechanism maps* that use *non-dimensional parameters*, which combine the basic constituent properties listed on Table I in mechanistically relevant ways. A list of these parameters is presented in Table II. The most successful methodology will be that using the *minimum* number of constituent properties needed to represent the constitutive behavior. At mechanism transitions, the mechanics needed to characterize composite behavior often change.[12,17]

2. BASIC RESULTS FOR 1-D MATERIALS

2.1 Phenomenology

Models for a range of damage phenomena found in 1-D CMCs, have been established and validated by experiment.[18-40] These models provide the basis upon which the behavior of 2-D and 3-D CMCs can be addressed. The underlying phenomenology involves matrix cracking and fiber failure. *Matrix cracks* form first and interact with predominantly intact fibers,[2,18-24] subject to interfaces that debond, at energy Γ_i, and then slide at a constant shear stress, τ .‡ This process commences at a lower bound stress, $\bar{\sigma}_{mc}$. The crack density increases with increase in stress above $\bar{\sigma}_{mc}$ and may eventually attain a saturation spacing, $\bar{\ell}_s$. The details of crack evolution are governed by the distribution of matrix flaws. The matrix cracks reduce the elastic

‡ More rigorous debonding and sliding behaviors have been analyzed,[21] but have not yet been found necessary for the derivation of useful constitutive laws.

modulus, $\bar{E}$, cause hysteresis in the presence of sliding interfaces, and also induce a permanent strain, ε_p. These matrix cracking effects are schematically illustrated in Fig. 1. The intent is to relate these quantities to the constituent properties (Table I) through non-dimensional parameters (Table II).

The matrix cracks may enhance the stress on the fibers and encourage fiber failure.[8,15] However, when a fiber fails, the stress does not reduce to zero everywhere along that fiber. Load transfer can still occur through the sliding stress, τ, even though the matrix has many cracks.[25-27] As a result, the ultimate tensile strength (UTS) may exceed the value expected for a 'dry bundle' (fibers with no matrix). Two bounds appear to be involved. When failed fibers and matrix cracks do not induce a significant *stress concentration* within *intact* fibers, global load sharing (GLS) applies.[25] Then, the effective gauge length relevant to fiber failure is governed by the load transfer length. Consequently, the UTS becomes independent of the actual gauge length. Conversely, when an unbridged segment of matrix crack exists (because of processing flaws, etc.), the stress concentration induced within the fibers reduces the UTS.[8,15] In this case, fiber pull-out appears to control the UTS.[41] Constituent properties that lead to this transition in behavior will be discussed below.

2.2 Matrix Cracks

A summary of the matrix cracking results is presented, which apply to materials with relatively small debond energies (SDE). More complete results are presented elsewhere.[21,24] *Long* matrix cracks interacting with fibers are subject to a steady-state condition, which leads to a *lower bound* cracking stress, given by[2,18,19]

$$\frac{\bar{\sigma}_{mc}}{E_L} = \left[\frac{6\tau\Gamma_m f^2 E_f}{(1-f)E_m^2 R E_L}\right]^{1/3} - q/E_m \qquad (1a)$$

where q is the residual axial stress in the matrix, which is related to the misfit strain, Ω^*, by;[19]

$$q/E_m = \beta\left[E_f/E_L(1-\nu)\right]f\Omega \tag{1b}$$

with $\beta \approx 1$. The first important non-dimensional relationship is thus (Table II),

$$\bar{\sigma}_{mc}/E_L = M^{2/3} - \beta Q \tag{1c}$$

As multiple matrix cracking develops, the slip zones from neighboring cracks overlap and produce a *shielding* effect.[20,22] When the shielding proceeds to completion, a *saturation* crack density results. This occurs at stress $\bar{\sigma}_s$, with an associated spacing, $\bar{\ell}_s$, given by[20]

$$\bar{\ell}_s/R = \chi\left[\Gamma_m(1-f)^2 E_f E_m/f\tau^2 E_L R\right]^{1/3} \tag{2a}$$

The coefficient χ depends on crack evolution: periodic, random, etc. Recent estimates[22] indicate that, $\chi \approx 1.6$. The second important non-dimensional formula is thus (Table II),

$$\bar{\ell}_s/R = \chi\mathcal{L}^{2/3} \tag{2b}$$

The actual *evolution of matrix cracks* at stresses above σ_{mc} is governed by the size and spatial distribution of matrix flaws. If this distribution is known, the evolution can

---

* Ω may be related to the thermal expansion coefficients of fiber α_f and matrix α_m by , $\Omega = (\alpha_m - \alpha_f)\Delta T$, where ΔT is the cooling range, taken as a positive quantity. However, in some cases, there are additional contributions from phase transformation, 'intrinsic' stress, etc.

be simulated[20] (Fig. 2).‡ A simple formula that can be used to approximate crack evolution is[9]

$$\bar{\ell} \approx \bar{\ell}_s \frac{\left[\bar{\sigma}_s/\bar{\sigma}_{mc} - 1\right]}{\left[\bar{\sigma}/\bar{\sigma}_{mc} - 1\right]} \tag{3}$$

Direct application of Eqns. (1) to (3) requires that the elastic properties be known and, moreover, that the constituent properties (τ, Γ_m and Ω) be independently measured.[9,30] However, it would be more convenient if a methodology existed that related the constituent properties to *readily measured macroscopic features.* With this objective, a series of formulae have been derived from basic solutions for debonding and sliding at interfaces, as matrix cracks evolve.[21,24,31] Matrix cracks *increase* the elastic compliance. Numerical calculations indicate that the *unloading elastic modulus*, E^*, is given by[31]

$$E_L/E^* - 1 = \left(R/\bar{\ell}\right)\alpha\left[f, E_f/E_m\right] \tag{4}$$

where α is another non-dimensional function (Fig. 3). Initial unloading occurs with modulus, E^*. However, the displacements caused by reverse sliding soon dominate.[32,33] These lead to an effective unloading/reloading modulus, $\bar{E}_L$ and generate a hysteresis loop, width $\delta\varepsilon$. When the stress $\bar{\sigma}_p$ is below $\bar{\sigma}_s$, such that limited slip zone overlap occurs, the unloading modulus and the loop width (Fig. 1) are independent of the misfit strain, Ω, but relate to the sliding stress, τ. They are also independent of Γ_i, for SDE.[24,32] The unloading modulus is given by[23,24,31,32]

---

‡ In some cases, *small* matrix cracks can form at stresses below $\bar{\sigma}_{mc}$.[28,29] These occur either within matrix-rich regions or around processing flaws. However, the non-linear composite properties are usually dominated by fully-developed matrix cracks that form at stresses above $\bar{\sigma}_{mc}$ (Fig. 1).

$$E^{\cdot}/\bar{E}_L = 1 + \mathcal{H} E^{\cdot}/\bar{\sigma}_p \tag{5}$$

where $\mathcal{H}$ is the third important non-dimensional parameter (Table II), given by

$$\mathcal{H} = b_2(1 - a_1 f)^2 R \bar{\sigma}_p^2 / 4\bar{\ell}\tau E_m f^2 \tag{6}$$

The width of the hysterisis loop $\delta\varepsilon$ is[24,32]

$$\delta\varepsilon = 2\mathcal{H}\left(\bar{\sigma}/\bar{\sigma}_p\right)\left[1 - \bar{\sigma}/\bar{\sigma}_p\right] \tag{7a}$$

such that the loop width at half maximum, $\delta\varepsilon_{1/2}$ (at $\bar{\sigma} = \bar{\sigma}_p/2$), is

$$\delta\varepsilon_{1/2} = \mathcal{H}/2 \tag{7b}$$

The *permanent strain*, ε_p, is sensitive to the sliding stress and the misfit, as well as the debond energy. It is given by,[21,24,32]

$$\varepsilon_p = 2\mathcal{H}\left[1 - \Sigma_i\right]\left[1 - \Sigma_i + 2\Sigma_T\right] + \varepsilon^{\cdot} \tag{8}$$

where Σ_i and Σ_T are two non-dimensional parameters (Table II) that introduce the influence of the debond energy Γ_i and the misfit strain Ω, given by[21,24,32]

$$\begin{aligned} \Sigma_T &\equiv \frac{\bar{\sigma}_T}{\bar{\sigma}_p} = (c_2/c_1) E_m \Omega/\bar{\sigma}_p \\ \Sigma_i &\equiv \frac{\bar{\sigma}_i}{\bar{\sigma}_p} = (1/c_1)\sqrt{E_m \Gamma_i / R\bar{\sigma}_p^2} - \Sigma_T \end{aligned} \tag{9}$$

and ε^* is the extension associated with relief of the residual stress caused by matrix cracks, in the absence of interface sliding,[31]

$$\varepsilon^* = (E_m \Omega/E)\left[f a_2/(1 - a_1 f)\right]\left[E/E_* - 1\right] \tag{10}$$

The above results can be combined to give an expression for the secant modulus, $\bar{E}_s$.[24] The resulting constitutive law may be used to simulate stress/strain curves.[24] The results may also be used to evaluate τ, Γ_i and Ω, provided that $\bar{\ell}_s$ has been measured, as elaborated below.

At stresses above $\bar{\sigma}_s$, the behavior is less well-documented. It has generally been assumed that the tangent modulus $\bar{E}_t$ is that associated exclusively with the fibers,[18]

$$\bar{E}_t = f E_f \tag{11}$$

However, deviations from Eqn. (11) often arise.[22]

Finally, it is noted that certain matrices (especially oxides) are susceptible to stress corrosion cracking.[25] This phenomenon leads to time-dependent matrix cracking, which can occur at stresses below $\bar{\sigma}_{mc}$.

2.3 Fiber Failure

Several factors are important concerning fiber failures within a composite matrix. (i) Fibers begin to fail prior to the UTS.[25-27] At the UTS, the fraction of failed fibers within the characteristic length, δ_c, is sufficient that the remaining intact fibers are unable to support the load. (ii) The stochastic nature of fiber failure dictates that the fiber failure sites have a *spatial* distribution around the fracture plane. Consequently, a frictional *pull-out resistance* exists. This resistance allows the material to sustain load, beyond the UTS. The associated pull-out strength S_p is an important property of the

composite. (iii) When unbridged flaws exist in the material, the matrix cracks introduce stress concentrations within intact fibers. This effect may lead to a reduced UTS.[8,15]

The basic stochastics of fiber failure have identified two non-dimensional parameters: a characteristic strength[25,36]

$$S_c = S_o \left[\tau L_o / R S_o\right]^{\gamma_{(m+1)}} \tag{12a}$$

and a characteristic length

$$\delta_c = L_o \left[S_o R / \tau L_o\right]^{\gamma_{(m+1)}} \tag{12b}$$

related by

$$S_c = \tau \delta_c / R \tag{12c}$$

When multiple matrix cracking precedes composite failure, and when GLS applies, the UTS is gauge length independent at large lengths ($L_g \gtrsim \delta_c$). The UTS is given by[25]

$$S_u = f S_c F(m) \tag{13}$$

where

$$F(m) = \left[2/(m+2)\right]^{\gamma_{(m+1)}} \left[(m+1)/(m+2)\right]$$

At shorter gauge lengths ($L_g < \delta_c$), the UTS increases as L_g decreases[26] (Fig. 4).

In principle, it is possible for composite failure to be preceded by relatively few matrix cracks, with GLS still applicable. Then, because the average stress on the fibers is

lower, the UTS is predicted to be higher than S_u. In the limit wherein only *one* matrix crack has formed, the UTS (subject to GLS) is

$$S_u^* = f S_c G(m) \tag{14}$$

where

$$G(m) \approx \left[(5m+1)/5m\right]\exp\left[-1/(m+1)\right]$$

The spatial distribution of the fiber failures that occur upon loading results in fiber pull-out on the matrix fracture plane. The mean pull-out length, $\bar{h}$ (for $L_g > \delta_c$), has the non-dimensional form[25,36]

$$\bar{h}\tau/RS_c = \lambda(m) \tag{15}$$

There are two bounding solutions for the function λ (Fig. 5). Composite failure subject to *multiple matrix cracking* gives the *upper bound*. Failure in the presence of *a single crack* gives the *lower bound*.

Because of pull-out, the system has a *residual* strength, S_p, (Fig. 6a) given by

$$\begin{aligned} S_p &= 2\tau f \bar{h}/R \\ &\equiv 2 f S_c \lambda(m) \end{aligned} \tag{16}$$

The preceding results are applicable provided that there are no unbridged segments along the matrix crack. Unbridged regions concentrate the stress in the adjacent fibers and weaken the composite. The effect can be addressed using Large-

Scale Bridging Mechanics (LSBM). Simple linear scaling considerations require that the strength S^* depend on a non-dimensional *flaw index*[8,15] (Table II),

$$\mathcal{A} = a_o S^2/E_L \Gamma_o \tag{17}$$

where Γ_o is the area under the stress/displacement curve for the bridging fibers, S is the fully-bridged UTS and $2a_o$ is the length of the unbridged segment. The flaw index $\mathcal{A}$ must be specified for each bridging law, based on Γ_o. The functional dependence of strength S^* on $\mathcal{A}$ has been determined by numerical analysis for two limiting cases.[37] A *lower bound* arises in the presence of bridging without pull-out ($S = S_u$, $S_p = 0$), with flaw index[8,15] (Table II),

$$\mathcal{A}_b = 3\left[f/(1-f)\right]^2 \left(E_f E_L/E_m^2\right)\left(a_o \tau/RS\right) \tag{18a}$$

The dependence of the UTS on $\mathcal{A}_b$ is plotted on Fig. 6a. An *upper bound* obtains when the UTS is pull-out dominated ($S = S_p$), with flaw index[8,37,41] (Table II),

$$\mathcal{A}_p = 2\left(a_o/\bar{h}\right)\left(S_p/E_L\right) \tag{18b}$$

The degradation is plotted on Fig. 6b. The behavior between the bounds has not been well-established. It involves coupled bridging and pull-out. One result[37] (plotted on Fig. 6a) suggests that the lower bound is more relevant when $\mathcal{A}_b \lesssim 0.3$, whereas the upper bound is a reasonable approximation when $\mathcal{A}_b > 1.5$.

Experimental validation of the above results requires independent measurement of S_c, and m. Tests conducted on pristine fibers are *not relevant*, because fiber degradation usually occurs upon composite processing.[10,38,42] Two approaches have been used. One approach entails removal of the matrix, by dissolution,[1] which is only feasible if further

fiber degradation does not occur. The second approach involves *fracture mirror* measurements on failed fibers, after tensile testing of the composite.[10,38,39,42]

3. CHARACTERISTICS OF 2-D MATERIALS

3.1 Matrix Cracking

General comparison between the stress/strain, $\sigma(\varepsilon)$, curves measured for 1-D and 2-D materials[41] (Figs. 7 and 8) provides important perspective. It is found that $\sigma(\varepsilon)$ for 2-D materials is quite closely matched by simply scaling down the 1-D curve from S to S/2. The behavior of 2-D materials must, therefore, be *dominated* by the 0° plies,‡ which provide a fiber volume fraction in the loading direction about half that present in 1-D material.

The only significant 2-D effects occur at the initial deviation from linearity. At this stage, matrix cracks that form either in matrix-rich regions or in 90° plies evolve at somewhat lower stresses than cracks in 1-D materials.[29,30] However, the associated non-linearities are usually slight and do not normally contribute in an important manner to the overall non-linear response of the material. For example, matrix cracking in the 90° plies often proceeds by a tunneling mechanism[9,43,44] (Fig. 9). Tunnel cracking occurs subject to a lower bound stress[11,43,44]

$$\sigma_r = \left[\Gamma_m E/g t\right]^{1/2} - \sigma_R (E_L + E_T)/2E_T \qquad (19)$$

where g is a function that ranges between 1/3 and 2/3.[44] The unloading modulus associated with tunnel cracks is[44]

‡ Furthermore, since some of the 2-D materials are woven, the S/2 scaling infers that the curvatures introduced by weaving have minimal effect on the stress/strain behaviors.

$$\bar{E}/E = h\left(E_f/E_m, f, t/\bar{L}\right) \tag{20}$$

with $\bar{L}$ being the mean crack spacing in the 90° plies. The function h varies between 1 and ~ 0.6 as $t/\bar{L}$ changes from ~ 0 to > 1. The corresponding permanent strain is[44]

$$\varepsilon_p = \left(1 - E_T \nu^2/E_L\right)\sigma_R/E_L \tag{21}$$

The actual evolution of cracks at stresses above σ_τ depends on the availability of flaws in the 90° plies.

Extension of these tunnel cracks into the matrix of the 0° plies results in behavior similar to that found in 1-D material. Moreover, if the stress $\bar{\sigma}_0$ acting on the 0° plies is known, the 1-D solutions may be used directly. Otherwise, this stress must be estimated. For a typical 0/90 system, $\bar{\sigma}_0$ ranges between $\bar{\sigma}$ and $2\bar{\sigma}$, depending upon the extent of matrix cracking in the 90° plies and upon E_T/E_L.[44] Preliminary analysis has been conducted below using, $\bar{\sigma}_0 = 2\bar{\sigma}$, as implied by the comparison between 1-D and 2-D stress/strain curves (Fig. 8). Additional modelling is required on this topic.

3.2 Fiber Failure

The matrix cracks that originate in the 90° plies and extend through the 0° plies must induce a stress concentration in the fibers. The phenomenon is analogous to that considered above for 1-D material containing unbridged segments. When the stress concentration is small, the UTS should be given by Eqn. (13), but with f replaced by f_ℓ. In a typical case ($f_\ell/f = 1/2$), the UTS would be $S_u/2$, consistent with experimental findings on several CMCs (Fig. 8). In other cases, the stress concentration is important and the UTS is significantly smaller than $S_u/2$.

Major factors governing the stress concentration are the modulus ratio, E_T/E_L, the crack spacing, $\bar{L}$, and τ. That is, small values of E_T/E_L, $\bar{L}$ and τ alleviate the stress concentration.[41]

3.3 Shear Damage

When loaded in shear, 2-D CMCs are subject to non-linear deformation.[45] The deformations are governed primarily by matrix cracks. Typical shear stress/strain, $T(\gamma)$ curves (Fig. 10) indicate that CMCs can normally sustain larger shear strains than tensile strains prior to failure. The matrix damage often consists of cracks oriented at 45° to the fiber axis. Since fiber sliding is inhibited in shear loading, the elastic compliance of the composite with matrix cracks may be a useful upper bound for the shear strength. Consequently, when normalized by the shear modulus of the composite (Fig. 10), the $T(\gamma)$ curves found for a range of CMCs tend to converge into a band.

4. TEST METHODOLOGY

The preceding characteristics suggest a methodology that can be used to efficiently evaluate constituent properties, which may then be used to make predictions about composite performance. The basic philosophy is that straightforward procedures be used, with consistency demonstrated between independent measurement approaches. The measurements that are experimentally convenient include: the fiber pull-out length, $\bar{h}$, the matrix crack spacing at saturation, $\bar{\ell}_s$, the stress/strain (σ, ε) behavior, the fracture mirror dimensions and the bending deformation of a bilayer (Table I).

The steps are as follows. Generally, the fiber modulus is known, whereupon E_m can be evaluated from the measured initial composite modulus. Both S_c and m are known, provided that fracture mirror measurements have been made. Curvature measurements made on bilayer provide Ω. At this stage, measurements of pull-out,

saturation crack spacing and unloading/reloading hysteresis are used to determine τ, Γ_i and Γ_m, as well as to provide checks on the magnitudes of S_c and Ω.[24,34] Specifically, the magnitude of τ is obtained from the hysteresis loop width at half maximum, $\delta\varepsilon_{1/2}$, measured as a function of $\bar{\sigma}_p$ (Eqn. 7b) and checked using the unloading modulus, $\bar{E}$ (Eqn. 5). Typical results are shown in Figs. 11 and 12. Then, the misfit strain, Ω, and the debond energy, Γ_i, are evaluated from the permanent strain ε_p (Fig. 13) by using Eqn. (8). Additional procedures have been devised to determine Ω.[24] The misfit is compared with the bilayer measurements. Thereafter, the fiber pull-out lengths are used to provide consistency checks on τ and S_c, by using Eqn. (15), with the appropriate bound for λ.

When the preceding measurements provide consistent information, two other results can be used. The saturation crack spacing, $\bar{\ell}_s$, allows estimation of Γ_m (Eqn. 2), which may be compared with values found for the monolithic matrix material. The same value of Γ_m can be used to calculate the matrix cracking stress, $\bar{\sigma}_{mc}$ (Eqn. 1), which can be compared with the onset of linearity found in the stress/strain curves.

Finally, with S_c and m known, the UTS may be compared with the strengths predicted from global load sharing analysis (Eqn. 13) and fiber pull-out analysis (Eqn. 16). This comparison gives insight about the influence of matrix flaws on stress concentrations expected in the fibers.

The procedure is briefly illustrated by referring to a comprehensive set of results obtained on both SiC/CAS[6,9,24,30] and SiC/SiC[29,34,46] (see Figs. 11–13). The constituent properties for these two CMC systems obtained using the above methodology are summarized in Table III. More complete assessments are provided elsewhere.[24,34] The comparison between these two systems is interesting, because the constituent properties are very different. (i) In the SiC/SiC system, the fibers have clearly been degraded during processing. (ii) The large difference in τ indicates that the C coating placed on the fibers in the SiC/SiC material (by vapor deposition) has very different properties

than the C interphase in the CAS system, which is governed by reaction during processing. The high stiffness of the SiC matrix may also have an important influence on τ. (iii) The SiC/SiC system has a substantially larger debond energy, Γ_i, which is the origin of the relatively small permanent strain.

5. SIMULATIONS

When the constituent properties have been evaluated in a consistent manner, the stress/strain curves, for SDE materials, at stresses prior to saturation may be simulated by using Eqns. (1) to (10).[24,34] The procedure is straightforward for 1-D material, provided that Eqn. (3) is a reasonable representation of matrix crack evolution. Some examples are presented in Fig. 14a.[24] Further work is needed to predict the behavior above $\bar{\sigma}_s$. The simulation capability for 2-D material depends on the assumption made about the stress $\bar{\sigma}_0$ acting on the 0° plies. If this stress is considered to be, $\bar{\sigma}_0 = 2\bar{\sigma}$, the simulations for SDE materials, based on SiC/CAS (Fig. 14b), agree quite well with experiments except at small plastic strain.[34] Further research is needed to understand the behaviors at small plastic strains.

6. EFFECTS OF STRAIN CONCENTRATIONS

6.1 General Considerations

When either holes or notches (or other strain concentrating sites) are introduced, experimental results have indicated that CMCs can exhibit (at least) three classes of behavior,[12,40] as sketched in Fig. 15. Class I materials exhibit a dominant (mode I) crack emanating from the notch, with fiber failures occurring as the crack extends across the material. Class II materials experience multiple (mode I) matrix cracking from the notch. These cracks usually extend across the net section prior to fiber failure. In class III

materials, shear damage occurs from the notch and extends normal to the notch plane prior to composite failure. In all three cases, *stresses are redistributed* by matrix cracking as well as by fiber pull-out.

The characterization of notch effects for CMCs exhibiting these three classes of behavior appears to require different *mechanics*, because the stress redistribution mechanism within each class operates over different physical scales. Class I behavior involves stress redistribution by fiber bridging/pull-out, which occurs along the crack plane. Large-Scale Bridging Mechanics (LSBM) is preferred for such materials.[8,13-15] Class II behavior allows stress redistribution by large-scale matrix cracking. Consequently, a mechanism-based, Continuum Damage Mechanics (CDM) is regarded as most appropriate.[16] Class III behavior involves material responses similar to those found in metals,[12,40,41] and a comparable mechanics might be used: either LEFM for small-scale yielding or non-linear fracture mechanics for large-scale yielding. Since a unified mechanics has not yet been identified, it is necessary to devise *mechanism maps* that distinguish the various classes, through constituent properties. Initial attempts are elaborated below.

6.2 Mechanism Transitions

The transition between class I and class II behaviors involves considerations of both matrix crack growth and fiber failure. One hypothesis for the transition may be analyzed using LSBM. Such analysis allows the condition for fiber failure at the end of an unbridged crack segment to be solved simultaneously with the energy release rate of the matrix front. The latter is equated to the matrix fracture energy.[15] By using this solution to specify that fiber failure occurs *before the matrix crack extends into steady-state*, class I behavior is presumed to ensue. Conversely, class II behavior is assigned when the steady-state matrix cracking condition is achieved prior to fiber failure. The resulting mechanism map involves two indices:[15]

$$\mathcal{S} = \left(RS/a_o\tau\right)\left(E_m^2/E_l E_f\right)\left[(1-f)/f\right]^2 \equiv 3/\mathcal{A}_b \tag{24a}$$

and

$$\mathcal{C}_m = \sigma_{inc}/S \tag{24b}$$

With $\mathcal{S}$ and $\mathcal{C}_m$ as coordinates, a mechanism map may be constructed that distinguishes class I and class II behavior (Fig. 16). While this map has qualitative features consistent with experience, the experiments required for validation have not been completed. In practice, the mechanism transition in CMCs must involve additional considerations.

The incidence of class III behavior is found at relatively small magnitudes of the ratio of shear strength, T, to tensile strength S. When T/S is small, a shear band develops at the notch front and extends normal to the notch plane.[10,40] Furthermore, since T is related to G (Fig. 10), the parameter G/S is selected as the ordinate of a mechanism map.[12,41] Experimental results suggest that class III behavior arises when $G/S \lesssim 50$ (Fig. 17).

6.3 Mechanics Methodology

i) Class I Materials

The class I mechanism, when dominant, has features compatible with LSBM. These mechanics may be used to characterize effects of notches, holes and manufacturing flaws on tensile properties, whenever a single matrix crack is prevalent. For cases wherein the flaw or notch is small compared with specimen dimensions, the tensile strength may be plotted as functions of *both* flaw indices: $\mathcal{A}_b$ and $\mathcal{A}_p$ (Fig. 6). For the former, the results are sensitive to the ratio of the pull-out strength S_p to the UTS. These

results should be used whenever the unnotched tensile properties are compatible with global load sharing. Conversely, $\mathcal{A}_p$ should be used as the notch index when the unnotched properties appear to be pull-out dominated.

When the notch and hole have dimensions that are significant fraction of the plate width ($a_o/w > 0$), *net section* effects must be included.[8,37] Some results (Fig. 18) illustrate the behavior.

Complete experimental validation of LSBM for class I materials has not been undertaken. Partial results for the material, SiC/C_B, are compatible with LSBM, as shown for data obtained with center notches and center holes[12] (Fig. 17), with $\mathcal{A} \approx 0.8$. For this material, the unnotched properties appear to be pull-out controlled,[10,12] and the constituent properties give a pull-out notch index, $\mathcal{A}_p \approx 0.76$.

ii) Class II Materials

The non-linear stress/strain behavior governed by matrix cracking, expressed through $\bar{E}$ (Eqn. 5) and ε_p (Eqn. 8) provide a basis for a Damage Mechanics approach that may be used to predict the effects of notches and holes. Such developments are in progress. An important factor that dictates whether continuum or discrete methods are used concerns the ratio of the matrix crack spacing to the radius of curvature of the notch.

In practice, several class II CMCs have been shown to exhibit notch insensitive behavior for holes and notches in the size range: 1–5 mm (Fig. 19). These materials include: SiC/CAS[6] and SiC/glass (1070).[7] The non-linearity provided by the matrix cracks thus appears to allow stress redistribution to an extent that essentially *eliminates* the stress concentration.[7,47] The elimination of the stress concentration has been established both by notch strength measurement[6,7] and by thermoelastic emission tests.[46]

iii) Class III Materials

Class III behavior has been found in several C matrix composites[10,12] (Fig. 16). In these materials, the extent of the shear deformation zone ℓ_p is found to be predictable from measured shear strengths, T, in approximate accordance with[12]

$$\ell_p/a_o \approx \sigma/T \tag{25}$$

Calculations have indicated that this shear zone diminishes the stress ahead of the notch,[12] analogous to the *effect of a plastic zone in metals,* and provides good notch properties. For several C/C materials, it has been found that the shear band lengths are small enough that LEFM characterizes the experimental data over a range of notch lengths. For edge notched specimens, it is found that,[12] $K_{IC} \approx 16$ MPa$\sqrt{m}$ (Fig. 20). However, conditions must exist where LEFM is violated. For example, when $\ell_p/a_o \lesssim 4$, the stress concentration is essentially eliminated and the material must then become notch insensitive.[12] Further work is needed to identify parameters that bound the applicability of LEFM, as well as establish the requirements for notch insensitivity.

7. SUMMARY

Test methods have been described that relate constituent properties to macroscopic behaviors in a consistent manner. The approach has been illustrated for two CMC systems. It is expected that the methodology will be used to predict stress/strain curves and examine their sensitivity to constituent properties. These properties may be used to delineate mechanism maps that represent transitions in macroscopic performance, especially in the presence of strain concentrations. Mechanics procedures for each mechanism have been described in a preliminary manner. A concerted effort is needed

to further develop and validate the mechanics, which should have applicability to a wide range of technologically important CMCs.

ACKNOWLEDGEMENTS

This work was supported by the Defense Advanced Research Projects Agency through the University Research Initiative under Office of Naval Research Contract No. N–00014–86–K–0753.

TABLE I

Measurement Methods

CONSTITUENT PROPERTY	MEASUREMENT
Sliding Stress, τ	• Pull-Out Length, $\bar{h}$[25,36] • Saturation Crack Spacing, $\bar{\ell}_s$[20,22] • Hysteresis Loop, $\delta\varepsilon_{1/2}$[23,24] • Unloading Modulus, $\bar{E}_L$[23,24]
Characteristic Strength, S_c, m	• Fracture Mirrors[38,39] • Ultimate Strength, S[25]
Misfit Strain , Ω	• Bilayer Distortion[9] • Permanent Strain, ε_p[23,24] • Residual Crack Opening[32]
Matrix Fracture Energy, Γ_m	• Monolithic Material • Saturation Crack Spacing, $\bar{\ell}_s$[22] • Matrix Cracking Stress, $\bar{\sigma}_{mc}$[19]
Debond Energy, Γ_i	• Permanent Strain, ε_p[21,24] • Residual Crack Opening[21,24]

TABLE II

Summary of Non-Dimensional Coefficients

$$\Sigma_T \equiv \frac{\bar{\sigma}_T}{\bar{\sigma}_p} = (c_2/c_1)E_m\Omega/\bar{\sigma}_p, \quad \text{Misfit Index}^{21,24,32}$$

$$\Sigma_i \equiv \frac{\bar{\sigma}_i}{\bar{\sigma}_p} = (1/c_1)\sqrt{E_m\Gamma_i/R\bar{\sigma}_p^2} - \Sigma_T, \quad \text{Debond Index}^{21,24}$$

$$\mathcal{H} = b_2(1-a_1 f)^2 R\bar{\sigma}_p^2/4\bar{\ell}\tau E_m f^2, \quad \text{Hysteresis Index}^{24,32}$$

$$\mathcal{L} = \Gamma_m(1-f)^2 E_f E_m/f\tau^2 E_L R, \quad \text{Crack Spacing Index}^{22}$$

$$\mathcal{M} = 6\tau\Gamma_m f^2 E_f/(1-f)E_m^2 R E_L, \quad \text{Matrix Cracking Index}^{2,18,19}$$

$$Q = E_f f\Omega/E_L(1-\nu), \quad \text{Residual Stress Index}^{19,24}$$

$$\mathcal{A} = a_o S^2/E_L\Gamma, \quad \text{Flaw Index}^{8}$$

$$\mathcal{A}_b = \left[f/(1-f)\right]^2\left(E_f E_L/E_m^2\right)\left(a_o\tau/RS_u\right), \quad \text{Flaw Index for Bridging}^{8,15}$$

$$\mathcal{A}_p = \left(a_o/\bar{h}\right)\left(S_p/E_L\right), \quad \text{Flaw Index for Pull-Out}^{37,41}$$

TABLE III

Important Constituent Properties For CMCs: Comparison Between SiC/SiC and SiC/CAS

PROPERTY		MATERIAL	
		SiC/CAS	SiC/SiC
CONSTITUENTS	Matrix Modulus, E_m (GPa)	1[illegible]	400
	Fiber Modulus, E_f (GPa)	200	200
	Sliding Stress, τ (MPa)	15–20	100–150
	Residual Stress, q (MPa)	80–100	50–100
	Fiber Strength, S_c (GPa)	2.0–2.2	1.3–1.6
	Shape Parameter, m	3.3–3.8	4.2–4.7
	Matrix Fracture Energy, Γ_m (Jm^{-2})	20–25	5–10
	Debond Energy, Γ_i (Jm^{-2})	~ 0.1	~ 2
DEPENDENT PROPERTIES	Matrix Cracking Stress, σ_{mc} (MPa)	140–160	200–220
	Saturation Crack Spacing , $\bar{d}_s$ (μm)	110–130	15–20
	Pull-out Length $\bar{h}$ (μm)	250–350	25–40

REFERENCES

[1] K.M. Prewo and J.J. Brennan, *J. Mater. Sci.*, **17** (1982) 1201–06.

[2] D.B. Marshall, B.N. Cox and A.G. Evans, *Acta Metall.*, **33** (1985) 2013.

[3] J.J. Brennan and K.M. Prewo, *J. Mater. Sci.*, **17** (1982) 2371–83.

[4] M. Bouquet, J.-M. Birbis, J.-M. Quenisset and R. Naslain, ICCM-VI, Elsevier, London. **Vol. 2** (1987) p. 248–49.

[5] J.M. Domergue, H.C. Cao, A.G. Evans and D. Petrak, *J. Am. Ceram. Soc.*, to be published.

[6] C. Cady and A.G. Evans, *J. Am. Ceram. Soc.*, to be published.

[7] S. Mall, D.E. Bullock and J.J. Pernot, to be published.

[8] G. Bao and Z. Suo, ASME Book No. AMR118, *Appl. Mech. Rev.*, **45** (1992) 355–66.

[9] D. Beyerle, S.M. Spearing and A.G. Evans, *J. Am. Ceram. Soc.*, **75** (1992) 3321–30.

[10] F.E. Heredia, S.M. Spearing, P. Mosher, A.G. Evans and W.A. Curtin, *J. Am. Ceram. Soc.*, **75** (1992) 3017–25.

[11] N. Laws and G. Dvorak, *Jnl. Composite Mtls.*, **22** (1980) 900.

[12] F.E. Heredia, S.M. Spearing, M.Y. He, T.J. Mackin, P.A. Brøndsted, A.G. Evans and P. Mosher, *J. Am. Ceram. Soc.*, to be published.

[13] B.N. Cox and D.B. Marshall, *Fatigue and Fracture of Eng. Mtls.*, **14** (1991) 847.

[14] B.N. Cox and C.S. Lo, *Acta Metall. Mater.*, **40** (1992) 69.

[15] L. Cui and B. Budiansky, to be published.

[16] D. Hayhurst, F.A. Leckie and A.G. Evans, *Proc. Roy. Soc.*, London, **A434** (1991) 369.

[17] A.G. Evans and F.W. Zok, *Topics In Fracture and Fatigue* (ed. A.S. Argon) 1992, pp. 271–308.

[18] J. Aveston, G.A. Cooper and A. Kelly, in *The Properties of Fiber Composites*, NPL Conf. Proc., pp. 15–26.

[19] B. Budiansky, J.W. Hutchinson and A.G. Evans, *J. Mech. Phys. Solids*, **34** (1986) 167.

[20] F.W. Zok and S.M. Spearing, *Acta Metall. Mater.*, **40** (1992) 2033.

[21] J.W. Hutchinson and H. Jensen, *Mech. of Mtls.*, **9**, (1990) 139.

[22] S.M. Spearing and F.W. Zok, *Jnl. Eng. Mtls. Tech.*, in press.

[23] A.W. Pryce and P. Smith, *J. Mater. Sci.*, **27** (1992) 2695–2704.

[24] E. Vagaggini, J.M. Domergue and A.G. Evans, *J. Am. Ceram. Soc.*, to be published.

[25] W.A. Curtin, *J. Am. Ceram. Soc.*, **74** (1991) 2837–45.

[26] L. Phoenix and R. Raj, *Acta Metall. Mater.*, **40** (1992) 2813–28.

[27] F. Hild, J.M. Domergue, F.A. Leckie and A.G. Evans, *Intl. Jnl. Solids Structures*, to be published.

[28] B.Y. Kim and N. Pagano, *J. Am. Ceram. Soc.*, **74** (1991) 1082–90.

[29] X. Aubart, Thèse de Doctorat de L'Université de Paris (Nov. 1991), "Modélisation et Identification du Comportement de Composites à Matrice Céramique."

[30] D. Beyerle, S.M. Spearing, F.W. Zok and A.G. Evans, *J. Am. Ceram. Soc.*, **75** (1992) 7519.

[31] M.Y. He, B.-X. Wu, A.G. Evans and J.W. Hutchinson, *Mech. of Mtls.*, to be published.

[32] D.B. Marshall, *Acta Metall. Mater.*, **40** (1992) 427–41.

[33] T.J. Kotil, J.W. Holmes and M. Cominou, *J. Am. Ceram. Soc.*, **73** (1990) 1879.

[34] J.M. Domergue, E. Vagaggini, A.G. Evans and D. Roach, *J. Am. Ceram. Soc.*, to be published.

[35] S.M. Spearing, F.W. Zok and A.G. Evans, *J. Am. Ceram. Soc.*, in press.

[36] M.D. Thouless and A.G. Evans, *Acta Metall.*, **36** (1988) 517.

[37] Z. Suo, S. Ho and X. Gong, *J. Matl. Engr. Tech.*, in press.

[38] A.J. Eckel and R.C. Bradt, *J. Am. Ceram. Soc.*, **72** (1989) 435.

[39] J.F. Jamet, D. Lewis and E.Y. Luh, *Ceram. Eng. Sci. Proc.*, **5** (1984) 625.

[40] A.G. Evans, *Mat. Sci. Eng.*, **A143** (1991) 63.

[41] A.G. Evans, F.W. Zok and T.J. Mackin, to be published.

[42] H.C. Cao, E. Bischoff, M. Rühle, A.G. Evans, D.B. Marshall and J.J. Brennan, *J. Am. Ceram. Soc.*, **73** (1990) 1691.

[43] J.W. Hutchinson and Z. Suo, *Appl. Mech. Rev.*, **28** (1991).

[44] C. Xia, R.R. Carr and J.W. Hutchinson, *Harvard Univ. Report Mech-202* (1992) to be published.

[45] P.A. Brøndsted, F.E. Heredia and A.G. Evans, *J. Am. Ceram. Soc.*, to be published.

[46] T.J. Mackin, A.G. Evans and T.E. Purcell, to be published.

FIGURE CAPTIONS

Fig. 1. A schematic indicating the consequence of matrix cracking in CMCs on the stress/strain behavior.

Fig. 2. A schematic indicating the parameters that influence the evolution of matrix cracks in 1-D CMCs.[30]

Fig. 3. Effects of matrix crack density on the elastic compliance of 1-D CMCs.[31]

Fig. 4. Effects of gauge length on the ultimate tensile strength predicted by global load sharing analysis.[27]

Fig. 5. Bounding solutions for the non-dimensional fiber pull-out length.[25]

Fig. 6. Strength degradation in elastically isotropic CMCs subject to unbridged segments (length $2a_o$) a) combined bridging and pull-out; b) pull-out.[8,37]

Fig. 7. A comparison of stress/strain curves for 2-D CMCs all reinforced with Nicalon fibers (with f = 0.4). The SiC/CAS is a laminate, the SiC/SiC_{CVI} has a plain weave: the other materials have a 8-harness satin weave.[41]

Fig. 8. A comparison of 1-D and 2-D CMC tensile properties obtained for SiC/CAS and SiC/SiC_{CVI}. The lines marked (1/2)1-D are the results for 1-D material reduced in scale by (1/2).[41]

Fig. 9. A typical matrix cracking mode in 2-D CMCs.[9]

Fig. 10. The shear strength of various CMCs normalized by the composite shear modulus.[45]

Fig. 11. The unloading modulus measured for 1-D and 2-D SiC/CAS and SiC/SiC_{CVI} showing comparisons with the model (Eqn. 5) for various sliding stresses.[24,34]

Fig. 12. Variations in the relative hysteresis loop width with crack density obtained for 2-D SiC/SiC_{CVI} showing comparisons with the model (Eqn. 7) for various sliding stresses.[24]

Fig. 13. Variation in permanent strain for a 1-D SiC/CAS material showing comparisons with the model (Eqn. 8) for various values of the sliding stress, using an independently determined value for the misfit strain, with ($\Gamma_i \approx 0$).[30]

Fig. 14. Simulated stress, strain curves for SDE material a) 1-D material with notational constituent properties. b) 2-D material simulation obtained by assuming $\bar{\sigma}_0 = 2\bar{\sigma}$, compared with experimental measurements (constituent properties relevant to SiC/CAS).

Fig. 15. The three classes of behavior found in CMCs and the associated mechanisms of stress redistribution.[40,41]

Fig. 16. A proposed mechanism map for the transition between class I and class II behaviors.[15,41]

Fig. 17. A proposed mechanism map for the transition to class III behavior.[45]

Fig. 18. Effects of holes and notches on the tensile strength predicted using LSBM. Also included are results obtained for SiC/C_B.[12]

Fig. 19. The notch strength of a 2-D SiC/CAS composite revealing that this is a notch insensitive material.[6]

Fig. 20. Use of LEFM to characterize the notch strength of C/C composites.[12]

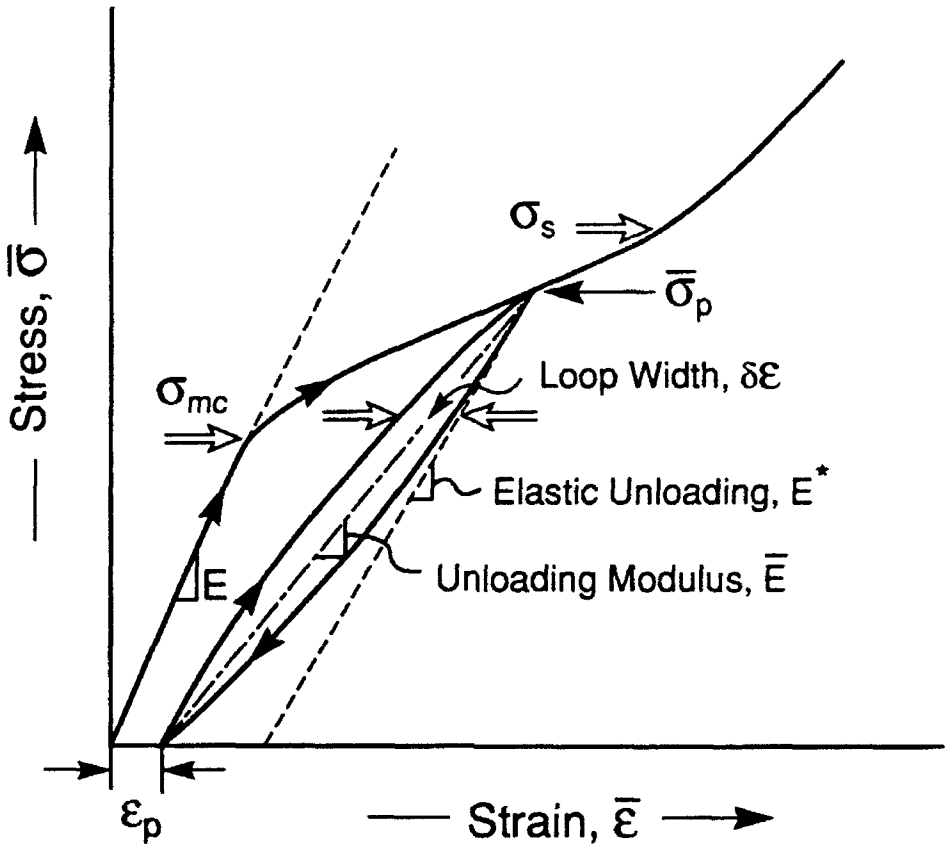
Stress, $\bar{\sigma}$
σ_s
$\bar{\sigma}_p$
σ_{mc}
Loop Width, $\delta\bar{\varepsilon}$
Elastic Unloading, E^*
Unloading Modulus, $\bar{E}$
E
ε_p
Strain, $\bar{\varepsilon}$

Figure 1

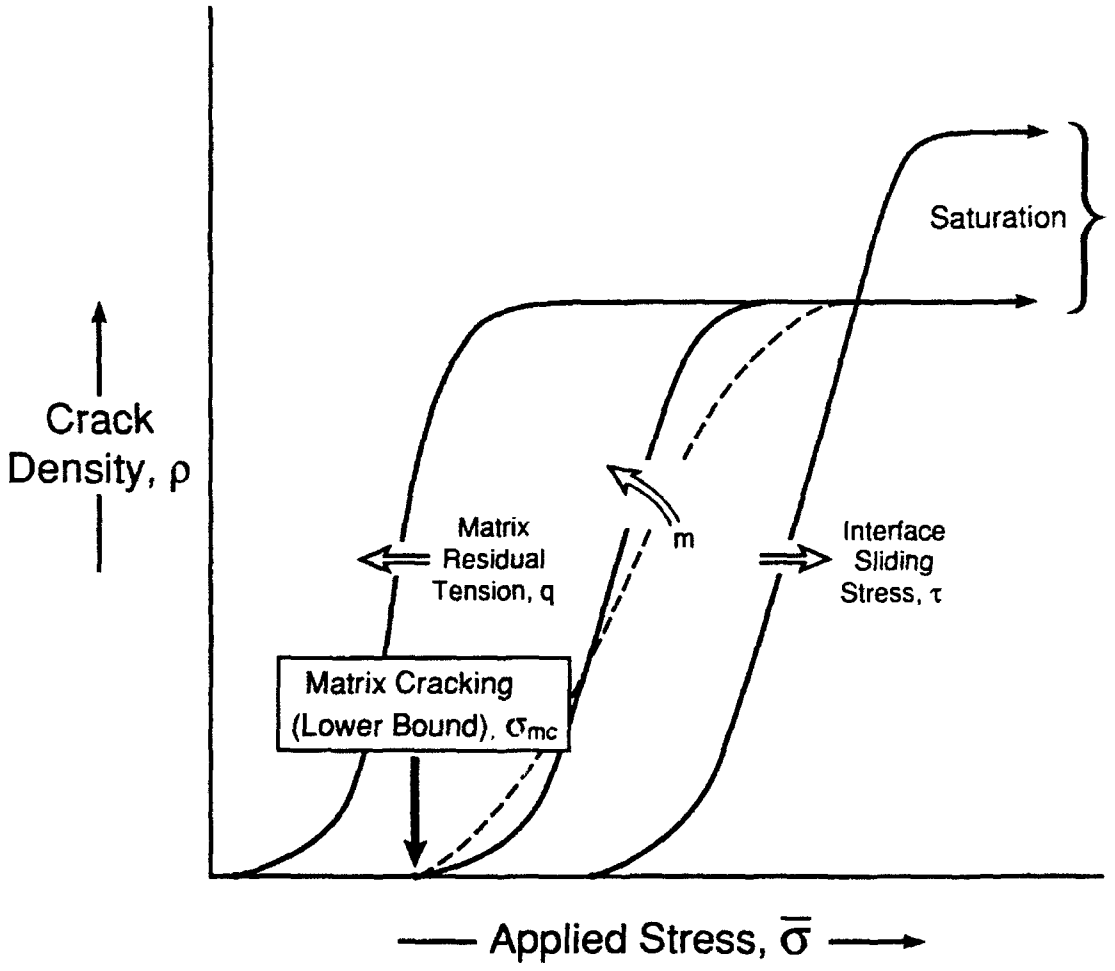
Saturation
Crack
Density, ρ
Matrix
Residual
Tension, q
m
Interface
Sliding
Stress, τ
Matrix Cracking
(Lower Bound), σmc
Applied Stress, σ̄

Figure 2

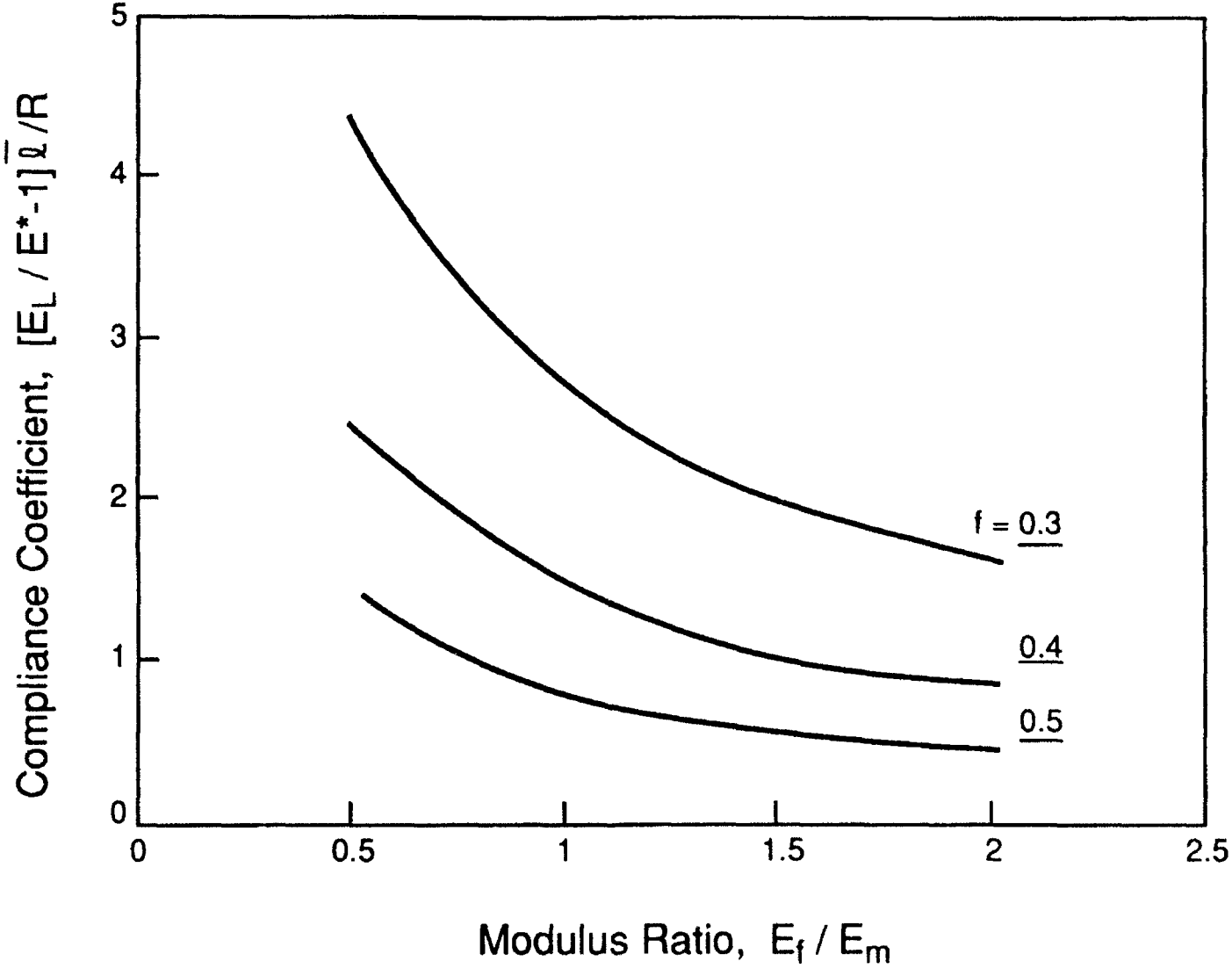
Compliance Coefficient, $[E_L / E^* - 1]\bar{\ell}/R$
5
4
3
2
1
0
0
0.5
1
1.5
2
2.5
f = 0.3
0.4
0.5
Modulus Ratio, E_f / E_m

Figure 3

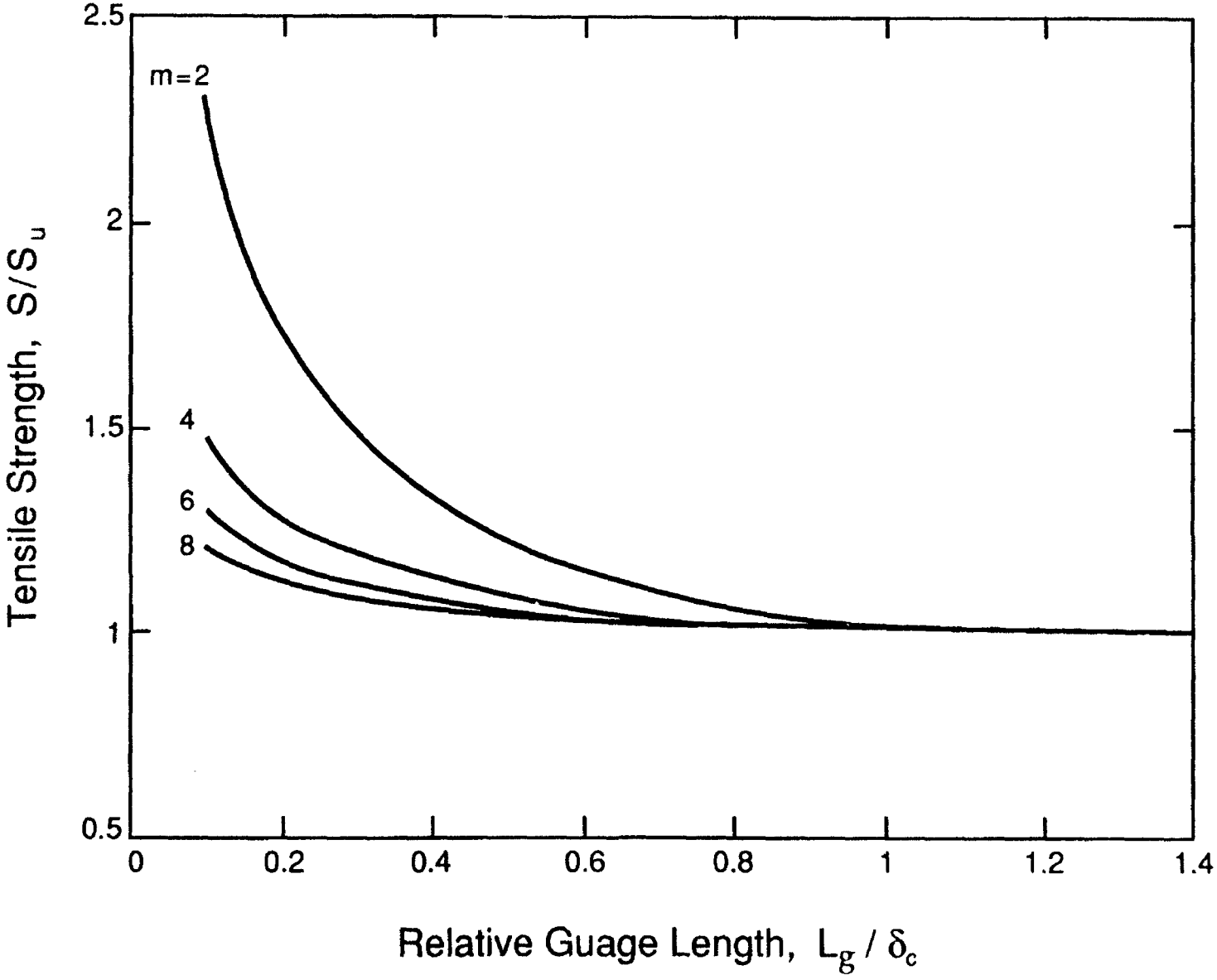
2.5
2
1.5
1
0.5
m=2
4
6
8
Tensile Strength, S/S$_u$
0
0.2
0.4
0.6
0.8
1
1.2
1.4
Relative Guage Length, L_g / δ_c

Figure 4

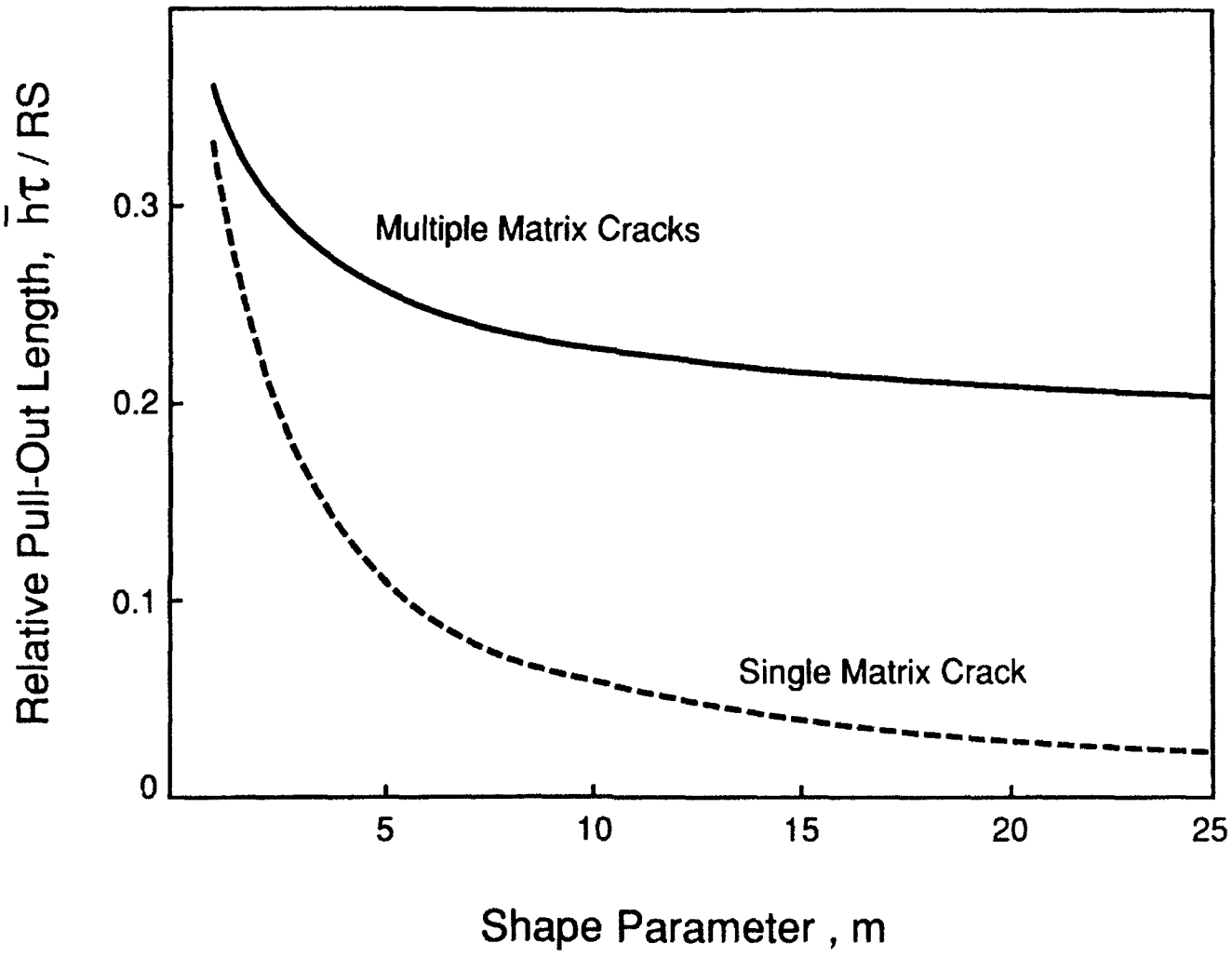
Relative Pull-Out Length, $\bar{h}\tau$ / RS
0.3
0.2
0.1
0
Multiple Matrix Cracks
Single Matrix Crack
5
10
15
20
25
Shape Parameter , m

Figure 5

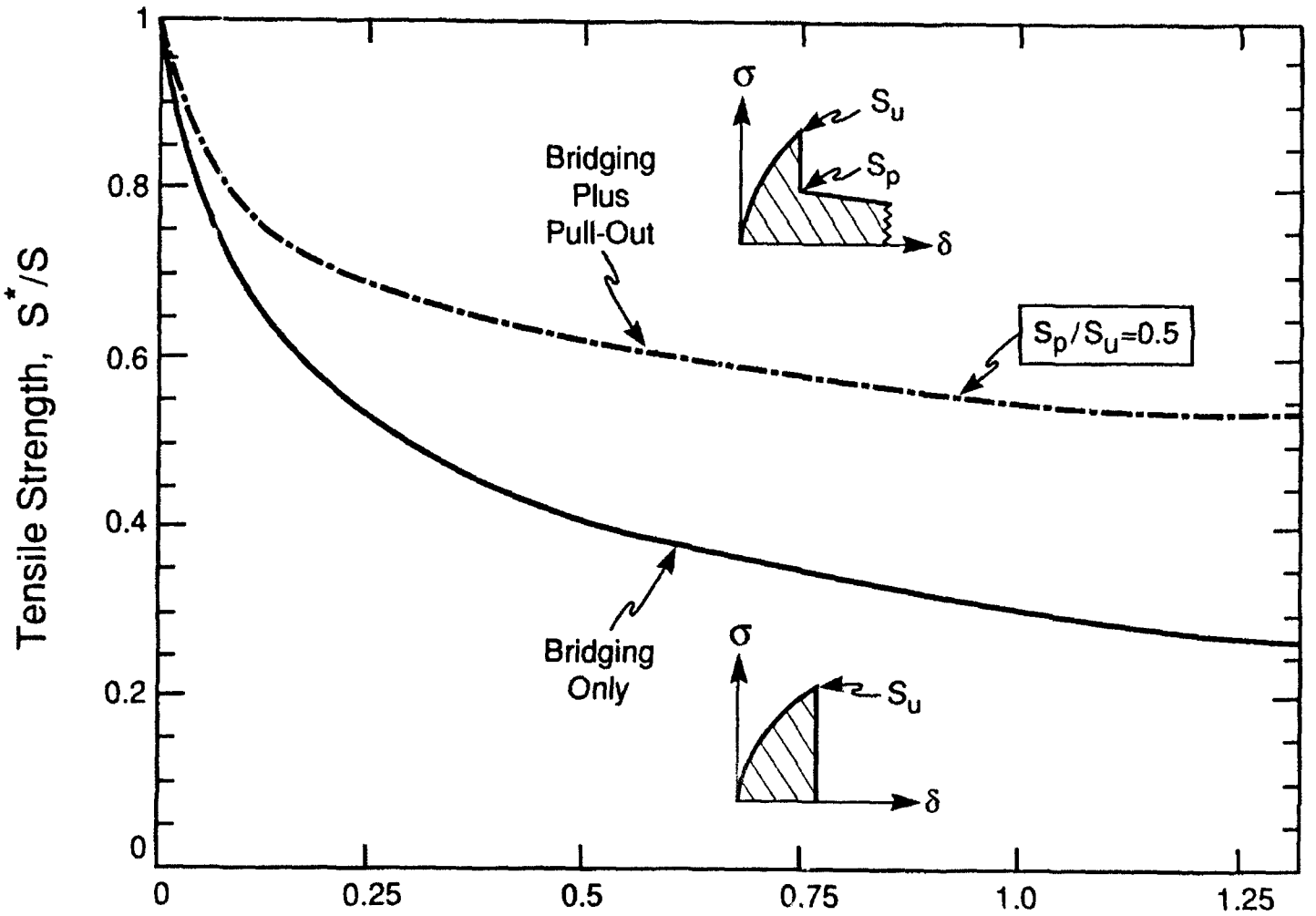

$$\text{Flaw Index, } A_b = \frac{f^2}{(1-f)^2}\left(\frac{E_f E}{E_m{}^2}\right)\left(\frac{a_o \tau}{RS}\right)$$

Figure 6a

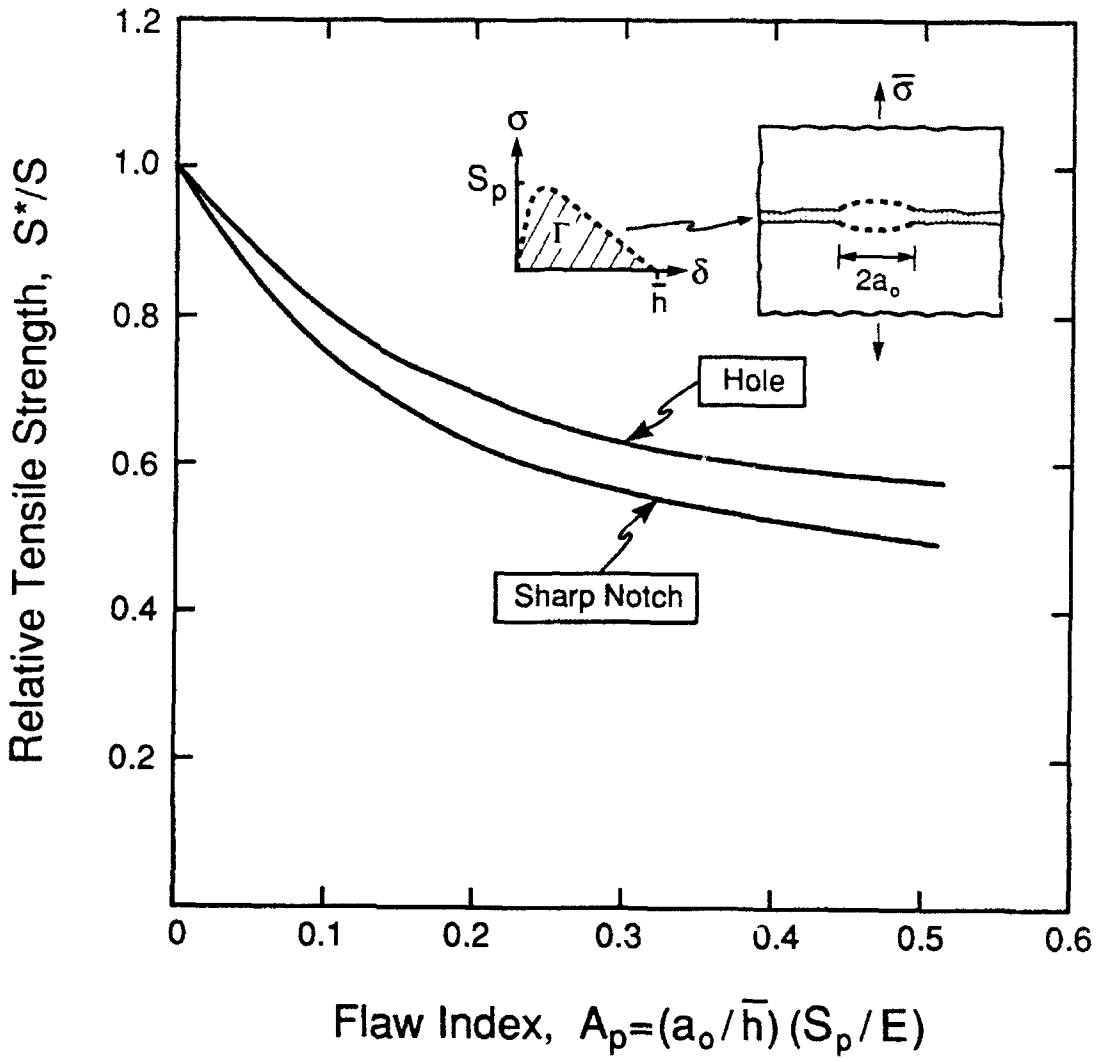
Relative Tensile Strength, S*/S
1.2
1.0
0.8
0.6
0.4
0.2
0
0.1
0.2
0.3
0.4
0.5
0.6
Flaw Index, $A_p=(a_o/\bar{h})(S_p/E)$
σ
S_p
Γ
δ
$\bar{h}$
$\bar{\sigma}$
$2a_o$
Hole
Sharp Notch

Figure 6b

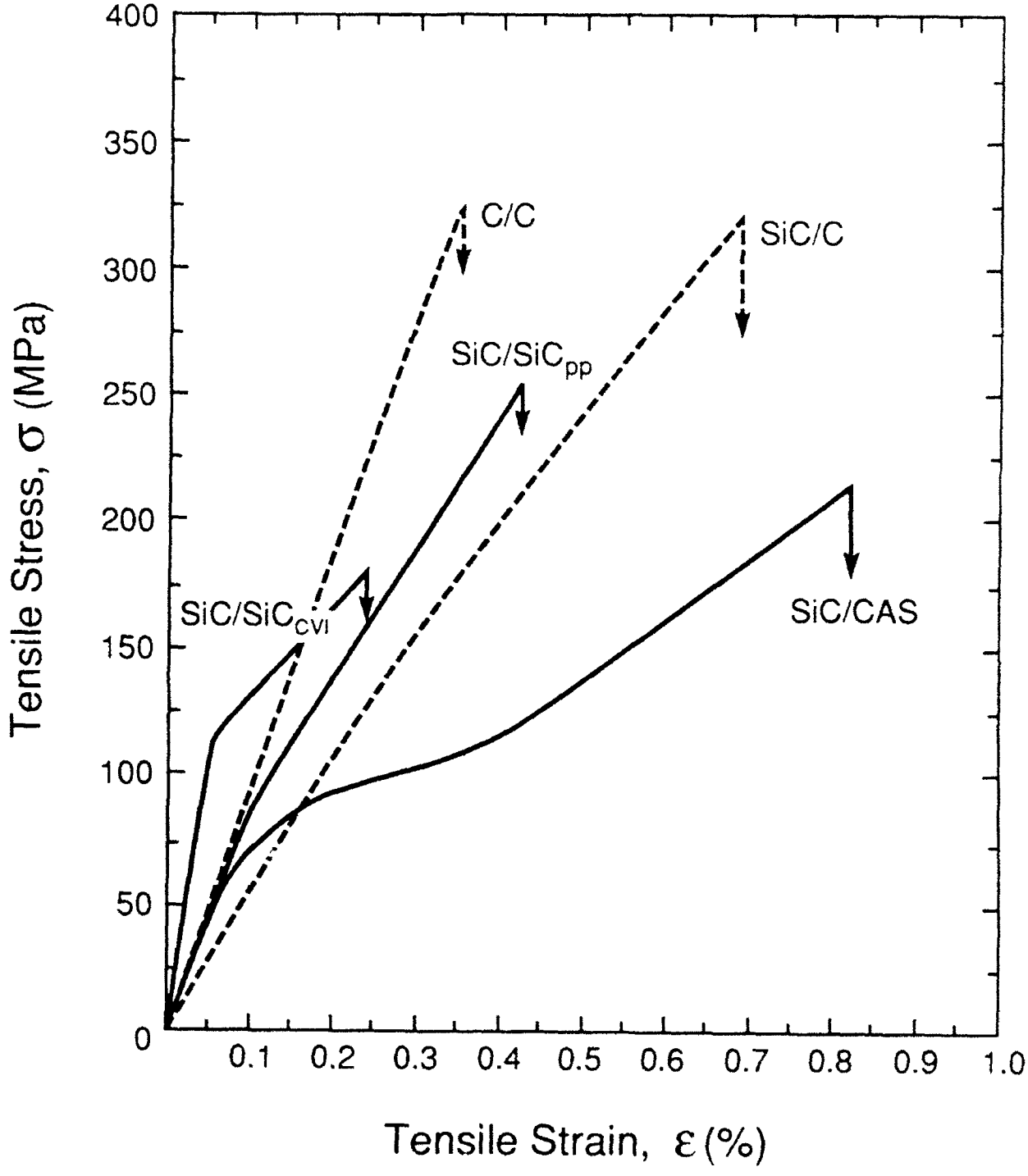
400
350
300
250
200
150
100
50
0
Tensile Stress, σ (MPa)
C/C
SiC/C
SiC/SiC$_{pp}$
SiC/SiC$_{CVI}$
SiC/CAS
0.1
0.2
0.3
0.4
0.5
0.6
0.7
0.8
0.9
1.0
Tensile Strain, ε (%)

Figure 7

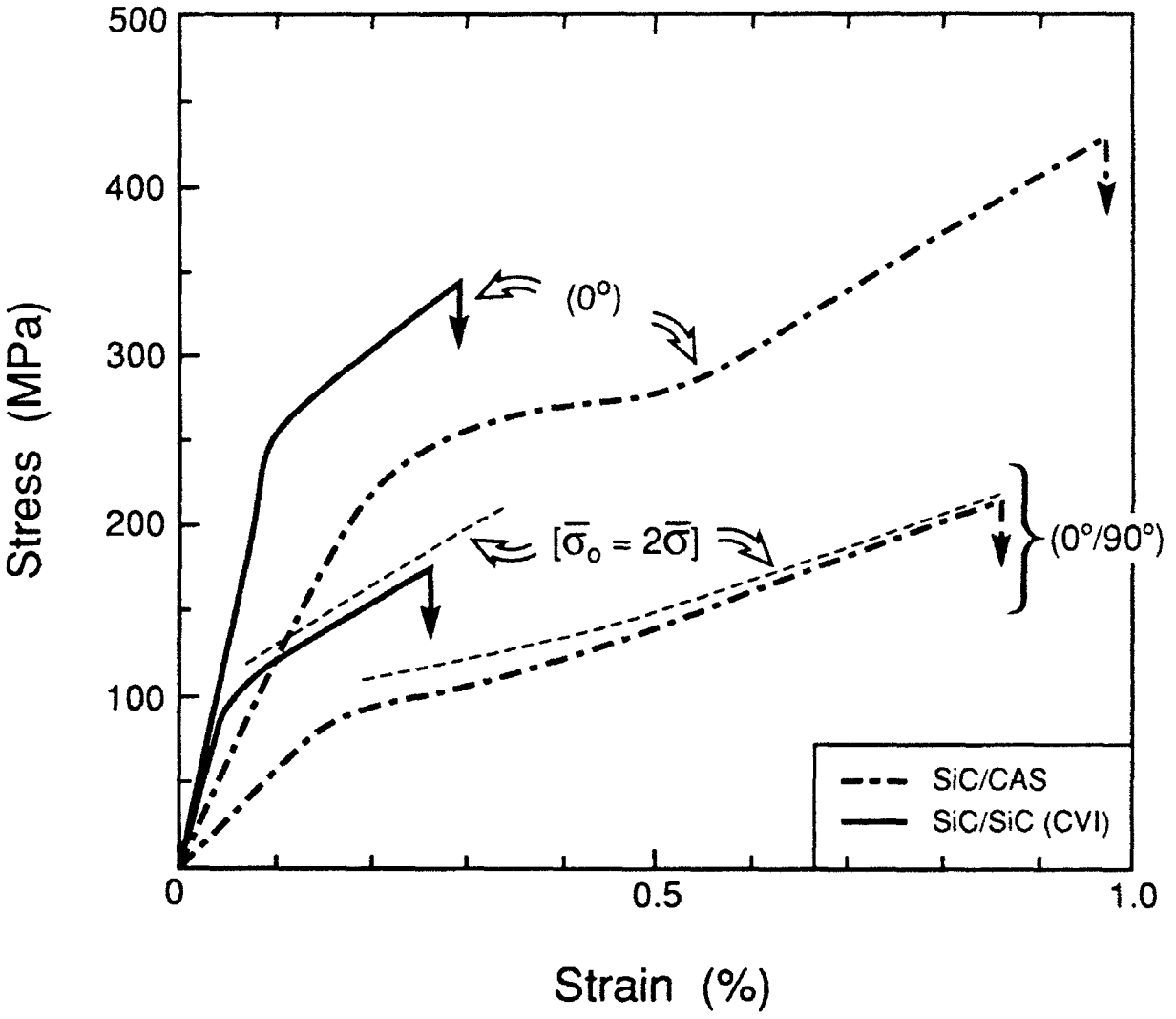
500
400
300
200
100
0
0.5
1.0
Stress (MPa)
Strain (%)
(0°)
[$\bar{\sigma}_o = 2\bar{\sigma}$]
(0°/90°)
SiC/CAS
SiC/SiC (CVI)

Figure 8

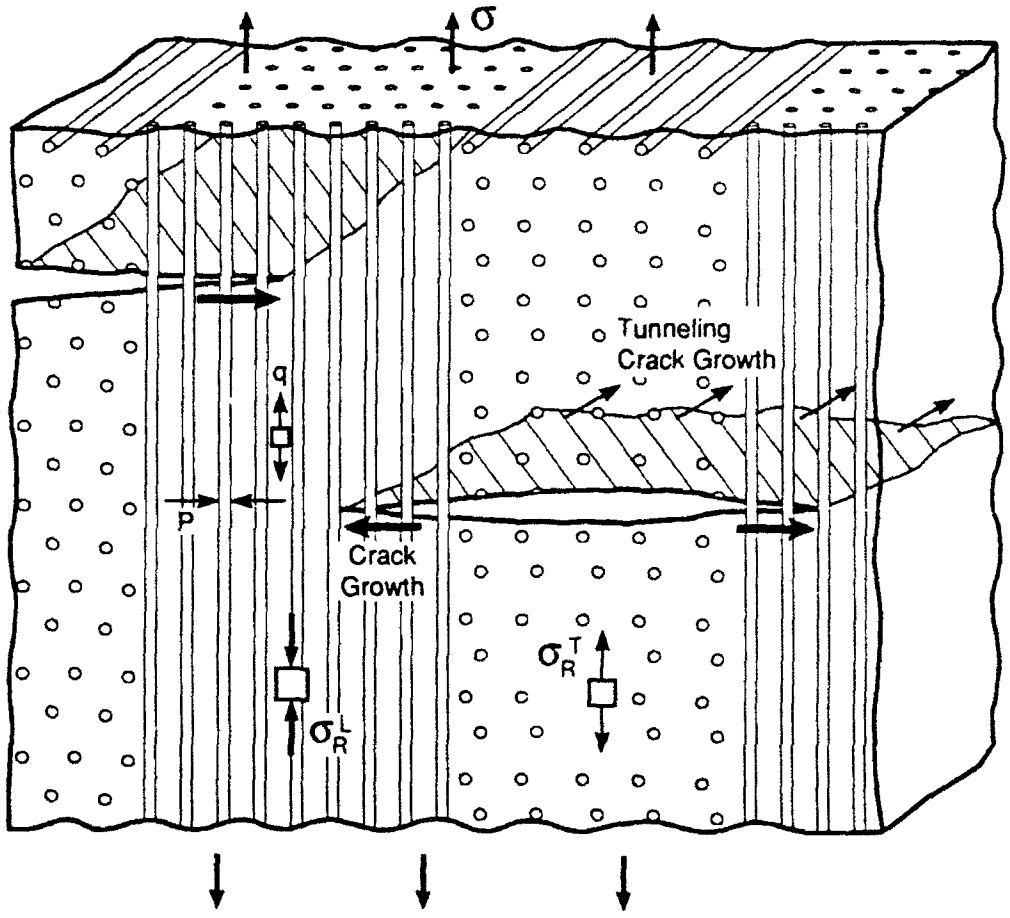

Figure 9

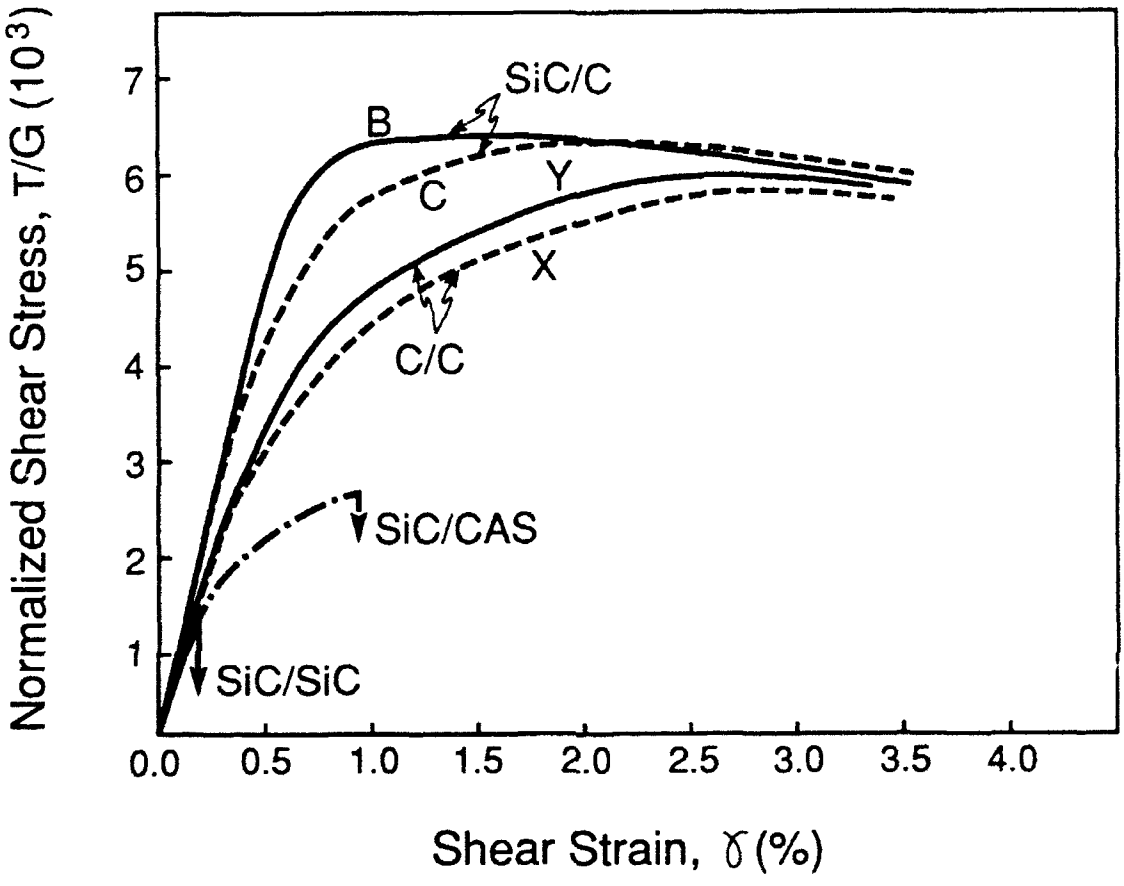
Normalized Shear Stress, T/G (10^3)
7
6
5
4
3
2
1
0.0
0.5
1.0
1.5
2.0
2.5
3.0
3.5
4.0
Shear Strain, γ (%)
SiC/C
B
C
Y
X
C/C
SiC/CAS
SiC/SiC

Figure 10

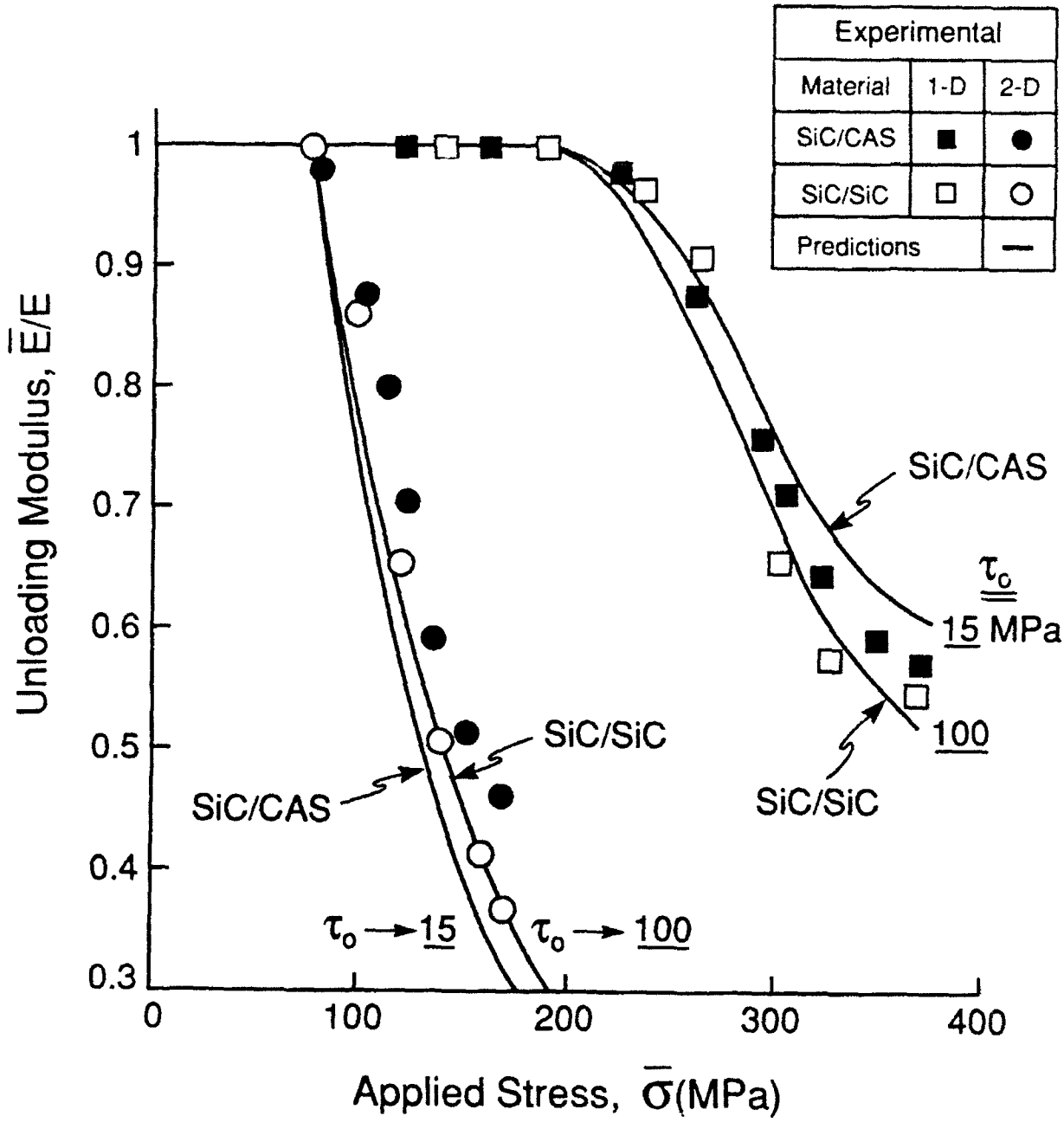
Experimental
Material
1-D
2-D
SiC/CAS
SiC/SiC
Predictions
Unloading Modulus, $\bar{E}/E$
1
0.9
0.8
0.7
0.6
0.5
0.4
0.3
0
100
200
300
400
Applied Stress, $\bar{\sigma}$(MPa)
SiC/CAS
τ_o = 15 MPa
SiC/SiC
100
SiC/SiC
SiC/CAS
$\tau_o \rightarrow$ 15
$\tau_o \rightarrow$ 100

Figure 11

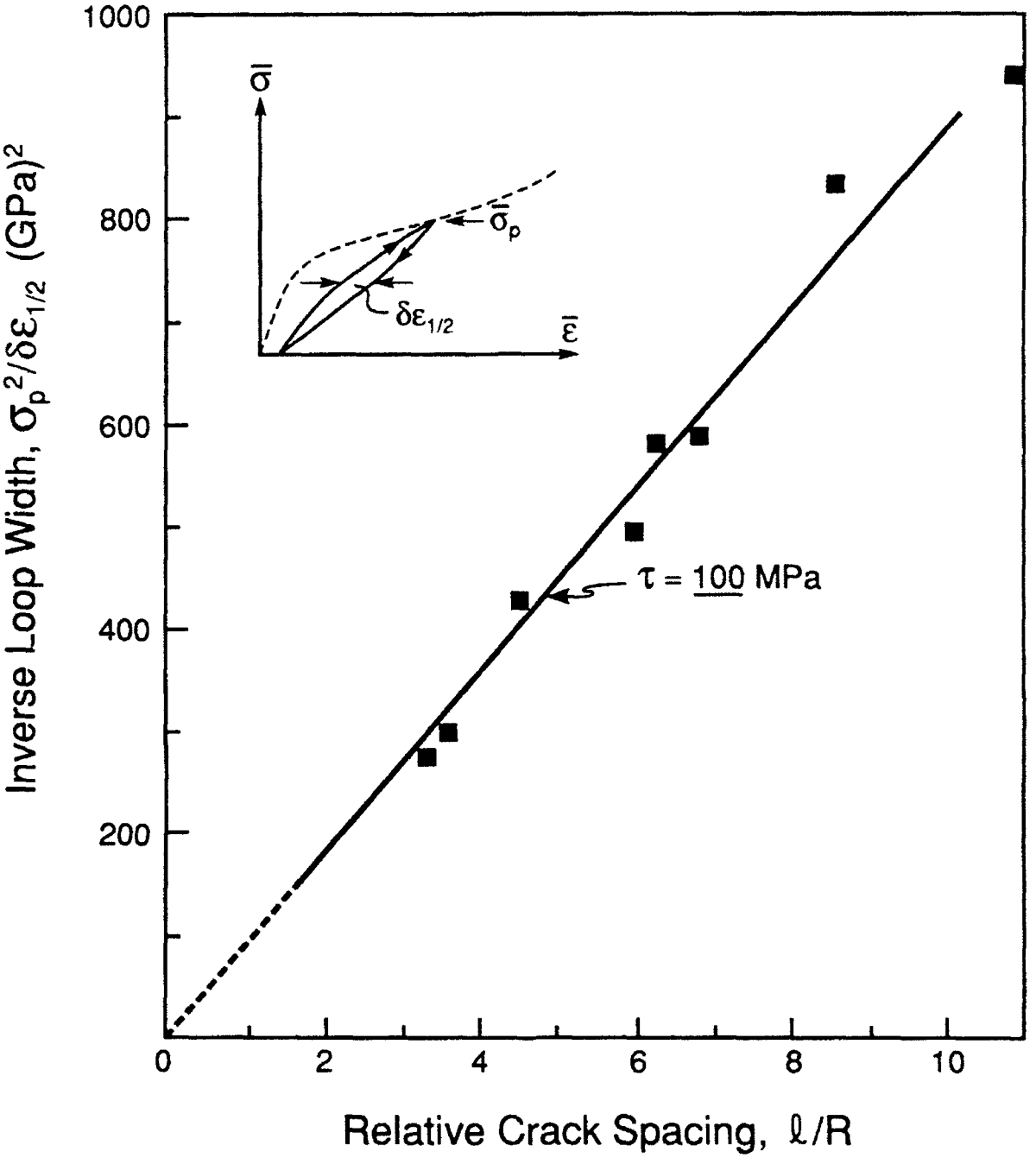
1000
800
600
400
200
0
2
4
6
8
10
Inverse Loop Width, $\sigma_p^2/\delta\varepsilon_{1/2}$ (GPa)^2
Relative Crack Spacing, ℓ/R
$\bar{\sigma}$
$\bar{\sigma}_p$
$\delta\varepsilon_{1/2}$
$\bar{\varepsilon}$
τ = 100 MPa

Figure 12

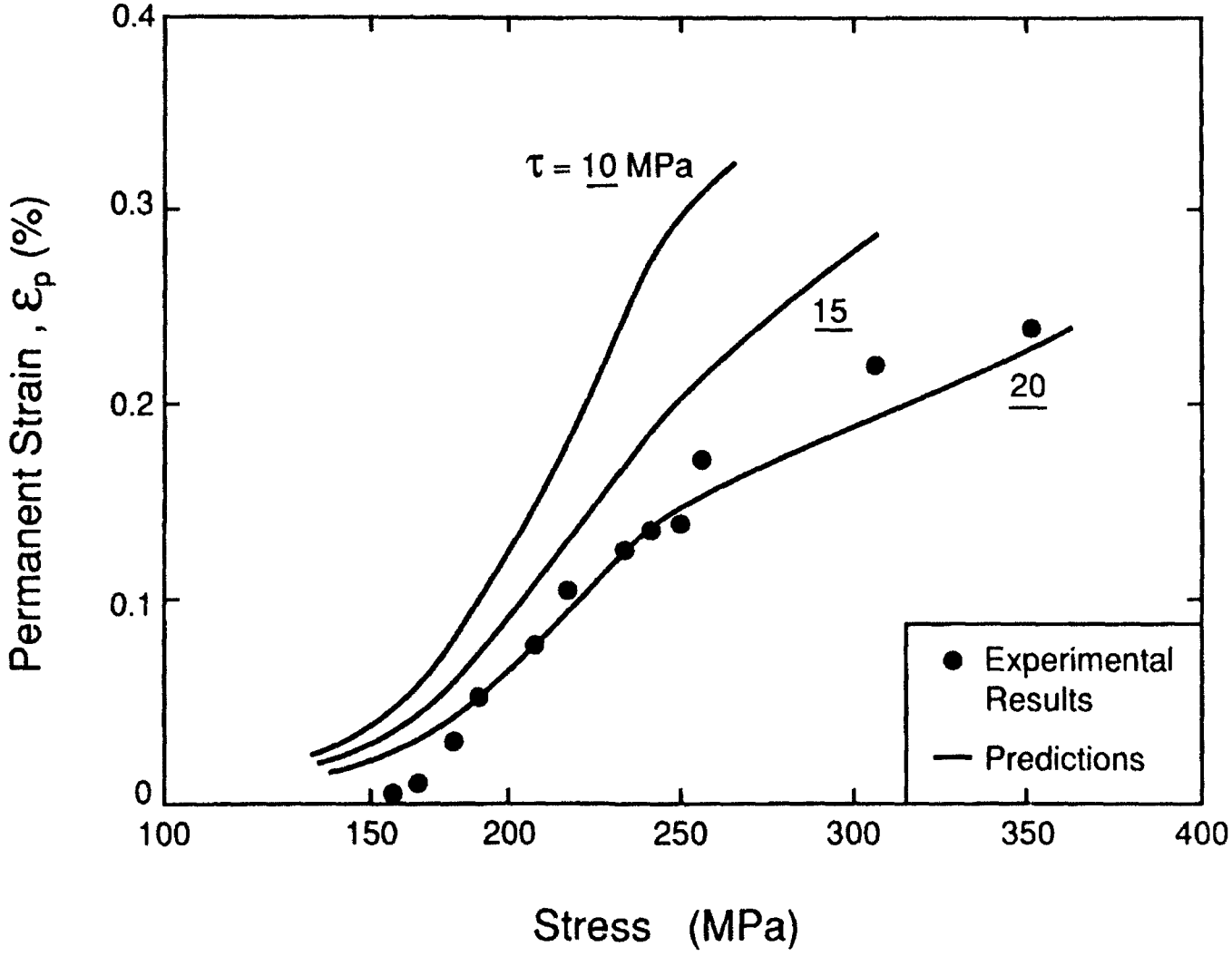
0.4
0.3
0.2
0.1
0
Permanent Strain , ε_p (%)
τ = 10 MPa
15
20
Experimental Results
Predictions
100
150
200
250
300
350
400
Stress (MPa)

Figure 13

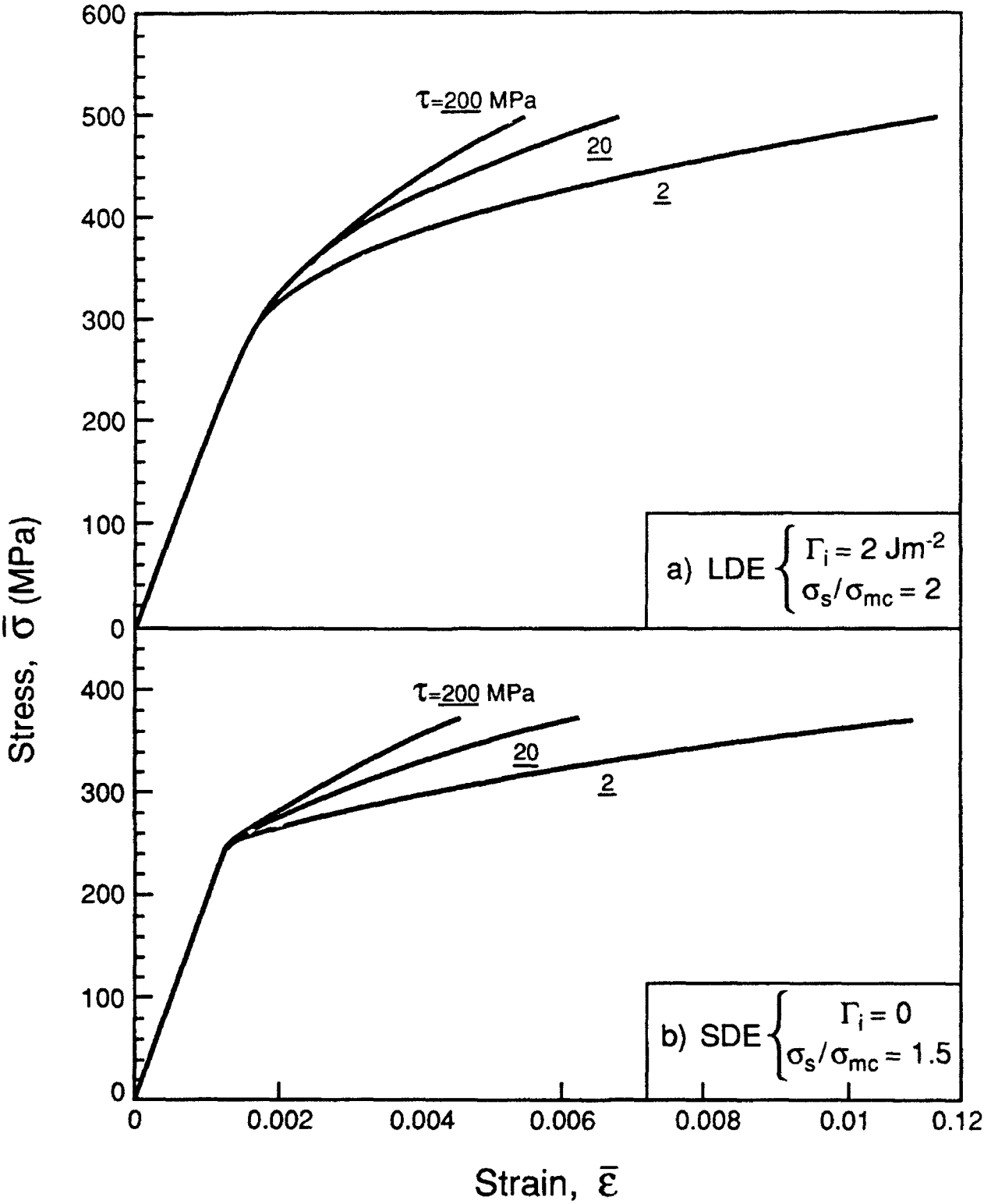

Figure 14a

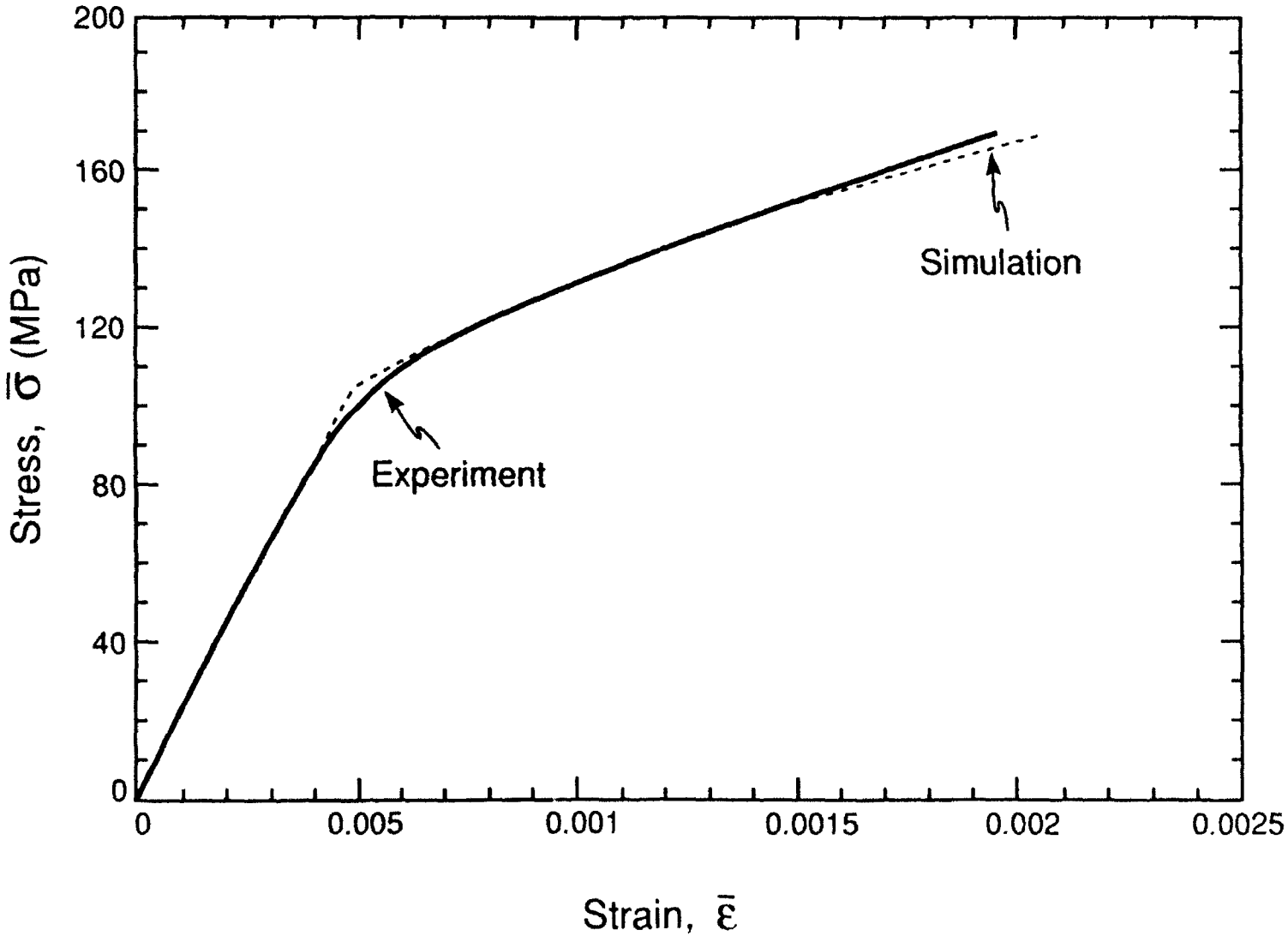
200
160
120
80
40
0
Stress, $\bar{\sigma}$ (MPa)
0
0.005
0.001
0.0015
0.002
0.0025
Strain, $\bar{\varepsilon}$
Simulation
Experiment

Figure 14b

Class I

Matrix Cracking + Fiber Failure

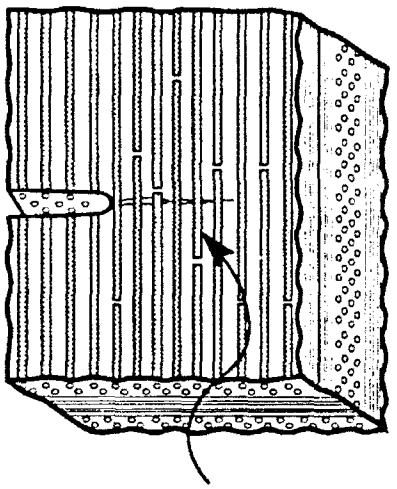

Pull-Out Tractions
Redistribute Stress

Class II

Matrix Cracking: No Fiber Failure

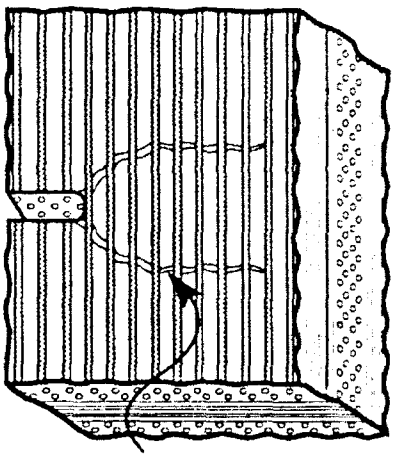

Matrix Cracks
Redistribute Stress

Class III

Shear Damage By Matrix Cracking

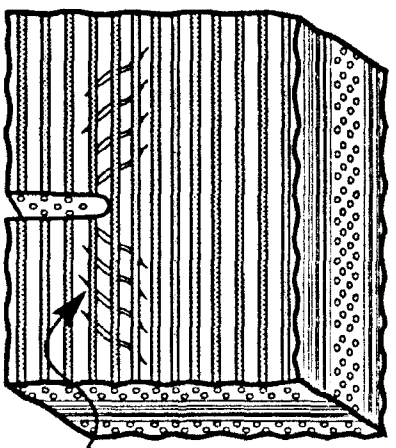

Shear Damage Zone
Redistributes Stress

Figure 15

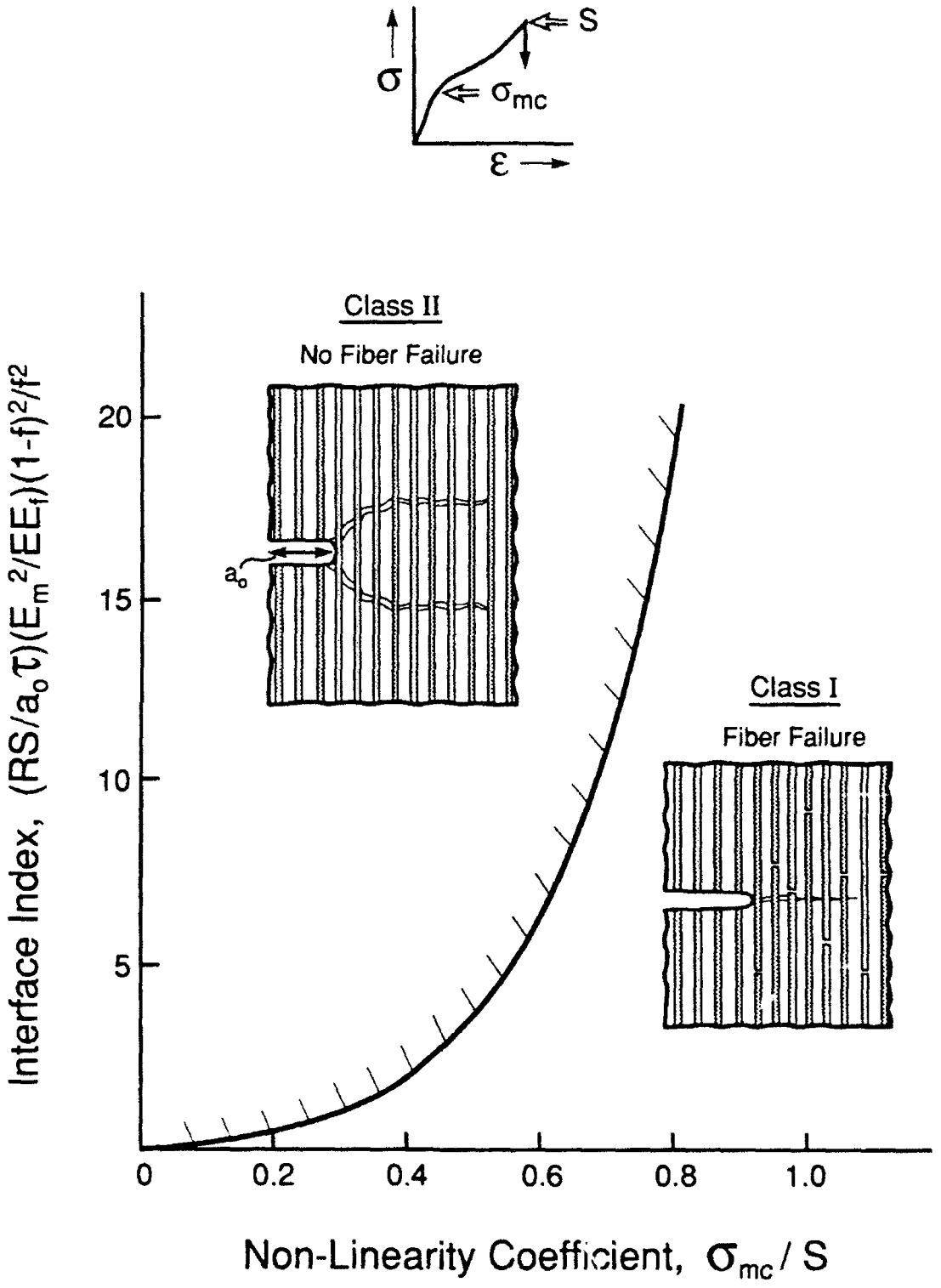
S
σ
σmc
ε
Class II
No Fiber Failure
a0
Class I
Fiber Failure
Interface Index, (RS/a0τ)(Em2/EEf)(1-f)2/f2
20
15
10
5
0
0.2
0.4
0.6
0.8
1.0
Non-Linearity Coefficient, σmc / S

Figure 16

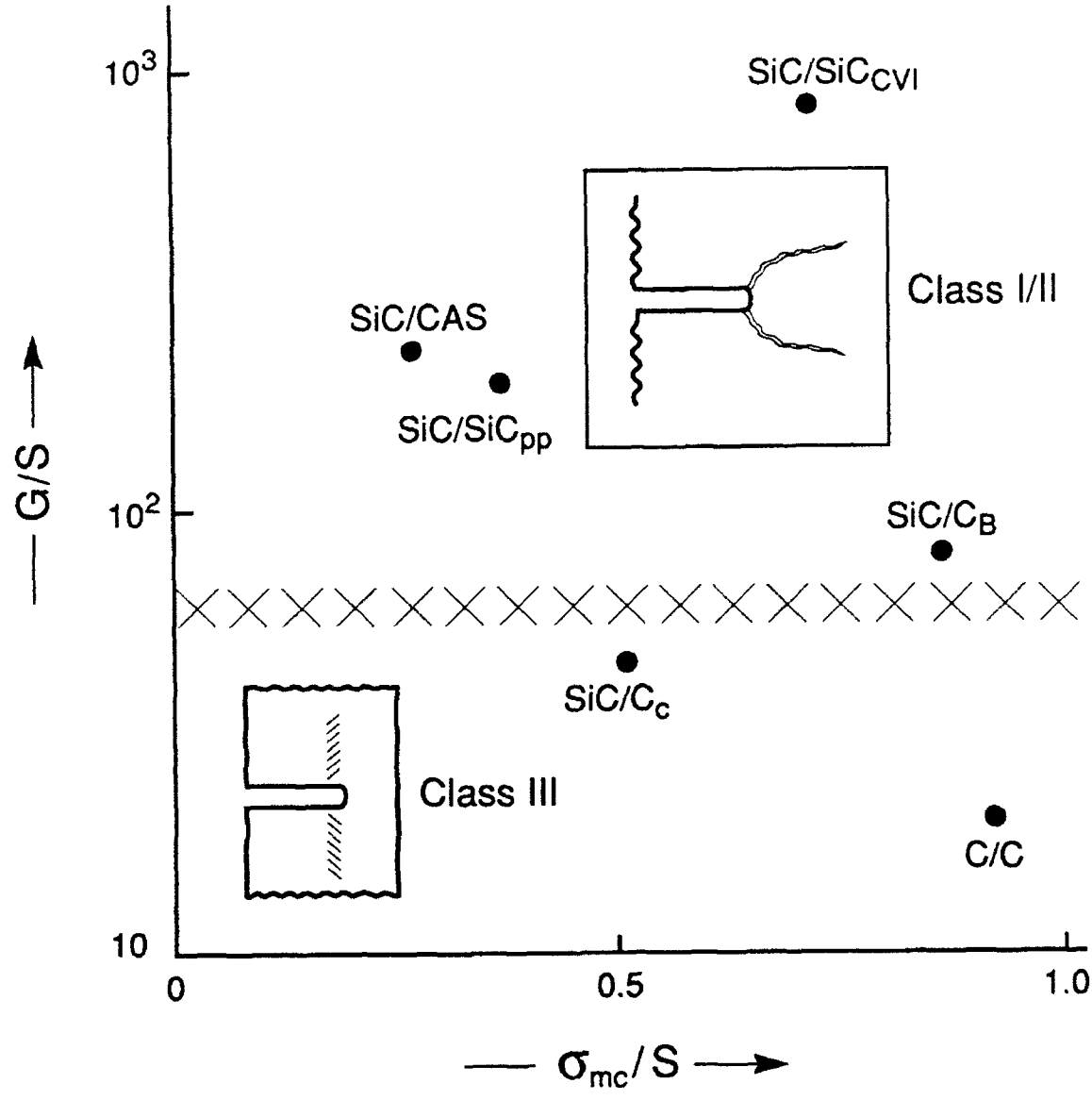
10^3
10^2
10
G/S
SiC/SiC$_{CVI}$
Class I/II
SiC/CAS
SiC/SiC$_{pp}$
SiC/C$_B$
SiC/C$_c$
Class III
C/C
0
0.5
1.0
σ_{mc}/S

Figure 17

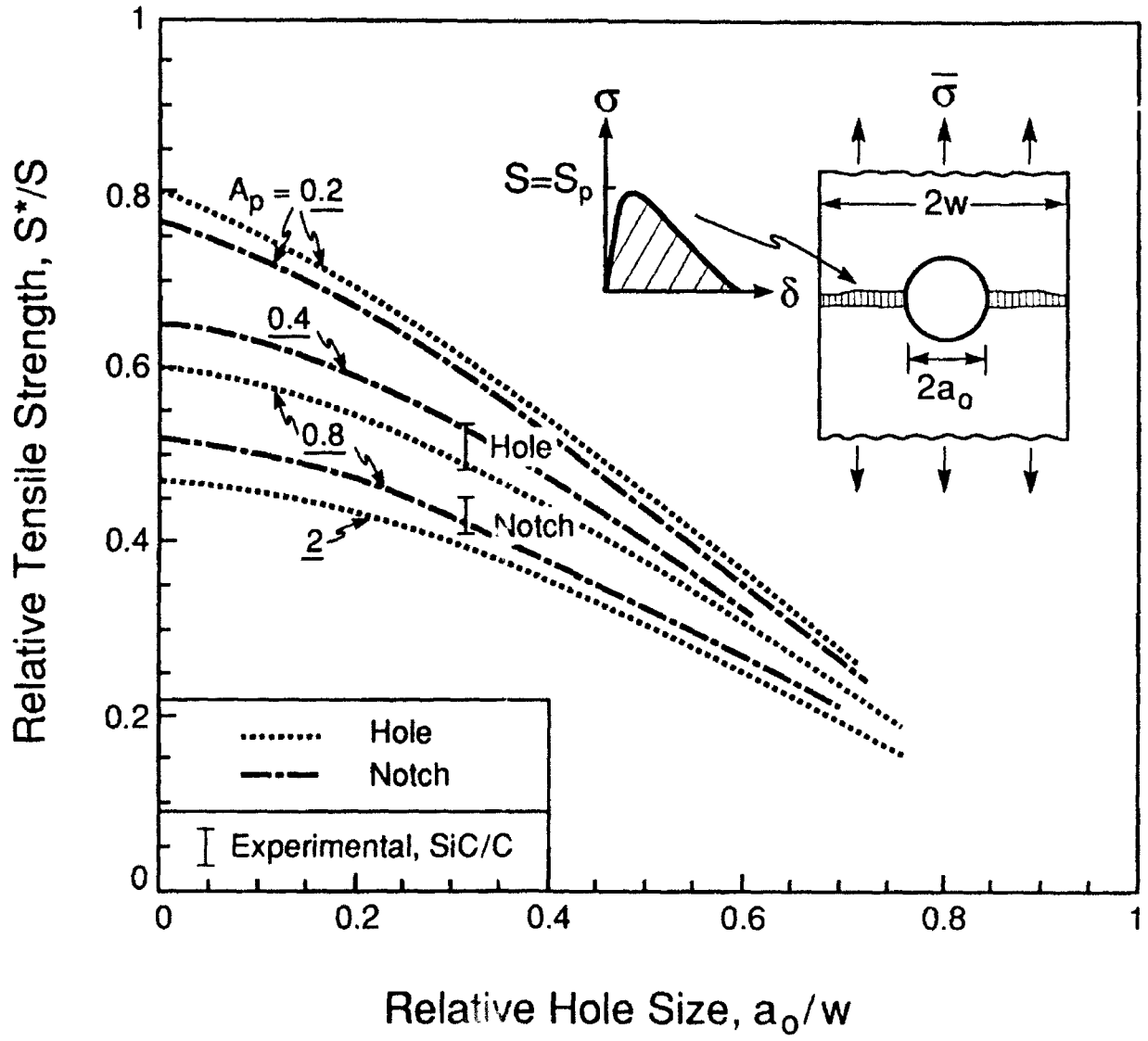
Relative Tensile Strength, S*/S
Relative Hole Size, a_o/w
A_p = 0.2
0.4
0.8
2
Hole
Notch
Hole
Notch
Experimental, SiC/C
σ
$\bar{\sigma}$
S=S_p
δ
2w
$2a_o$
0
0.2
0.4
0.6
0.8
1

Figure 18

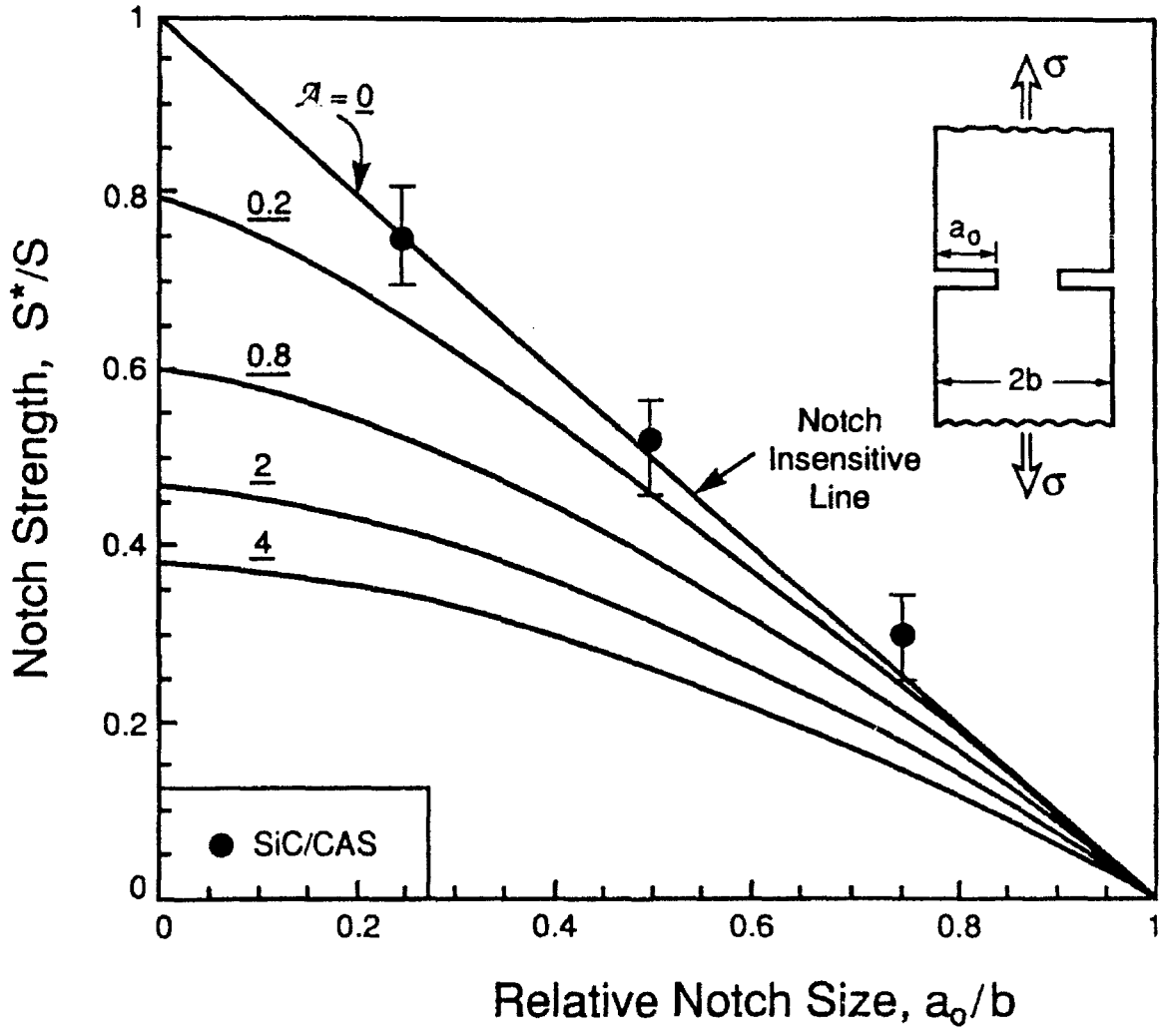
Notch Strength, S*/S
Relative Notch Size, a_o/b
$\mathcal{A} = 0$
0.2
0.8
2
4
Notch Insensitive Line
a_o
2b
σ
σ
SiC/CAS
0
0.2
0.4
0.6
0.8
1

Figure 19

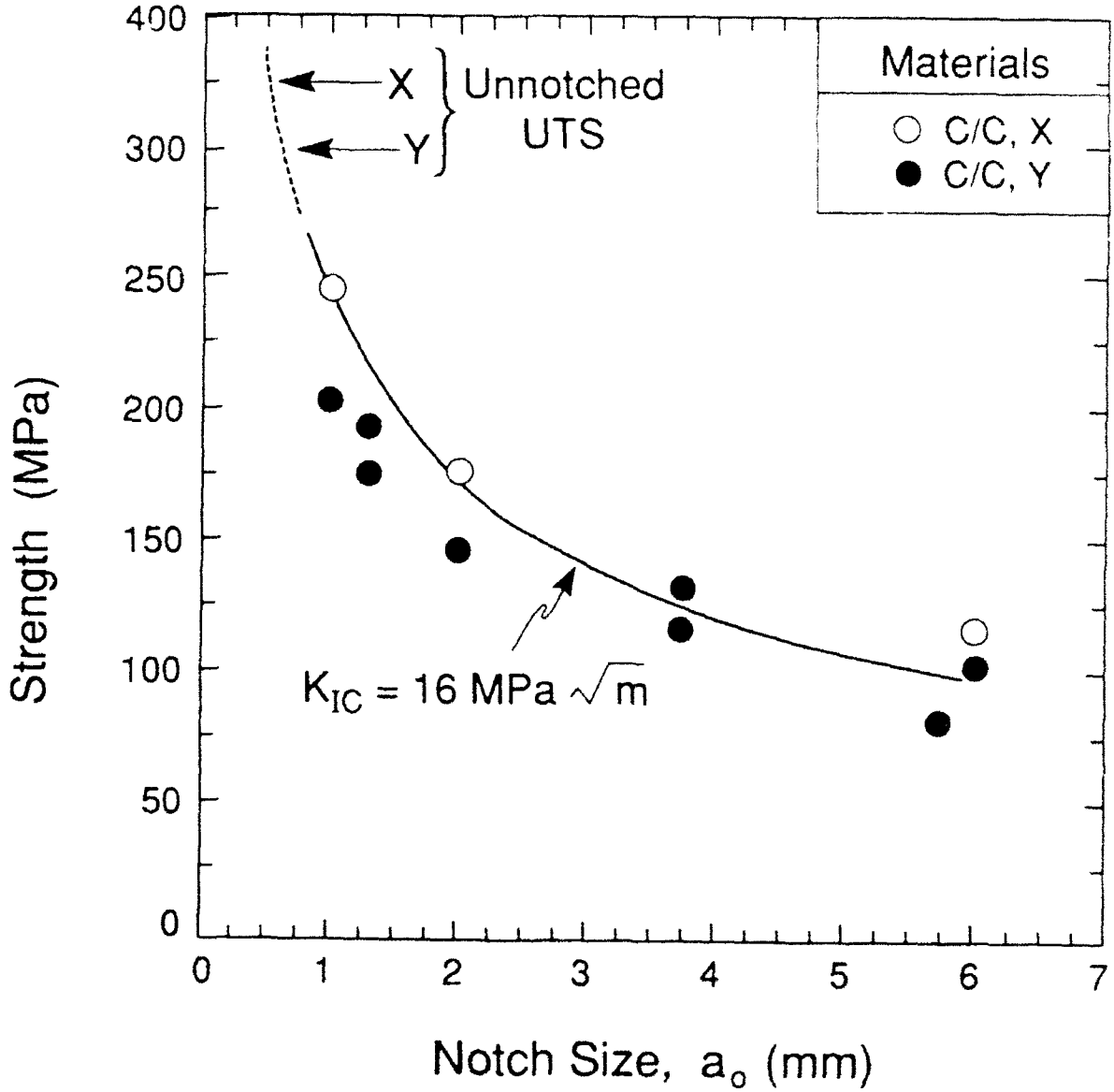
400
300
250
200
150
100
50
0
0
1
2
3
4
5
6
7
Strength (MPa)
Notch Size, a_o (mm)
X
Y
Unnotched
UTS
Materials
C/C, X
C/C, Y
K_{IC} = 16 MPa $\sqrt{m}$

Figure 20

MATERIALS

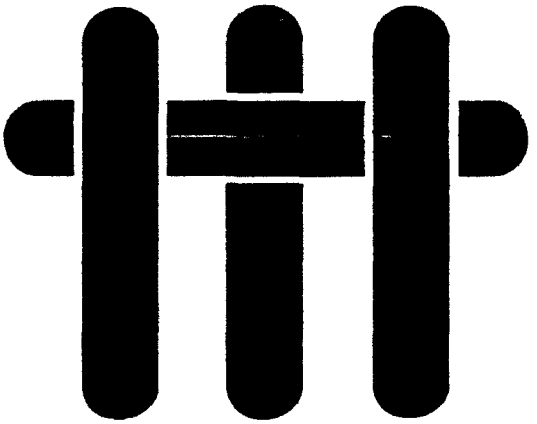

DAMAGE AND FAILURE IN UNIDIRECTIONAL CERAMIC-MATRIX COMPOSITES

by

D. S. Beyerle, S. M. Spearing, F. W. Zok and A. G. Evans
Materials Department
College of Engineering
University of California
Santa Barbara, California 93106

ms 6-4-92

ABSTRACT

A study of the mechanical characteristics of a unidirectional fiber-reinforced CAS matrix composite has been conducted. The properties have been related to the individual properties of the matrix, fibers and the interfaces, as well as the residual stress, using available models of matrix cracking and fiber fracture. Comparisons have been made with LAS matrix composites. Predictions of initial matrix cracking and of ultimate strength using the models are found to correlate well with the measured values. However, deficiencies have been noted in the ability of the models to predict the evolution of matrix cracks, plus associated changes in the modulus.

1. INTRODUCTION

The response of unidirectional ceramic matrix composites to loading in the longitudinal direction involves consideration of the properties of the fibers, the matrix and the interface *in situ* in the composite, as well as residual stresses caused by thermal expansion misfit. Present understanding is as follows. Most composites are reinforced with SiC (Nicalon) fibers with thin coatings of C on the fibers.[1-6] Such composites usually exhibit non-linearity prior to failure,[1,4-7] dominated by damage in the form of multiple matrix cracking. The non-linearity is manifest as a reduction of tensile modulus $\bar{E}$ with applied stress, σ, coupled with a permanent deformation, as well as changes in thermal diffusivity and thermal expansion coefficient. These effects can be important for structural applications, especially the damage that occurs in the vicinity of holes, notches and around attachments. Mechanism-based relationships between $\bar{E}$ and σ represent important properties of the composite. The ultimate tensile strength of the composite and its dependence on the properties of the fibers and fiber coatings *in situ* [8-10] constitutes an additional composite property.

Micromechanics models representing each of the above phenomena have been developed: matrix cracking,[11-14] failure[15] and debonding.[16] Such models provide valuable insight into the effects of the constituent and interface properties on the mechanical behavior of the composite. However, comparison with experiment, especially with regard to matrix cracking, has lead to contradictory conclusions.[5,7,17,18] The apparent discrepancies arise either from widely differing choices of the properties of the composite constituents (fiber, matrix, interface), *in situ* in the composite, or from differing assumptions about the flaw distributions in the matrix. A clarification of the issues is attempted in the present study by conducting an investigation of the properties of a unidirectional composite with a calcium alumina silicate (CAS) matrix, reinforced with Nicalon (SiC) fibers,[3] and comparing with results from the literature on a lithium

alumino silicate (LAS) matrix composite with the same fibers.[1,2] For this purpose, the status of the salient modelling efforts is briefly reviewed, in a manner that explicitly identifies the constituent and composite properties that require measurement. Then, measurements are made that enable comparison with the models.

2. MODELLING BACKGROUND

2.1 Interfaces

In general, composite interfaces are characterized by two parameters: a debond energy Γ_i and a sliding stress along the debonded interface, τ.[19] For most C coatings, Γ_i appears to be small[6] and will be neglected in the following summary. Also, in general, τ has a Coulomb friction component and varies as the matrix crack opens.[19] However, again the effect appears to be small for most ceramic matrix composites[6,20] and, in the following, τ is regarded as a constant.

2.2 Matrix Cracking

A fundamental notion in matrix cracking, first introduced by Aveston, Cooper and Kelly[11] (ACK), concerns the concept of steady-state, wherein the energy release rate for a single matrix crack $\mathcal{G}_o$ is *independent of matrix crack length* and given by[12,13]

$$\mathcal{G}_o = \frac{(\sigma + qE/E_m)^3 E_m^2 (1 - f)^2 R}{6\tau f^2 E_f E^2} \qquad (1)$$

where σ is the imposed stress, E is Young's modulus, f is the fiber volume fraction, R is the fiber radius, q is the residual axial stress in the matrix (positive being tensile) and the subscripts m and f refer to matrix and fiber, with $E = f E_f + (1 - f)E_m$. Steady-state

conditions apply provided that the initial flaws in the matrix, length a_o, *exceed* a critical value, a_c given by,[13,14]

$$a_c = \frac{1}{2} E_m \Gamma_m \left[\frac{(1-f)^2 R(1+\xi)}{\tau f^2 E_f} \right] \tag{2}$$

where $\xi = E_f f / E_m (1 - f)$ and Γ_m is the matrix fracture energy. When $a_o > a_c$, a *lower bound to the matrix cracking stress*, σ_o, is obtained by setting $\mathcal{G}_o$ to the matrix fracture resistance,[11,12]

$$\mathcal{G}_o = \Gamma_m (1 - f) \tag{3}$$

such that,

$$\sigma_o = \sigma_* - qE/E_m \tag{4}$$

where

$$\sigma_* = \left[\frac{6\tau\Gamma_m f^2 E_f E^2}{(1 - f) E_m^2 R} \right]^{1/3} \tag{5}$$

When $a_o < a_c$, $\mathcal{G} < \mathcal{G}_o$ and the cracking stress σ_c exceeds σ_o.[13,14]

The development of cracks at stresses above σ_o has aspects of both mechanics and stochastics. The mechanics considers the mutual interactions between well-developed cracks that affect the steady-state energy release rate.[21] Stochastics involves the distribution of matrix flaws having size $a_o \lesssim a_c$ and the resulting influence on crack evolution, through coupled effects of weakest link statistics and mechanics.[22,23]

A comprehensive model that includes all aspects of the mechanics and stochastics does not yet exist. However, the mechanics plus some simplified statistics addresses several of the important factors. An important governing quantity is the slip length, d, between matrix and fiber which in the presence of a steady-state matrix crack is given by,[4,21]

$$d/R = (\sigma + qE/E_m)E_m(1 - f)/2Ef\tau \tag{6a}$$

which has the reference value

$$d_o/R = \sigma_o E_m(1 - f)/2Ef\tau \tag{6b}$$

When the slip zones between neighboring cracks overlap, $\mathcal{G}$ for steady-state cracks differs from $\mathcal{G}_o$. The relationship between $\mathcal{G}$ and $\mathcal{G}_o$ is dictated by the *location of the neighboring cracks*. When a crack forms *midway* between two existing cracks with a separation 2ℓ, $\mathcal{G}$ is related to $\mathcal{G}_o$ by[21]

$$\mathcal{G}/\mathcal{G}_o = 4(\ell/2d)^3 \qquad \text{for } 0 \le \ell/d \le 1 \tag{7a}$$

and

$$\mathcal{G}/\mathcal{G}_o = 1 - 4(1 - \ell/2d)^3 \qquad \text{for } 1 \le \ell/d \le 2 \tag{7b}$$

Consequently, if matrix cracks develop in a strictly periodic manner, the evolution of the crack density with stress can be predicted by combining Eqns. (3), (6) and (7), leading to the result plotted in Fig. 1. In general, non-periodic crack locations exist. However, a similar trend in crack spacing is obtained by placing the steady-state cracks at spatially random locations relative to existing cracks, achieved by using a Monte

Carlo simulation [21](Fig. 1). These results indicate that the average crack spacing reaches a saturation value, $\bar{\ell} = 1.75 d_*$, when $\sigma/\sigma_* \geq 1.3$. This solution provides a relationship between the sliding stress and the saturation crack spacing (through Eqns. (5) and (6b)), given by;

$$\tau = 2.0\, R(1-f)\left(\Gamma_m E_f E_m / f E \bar{\ell}^3\right)^{1/2} \tag{8}$$

The actual evolution of matrix cracks would deviate from these predictions when the initial matrix flaws are smaller than a_c. The analysis of matrix cracking then relies on information about the size and spatial distribution of matrix flaws and on the mechanics of flaws smaller than a_c.[13,14] In general, the solution requires combined analysis of the initial flaw distribution and interaction with matrix cracks already formed. However, some useful results can be obtained by using the mechanics of non-interacting short cracks[13] with an extreme value matrix flaw size distribution.[22,23] The principal result arising from such analysis is that extensive matrix cracking is not predicted until stresses are *appreciably above* σ_0, as governed by the magnitude of the shape parameter for matrix flaws: a quantity related to the Weibull modulus, m. A schematic that combines the principal aspects of the above behaviors is presented in Fig. 2.

2.3 Residual Stresses

The residual stress q is governed by the misfit strain Ω between the fiber and the matrix. For matrix and fibers having the same Poisson's ratio, q is given by;[12]

$$q = \frac{\lambda_2 E_m E_f f \Omega}{\lambda_1 E(1-\nu)} \tag{9a}$$

where ν is the Poisson's ratio,

$$\lambda_1 = 1 - \frac{(1-2\nu)}{2(1-\nu)}(1 - E/E_f) \tag{9b}$$

and

$$\lambda_2 = (1 + E/E_f)/2 \tag{9c}$$

For $\nu = 0.3$ and for E/E_f representative of the present composite (Table I), $\lambda_1 = 0.9$ and $\lambda_2 = 0.85$. Similarly, the radial stress, p, at the fiber/matrix interface is[12]

$$p = -\frac{E_f(1-f)\Omega}{2\lambda_1(1-\nu)} \tag{10}$$

The interfacial sliding stress is expected to be influenced by both the sign and magnitude of p. When the misfit arises solely from thermal expansion differences, $\Omega = (\alpha_f - \alpha_m)\Delta T$, where α is the thermal expansion coefficient and ΔT is the temperature difference between softening and ambient.

The periodic matrix cracking is predicted to change the unloading (or reloading) modulus in accordance with,[17,23]

$$E/\bar{E} = S(\bar{\ell}/R) + RE_m^2(1-f)^2\Delta\sigma/4\bar{\ell}\tau E_f E f^2 \tag{11}$$

where S is an elastic compliance associated with the matrix cracks (of order 1 to 1.2) and $\Delta\sigma$ is the incremental reduction in stress used to measure the modulus.. The modulus thus decreases as the mean crack spacing increases and can be predicted by inserting measured crack spacings into Eqn. (11).

2.4 Fiber Fracture and Composite Ultimate Strength

The factors governing the ultimate strength of a fiber reinforced composite have been modelled using weakest link statistics.[9,10,15] The calculations assume that both the debond energy and sliding stress are small, such that the fibers are non-interacting, and that the matrix exhibits *multiple cracking* prior to composite failure. In this case, the matrix allows load transfer along a fiber from a fiber failure site, through the interfacial shear tractions, with global load sharing. As a result, fibers can experience multiple cracking along their length.‡ Since the load transfer is governed by τ, parameters such as the pullout length and the fiber strength can be explicitly linked with τ. Following this approach, the ultimate strength of the composite σ_u is predicted to be:[15]

$$\sigma_u = f S_c \left[\frac{2}{(m+2)}\right]^{1/(m+1)} \left[\frac{m+1}{m+2}\right] \tag{12}$$

where m is the Weibull shape parameter and S_c is a characteristic fiber strength,[9,15] which may be obtained *directly* from fracture mirror measurements.[10,15]

Another important result relates the mean fiber pullout length to the interfacial shear stress: [9,15]

$$\bar{h} = \lambda(m) R S_c / 4\tau \tag{13}$$

where $\lambda(m)$ takes a value close to unity for m>3. This expression gives an alternative means of estimating τ.

---

‡ This multiple fiber cracking phenomenon associated with the stresses carried by failed fiber causes the ultimate strength prediction to differ from that given by Cao *et al.*,[5] which ignores this factor.

2.5 Implications For Measurements

For CAS composites reinforced with Nicalon fibers, several constituent properties are relatively well known: including the elastic properties and expansion coefficients, as well as fiber radius and fiber volume fractions (Table I). The important constituent properties that require *independent* measurement are τ, Γ_m and q. In principle, q can be obtained from Eqn. (9), if the misfit strain Ω is known. However, ΔT is ill-defined and, in some cases, additional stresses may develop as a result of matrix crystallization.

Additional measurements needed to correlate experiment with theory include the matrix cracking stress and the crack spacing, both measured *in situ*. Moreover, measurements to be performed on fracture surfaces include fracture mirror radii[5,15] and fiber pull-out distributions.[10,15]

3. EXPERIMENTAL PROCEDURES

3.1 Testing

All experiments were conducted on a unidirectional laminate of CAS/Nicalon material provided by Corning.[3] Flexural specimens having dimensions 50 x 3 x 2.8 mm, (with the fibers oriented along the axis) were prepared by diamond machining. The tensile face and one side face were polished to facilitate the direct observation of matrix cracks. The tests were conducted in four-point bending with inner and outer spans of 20 and 40 mm, respectively. The bending fixture was located within an optical microscope, allowing high-resolution *in situ* observations of matrix cracking.

Tensile specimens were prepared by machining beams having dimensions 150 x 3 x 2.8 mm, followed by polishing. Aluminum tabs were bonded to the ends, to ensure even load transfer and to avoid crushing of the specimen. Strains were measured along a gauge length using an axial extensometer in contact with the specimen. Tests

were performed in a servohydraulic machine with hydraulic grips. Care was taken to eliminate bending; strain gauge measurements confirmed that this was largely achieved. Following mechanical testing, the specimens were examined in the optical microscope and scanning electron microscope (SEM). In some cases, tests were interrupted prior to failure and the specimens examined in the SEM. Several tests were performed with partial unloading ($\Delta\sigma$ = 25 MPa) conducted at discrete strain intervals, as needed to determine the change in composite unloading modulus $\bar{E}$ as a function of strain. There is a corresponding permanent strain, but this was not measured A few tensile tests were conducted with two faces of the specimen having a *matrix-only layer* on the outside, ~ 30 μm thick. In all cases, loading durations were short (< 10s) to minimize the influence of stress corrosion on the matrix cracking behavior. Time dependent effects will be reported in a subsequent publication.[23]

The matrix fracture energy was determined by testing chevron-notched flexure specimens of unreinforced CAS. The load/displacement behavior was monitored during testing to determine whether there was stable crack growth prior to catastrophic failure. Tests were conducted rapidly (failure time < 10s) to minimize the effect of stress corrosion.

3.2 Observations

The onset and evolution of matrix cracks were studied by conducting experiments on specimens with polished surfaces *in situ* within an optical microscope. Such measurements were made under load, since some cracks were found to close upon unloading, making them essentially invisible in the optical microscope (Fig. 3). Edge replicates were taken during tensile tests, for the same purpose. Initial cracking was also monitored using an acoustic emission transducer attached to the specimen. *In situ* measurements were verified by *ex situ* measurements performed both in optical and

scanning electron (SEM) microscopes. The SEM was also used to measure fracture mirror radii and fiber pull-out lengths.

3.3 Residual Stresses

Residual stresses were measured using a dissolution technique described elsewhere.[24] Long, thin strips were cut from the composite parallel to the fiber direction. The strips were polished and mounted on a plate parallel to a steel reference strip. Surface features were photographed at high magnification, and their positions relative to marks on the steel strip were recorded. The ends of the composite strip were masked with silicon rubber and the matrix dissolved using a dilute HF solution. The length, w, of the dissolved section was varied between 40 and 120 mm. The masks were subsequently removed and the relative positions of the same surface features were again documented. The displacement, δ, of the masked section was obtained from measurements on the micrographs. Provided that w is much larger than the zero-load slip length, the residual stress, q, is related to δ by:

$$q = \delta E_f f / w(1-f) \tag{14}$$

4. MECHANICAL BEHAVIOR

Flexural tests gave load/displacement curves typical of those reported elsewhere.[4] The loads, when converted into a *nominal* maximum tensile stress, resulted in stress/displacement curves with a non-linearity at about 200 MPa and an ultimate strength (modulus of rupture) of about 650 MPa. Optical observations during testing indicated that matrix cracks first developed on the tensile face at stresses between 130 and 150 MPa, consistent with the value ascertained for a similar material using acoustic emission.[8] At higher stresses, additional matrix cracks formed, until a saturation

spacing was attained. The distribution of crack spacing at saturation is depicted in Fig. 4, with the average value being 103 ± 15 μm. Final failure occurred by delamination in the region between the inner and outer loading points, as also observed in the LAS/Nicalon composites.[1,2,4]

Tensile stress/strain curves had the features illustrated in Fig. 5a. Based on 6 tests, the non-linearity was found to occur at stresses in the range 150–200 MPa, with an ultimate strength of 430 ± 30 MPa at a tensile strain of ~ 0.8%. *In situ* observations made with an optical telescope confirmed that the onset of matrix cracking again occurred in the range 130–150 MPa. Acoustic emission events first occurred within a similar range (Fig. 5b). Partial unloading to obtain information about changes in modulus provided the results summarized in Fig. 6. These results are in broad agreement with results reported by Pryce and Smith.[17] Corresponding measurements of the change in crack density with applied stress are plotted on Fig. 7.

Tests conducted on specimens with a thin matrix-only outer layer gave essentially the same stress-strain curves. However, *in situ* observations indicated that cracks first formed in the surface layer at stresses as low as 50 MPa. Such measurements demonstrate the important role of the *local* fiber content on matrix cracking and exemplify the need for removing the matrix-rich layer prior to testing.

Matrix dissolution experiments resulted in the displacements plotted on Fig. 8. Combining the measurements with Eqn. (13) gives the residual stress in the matrix, $q = 89 \pm 13$ MPa.

Chevron-notched flexure tests conducted on 10 specimens of the unreinforced matrix material yielded a matrix fracture energy, $\Gamma_m = 25 \pm 2\ Jm^{-2}$. Non-linearity in the load/displacement plot prior to the load maximum indicated that stable crack growth had occurred before catastrophic failure.

5. OBSERVATIONS

The material exhibited extensive fiber pull-out during failure (Fig. 9) with distributed fiber failure sites and no obvious clustering. A typical distribution of fiber pull-out lengths is shown in Fig. 10. The average pull-out length, $\bar{h}$, lies in the range 250–350 μm, which is much smaller than that found for LAS matrix material[4,5] ($\bar{h} \approx 2$ mm). Fracture mirror radii converted into the *in situ* fiber strength parameter, S_c, are plotted on Fig. 11, giving the parameters, m = 3.6 and S_c = 2.0 GPa. Dissolution of the matrix in a specimen loaded to 400 MPa revealed a substantial number of broken fibers, with the fracture sites distributed evenly throughout the composite.

6. ASSESSMENT OF THE RESULTS

6.1 Constituent Properties

Values of the interface sliding stress can be inferred from the various methods described in Section 2, coupled with the experimental measurements. The crack spacing and matrix toughness measurements in conjunction with Eqn. (8) yield the estimate τ = 25–28 MPa. The values inferred from the fiber pull-out lengths, obtained using Eqn. (13), are somewhat lower, being ~10–15 MPa. Evidently, the range of values obtained through the two methods is broad (10–28 MPa). This is, perhaps, a result of both the underlying assumptions in the micromechanical models and uncertainties in the experimental measurements. Similar trends have also been observed in the LAS/SiC composites, wherein τ has been estimated to be in the range of 1–3 MPa[5]. The relative values of τ in the CAS and LAS matrix composites (Table 1) partially reflect the different thermal expansion mismatches of the two materials. In the LAS material, the radial stress, p, is tensile and consequently, τ is low. Conversely, in the CAS material, p is compressive and thus, τ is relatively high.

The matrix fracture energy, $\Gamma_m \approx 25\ Jm^{-2}$, is comparable to literature values for monolithic glass ceramic matrices[25] ($\Gamma_m = 15–30\ Jm^{-2}$). Other researchers have assumed widely differing values, leading to conclusions that also differ from those presented below. At one extreme, Kim and Pagano[7] assumed that $\Gamma_m \equiv 2\gamma = 80\ Jm^{-2}$ and concluded that matrix cracking is observed at a stress below the ACK lower bound. At another extreme, Pryce and Smith[17] used $\Gamma_m = 6\ Jm^{-2}$, and propose that matrix cracks first form at stresses above the ACK lower bound.

6.2 Matrix Cracking

The experimental measurements of matrix cracking can be compared with deterministic cracking stress predicted using steady-state mechanics. The lower bound ACK result is first computed as a function of the interface sliding stress (Fig. 12). Superposition of the stress range at which the first matrix cracks have been detected, both in this study and that of Kim and Pagano,[7] reveals that the ACK prediction is in accord with the measurements, provided that τ is chosen to be in the range 10–15 MPa. This is consistent with the lower end of the values inferred from the measurement techniques described above. The model also correctly identifies the effect of residual stress, as manifest in the difference in matrix cracking stresses of the CAS and LAS matrix composites.

The evolution of matrix cracks at stresses above the first cracking stress can be addressed by predicting the change in modulus, $\bar{E}$. This is done in a consistent manner by selecting the magnitude of τ that gives best agreement with the first cracking measurements ($\tau = 10–15$ MPa, Fig. 12) and using this value throughout. Comparison with measured values has two steps: i) the change in crack density with stress is compared with predictions based on steady-state mechanics (Fig. 1), ii) the measured crack densities (Fig. 7) are used with Eqn. (11) to predict $\bar{E}/E$. In the first step, insight regarding the evolution in crack spacing is obtained by superposing the crack density

predictions from Fig. 1 onto the experimental results (Fig. 7). It is apparent that the abrupt increase in crack density at $\sigma/\sigma_* = 1$, predicted by the mechanics model, based on steady-state cracks, does not happen. Instead, the results are qualitatively consistent with Fig. 2, indicative of a majority of matrix flaws having size smaller than the critical size a_c needed for steady-state conditions to apply. Complete quantitative results for matrix cracking in this flaw size regime are not yet available.[22,23] Further interpretation of matrix crack evolution awaits these models and emphasizes their importance to the rigorous prediction of matrix crack evolution. Nevertheless, it is apparent that one important feature, the saturation crack density, is predicted with reasonably accuracy by the model.

In the second step, the modulus changes predicted by inserting the *measured* crack densities (Fig. 7) into Eqns. (11) are compared with experiments on Fig. 6. The comparison indicates that the model slightly underestimates the modulus reduction for the same range of τ. This discrepancty is believed to be due to fiber failure[26]: an effect yet to be incorporated into the model.

6.3 Ultimate Strength

Based on the *in situ* strength parameter, $S_c = 2.0$ GPa and the shape parameter, $m = 3.6$, the predicted ultimate strength (Eqn. 11) is $\sigma_u = 480$ MPa, compared with a measured values of 430 ± 30 MPa. Values measured by Kim and Pagano[7] (505 MPa) and Pryce and Smith[17] (400 MPa) on this material are within the range of the present measurements and predictions.‡ The reasonable agreement suggests that the assumptions inherent in the non-interacting fiber failure model are appropriate for this composite. This result is further supported by the observation of evenly distributed fiber failure sites prior to composite failure. The magnitudes of S_c and m can also be

‡ The difference may be related to either batch to batch variation reflected in different fiber strengths, S_c, or to time-dependent effects.

used to evaluate the bundle strength S_b of the fibers within the composite.[15] For a 25 mm gauge length: $S_b \approx 0.42$ GPa. Comparison with the bundle strength of *pristine* Nicalon fibers at the same gauge length[27] ($S_b \approx 1.8$ GPa) suggests that significant degradation of the fibers has occurred during processing.

7. CONCLUDING REMARKS

Some of the mechanical properties of a unidirectional CAS matrix composite reinforced with Nicalon fibers, such as the initial matrix cracking stress and ultimate strength, appear to be consistent with available models and can be predicted with good accuracy, provided that the appropriate properties of the interface, the matrix and the fibers, *in situ* in the composite, as well as the residual stress, are taken into account. A particularly important feature is the existence of a *tensile* longitudinal residual stress in the matrix. This residual stress lowers the matrix cracking stress relative to that found for other matrices, such as LAS. Moreover, the *compressive* radial residual stress at the interface results in a high interface sliding stress, being almost an order of magnitude higher than the value in the LAS material.

The evolution in crack density with stress, above initial cracking, is not accurately predictable from available models, except for the saturation crack density, which seems to be reasonably well described. Consequently, it is not yet possible to predict changes in modulus $\bar{E}$ with applied stress. Nevertheless, formulae that relate $\bar{E}$ to stress, σ, subject to *independent* information about the crack density have reasonable applicability. Three issues are highlighted for further research. i) The need to address initial matrix flaws smaller than the steady-state critical size in matrix cracking models. Such activities are in progress,[22,23,27] based on the mechanics of short matrix cracks coupled with distributions of matrix flaws, using extreme value statistics. ii) The application to matrix cracking problems of interface models[19] more complex than constant τ. iii) The

effect of fiber failure on modulus reduction, particularly at stresses approaching the fiber bundle strength.[26] Further interpretation and analysis await these results.

ACKNOWLEDGEMENTS

This work was supported by the Defense Advanced Research Projects Agency through the University Research Initiative under ONR contract N-00014086-K-0753. The authors would like to thank Dr. K. Chyung for supplying the test material and for useful discussions.

TABLE I

Properties of CAS Matrix Composites Compared with LAS

Property		CAS	LAS
Fiber Volume Fraction, f		0.37[a]	0.4–0.5[b]
Matrix Modulus, E_m (GPa)		97[a]	86[b]
Matrix Thermal Expansion Coefficient, α_m ($10^6 C^{-1}$)		5[a]	1[b]
Sliding Stress τ (MPa)		10–15 (Eqn 4 and 5) 10–15 (Eqn 13) 25–28 (Eqn 8)	1–3[b]
Residual Stresses	p(MPa)	– 65	20[b]
	q(MPa)	89	– 50[b]
Matrix Cracking Stress, σ_o (MPa)		130–150	280–300[b]
Matrix Fracture Energy, Γ_m (J/m^2)		25	20–30

Other Salient Properties of CAS Matrix Composite Reinforced With Nicalon Fibers

$R = 7.5\ \mu m$, $\alpha_f \approx 4 \times 10^{-6}\ C^{-1}$, $E_f \approx 200$ GPa

a. K. Chyung, Corning Labs

b. Reference [5]

REFERENCES

[1] K. M. Prewo and J. J. Brennan, "Silicon Carbide-Fiber-Reinforced Glass-Ceramic Matrix Composites Exhibiting High Strength and Toughness," *J. Mater. Sci.*, **17**, 1201–206 (1982).

[2] K. M. Prewo, "Tension and Flexural Strength of Silicon Carbide Fiber-Reinforced Glass Ceramics," *J. Mater. Sci.*, **21**, 3590–600 (1986).

[3] K. Chyung, U.S. Patent 4,615,987 (7 Oct., 1986).

[4] D.B. Marshall and A.G. Evans, "Failure Mechanisms in Ceramic Fiber/Ceramic Matrix Composites," *J. Am. Ceram. Soc.*, **68[5]** 225–34 (1985).

[5] H.C. Cao, E. Bischoff, O. Sbaizero, M. Rühle A.G. Evans, D.B. Marshall and J.J. Brennan, "Effect of Interfaces on the Properties of Fiber-Reinforced Ceramics," *J. Am. Ceram. Soc.*, **73[6]** 1691–99 (1990).

[6] A.G. Evans and D.B. Marshall, "The Mechanical Behavior of Ceramic Matrix Composites," *Acta Metall.*, **37[10]** 2567–83 (1989).

[7] R.Y. Kim and N. Pagano, "Crack Initiation in Unidirectional Brittle Matrix Composites," *J. Am. Ceram. Soc.*, 74**[5]** 1082–90 (1991).

[8] J.J. Brennan, "Interfacial Studies of Chemical Vapor Infiltrated Ceramic Matrix Composite," *Mat. Sci and Engineering*. **A126** 203–23 (1990).

[9] M.D. Thouless and A.G. Evans, "Effects of Pullout on the Mechanical Properties of Ceramic Matrix Composites," *Acta Metall.*, **36[3]** 517–22 (1988).

[10] M.D. Thouless, O. Sbaizero, L.S. Sigl and A.G. Evans, "Effect of Interface Mechanical Properties on Pullout in SiC-Fiber-Reinforced Lithium Aluminum Silicate Glass Ceramic," *J. Am. Ceram. Soc.*, **72[4]** 525–32 (1989).

[11] J. Aveston, G.A. Cooper and A. Kelly, "Single and Multiple Fracture in the Properties of Fiber Composites," *The Properties of Fiber Composites, IPC*, (1971).

[12] B. Budiansky, J.W. Hutchinson and A.G. Evans, "Matrix Fracture in Fiber-Reinforced Ceramics," *J. Mech. Phys. Solids*, **34[2]** 164–189 (1986).

[13] D.B. Marshall, B.N. Cox and A.G. Evans, "The Mechanics of Matrix Cracking in Brittle Matrix Fiber Composites," *Acta Metall.*, **33[11]** 2013–21 (1985).

[14] L.N. McCartney, "Mechanics of Matrix Cracking in Brittle Matrix Fiber-Reinforced Composites," *Proc. Roy. Soc.*, Series A—Mathematical and Physical Sciences, **409[1837]** 329–50 (1987).

[15] W.A. Curtin, "Theory of Mechanical Properties of Ceramic-Matrix Composites," *J. Am. Ceram. Soc.*, **74[11]** 2837–45 (1991).

[16] M.-Y. He and J.W. Hutchinson, "Crack Deflection at an Interface Between Dissimilar Elastic Materials," *Intl. Jnl. Solids Structures*, **25**, 1053–67 (1989).

[17] A. Pryce and P. Smith, "Modelling the Stress/Strain Behaviour of Unidirectional Ceramic Matrix Composite Laminates," submitted to *J. Mater. Sci.*, (1991).

[18] R.N. Singh, "Fiber-Matrix Interfacial Characteristics in a Fiber-Reinforced Ceramic Matrix Composite," *J. Am. Ceram. Soc.*, **72[9]** 1764–67 (1989)

[19] J.W. Hutchinson and H.M. Jensen, "Models of Fiber Debonding and Pullout in Brittle Composites with Friction," *Mech. Mater.* **9**, 139–63 (1990)

[20] D.B. Marshall and W. Oliver, "Measurement of Interfacial Mechanical Properties in Fiber-Reinforced Ceramic Composites," *J. Am. Ceram. Soc.*, **70**[8] 542–48 (1987).

[21] F.W. Zok and S.M. Spearing, "Matrix Crack Spacing in Brittle Matrix Composites," *Acta Metall. Mater.*, to be published (1992).

[22] W.A. Curtin, "The Tough to Brittle Transition in Brittle Matrix Composites," to be published.

[23] S.M. Spearing, F.W. Zok and A.G. Evans, "Stress Corrosion Cracking in a Unidirectional Ceramic Matrix Composite," to be published.

[24] B.N. Cox, M.R. James, D.B. Marshall and R.C. Addison, Jr., "Determination of Residual Stresses in Thin Sheet Titanium Aluminide Composites," *Metall. Trans.*, **21A**, 2701–07 (1990).

[25] B. Pletka and S.M. Weiderhorn, "Subcritical Crack Growth in Glass Ceramics," *Fracture Mechanics of Ceramics* (Ed. R.C. Bradt *et al.*) Plenum, NY, 745–59 (1983).

[26] F. Hild, J.M. Domergue, F.A. Leckie and A.G. Evans, "Tensile and Flexural Ultimate Strength of Fiber-Reinforced Ceramic-Matrix Composites," *Intl. Jnl. Solids Structures*, in press (1992).

[27] G. Simon and A.R. Bunsell, "Mechanical and Structural Characterization of Nicalon Silicon Carbide Fiber, *J. Mater. Sci.*, **19**, 3649–57 (1984).

[28] S.M. Spearing and F.W. Zok, "Stochastic Aspects of Matrix Cracking in Brittle Matrix Composites," to be published.

FIGURE CAPTIONS

Fig. 1. Prediction of the evolution of crack density with increasing stress, for periodic and non-periodic crack spacings.

Fig. 2. Schematic of crack densities with stress based on combined mechanics and stochastics.

Fig. 3. (a) Optical micrograph of matrix cracks on the tensile surface of a bend specimen at a nominal stress of 350 MPa.
(b) Micrograph of the same region after unloading.

Fig. 4. Histogram of matrix crack spacings measured under load.

Fig. 5. (a) A tensile stress-strain curve indicating the unloading modulus and the permanent strain.
(b) A corresponding acoustic emission curve.

Fig. 6. Unloading modulus as a function of applied stress obtained from uniaxial tension tests. The model predictions are obtained by inserting the measured crack densities (Fig. 7) into Eqns (11).

Fig. 7. Change in crack density, $R/\bar{\ell}$, with applied stress, σ. Also shown are predicted curves obtained from Fig. 1

Fig. 8. Matrix residual stress measurements showing the displacement of the masked composite as a function of the length of the dissolved region.

Fig. 9. Tensile fracture surfaces showing fiber pull-out.

Fig. 10. A typical distribution of fiber pullout lengths from a tensile fracture surface.

Fig. 11. *In situ* fiber strength distribution obtained from fracture mirror measurements.

Fig. 12. The effect of interface sliding stress on the lower bound matrix cracking stress, calculated using Eqns. (4) and (5). Also superposed, as shaded rectangles, are the experimentally measured ranges of first matrix cracking stresses and sliding stresses for both the CAS and LAS matrix composites.

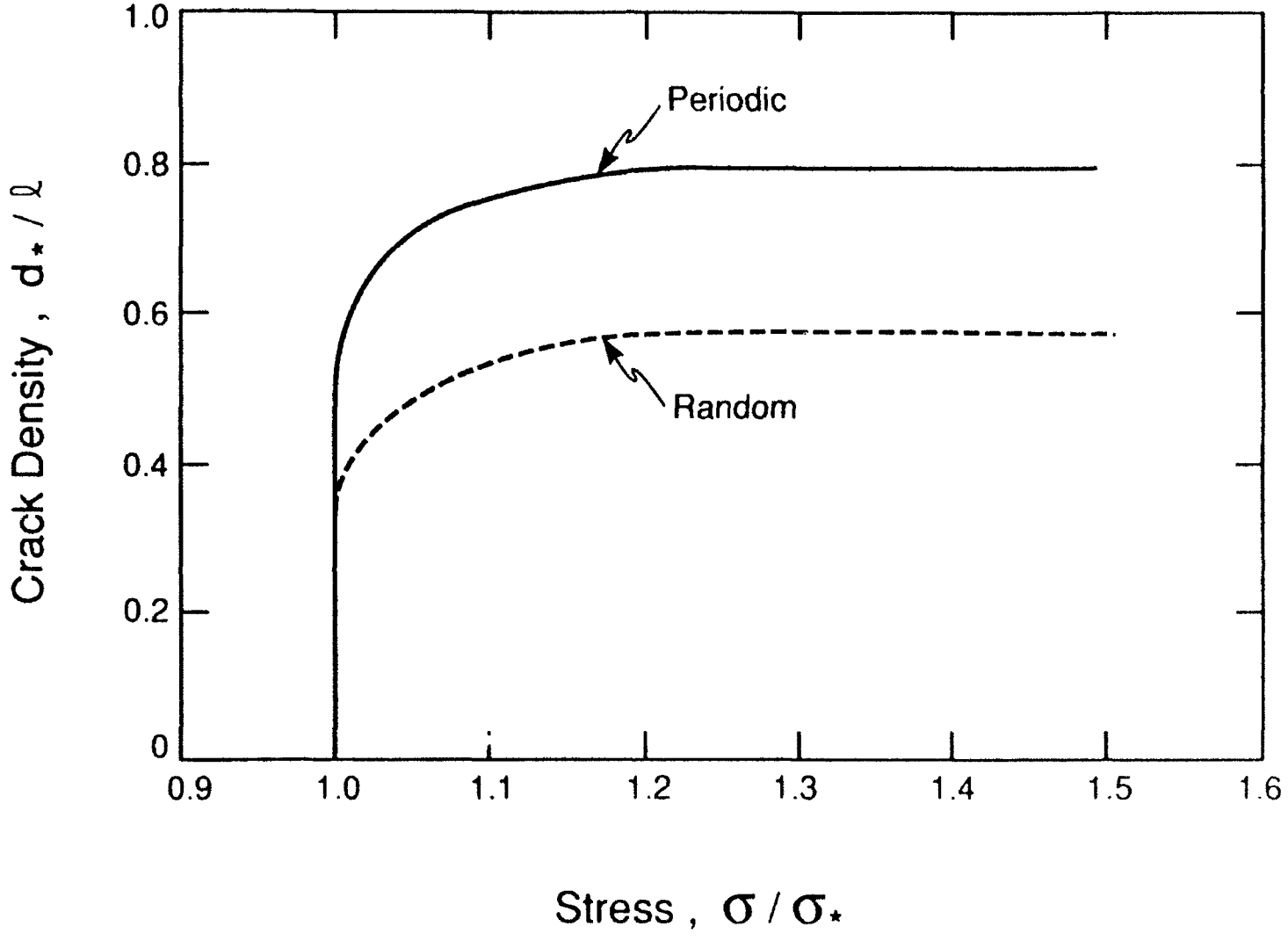

Fig. 1. Prediction of the evolution of crack density with increasing stress, for periodic and non-periodic crack spacings.

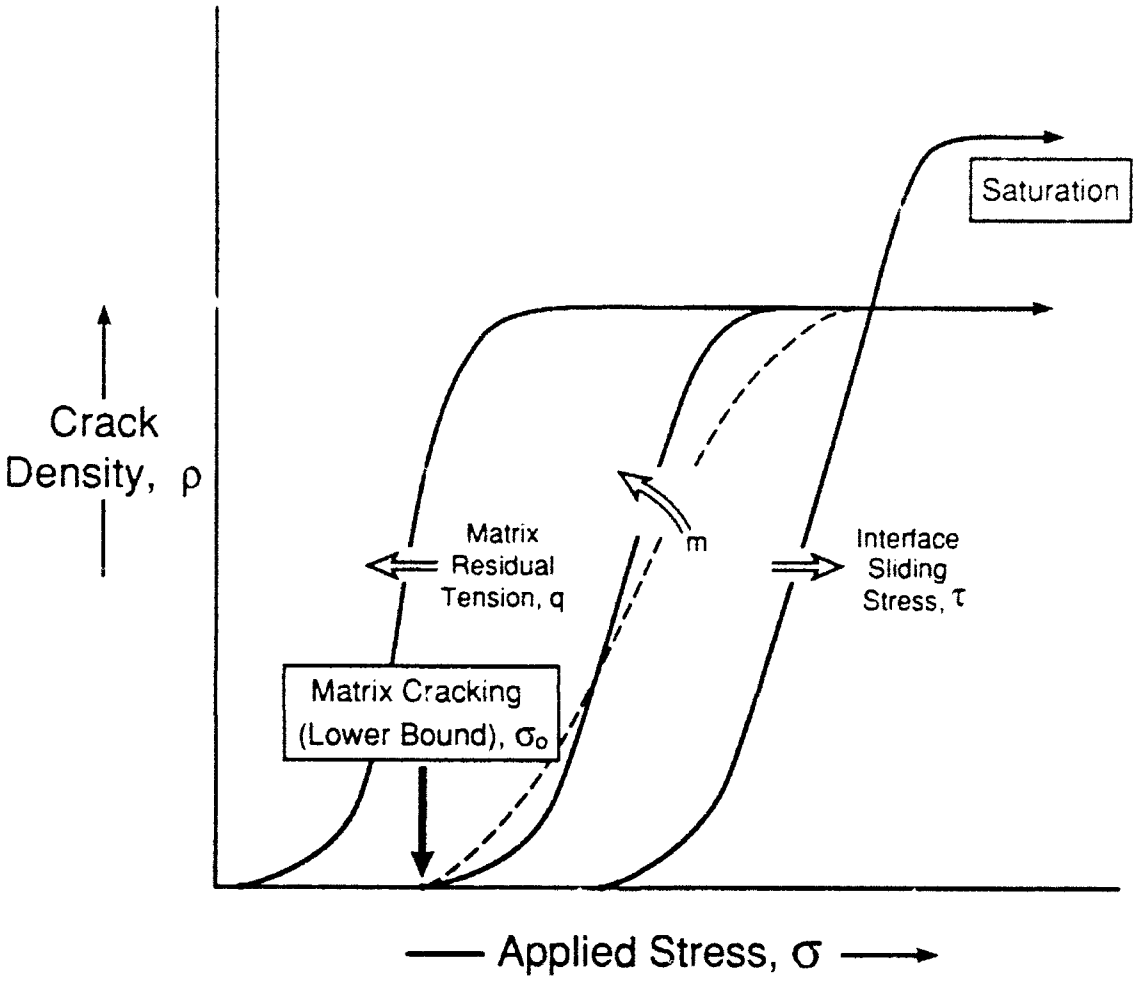

Fig. 2. Schematic of crack densities with stress based on combined mechanics and stochastics.

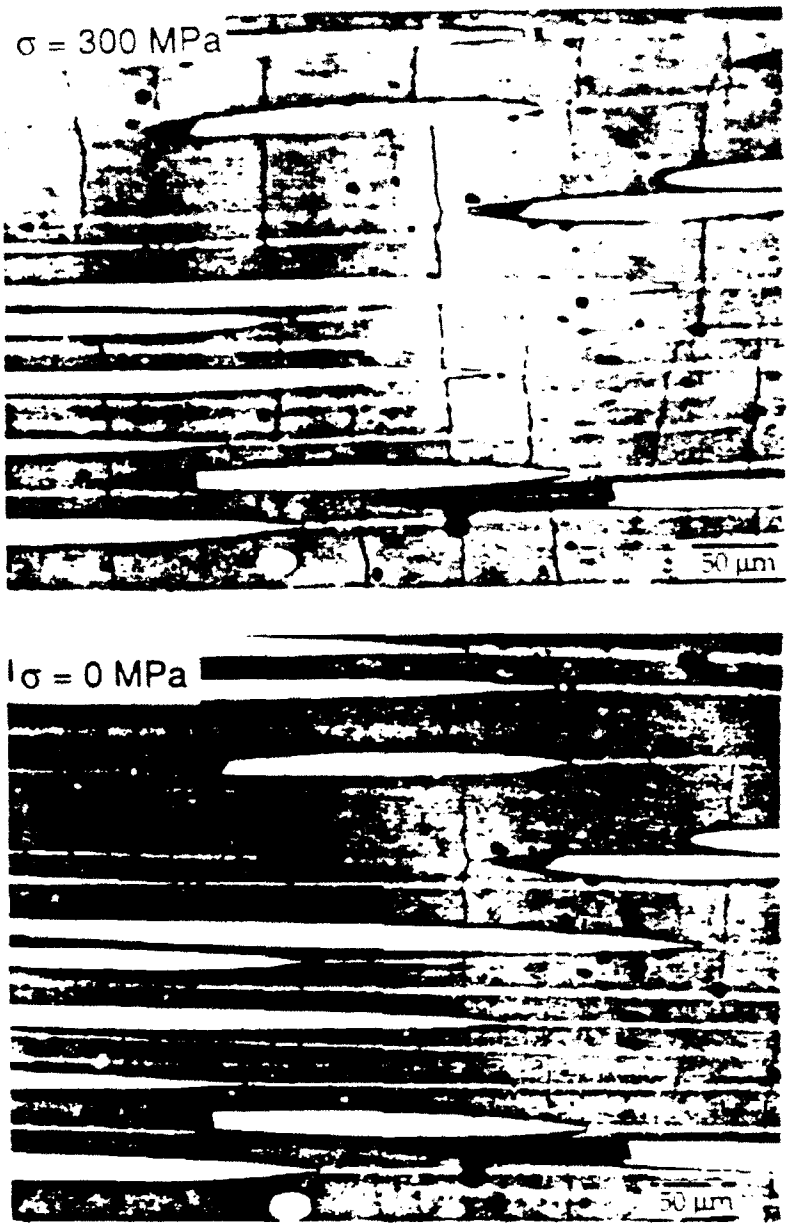

Fig 3. (a) Optical micrograph of matrix cracks on the tensile surface of a bend specimen at a nominal stress of 300 MPa.
(b) Micrograph of same region after unloading

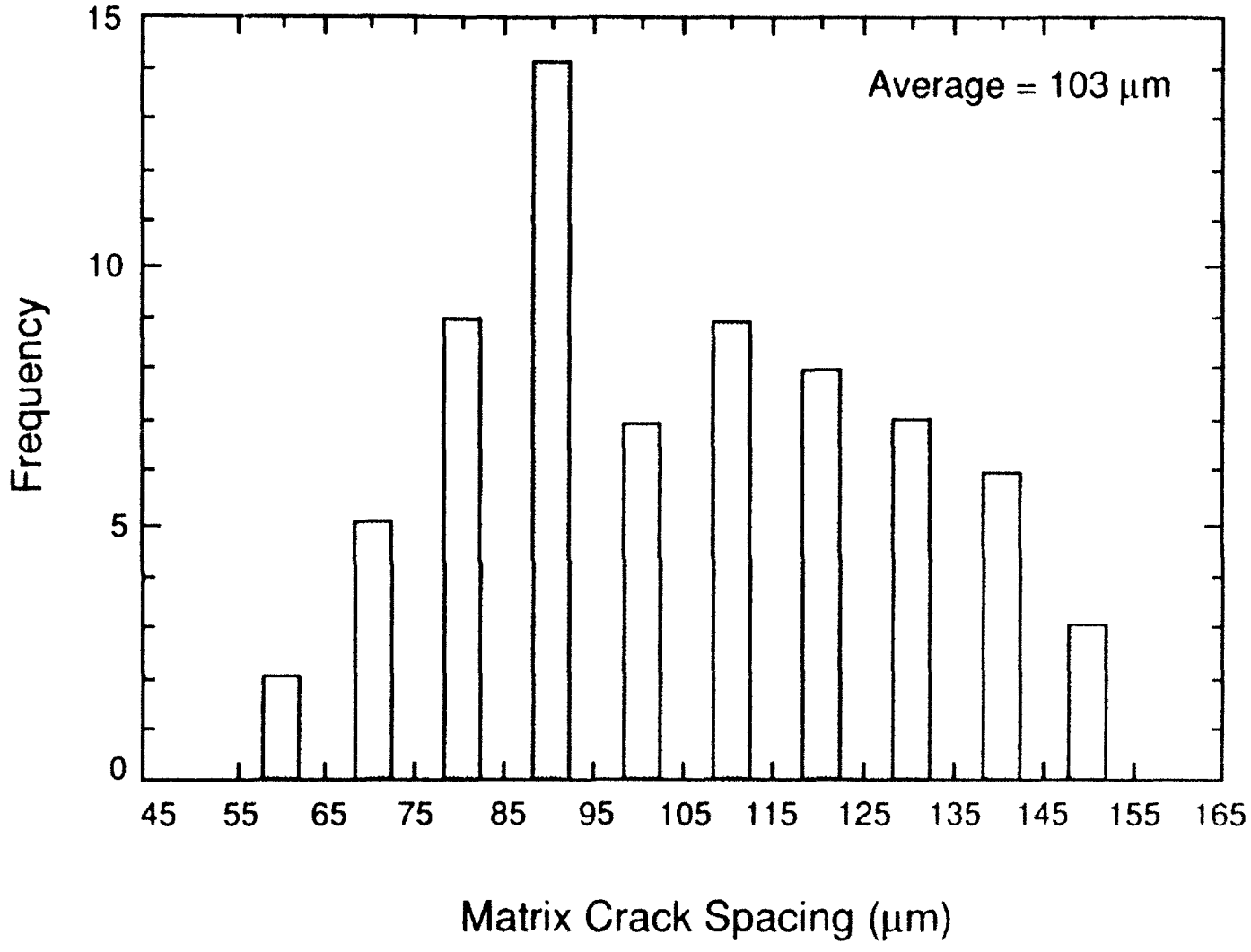

Fig. 4. Histogram of matrix crack spacings measured under load.

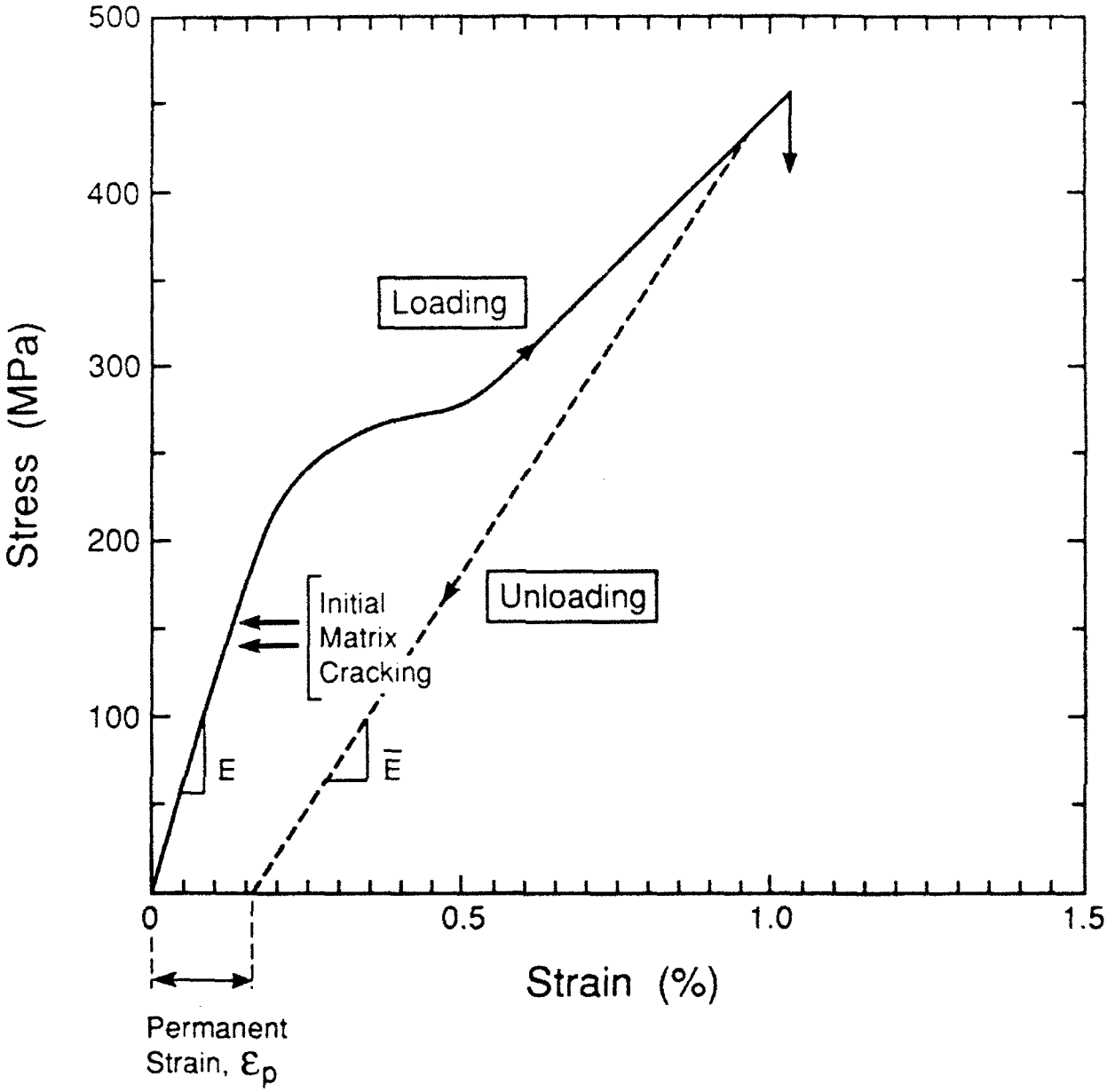

Fig. 5. (a) A tensile stress-strain curve indicating the unloading modulus and the permanent strain.

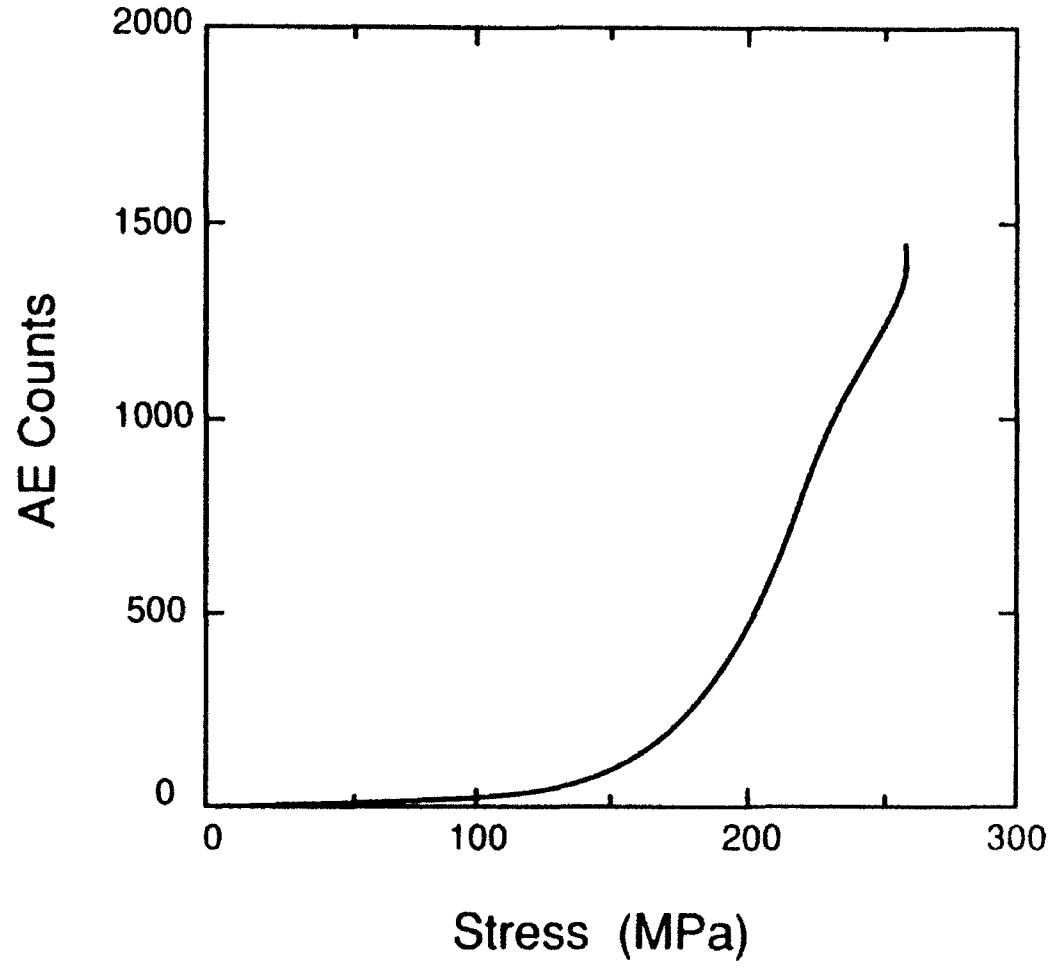

Fig. 5(b) A corresponding acoustic emmission curve.

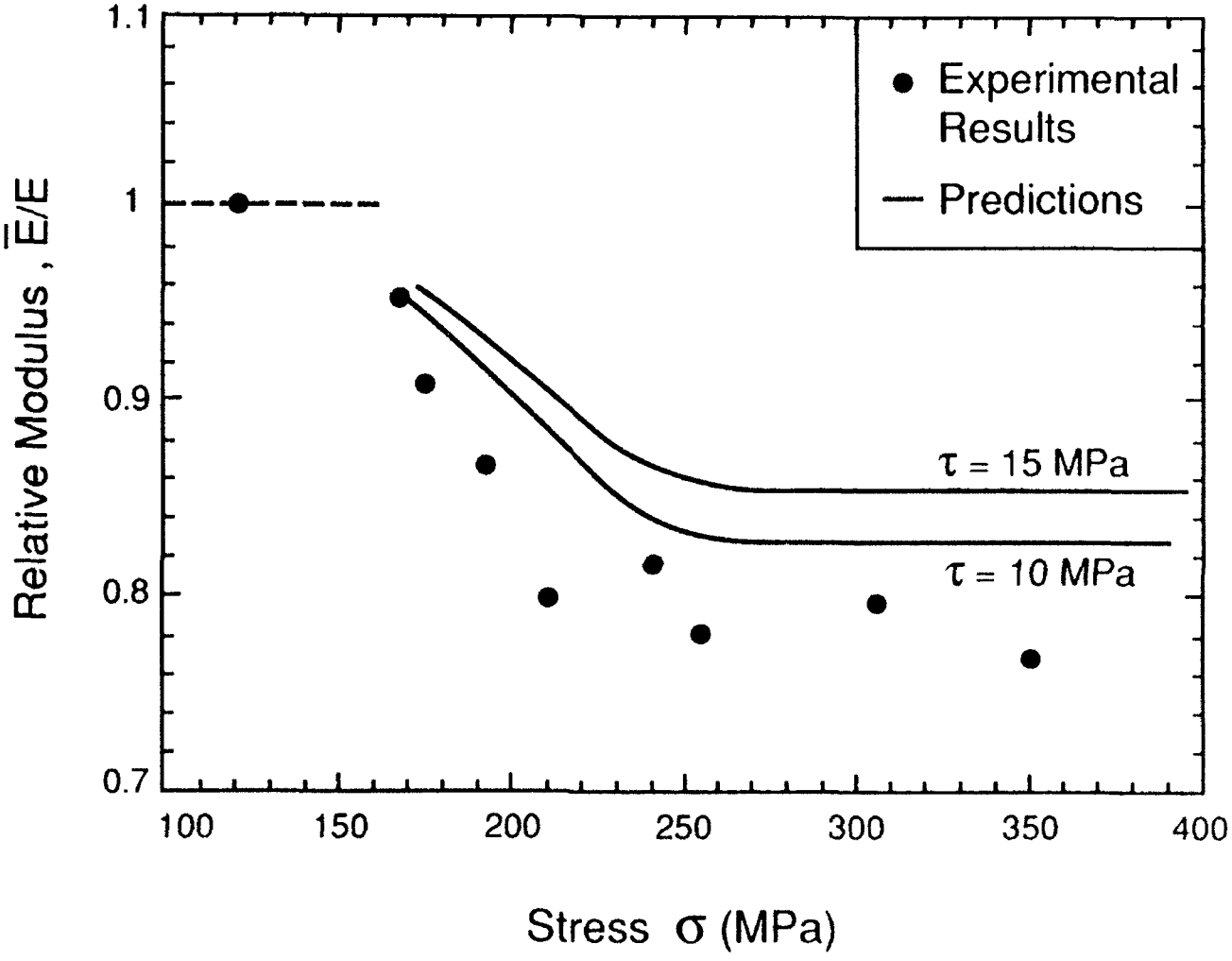
1.1
1
0.9
0.8
0.7
Relative Modulus , $\bar{E}/E$
100
150
200
250
300
350
400
Stress σ (MPa)
Experimental Results
Predictions
τ = 15 MPa
τ = 10 MPa

Fig. 6

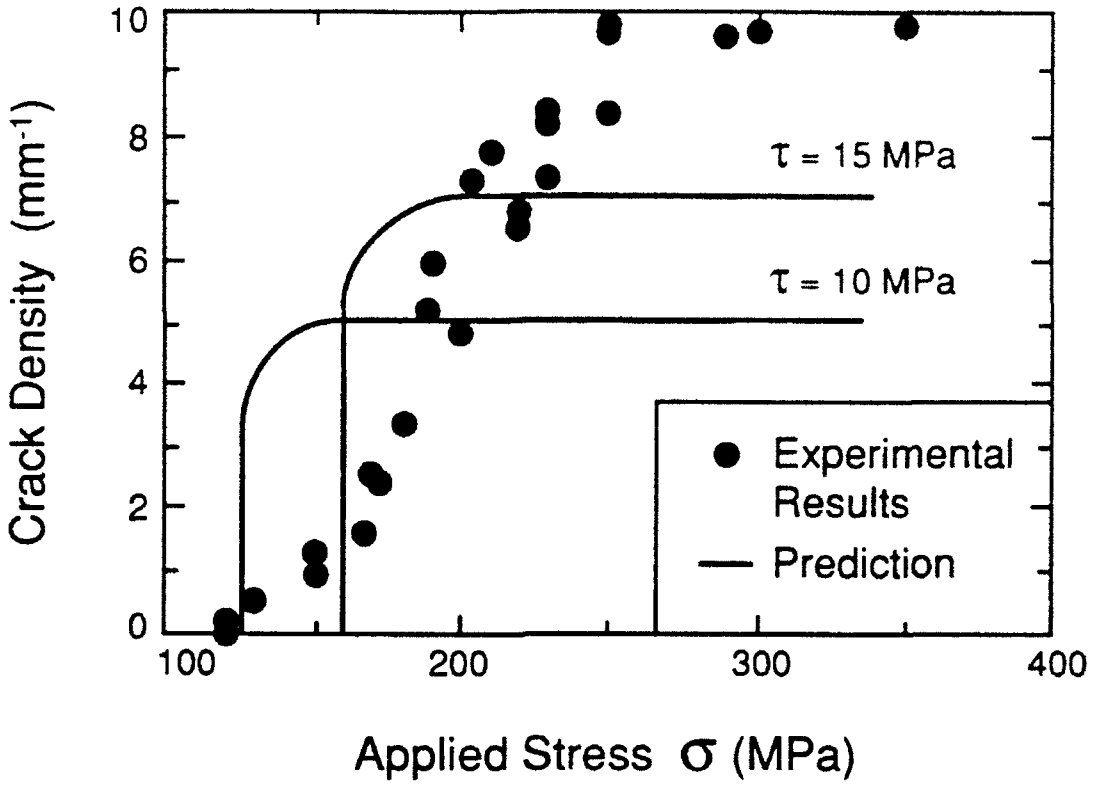

Fig. 7. Change in crack density, $R/\bar{\ell}$, with applied stress, σ. Also shown are predicted curves obtained from Fig. 1.

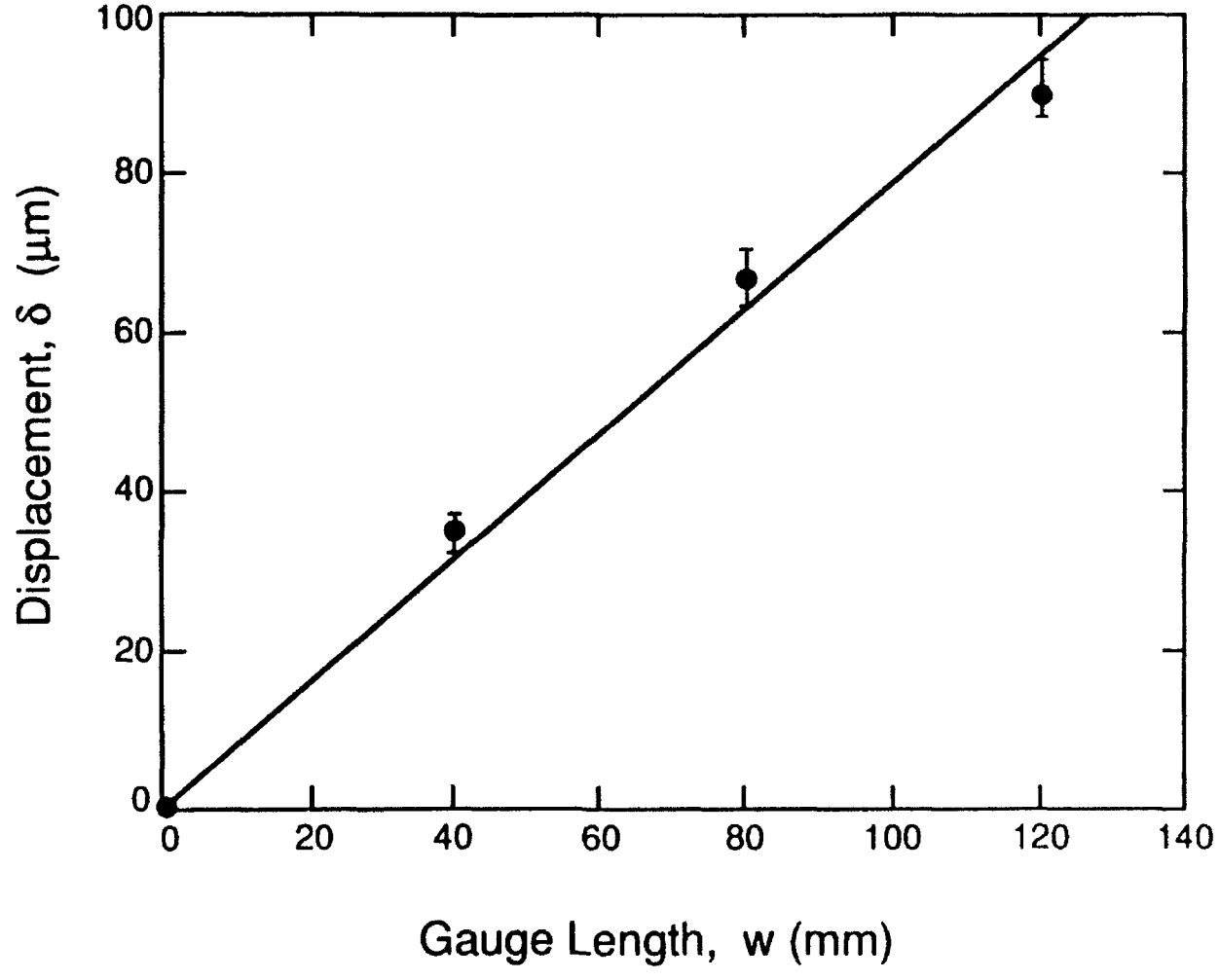

Fig. 8. Matrix residual stress measurements showing the displacement of the masked composite as a function of the length of the dissolved region.

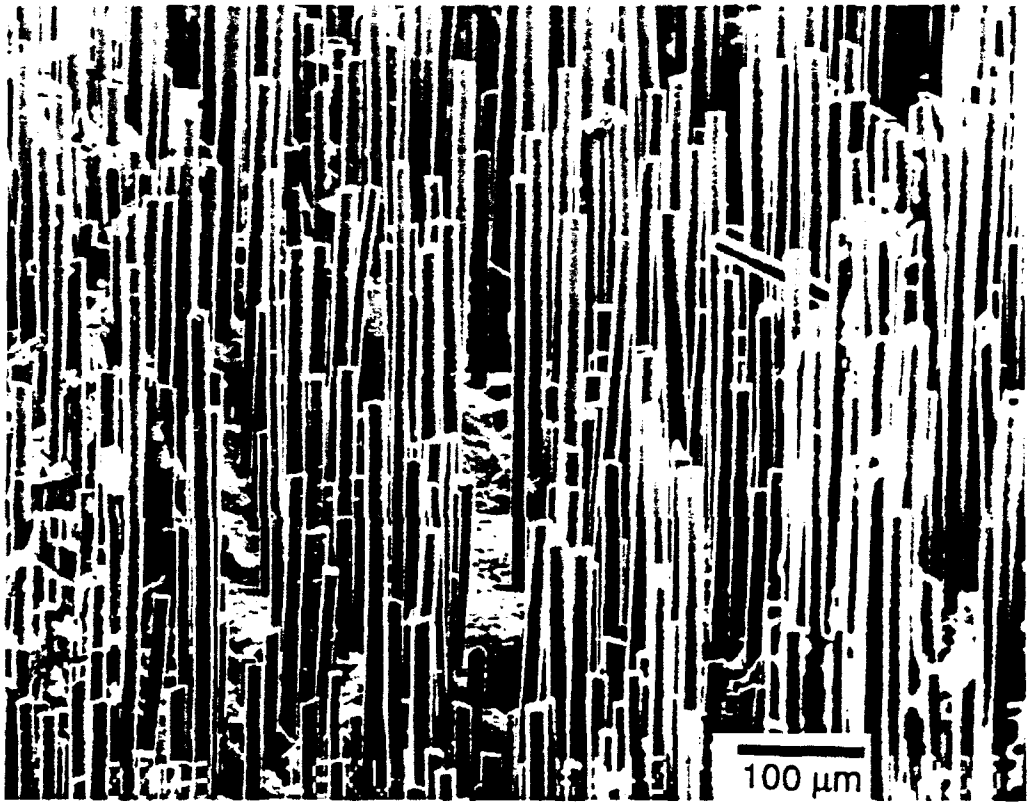

Fig. 9 Tensile fracture surfaces showing fiber pull-out.

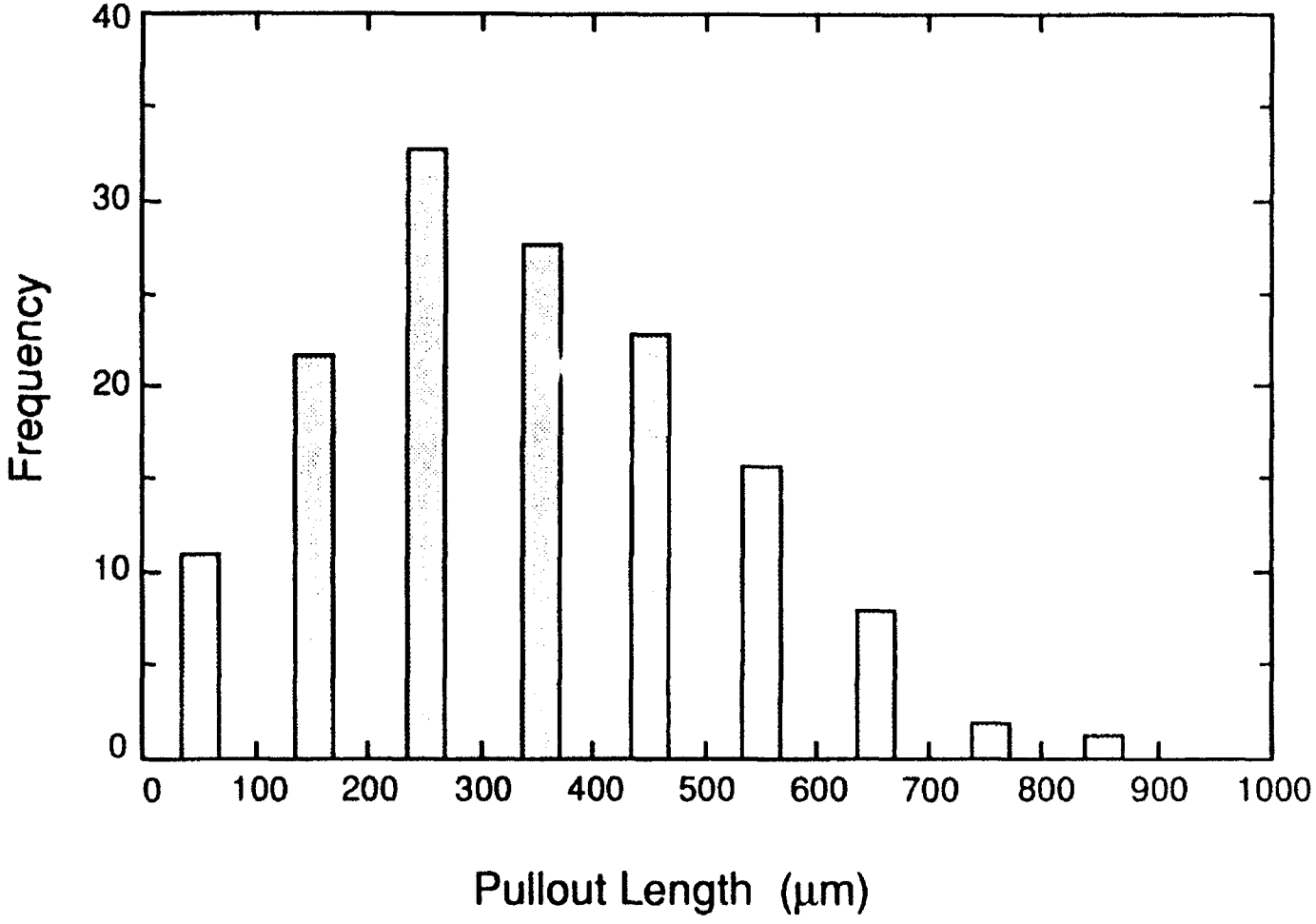

Fig. 10. A typical distribution of fiber pullout lengths from a tensile fracture surface.

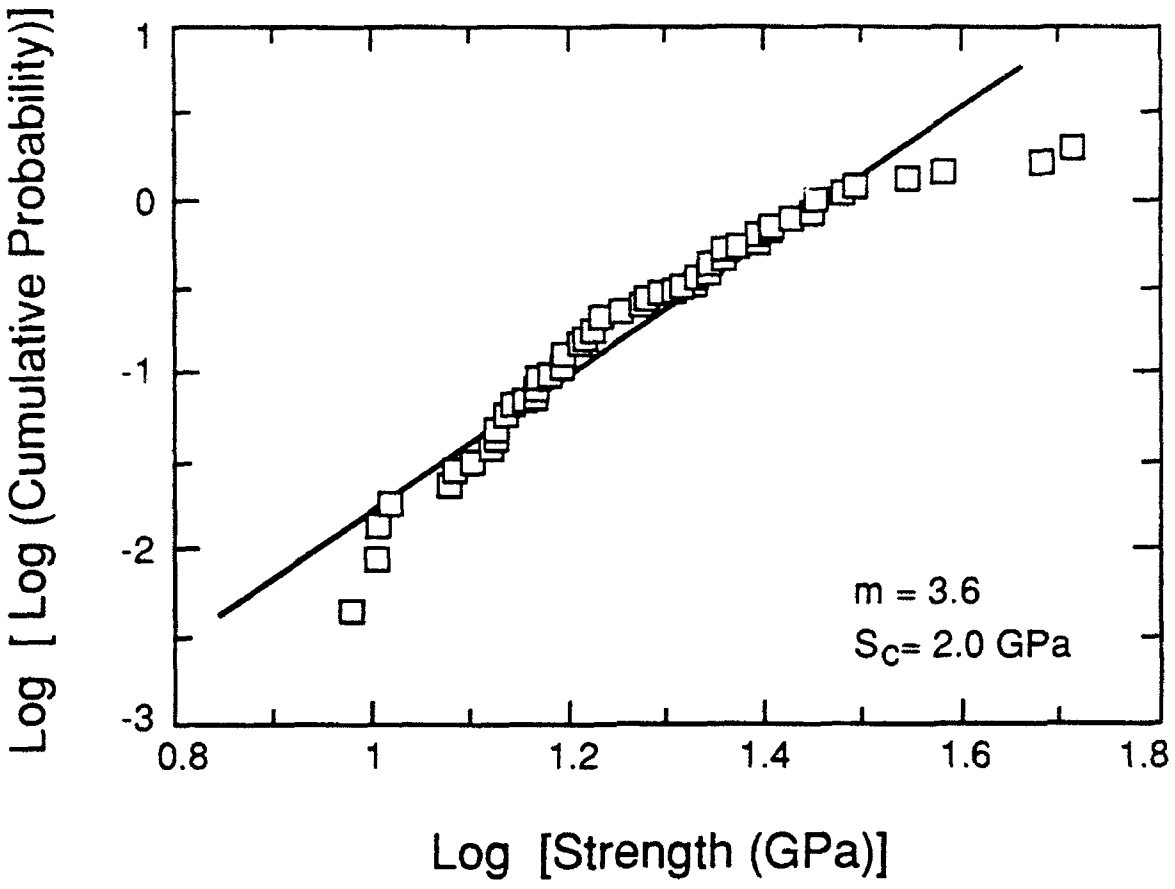

Fig. 11. *In situ* fiber strength distribution obtained from fracture mirror measurements.

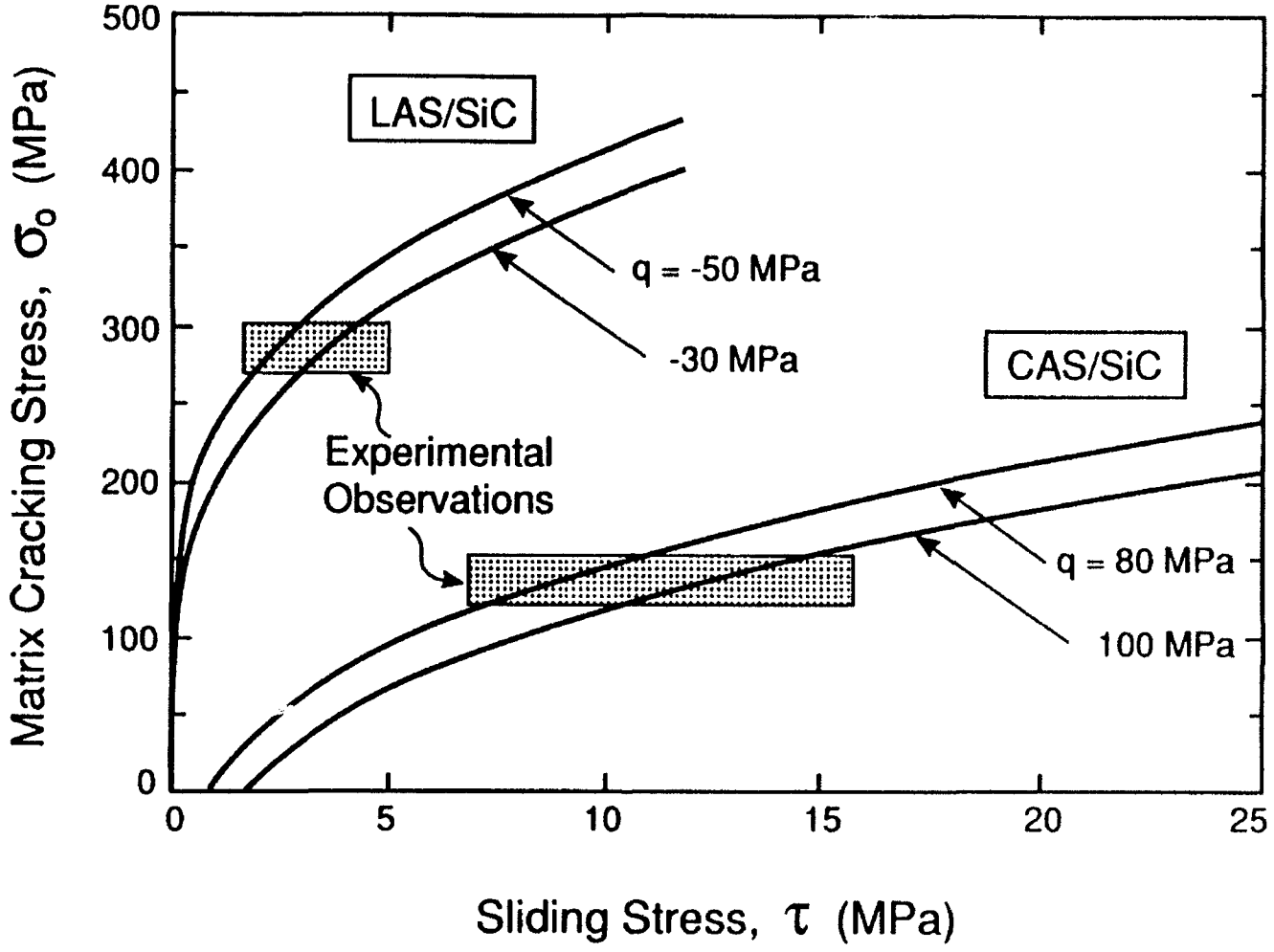

Fig. 12. The effect of interface sliding stress on the lower bound matrix cracking stress, calculated using Eqns. (4) and (5). Also superposed, as shaded rectangles, are the experimentally measured ranges of first matrix cracking stresses and sliding stresses for both the CAS and LAS matrix composites.

Int. J. Solids Structures Vol. 30, No. 3, pp. 385–398, 1993
Printed in Great Britain

A SELF-CONSISTENT MODEL FOR MULTI-FIBER CRACK BRIDGING

WILLIAM S. SLAUGHTER†
Division of Applied Sciences, Harvard University, Cambridge, MA 02138, U.S.A.

(*Received* 19 *September* 1991; *in revised form* 1 *April* 1992)

Abstract—A self-consistent model for determining the equivalent spring stiffness in fiber crack-bridging problems is proposed. The model is compared with the shear-lag model for ideal bonding of the fiber–matrix interface, in which case the springs have a linear spring constant. A comparison is also made, in the homogeneous limit when fiber and matrix elastic properties are identical, with results from particle and ligament crack-bridging analyses. The self-consistent model is seen to agree with these other models. A simplified parametric equation is given which approximates the results over the considered range of material properties.

INTRODUCTION

A great deal of interest in recent years has centered around the subject of fiber-reinforced materials. This is due, largely, to experimental studies that have demonstrated that fiber-reinforcing can substantially increase the fracture toughness of ceramics, which are normally very brittle (Prewo and Brennan, 1980). It is anticipated that if ceramic materials can be adequately toughened, either through fiber-reinforcing or some other mechanism, the excellent thermal properties (and perhaps electrical properties) which they exhibit will provide a significant technological advance.

It has been demonstrated how a steady-state crack, growing normal to an aligned array of reinforcing fibers, can be modeled by analysing a configuration in which there are no fibers but a continuous distribution of springs restraining the two crack faces (Budiansky and Amazigo, 1989). The spring stress is a function of the crack opening displacement and is zero when the displacement is zero. The model material on which the springs act is assumed to be homogeneous and transversely isotropic with elastic constants equal to those of the composite. The critical energy release rate is modified to account for the increase in crack area due to the absence of fibers. Budiansky and Amazigo used this model to examine a semi-infinite crack growing through an infinite, reinforced material where the fibers break at some critical fiber stress. This condition results in a zone, starting at the crack-tip, in which fiber bridging is contained. This zone extends back to infinity as the critical fiber stress becomes large. The manner in which an "equivalent" spring strength is determined, so that the fracture toughness is the same for the model as it would be for the fiber-reinforced material, is the subject of this paper. Budiansky and Amazigo assumed fiber–matrix interface conditions in which sliding occurs when the interfacial shear stress reaches a maximum value, resulting in a nonlinear spring stiffness. Only the limiting condition of ideal bonding, in which the spring stiffness can be expressed as a linear spring constant, is considered here.

Budiansky and Amazigo used a shear-lag model, developed by Budiansky *et al.* (1986), to determine an equivalent spring stiffness for their model. A similar method was devised by Aveston and Kelly (1973). In the shear-lag model, a representative problem is examined in which a fiber is concentrically embedded in a cylindrical matrix. The ratio of fiber and matrix radii is chosen so that the fiber volume concentration of the composite is preserved. It is further supposed that all axial stresses in the matrix are concentrated at an intermediate, "effective" radius and that the volume of matrix between this effective radius and the fiber supports only shear stresses. The effective radius is chosen through complementary energy considerations. Alternatively, Aveston and Kelly defined the effective radius as that at which the axial displacement equals the average for the matrix, though they did not

† Current address: Department of Engineering, Trumpington Street, Cambridge CB2 1PZ, U.K.

explicitly solve for it. The result is an approximate solution for fiber and matrix stresses far downstream of the crack-tip from which an equivalent spring stiffness can be determined.

The assumptions of the shear-lag model result in a method that is adaptable to a wide range of fiber–matrix interface conditions. These include ideal bonding, sliding with constant frictional stress, Coulomb frictional sliding (Hutchinson and Jensen, 1990), and non-frictional debonding with a critical debonding energy release rate (Budiansky *et al.*, 1986). At the same time, however, it has not been shown to what extent these assumptions affect the accuracy of the results. For example, in the limit as fiber volume concentration tends to zero, no axial load is transferred between the fiber and matrix. This indicates that there *might* be some range of small fiber volume concentrations over which the shear-lag model is unsuitable.

Proposed here is a self-consistent model for determining the equivalent spring constant in fiber crack-bridging problems. Incorporated into this model is the method for analysing fiber load-diffusion problems that was developed by Slaughter and Sanders (1991). Also utilized is the assumption, made by Budiansky and Amazigo (1989), that the elastic field in the composite can be approximated by a homogeneous system. In contrast to the shear-lag model (which may be unreliable for small concentrations), the assumptions of this model tend to break down for high fiber volume concentrations. The two models should, therefore, provide a good check on each other.

SELF-CONSISTENT APPROXIMATION

Consider a semi-infinite, plane crack driven by an average far-field stress, $\bar{\sigma}$. The crack grows through an infinite matrix that is reinforced by an aligned array of fibers. The fibers are normal to the crack plane and the crack is presumed to grow around the fibers, leaving them intact in its wake. Downstream of the crack tip the elastic field approaches that represented in Fig. 1. In this three-dimensional field, the fibers are of radius a and the fiber volume concentration is c. Both the fibers and matrix are homogeneous and isotropic, linear elastic solids with Young's modulus and Poisson's ratio taken, respectively, to be E_f and ν_f for the fibers and E_m and ν_m for the matrix. The z-direction is defined as that in which the applied stress, $\bar{\sigma}$, acts and in which the fibers are aligned, i.e. normal to the crack, with $z = 0$ at the crack plane.

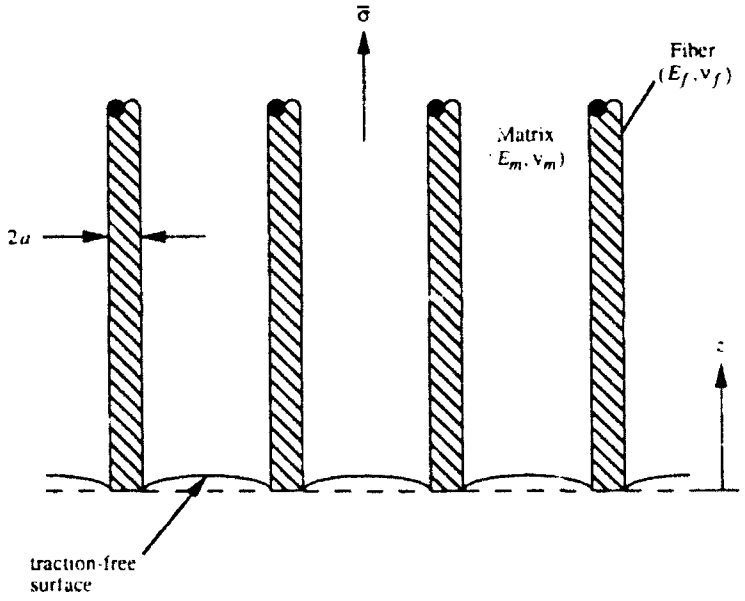

Fig. 1. Elastic field far behind the crack-tip in a fiber crack-bridging problem in which the fibers are aligned and remain unbroken. The fiber–matrix interface is ideally bonded.

The overall elastic response of an aligned fiber composite can be expressed in terms of transversely isotropic elastic moduli. A theory for approximating these moduli, for an arbitrary aligned fiber composite, has been developed using self-consistent arguments (Hill, 1965). The five moduli are, in this instance, most conveniently given as the stiffnesses C_{11}, C_{33}, C_{23}, C_{13} and C_{44}. The composite Young's modulus for axial extension

$$E_z = C_{33} - 2C_{13}^2/(C_{11} + C_{12}) \approx cE_f + (1-c)E_m,$$

will also prove useful. For a more detailed discussion of the overall elastic moduli see Appendix A. Referring to Fig. 1, the following conditions on axial displacement, w, and radial and axial stress, σ_r and σ_z, respectively, are noted:

$$\begin{aligned} &\text{at } z = 0: \quad w = 0 \quad \sigma_r^m = 0, \quad \sigma_z = \frac{1}{c}\bar{\sigma}, \\ &\text{at } z \to \infty: \quad \sigma_r \approx \sigma_r^m \approx 0, \quad \sigma_z^m \approx E_m\bar{\varepsilon}, \quad \sigma_z = E_f\bar{\varepsilon}, \end{aligned} \tag{1}$$

where $\bar{\varepsilon} \equiv \bar{\sigma}/E_f$ is the uniform, far-field axial strain. Matrix quantities are denoted by superscript m while fiber quantities are without denotation and represent the average over a fiber cross-section. It is assumed that the elastic response of a fiber, in an aligned fiber composite, can be approximated by the response of a single fiber embedded in a homogeneous, transversely isotropic material with elastic moduli equal to those of the composite.

The contribution to the far-field axial displacement, due to the passage of the crack in the composite, is given by

$$\Delta = \lim_{l \to \infty} \int_0^l (\varepsilon_z - \bar{\varepsilon})\, \mathrm{d}z. \tag{2}$$

The equivalent spring constant, k, that is needed to analyse the fracture toughening effect of the fiber reinforcement, using Budiansky and Amazigo's method, relates this displacement to the far-field stress,

$$\bar{\sigma} = k\Delta. \tag{3}$$

For ideal bonding of the fiber–matrix interface, k depends only on material properties and the fiber volume concentration, c. This spring constant can be used to model the effects of fiber crack bridging. More specifically, in this case, it is assumed that the effect on the elastic response of a fiber in the composite, due to crack bridging by all other fibers, can be approximated by that due to a continuous distribution of springs, relating normal tractions to surface displacements via the linear spring stiffness, k.

The self-consistent method for determining k makes use of both the aforementioned methods for approximating the effects of discrete fibers. This results in the assumption that the reaction in one of the fibers shown in Fig. 1 can be modeled by the single fiber problem shown in Fig. 2. In this problem the matrix has the elastic properties of the fiber composite. The fiber properties remain unchanged. The surface at $z = 0$ is restrained by the linear springs with equivalent spring constant k, as defined above. A polar coordinate system is defined with r measured from the fiber center. This leads to the following modifications of the conditions given in eqns (1):

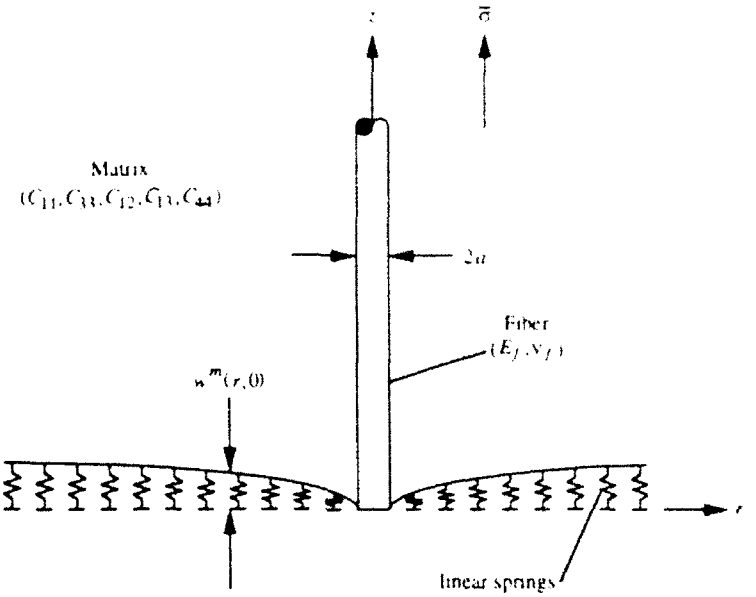

Fig. 2. Self-consistent approximation to the fiber crack-bridging problem. The matrix has the transversely isotropic elastic properties of the fiber/matrix composite.

$$\text{at } z = 0: \quad w = 0, \quad \sigma_z^m = k w^m, \quad \sigma_z = \frac{1}{c}\bar{\sigma},$$

$$\text{at } z \to \infty: \quad \sigma_r \approx \sigma_r^m \approx 0, \quad \sigma_z^m = \bar{\sigma}, \quad \sigma_z = E_z \bar{\varepsilon} = \frac{E_z}{E_z^*}\bar{\sigma}, \tag{4}$$

along with the observation that at $z = 0$

$$\lim_{r \to \infty} w^m = \Delta. \tag{5}$$

For a given fiber volume concentration, c, which spring constant, k, will cause the zero fiber displacement constraint at $z = 0$, given in eqns (4), to be satisfied? A similar self-consistent model, for unbroken ligaments between crack faces in a homogeneous, isotropic material, was considered by Rose (1987). For numerical reasons to come later it will prove advantageous to consider the inverse form of this: for a given spring constant k (and given material properties), what fiber volume concentration c will cause the zero fiber displacement constraint at $z = 0$ to be satisfied?

The elastic field shown in Fig. 2 has nonzero components at $(r, z) \to \infty$. This is eliminated by superposing a uniform compressive strain $\varepsilon_z = \bar{\varepsilon}^m = -\bar{\varepsilon}$, $\sigma_r^m = -\bar{\sigma}$, $\sigma_z = -E_f\bar{\sigma}/E_z$. The problem becomes that shown in Fig. 3. Displacements and stresses now vanish at infinity, while at $z = 0$

$$w = -\Delta,$$

$$\sigma_z^m = k w^m,$$

$$\sigma_z \equiv \frac{F}{\pi a^2} = \left(\frac{1}{c} - \frac{E_f}{E_z}\right)\bar{\sigma}. \tag{6}$$

This superposition facilitates the application of the fiber load-diffusion analysis method introduced in Slaughter and Sanders (1991). F is defined as the load on the end of the fiber. For a given k, what fiber volume concentration c will result in the satisfaction of eqns (6)?

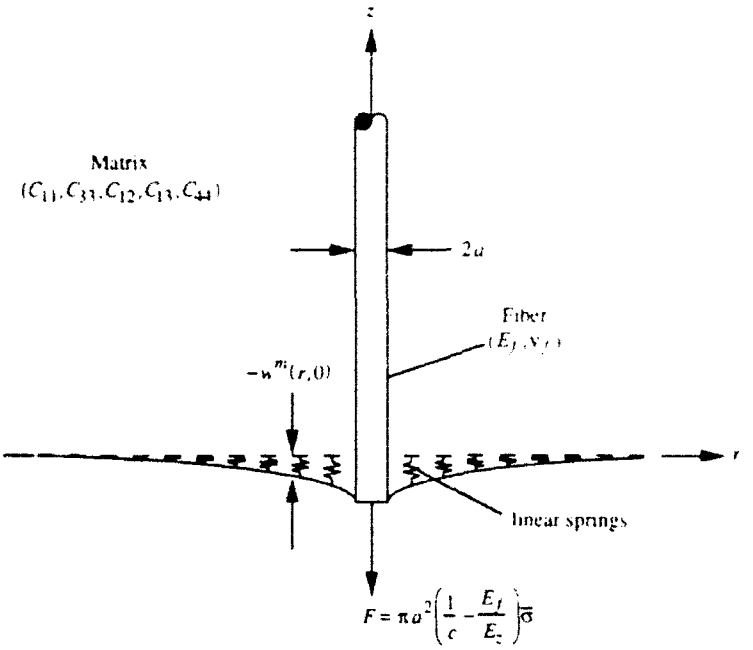

Fig. 3. Self-consistent approximation to the fiber crack-bridging problem plus the superposition of a uniform axial strain to nullify far-field stresses.

THE EQUIVALENT SPRING CONSTANT

In solving for the equivalent spring constant, k, in Fig. 3, the model for load-transfer from an embedded fiber to an elastic matrix, introduced in Slaughter and Sanders (1991), is adopted. The fiber is approximated as an axisymmetric, elastic rod with axial stress σ_z. Shear strains in the fiber are ignored and $\varepsilon_\theta = \varepsilon_r$, ε_z, $\sigma_r = \sigma_\theta$ and σ_z are functions of z only. Constitutive equations for the fiber reduce to the following.

$$\sigma_z = E_f \varepsilon_z + 2\nu_f \sigma_r, \tag{7}$$

$$E_f \varepsilon_\theta + \nu_f E_f \varepsilon_z - (1 - 2\nu_f)(1 + \nu_f)\sigma_r = 0. \tag{8}$$

Forces acting on the fiber are an applied load F, at the fiber end, and bonding tractions with the matrix, $\tau = \tau_{rz}^m(a, z)$ and $\sigma_r = \sigma_r^m(a, z)$, along the fiber–matrix interface at $r = a$. The fiber is in equilibrium if, for all $z \geq 0$,

$$\pi a^2 \sigma_z + 2\pi a \int_0^z \tau \, dz' = F. \tag{9}$$

The fiber quantities ε_θ, σ_r and ε_z remain to be related to quantities in the matrix.

In contrast to the problem of load-transfer from a single fiber to a semi-infinite matrix analysed in Slaughter and Sanders (1991), compressive normal tractions, $t(r) \equiv -\sigma_z^m(r, 0)$, act along the surface of the matrix at $z = 0$ where

$$t(r) = -k w^m(r, 0). \tag{10}$$

Over-all equilibrium for the fiber–matrix system requires that

$$2\pi \int_0^a t(r) r \, dr = F \tag{11}$$

In addition, the matrix is transversely isotropic with elastic moduli C_{11}, C_{12}, C_{13}, C_{33} and C_{44}. Elliott (1948, 1949) showed how the elastic field in such a material can be expressed in terms of two "harmonic" functions, ϕ_1 and ϕ_2, where

$$\left(\nabla_1^2 + \mu_i \frac{\partial^2}{\partial z^2}\right)\phi_i = 0, \quad (i = 1, 2), \tag{12}$$

and μ_1 and μ_2 are the roots of

$$C_{11}C_{44}\mu^2 + [C_{13}(2C_{44} + C_{13}) - C_{11}C_{33}]\mu + C_{33}C_{44} = 0. \tag{13}$$

For axially symmetric fields

$$\nabla_1^2 \equiv \frac{\partial^2}{\partial r^2} + \frac{1}{r}\frac{\partial}{\partial r} \tag{14}$$

and the radial and axial displacements, u and w, respectively, are given by

$$u = \frac{\partial \phi_1}{\partial r} + \frac{\partial \phi_2}{\partial r}, \quad w = \kappa_1 \frac{\partial \phi_1}{\partial z} + \kappa_2 \frac{\partial \phi_2}{\partial z}, \tag{15}$$

where

$$\kappa_i \equiv \frac{C_{11}\mu_i - C_{44}}{C_{13} + C_{44}}, \quad (i = 1, 2). \tag{16}$$

The roots of eqn (13) are either real and positive, in which case ϕ_1 and ϕ_2 are real, or they are complex conjugates, in which case ϕ_1 and ϕ_2 are complex conjugates as well.

The elastic field in this problem is approximated by that due to a point force of magnitude F, acting at the origin in the negative z-direction, along with distributions along the z-axis of point forces and point dilatations, $p(z)$ and $q(z)$, and the traction distribution, $t(r)$. The point forces are in the negative z-direction and the point force distribution must be self-equilibrating;

$$\int_0^c p(\zeta)\, d\zeta = 0. \tag{17}$$

In terms of the Elliott harmonic functions, this approximate field is expressed as

$$\phi_i = \int_0^c \{\phi_i^A(r, z, \zeta)[F\delta(\zeta) + p(\zeta)] + \phi_i^B(r, z, \zeta)q(\zeta)\}\, d\zeta + \int_a^c \phi_i^C(r, z, \rho)t(\rho)\, d\rho, \quad (i = 1, 2), \tag{18}$$

where $\phi_i^A(r, z, \zeta)$ and $\phi_i^B(r, z, \zeta)$ are the elastic solutions at (r, z) for a point force and a point dilatation, respectively, acting at $(0, \zeta)$ and $\phi_i^C(r, z, \rho)$ is the elastic solution at (r, z) for a ring of point forces at $(\rho, 0)$. $\delta(z)$ is the Dirac function. See Appendix B for a more detailed discussion and explicit expressions for these and following kernel functions. ϕ_i^A and ϕ_i^B are well behaved analytic functions for $r \neq 0$. ϕ_i^C has an integrable singularity, when $z = 0$, at $r = \rho$. As a result, the elastic field given by eqn (18) has real, analytic displacements, strains, and stresses when $r \neq 0$. Each of these quantities is expressible, through eqns (15) and (18), as integrals of known kernel functions times the unknown distributions.

The governing equations for this problem are (8), (9) and (10). Over-all equilibrium of the problem, eqn (11), and the self-equilibrating condition on the point force distribution, eqn (17), offer additional constraint on the solution. Equation (7) is used to eliminate σ_z from (9). In order to express the governing equations in terms of the unknown distributions, the fiber quantities ε_m, σ_r and ε_z need to be related to quantities in the matrix. Following the method in the solution of the single fiber problem (Slaughter and Sanders, 1991).

$$\varepsilon_m = \frac{1}{a} u^m(a, z), \tag{19}$$

$$\sigma_r = \sigma_r^m(a, z). \tag{20}$$

For the axial fiber strain,

$$\varepsilon_z = \varepsilon_z^m(a, z), \tag{21}$$

when used in eqn (8), while

$$\varepsilon_z = \frac{1}{\pi a^2 E_f} \int_0^z H(z-\zeta)\left[1-\operatorname{erf}\left(\frac{z-\zeta}{a}\right)\right][F\delta(\zeta)+p(\zeta)]\,d\zeta + \varepsilon_z^m(a, z). \tag{22}$$

when used in eqn (9), where $H(z)$ is the Heaviside step function. The relation (22) compensates for the discontinuity in axial strain in the fiber across an applied step loading. The discontinuity is necessary under the elastic rod approximation if σ_r is assumed to be continuous.

Using the relationship between fiber and matrix quantities, established in eqns (19) through (22), and the expression for the elastic field in the matrix, eqn (18), the governing equations can be rewritten as coupled integral equations for the unknown distributions $p(z)$, $q(z)$ and $t(r)$. Non-dimensionalizing in a and F such that $k \Rightarrow E_f k/a$,

$$\int_0^z p(\zeta)\,d\zeta + \int_0^z [\Gamma_{11}(z,\zeta)p(\zeta)+\Gamma_{12}(z,\zeta)q(\zeta)]\,d\zeta + \int_1^z \Gamma_{13}(z,\rho)t(\rho)\,d\rho = -\Gamma_{11}(z,0). \tag{23}$$

$$\int_0^z [\Gamma_{21}(z,\zeta)p(\zeta)+\Gamma_{22}(z,\zeta)q(\zeta)]\,d\zeta + \int_1^z \Gamma_{23}(z,\rho)t(\rho)\,d\rho = -\Gamma_{21}(z,0). \tag{24}$$

$$\int_0^r [\Gamma_{31}(r,\zeta)p(\zeta)+\Gamma_{32}(r,\zeta)q(\zeta)]\,d\zeta + \frac{\pi}{k} t(r) + \int_1^r \Gamma_{33}(r,\rho)t(\rho)\,d\rho = -\Gamma_{31}(r,0), \tag{25}$$

where the kernels $\Gamma_{\alpha\beta}$ ($\alpha, \beta = 1, 2, 3$) are real functions. See Appendix B for explicit expressions for the kernels and non-dimensionalizations. All subsequent expressions are in non-dimensional form. To solve for the distributions, the system of coupled integral equations (23), (24) and (25) is reduced to a set of discrete linear equations. The integrals are approximated using the mapped Gauss-Legendre rule and each equation is enforced at the quadrature points, in accordance with the Nystrom method (Delves and Mohamed, 1985). The constraints (11) and (17), which in non-dimensional form are

$$\int_{a}^{b} r(\rho)\rho \, d\rho = \frac{1}{2\pi}, \tag{26}$$

$$\int_{a}^{b} p(\zeta) \, d\zeta = 0, \tag{27}$$

are added to this set of linear equations. The resulting system exhibits some ill-posed tendencies due to the nature of the integral equations. These problems are dealt with by using singular value decomposition (SVD) to solve the set of linear equations.

To solve for the fiber volume concentration, c, that corresponds to a given spring constant, k, requires an iterative approach. The transversely isotropic material stiffnesses of the matrix depend on c and, therefore, so do the kernel functions, $\Gamma_{\alpha\beta}(\alpha, \beta = 1, 2, 3)$. If an estimate of c is used and the distributions solved for, then a new estimate for c can be calculated from the definition of the load applied to the end of the fiber [eqn (6)]

$$c = k\Delta\left[1 + \left(\frac{E_f}{E_m}\right)k\Delta\right]^{-1}, \tag{28}$$

where $\Delta = w^m(1, 0)$ and

$$w^m(1, 0) = \Gamma_{31}(r, 0) + \int_{a}^{b} [\Gamma_{31}(r, \zeta)p(\zeta) + \Gamma_{32}(r, \zeta)q(\zeta)] \, d\zeta + \int_{a}^{b} \Gamma_{33}(r, \rho)r(\rho) \, d\rho. \tag{29}$$

Equation (29) is theoretically equivalent to $w^m(r, 0) = -\pi r(r)\, k$ but converges more steadily during numerical analysis. In this way, the estimate for c is refined until there is convergence.

The results from this analysis are compared with those from the shear-lag model (Budiansky and Amazigo, 1989) in the instance that the fiber and matrix remain ideally bonded. In addition, in the limit that fiber and matrix elastic properties are the same, comparison can be made with Rose's analysis for unbroken ligaments bridging the crack faces (Rose, 1987) as well as with an analysis of crack bridging by particulate reinforcements (Budiansky *et al.*, 1988). Comparisons for the case when fiber and matrix elastic properties are the same are shown in Fig. 4 and those for dissimilar fiber and matrix elastic properties

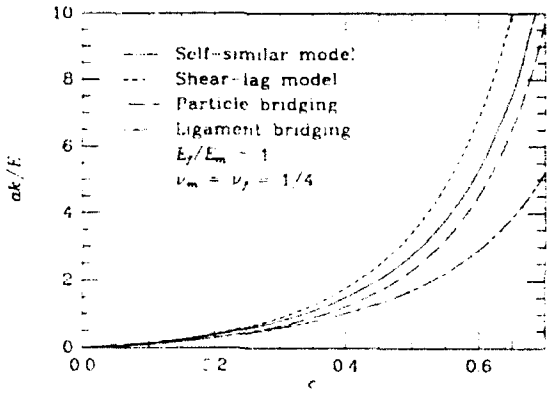

Fig. 4. The equivalent spring constant versus fiber volume concentration in the homogeneous limit when the fiber and matrix elastic properties coincide. In addition to the self-consistent model, results from the shear-lag model (Budiansky and Amazigo, 1989), a particle crack-bridging analysis (Budiansky *et al.*, 1988), and a ligament crack-bridging analysis (Rose, 1987) are plotted.

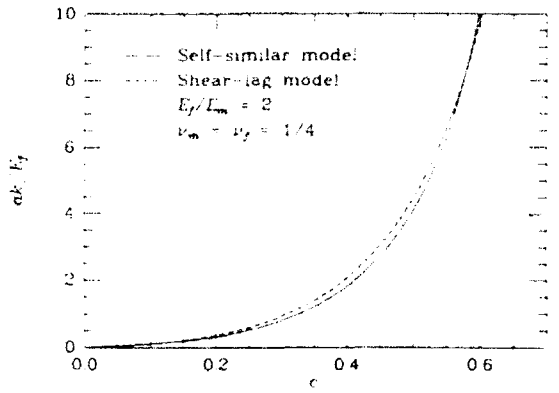

Fig. 5. The equivalent spring constant versus fiber volume concentration for the self-consistent model and the shear-lag model (Budiansky and Amazigo, 1989) when the ratio of the fiber to matrix Young's moduli is 2 and both Poisson's ratios are 1/4.

are shown in Figs 5–7. It is noted that variations in the Poisson's ratio of either the fiber or matrix have little effect on any of these models. The following parametric curve-fitting equation approximates the results from the self-consistent model for the equivalent spring constant as a function of fiber volume concentration:

$$k = \alpha c(1-c)^{\gamma}. \tag{30}$$

where

$$\alpha = 2.8\left(\frac{E_f}{E_m}+1\right)^{-1}. \tag{31}$$

$$\gamma = 0.73 - 2.73\sqrt{\frac{E_f}{E_m}}. \tag{32}$$

Plots of this approximate formula are given, along with results from the self-consistent analysis, in Fig. 8.

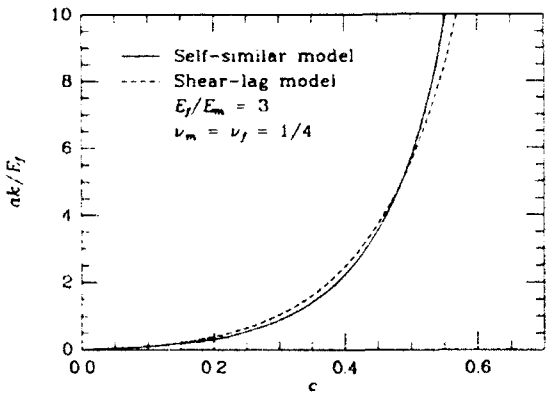

Fig. 6. The equivalent spring constant versus fiber volume concentration for the self-consistent model and the shear-lag model (Budiansky and Amazigo, 1989) when the ratio of the fiber to matrix Young's moduli is 3 and both Poisson's ratios are 1/4.

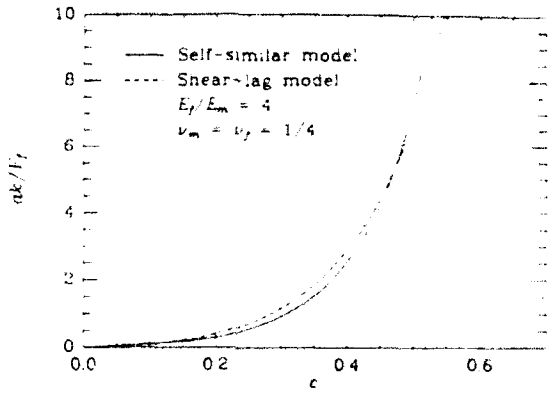

Fig. 7. The equivalent spring constant versus fiber volume concentration for the self-consistent model and the shear-lag model (Budiansky and Amazigo, 1989) when the ratio of the fiber to matrix Young's moduli is 4 and both Poisson's ratios are 1/4.

CONCLUDING REMARKS

It can be seen in Fig. 4 that, in the homogeneous limit of equivalent fiber and matrix material properties, the self-consistent model is in agreement with other available models. Surprisingly, the model developed by Rose (1987) for crack bridging by equiaxed ligaments, which is conceptually most like the self-consistent model, exhibits the greatest divergence in results. This is due to different assumptions on how discrete crack-bridging ligaments can be modeled by continuous spring distributions and how the resulting single ligament problem (or single fiber problem in this paper) is approximately solved. Both the shear-lag model and the particulate reinforcement model agree fairly well with the self-consistent model.

An examination of Figs 5–7 shows that the self-consistent and shear-lag models continue to give closely matched results throughout the range of material properties considered. The proposition that the two might be best applied to different ranges of fiber volume concentrations is not borne out. The results shown here indicate that either model would be suitable for the full range of concentrations. Ease of use suggests that, as long as only ideal bonding of the fiber–matrix interface is considered, the parametric equation (30), derived from the self-consistent model, may prove more convenient. It should be noted, however, that effective toughening in fiber-reinforced ceramics is seen to be associated with debonding of the fiber–matrix interface and fiber pull-out. The shear-lag model continues to enjoy a considerable advantage in calculating the nonlinear spring stiffnesses that follow from these conditions. These results serve to confirm the reliability of the shear-lag model when extended into problems of complicated fiber–matrix interface conditions.

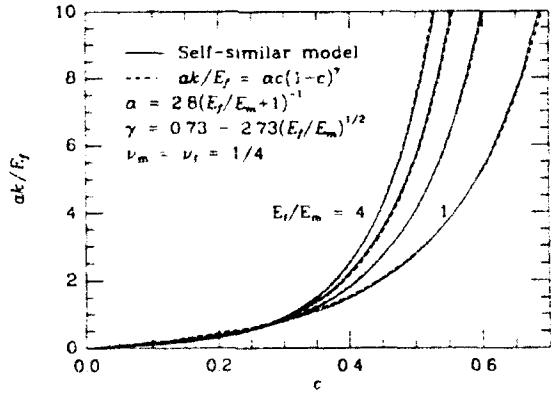

Fig. 8. The equivalent spring constant versus fiber volume concentration for the self-consistent model and the parametric curve-fitting equation.

Acknowledgements—This work was supported in part by the DARPA University Research Initiative (Subagreement P.O. VB38639-0 with the University of California, Santa Barbara, ONR Prime Contract N00014-86-K-0753), the Office of Naval Research (Contract N00014-90-J-1377), and the Division of Applied Sciences, Harvard University.

REFERENCES

Aveston, J. and Kelly, A. (1973) Theory of multiple fracture of fibrous composites. *J. Mater. Sci.* **8**, 352–362.
Budiansky, B. and Amazigo, J. C. (1989) Toughening by aligned, frictionally constrained fibers. *J. Mech. Phys. Solids* **37**, 93–109.
Budiansky, B., Amazigo, J. C. and Evans, A. G. (1988) Small-scale crack bridging and the fracture toughness of particulate-reinforced ceramics. *J. Mech. Phys. Solids* **36**, 167–187.
Budiansky, B., Hutchinson, J. W. and Evans, A. G. (1986) Matrix fracture in fiber-reinforced ceramics. *J. Mech. Phys. Solids* **34**, 167–189.
Delves, L. M. and Mohamed, J. L. (1985) *Computational Methods for Integral Equations*. Cambridge University Press, Cambridge.
Elliott, H. A. (1948) Three dimensional stress distributions in hexagonal aeolotropic crystals. *Proc. Cambridge Phil. Soc.* **44**, 522–533.
Elliott, H. A. (1949) Axial symmetric stress distributions in aeolotropic hexagonal crystals. The problem of the plane and related problems. *Proc. Cambridge Phil. Soc.* **45**, 621–630.
Hill, R. (1964) Theory of mechanical properties of fibre-strengthened materials. I. Elastic behaviour. *J. Mech. Phys. Solids* **12**, 199–212.
Hill, R. (1965) Theory of mechanical properties of fibre-strengthened materials. III. Self-consistent model. *J. Mech. Phys. Solids* **13**, 189–198.
Hutchinson, J. W. and Jensen, H. M. (1990) Models of fiber debonding and pullout in brittle composites with friction. *Mech. Mater.* **9**, 139–163.
Prewo, K. M. and Brennan, J. J. (1980). High-strength silicon carbide fiber-reinforced glass-matrix composites. *J. Mater. Sci.* **15**, 463–468.
Rose, L. R. F. (1987) Effective spring constant for unbroken ligaments between crack faces. *Int. J. Fract.* **33**, 145–152.
Shield, R. T. (1951) Notes on problems in hexagonal aeolotropic materials. *Proc. Cambridge Phil. Soc.* **47**, 401–409.
Slaughter, W. S. and Sanders, J. L. (1991) A model for load-diffusion from an embedded fiber to an elastic matrix. *Int. J. Solids Structures* **28**, 1041–1052.

APPENDIX A

Approximate composite elastic moduli

Hill (1965) used a self-consistent model to determine approximately the composite elastic moduli of fiber-reinforced materials. This approximation is independent of the spatial arrangement of the fibers. The only requirement is that the fibers be perfectly aligned and the composite exhibit statistical homogeneity. Hill showed further that the results from this model fall within bounds established as the best possible without considering detailed geometry (Hill, 1964). The composite is transversely isotropic with rigidity for transverse shearing over any axial plane, η; plane-strain bulk modulus for lateral dilation without fiber extension, γ; Young's modulus and Poisson's ratio under uniaxial loading, E_z and ν_{zr}; and rigidity for longitudinal shearing over any axial plane, G. The shearing rigidities are given by the positive roots of

$$\frac{c\gamma_f}{\gamma_f+\eta}+\frac{(1-c)\gamma_m}{\gamma_m+\eta}=2\left[\frac{c\eta_m}{\eta_m-\eta}+\frac{(1-c)\eta_f}{\eta_f-\eta}\right], \tag{A1}$$

$$\frac{c}{G-G_m}+\frac{1-c}{G-G_f}=\frac{1}{2G}, \tag{A2}$$

where subscript f and m signify fiber and matrix moduli, respectively, which for isotropic materials are given in terms of the isotropic Young's moduli, E, and Poisson's ratio, ν, by

$$\eta=G=\frac{E}{2(1+\nu)}, \tag{A3}$$

$$\gamma=\frac{E}{2(1+\nu)(1-2\nu)}. \tag{A4}$$

Using the result from (A1) then the remaining composite moduli are

$$E_z=cE_f+(1-c)E_m+4c(1-c)(\nu_f-\nu_m)^2\left(\frac{c}{\gamma_m}+\frac{1-c}{\gamma_f}+\frac{1}{\eta}\right)^{-1}, \tag{A5}$$

$$\nu_{zr}=c\nu_f+(1-c)\nu_m+c(1-c)(\nu_f-\nu_m)\left(\frac{1}{\gamma_m}-\frac{1}{\gamma_f}\right)\left(\frac{c}{\gamma_m}+\frac{1-c}{\gamma_f}+\frac{1}{\eta}\right)^{-1}. \tag{A6}$$

$$= \left(\frac{\quad}{\quad} + \frac{\quad}{\quad} \right) \eta \tag{A7}$$

The composite stiffnesses are defined so that

$$\begin{matrix} \sigma_{\quad} & C_{\quad} & C_{\quad} & C_{\quad} & 0 & 0 & 0 & \cdot \\ \sigma_{\quad} & C_{\quad} & C_{\quad} & C_{\quad} & 0 & 0 & 0 & \cdot \\ \sigma_{\quad} & C_{\quad} & C_{\quad} & C_{\quad} & 0 & 0 & 0 & \cdot \\ \tau_{\quad} & 0 & 0 & 0 & 2C_{\quad} & 0 & 0 & \cdot \\ \tau_{\quad} & 0 & 0 & 0 & 0 & 2C_{44} & 0 & \cdot \\ \tau_{\quad} & 0 & 0 & 0 & 0 & 0 & C_{\quad} - C_{\quad} & \cdot \end{matrix} \tag{A8}$$

In terms of the moduli used by Hill the stiffnesses are

$$C_{\quad} = \eta \tag{A9}$$

$$C_{\quad} = \eta \tag{A10}$$

$$C_{\quad} = 2\eta \tag{A11}$$

$$C_{\quad} = E - 4\eta \tag{A12}$$

$$C_{44} = G \tag{A13}$$

APPENDIX B

Singular solutions in a transversely isotropic elastic half-space

The solution for a point force acting in a transversely isotropic half-space has been previously studied (Shield, 1951). The solution for a unit force acting at $(r, z) = (0, \zeta)$ in the negative z-direction as required in eqn (18) is given by

$$\phi_1^{\Delta} = \frac{-P}{8\pi(\mu_1 - \mu_2)} \left[\ln\left(\frac{R_1 + z_1 - \zeta_1}{R_1 - z_1 + \zeta_1}\right) - \ln\left(\frac{\bar{R}_1 + z_1 - \zeta_1}{\bar{R}_1 - z_1 - \zeta_1}\right) \right] + \frac{P}{2\pi\beta(\mu_1 - \mu_2)} \left[\frac{\kappa_1 C_{13} - \mu_1 C_{33}}{(1+\kappa_1)\mu_1} \ln(\bar{R}_1 + z_1 + \zeta_1) - \frac{\kappa_2 C_{13} - \mu_2 C_{33}}{(1+\kappa_2)\mu_2} \ln(\delta_{12} + z_1 + \zeta_2) \right]. \tag{B1}$$

$$\phi_2^{\Delta} = \frac{P}{8\pi(\mu_1 - \mu_2)} \left[\ln\left(\frac{R_2 + z_2 - \zeta_2}{R_2 - z_2 + \zeta_2}\right) - \ln\left(\frac{\bar{R}_2 + z_2 + \zeta_2}{\bar{R}_2 - z_2 - \zeta_2}\right) \right] + \frac{P}{2\pi\beta(\mu_1 - \mu_2)} \left[\frac{\kappa_1 C_{13} - \mu_1 C_{33}}{(1+\kappa_2)\mu_1} \ln(\delta_{21} + z_2 + \zeta_1) - \frac{\kappa_2 C_{13} - \mu_2 C_{33}}{(1+\kappa_2)\mu_2} \ln(\bar{R}_2 + z_2 + \zeta_2) \right]. \tag{B2}$$

where

$$P = \frac{C_{13} + C_{44}}{C_{33} C_{44}}, \tag{B3}$$

$$\beta = \frac{\kappa_1 C_{13} - \mu_1 C_{33}}{(1+\kappa_1)\mu_1} - \frac{\kappa_2 C_{13} - \mu_2 C_{33}}{(1+\kappa_2)\mu_2}, \tag{B4}$$

$$z = \frac{z}{\mu}, \quad \zeta = \frac{\zeta}{\mu}, \tag{B5}$$

$$R_1 = \sqrt{r^2 + (z - \zeta)^2}, \quad \bar{R} = \sqrt{r^2 + (z + \zeta)^2}, \tag{B6}$$

$$\delta_{12} = \sqrt{r^2 + (z + \zeta)^2}. \tag{B7}$$

Recall the definitions of μ_i and κ_i in eqns (13) and (16).

No solution for a point dilatation was found in the literature. Therefore, with the nature of the self-consistent model considered, a unit point "dilatation" at $(0, \zeta)$ is defined such that the net normal displacement through an infinitely long circular cylinder, with centroidal axis coincident with the z-axis, approaches unity as the radius approaches zero. The elastic field is axisymmetric. This condition is not sufficient to define a unique solution. The solution used in this application, chosen for convenience, is

$$\phi_1^B = \frac{-1}{4\pi(\sqrt{\ } - \sqrt{\ })}\left[\frac{1}{R_1} + \left(1 + \frac{a/b}{\beta}\right)\frac{1}{\bar{R}_1} + \left(\frac{a/b}{\beta}\right)_0^1\right], \tag{B8}$$

$$\phi_2^B = \frac{-1}{4\pi(\sqrt{\ } - \sqrt{\ })}\left[\frac{1}{R_2} + \left(1 + \frac{a/b}{\beta}\right)\frac{1}{\bar{R}_2} + \left(\frac{a/b}{\beta}\right)_0^1\right], \tag{B9}$$

where

$$a = \frac{2\sqrt{\ }}{1-\kappa}, \quad b = C_{11} - C_{12}\frac{\kappa}{\mu}. \tag{B10}$$

The solution for a circular ring of compressive normal tractions of radius ρ on the surface $z = 0$ can be derived from the point force solution [eqns (B1) and (B2)]. The resulting elastic field is given by

$$\phi_1^A = \frac{1}{\pi\beta}\left(\frac{\sqrt{\ }}{1-\kappa_1}\right)\int_0^{\pi} \ln(\bar{R}_1 - z_1)\rho\,d\theta, \tag{B11}$$

$$\phi_2^A = \frac{-1}{\pi\beta}\left(\frac{\sqrt{\ }}{1-\kappa_2}\right)\int_0^{\pi} \ln(\bar{R}_2 - z_2)\rho\,d\theta, \tag{B12}$$

where

$$\bar{R}_i = \sqrt{\bar{r}^2 - z_i^2}, \quad \bar{r}^2 = r^2 + \rho^2 - 2r\rho\cos\theta \tag{B13}$$

This ring has a net force of $2\pi\rho$.

Expressions for required elastic quantities

Listed below are those elastic quantities that are needed for the implementation of the self-consistent model. They are given in terms of the Elliott "harmonic" functions ϕ_1 and ϕ_2 as defined in eqns (12)–(16):

$$u = \frac{\partial}{\partial r}(\phi_1 + \phi_2). \tag{B14}$$

$$\varepsilon_z = \frac{\partial^2}{\partial z^2}(\kappa_1\phi_1 + \kappa_2\phi_2). \tag{B15}$$

$$\tau_{rz} = C_{44}\left[(1+\kappa_1)\frac{\partial^2\phi_1}{\partial r\,\partial z} + (1+\kappa_2)\frac{\partial^2\phi_2}{\partial r\,\partial z}\right]. \tag{B16}$$

$$\sigma_r = \left(C_{11}\frac{\partial^2}{\partial r^2} + C_{12}\frac{1}{r}\frac{\partial}{\partial r}\right)(\phi_1 + \phi_2) + C_{13}\frac{\partial^2}{\partial z^2}(\kappa_1\phi_1 + \kappa_2\phi_2). \tag{B17}$$

Non-dimensionalizations and kernels for the coupled integral equations

The kernel functions for the three integral equations (23)–(25) are arrived at by substituting (B14)–(B17) [with ϕ_1 and ϕ_2 given by (18)] into the governing equations (8)–(10) using the fiber–matrix relations (19)–(22). To non-dimensionalize with a and F the following substitutions are made:

$$z \to az, \quad \zeta \to a\zeta, \quad r \to ar, \quad \rho \to a\rho, \quad k \to \frac{E_2}{a}k, \quad p(\zeta) \to \frac{F}{a}p(\zeta),$$

$$q(\zeta) \to \frac{F}{E_1}q(\zeta), \quad t(\rho) \to \frac{F}{a^2}t(\rho), \quad \phi_i^A \to \frac{1}{\pi E_2}\phi_i^A, \quad \phi_i^B \to \frac{1}{\pi a}\phi_i^B, \quad \text{and} \quad \phi^C \to \frac{a}{\pi L}\phi^C$$

The resulting expressions for the kernel functions are

$$\Gamma_{11} = -H(z-\zeta)\,\mathrm{erf}(z-\zeta) + \alpha_1\frac{\partial}{\partial r}(\phi_1^A + \phi_2^A)_{z=1} + \alpha_2\frac{\partial^2}{\partial r^2}(\phi_1^A + \phi_2^A)_{z=1}$$
$$+ \alpha_3\frac{\partial^2}{\partial z^2}(\kappa_1\phi_1^A + \kappa_2\phi_2^A)_{z=1} + \alpha_4\frac{\partial}{\partial r}[(1+\kappa_1)\phi_1^A - (1+\kappa_2)\phi_2^A]_{z=1}\Big|_{-\infty}^{\infty}, \tag{B18}$$

$$\Gamma_{12} = \alpha_1\frac{\partial}{\partial r}(\phi_1^B + \phi_2^B)_{z=1} + \alpha_2\frac{\partial^2}{\partial r^2}(\phi_1^B + \phi_2^B)_{z=1}$$
$$+ \alpha_3\frac{\partial^2}{\partial z^2}(\kappa_1\phi_1^B + \kappa_2\phi_2^B)_{z=1} + \alpha_4\frac{\partial}{\partial r}[(1+\kappa_1)\phi_1^B - (1+\kappa_2)\phi_2^B]_{z=1}\Big|_{-\infty}^{\infty}, \tag{B19}$$

$$\Gamma_{11} = \alpha_1 \frac{\partial}{\partial r}(\phi_1^S - \phi_2^S)_{r=1} + \alpha_2 \frac{\partial^2}{\partial r^2}(\phi_1^S + \phi_2^S)_{r=1}$$

$$+ \alpha_3 \frac{\partial^2}{\partial z^2}(\kappa_1\phi_1^S + \kappa_2\phi_2^S)_{r=1} + \alpha_4 \frac{\partial}{\partial r}[(1+\kappa_1)\phi_1^C + (1+\kappa_2)\phi_2^C] \quad \text{(B20)}$$

$$\Gamma_{12} = \alpha_1 \frac{\partial}{\partial r}(\phi_1^A - \phi_2^A)_{r=1} - \alpha_2 \frac{\partial^2}{\partial r^2}(\phi_1^A - \phi_2^A)_{r=1} + \alpha_3 \frac{\partial^2}{\partial z^2}(\kappa_1\phi_1^A + \kappa_2\phi_2^A) \quad \text{(B21)}$$

$$\Gamma_{22} = \alpha_1 \frac{\partial}{\partial r}(\phi_1^B - \phi_2^B)_{r=1} - \alpha_2 \frac{\partial^2}{\partial r^2}(\phi_1^B - \phi_2^B)_{r=1} + \alpha_3 \frac{\partial^2}{\partial z^2}(\kappa_1\phi_1^B + \kappa_2\phi_2^B) \quad \text{(B22)}$$

$$\Gamma_{23} = \alpha_1 \frac{\partial}{\partial r}(\phi_1^S - \phi_2^S)_{r=1} + \alpha_2 \frac{\partial^2}{\partial r^2}(\phi_1^S - \phi_2^S)_{r=1} + \alpha_3 \frac{\partial^2}{\partial z^2}(\kappa_1\phi_1^S + \kappa_2\phi_2^S)_{r=1} \quad \text{(B23)}$$

$$\Gamma_{31} = \frac{\partial}{\partial z}(\kappa_1\phi_1^A + \kappa_2\phi_2^A)_{r=1}, \quad \text{(B24)}$$

$$\Gamma_{32} = \frac{\partial}{\partial z}(\kappa_1\phi_1^B + \kappa_2\phi_2^B)_{r=1}, \quad \text{(B25)}$$

$$\Gamma_{33} = \frac{\partial}{\partial z}(\kappa_1\phi_1^S + \kappa_2\phi_2^S)_{r=1}, \quad \text{(B26)}$$

where

$$\alpha_1 = 2\nu_f \frac{C_{12}}{E_f}, \quad \text{(B27)}$$

$$\alpha_2 = 2\nu_f \frac{C_{11}}{E_f}, \quad \text{(B28)}$$

$$\alpha_3 = 1 + 2\nu_f \frac{C_{13}}{E_f}, \quad \text{(B29)}$$

$$\alpha_4 = 2\frac{C_{44}}{E_f}, \quad \text{(B30)}$$

$$\alpha_5 = (1-\nu_f)(1-2\nu_f)\frac{C_{12}}{E_f} - 1, \quad \text{(B31)}$$

$$\alpha_6 = (1+\nu_f)(1-2\nu_f)\frac{C_{11}}{E_f}, \quad \text{(B32)}$$

$$\alpha_7 = (1+\nu_f)(1-2\nu_f)\frac{C_{13}}{E_f} - \nu_f. \quad \text{(B33)}$$

journal

Damage Mechanisms and the Mechanical Properties of a Laminated 0/90 Ceramic/Matrix Composite

Douglas S. Beyerle,* S. Mark Spearing, and Anthony G. Evans*

Materials Department, College of Engineering, University of California, Santa Barbara, California 93106-5050

The tensile properties of a 0/90 laminated CAS matrix composite reinforced with Nicalon fibers have been measured. Some effects of notches have also been explored. Changes in modulus and permanent strain caused by matrix cracking have been measured and compared with available models. For this comparison, independent measurements have been made of the constituent properties and the residual stress. The ultimate tensile strength has also been measured and compared with a global load-sharing model. It is concluded that lower-bound matrix cracking models provide good predictability of the stresses at which various matrix cracking mechanisms first operate. Also, the ultimate tensile strength is found to be consistent with a global load-sharing model, based on the in situ strength properties of the fibers. Conversely, the evolution of matrix cracks at stresses above the lower bound has yet to be adequately modeled. In addition, a need is identified for improved models relating elastic properties and permanent strains to matrix crack spacing.

I. Introduction

THE macroscopic tensile properties of *unidirectional* continuous fiber-reinforced ceramic-matrix composites (CMC) have been extensively studied and related to the in situ properties of the fiber, matrix, and the fiber coating.[1-9] The main effort has been concerned with clarifying the role of the interface, in terms of the fiber coating, and relating its properties to those of the composite.[9] There has been a more limited effort attempting to relate the mechanical performance of 2-D-reinforced CMCs to the constituent properties. Preliminary attempts were made on a 0/90 laminated glass ceramic matrix composite (lithium-alumino silicate, LAS) reinforced with Nicalon fibers,[10] but with limited attention given to relationships between the macroscopic composite properties and the in situ properties of the constituents. More recently, progress has been made on woven composites, consisting of Nicalon fibers in C-based matrices.[11] The intent of the present article is to conduct a comprehensive study that relates the macroscopic properties of a 0/90 laminate to the in situ constituent properties. The material of choice is a calcium alumino silicate (CAS) reinforced with Nicalon fibers,[12] because many of the salient in situ properties of this composite system have been obtained from measurements performed on a unidirectional material processed in the same manner.[9] The principal objectives of this study are to measure and rationalize the tensile properties along one of the fiber directions and to provide preliminary information on the influence of notches.

The macroscopic properties of primary interest are the elastic moduli and permanent strain (as influenced by the applied load) and the ultimate tensile strength. The constituent properties having relevance to these macroscopic quantities (summarized in Table I) include the interfacial sliding stresses, τ_i; the elastic properties of the fiber and matrix, E_f and E_m; the fiber radius, R, the in situ fiber strength, S_f; the matrix fracture energy, Γ_m; and the misfit strain, Ω, which indicates the residual stresses. Some of the basic formulae relating the *linear* properties of the laminated composites are summarized in Table II. The corresponding relationships for the nonlinear composite properties are subject to information about the dominant damage mechanisms. Assessment of such mechanisms involves experiments that observe and monitor the dominant damage phenomena. Such experiments are conducted in this study and damage models are used to rationalize the measured nonlinear properties.

Table I. Initial Properties of Composites[9]

		Values		
		Fibers (Nicalon)	Matrix (CAS)	Measured
Young's modulus (GPa)	E_1	136	136	
	E_2	120	80	
	E	128	93	90–100
Residual stresses (MPa)	p	−62		
	q	85		90
	σ_m		20	25–30

Fiber modulus: E_f = 200 GPa
Matrix modulus: E_m = 97 GPa
Ply thickness: t = 180 μm
Matrix fracture energy: Γ_m = 25 J/m²
Fiber radius: R = 7.5 μm
Misfit strain between fibers and matrix: Ω_1 = 1.25 × 10⁻³
Misfit strain between laminae: Ω_2 = 2.5 × 10⁻³
Sliding stress: τ_i = 10–20 MPa
In situ fiber strength parameters: S_0 = 2.0 GPa
m = 3.6
δ = 3.5
δ_c = 8–10

II. Experimental

(1) Procedures

Experiments were conducted on a CAS matrix composite reinforced with Nicalon fibers in a crossply $[(0/90)_2]_s$ configuration provided by Corning.[12] The nominal ply thickness, t = 180 μm. All test specimens were cut from 150-mm × 130-mm × 3.1-mm plates. *Tensile specimens* were prepared by machining beams having dimensions 150 mm × 3 mm × 3.1 mm, followed by polishing. Aluminum tabs were bonded to the ends to ensure uniform load transfer and to avoid crushing of the specimen. Strains were measured along a gauge length using an axial extensometer in contact with the specimen. An

Table II. Formulae for Linear Properties of Laminate ($t_0 = t_{90} = t$)

Composite modulus, E_c	$= E_1 + E_2$
Residual stress, σ_R	$= +E_1E_2\Omega/E_c$
Stress on longitudinal plies, σ_1	$= \sigma E_1/E_c$
Stress on transverse plies, σ_2	$= \sigma E_2/E_c$

W. K. Treadway — *contributing editor*

Manuscript No. 195908. Received March 11, 1992; approved July 24, 1992.
*Member, American Ceramic Society.

acoustic emission technique and a traveling microscope were employed to monitor damage. Several tests were performed with either partial or full unloading conducted at discrete strain intervals, as needed to determine the change in unloading modulus and the permanent strain, as a function of applied stress. Some specimens were edge-notched using a diamond saw prior to testing, in order to ascertain the notch properties. Unloaded specimens and fracture surfaces were characterized in the scanning electron microscope (SEM).

Two types of *flexural test* were conducted to explore both tensile and shear damage. For the study of tensile behavior, the flexure beams were typically 55 mm × 3 mm × 3.1 mm, and the tests were conducted in four-point bending, with inner and outer spans of 20 and 40 mm, respectively. One side face and the tensile face were polished to enhance microscopic imaging. To detect damage, experiments were performed in situ within an optical microscope. Photomicrographs were taken under load at a series of stress levels in order to document the formation and propagation of damage, such as matrix cracks. In some cases, the loading was interrupted and then resumed to failure. To investigate the shear characteristics, short flexural beams (25 mm) were used. Again, the side faces were polished in order to investigate the damage in situ in the SEM. Interrupted tests were also used.

A few specimens were used to measure the residual stress. For this purpose, a series of crossply laminate bend specimens were mounted on a steel plate and surface ground until only two laminae (a single 90° layer and single 0° layer) remained. Upon removal from the mount, bending occurred and the radius of curvature was measured. The residual stress was ascertained from the curvature, using beam theory (Appendix A, Eq. (A–4)).

(2) Measurements and Observations

(A) Tensile Behavior: Tensile stress/strain curves had the features illustrated in Fig. 1. Nonlinearity occurred at stresses in the range 40–60 MPa, following an initial tensile modulus, $E \approx 100$ GPa, with an ultimate strength of $S_u = 230 \pm 20$ MPa, at a tensile strain to failure, $\varepsilon_f = 0.8\%$. Corresponding changes in tensile modulus obtained by partial unloading by 25 MPa, as well as in permanent strain, are indicated on Fig. 2. Acoustic emission events first occurred within a stress range similar to the onset of nonlinearity. Flexural measurements obtained with long beams exhibited similar characteristics, with a nonlinearity at about 60 MPa and an ultimate strength of about 320 MPa. Optical observations performed in situ (Fig. 3) are summarized on Fig. 4. Matrix cracks first developed at stresses between 40 and 50 MPa. In all cases, the first cracks were observed *in the central 90/90 double layer* and always spanned the entire double ply but arrested at the 90/0 interfaces. Upon increasing the stress to about 50–60 MPa, matrix cracks appeared abruptly in all other 90° plies and additional matrix cracks developed in the central ply. Again, these cracks spanned the entire ply but arrested at the laminae interfaces at ~60 MPa. The crack spacing L in the single 90° layers was substantially less than the crack spacing in the central double 90° ply. Matrix cracks in alternating 90° layers were never coplanar, but always offset.

Upon increasing the stress to about 70–80 MPa, no further cracking was observed in the 90° layers, as indicated by a plot of the inverse crack spacing t/L with stress (Fig. 5). However, the preexisting cracks began to extend into the adjacent 0° layers. This process occurred stably with increasing stress, without obvious fiber failure. At higher stress, around 110 MPa, the extended matrix cracks overlapped in the 0° layers. Eventually, at ~170 MPa, these cracks entered the adjacent 90° layers (Fig. 3(C)) and reoriented toward preexisting cracks. At this stage, few fiber failures were visible. After testing to failure, the average crack spacing $\bar{d}$ in the 0° layers was ~150 μm compared with a spacing L in the single 90° layers of ~200 μm and ~300 μm in the double 90° layers (Fig. 6). The saturation crack spacing observed in unidirectional material was 103 μm.[7]

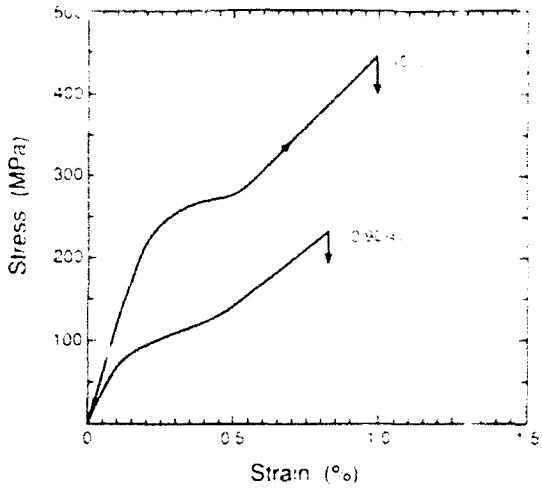

Fig. 1. Tensile stress/strain curve for the 0/90 material compared that for unidirectional material.

Subsequent to tensile failure, SEM examination revealed a relatively planar mode I fracture, with extensive pullout of the fibers within the 0° plies (Fig. 7(A)). Measurement of the pullout lengths h gave the distribution summarized in Fig. 7(B), with an average value, $\bar{h} = 285$ μm (similar to that found for unidirectional material[7]).

The notch characteristics are dominated by multiple delaminations that occur from the notch tip (Fig. 8). The nominal energy release rates associated with the extension of these delamination cracks are thus relatively large and exceed those found for 0/90 LAS composites.[7]

Double-layer 0/90 laminae (prepared for residual stress measurements, as described above) were found to have radii of curvature in the range 450–800 mm. The residual stress determined from this curvature, using beam theory (Appendix A, Eq. (A–4)) is $\sigma_R = 25 \pm 5$ MPa.

(B) Shear Behavior: The nominal shear stress displacement curves measured on short beams in flexure exhibit nonlinearity at a shear stress of about 50 MPa and a peak shear stress of about 85 MPa. The first shear damage to be observed consisted of a few matrix cracks that extended through both the 0°

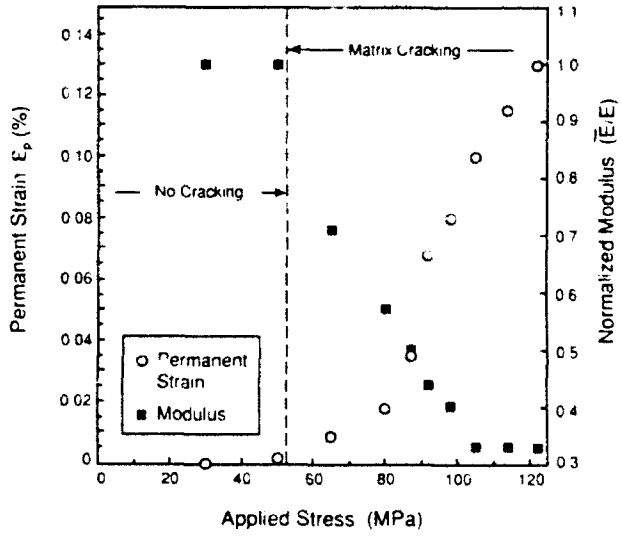

Fig. 2. Changes with applied stress in unloading tensile modulus upon partial unloading by 25 MPa and permanent strain.

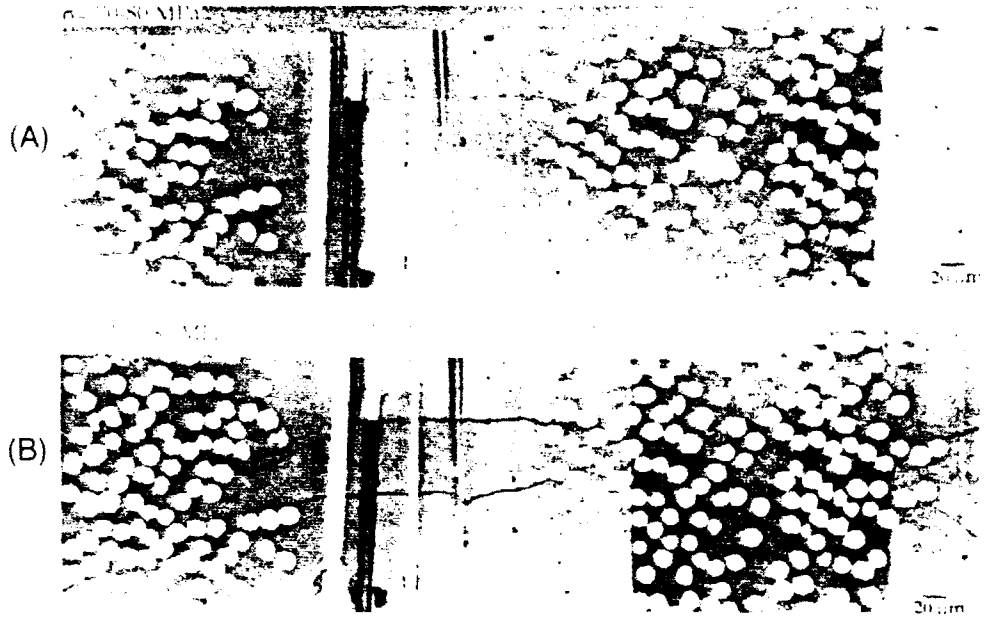

Fig. 3. Matrix cracks observed in situ in the optical microscope (A) stressed to 70 MPa, (B) stressed to 170 MPa

and 90° plies, at an inclination of ~35° (Fig. 9(A)). However, these cracks originated from previously formed tensile matrix cracks. At higher stresses, damage tended to concentrate in the matrix-only region (Fig. 9(B)), manifest as an *en echelon* crack array, inclined at ~68°. These cracks eventually coalesced, leading to shear failure by fragmentation of the matrix-only layer. Analogous behavior has been documented for unidirectional LAS composites.[14]

III. Models of Damage and Failure

The *nonlinearity* in the stress-strain curves found upon tension and shear testing must be governed by the *matrix cracks*, whereas the *ultimate tensile strength* should be dominated by the properties of the *fibers and interfaces*, subject to weakest-link statistics. In order to simulate the mechanical properties dictated by matrix cracks, two types are of interest: (i) *tunneling* cracks in 90° layers and (ii) *normal matrix* cracks in 0° layers. For both types, it is necessary to determine the applied loads that cause the cracks to form (subject to residual stresses), as well as evaluate their influence on the elastic moduli and the permanent strain. Analyses of these effects are presented below.

(1) *Tunneling Cracks in 90° Layers*

(A) Tensile Loading: Analyses of tunneling cracks[7,10] provide the background needed to predict the formation of cracks in the 90° layers. Tunneling cracks arise when flaws preexist that span the layer thickness and then propagate *along* the layer (Fig. 10(A)). Such initial flaws are expected in CMCs, especially at edges, caused by the combined effects of machining and thermal expansion misfit stresses. The principal feature of tunneling cracks of present relevance is the existence of a *lower-bound*, steady-state, cracking stress σ_c, that relates explicitly to the layer thickness, t, through the nondimensional function

$$\sigma_c^2 t/E_1\Gamma_1 = g(\chi) \tag{1}$$

where χ is an elastic mismatch parameter,

$$\chi = (E_1 - E_2)/(E_1 + E_2) \tag{2}$$

and

$$E' = E/(1 - \nu^2)$$

with the subscripts L and T referring to longitudinal and transverse plies, and $g(\chi)$ [15] is the function plotted on Fig. 10(B). Γ_1 is the energy for matrix cracking in the transverse layers, given by

$$\Gamma_1 = \Gamma_m(1 - f) \tag{3}$$

with f being the fiber concentration. The relevant critical stress in the *transverse layers* σ_c (which arises from the applied loads, plus the thermal expansion misfit) is given by

$$\sigma_c = E_1(\sigma + \varepsilon_1 E_1)/E \tag{4}$$

where ε_1 is the misfit strain between the longitudinal and transverse plies (which is related to the residual stress, σ_R, Table II) and σ is the applied stress. The magnitude of the *applied stress* at which tunneling cracks first occur, σ_c, can be derived by equating σ_c to σ_c:

$$\begin{aligned}\sigma_c &= (E/E_1)[gE_1\Gamma_1/t]^{1/2} - \varepsilon_1 E_1 \\ &= E[g\Gamma_1/E_1 t]^{1/2} - \sigma_R E/E_1\end{aligned} \tag{5}$$

The relevant magnitudes of the elastic modulus E_1 and E require some discussion. The magnitude of E_1, being independent of the interface properties, is well-defined and given by

$$E_1 = fE_f + (1 - f)E_m \tag{6}$$

However, E depends on the interface and the expansion misfit but in general can be expressed as[16]

$$E = E_c \left\{ \frac{1 - f[(E_m/E_c - 1)(E_m/E_c + Q)]}{1 + Qf[(E_m/E_c - 1)(E_m/E_c + Q)]} \right\} \tag{7}$$

where Q depends on the spatial arrangement of the fibers but typically has magnitude, $Q \approx 1.2$. If the fiber and the matrix are in mutual contact, either because the interfaces are bonded or

A related result has been reported by Laws and Dvorak[13] based on a global energy balance.

It is assumed that there is no contribution to Γ_1 from the interfaces, which have a negligible fracture energy. It is also assumed that the tunnel cracks are not subject to bridging tractions from the fibers in the 90° layers.

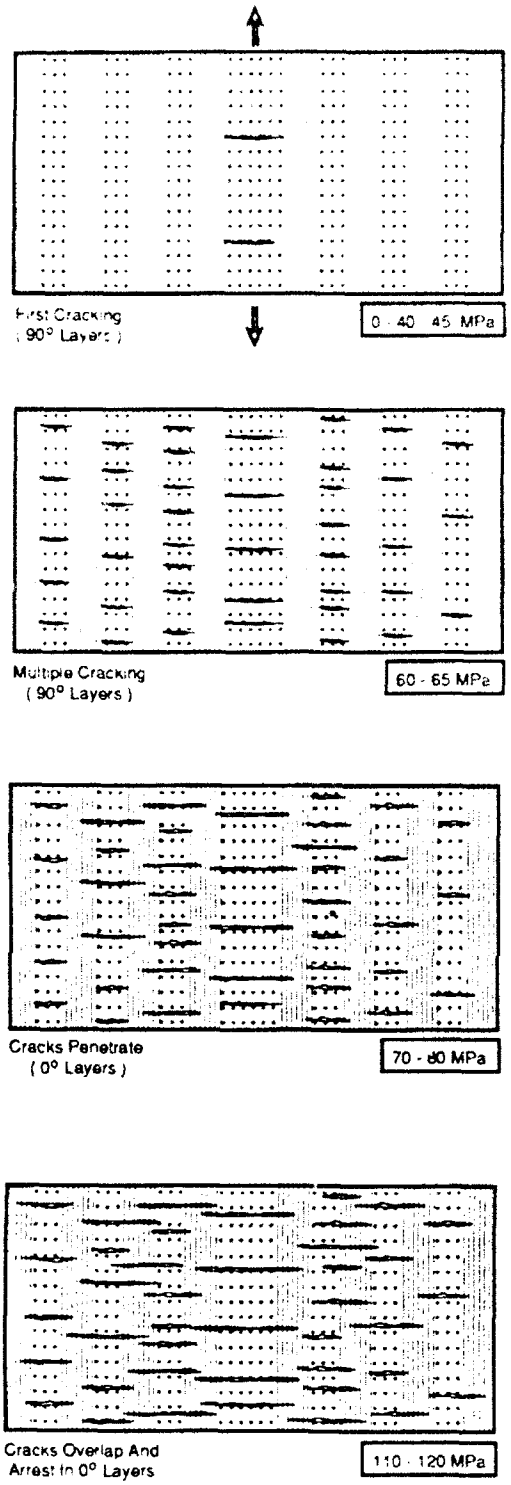

Fig. 4. Schematic indicating the sequence of matrix cracking based on direct observations of the type indicated on Fig. 3

because they are subject to a net compression (residual plus applied), then E_n in Eq. (7) is the transverse modulus of the fibers, E_t. However, if the interfaces separate upon loading, E_n would be much smaller. For the present composite, which has a "weak" interface, interface separation is likely to occur when the transverse stress exceeds the residual compression at the interface [9] At this stage, there would be an abrupt drop in transverse modulus. It will be shown below that the experimental results are consistent with a separated interface ($E_n \to 0$)

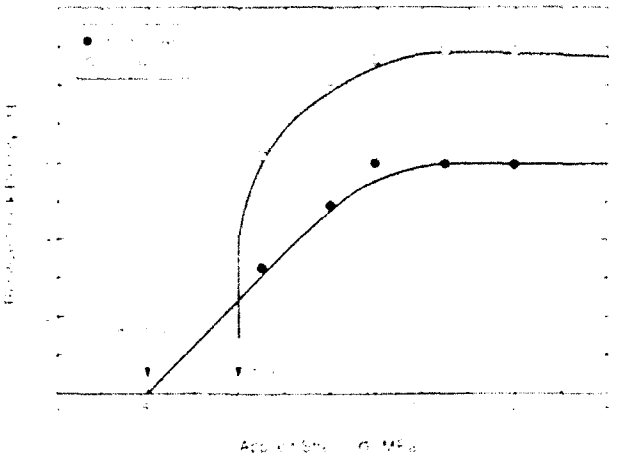

Fig. 5. Effects of stress on crack density in the 90° ply

(B) Shear Loading. The basic tunnel crack formulation also applies for matrix cracks formed upon shear loading if it is presumed that the matrix tunnel cracks follow a mode I trajectory [9] Then, if elastic mismatch effects are neglected, the lower-bound shear stress, τ, for growth of the tunnel cracks is given by

$$\tau \sqrt{t/T} = \sqrt{\pi \sin\theta 2\cos\theta} \tag{8}$$

where θ is the crack inclination with respect to the ply normal, which is related to the residual stress σ_r by

$$\sqrt{2}\tan\theta = \sigma_r \sqrt{T} + \sqrt{2 + (\sigma_r \sqrt{T})} \tag{9}$$

with t being the layer thickness and Γ the relevant fracture energy. Combining Eqs. (8) and (9) leads to an explicit relationship between τ and σ_r. Multiple cracking is expected at higher shear stress, analogous to that found in tensile loading.

(2) Matrix Cracking of 0° Layer

Upon tensile loading, cracks in the 90° layer precede those in the 0° layer and, furthermore, the latter form by extension of the previously formed cracks in the 90° layers. Consequently, the cracking problem in the 0° plies commences with a plane strain matrix crack of length t (Fig. 10(A)) that subsequently penetrates the 0° fiber bundles. In order to obtain approximate *analytical* solutions for crack penetration that illustrate the key trends, consideration is first given to identifying the most reasonable simplifications concerning the relative layer thickness

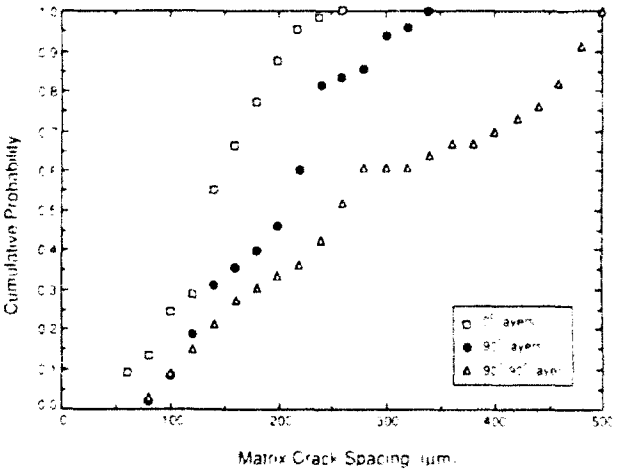

Fig. 6. Cumulative distributions of crack spacing after failure (0° layer, 90° layer, double 90° layer)

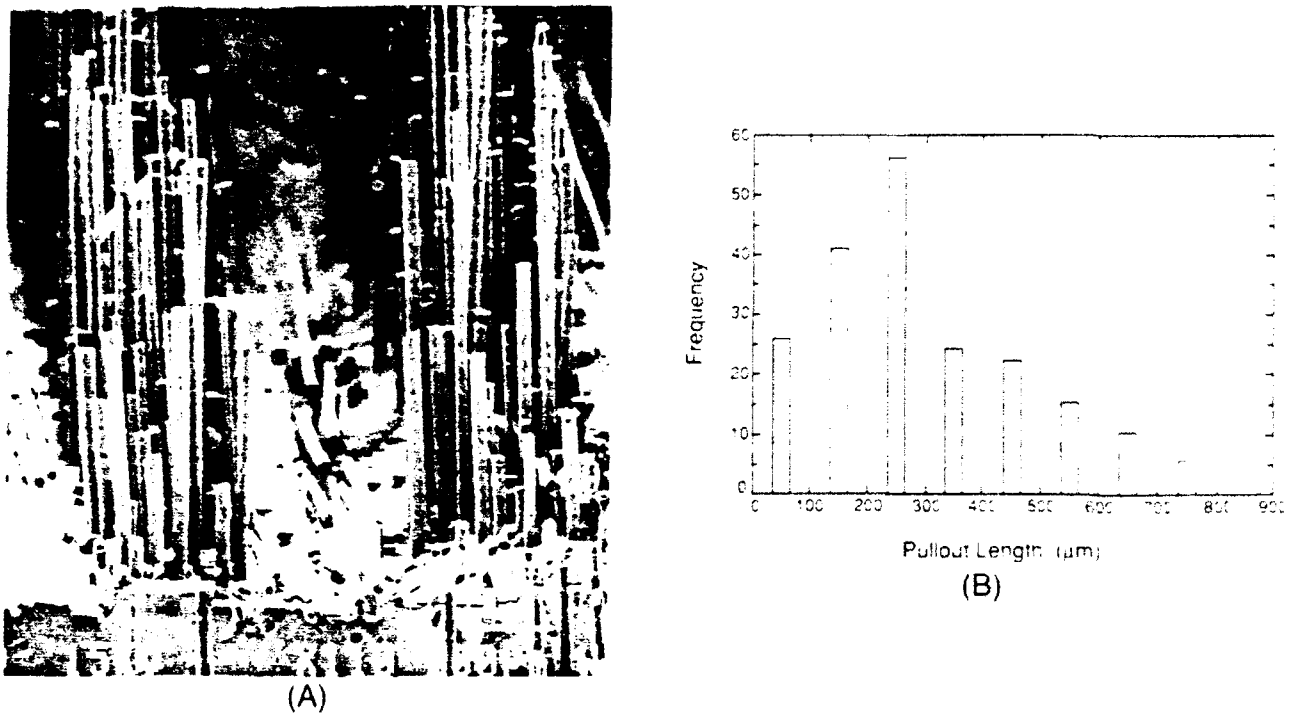

Fig. 7. (A) Fracture surface indicating fiber pullout, (B) the pullout distribution

and stiffness, as well as the failure mode in the 0° bundles. The laminate layers generally have about equal thickness and, hence, the thickness ratio is taken to be unity. It is also believed that the main features of the cracking phenomenon can be elucidated by assuming elastic homogeneity, $E_f \approx E_m \approx E$. Moreover, the problem consists of a crack penetrating into a longitudinal fiber bundle *with the fibers remaining intact*. Consequently, the bridging tractions, $\sigma_b(u)$, satisfy[21]

$$\sigma_b(u) = 2f[\tau_0 E/(1-f)R]^{1/2}u^{1/2} \tag{10}$$

where, τ_0 is the interface sliding stress and u the crack opening displacement. Near the crack tip in the 0° layer, the crack opening is related to the tip stress intensity factor K_{tip} by[21,22]

$$Eu(x) = (2\sqrt{\pi})K_{tip}\sqrt{c}\sqrt{1-(x/c)^2} \tag{11}$$

where x is the distance from the crack center and $2c$ the crack length. In previous analyses,[21] it has been found that Eq. (11) also provides a reasonable representation of $u(x)$ over most of the bridged segment. This assumption will be used here. It will also be assumed that a critical-stress-based fracture criterion applies, given by[21]

$$K_{tip} = \sqrt{EI_0} \tag{12}$$

Then, $\sigma_b(x)$ becomes

$$\sigma_b(x) = \frac{2\sqrt{2}}{\pi^{1/2}} f\left[\frac{\tau_0 E}{(1-f)}\right]^{1/2}\left(\frac{I_0 c}{ER^2}\right)^{1/4}\left[1-(x/c)^2\right]^{-1/4} \tag{13}$$

For an elastically homogeneous system, K_{tip} can also be related to the *net* tractions $\sigma_n(x)$ by[21,22]

$$K_{tip} = \frac{2\sqrt{c}}{\sqrt{\pi}}\int_0^c \frac{\sigma_n(x)\,dx}{\sqrt{c^2-x^2}} \tag{14}$$

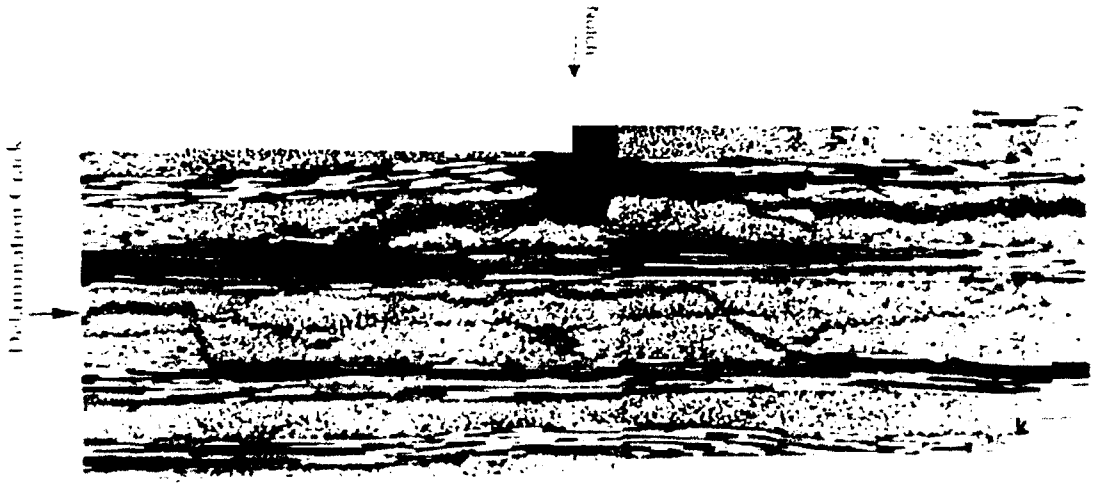

Fig. 8. Result of notch tests showing multiple delamination cracks

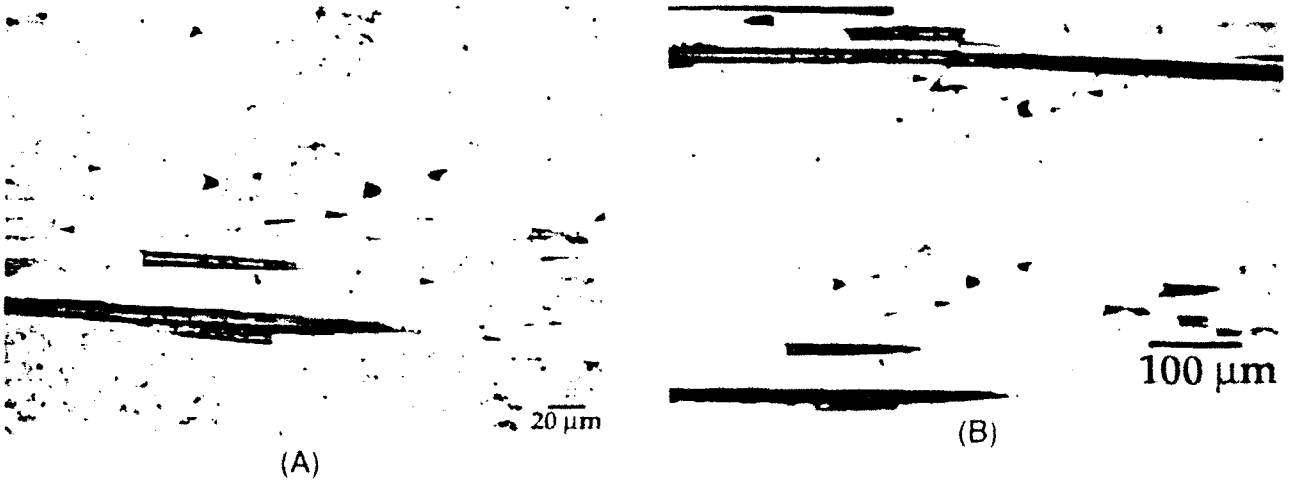

Fig. 9. Shear damage found in short beam tests. (A) Initial matrix cracking at ~50 MPa. (B) Concentrated shear damage prior to failure occurring in the matrix-only layer. Arrows indicate locations of matrix cracks.

such that, with Eq. (12)

$$\sqrt{\frac{\overline{EK_i}}{c}} = \frac{2}{\sqrt{\pi}} \int_0^c \frac{\sigma_i(x)\,dx}{\sqrt{c^2 - x^2}} \tag{15}$$

A solution to the problem of interest is now obtained from Eq. (15) by providing information about $\sigma_i(x)$:

$$\sigma_i(x) = \sigma + \sigma_R \qquad (x \leq t/2) \tag{16}$$

$$\sigma_i(x) = \sigma - \sigma_R - \sigma_R(x) \qquad (x \geq t/2) \tag{17}$$

where σ is the applied stress and σ_R the residual stress.[7] Inserting the stresses from Eqs. (16) and (17) into Eq. (15) and integrating, the crack growth stress $\sigma(c)$ becomes

$$\left(\frac{2\pi}{\lambda_1^2}\right)\frac{\sigma}{\sigma_0} = \frac{\pi}{2} + \frac{\lambda_2\sqrt{\pi/2}}{\sqrt{\alpha}} - 2\sin^{-1}(1/\alpha) + \lambda_2\alpha^{3/2}F(\alpha) \tag{18}$$

where

$$\lambda_1 = (E_1\sigma_R)\sqrt{\Gamma_1 E_1}$$

$$\lambda_2 = 2/(2\pi)^{1/2}\left[\frac{\pi\Gamma_2 E_2}{\sigma_R^2}\left(\frac{\tau}{R(1-f)}\right)^2\right]^{1/4}$$

$$\alpha = 2c/t$$

$$F(\alpha) = \int_{1/\alpha}^{1} \frac{d\omega}{(1-\omega^2)^{1/2}}$$

Before evaluating Eq. (18), it is convenient to reexpress λ_2 in terms of the steady-state matrix cracking stress for unidirectional material

[7] Since the layers are taken to have equal thickness and the system is elastically homogeneous, the residual stresses must have equal magnitude but opposite sign in alternating layers.

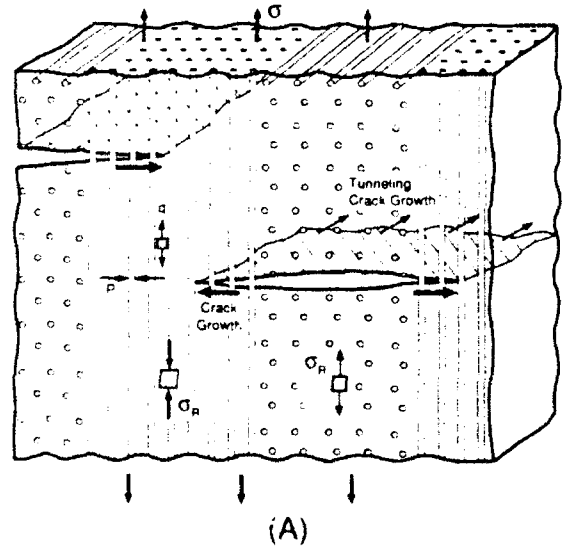

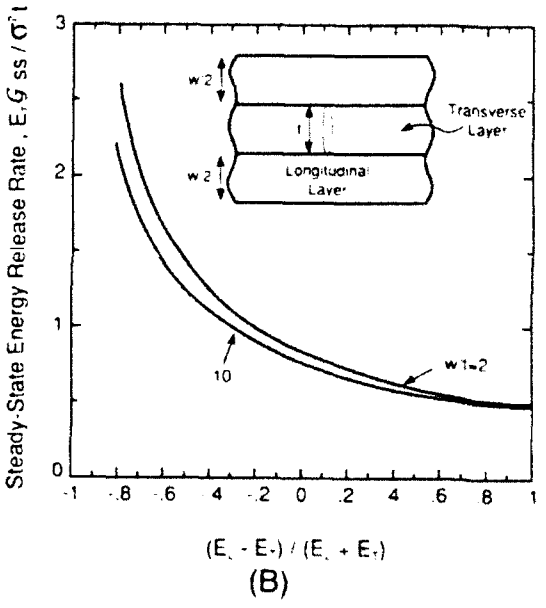

Fig. 10. (A) Schematic of tunneling cracks in 90° layers. (B) Effects of elastic mismatch on the lower-bound criterion for tunnel cracking.[7]

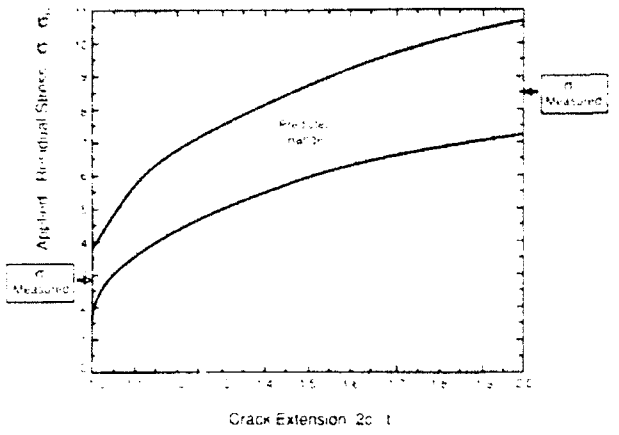

Fig. 11. Stresses needed to propagate matrix cracks through the 0° layers. The lower and upper bounds correspond to $\lambda_2 = 5.8$ and 5.10, respectively. Also shown is the comparison of measured and calculated cracking stresses, σ_i and σ.

$$\sigma_{ss} = \left[\frac{6\tau_i L_s f^2 E}{R(1-f)}\right]^{1/2} \tag{19}$$

giving

$$\lambda_1 = 2\left(\frac{2}{3\pi}\right)^{1/2} \frac{\sqrt{\bar{l}}}{(1-f)^{1/2}} \left(\frac{\tau_i E_c t}{\Gamma_m \sigma_R R}\right)^{1/2} \left(\frac{\sigma_c}{\sigma_R}\right)^{1/2}$$

For ceramic/matrix composites, it can be readily ascertained that λ_1 and λ_2 are both *of order unity* and range between 0.1 and 10 (Table I). This range is used to address the trends predicted by Eq. (18). Additionally, the important range for α is between 1 and 2. With this background, plots of σ/σ_R as a function of α (Fig. 11) illustrate the major trends. It is apparent that, for this range of λ_1 and λ_2, the cracks penetrate into the 0° bundles at a critical stress, σ_i. Subsequently, the cracks extend *stably*, subject to increasing load until they exit the 0° bundles. Thereafter, they grow unstably across the next 90° layer. Consequently, the stress σ_i' at $\alpha = 2$ would typically represent the maximum stress at which matrix cracking occurs. This stress is obtained from Eq. (18) as

$$\sigma_i'/\sigma_R = 0.56\lambda_1 - 0.67 + 0.82\lambda_2 \tag{20}$$

The loading range wherein changes in modulus and permanent strains are associated with crack growth across the 0° plies is thus bounded by the stresses σ_i and σ_i' (Fig. 11).

(3) Fiber Fracture and Ultimate Strength

Final failure of the composite is considered to be dominated by the fibers in the 0° plies, whereupon the ultimate strength is determined by consideration of weakest-link statistics. By assuming that both the debond energy and sliding stress are small, such that the fibers are noninteracting, the matrix allows load transfer through the interfacial shear tractions, with global load sharing, and parameters such as the pullout length and the in situ fiber strength can be explicitly linked with τ_i. Following this approach, the ultimate strength of the composite is predicted to be[10]

$$S_u = f_1 S_o \left[\frac{2}{(m+2)}\right]^{1/(m+1)} \left[\frac{m+1}{m+2}\right] \tag{21}$$

where f_1 is the volume fraction of the fibers in the longitudinal orientation, m is the Weibull shape parameter and S_o is a characteristic fiber strength. The values of S_o and m for Nicalon fibers in CAS have been obtained from measurements of fracture mirrors on broken fibers in unidirectional material (Table I). The corresponding result for the average pullout length is[10]

$$\bar{h} = (RS_o \tau_i)(\lambda(m)) \tag{22}$$

where λ is a nondimensional quantity of order unity.

(4) Stress Strain Curves

The tensile stress strain curves can be simulated by using the above information about matrix cracks to determine the changes in modulus, plus the permanent strains coupled with the analysis of fiber failure. Solutions for periodic multiple cracks in the 90° layers have been expressed in terms of a "shear lag" parameter, ξ,[11] which is a measure of the shear response of the matrix layer between the 0° and 90° plies. With this parameter, the stress strain curve $\sigma(\varepsilon)$ is given by

$$\sigma/\bar{E} = \frac{\varepsilon - \alpha(L_c/2t)\sigma_T[\tanh(\xi/L_c/2t)]/\xi}{1 + \alpha(L_c/2t)(E_m/E_1)\tanh(\xi/L_c/2t)} \tag{23}$$

such that the Young's modulus is

$$E/\bar{E} = 1 + \alpha(L_c/2t)(E_m/E_1)\tanh(\xi/L_c/2t) \tag{24}$$

and the permanent strain is

$$\varepsilon_r = \alpha(L_c/2t)\sigma_R/E_1)\tanh(\xi/L_c/2t) \tag{25}$$

The magnitude of ξ has been assessed both by finite element procedures[11] and by an approximate elasticity method,[12] which agrees well with the numerical results. The latter is given for equal numbers of 0° and 90° plies by[12]

$$\xi = \sqrt{3E_1 E_2 (1+\nu_{12})} \tag{26}$$

where ν_{12} is Poisson's ratio. Hence, by using *measured* values of t/L_c, both $\bar{E}$ and ε_r may be calculated.

The modulus changes that occur when the tunnel cracks extend into the 0° bundles have not yet been calculated. Consideration of a lower bound provides some perspective. When the 0° layers have fully developed matrix cracks (at stress σ_i', Eq. (20)), the unloading modulus of these layers $\bar{E}_1$ upon full unloading, when $\bar{d}$ is less than the saturation value, becomes[13]

$$E_1/\bar{E}_1 = RE_m^2(1-f)^2\dot{\sigma}_1/4\bar{d}\tau_i E_1 E_f^2 + s(\bar{d}/R) \tag{27}$$

where $\dot{\sigma}_1$ is the peak stress (applied plus residual) reached in these layers and s is a compliance function of order 1.0–1.2. A similar expression applies for partial unloading.[13] By knowing how $\bar{d}$ changes with stress $\dot{\sigma}_1$, Eq. (27) provides a lower bound for the change in composite modulus with stress. The corresponding permanent strain is[4]

$$\bar{\varepsilon}_{ss} = \frac{R(1-f)^2 q^2}{4\bar{d}f^2\tau_i E_f}\left[\left(\frac{\dot{\sigma}_1 E_m}{qE}\right)^2 + 4\left(\frac{\dot{\sigma}_1 E_m}{qE}\right) - 2\right] \tag{28}$$

where $\dot{\sigma}_1$ is, again, the net stress (residual plus applied) reached in the 0° plies.

IV. Comparison between Theory and Experiment

(1) Initial Properties

A comparison between theory and experiment can be made by first evaluating the elastic properties, the residual stress, and the interface properties, following some general remarks that provide the necessary context. The overall residual stress in the plies, σ_R, caused by thermal expansion anisotropy is biaxial, with the normal and shear stresses at the ply boundaries being zero (except near the edges). However, prior to bonding of the plies, residual stresses exist within the fibers and the matrix, characterized by a compression p normal to the interface and a longitudinal tension q in the matrix having magnitudes ($p = -62$ MPa, $q = 85$ MPa). Upon bonding, both p and q are changed—q uniformly and p nonuniformly.

When a stress is applied to the laminated composite, p is further reduced and interface separation may occur. This situation leads to uncertainty about the influence of the fibers on the transverse modulus. However, comparison of the measured,

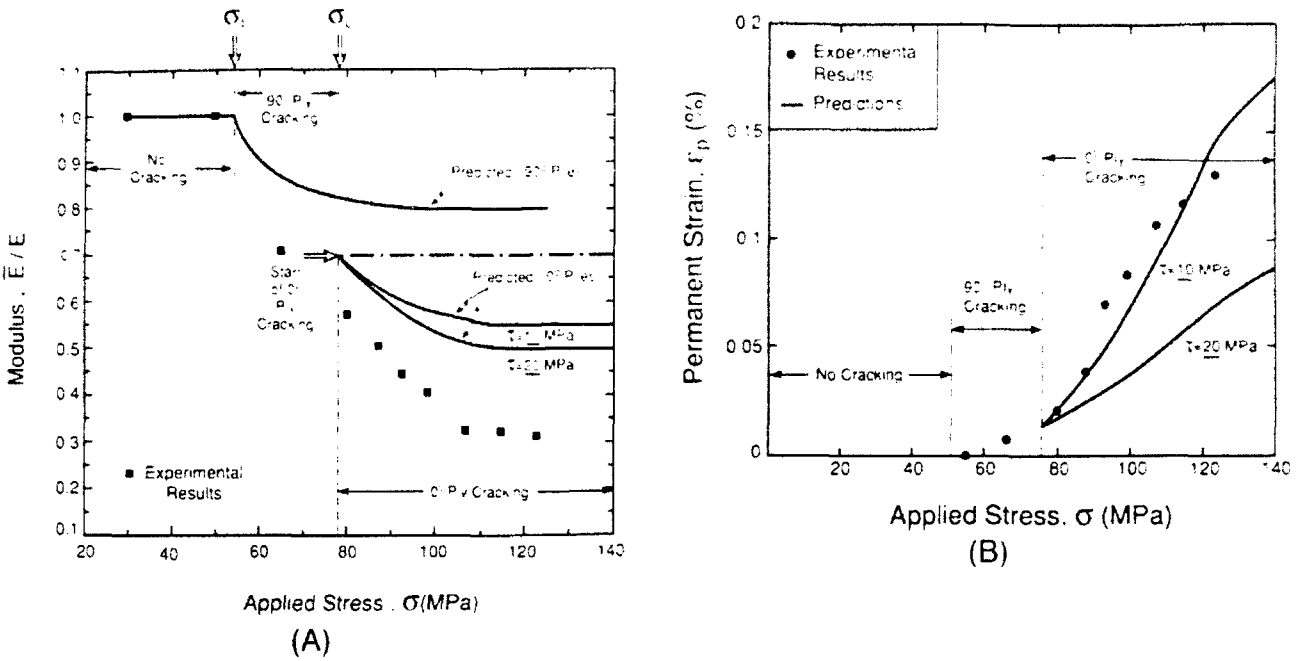

Fig. 12. Comparisons of measured and calculated values of (A) modulus change, (B) permanent strain

initial composite modulus with the values expected, either for an intact interface ($E_0 = E_1$ in Eq. (7)) or a separated interfaces ($E_0 = 0$), indicates (Table I) that the interfaces can be regarded as separated, such that the effective transverse modulus, $E_1 \approx 50$ GPa. This value for E_1 is used in subsequent comparisons between theory and measurement. Based on the above choice for E_1, the beam curvature measurements (Section II(2)) indicate a residual stress, $\sigma_R = 25 \pm 5$ MPa. This value is consistent with the magnitude expected from the thermal expansion misfit between the fiber and matrix (Table II).

The interface sliding stress τ_0 can be estimated from the fiber pullout length (Fig. 7(B)), using Eq. (22), by assuming that the in situ properties of the fibers are the same as those found for unidirectional material[3] (Table I, $S_f = 2.0$ GPa, $m = 3.6$). Then Eq. (22) gives $\tau_0 \approx 13$ MPa. This value is essentially the same as that established for unidirectional material,[3] even though the residual stress, p, has been modified upon forming the laminate.

(2) Matrix Cracking

(A) Transverse Plies: The stresses at which cracking of the *transverse plies* commences can be predicted by assuming that the tunneling crack mechanism obtains, whereupon Eq. (5) may be used in conjunction with the properties indicated on Table I and g obtained from Fig. 10(B) ($g \approx 1.53$). The inner double 90° layer is predicted to crack first at an applied stress $\sigma_c \approx 40$ MPa, whereas cracking of the other 90° layers is expected at stresses $\sigma_c \approx 60$ MPa, compared with measured values of 40–50 and 50–60 MPa, respectively. Consequently, the predicted sequence of cracking between layers, as well as the level of stress, is consistent with the present measurements, validating the tunnel crack mechanism.

Inserting the *measured* values of the crack spacing (Figs. 5 and 6) into Eqs. (24) and (25) and using the measured values of the elastic properties and residual stress (Table I), the modulus changes and the permanent stress, caused by cracking of the 90° layers, are predicted and compared with the experimental results on Figs. 12(A) and (B), respectively. The comparison is based on the independent knowledge that cracking of the 90° plies saturates at ~80 MPa, leading to the distinction between cracking mechanisms indicated on Fig. 12. With this specification, it is noted that the modulus decrease predicted by the model is smaller than that found experimentally (Fig. 12(A)). The reasons for this discrepancy are not understood. Also, the permanent strains caused by 90° tunnel cracks are small, both by measurement and predictions (Fig. 12(B)).

(B) Longitudinal Plies: Comparison between theory and experiment for cracking of the 0° plies is achieved by first comparing the calculated (Eq. (18)) and measured values of the stresses, σ_1, and σ_1', at which cracks (a) just penetrate the 0° plies and (b) have extended stably across these plies. For this purpose, it is noted that λ_1 and λ_2 are in the range 3–5 and 8–10, respectively, giving the range of predicted crack growth stresses plotted on Fig. 11. The predicted range encompasses the measured values of σ_1, and σ_1', despite the simplification concerning elastic homogeneity used for the calculations. The basic model thus appears to be reasonable.

The change in modulus and permanent strain induced by cracking of the 0° plies can now be predicted based on the knowledge that cracks begin forming at ~80 MPa and saturate at ~170 MPa. Then, by using the measured crack spacings, $\bar{E}$ and ϵ_p are predicted. The calculations have been performed by adopting the following homogenization procedure. The fibers are considered to be distributed uniformly, with an average volume fraction ($f = 0.19$), and the matrix is assigned a composite modulus based on the properties of the laminate. Values of sliding stress in the range, $\tau_0 = 10$–20 MPa, are used as ascertained both in this study and in previous analyses.[3] Comparison with experiment (Fig. 13) indicates that this approach significantly underestimates the modulus reduction found experimentally (Fig. 12(A)). Furthermore, the discrepancy is larger than that previously found for unidirectional material.[3] A model that more completely incorporates the compliance of the combined 90°/0° crack configuration appears to be necessary before modulus changes can be accurately simulated. Conversely, the permanent strain prediction is quite good (Fig. 12(B)), even though the same interface model is used. Similarly good agreement with the models was found for unidirectional material.[3]

(3) Ultimate Strength

The interface sliding stress, τ_0, and pullout lengths are essentially the same as those previously found for unidirectional material.[3] Consequently, the fiber strength parameter S and the

Weibull modulus, m, (Table I) should be the same, provided that fiber degradation effects caused by processing are similar in unidirectional and 0/90 materials. With this assumption, the ultimate strength predicted by Eq. (21) is 250 MPa, compared with the measured value of 230 ± 20 MPa. The agreement is good and consistent with the behavior found for unidirectional material.[7]

V. Concluding Remarks

The basic matrix cracking models for 0/90 ceramic matrix composites appear to provide a reasonably accurate description of the *incidence* of cracking. However, models of the influence of such cracks on the elastic modulus E are less satisfactory, even with independent information about the crack density. Furthermore, models for crack evolution with load are not well developed. It is thus concluded that improved models of crack evolution are needed in order to provide constitutive laws suitable for design calculations, including more sophisticated representations of the interface properties[7] and of the effects of matrix cracks on the elastic compliance.[2]

Residual stress and interfacial effects have been shown to be of considerable importance. It is necessary to have independent knowledge of the associated misfit parameters in order to provide meaningful predictions of matrix crack formation. It is also necessary to know the matrix fracture energy.

The ultimate strength S_u is found to be consistent with the predictions of global load-sharing models and to have a correspondence with S_u for 1-D material, simply through the reduced fiber volume fraction in the loading orientation.

Finally, the elastic modulus in the 90° layer is found to be unexpectedly low. This effect has been attributed to the weak interfaces, combined with the residual tension in the 90° layers. The residual tension seemingly causes the interfaces to separate, even though its magnitude is too small to predict actual interface separation prior to loading. This discrepancy has yet to be resolved.

APPENDIX A

Relationship between Residual Stress and Curvature

The residual stresses in the plies can be derived from the curvature of a 0/90 layer prepared as described in the text. From equilibrium, the residual force on these laminae must be zero, and since the layers have equal thickness, t, then

$$\sigma_{R0} + \sigma_{R90} = 0 \tag{A-1}$$

where σ_R is residual stress and the subscripts 0 and 90 refer to the 0° and 90° layers, respectively. The residual stress in each layer can also be related to the bending moment, per unit width, M_R by

$$M_R = \sigma_R t^2 \tag{A-2}$$

where

$$M_R = \frac{EI}{\mathcal{R}} \tag{A-3}$$

with E being the Young's modulus of one of the layers, I the associated second moment of inertia, and $\mathcal{R}$ the radius of curvature. Combining Eqs. (A-2) and (A-3), the residual stress may be deduced as

$$\sigma_R = \frac{E_1 I_0}{\mathcal{R} t^2} \tag{A-4}$$

where I_0 is given by

$$12I_0/t^3 = \Sigma + 1 + 3(2\kappa - 1)^2 + 3(3 - 2\kappa)^2 \tag{A-5}$$

where Σ is the ratio of Young's modulus, E_1/E_2, w is the beam width, and κ defines the location of the neutral axis

$$\kappa = (3\Sigma + 1)/2(1 + \Sigma) \tag{A-6}$$

For the present composite (E_1 = 130 GPa, E_2 = 80 GPa), Σ = 0.36 and κ = 0.77.

APPENDIX B

Notation

c	Crack length
d	Mean crack spacing in 0° plies
E	Young's modulus of composite
E'	Plane strain modulus, $E/(1 - \nu^2)$
$\bar{E}$	Young's modulus of composite subject to damage
E_f	Young's modulus of fibers
E_m	Young's modulus of matrix
E_1	Longitudinal modulus of ply
E_2	Transverse modulus of ply
f	Fiber volume fraction
g	Tunnel crack parameter
h	Mean fiber pullout length
K_{tip}	Tip stress intensity factor
L	Mean crack spacing in 90° layers
m	Shape parameter for fiber strengths (Weibull modulus)
p	Residual stress normal to interface
q	Axial residual stress in matrix
R	Fiber radius
S_u	Ultimate strength
S_o	In situ fiber strength parameter
t	Ply thickness
t_m	Matrix layer thickness
T	Shear strength
u	Crack opening displacement
σ	Applied stress
σ_1	Stress at which crack in 90° layers penetrate into 0° layers
σ_1'	Stress at which matrix cracks extend completely across 0° plies
σ_b	Bridging traction
σ_R	Residual stress *within* ply
σ_s	Steady-state stress for tunnel cracks
σ_t	Net stress in transverse plies (applied plus residual)
σ_t'	Critical applied stress for tunnel cracking of 90° plies
σ_0	Matrix cracking parameter for 0° plies
Γ_m	Matrix fracture energy
Γ_1	Transverse fracture energy of ply
Ω	Thermal expansion misfit strain between fibers and matrix
τ_0	Interface sliding stress
ε_p	Permanent strain
ε_1	Misfit strain between longitudinal and transverse plies
ε_1^*	Failure strain of composite
λ	Elastic mismatch parameter $(E_1 - E_2)/(E_1 + E_2)$
ν	Poisson's ratio
λ	Pullout parameter
λ_1, λ_2	0° ply cracking parameters

References

A. G. Evans and D. B. Marshall, "The Mechanical Behavior of Ceramic Matrix Composites," *Acta Metall.*, **37** [10] 2567–83 (1989).

W. A. Curtin, "Theory of Mechanical Properties of Ceramic Matrix Composites," *J. Am. Ceram. Soc.*, **74** [11] 2837–45 (1991).

R. Y. Kim and N. Pagano, "Crack Initiation in Unidirectional Brittle Matrix Composites," *J. Am. Ceram. Soc.*, **74** [5] 1082–90 (1991).

A. Pryce and P. Smith, "Modelling the Stress Strain Behaviour of Unidirectional Ceramic Matrix Composite Laminates," *J. Mater. Sci.*, in review.

R. W. Rice, J. R. Spann, D. Lewis, and W. Coblenz, "The Effect of Ceramic Fiber Coatings on the Room Temperature Mechanical Behavior of Ceramic Fiber Composites," *Ceram. Eng. Sci. Proc.*, **5**, 614 (1984).

[8] C. Cao, E. Bischoff, O. Sbaizero, M. Ruhle, A. G. Evans, D. B. Marshall, and J. J. Brennan, "Effect of Interfaces on the Properties of Fiber-Reinforced Ceramics," *J. Am. Ceram. Soc.*, **73** [6] 1691–99 (1990).

[9] K. M. Prewo and J. J. Brennan, "High Strength Silicon Carbide Fiber Reinforced Glass Matrix Composites," *J. Mater. Sci.*, **15**, 2199–206 (1980).

[10] D. Beyerle, S. M. Spearing, F. W. Zok, and A. G. Evans, "Damage and Failure in Unidirectional Ceramic Matrix Composites," *J. Am. Ceram. Soc.*, in press.

[11] A. G. Evans, F. W. Zok, and J. B. Davis, "The Role of Interfaces in Fiber Reinforced Brittle Matrix Composites," *Compos. Sci. Technol.*, **42**, 3–24 (1991).

[12] O. Sbaizero and A. G. Evans, "Tensile and Shear Properties of Laminated Ceramic Matrix Composites," *J. Am. Ceram. Soc.*, **69** [6] 481–86 (1986).

[13] F. E. Heredia, S. M. Spearing, A. G. Evans, P. Mosher, and W. A. Curtin, "Some Mechanical Properties of C/Matrix Composites Reinforced with Nicalon Fibers," *J. Am. Ceram. Soc.*, in press.

[14] K. Chyung, U.S. Pat. No. 4,615,987, October 1986.

[15] O. Sbaizero, P. G. Charalambides, and A. G. Evans, "Delamination Cracking in a Laminated Ceramic Matrix Composite," *J. Am. Ceram. Soc.*, **73** [7] 1936–40 (1991).

[16] A. G. Evans, "The Mechanical Properties of Reinforced Ceramic, Metal and Intermetallic Matrix Composites," *Mater. Sci. Eng.*, **A143**, 63–76 (1991).

[17] J. W. Hutchinson and Z. Suo, "Mixed Mode Cracking in Layered Materials," *Adv. Appl. Mech.*, **28** (1991).

[18] S. He and Z. Suo, "Tunnelling Cracks in Constrained Layers," unpublished work.

[19] N. Laws and G. Dvorak, "Progressive Transverse Cracking in Composite Laminates," *J. Comp. Mater.*, **22**, 900–16 (1988).

[20] D. B. Marshall and W. Oliver, "Measurement of Interfacial Mechanical Properties in Fiber-Reinforced Ceramic Composites," *J. Am. Ceram. Soc.*, **70** [8] 542–48 (1987).

[21] J. C. Halpin and S. W. Tsai, "Environmental Factors Estimation for Composite Materials Design," AFML TR 67-423 (1969).

[22] S. Janssen, H. E. Deve, and A. G. Evans, "The Anisotropic Mechanical Properties of a Ti Matrix Composite Reinforced with SiC Fibers," *Metall. Trans. A*, **22**, 2975–84 (1991).

[23] D. B. Marshall, B. N. Cox, and A. G. Evans, "The Mechanics of Matrix Cracking in Brittle-Matrix Fiber Composites," *Acta Metall.*, **33** [11] 2013–21 (1985).

[24] R. M. McMeeking and A. G. Evans, "Matrix Fatigue Cracking in Fiber Composites," *Mech. Mater.*, **9**, 217–27 (1990).

[25] S. M. Spearing, F. W. Zok, and A. G. Evans, "Stress Corrosion Cracking in a Unidirectional Ceramic Matrix Composite," unpublished work.

[26] P. Steif, referenced in S. T. Ogin, P. A. Smith, and P. W. R. Beaumont, *J. Compos. Sci. Technol.*, **24**, 23–31 (1985).

[27] J. W. Hutchinson and H. Jensen, "Models of Fiber Debonding and Pullout in Brittle Composites with Friction," *Mech. Mater.*, **9**, 139–63 (1990).

journal

Reprinted from the Journal of the American Ceramic Society, Vol. 75, No. 11, November 1992

J. Am. Ceram. Soc., 75 [11] 3017–25 (1992)

Mechanical Properties of Continuous-Fiber-Reinforced Carbon Matrix Composites and Relationships to Constituent Properties

Fernando E. Heredia, S. Mark Spearing, and Anthony G. Evans

Materials Department, College of Engineering, University of California, Santa Barbara, California 93106

Paul Mosher

B. P. Chemicals (HITCO) Inc., Gardena, California 90249

William A. Curtin

B. P. Research, Warrensville, Ohio 44128

The tensile properties of three carbon matrix composites reinforced with SiC (Nicalon) fibers (materials A, B, C) have been measured with and without notches. One of the three materials (material B) had a relatively low strength and exhibited notch brittleness. This material had both a high interface sliding stress and a low fiber bundle strength, caused by particulates in the matrix. These characteristics have been shown to result in a change in failure mechanism that leads to the inferior properties exhibited by material B. The notch properties of the higher-toughness materials were shown to involve splitting, which alleviates the notch stress concentration and diminishes the notch sensitivity.

I. Introduction

A GENERAL understanding now exists regarding the mechanical properties of brittle matrix composites reinforced with continuous brittle fibers.[1-4] In particular, the relationships between the properties of unidirectional material in longitudinal and transverse tension and the in situ properties of the fibers, the matrix, and the fiber/matrix interfaces have been identified.[5-8] Some relationships between the properties obtained on unidirectional material and the corresponding properties of 2-D structures have also been developed.[9] However, there have apparently been no *quantitative* attempts to assess the properties of carbon matrix composites within this framework. The intent of the present article is to examine and evaluate the tensile and notch-tensile properties of several 2-D carbon matrix composites.

In brittle matrix composites, the ultimate tensile strength and the longitudinal modulus along one of the fiber directions are dominated by the in situ properties of the fibers. A useful normalization for the stress σ is thus[10] $\sigma/f_f S_o$, where f_f is the fiber volume fraction in the loading direction and S_o the in situ fiber strength at a particular gauge length.[5,11,12] A corresponding normalization for the strain is[10] $\varepsilon/\varepsilon_f$, where ε_f is the failure strain for the fibers. With these normalizations, *high-performance* composites have ultimate strengths ($\sigma_u/f_f S_o$) and failure strains ($\varepsilon_u/\varepsilon_f$) *close to unity*. Such values occur when the interfaces are "weak."[10] The characteristic "weakness" of fiber/matrix interfaces can be specified in terms of a debond fracture energy for the interface, Γ_i, as well as the sliding stress along the debonded interface, τ.[13,14] Both Γ_i and τ must be *small* for the composite to exhibit normalized strengths and failure strains approaching unity. Consequently, it is possible to rank the tensile properties through the *in situ characteristics of the fibers and the fiber/matrix interface*.

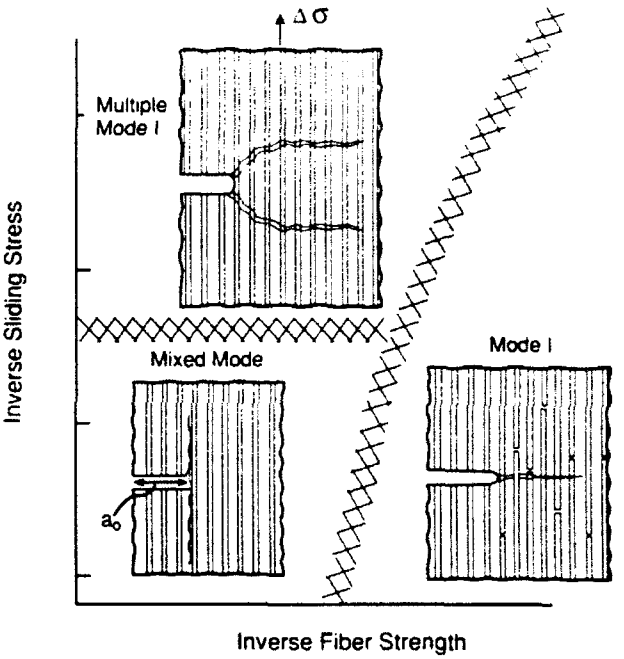

Fig. 1. Map indicating the various damage modes found in brittle matrix composites.

The notch properties are reflected in a notch sensitivity, which can range from notch-insensitive behavior[15] (wherein the tensile strength can be expressed simply in terms of the net section stress) to an extreme notch sensitivity characterized by fracture mechanics.[16] Typically, brittle matrix composites exhibit behavior between these extremes. A range of damage phenomena, illustrated in Fig. 1, govern the notch properties.[10] These phenomena include mode I matrix cracking with fiber pullout,[6,8] delamination cracking from the notch,[15,17] and multiple (mode I) microcrack damage.[2,4,5] The notch sensitivity is intimately related to the operative damage phenomenon. In some cases, models have been developed that relate the notch strength to various properties of the matrix, fibers, and interfaces.[18,19]

M. D. Thouless—contributing editor

Manuscript No. 196349. Received September 17, 1991; approved June 17, 1992.
*Member, American Ceramic Society.

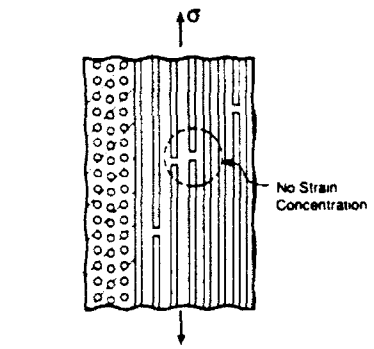

a) Non-Interacting Fiber Bundle Failure

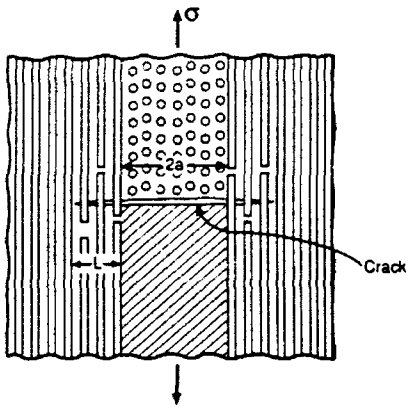

b) Crack Extension With Fiber Pull-Out

Fig. 2. Mode I failure mechanisms in brittle matrix composites: (a) noninteracting fiber bundle failure with multiple matrix cracking; (b) failure by growth of a dominant mode I crack through a fiber bundle.

Techniques that have been particularly useful in diagnosing the properties of brittle matrix composites involve measurements of fracture mirrors on failed fibers, as well as fiber pullout lengths.[5,11,12] Fracture mirror measurements allow determination of the in situ strengths of the fibers, S_c. Fiber pullout lengths, h, provide information about the interface sliding stress, τ. Both relate to the ultimate strength, σ_u. The present study has been conducted on *carbon matrix composites reinforced with Nicalon SiC fibers*, which have a well-established fracture mirror response.[5] Furthermore, such composites have been shown to exhibit an oxidation resistance much superior to that of carbon/carbon composites and thus have interesting potential as high-temperature structural composites.[20]

II. Analytical Background

While a range of possible damage mechanisms can operate in brittle matrix composites (Fig. 1), previous research on carbon matrix composites has suggested that the tensile fracture process in either notched or unnotched materials usually occurs by a mode I mechanism (wherein the primary fracture plane is normal to the loading axis).[21-23] In general, there are two mode I failure regimes, depending upon the stress concentration experienced by intact fibers neighboring a previously failed fiber. In one limit, the interface and/or the matrix are sufficiently "weak" that the matrix does *not* transmit such a stress concentration, whereupon each of the fibers is *statistically independent* (Fig. 2(a)).[7,11,12] Conversely, when a stress concentration develops, failure involves the *progressive propagation of a crack* with simultaneous failure of the fibers[5,6] (Fig. 2(b)). Both regimes are briefly outlined below, to provide a rationale for conducting and interpreting the experiments.

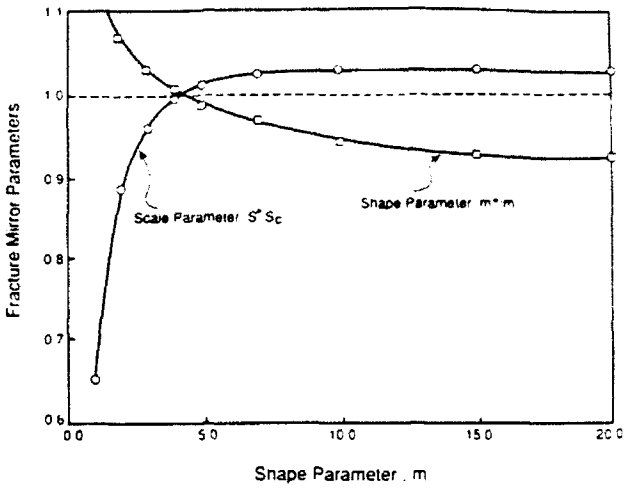

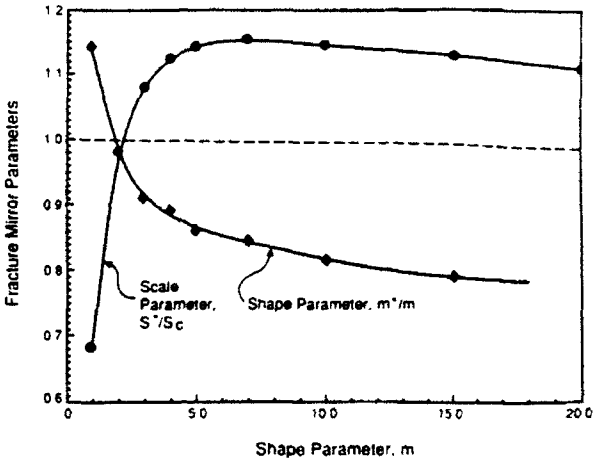

Fig. 3. Statistical parameters associated with fracture mirror measurements: (a) noninteracting fibers; (b) single matrix crack.

(1) Bundle Failure

A number of important results for fiber bundle failure in brittle matrix composites[7,8,12] have been derived using *weakest-link statistics*. The results apply, subject to a *global load-sharing (GLS) criterion* which gives rise to *uncorrelated* fiber failure sites (Fig. 2(a)). This criterion assumes that the interfaces have sufficiently low debond energy and sliding stress that the failed fibers do not concentrate stress. It is also implied that the *matrix* is subject to *multiple cracking*, prior to composite failure. In such a case, the matrix influences composite fracture by transferring load from a failed fiber to *all* remaining intact fibers, equally. Then, load recovery from a fiber failure site occurs *along* a fiber, through the sliding stress, τ.[8,12] As a result, *fibers* can also experience *multiple cracks*. Since the load recovery length is related to τ, composite parameters such as the pullout length and the in situ fiber strength have a direct connection with τ.

Global load-sharing results are based on weakest-link statistics plus fracture mirror information.[5] The fracture mirror measurements determine the local stress, S, acting on the fiber, upon failure, at the location of the fracture flaw. The measurements of S are correlated through the cumulative function[11,12]

$$G(S) = 1 - \exp[-(S/S_c)]^{m_c} \quad (1)$$

where m_c is a shape parameter and S_c a scale parameter. Weakest-link analysis of this phenomenon[12] has demonstrated relationships between m_c, S_c, and the properties of the fibers in situ

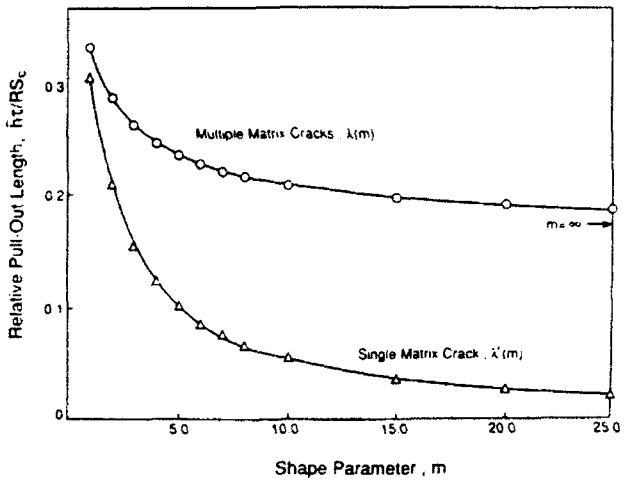

Fig. 4. Nondimensional fiber pullout lengths.

within the composite. These relationships connect the fracture mirror shape parameter m_c with the shape parameter m for the *actual fiber strength distribution*, as well as the fracture mirror scale parameter S_c with a characteristic fiber strength S_c (Fig. 3(a)).[12] The characteristic strength S_c is the mean fiber strength at a gauge length governed by the load transfer length. It is defined as

$$S_c^{m+1} = \frac{S_0^m \tau \ell_0}{R} \tag{2}$$

where S_0 is the stress scale parameter for the fiber strength distribution and ℓ_0 is a normalizing length (usually taken to be 1 m).[†] In order to relate S_c to the strength of the fibers measured in a bundle (without matrix), S_b, the difference in gauge lengths must be taken into account. The fiber bundle strength at gauge length ℓ is given by

$$S_b \equiv S_0(\ell_0/\ell me)^{1/m} \tag{3}$$

Consequently, S_c and S_b are related by

$$S_b = S_c^{(m+1)/m}(R/\tau \ell me)^{1/m} \tag{4}$$

where e is the base of natural logarithms. Hence, with S_c and m ascertained from fracture mirror data, S_b can be determined from Eq. (4), provided that τ is known.

The sliding stress τ is related to the pullout length $\bar{h}$ by[8,12]

$$\bar{h}\tau/RS_c = \lambda(m)/4 \tag{5}$$

with $\lambda(m)$ being a nondimensional function determined from the statistics of fiber failure, plotted on Fig. 4. Consequently, τ can be obtained from independent measurement of $\bar{h}$.

The final result of importance concerns the ultimate strength of the composite, σ_u, given by[12]

$$\sigma_u = f_f S_c \left[\frac{2}{(m+2)}\right]^{1/(m+1)} \left[\frac{m+1}{m+2}\right] \tag{6}$$

where f_f is the fiber fraction *along the loading direction*. It is of significance to appreciate that σ_u expressed in terms of S_c, through Eq. (6), has an implicit dependence in τ, as indicated by Eq. (2).

In summary, the above formulae (Eqs. (1)–(6)) may be used as follows. (i) Determine S_c and m_c (Eq. (1)) based on fracture mirror measurements, and then obtain S_c and m from Fig. 3(a). (ii) Determine $\bar{h}$ and evaluate τ from Eq. (5), with m and S_c now known. (iii) With S_c, τ, and m known, the fiber bundle strength S_b can be obtained from Eq. (4). (iv) If S_c is known from independent fiber strength data, Eq. (3) may be used to check on the magnitude of S_0. (v) Calculate the ultimate strength σ_u from Eq. (6).

(2) *Crack Extension*

Various studies on ceramic matrix composites[5,7] have indicated that a transition in failure mechanism occurs as the ratio τ/S_c increases. This transition is not well understood but undoubtedly involves some deviation from global load sharing, such that fiber failure occurs in conjunction with matrix crack propagation, as illustrated in Fig. 2(b). In this local load-sharing (LLS) regime, mode I cracks propagate subject to a resistance curve.[7] A simplified crack growth model is presented that addresses this failure mode in 2-D CMCs. When the fiber pullout length, $\bar{h}$, is relatively large ($\bar{h}/R \gg 1$), it has been shown that the resistance is dominated by friction exerted over the *entire* pullout length, such that $\bar{h}$ correlates with the fracture resistance in accordance with[7]

$$K_R = K_0 + 4\sqrt{\frac{2}{\pi}\left(\frac{\tau f_f \bar{h}}{R}\right)}\sqrt{L} \tag{7}$$

where K_0 is the fracture resistance of the matrix, L is the crack extension, and f_f is the fiber fraction *within the bundle*. For a small surface crack in a tensile body, the stress intensity factor K is given by

$$K \approx 1.98\sigma\sqrt{a_0 + L} \tag{8}$$

where σ is the imposed stress and a_0 is the initial crack length. Crack extension occurs when $K = K_R$ and hence, from Eqs. (7) and (8), the stress and crack length are related by

$$1.98\sigma\sqrt{a_0 + L} = K_0 + 4\sqrt{\frac{2}{\pi}\left(\frac{\tau f_f \bar{h}}{R}\right)}\sqrt{L} \tag{9}$$

This result can be reexpressed in terms of the fiber properties ascertained from fracture mirror measurements. For this purpose, when fracture occurs by growth of a single crack, the statistical results associated both with pullout and fracture mirrors differ from those for multiple matrix cracking.[12] Modified results for single cracks are summarized on Figs. 3(b) and 4. In particular, the pullout length $\bar{h}$ relates to the new characteristic fiber strength S_c' through[12]

$$\frac{\bar{h}\tau}{RS_c'} = \lambda'(m)/4 \tag{10}$$

as plotted in Fig. 4. Combining Eqs. (9) and (10), the predicted crack growth stress becomes

$$\sigma = \frac{1}{1.98\sqrt{a_0 + L}}\left[K_0 + \sqrt{\frac{2}{\pi}} f_f S_c' \lambda'(m)\sqrt{L}\right] \tag{11}$$

It is apparent from Eq. (11) that the crack extension stress increases continuously as the crack propagates through the bundle. Consequently, σ reaches a maximum as the crack exits the bundle, into the adjoining matrix layer (where the resistance drops). In a woven architecture, the bundle dimensions are such

[†] This scaling quantity implicitly includes the distribution of fiber radii, which are not yet determined separately.

[‡] While only S_c and m are needed to predict σ_u, values of τ, S_b, and S_0 provide important insight about the composite.

Table I. Carbon Matrix Materials Used In This Study

Material	Density (g/cm³)	Fiber volume fraction, f_f	Porosity (%)	Fiber coating	Matrix
A	1.98	0.44	10	None	C
B	2.04	0.45	9	None	C + particulate
C	2.00	0.40	12	C	C + particulate

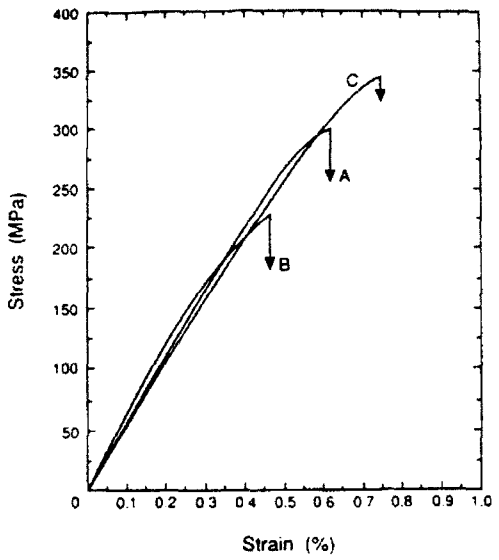

Fig. 5. Tensile stress–strain curves obtained for each material.

that the stress maximum arises when $L \approx a_0$ (Fig. 2(b)), whereupon Eq. (11) predicts a *peak* crack extension stress σ_* given by

$$\sigma_* = \frac{0.36K_0}{\sqrt{a_0}} + 0.28f_b S_0' \lambda'(m) \qquad (12)$$

When residual stresses are present because of thermal expansion mismatch between fiber and matrix, σ_* is modified and is typically lower than the magnitude predicted by Eq. (12).

Table II. Comparison of Measured and Predicted Ultimate Strengths

Material	Measured strength (MPa)	Predicted strength (MPa)	
		Bundle failure (Eq. (7))	Crack propagation (Eq. (12))
A	300 ± 30	330 ± 40	
B	225 ± 30	385 ± 35	205 ± 25
C	345 ± 30	315 ± 35	

A 1 MPa $\sqrt{m}$ = 90 μm

III. Materials

Three different carbon matrix composites reinforced with Nicalon fibers (average radius, R = 7 μm) were supplied by B. P. Chemicals (HITCO) Inc. (BPCHI). They are from BPCHI's Ceracarb[TM] composites line and are referred to here as materials A, B, and C (Table I).[20] All of the composites were fabricated by conventional lamination methods, followed by pyrolysis and carbon chemical vapor infiltration (CVI). Material A is a reference material, wherein no elements other than carbon are present in the matrix. Material B contains particulates that were introduced into the matrix during the impregnation of the fabric. Material C also contains particulates, but the fibers were precoated with a thin layer of pyrolytic carbon prior to their impregnation. All materials were made from a balanced 2-D Nicalon cloth with an 8 harness satin weave. The layers of fabric were laid up in a 0°/90° fashion to yield a nominal fiber fraction, $f \approx 0.43$ and a fiber fraction aligned with each of the two principal axes of $f_i \approx 0.22$. The fiber fraction within each bundle is $f_b \approx 0.67$.

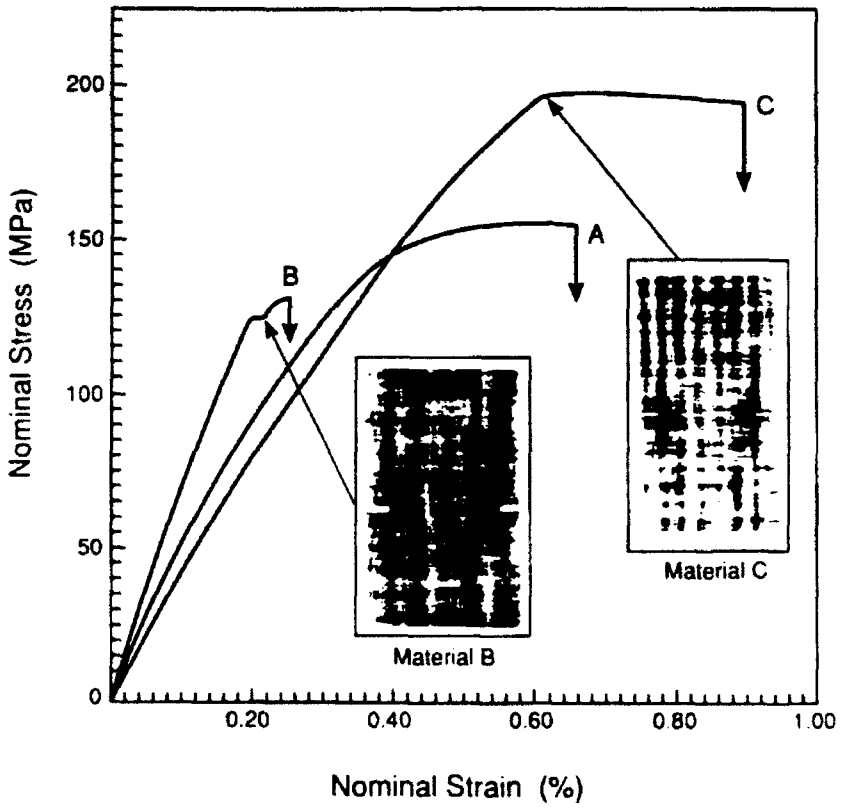

Fig. 6. Nominal stress–strain curves obtained using double-notch specimens.

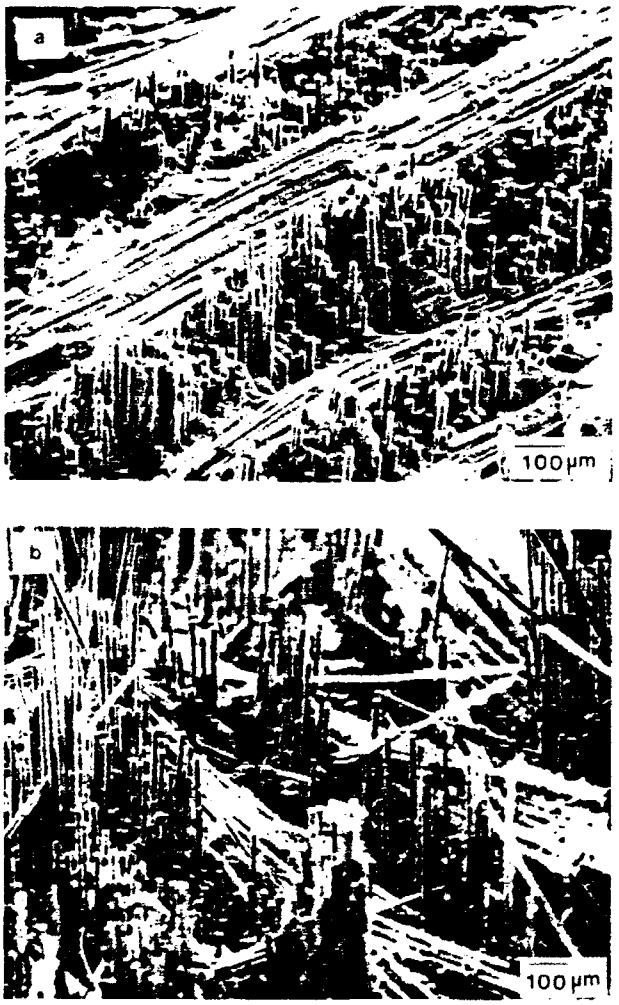

Fig. 7. Comparison of fracture surfaces revealing differences between (a) material C and (b) material B.

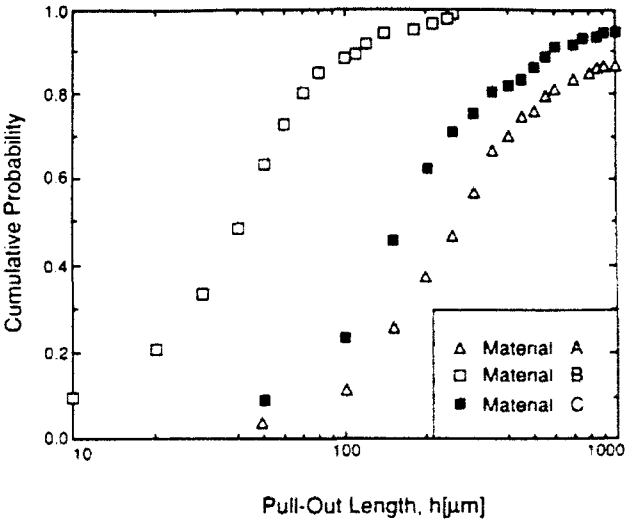

Fig. 8. Fiber pullout distributions for each material

IV. Experimental

(1) Procedures

Tensile tests have been conducted using friction grips to provide alignment. Displacements are measured by means of an extensometer in contact with the gauge section. The effects of notches on the tensile properties have been investigated by using a double-notch tensile configuration, with the notches introduced using a profiled diamond wheel. In the notch tests, damage development was monitored by infiltrating the material, while under load, with a ZnI_2 solution, and then using an X-ray method to image damaged regions.[19] Fracture surfaces and polished cross sections were studied using scanning electron microscopy (SEM).

(2) Measurements

Typical tensile stress/strain curves obtained on each of the three materials tested in the warp direction are summarized in Fig. 5. Ultimate strength results obtained on 10 specimens of each material are summarized in Table II. It is apparent from a comparison of the properties of these materials that the use of hard particulates in the matrix in material B reduces the tensile strength compared with the reference material A. However, when a carbon fiber coating is used before incorporation of the particulates (material C), the strength essentially reverts to that for the reference material. A similar trend is evident in the failure strain.

The notch tensile properties obtained along one fiber direction are summarized in Fig. 6, wherein the nominal stress is plotted as a function of the nominal strain. All materials exhibit appreciable nonlinearity prior to failure. The magnitude of the notch strength, and the extent of the nonlinear deformation prior to failure, increase in the same order as the tensile strength and tensile failure strain: notably, the properties *increase* in the order $B \rightarrow A \approx C$.

The ratio of the notch strength, σ_N, to the tensile strength, σ_u, is essentially the same for all three materials. Conversely, the extent of nonlinear deformation in the notched specimens prior to failure is strongly material-dependent, again increasing in the order $B \rightarrow A \approx C$.

(3) Observations

All of the *notched* specimens fractured in nominal mode 1 wherein the principal fracture plane was normal to the tensile axis, such that the fracture surfaces were amenable to explicit measurements of the fiber pullout distributions and the fracture mirror radii. One immediate difference between material B and either of the other materials concerns the failure location. In material B, fracture is essentially coplanar, with the longitudinal bundles failing on the same plane as both the transverse bundles and the matrix (Fig. 7(a)). However, in materials A or C, the longitudinal bundles fail on planes offset from the plane at which the transverse bundles and the matrix fracture (Fig. 7(b)). Pullout measurements are conducted in all cases with reference to the matrix failure plane *within the bundles*, using the SEM technique described elsewhere.[11] The cumulative distribution of pullout lengths, h, obtained for the three materials (Fig. 8) reveals that h is appreciably smaller for material B than for either of the other two materials.

Fracture mirror measurements (see Fig. 10(a)) lead to the strength distributions summarized on Fig. 9. It is apparent that this measure of the in situ strength indicates no significant difference between the three materials. However, because of the implicit influence of the slip distance on S_c (Eq. (2)), *these results do not necessarily imply that the fiber bundle strength is the same for each composite*.

Direct observations of the fibers after testing have provided additional information. The fibers in reference material A exhibit smooth surfaces (Fig. 10(a)), characteristic of the original fiber,[1] whereas material B exhibits particulates attached to the fiber surfaces (Fig. 10(b)). In composite C, the carbon fiber coating is evident (Fig. 10(c)). In some areas, the coating has

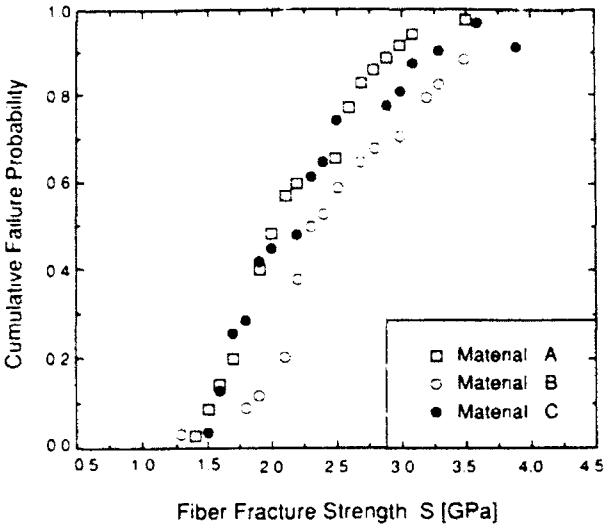

Fig. 9. In situ fiber strength distributions obtained from fracture mirrors

been detached from the fiber, exposing a pristine surface on the underlying fiber.

The X-ray penetrant observations conducted on notched specimens of materials B and C provide important information (Fig. 11). In all materials, damage in the form of either the T-cracks or H-cracks (indicated on the figure) form at relatively low loads. These cracks are believed to occur at bundle/bundle and bundle/matrix interfaces. However, this damage appears to be stable and does not directly contribute to composite failure. More importantly, in materials A and C, split cracks extend from the notches, comparable to those found in certain CMCs and in polymer matrix composites in fatigue.[10] The growth of the split cracks is stable such that the crack length, ℓ, increases with increase in load, as plotted on Fig. 12. These splits reduce the stress concentration at the notch tip and diminish the notch sensitivity of the material, analogous to the effect of the plastic zone in metals. In material B, split cracks are not apparent. Instead, a concentration of *mode I* damage appears to occur at the notch prior to fracture.

Subsequent to failure, polished sections examined in the SEM revealed a difference in matrix cracking between material B and either A or C. In the latter materials, multiple matrix cracks were evident, especially in regions where the fiber volume fraction was low and the matrix regions were readily resolved in the SEM (Fig. 13). Some of these cracks were present as a result of processing, but others formed during testing.

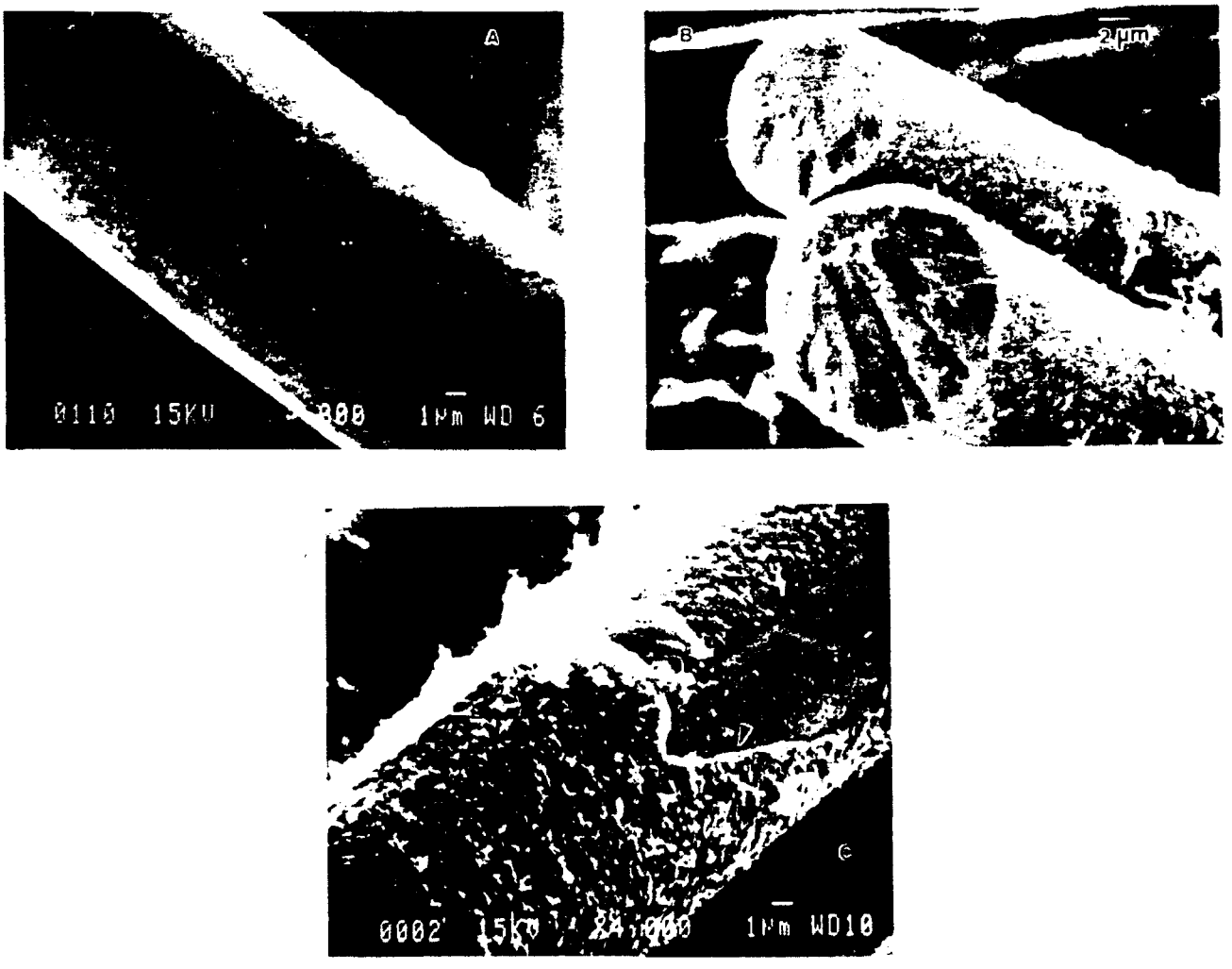

Fig. 10. SEM observations of the surfaces of pulled-out fibers

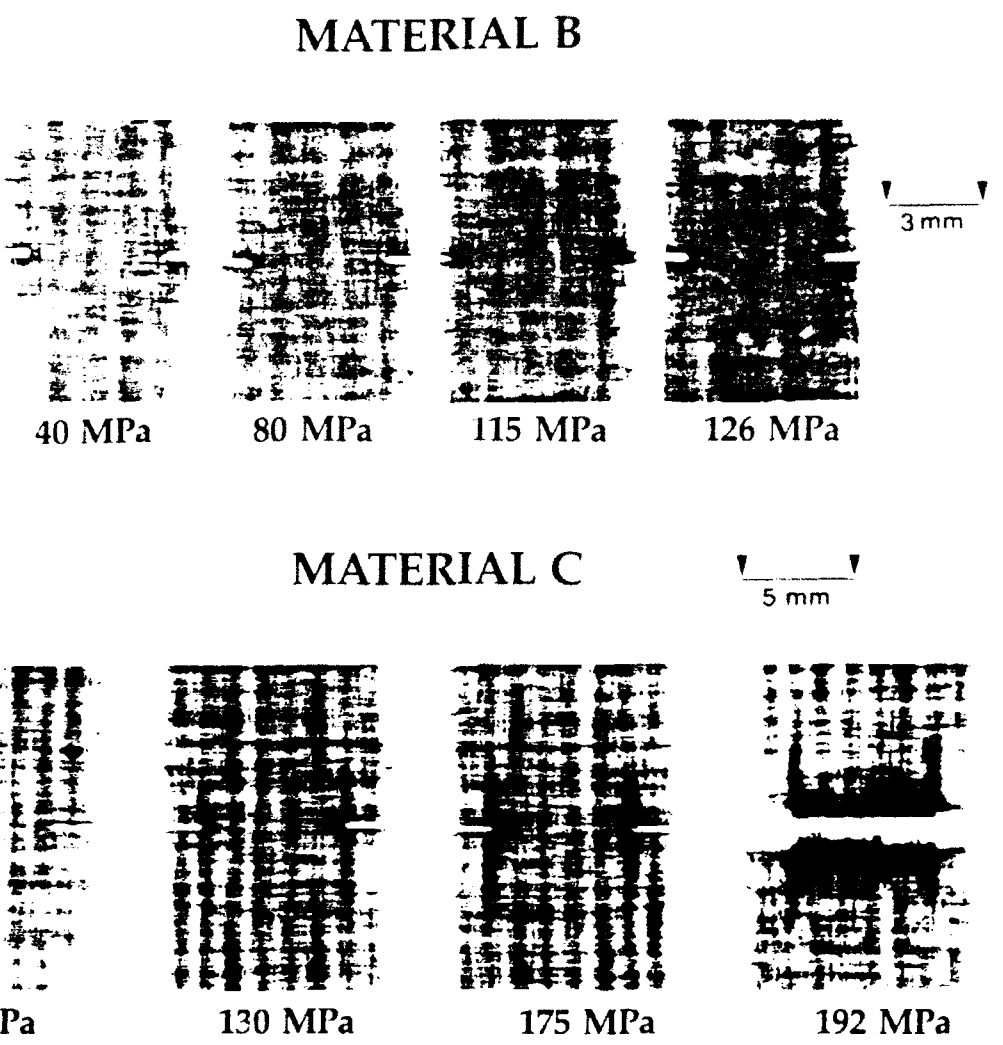

Fig. 11. Sequence of X-ray penetrant observations on notched tensile specimens of materials B and C.

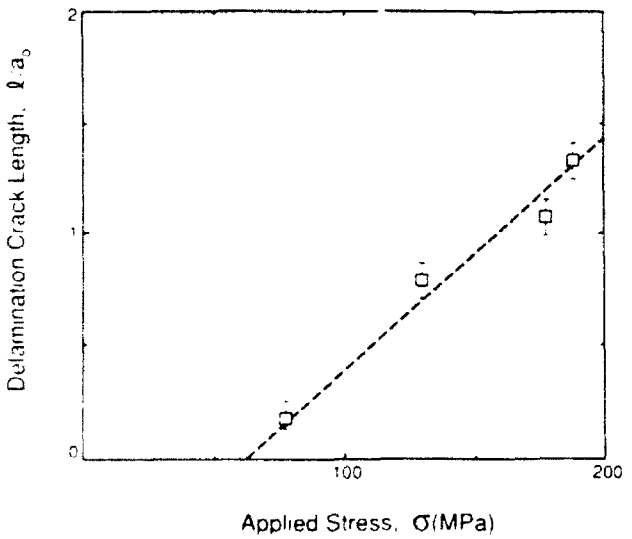

Fig. 12. Variation in delamination crack length ℓ with stress, σ. a_o is the notch depth.

Conversely, in material B, there was no clear evidence of multiple matrix cracking. Instead, where cracks were detectable, they usually caused fiber failures.

V. Analysis

Various observations suggest that materials A and C are subject to a damage mechanism involving multiple matrix cracks, with failure governed by global load sharing (Fig. 2(a)). These include direct observations of matrix microcracks (Fig. 13), as well as the uncorrelated nature of fiber failure (Fig. 7). Conversely, for material B, matrix cracking was not evident. Instead, fracture by a dominant mode I crack, accompanied by fiber failure, is considered to be the composite failure mechanism (Fig. 2(b)), consistent with the fracture morphology (Fig. 7).

Based on this distinction between mechanisms, values for S_o, S_o, τ, and m are obtained in the manner described in Section II and summarized in Table III.[3] The principal features of importance are the differences in the fiber bundle strength S_o, as well as the interface sliding stress among the three materials. Notably, S_o is lower and τ is larger for material B than for either material A or C. These differences are considered to be related to the particulates attached to the fibers in material B (Fig.

[3] For reference purposes, material B is also analyzed as if failure involved global load sharing.

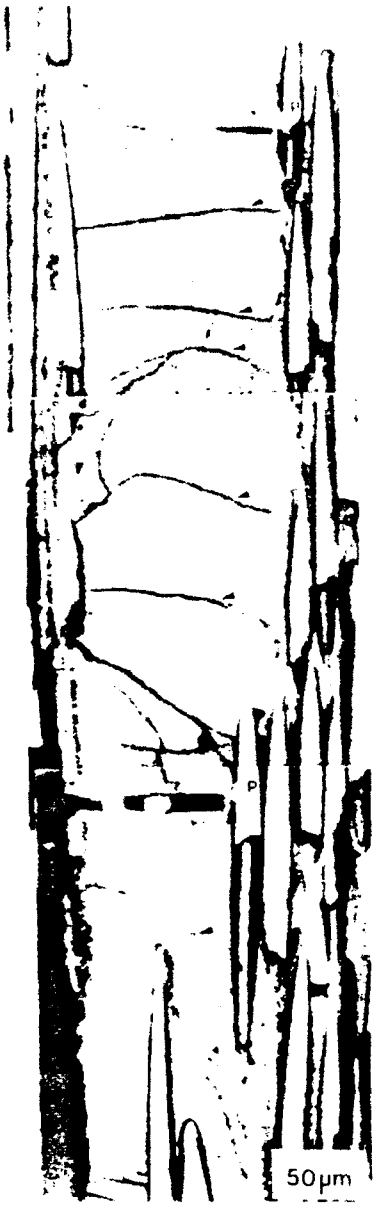

Fig. 13. SEM observation of a polished section after testing to failure showing matrix cracks in material C. Processing cracks are identified (P) with white arrows, while loading cracks are marked with black arrows. (Courtesy, K. Turner.)

10(b)). The particulates act as asperities that increase τ and also reduce the bundle strength of the fibers (either by abrasion or as a result of thermal expansion mismatch). In all these materials, the fibers have a bundle strength (at gauge length, ℓ = 2.5 cm) lower than that for pristine Nicalon fibers (S_o = 0.9 GPa for ℓ = 2.5 cm), signifying that moderate fiber degradation occurs during composite processing.

(1) Strength

Preliminary assessment of the tensile properties (in the warp direction) is made by assuming global load sharing (Fig. 2(a)) and predicting the ultimate strengths using the associated fiber and interface properties (Table III), in conjunction with Eq. (7). The results are summarized in Table II. Direct comparison with the measured strengths indicates good agreement for materials A and C. Conversely, the strength of material B is lower than

Table III. Composite Properties Based on Fracture Mirror and Pullout Measurements

	Matrix [ref.]	Failure [ref.]	m	S_o (GPa)	τ (MPa)
A	410	GLS	2.2 ± 0.2	1.6 ± 0.2	0.1–0.2
C	300	GLS	2.5 ± 0.2	1.4 ± 0.1	0.1–0.2
B	50	GLS	2.5 ± 0.3	0.91 ± 0.11	0.5–1.0
		LLS	2.2 ± 0.3	0.85 ± 0.05	0.1–0.2

State of stress: σ_x = σ_y = τ_{xy} = 0; σ_z = σ_{zo} + σ_{zm}.

predicted, as anticipated from the applicability of global load sharing. For this material, the single-crack LLS model (Eq. (12)) predicts strengths in close agreement with measurements (Table II). A transition in failure mechanism has thus occurred between composite B and composites A or C. This GLS to LLS transition is related to the magnitude of the ratio τ/S_o. As this ratio becomes relatively large in composite B, fiber failure occurs in conjunction with matrix cracking, leading to failure by a dominant crack mechanism. However, an explicit criterion for the mechanism transition has yet to be developed.

(2) Notch Strength

The notch tensile properties are strongly influenced by the formation of split cracks (Fig. 11) manifest in the much larger work of rupture for materials A and C than for material B (Fig. 6). Similar notch-strengthening effects have been found in polymer matrix composites following split cracking induced by fatigue.[25,26] Analogy with these results suggests that the splitting reduces the stress concentration at the notch. Further studies would be needed to derive explicit relationships between the notch strength and the properties of the fibers and interfaces. However, the relatively large interface sliding stress τ in material B represents a major difference and is probably the origin of the diminished splitting and the inferior notch properties.

VI. Concluding Remarks

The present study has explored some of the fundamental relationships between the macroscopic properties of carbon matrix composites and the in situ properties of the fibers and the interface. This has been achieved through the use of straightforward models based on the observed failure mechanisms. Two of the three carbon matrix composites investigated here exhibit fracture and notch characteristics indicative of a multiple-matrix cracking, global load-sharing mechanism; and the measured tensile strengths are in good agreement with model predictions based on such a mechanism. One of the three materials was found to have inferior strength and notch sensitivity and a different fracture surface morphology. The differences relative to the other two materials are attributed to a combination of a large interface sliding stress and a low fiber bundle strength for the composite, caused by particulates in the matrix that adhered to the fiber, which lead to a transition in the fracture mechanism.

The behavior of these materials in the presence of notches is similar to that observed in polymer matrix composites subject to fatigue.[25] This analogy suggests an approach for predicting the notch properties that will be explored in further studies.

References

R. Kerans, R. S. Hay, N. J. Pagano, and T. A. Parthasarathy, "The Role of the Fiber-Matrix Interface in Ceramic Composites," *Am. Ceram. Soc. Bull.*, **68** [2] 429–42 (1989).

A. G. Evans and D. B. Marshall, "The Mechanical Behavior of Ceramic Matrix Composites," *Acta Metall.*, **37** [10] 2567–83 (1989).

D. B. Marshall and B. N. Cox, "A J-Integral Method for Calculating Steady-State Matrix Cracking Stresses in Composites," *Mech. Mater.*, **7** [2] 127–33 (1988).

J. Aveston, G. A. Cooper, and A. Kelly, "Single and Multiple Fracture," pp. 15–26 in Proceedings of the Conference on the Properties of Fiber Composites, National Physical Laboratory, England, November 4, 1971. IPC Science and Technology Press, Guildford, U.K., 1971.

[8] C. Cao, E. Bischoff, O. Sbaizero, M. Ruhle, A. G. Evans, D. B. Marshall, and J. J. Brennan, "Effect of Interfaces on the Properties of Fiber Reinforced Ceramics," *J. Am. Ceram. Soc.*, **73** [6] 1691–99 (1990).

[9] F. W. Zok, O. Sbaizero, C. L. Horn, and A. G. Evans, "Mode I Fracture Resistance of a Laminated Fiber-Reinforced Ceramic," *J. Am. Ceram. Soc.*, **74** [1] 187–93 (1991).

[10] W. A. Curtin, "Fiber Fragmentation in a Single Filament Composite," *Appl. Phys. Lett.*, **58**, 1155–57 (1991).

[11] M. D. Thouless and A. G. Evans, "Effects of Pull-Out on the Mechanical Properties of Ceramic Matrix Composites," *Acta Metall.*, **36** [3] 517–22 (1988).

[12] O. Sbaizero and A. G. Evans, "Tensile and Shear Properties of Laminated Ceramic Matrix Composites," *J. Am. Ceram. Soc.*, **69** [6] 481–86 (1986).

[13] A. G. Evans, "The Mechanical Properties of Reinforced Ceramics: Metal and Intermetallic Matrix Composites," *Mater. Sci. Eng.*, **A143**, 63–76 (1991).

[14] M. D. Thouless, O. Sbaizero, L. S. Sigl, and A. G. Evans, "Effect of Interface Mechanical Properties on a Pullout in a SiC Fiber-Reinforced Lithium Aluminum Silicate Glass Ceramic," *J. Am. Ceram. Soc.*, **72** [4] 525–32 (1989).

[15] W. A. Curtin, "Theory of Mechanical Properties of Ceramic Matrix Composites," *J. Am. Ceram. Soc.*, **74** [11] 2837–45 (1991).

[16] J. W. Hutchinson and H. M. Jensen, "Models of Fiber Debonding and Pull-out in Brittle Composites with Friction," *Mech. Mater.*, **9**, 139–63 (1990).

[17] A. G. Evans, F. W. Zok, and J. B. Davis, "The Role of Interfaces in Fiber-Reinforced Brittle Matrix Composites," *Compos. Sci. Technol.*, **42**, 3–24 (1991).

[18] O. Sbaizero, P. G. Charalambides, and A. G. Evans, "Delamination Cracking in a Laminated Ceramic Matrix Composite," *J. Am. Ceram. Soc.*, **73** [7] 1936–40 (1990).

[19] A. G. Evans, "Perspective on the Development of High-Toughness Ceramics," *J. Am. Ceram. Soc.*, **73** [2] 187–206 (1990).

[20] R. Pordia, B. J. Dalgleish, P. G. Charalambides, and A. G. Evans, "Cracking and Damage in a Notched Unidirectional Fiber-Reinforced Brittle Matrix Composite," *J. Am. Ceram. Soc.*, **74** [11] 2776–80 (1991).

[21] M. Spearing, P. W. R. Beaumont, and M. F. Ashby, "Fatigue Damage Mechanics of Notched Graphite/Epoxy Laminates," pp. 806–28 in *Composite Materials: Fatigue and Fracture*. ASTM STP 1110. Edited by T. K. O'Brien. American Society for Testing and Materials, Philadelphia, PA, 1991.

[22] M. F. Kortschot and P. W. R. Beaumont, "Damage-Based Notched Strength Modeling: A Summary," sec. 8.2, 18 pp. (date ?).

[23] P. Mosher, private communication.

[24] J. L. Perry and D. F. Adams, "Mechanical Tests of a Three-Dimensionally Reinforced Carbon-Carbon Material," *Carbon*, **14**, 65–71 (1976).

[25] S. Sato, A. Kurumada, H. Iwata, and Y. Komatsu, "Tensile Properties and Fracture Toughness of Carbon Fiber Felt Reinforced Carbon Composites at High Temperature," *Carbon*, **27** [6] 791–801 (1989).

[26] W. Kowbel and C. H. Shatt, "The Mechanism of Fiber-Matrix Interactions in Carbon-Carbon Composites," *Carbon*, **28** [2–3] 287–90 (1990).

MATERIALS

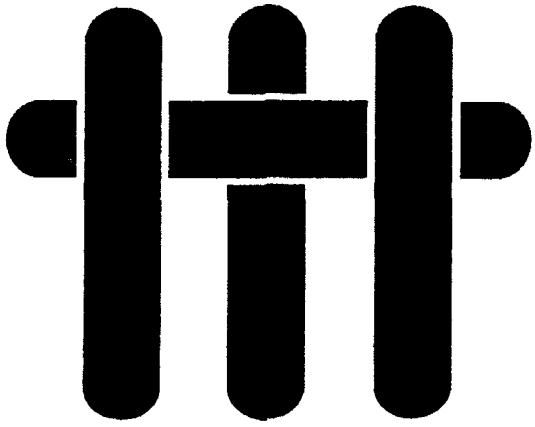

NOTCH EFFECTS IN CARBON MATRIX COMPOSITES

by

Fernando E. Heredia, S. Mark Spearing*, Thomas J. Mackin,
Ming Y. He, Anthony G. Evans,

Materials Department
College of Engineering
University of California
Santa Barbara, California 93106–5050

Paul Mosher

BP Chemicals (HITCO), Inc.
Gardena, California 90249

and

Povl Brøndsted

Risø National Laboratory
Roskilde, Denmark

* Present address: B.P. Research, Warrenville, Ohio 44128

Submitted to the Journal of the American Ceramic Society, November 1992

KJS 11/13/92

ABSTRACT

The tensile properties of various carbon matrix composites, reinforced with C and SiC fibers, have been evaluated. The objective is to assess mechanics procedures for characterizing the influence of holes and notches. Interpretation has been attempted using large-scale bridging mechanics, with linear elastic fracture mechanics as one limit and notch insensitivity as the other. Important differences between the materials, associated primarily with the fiber/matrix interfaces and the in-plane shear strength, have been identified and attempts made to rationalize these differences.

1. INTRODUCTION

One of the important macroscopic mechanical properties of 2-D brittle matrix composites is the effect of notches and holes on the tensile fracture strength. This information is required both for design and for the development of improved materials. The approach used to represent this behavior is governed by the *mechanisms of damage* that occur near the notch and their influence on the stress field around the notch. For design, a simple representation of the results is needed. Various representations have been used for structural materials. One is based on elastic stress concentration factors.[1] Another uses linear elastic fracture mechanics (LEFM).[2] Intermediate behaviors are frequently found in brittle matrix composites.[3] Two approaches for characterizing notch size effects in this intermediate regime have recently been proposed using either the mechanics of large-scale bridging (LSBM) or continuum damage mechanics (CDM).[4-7] The LSBM approach is relevant whenever fracture from the notch involves a single matrix crack with bridging tractions acting across the crack, provided by fiber reinforcements.[8,9] The CDM approach is more applicable whenever multiple matrix cracks emanate from the notch. The essential non-dimensional parameters that interpolate between notch-sensitive and notch-insensitive behavior are described in the Appendix. One objective of the present study is to examine various mechanics approaches for several carbon matrix composites, all having the same fiber architecture.

Brittle-matrix composites exhibit at least three dominant behavioral *classes* (I, II, III), governed by the operation of different damage mechanisms[10-12] (Fig. 1). Some of the differences in notch properties between these classes are described in the Appendix. The mechanics used to predict trends in notch properties for a particular composite require that the behavioral class be identified. Such mechanism identification represents another objective of this study.

2. EXPERIMENTAL PROCEDURES

2.1 Materials

Four carbon matrix composites were supplied by BP Chemicals (HITCO), Inc. Two were carbon/carbon (C/C) materials, designated here as materials *X* and *Y*. The others were SiC/C Ceracarb™ composites, designated materials *B* and *C*.[3] All of the composites had a fiber architecture comprising an eight harness satin weave. The layers of fabric were laid up in a 0/90 fashion to yield a nominal fiber volume fraction, $f \approx 0.43$, and a fiber fraction aligned with each of the two principal axes, $f_{\ell} \approx 0.22$. All the materials were fabricated by conventional lamination, followed by pyrolysis and chemical vapor infiltration. The C/C materials have Thornel T300™ fibers as reinforcements. Material *X* is a reference material, wherein no elements other than carbon are present in the matrix. Material *Y* contains particulates introduced into the matrix during impregnation of the fabric. The Ceracarb™ materials contain Nicalon™ fibers in a matrix similar to that of C/C material *Y*. In material *C*, the fibers are coated with a thin layer of pyrolitic carbon. Material *B* has no fiber coating.

2.2 Test Procedures

Rectangular specimen blanks 130 mm long were prepared by diamond machining. In some specimens, double-edge notches were introduced using a 500 μm thick profiled diamond wheel with a 250 μm tip radius. In others, either a center notch or hole was produced. For the C/C composite, three effects of notch geometry were investigated. One series of tests was conducted on specimens of width, $2b = 15$ mm, but with three edge notch sizes, $a_o = 1.875$ mm, 3.75 mm and 5.625 mm. These tests gave a range in $a_o/b = 0.25$, 0.5 and 0.75. The purpose of these tests was to investigate notch sensitivity at a *single specimen* scale. A second series of edge-notch tests consisted of specimens with fixed ratio $a_o/b = 0.5$, but with variable specimen widths, $2b = 5$, 10, 15 or

24 mm, with the aim of investigating the effect of *absolute scale*. These results were then compared with the behavior found for center notches. For the SiC/C material, tests were conducted with edge notches, center notches and center holes, all with $a_o/b = 0.32$.

Baseline strength data were obtained from tensile coupons slightly waisted over their gauge lengths. Waisting was achieved by using a 150 mm diameter grinding wheel to give a reduction in width conforming to a circular arc, with a maximum reduction of 1 mm from each side. For the C/C materials, two width scales were used in the gauge length: 8 and 2 mm. For the SiC/C composites, only 8 mm widths were tested. Six specimens were tested for each condition. The specimens were loaded in tension in a servohydraulic load frame. Loads were introduced using aligned hydraulic grips. Tests were conducted in displacement control at an actuator speed of 2 μm/s. Displacements were measured using a centrally mounted 10 mm clip gauge. For measuring the local strains in the longitudinal and in the transverse directions, strain gauges consisting of single foils and with a gauge length of 0.75 mm, were used*. The strain gauge signals were monitored using Micro Measurement amplifiers.** The analog signals from the strain gauge amplifier were digitized using an A/D board,*** and all data from the tests were sampled using a PC data acquisition program, which also controlled the test machine. The tests were conducted either as monotonic loading to fracture or as loading-unloading tests to measure the influence of accumulated damage on the stiffness of the materials.

Damage development was monitored by infiltrating the material with a ZnI_2 solution, while under load, and then using an X-ray method to image damaged regions. Fracture surfaces were studied using scanning electron microscopy (SEM). Preliminary

---

* Micro Measurement type EA-06-031DE-120

** Measurement Group, model 2120A, strain gauge conditioners with a model 2110A power supply

*** Instron, model 8500-133

information about the notch tip stress distributions was obtained on the C/C composites by Stress Pattern Analysis using Thermal Emission (SPATE):[13,14] a procedure by which surface temperature distributions were measured while the specimen was cyclically loaded between 0 and 50 MPa. These temperatures are, in turn, related to the sum of the in-plane principal stresses. A comparison is made between the material prior to testing and after preloading to 120 MPa.

3. MEASUREMENTS AND OBSERVATIONS

3.1 Tension Tests

The tensile tests gave reasonably consistent results (Fig. 2, Table I). All materials are slightly non-linear . The C/C material *X* and the SiC/C material *C* exhibited similar strengths. There was no significant influence of specimen width, except for the greater variability for the narrower specimens, probably reflecting the inconsistent number of 0° tows in the cross section. The C/C material *Y* was weaker than *X*, while the SiC/C material *B* had the lowest strength.‡

The non-linearities are reflected in the measurements of unloading modulus, $\bar{E}$, and Poisson's ratio, $\bar{\nu}$ (Fig. 3). It is apparent that the SiC/C materials develop significant non-linearity, commencing at ~ 100 MPa, manifest in a reduced $\bar{E}$ and $\bar{\nu}$. These changes are attributed to combined effects of matrix cracks and fiber failure. The reduction in $\bar{E}$ and, particularly, $\bar{\nu}$ is more pronounced for material C, suggesting a greater incidence of matrix cracks prior to failure. Conversely, $\bar{E}$ for the C/C materials changes by < 3% prior to composite failure. For these materials, ν is negative and ranges between – 0.1 and 0, but does not appear to vary in a systematic manner as loads are applied.

‡ Two C/C specimens were cyclically loaded up to one million cycles. The compliance did not change significantly and the final damage was not visibly larger than that of specimens loaded to the same stress level under monotonic loading.

3.2 Notched Tension Tests

Load/deflection curves obtained on edge-notched specimens indicate various levels of non-linearity prior to unstable fracture, as illustrated by results for the C/C composites (Fig. 4). The non-linearities also coincide with an increase in compliance. Furthermore, loading/unloading cycles conducted on specimens previously loaded close to their failure stress revealed significant hysteresis. The specimens with $a_o/b = 0.75$ retained a load bearing capability after achieving their maximum load. Specimens with smaller notches all failed catastrophically. The C/C specimens with fixed a_o/b (= 0.5), but of varying widths, showed a pronounced size effect (Fig. 5a). Material *X* consistently exhibited a higher notch strength than material *Y*. There was also a strong effect on strength of relative notch depth, a_o/b, at fixed width (Fig. 5b, Table II).

The SiC/C materials exhibited a similar set of notch characteristics, with material C superior to material *B*. The results are summarized in Table II, which compares the notch strength, S_N, with the net section stress, σ_N. Evidently, the relative degradation in tensile strength caused by notches is similar in both materials. Moreover, notches result in a greater degradation than holes. Strain gauge measurements made around holes and notches, as the materials are loaded to failure, gave the strain concentration factors at composite failure, summarized in Table II. In each case, the strain concentrations are either comparable to, or somewhat lower than the values expected for an isotropic elastic system.[1]

3.3 Damage Observations

The X-ray die penetrant measurements indicate that, in three of the materials (C/C, *X*, *Y*, and SiC/C, C), damage occurs and concentrates within a narrow zone normal to the notch (Fig. 6). Related studies of sectioned specimens[15] have revealed that the

damage consists of a network of matrix microcracks, with the majority of the fibers intact, similar to the shear damage found in other brittle systems.[16] The lateral width of the zone, ℓ, increases as the stress increases. Furthermore, when normalized with the notch depth, a_o, the *damage extent* for each notch geometry appears to be uniquely related to the *applied stress* for each class of material (Fig. 7). The zone size is consistently larger for edge notched than center notch specimens. The two C/C materials exhibited similar damage propagation behaviors. The SiC/C material C exhibited relatively less damage. The SiC/C material *B* , on the other hand, had no discernible damage (Fig. 6b).

Tests conducted using SPATE on one of the C/C composites had the features illustrated in Fig. 8. The principal comparison is between the temperature contours in the pristine state (Fig. 8a) and those evident after introducing damage by preloading (Fig. 8b). The preload used coincided with a damage zone size, $\ell / a_o \approx 1$. A qualitative comparison of Figs. 8a/b indicates that a significant stress redistribution has been caused by damage. The uncalibrated temperature scales that accompany the SPATE images provide a relative measure of the temperature range in the specimen, and are scaled to range between the lowest, far field temperature, and the highest notch tip temperature.

Observations of fracture specimens conducted in the scanning electron microscope revealed differences between the C/C and SiC/C materials. In the former, the 0° fiber bundles closest to the notch typically failed at some distance from the notch plane (Fig. 9), leading to *bundles* pulled out of the composite. In the latter, there are no obvious preferred *bundle* pull-outs near the notch root (Fig. 11). However, some generalized bundle pull-out is evident in material C. Fiber pull-out was evident in all cases (Table III) with the pull-out lengths being smallest in SiC/C composite *B* (Fig. 10), attributed[3] to a large value of the interface sliding stress, τ (Table III).

In all composite systems, cracks are evident in the 90° bundles at the notch root (Fig. 11). Some have a large opening displacement, consistent with their formation

during processing. Others appear to be stress induced and are indicative of the failure sequence, elaborated below.

4. ANALYSIS

4.1 Overall Assessment

The good notch properties of the present composites, relative to those of the unreinforced matrices, are believed to be attributable to damage, consisting of matrix cracks coupled with fiber bridging effects along the plane of final failure. The damage redistributes stresses and reduces the tensile stress at the notch tip. These phenomena are somewhat analogous to the role of the plastic zone in metals.[2,17] In order to rationalize the experimental results, it is necessary to have appreciation that several behavioral classes are possible (Appendix). Three of the materials (C/C, *X*, *Y*, and SiC/C, *C*) exhibit a distinct shear damage zone and will be treated as class III systems. One material (SiC/C, *B*) fails in mode I and is regarded as class I.[3]

In class III materials, stress redistribution occurs as a result of shear band formation at the notch. When the band size ℓ is relatively small, LEFM should be applicable. Deviations from LEFM are expected when ℓ is large. Consequently, the important issues are:[12,18] (i) the ratio of the damage zone size to the notch size, (ii) the stress and strain distributions ahead of the crack, (iii) the failure criterion, which dictates the magnitude of the local stress at the fracture criticality. The interpretation of the notch properties involves separate considerations of each of these issues.

For class I materials, stress redistribution is associated with the tractions across the crack, governed by fibers that bridge and pull-out as the crack extends.[4-7] The magnitude and geometric scale of these tractions are of primary relevance, as governed by the sliding stress, τ , the characteristic fiber strength, S_c, and the pull-out length, $\bar{h}$. When the bridging zone is small compared with the notch size, LEFM should be

applicable. Conversely, when the bridging zone is large, the notch properties are expected to be represented by large-scale bridging mechanics (LSBM), as described in the Appendix.

The presence of cracks near the notch tip in the 90° bundles (Fig. 11) suggests that first damage consists of matrix cracks in these bundles. Similar behavior has been found in other CMCs[19] and analyzed using a tunnel cracking model.[20] Subsequent damage appears to be dependent on the material, via the behavioral class. Consequently, each class is considered separately.

4.2 Class III Systems

In the C/C composites, as well as in SiC/C material C, transverse damage is prevalent, indicative of class III behavior. The form of the damage growth curve (Fig. 7) suggests that the damage can be regarded as a band subject to shear strength, T. The growth of a shear band has the following characteristics:[21,22] when the band length, ℓ, is small compared with the notch depth, a_o ($\ell / a_o \lesssim 0.3$), its magnitude is given by the small-scale yielding (SSY) result,

$$\ell/a_o \approx 0.052\pi(\sigma/T)^2 \qquad (2a)$$

At larger zone sizes, $\ell / a_o \gtrsim 2$, the zone length conforms to a shear lag (SL) solution,

$$\ell/a_o \approx \sigma/T \qquad (2b)$$

At intermediate ℓ / a_o, numerical solutions provide the appropriate relationship.[21,22]

The band growth curves predicted by these solutions are found to superpose onto the experimental measurements (Fig. 7), upon choosing explicit magnitudes for T, somewhat dependent on notch geometry. For double edge notch specimens,

T ≈ 50 MPa for the C/C composites and T ≈ 60 MPa for SiC/C composite C. Somewhat larger values apply for the center notch: T ≈ 60 and 70 MPa, respectively. These values are consistent with independent measurements of the in-plane shear strength of these materials.[23] This consistency with a shear band model is the basis for conducting further analysis. The smaller values of T found for edge notches than center notches may reflect the existence of appreciable normal tension along the shear zone, in the edge configuration.[20] Superposed tension is known to facilitate the propagation of a shear damage zone in brittle solids.[16]

In the presence of a shear band at a notch in a tensile specimen, the stresses ahead of the notch are redistributed. Finite element calculations (Fig. 12a) indicate that the σ_{yy} stresses immediately ahead of the notch are dramatically reduced by shear damage, with a corresponding relative increase further from the notch. The reduced stress occurs in the range

$$x/a_o \lesssim 0.1 \tag{3}$$

where x is the distance from the notch tip. The associated hydrostatic stress contours (Fig. 23b) are also qualitatively consistent with the SPATE temperature contours (Fig. 8). The relatively low σ_{yy} stresses close to the notch induced by the shear band is considered to be the origin of the notch resistance found in class III composites.

Given the phenomenological similarity of the shear band behavior to the influence of a plastic zone in metals, LEFM is used to obtain a critical mode I stress intensity factor, K_{IC}, from the results. The magnitude of K_{IC} is obtained for one notch configuration and then, the notch strengths measured for all other geometries are checked for consistency using standard stress intensity formulae. For double edge notched (DEN) specimens,[24]

$$K_{IC} = S_N\sqrt{a_o}\left[1.98 + 0.36(a_o/b) - 2.12(a_o/b)^2 + 3.42(a_o/b)^3\right] \quad (4a)$$

whereas, for center notched (CN) specimens[24]

$$K_{IC} = S_N\sqrt{a_o}\left[1.77 + 0.227(a_o/b) - 0.51(a_o/b)^2 + 2.7(a_o/b)^3\right] \quad (4b)$$

with S_N being the measured notch strength.

The results (Fig. 5) obtained for edge notched C/C specimens indicate good correspondence, with K_{IC} = 16 MPa$\sqrt{m}$ for material X and 15 MPa$\sqrt{m}$ for material Y. However, the corresponding values inferred from the center notch specimens are consistently larger (Table IV). Consequently, there are limitations to the universality of LEFM, which need to be further explored. The difference in behavior found between edge and center notches may reflect differences in the shear strength, T (Fig. 7), and associated stress redistribution effects.

It would be anticipated that LEFM is less likely to apply for small notches and manufacturing flaws because of the relatively large-scale influence of the shear band on the notch tip stress field. Nevertheless, it is of interest to interpret the unnotched tensile strength by invoking LEFM. This is accomplished by extrapolating the LEFM curve (Fig. 5a) to the measured tensile strength and inferring a flaw size. This procedure infers flaws having size, $a_o \approx 500$ μm. This size is similar to the dimensions of the 90° bundles. Since cracks form readily in these bundles (Fig. 11), LEFM appears to describe the unnotched properties, surprisingly well. Again, however, additional testing is needed to fully appreciate the limits on the use of LEFM.

The corresponding results for SiC/C material C are not sufficient to address the corresponding applicability of either LEFM or LSBM. However, estimates of K_{IC}, with comparison between edge and center notched specimens (Table IV), indicate

comparable toughness levels and a discrepancy between DEN and CN results similar to that for the C/C materials.

4.3 Class I Systems

It is believed from previous studies[3] that the SiC/C material *B* is class I, whereupon LSBM would be expected to have greater applicability than LEFM. Indeed, the use of LEFM, based on K_{IC} estimates (Table IV), indicates a major discrepancy between DEN and CN results. Consequently, LSBM analysis is attempted. Before proceeding, the prerequisite that the material be class I is addressed by comparison with the mechanism map (Appendix). The experimental stress/strain relationships (Fig. 3) combined with the constituent properties (Table III) for a notch size a_o = 1.5 mm, establish that the (S, Σ) coordinates on this map (Fig. A1) are (0.04, 0.3). These coordinates are consistent with class I being the operative behavior. As further background, it is noted that the pull-out stress (Eqn. A4) obtained using the parameters from Table III (σ_p = 270 MPa) is a reasonably close lower bound for the measured UTS (S = 225 MPa), whereas the strength predicted by assuming global load sharing (Eqn. A4, S_u = 380 MPa) is considerably larger than the UTS.

A procedure for using LSBM requires that the relative strengths measured on the specimens with center notches and center holes (Table II) be superposed onto the design diagram (Fig. A2b). When this is done (Fig. 13), all results are found to be consistent with a pull-out flaw index having magnitude, $\mathcal{A}_p$ = 0.2–0.4. Independent evaluation of this index (using Eqn. A6), gives, $\mathcal{A}_p \approx 0.1$ for 1.5 mm radius holes and notches. The correspondence is reasonable and encouraging, but the results are insufficient to establish that LSBM is the preferred mechanics approach for this material.

5. CONCLUSIONS

An effort has been made to understand the stress redistribution mechanisms that operate in various C matrix composites subject to strain concentrations, such as holes and notches. Based on these mechanisms, plus associated implications for the *scale* of stress redistribution, a preliminary assessment has been made of various mechanics methodologies. It is found for class III materials, in which shear bands constitute a major mode of stress redistribution, LEFM applies reasonably well, despite quite large-scale non-linear zones around the notch. In a class I material (SiC/C material *B*) that does not exhibit shear banding and also has relatively small fiber pull-out lengths, the LSBM approach appears to provide consistent predictions of the influence of center notches and holes. However, considerable additional data would be required to provide a rigorous assessment of LSBM compared with LEFM.

6. ACKNOWLEDGMENTS

This work was supported by the Defense Advance Research Projects Agency through the University Research Initiative under ONR contract N-00014086-K-0753.

APPENDIX

Mechanics Methodology for CMCs

For each of the three classes of behavior illustrated in Fig. 1, a different mechanics appears to be required, which combines aspects of LEFM, CDM and LSBM. In this appendix, some of the key results applicable to LSBM are presented. The first important LSBM result is the mechanism map that distinguishes class I and class II behaviors[11] (Fig. A1). *LSBM is only strictly applicable when class I behavior arises.*[4,5] The indices on this diagram are as follows: (i) An interface index for *fiber bridging*, S (which is the inverse of the flaw index),[11]

$$S^{-1} \equiv \mathcal{A}_b = \left[f_f/(1-f_f)^2\right]\left[EE_f/E_m\right]^2\left[a_o\tau/RS_cF(m)\right] \qquad (A1)$$

where E is Young's modulus, τ the sliding stress, R the fiber radius, S_c the characteristic strength,[25] f_f the fiber volume fraction and

$$F(m) = \left[2/(m+2)\right]^{\gamma_{(m+1)}}\left[(m+1)/(m+2)\right] \qquad (A2)$$

(ii) A non-linearity index,[11]

$$\Sigma = \sigma_{mc}/f_c S_c F(m) \qquad (A3)$$

where σ_{mc} is the matrix cracking stress, which approximately coincides with the onset of non-linearity in the unnotched stress/strain curve.

Whenever the unnotched tensile properties of the composite are consistent with global load sharing (GLS) predictions, the UTS is[25]

$$S_u = f_\ell S_c F(m) \tag{A4}$$

In some cases, the tensile properties in the unnotched state are controlled by the pull-out stress,[26]

$$\sigma_p = 2f_\ell \tau \bar{h}/R \tag{A5}$$

where $\bar{h}$ is the pull-out length. For materials having the latter characteristic, LSBM establishes a *pull-out* flaw index[4]

$$\begin{aligned} \mathcal{A}_p &= \left(a_o/\bar{h}\right)\left(\sigma_p/E\right) \\ &\equiv 2f_\ell\left(a_o\tau/RE\right) \end{aligned} \tag{A6}$$

Subject to the pull-out index, the tensile properties are straightforward and are predicted to vary in accordance with design diagrams (Figs. A2a, b). When GLS governs the unnotched properties, the appropriate flaw index is $\mathcal{A}_b$ (Eqn. A1). The corresponding notch tensile characteristics also depend on σ_p / S_u (Fig. A2c). However, these results are only strictly applicable when class I behavior occurs. Materials compatible with GLS predictions often exhibit *multiple matrix cracking*, which introduces other stress redistribution mechanisms.

TABLE I

Summary of Measurements Obtained From Unnotched Tension Tests

Material		Specimen Width (mm)	Ultimate Strength (MPa)
C/C	*X*	2	345 ± 25
		8	341 ± 7
	Y	2	292 ± 27
		8	289 ± 10
SiC/C	*B*	8	225 ± 30
	C	8	345 ± 30

TABLE II

Summary of Notch Properties

NOTCH CHARACTERISTICS			RELATIVE NOTCH STRENGTH, S_N/σ_N				STRAIN CONCENTRATION			
Type	Size		SiC/C		C/C		SiC/C		C/C	
	a_o/b	2b(mm)	B	C	X	Y	B	C	X	Y
Double Edge Notch	0.25	15	—	0.58	0.71	—	2.55	—	—	
	0.32		0.57		—	0.57				
	0.50		—		0.50	0.42				
	0.75		—			0.23				
Center Notch	0.32	20	0.50	0.56	0.67	0.53	1.85	1.5	1.30	2.2
Center Hole	0.32	20	0.59	0.52	0.67	0.48	3.0	2.5	2.5	3.3

TABLE III

Summary of Constituent Parameters for SiC/C Composites[3]

	MATERIAL	
	B	C
f_ℓ	0.22	0.22
τ (MPa)*	90	10
E_m (GPa)	30	20
E_f (GPa)	200	200
E (GPa)	70	59
S_c (GPa)	2.5	2.3
R (μm)	7	7
$\bar{h}$ (μm)	50	300

* τ is evaluated from $\bar{h}$ by considering that multiple matrix cracking occurs in both materials.

TABLE IV

Summary of LEFM Based Analysis of Notch Properties

MATERIAL		NOTCH TYPE	a_o/b	K_{IC} (MPa$\sqrt{m}$)
SiC/C	*B*	DEN*	0.30	8
		CN‡	0.32	12
	C	DEN	0.40	15
		CN	0.32	18
C/C	*X*	DEN	0.50	18
		CN	0.32	24
	Y	DEN	0.50	15
		CN	0.32	17

* DEN — Double Edge Notched

‡ CN — Center Notched

REFERENCES

[1] R.E. Peterson, *Stress Concentration Factors*, John Wiley, NY (1974).

[2] M.F. Kanninen and C.H.Y. Popelar, *Advanced Fracture Mechanics*, Oxford Univ. Press (1985).

[3] F.E. Heredia, S.M. Spearing, A.G. Evans, P. Mosher and W.A. Curtin, "Mechanical Properties of Continuous Fiber-Reinforced Carbon Matrix Composites and Relationships to Constituent Properties," *J. Am. Ceram. Soc.*, in press.

[4] G. Bao and Z. Suo, "Remarks on Crack Bridging Concepts," *Appl. Mech. Rev.*, in press.

[5] Z. Suo, S. Ho and X. Gong, "Notch Ductile-to-Brittle Transition Due to Localized Inelastic Band," *J. Mech. Phys. Solids*, in press.

[6] D.R. Hayhurst, P.R. Brown and C.J. Morrison, "The Role of Continuum Damage in Creep Crack Growth," *Phil. Trans. R. Soc. Lond.*, **A311**, 131-158 (1984).

[7] D.R. Hayhurst, F.A. Leckie and A.G. Evans, "Component Design-Based Model for Deformation and Rupture of Tough Fibre-Reinforced Ceramic Matrix Composites," *Proc. R. Soc. Lond.*, **A434**, 369-381(1991).

[8] D.B. Marshall and B.N. Cox, "Tensile Fracture of Brittle Matrix Composites: Influence of Fiber Strength," *Acta Metall.*, **35**, 2607–2619 (1987).

[9] F.W. Zok and C. Hom, "Large-Scale Bridging in Brittle Matrix Composites," *Acta Metall.*, **38**, 1895–1904 (1990).

[10] A.G. Evans, "The Mechanical Properties of Reinforced Ceramics, Metal and Intermetallic Matrix Composites," *Mat. Sci. Eng.*, **A143**, 63–76 (1991).

[11] L. Cui and B. Budiansky, private communication.

[12] M.T. Kortschott, P.W.R. Beaumont and M.F. Ashby, "Damage Mechanics of Composite Materials III: Prediction of Damage Growth and Notched Strength," *Composites Sci. and Technol.*, **40**, 147–165 (1991).

[13] N.F. Enke, "Thermographic Stress Analysis of Isotropic Materials," Ph.D. Thesis, Department of Engineering Mechanics, University of Wisconsin-Madison, 1989.

[14] N. Harwood and W.M. Cummings, *Thermoelastic Stress Analysis*, Adam Hilger Press., Philadelphia, 1991.

[15] K. Turner, J.S. Speck and A.G. Evans, unpublished results.

[16] N. Fleck," Brittle Fracture Due to an Array of Microcracks," *Proc. R. Soc. Lond.*, **A432**, 55-76 (1991).

[17] J.W. Hutchinson, *Non-Linear Fracture Mechanics*, Technical University of Denmark (1979).

[18] M. Spearing, P.W.R. Beaumont and M.F. Ashby, "Fatigue Damage Mechanics of Notched Graphite-Epoxy Laminates," in *Composite Materials: Fatigue and Fracture*, ASTM STP 1110, edited by T.K. O'Brien, pp. 596–616 (1991).

[19] D. Beyerle, S.M. Spearing and A.G. Evans, "Damage Mechanisms and the Mechanical Properties of a Laminated 0/90 Ceramic Matrix Composite," *J. Am. Ceram. Soc.*, in press.

[20] J.W. Hutchinson and Z. Suo, "Mixed Mode Cracking in Layered Materials," *Advances in Appl. Mech.*, **29**, 63 (1992).

[21] H.C. Cao and A.G. Evans, "On Crack Extension in Ductile/Brittle Laminates," *Acta Metall. Mater.*, **39[12]**, 2997–3007 (1991).

[22] K.S. Chan, M.Y. He and J.W. Hutchinson, "Cracking and Stress Redistribution in Ceramic Layered Composites," *J. Mater. Sci. and Eng.*, in press.

[23] P.A. Brøndsted, F.E. Heredia and A.G. Evans, to be published.

[24] H. Tada, P.C. Paris and G. Irwin, *The Stress Analysis of Cracks Handbook*, Del Research, St. Louis, MO.

[25] A.G. Evans, M.Y. He, F.E. Heredia, P. Brøndsted, to be published.

[26] W.A. Curtin, "Theory of Mechanical Properties of Ceramic Matrix Composites," *J. Am. Ceram. Soc.*, **74**, 2837–45 (1991).

FIGURE CAPTIONS

Fig. 1. A schematic of the three behavioral classes found in CMCs.

Fig. 2. Tensile stress/strain curves obtained on unnotched specimens.

Fig. 3. Changes in unloading modulus E and Poisson's ratio, $\bar{\nu}$, following loading.

Fig. 4. Stress/displacement curves obtained for notched C/C materials indicating varying degrees of non-linearity prior to failure.

Fig. 5. a) The influence of notch depth on the failure strength of C/C composites with fixed $a_o/b = 0.5$. b) The effect of a/b at fixed specimen width. Also shown are the curves associated with LEFM characterization, extrapolated to the unnotched tensile strength.

Fig. 6. The damage zone at failure in each of the materials, visualized using an X-ray die penetrant method. a) C/C material *X*, b) SiC/C material *B*, c) SiC/C material *C*. The damage zone for the C/C material *Y* is similar to that of the C/C material *X*.

Fig. 7. The normalized shear band length as a function of stress obtained for C/C materials *X* and *Y*, and SiC/C material *C* : a) edge notched specimens, b) center notched specimens. Also shown are curves calculated for values of shear strength, T, consistent with the measurements.

Fig. 8. Temperature amplitude distribution ahead of a notch in C/C material *X* measured using SPATE: a) as-notched, b) after preloading to 120 MPa.

Fig. 9. Scanning electron microscope views of a failure plane in a notched C/C composite: a) global view of the fracture plane, b) and c) are matching fracture surfaces. Note the bundle pull-outs near the notch root.

Fig. 10. Failure planes in SiC/C materials: a) material *B*, b) material C.

Fig. 11. Cracks in 90° bundles formed at the notch root upon testing to failure, indicated by the arrows.

Fig. 12. Finite element calculations of the stress ahead of a notch a) σ_{yy} stress on notch plane as a function of slip zone length, ℓ / a_o, b) stress contours, $\sigma_{11} + \sigma_{22}$,

normalized by the net section stress, σ_N (for $a_o/b = 0.5$), for comparison with the SPATE contours (Fig. 8b).

Fig. 13. A superposition of the results from center notched specimens and specimens with a center hole on the LSBM design diagram.

Fig. A1. A mechanism map for class I and class II brittle matrix composites.

Fig. A2. Notch sensitivity diagrams for class I composites: a) Pull-out dominated failure $a_o/b \rightarrow 0$, b) Effects of plate width, c) Combined bridging and pull-out, $a_o/b \rightarrow 0$.

Class I

Matrix Cracking + Fiber Failure

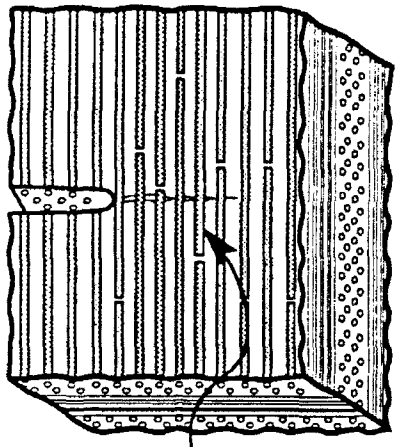

Pull-Out Tractions
Redistribute Stress

Class II

Matrix Cracking: No Fiber Failure

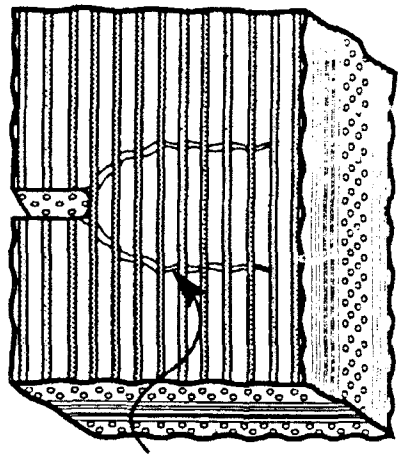

Matrix Cracks
Redistribute Stress

Class III

Shear Damage By Matrix Cracking

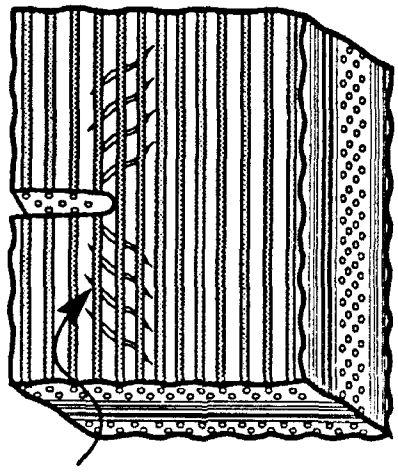

Shear Damage Zone
Redistributes Stress

FIGURE 1

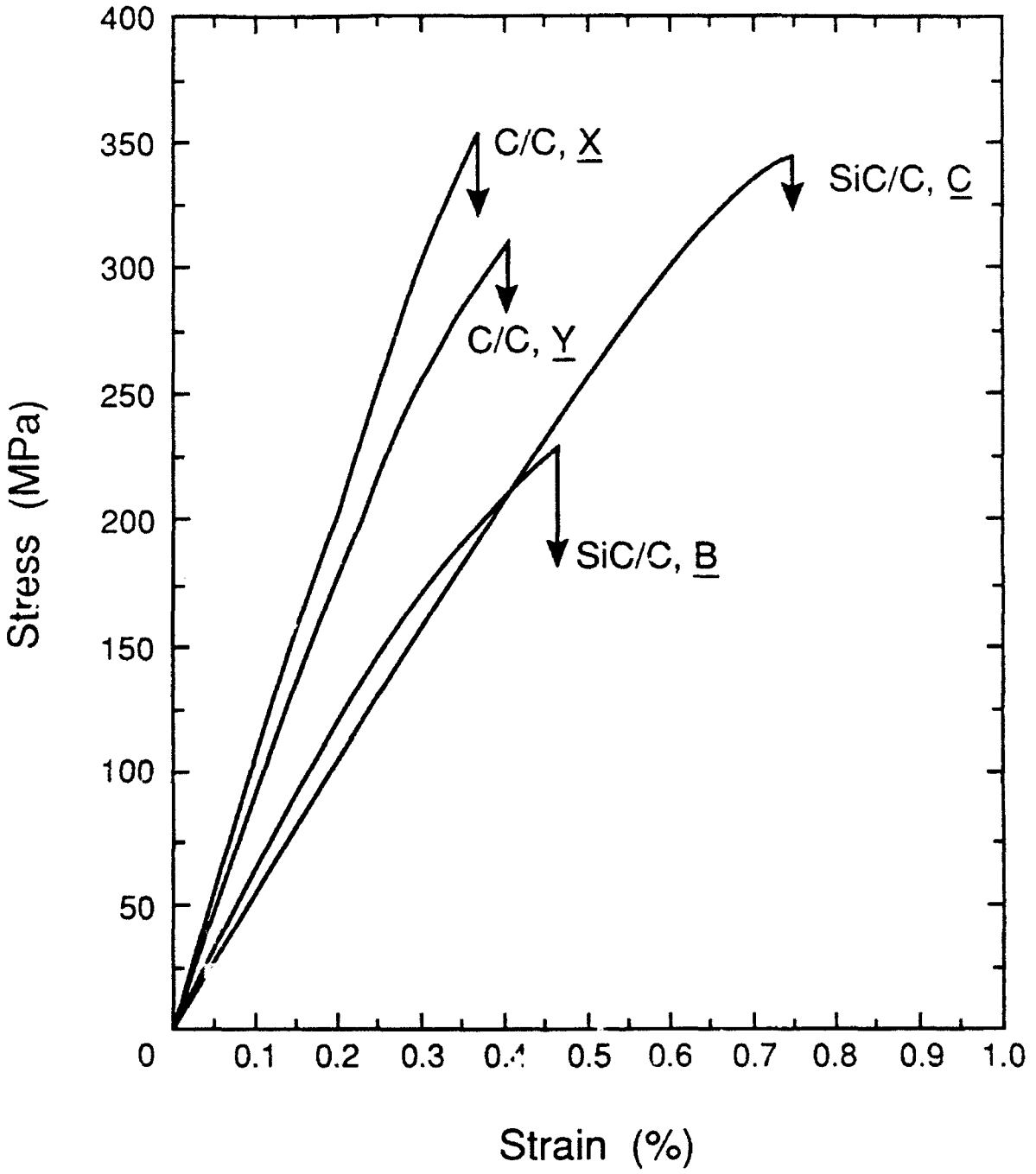

Heredia Evans URI 9/92 amk D2#870-1

FIGURE 2

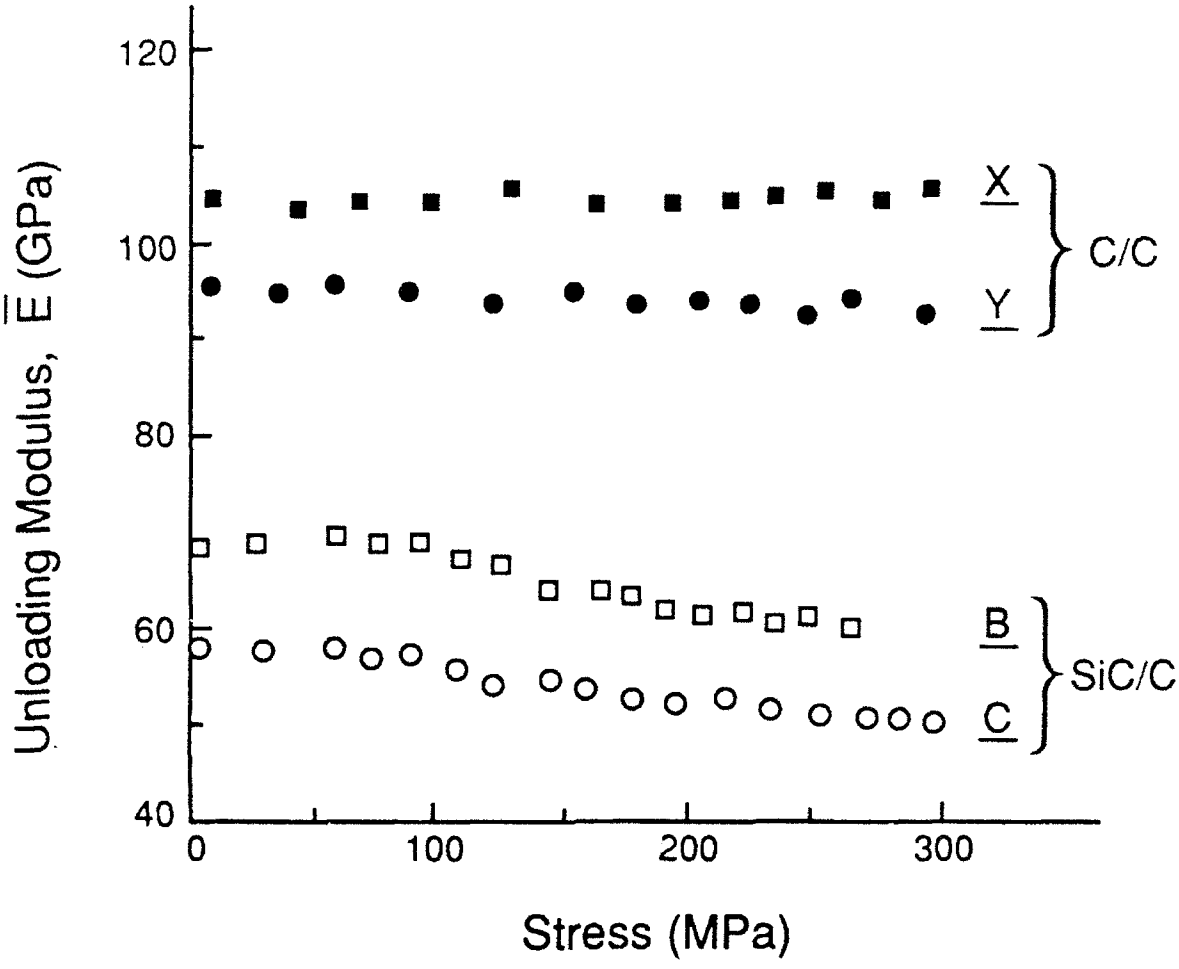
120
100
80
60
40
0
100
200
300
Unloading Modulus, $\bar{E}$ (GPa)
Stress (MPa)
X
Y
C/C
B
C
SiC/C

FIGURE 3 a

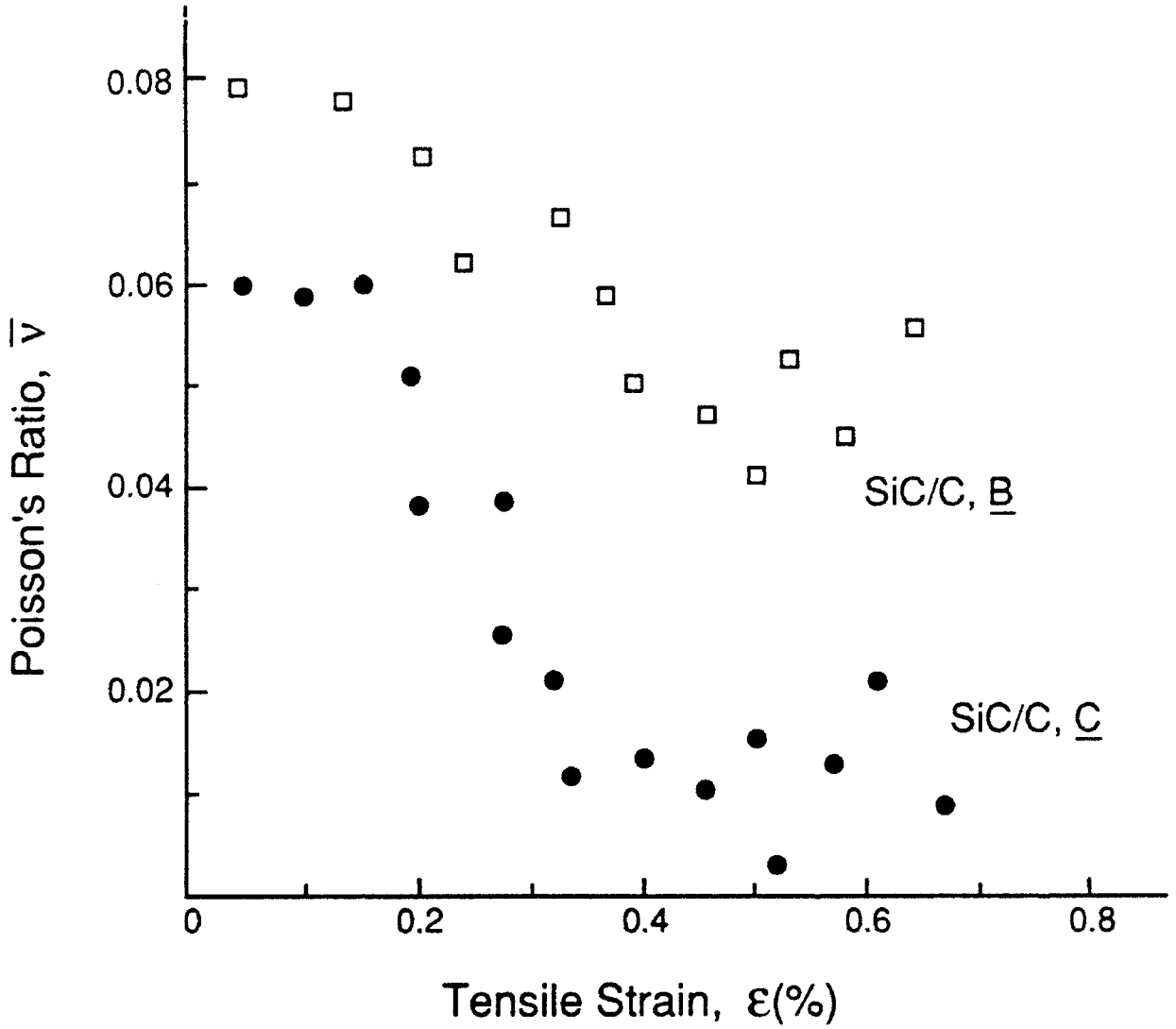
0.08
0.06
0.04
0.02
Poisson's Ratio, $\bar{\nu}$
SiC/C, B
SiC/C, C
0
0.2
0.4
0.6
0.8
Tensile Strain, ε(%)

FIGURE 3b

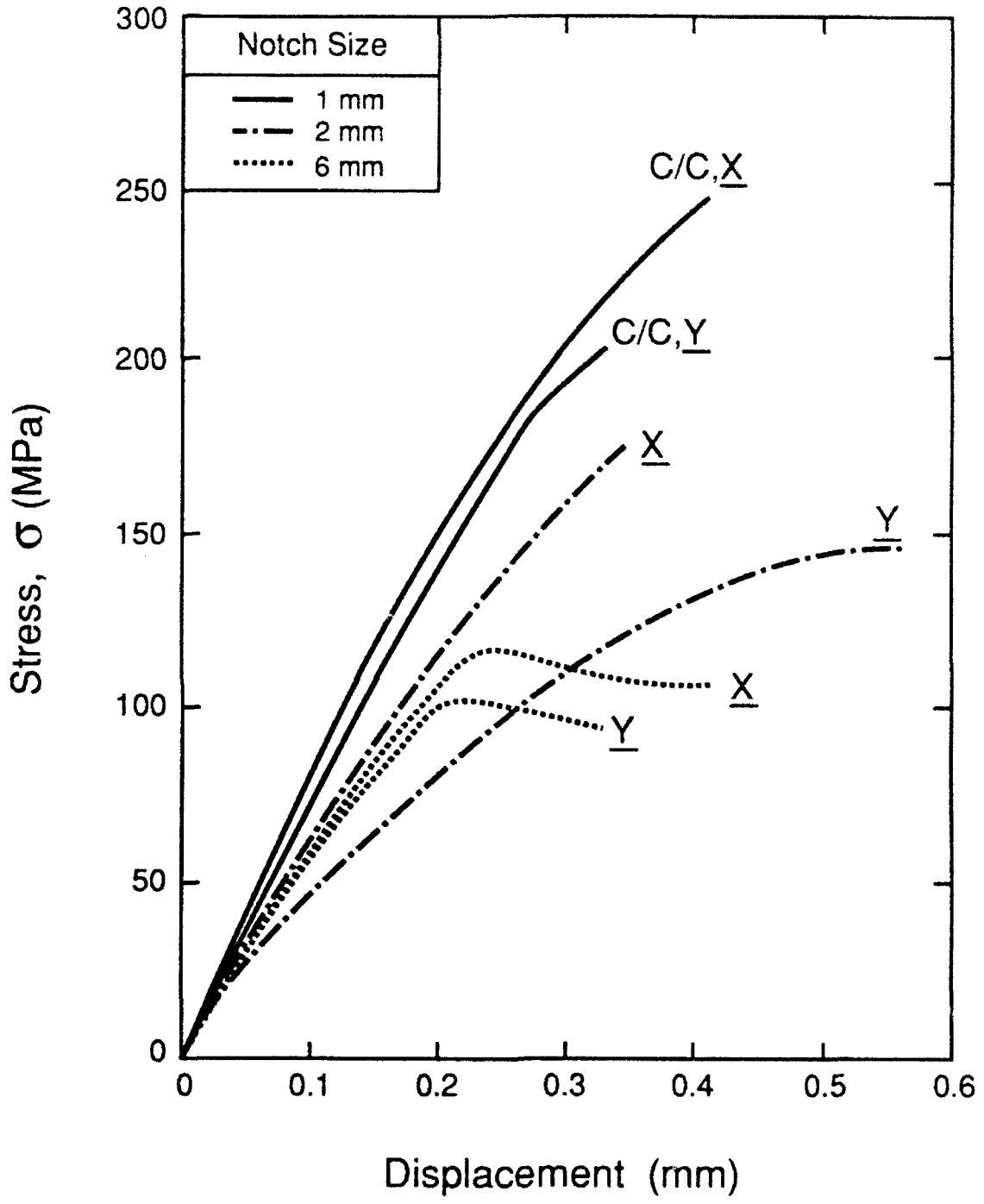
Notch Size
1 mm
2 mm
6 mm
C/C,X
C/C,Y
X
Y
X
Y
300
250
200
150
100
50
0
0
0.1
0.2
0.3
0.4
0.5
0.6
Stress, σ (MPa)
Displacement (mm)

FIGURE 4

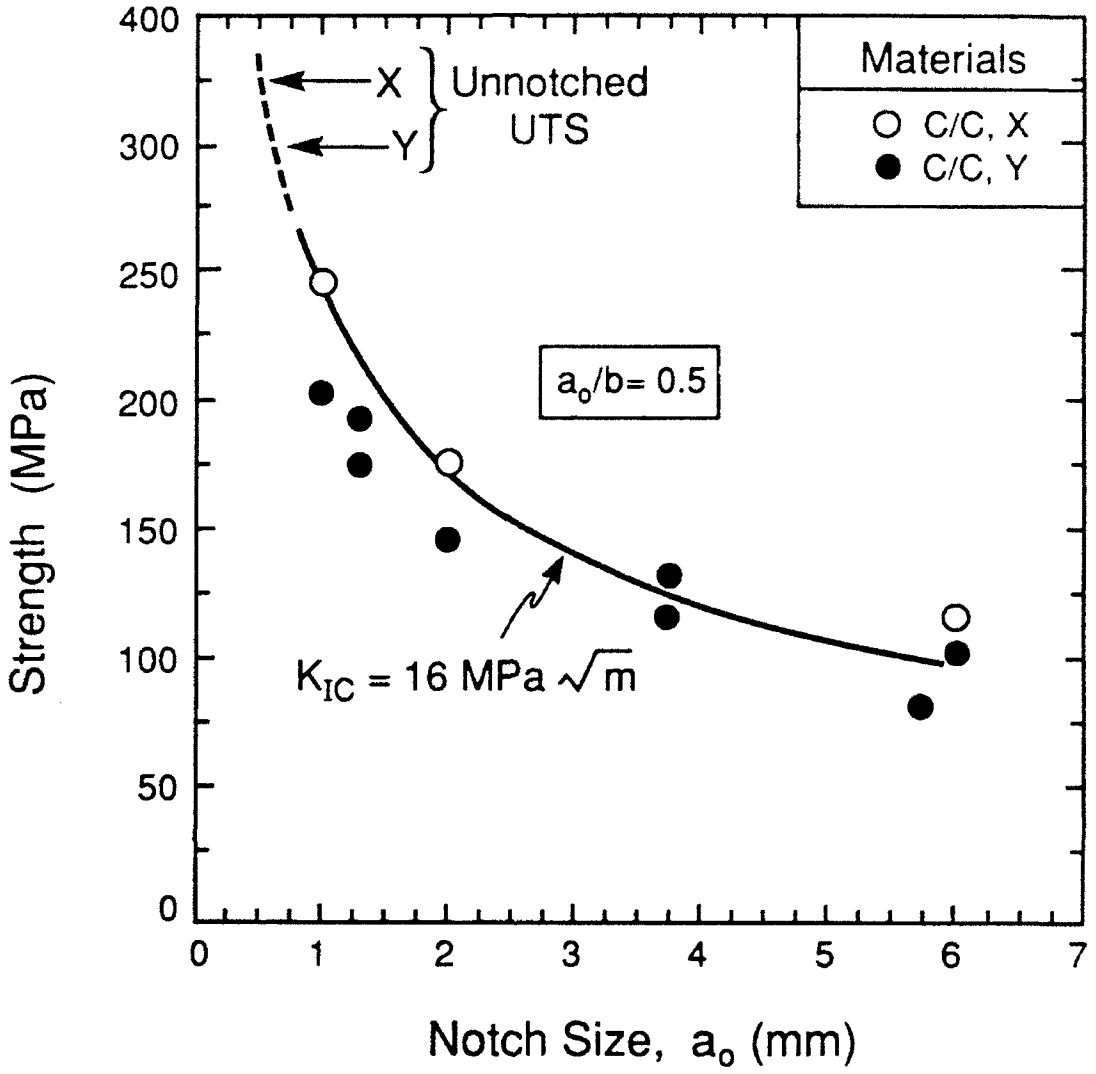
Materials
C/C, X
C/C, Y
X
Y
Unnotched
UTS
$a_o/b = 0.5$
K_{IC} = 16 MPa $\sqrt{m}$
Strength (MPa)
Notch Size, a_o (mm)
400
300
250
200
150
100
50
0
0
1
2
3
4
5
6
7

FIGURE 5a

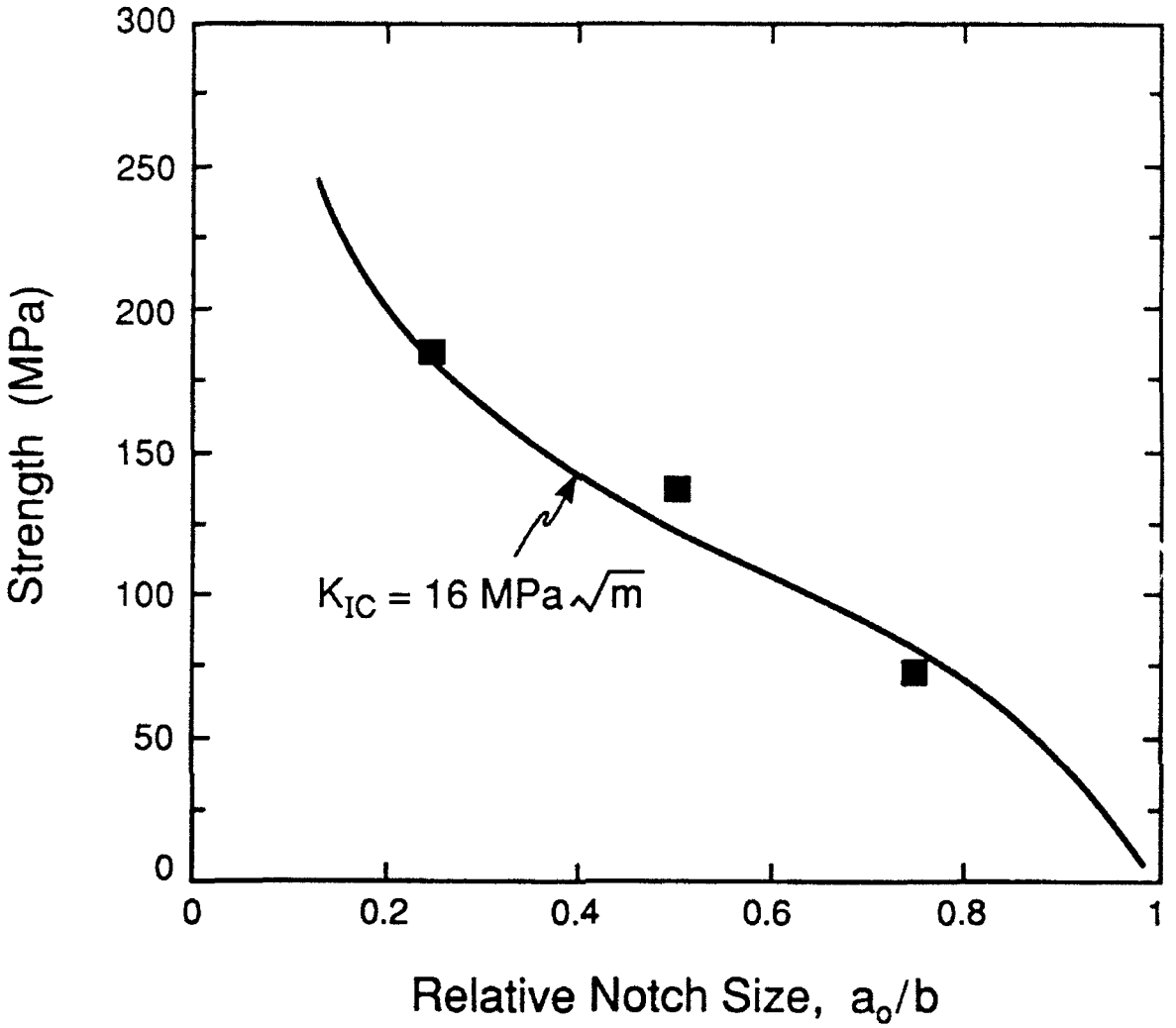
300
250
200
150
100
50
0
Strength (MPa)
0
0.2
0.4
0.6
0.8
1
Relative Notch Size, a_o/b
K_{IC} = 16 MPa$\sqrt{m}$

FIGURE 5b

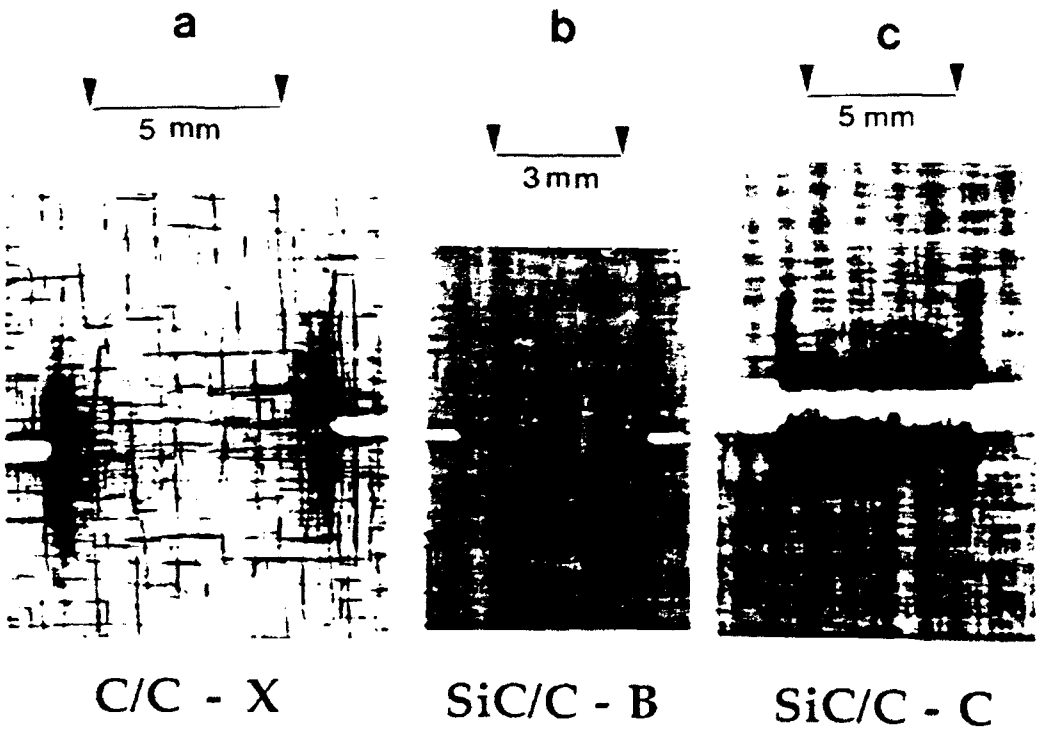

Figure 6

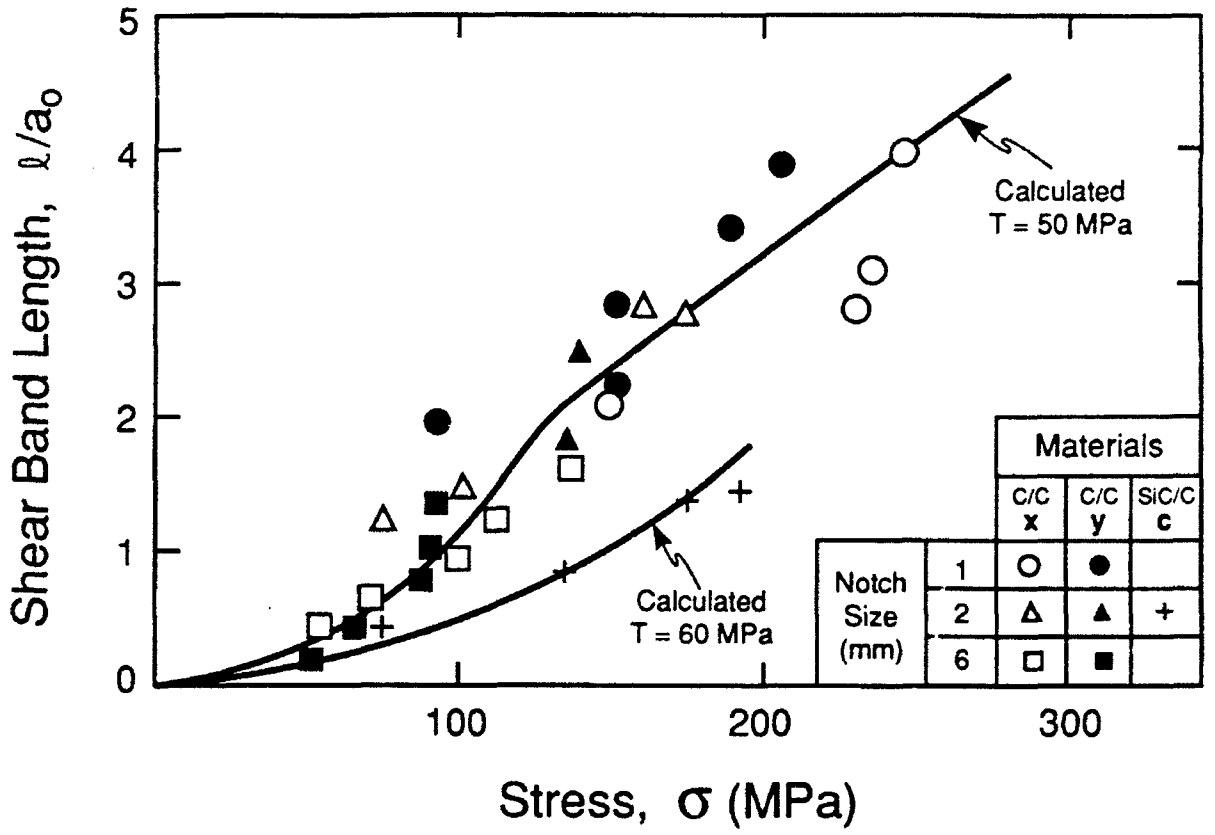

Heredia.Evans.DARPA•6/92•amk•D1#747-2

FIGURE 7a

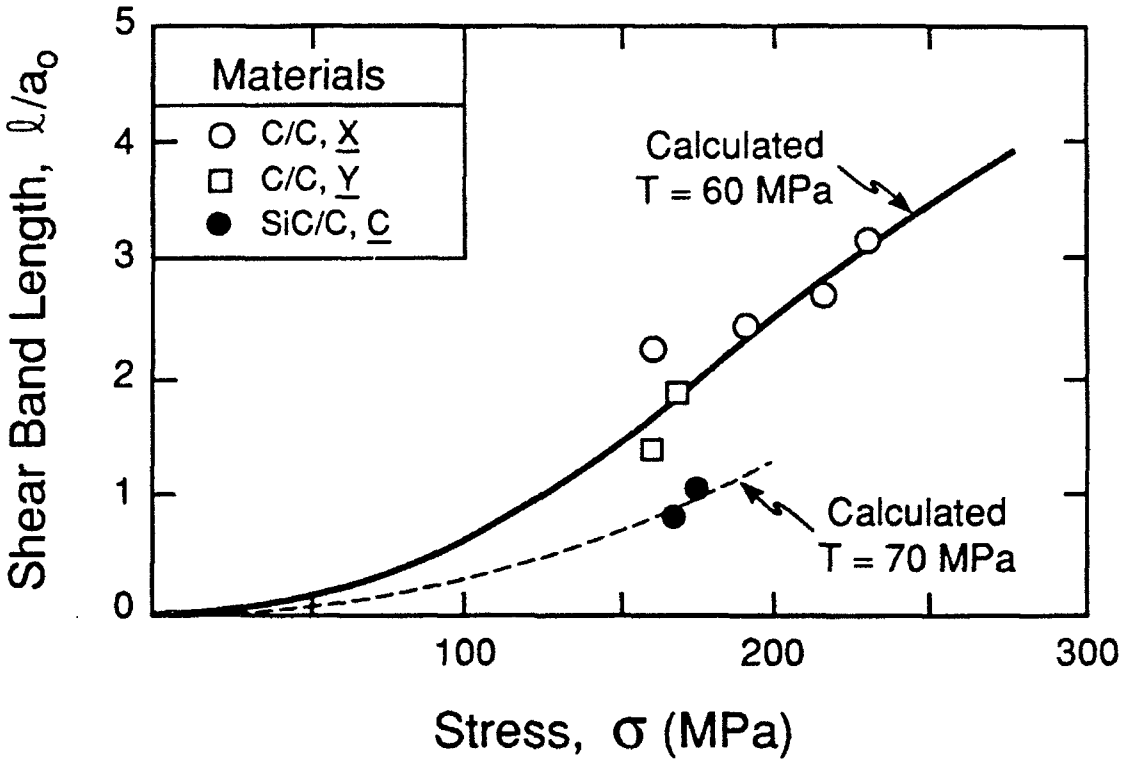
Materials
C/C, X
C/C, Y
SiC/C, C
Calculated
T = 60 MPa
Calculated
T = 70 MPa
Shear Band Length, ℓ/a$_o$
Stress, σ (MPa)
0
1
2
3
4
5
100
200
300

FIGURE 7b

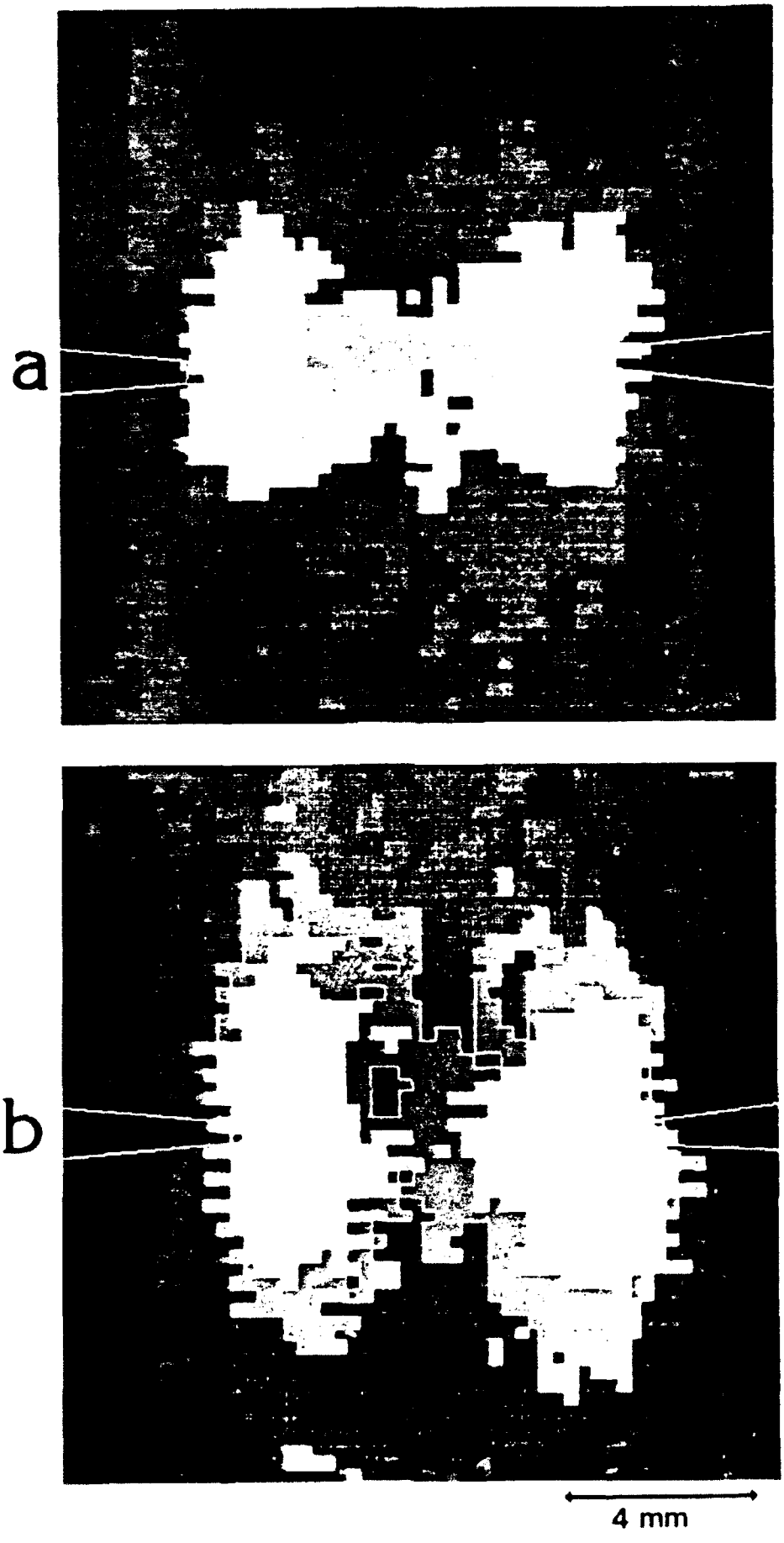

Figure 8

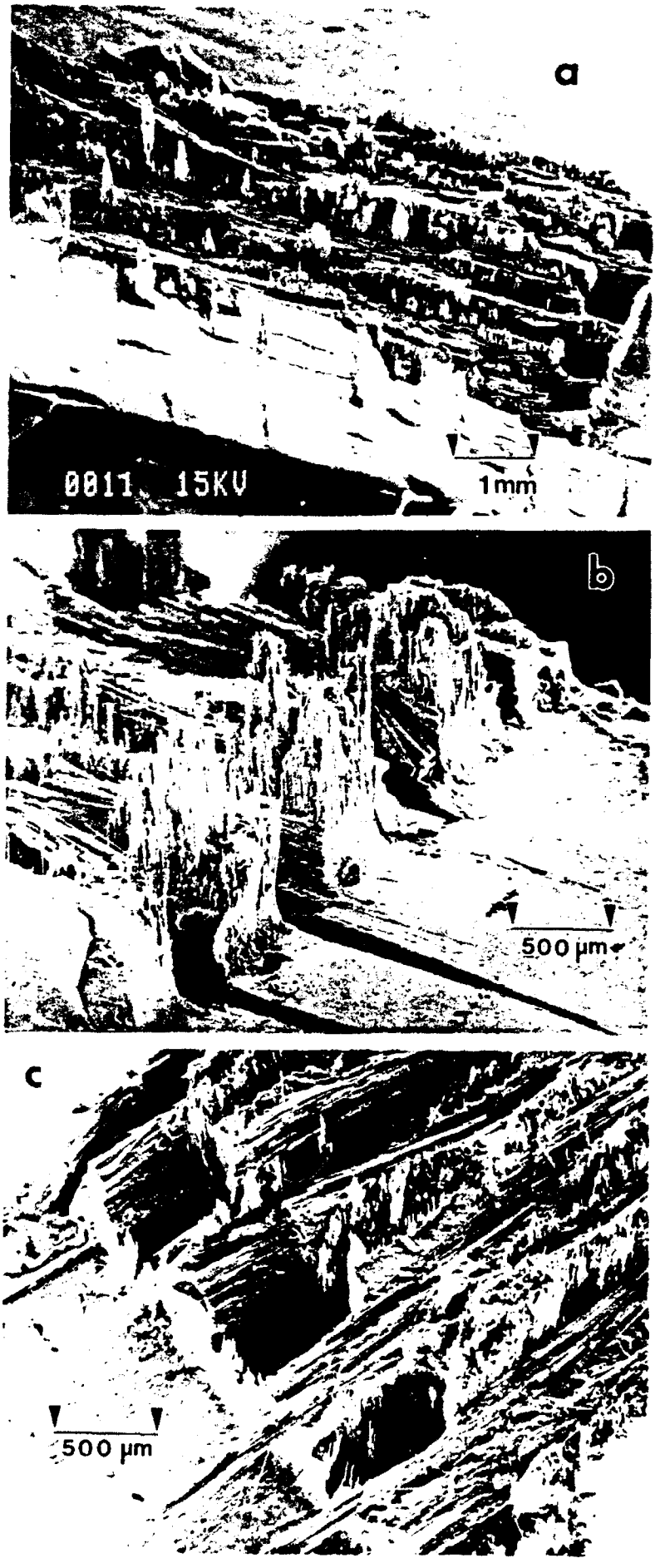

Figure 9

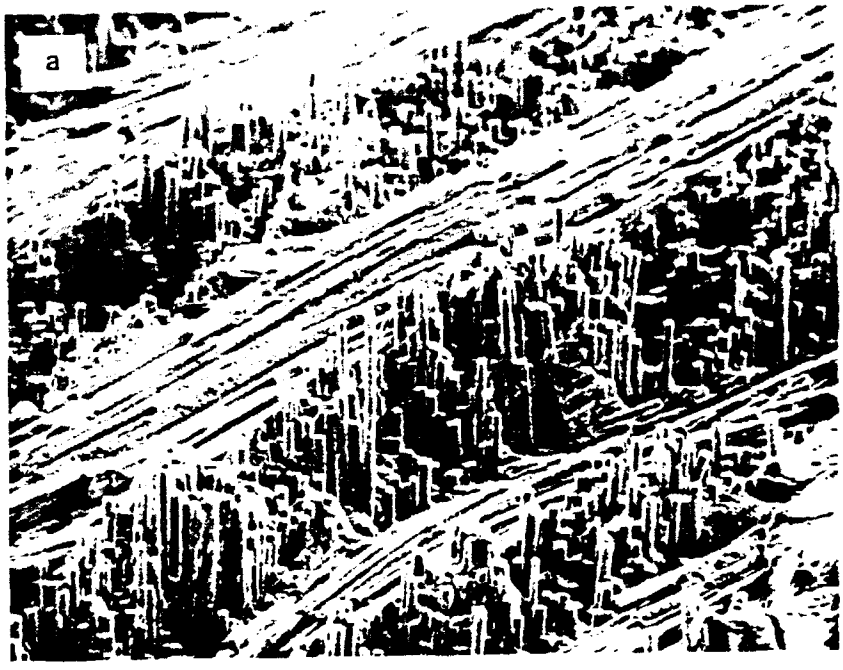

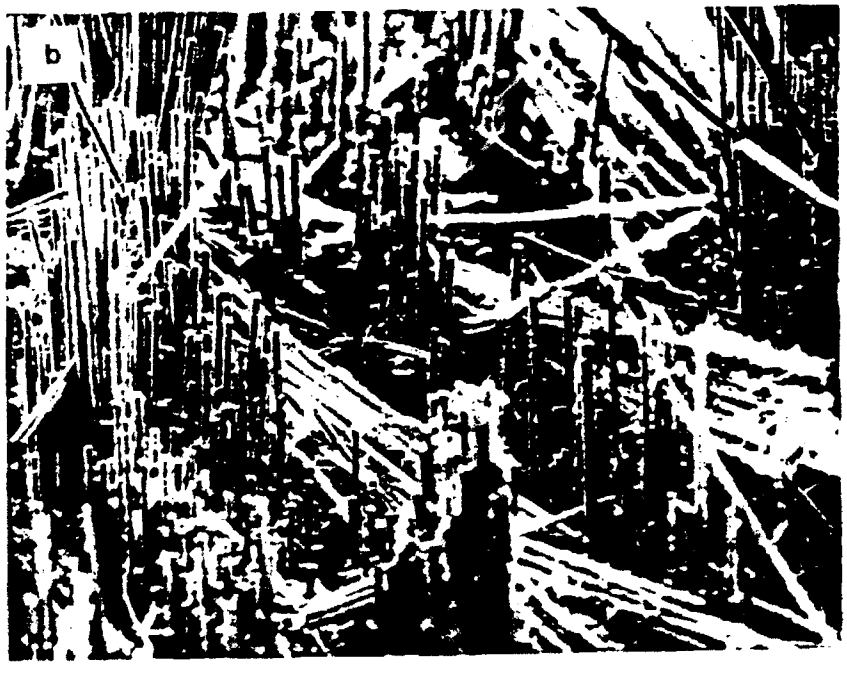

Figure 10

Figure 11

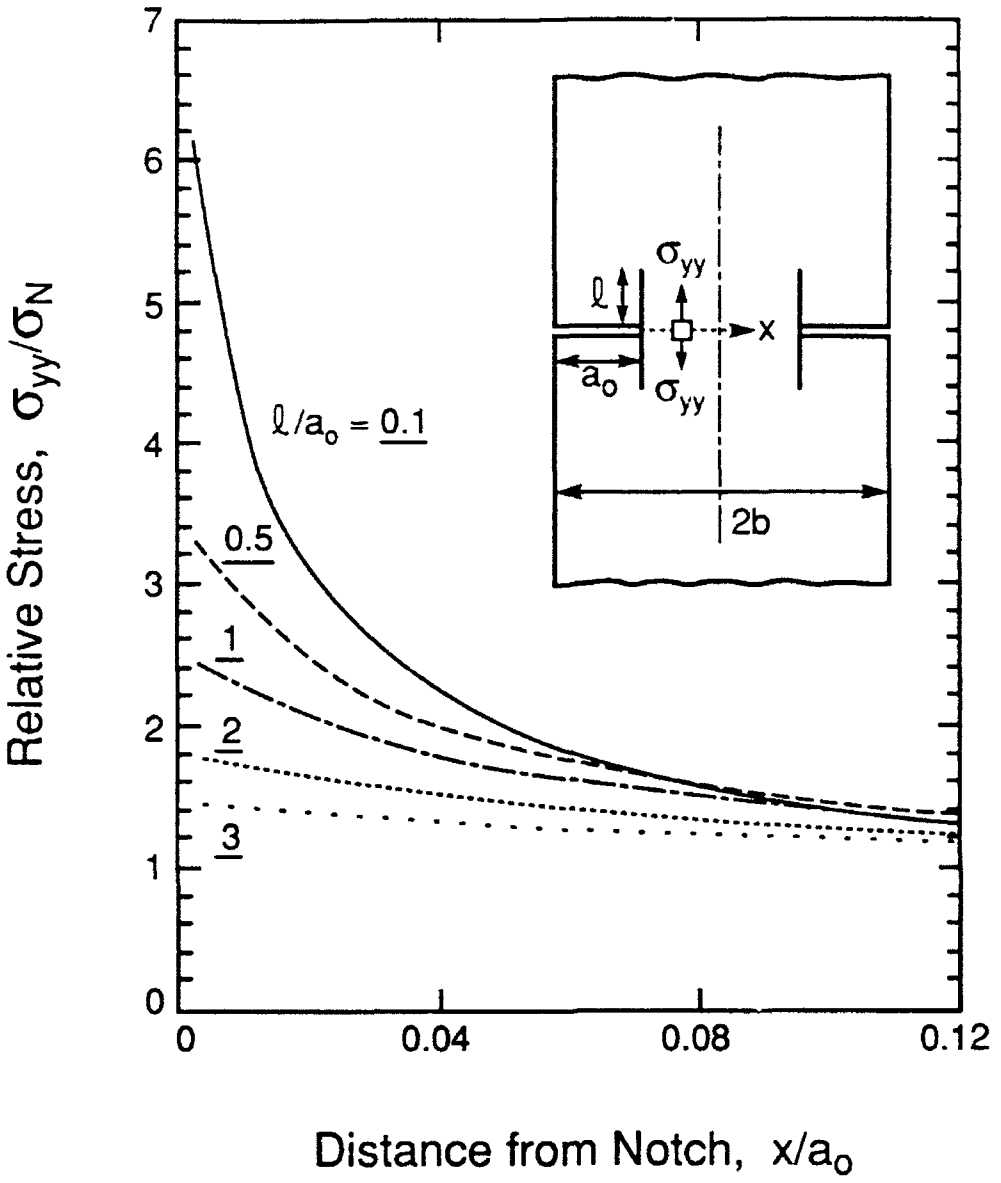

Heredia.Evans.DARPA-6/92-amk-D18747-1

FIGURE 12a

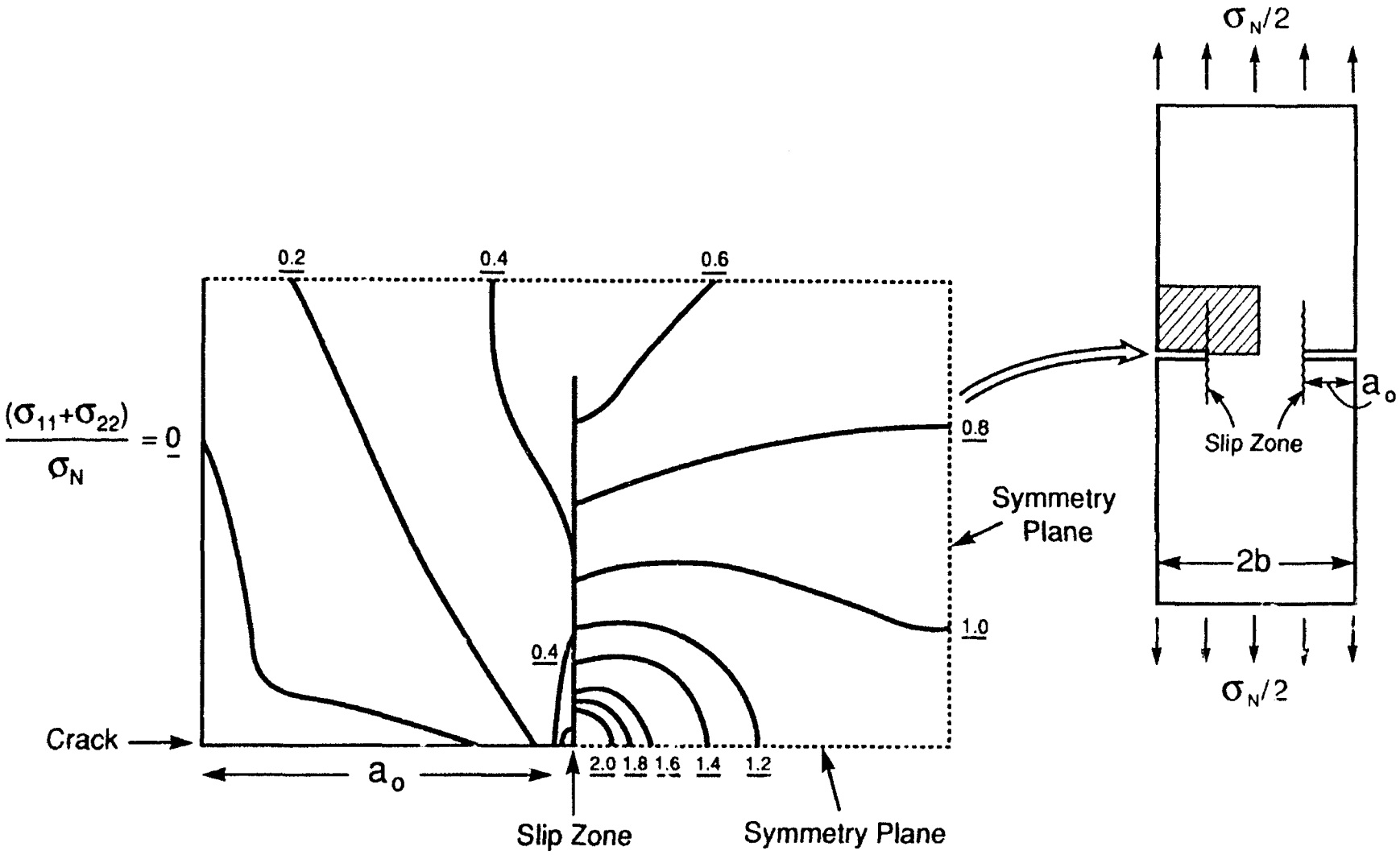
$\sigma_N/2$
$\frac{(\sigma_{11}+\sigma_{22})}{\sigma_N} = 0$
0.2
0.4
0.6
0.8
1.0
0.4
Crack
a_o
2.0 1.8 1.6 1.4 1.2
Slip Zone
Symmetry Plane
Symmetry Plane
Slip Zone
a_o
2b
$\sigma_N/2$

FIGURE 12b

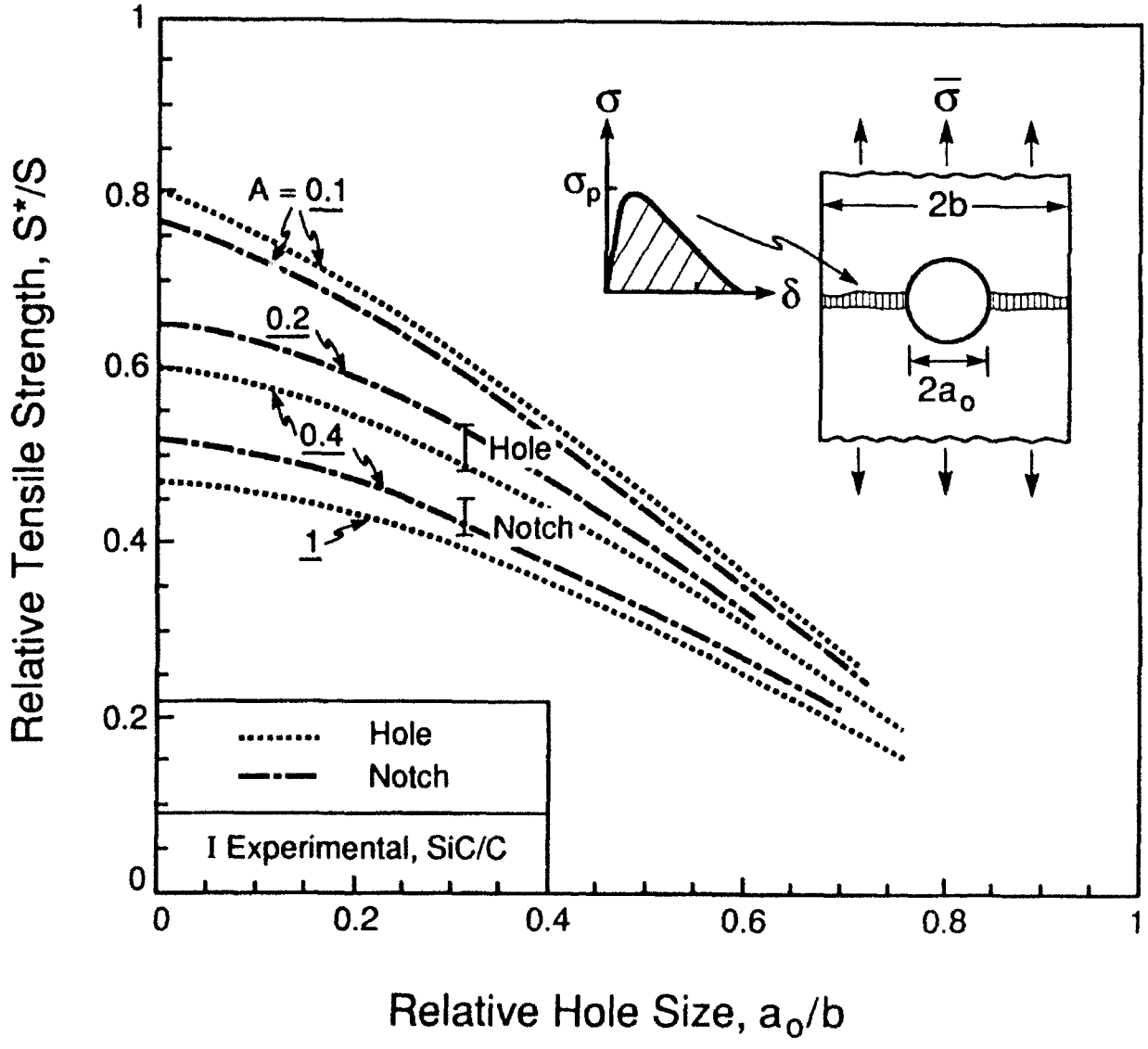
Relative Tensile Strength, S*/S
Relative Hole Size, a_o/b
A = 0.1
0.2
0.4
1
Hole
Notch
Hole
Notch
I Experimental, SiC/C
σ
σ_p
δ
$\bar{\sigma}$
2b
$2a_o$
0
0.2
0.4
0.6
0.8
1

FIGURE 13

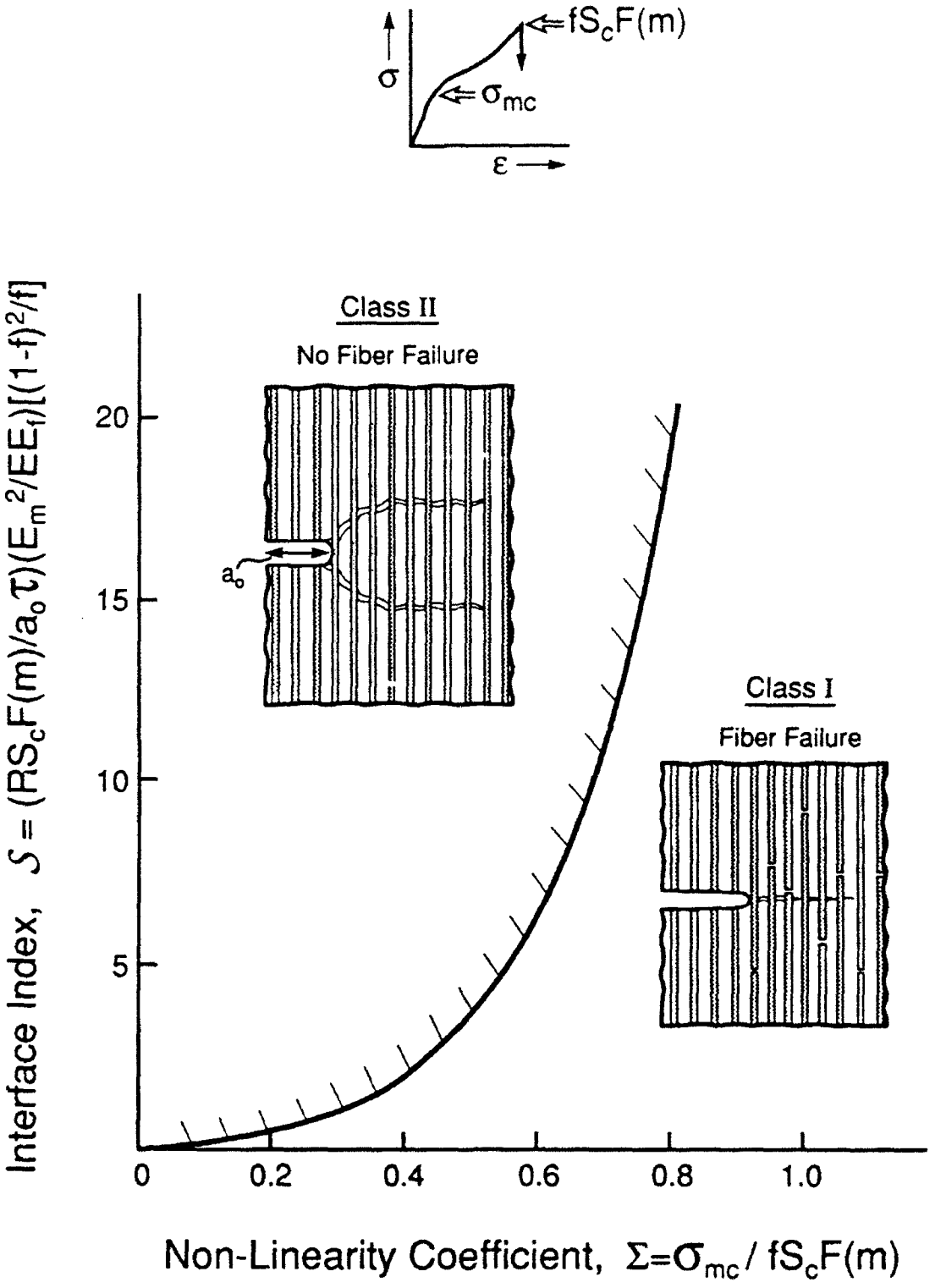
σ
fS_cF(m)
σ_mc
ε
Class II
No Fiber Failure
a_o
Class I
Fiber Failure
Interface Index, S = (RS_cF(m)/a_oτ)(E_m^2/EE_f)[(1-f)^2/f]
20
15
10
5
0
0.2
0.4
0.6
0.8
1.0
Non-Linearity Coefficient, Σ=σ_mc / fS_cF(m)

FIGURE A1

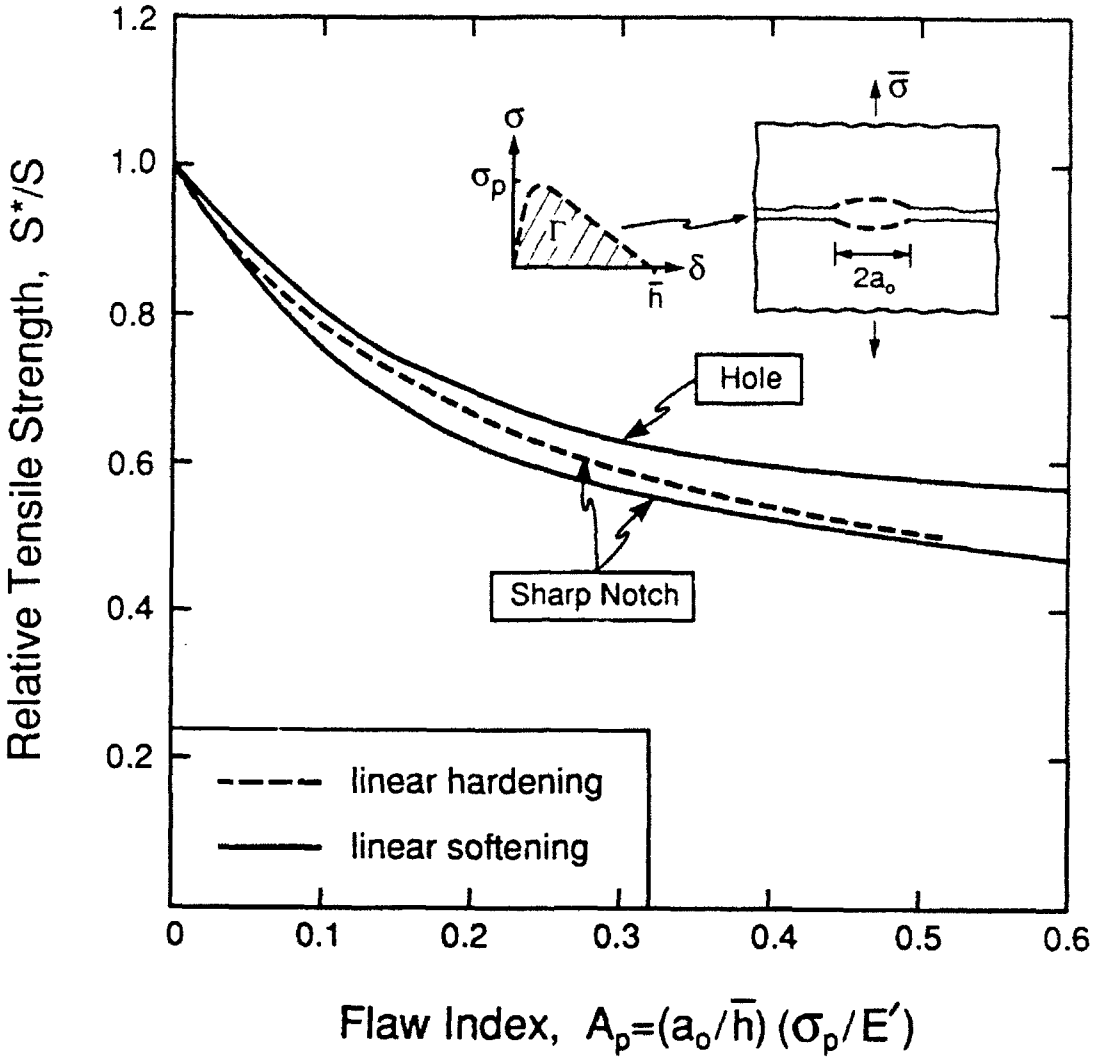

Evans..URI-9/92-amk-D40#866-5

FIGURE A2a

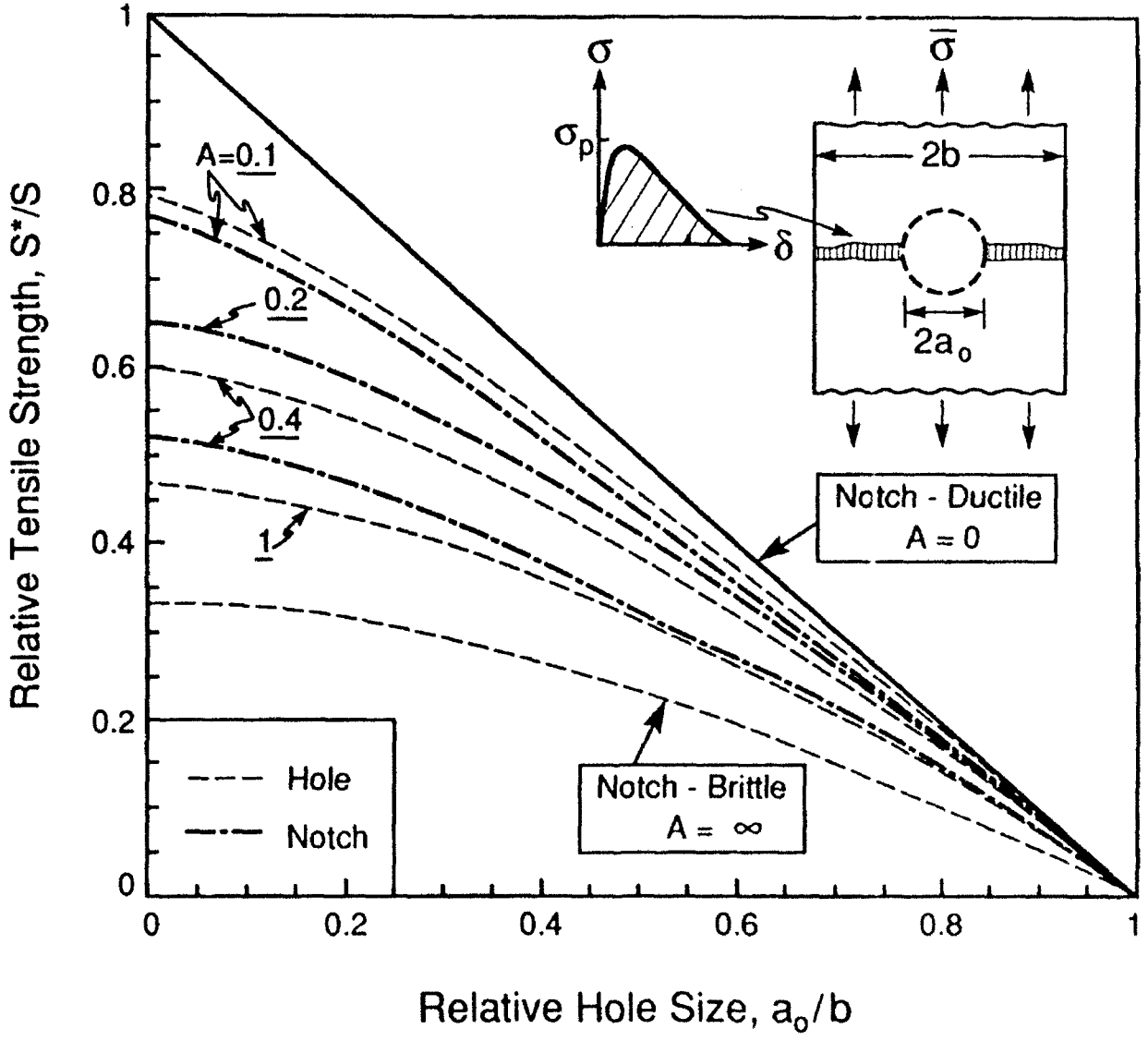
Relative Tensile Strength, S*/S
Relative Hole Size, a_o/b
A=0.1
0.2
0.4
1
Hole
Notch
Notch - Ductile
A = 0
Notch - Brittle
A = ∞
σ
σ_p
δ
$\bar{\sigma}$
2b
$2a_o$
0
0.2
0.4
0.6
0.8
1

FIGURE A2b

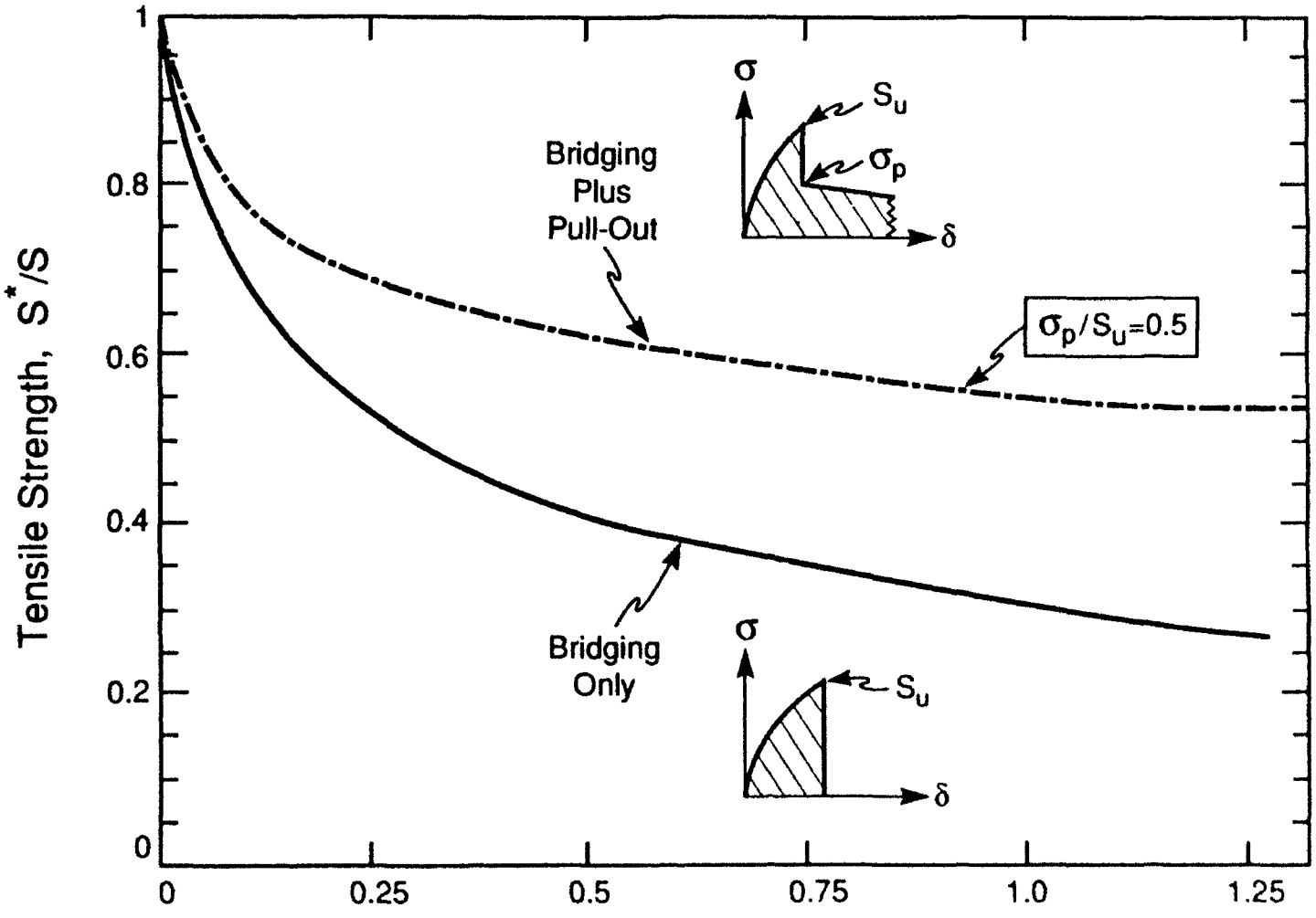

$$\text{Flaw Index, } A_b = \frac{f}{(1-f)^2}\left(\frac{E_f E}{E_m^2}\right)\left(\frac{a_o \tau}{RS}\right)$$

Figure A2c

Acta metall. mater. Vol. 40, No. 11, pp. 2967–2978, 1992
Printed in Great Britain

0956-7151/92 $5.00 + 0.00

THE MECHANICS OF FAILURE OF SILICON CARBIDE FIBER-REINFORCED GLASS-MATRIX COMPOSITES

S. JANSSON and F. A. LECKIE

Department of Mechanical and Environmental Engineering, University of California, Santa Barbara, CA 93106, U.S.A.

(*Received* 20 *November* 1991; *in revised form* 8 *April* 1992)

Abstract—Tensile and bending tests have been performed on a high-strength silicon carbide fiber-reinforced glass-matrix (LAS) composite. The experimental results indicate that the strength of the composite component is strongly dependent on the geometry and loading. A model of failure is developed which allows a uniform interpretation of the experiments when due account is taken of the strength of the matrix, the statistical nature of the properties of the fibers, and the dimension of the fiber pull-out length.

Résumé—On effectue des essais en traction et en flexion sur des composites à haute résistance formés d'une matrice de verre renforcée par des fibres de carbure de silicium. Les résultats expérimentaux indiquent que la résistance mécanique du composite dépend fortement de la géométrie et de la charge. Un modèle de rupture est développé qui permet une interprétation unique des expériences lorsque l'on tient compte de la résistance mécanique de la matrice, de la nature statistique des propriétés des fibres et de la longueur d'arrachage des fibres.

Zusammenfassung—Zug- und Biegeversuche werden an hochfesten Verbundwerkstoffen mit Glasmatrix und einer Verstärkung mit Fasern aus Siliziumkarbid durchgeführt. Die Ergebnisse zeigen, daß die Festigkeit der verstärkenden Komponente stark von der Geometrie und der Belastung abhängt. Ein Bruchmodell wird entwickelt, mit dem die Experimente einheitlich erklärt werden können, wenn die Festigkeit der Matrix, die statistische Natur der Fasereigenschaften und die Größe der Faser-Auszugslänge richtig berücksichtigt werden.

1. INTRODUCTION

Silicon carbon fiber reinforced glass–ceramic matrix composites have a high strength/weight ratio and offer the prospect of a material with good high temperature properties [1, 2]. Since there is little difference in the coefficient of thermal expansion between fibers and matrix the stresses induced by thermal loading are small. It has been demonstrated for example that the tensile residual stresses after processing are low [3]. The properties of the fibers with the commercial name Nicalon are unimpaired up to temperatures of 1000 [1] although it is known that the mechanisms of fracture are substantially different at elevated and room temperature [4]. The mechanism of failure of these materials have been extensively studied but by contrast less attention has been devoted to establishing the mechanics which dictates the strength and potential failure of the engineering components now being made from such materials.

Because of the relative ease of the bending test most material data has been obtained from this source. The strength however is known to be geometry dependent with substantial differences existing, for example, between the results of tensile and bending specimens [3]. Such differences must be reconciled before a reliable mechanics theory is established which can be widely applied. An early effort to develop a theory of mechanics is the work of Weibull [5, 6] whose procedures are widely used to define the statistical strength of fibers. Weibull also developed the weakest link concept and this method is also widely practiced when establishing the strength of components [7]. Considerable attention has also been devoted to predicting tensile strength from the properties of the composite constituents including the studies of Thouless and Evans [8], Aveston *et al.* [9], Schwietert and Steiff [10], and Zweben and Rosen [11]. In this study a variety of component geometries are tested under different loading conditions and an attempt is made to establish a model which can be used to determine the strength of engineering components, and to define the underlying failure mechanisms.

2. THE TEST PROGRAM

The material used in this study consists of silicon fibers (commercial name Nicalon) in a uniaxial lay-up whose elastic modulus is 200 GPa embedded in a matrix of lithium aluminosilicate (LAS) whose modulus is 85 GPa. The average tensile strength of the

fibers are reduced during the processing from 2000 to 1500 MPa based on a reference length of 25 mm [12]. The exponent in Weibull statistics is $m = 4.0$ [1, 13] and the average diameter is 12 μm.

The behavior of the material is investigated by observing the response and failure mechanism of beams of different sizes and cross-sections when subjected to three and four point bending. In these tests it is possible to adjust the relative value and spatial distribution of the shear and tensile stresses which are representative of loadings occurring in practice. Tensile tests are also performed. The material was supplied in plate form 3 mm thick and was cut by diamond grinding into beams and uniaxial specimens. Because the supply of material was limited it was only possible to perform two tests of each component and loading. In all cases the experimental variation were within 5%.

2.1. *Three-point bend test (rectangular and triangular cross-section)*

Three-point bend tests [Fig. 1(a)] were performed on beams of rectangular cross section with three different ratios of the span (l) to depth (h) of 6.67, 13.3 and 30 and on beams with triangular cross-section. For three-point bending of rectangular beams with the definitions shown in Fig. 1(a) classical elastic beam theory gives the maximum bending stress σ at the outer surfaces, the maximum shear stress τ at the beam center and beam bending deflection δ as

$$\sigma = \frac{3Pl}{2bh^2} \qquad \tau = \frac{3P}{4bh} \qquad \delta = \frac{Pl^3}{4Ebh^3} = \frac{l\sigma}{6Eh} \qquad (1a\text{–}c)$$

The ratio of maximum bending to shear stress is

$$\frac{\sigma}{\tau} = \frac{2l}{h} \qquad (1d)$$

so that the ratio may be adjusted by appropriate selection of the ratio (l/h). While the short beam may fail in shear the dimensions are such that deflection is dominated by bending.

The beams were loaded until failure occurred and the applied load and central displacement were continuously measured as indicated in Fig. 2(a). Using equation (1) the test results shown in Fig. 2(b,c) are expressed in terms of bending stress deflection and shear stress deflection curves respectively.

The modes of failure of the three-point bending specimens shown in Fig. 3(a–c) are indicative of the different stress–deflection characteristics observed in Fig. 2. The mode of failure for the short beam ($l/h_1 = 7.2$) shown in Fig. 3(a) indicates that shear cracks formed uniformly throughout the specimen. The formation of the cracks corresponds to the flat portion of the load maxima in Fig. 2(b). Thereafter the load decreases steadily with increase of central displacement.

The failure modes for the intermediate length beam ($l/h_1 = 13$) shown in Fig. 3(b) indicate that lengthwise shear cracks propagate along the middle of the beam from the center to the beam extremity. The formation of this crack corresponds to the first major load drop evident in Fig. 2(a). With continued loading a second crack pattern in formed at the quarter points of the cross-section and correspond to the second load drop shown in Fig. 2(c).

The failure of the long beam shown in Fig. 3(c) is a fibrous tensile fracture and occurs in the cross-section under the loading point. Initial failure is followed by a major load drop as indicated in Fig. 2(b) which is followed by the formation of a longitudinal shear crack. Some compressive crushing occurred at the center point of load application. However, there is no evidence of debonding between the compressive kink and the remainder of the beam.

The results of these tests indicate that fibrous tensile failure occurs when the tensile bending stress is 1180 MPa while shear crack formation occurs when the shear stress reached 29 MPa. Using equation (1a), it is evident that the failure mechanism changes from one of shear to fibrous bending failure when the ratio l/h_1 exceeds 20.3. As noted earlier when failure is by

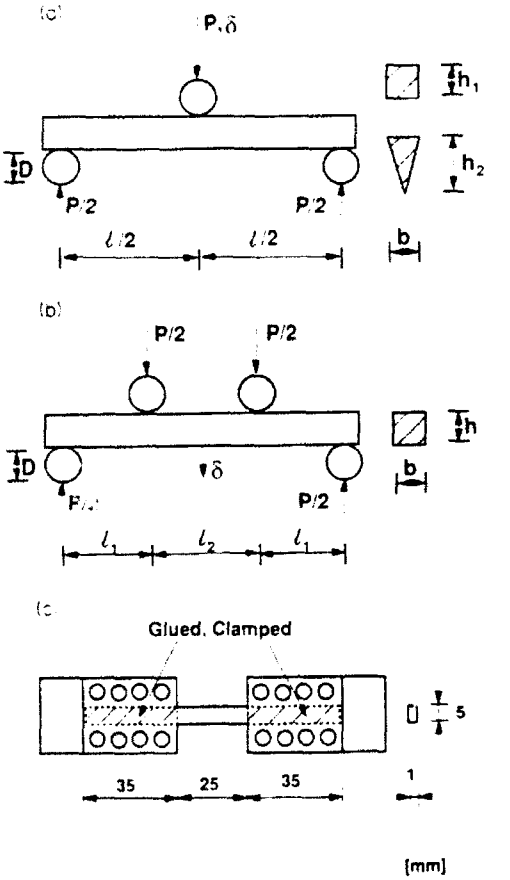

Fig. 1. Specimen geometries, dimensions $D = 10$ mm, $l = 20$, 40, 90 mm, $h = h_1 = b = 3$ mm, $h_2 = b$ mm, $l' = 20$ mm, and $l_2 = 35$ mm.

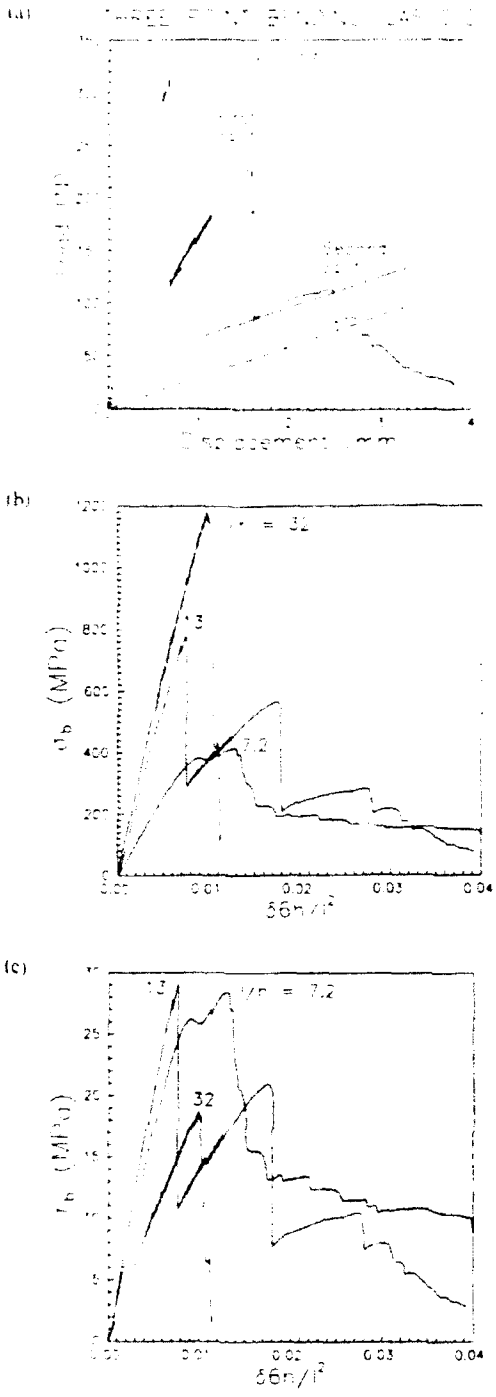

Fig. 2. Load displacement relationship for three-point bending ($l/h = 13$). (b) Nominal bending stress–displacement relationship. (c) Nominal shear stress–displacement relationship.

fibrous tension it is followed by catastrophic load drop. By contrast when failure is by shear crack formation the load drop is less dramatic and a diminished load is maintained during further deformation.

When the long beam of rectangular cross-section is subjected to three-point bending the fiber tensile failure is followed by dramatic decrease of load. When the long beam with triangular cross-section [Fig. 1(a)] is subjected to three-point bending failure is again by fiber tensile fracture. However, the failure process is less dramatic and is extended over a large deflection as shown in Fig. 4.

2.2. The four-point bend test

The arrangement of the four-point bend test is shown in Fig. 1(b). Using the classical elastic beam theory the bending stress and central deflection are given by

$$\sigma_b = \frac{3Pl}{bh^2} \qquad \delta = \frac{\sigma_b l^2}{4Eh} \tag{2a, b}$$

There is no shear on the central section of length l. To avoid shear failure in the cantilevered portion the ends of the beam were reinforced by aluminum sleeves glued into position.

The experimental results for the variation of bending stress with the central deflection are shown in Fig. 5. Fracture started with delamination of a thin surface foil on the compression side of the specimen [Fig. 3(d)]. Extensive compressive failure occurred thereafter in the matrix and during this period the load displacement diagram showed erratic behavior with increased displacement accompanied by alternate load increase and decrease. Generally, the load increased with displacement until fiber tensile fracture occurred in the tensile portion of the beam at a nominal bending stress of 1000 MPa. The final fracture is accompanied by load reduction which is less dramatic than evident in the three-point load test (Fig. 4).

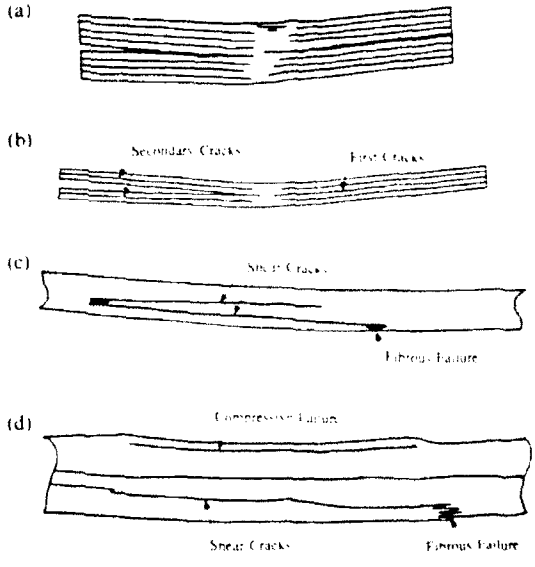

Fig. 3. (a) Schematic of multiple shear failure. (b) Schematic of mid-plane shear failure. (c) Schematic of fiber tensile failure. (d) Schematic of four-point bending failure.

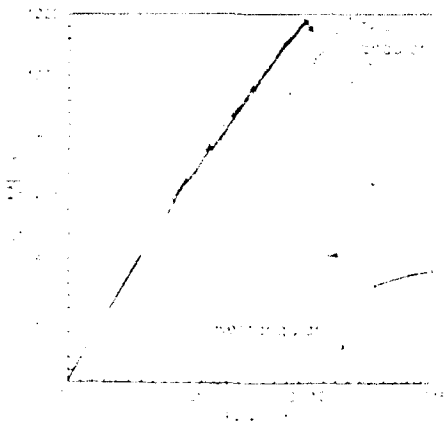

Fig. 4. Nominal bending stress displacement relationship for rectangular and triangular cross-section.

The four-point load test indicates that a crushing compressive stress occurs at 900 MPa. Failure by fiber kinking is not apparent which is to be expected since the buckling stress calculated according to the model by Rosen and Ketler [14] is 44 GPa, a value much higher than the observed failure stresses. From the rule of mixtures the matrix stress in compressive failure is estimated to be 540 MPa. Micrographic examination reveals that matrix microcracking appears in the compressive region.

2.3. *The uniaxial test*

The combination of the high tensile strength of the fibers and the poor shear properties of the matrix introduces major difficulties when the material is tested in tension. After experimentation with different geometries and gripping systems the geometry illustrated in Fig. 1(c) was found to give repeatable results and avoided failure within the gripping section of the specimens. In order to minimize bending stresses the specimens were glued to the grips, after which the grips were mounted in the load frame using a two component epoxy glue. After the glue had set a low clamping-pressure was applied to improve the strength of the adhesive joint. In order to reduce the shear stress in the matrix the test specimens were designed to be long and thin. The results of the three-point bending tests indicate that the ratio of the maximum tensile strength to the matrix shear strength is 30. For the geometry selected the ratio of the average tensile stress is 70 times that of the interlaminar shear stress so that failure inside the grips was avoided. Both strain gauge and cross-head displacement measurements were made. The strain was measured with a 6.3 mm long strain gauge mounted on the specimen and the ram-displacement was measured by a displacement transducer. The strain-gauge stress–strain relation and the estimated value using the ram displacement are shown in Fig. 11. While shear failures in the grips were avoided, it was observed that the deformatio, the glued joint was significant.

The strain-gauge results indicate a reduction in stiffness occurs when the stress is 180 MPa and continues until the stress is 250 MPa. The onset of the reduction coincides with the visual appearance of matrix cracking. Dramatic failure occurs at 790 MPa, with visual observation of the failure surface being reminiscent of fiber bundle failure. Referring to Fig. 7(b) it may be observed that single fiber pull-out is accompanied by the formation of bundles.

A second specimen was pre-loaded to a stress of 300 MPa and the subsequent stress strain curve showed no sign of softening at 250 MPa (Fig. 6). The value of Young's modulus for the uncracked specimen before softening occurred was 160 GPa. After softening the value of Young's modulus is 133 GPa and it is observed that the preloaded specimen has the same value. Consequently it can be deduced that cracking occurs in the matrix at 250 MPa and that its effect is to reduce Young's modulus from 160 to 133 GPa or by 16%. The additional strain observed on cracking is $\Delta\varepsilon_c = 0.08\%$.

The growth and density of cracks in the matrix were measured throughout the test by taking replicas of the surface. The replica procedure consisted of melting an acetate replicating tape onto the surface and peeling it from the surface after a period of 1 min. By counting the spacing along fifty fibers at each stress level it was possible to determine the variation of average crack spacing with stress. Referring to Fig. 8 it is seen that the crack spacing reaches a saturation value of approximately 100 μm for stresses of 300 MPa and above. This value of stress coincides with the onset of softening indicated in Fig. 6.

The failure mode in tension is illustrated in Fig. 7 from which it can be observed that the fracture runs along the whole gauge length at a small angle and then branches to the side at the grips. Examination of the failure surface shown in Fig. 7 indicates the formation of bundles of fibers, the bundles being

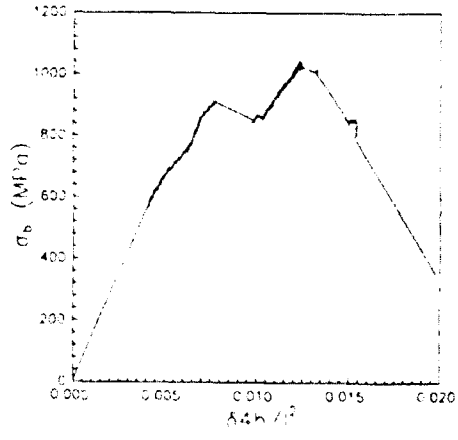

Fig. 5. Four-point bending stress–displacement relationship

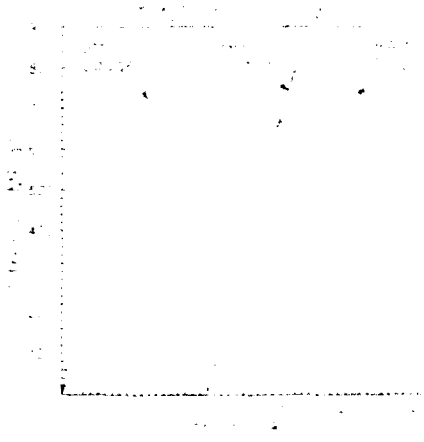

Fig. 6. Stress–strain for uniaxial specimen

approximately 120 μm diameter and of length 750 μm.

2.4 *Summary of experimental results*

The modes of failure evident from the test program are fiber tensile failure, matrix compression failure, interlaminar matrix shear and matrix tensile cracking.

The stresses corresponding to the failure are given in Table 1.

3. MATRIX FAILURE AND LOAD TRANSFER DISTANCE

The experiments indicate that matrix failure can take one of two forms. In the uniaxial test matrix tensile failure is evident with the appearance of cracks normal to the direction of the loading and with a uniform spacing of 0.1 mm. Matrix shear failure occurs when the shear stress is 29 MPa. When fiber tensile failure occurs it is followed by a splitting fracture in the matrix which propagates in the direction of the fibers.

The uniaxial test indicates that cracking starts to occur at a stress of 180 MPa and continues to saturate until the stress is 260 MPa. Since residual stresses from the processing are small the formula for the stresses in the fiber and matrix in Appendix I indicate that a composite stress of 180 MPa corresponds to a tensile stress of 110 MPa in the matrix. The steady state crack spacing in the matrix is measured to be 100 μm and remains constant with increasing load. This observation would indicate that the matrix stress remains constant after crack saturation and implies continuous slipping between fiber and matrix.

An expression for the spacing S of the matrix tension cracks is derived in Appendix I and is given by

$$\frac{S}{d} = \frac{\sigma_f}{2\tau_i}\left[\frac{1}{1+\dfrac{f}{1-f}\dfrac{E_f}{E_m}}\right] \tag{3}$$

where σ_f is the far field stress when the matrix cracking saturates, f is the volume fraction of fibers, d is the fiber diameter, τ_i is the shear stress between fiber and matrix and E_f and E_m are the elastic moduli of fibers and matrix respectively. When $S = 100\ \mu$m, $f = 0.5$, $d = 12\ \mu$m, $E_f/E_m = 2.35$ and $\sigma_f = 280$ MPa the formula gives the value of the shear stress $\tau_i = 5$ MPa. This value corresponds to that obtained by Weiks *et al.* [5] from fiber push-through tests.

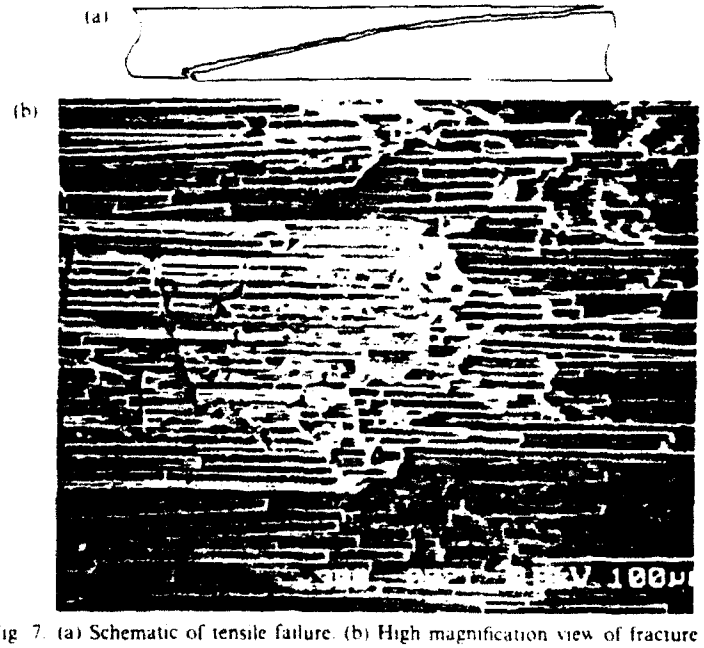

Fig. 7. (a) Schematic of tensile failure. (b) High magnification view of fracture surface

Table 1. Failure modes and stresses

Specimen	Dominant failure mode	Failure stress (MPa)
Uniaxial	Matrix tensile cracking	110
	Fiber tensile failure	790
[±45°]$_{2s}$	Matrix shear cracking	58
	Fiber tensile failure	1190
[0°/90°]$_{2s}$ Reinforced	Fiber tensile failure	1190
[0°/90°]$_{2s}$ Reinforced	Matrix shear cracking	58
[0°/90°]$_{2s}$ Unreinforced	Fiber tensile failure	1190

Shear failure occurs in the matrix in a direction parallel to the fibers when the shear stress is $\tau = 29$ MPa. If it is assumed that the fibers are randomly distributed then the effective area of the matrix in shear is the same as the volume fraction ratio f. Since $f = 0.5$ the shear matrix failure stress is 58 MPa. The matrix tensile failure stress estimated from the uniaxial tensile test is 110 MPa. Comparison of the failure shear stress of 58 MPa, with the matrix failure stress of 110 MPa suggests that the criterion for matrix failure is a maximum shear stress of approximately 55 MPa. Stress concentration effects have not been included but these are likely to be modest.

The fiber transfer length L_T is the distance required to transfer stress from a broken fiber to the matrix. This transfer length is readily found to be

$$L_T = \frac{\sigma_c}{f\tau_c}\frac{d}{4} \tag{4}$$

where σ_c is the far field composite area. The stress for tensile fiber failure varies between 800 and 1200 MPa according to the loading state. With $d = 12\ \mu$m, $f = 0.5$ and $\tau_c = 5$ MPa in equation (4) gives transfer lengths between 1.07 and 1.6 mm. The spacing of the matrix cracks in uniaxial tension is 100 μm so that the transfer length is approximately ten times the matrix crack spacing. In terms of the fiber diameter d, the matrix crack spacing is $S = 12.5d$ and the transfer length L_T varies between $125d$ and $185d$ depending on the loading condition.

4. FIBER TENSILE FAILURE

The experiments indicate that the stress at which tensile failure occurs in the fiber is dependent on the geometry of the specimen. The observed stresses for fiber tensile failure of the different specimens are given in Table 2 which indicates that the failure strengths vary between 790 and 1190 MPa. The failure tensile stress of the matrix is an order of magnitude smaller at 110 MPa and the interface shear strength between matrix and fiber is 5 MPa. It seems plausible to assume that the strength of specimen is dictated by fiber strength and that the contribution of the matrix to the final strength is negligible. The implications of this assertion is now studied.

4.1. Strength of fiber systems neglecting the matrix contribution

Weibull statistics are known to be an effective means of describing the strength of fiber systems. Andersson and Warren [13] have studied the strength of as received Nicalon fibers and concluded that the strength of the fiber can be described by the probability $P(f)$ of failure according to the Weibull relation

$$P(f) = 1 - \exp\left[-\frac{l}{l_0}\left(\frac{\sigma}{\sigma_0}\right)^m\right] \tag{5}$$

where l_0 is the gage length and m and σ_0 are material constants.

In a study by Prewo [12] the strength of Nicalon fibers were measured after subjecting them to the processing route used in the production of the composite. The statistics defining fiber strength can again be described by equation (5). Prewo [12] chose to present his results in terms of the average strength $\bar{\sigma}$ of fibers 25 mm long for which

$$\bar{\sigma} = 1500\ \text{MPa}$$

$$m = 4.0$$

for

$$l_0 = 25\ \text{mm}.$$

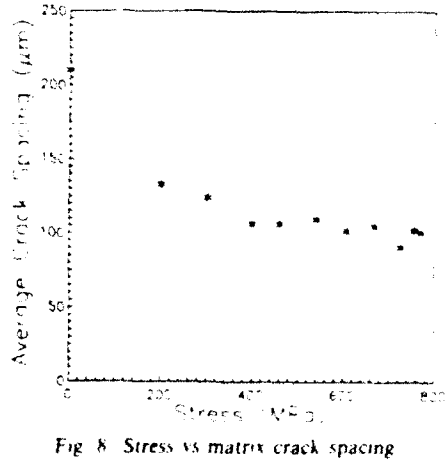

Fig. 8. Stress vs matrix crack spacing

Table 2. Effect of Weibull index m on strength

Loading	Experimental strength, MPa	Experimental strength factor	Computed strength factor $m = 4$	m	m	Modified experimental strength, MPa	Modified experimental strength factor
Uniaxial tension σ	790	1.00	1.00	1.00	1.00	790	1.00
Four-point bending	1050	1.33	1.42	1.32	1.27	1050	1.33
Three-point bending $\frac{L}{D}$	1180	1.50	1.67	1.50	1.27	1236	1.56
Three-point bending $\frac{L}{D}$	1390	1.81	2.26	1.86	1.43	1340	1.44

The average strength of the fibers before processing is 2300 MPa so that processing apparently reduces the fiber strength by 35%.

The relationship between the average strength $\bar{\sigma}(l_e)$ for fibers of gage length l_e and σ_r for reference length l in the Weibull relationship is from equation (A1)

$$\bar{\sigma}(l_e) = \left(\frac{l}{l_e}\right)^{\frac{1}{m}} \sigma_r \Gamma\left(1 + \frac{1}{m}\right) \tag{6}$$

where Γ is the Gamma function. When $l = l_e = 25$ mm and $m = 4$ equation (6) gives the result $\sigma_r = 1650$ MPa.

The expression for the bundle strength σ_B in terms of the average fiber strength $\bar{\sigma}_f$ is given by (A2) which is

$$\frac{\sigma_B}{\bar{\sigma}_f} = \frac{f(m\,e)^{\frac{1}{m}}}{\Gamma[(m+1)\,m]}. \tag{7}$$

Using $\sigma_r = 1650$ MPa and $m = 4.0$ for a length of 25 mm the bundle strength is predicted to be $\sigma_B = 450$ MPa which is substantially less than the value of 790 MPa observed in tensile tests.

Weibull weakest link theory has been used to determine the strength of the beam components using the procedures given in Appendix 2. For ease of comparison with experiments the strengths have been normalized with respect to the strength of the longitudinal tensile specimen. This method of presentation has the advantage that the geometry dependence of the strength of the exponent m can be assessed separately. The resulting strength factors have been calculated for different values of Weibull index m and the results are shown in Table 2.

While the predicted strength factors order correctly the strength of the components, the predicted range of strength for $m = 4$ is generally greater than that observed in experiment. It has been observed by Prewo and Brennan [2] and Curtin [16] that the measured uniaxial strength corresponds to that of fiber bundle of a length close to the stress transfer length of 1.07 mm which is substantially shorter than the gauge length. The uniaxial bundle strength for gauge length of 1.07 mm is 910 MPa which overestimates the experimental uniaxial strength by 15%. This crude calculation does indicate however that the matrix is likely to play a significant role in establishing the composite strength. A more detailed analysis is now performed in which the role of the matrix is included.

4.2 Bundle element model

Examination of the failure surface [Fig. 7(b)] indicates a combination of individual fiber pull-out and bundle pull-out. The bundle diameter is approximately 10 fiber diameters and the pull-out length 100 fiber diameters long. Consider that the failure element consists of n fibers of diameter d embedded in a cylinder of matrix of diameter D. The load transfer distance for the fibers is

$$l_t = \frac{d\sigma_f}{4\tau_s}$$

where σ_f is the far field stress and τ_s is the shear strength of the fiber–matrix interface. Since the fiber can break anywhere in the element and still pull-out from the matrix the bundle element length is $l_B = 2l_t$.

As the number of breaking fibers increases the restraining matrix shear stress on the element increases until failure occurs by the bundle pulling out from the matrix (Fig. 9). Then equating the shear force from the fibers to the shear force from the surrounding matrix gives the result

$$\tau_c D = nd\tau_s$$

where τ_c is the composite shear strength and τ_s is the interface shear stress. Using this result together with the definition of the volume fraction f gives the number of fibers in the bundle and its diameter by

$$n = \frac{1}{f}\left(\frac{\tau_c}{\tau_s}\right)^2 \quad \text{and} \quad \frac{D}{d} = \frac{\tau_c}{f\tau_s} \tag{8a,b}$$

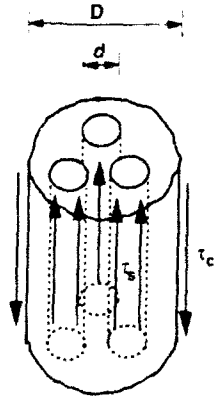

Fig. 9. Shear stress distribution of bundle pull-out.

The volume of the element is then

$$V_B = \frac{\Pi d^2 \tau \sigma_f}{S_0 (\sigma_f)} \tag{9}$$

The element strength is computed in Appendix 3 from the sum of the strength of the unbroken fibers and the pull-out contributions of the broken fibers.

The stress, σ_f, in unbroken fibers at the load maximum for the fiber bundle is given by the condition (Appendix 3)

$$\sigma_f^{m+1} = \frac{2l_f \sigma_0^m \tau}{(m+1)d}\left[1 + \frac{m-1}{2}\left[\frac{d}{2l_f}\frac{\sigma_f}{\tau}\right]^{m+1}\left(\frac{\sigma_f}{\sigma_0}\right)^m\right] \tag{10}$$

Since there are twenty matrix cracks within the bundle element of length $2l_f$ it is expected that the contribution of the matrix to the far stress σ_0 may be neglected. Assuming further that a weak element reaches the load maximum locally and that the strain is constant throughout then the contribution of fibers to the far field stress σ_0 is

$$\sigma_0 = f\sigma_f \tag{11}$$

where f is the fiber volume ratio.

Equation (10) is solved by iteration and when $\tau_i = 5$ MPa the element strength is found to be 1220 MPa. Using equation (8) the number of fibers in the element is $n = 72$, the diameter is $D = 12d$ and length $l_B = 64d$. These predictions are in good agreement with the observed values in Fig. 7(b).

It remains to relate the strength of the element bundle to the strength of the uniaxial specimens used in the test program. Since the bundle element contains 72 fibers, the statistical variation of bundle strength is less than that of the individual fiber strength for which $m = 4$. If the statistical variation of the element bundle strength is defined by the Weibull exponent M then from Appendix 3 the relationship between m and M is

$$M = \left(\frac{1.44n}{\exp\left(\frac{1}{m+1}\right) - 1}\right)^{1/2} \tag{12}$$

With the number of fibers in the bundle $n = 72$ and $m = 4$ the value for M is predicted to be

$$M = 21.6.$$

This high value implies small statistical variation in the bundle strength. Nevertheless, when using the weakest link procedure described in Appendix 2 with the bundle volume given by equation (9) predicts the strength of the uniaxial test specimen to be

$$\sigma = 845 \text{ MPa}.$$

This value is 7% greater than the experimental value of 790 MPa.

As an aside it is interesting to use the model to determine the value of the interface shear strength τ_i which gives the greatest strength. Repeating the calculations for different values of τ_i it is found that the uniaxial strength can be increased to 920 MPa for $\tau_i = 2.5$ MPa.

It remains to determine how well the model predicts the strength of the bending components. Reference to Table 2 indicates the effect of m on the computed strength factor of m. When $m = 21$ the element model predicts a range of strength which agrees well with experiment. However, the predictions of the strength factor for beams with rectangular cross-section are 12% lower than the experimental values.

An attempt is now made to study the factors which might account for the observed differences. In the first place the bending stresses in the beams are determined using simple elastic beam theory with no allowance made for the matrix cracking which causes a 16% reduction in the tensile elastic modulus. An elastic solution which allows for the different values of elastic modulus in tension and compression is given in Appendix 4. The results of the simple calculation suggest that the maximum tensile stresses are 5% less than those calculated using simple beam theory. The modified experimental stresses and the corresponding strength factors are given in Table 2. Another effect may be introduced by considering the possibility of failure on the surface. If the calculations whose results are given by equation (8) are repeated for bundle failure which occur on free surfaces then the failure elements now contain 36 fibers which is half of those in an interior element. From equation (12) the corresponding Weibull is 15. The predicted failure stresses using the internal and surface elements are shown in Table 3. The volume and surface predictions show little difference and generally agree with experimental observations.

5. PROGRESSIVE DAMAGE

In the majority of the tests the attainment of the maximum load was followed by dramatic collapse. However, in the case of the three-point bend tests on the short and intermediate beams the attainment of the maximum load was followed by progressive shear failure of the matrix so that the load drop was less precipitous (Fig. 2) and damage formation was accompanied by substantial energy absorption. The three-point bending response of the long beam with

Table 3. Comparison of model predictions with experiments

Loading	Modified experimental strength	Model prediction: Volume element	Model prediction: Surface element
Uniaxial tension	790	845	756
Four-point bending	998	990	949
Three-point bending ☐	1130	1070	986
Three-point bending ☐	1140	1210	1175

rectangular cross-section (Fig. 4) also indicated that progressive tensile fibers damage resulted in an ability to sustain load with continued displacement. The two forms of progressive damage are now discussed.

5.1. *Progressive shear damage*

When the intermediate rectangular beams are loaded in three point bending shear damage occurs when $\tau_c = 29$ MPa. The onset of the crack along the mid-plane of the beam is accompanied by a sudden load drop, but thereafter the load increases with further increase of central deflection [Fig. 2(a)]. The dotted line indicates the load displacement diagrams for the combined effect of two beams of half the original thickness. The experimental results indicate stiffer responses than the model predictions. However, no influence of the sliding resistance at the shear cracks has been taken into account and a consistent bound calculation can be made by assuming a stress state distribution consisting of the two stress fields indicated in Fig. 10. The first field corresponds to beam with a maximum shear stress of $\tau_s = 5.0$ MPa which corresponds to the sliding resistance after fracture (Fig. 2). The second stress field corresponds to that in two independent beams each of half the original beam depth. The resulting load indicated by the solid line in Fig. 2(a) displacement prediction is close to the experimental observations.

The next shear cracks split the beam into fourths when the shear stress reaches τ_c [Fig. 10(a)]. The second split occurs when $\tau + 0.75\tau_s \approx \tau_c$, and following a similar procedure predicts $P = 248$ N. This is in reasonable agreement with experiments which indicate the second split occurs at a load of 230 N [Fig. 2(a)].

In the case of the short beam shear failure cracks appear to occur more uniformly over the section [Fig. 3(a)]. Assuming that the progression of cracking continues in the manner described previously then a multiple cracking stress finally would have the form shown in Fig. 10(b) with a parabolic distribution of shear stress with each element of maximum value τ_s.

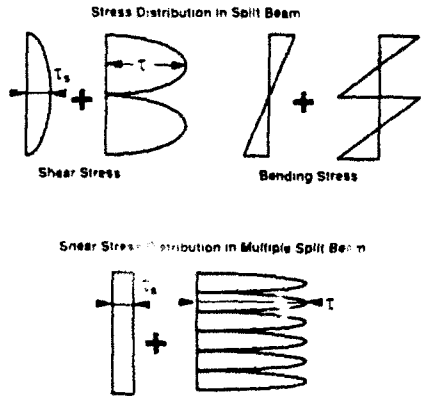

Fig. 10. Stress distribution for split beams.

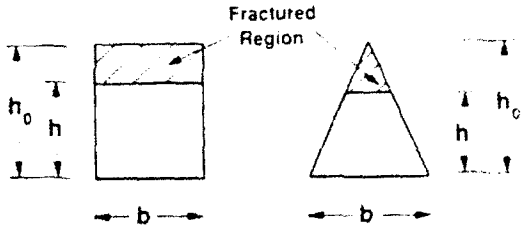

Fig. 11. Progressive damage growth in rectangular and triangular beam.

The load P_i at first shear failure is given by

$$\frac{P}{bh} = \frac{2}{3}\tau_c$$

while the load P_m for multiple cracking is

$$\frac{P_m}{bh} \approx 2\tau_s + \frac{1}{3}(\tau_c - \tau_s)$$

With $\tau_c = 29$ MPa and $\tau_s = 5$ MPa these results give

$$\frac{P_i}{bh} = 38.6 \text{ MPa} \qquad \frac{P_m}{bh} = 43.3 \text{ MPa}$$

which indicate that the initial and multicrack loading are almost equal with the multicracking load being slightly larger. This is confirmed by experiment [Fig. 2(b)] for which the corresponding values are 35.5 and 38.6 MPa.

5.2. *Progressive fiber failure*

Referring to the load displacement relationship for three-point tests carried out on the rectangular and triangular cross section (Fig. 4) it can be observed that the maximum bending stresses for both cases is approximately equal but that the triangular cross-section can withstand additional deformation before losing its load-bearing capacity. Visual observation during the test suggests that local tensile failure occurs at the tip of the triangular section and that damage in the form of fiber tensile failure grows

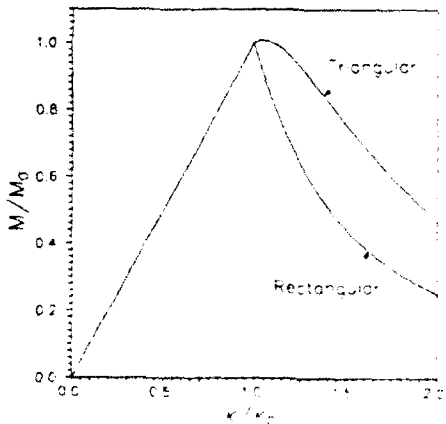

Fig. 12. Calculation response of rectangular and triangular section beams.

progressively through the section before total failure occurs.

In Appendix 5 a calculation has been performed in which a damage front is assumed to advance across the beam section. The calculation is based on the assumption that failure occurs when the bending stress attains a value of bending stress of 1200 MPa. The results of these calculations are shown in Fig. 12 for the beams with rectangular and triangular sections. The comparison of the predictions with experimental observation in Fig. 4 suggests that the supporting assumptions capture the essence of the beam failure. In the case of the triangular beam the progressive failure imparts ductile characteristics.

6. CONCLUSIONS

The strength of simple components consisting of a glass matrix reinforced by silicon fiber fibers has been investigated. The tensile strength of the brittle matrix is approximately 110 MPa while the tensile strength of the composite varies between 790 and 1190 MPa depending on the form of the loading. Observation of the failure surface suggests the existence of a fiber bundle element whose size is dependent on the properties of the matrix and the fiber–matrix interface. The fiber bundle element has a strength of 1220 MPa and a Weibull index of $M = 21$. When the element is used as the basis of the Weibull weakest link calculations it is found that the predictions of the model agree to within 8% of the experimental observations.

An unavoidable drawback in this study has been the very limited availability of the material, but since the value of M for the unit cell is large it is expected that statistical variation is small. There is an apparent lack of tests on large specimens which would help establish the importance of scaling effects. The present model would suggest that scaling effects should be modest.

Acknowledgements—The support from the Air Force Office of Scientific Research under Grant 90-0132 are greatly acknowledged. Helpful discussions and suggestions from Professor A. G. Evans are also acknowledged.

REFERENCES

1. K. M. Prewo and John J. Brennan, *J. Mater. Sci.* **15**, 463 (1980).
2. K. M. Prewo and J. J. Brennan, *J. Mater. Sci.* **17**, 1201 (1982).
3. D. B. Marshall and A. G. Evans, *J. Am. Ceram. Soc.* **68**, 225 (1985).
4. E. Y. Luh and Anthony G. Evans, *J. Am. Ceram. Soc.* **70**, 466 (1987).
5. W. Weibull, *A Statistical Theory of the Strength of Materials*, Proc. Royal Swedish Institute, Stockholm, No. 151 (1939).
6. W. Weibull, *The Phenomenon of Rupture in Solids*, Proc. Royal Swedish Institute Stockholm, No. 153 (1939).
7. H. L. Lo and I. Finnie, *Int. J. Fract.* **6**, 287 (1970).
8. M. D. Thouless and A. G. Evans, *Acta metall.* **36**, 517 (1988).
9. J. Aveston, A. A. Cooper and A. Kelly, *The Properties of Fibre Composites, Conf. Proc.*, National Physical Laboratory, Guildford. I.P.C. Science and Technology Press (1971).
10. H. R. Schwietert and P. S. Steif, *J. Mech. Phys. Solids* **38**, 325 (1990).
11. C. Zweben and B. W. Rosen, *J. Mech. Phys. Solids* **18**, 180 (1970).
12. K. M. Prewo, *J. Mater. Sci.* **21**, 3590 (1986).
13. C. H. Andersson and R. Warren, *Composites* **15**, 16 (1984).
14. B. W. Rosen and A. F. Kettler, *Handbook Glass Fiber Reinforced Plastics*, Final Report, Contract No. NOw 61-0613-d, Bureau of Naval Weapons, Washington, D.C. (Nov. 30, 1982).
15. T. P. Weihs, C. M. Dick and W. D. Nix, *Proc. Mat. Res. Soc. Symp.*, pp. 147–152. Material Research Society, Pittsburg, Pa. (1988).
16. W. A. Curtin, Theory of mechanical properties of ceramic matrix composites, private communication (1990).
17. H. E. Daniels, *Proc. R. Soc. Lond.* A **183**, 405 (1945).
18. G. R. Irwin, Relatively unexplored aspects of fracture mechanics, Univ. of Illinois, TAM Report No. 240 (Feb. 1963).
19. Z. Suo, G. Bao, B. Fan and T. C. Wang, Orthotropy rescaling and implications for fracture in composites, Report Mechanical Engineering and Materials Department, UC Santa Barbara (July 1990).

APPENDIX 1

Crack Spacing in Matrix and Pull-Out Length

When the matrix is uncracked the stresses σ_M in the matrix and σ_f in the fiber are

$$\frac{\sigma_f}{\sigma_c} = \frac{1}{\left[f + (1-f)\dfrac{E_m}{E_f}\right]} \qquad \frac{\sigma_M}{\sigma_c} = \frac{1}{\left[f\dfrac{E_f}{E_M} + (1-f)\right]}$$

where f is the fiber volume fraction and E_f and E_M are the elastic moduli of fiber and matrix respectively. When the matrix stress reaches a critical value matrix cracks form and shear stresses arise between fiber and matrix. If it is assumed that the shear stress at the fiber matrix interface is τ_i then the distance L over which slip occurs can be shown to be

$$\frac{L}{d} = \frac{\sigma_c}{4\tau_i f}\left[1 + \frac{f}{1-f}\frac{E_f}{E_m}\right]$$

where d is the diameter of the fiber.

Saturation is reached when the crack spacing S is twice the slip distance L which gives the condition

$$\frac{S}{d} = \frac{\sigma_c}{2\tau_i f\left[1 + \dfrac{f}{(1-f)}\dfrac{E_f}{E_m}\right]}$$

With the values $E_f = 200$ GPa, $E_m = 85$ GPa, $\tau_i = 5$ MPa, $\sigma_c = 290$ MPa and $f = 0.5$ gives the saturation crack spacing

$$\frac{S}{d} = 8.4$$

If a single fiber is able to pull-out after fracture then the pull-out distance is less than L_r

$$L_r = \frac{\sigma_f d}{4\tau_i}$$

where τ_i is the interface shear stress which in this case is 5 MPa.

Experiments indicate that it is also possible for a bundle of fibers to pull-out. If L_B is the pull-out distance of the bundle and D_B is the diameter of the bundle then

$$L_B = \frac{f\sigma_f d}{4\tau_M}$$

APPENDIX 2

Weibull Fiber Bundle and Weakest Link Statistics

The procedures developed by Weibull [5, 6] are developed in the original papers but for completeness the calculations are completed in some detail.

Fibers and fiber bundle

The probability of survival of fibers subjected to stress σ is

$$P_s = \exp\left[-\frac{l}{l_0}\left(\frac{\sigma}{\sigma_0}\right)^m\right]$$

where l = length of the fiber, σ = applied stress, l_0 = reference length corresponding to stress σ_0, σ_0 = material property (stress when probability of survival is $P_s = 1/e$), and m = material constant. The probability of failure is

$$P_f = 1 - P_s$$

The average failure stress of fibers is

$$\bar{\sigma}_f = \int_0^\infty \sigma \frac{\partial P_f}{\partial \sigma}\, d\sigma = \frac{ml}{\sigma_0^m l_0}\int_0^\infty \sigma^m \exp\left(-\frac{l}{l_0}\frac{\sigma^m}{\sigma_0^m}\right) d\sigma$$
$$= \left(\frac{l_0}{l}\right)^{1/m}\sigma_0\Gamma(1 + 1/m) \quad \text{(A1)}$$

where Γ is the gamma function.

Properties of fiber bundle

Consider now the properties of a bundle of N fibers be loaded simultaneously by a load Q. Let

N = number of fibers in bundle
n = numbers of broken fibers
Q = applied load
σ = average stress of N fibers
σ_B = average stress of n fibers.

Then

$$P_s = 1 - \frac{n}{N}$$

and

$$\sigma_B = \sigma\left(1 - \frac{n}{N}\right) = \sigma P_s = \sigma \exp\left[-\frac{l}{l_0}\left(\frac{\sigma}{\sigma_0}\right)^m\right].$$

The maximum of the average stress occurs when

$$\frac{\partial \sigma_B}{\partial \sigma} = 0$$

which gives the result

$$\frac{\sigma}{\sigma_0} = \left[\frac{l}{l_0}m\right]^{-1/m}$$

and the maximum stress $\bar{\sigma}_B$

$$\frac{\bar{\sigma}_B}{\sigma_0} = \left(\frac{l}{l_0}m\right)^{-1/m}\exp\left(-\frac{1}{m}\right).$$

The ratio of the bundle strength to the mean fiber strength $\bar{\sigma}_f$ is

$$\frac{\bar{\sigma}_B}{\bar{\sigma}_f} = \frac{(m\,e)^{-1/m}}{\Gamma[(m+1)/m]}. \quad \text{(A2)}$$

The weakest link theory

Using the weakest link concept the probability of survival of the component is the product of the survival of the subelements. Hence

$$P_s = \exp\left[-\int_\Gamma \left(\frac{\sigma}{\sigma_0}\right)^m \frac{d\Gamma}{\Gamma_0}\right] = \exp(-B)$$

where the integral is computed over that part of the volume Γ for which the stress is tensile.

The value of B has been determined for the geometries studied in the program.

(1) Uniform bending beam of length l and rectangular cross-section

$$B = \frac{\Gamma}{2l_0}\left(\frac{\sigma_{max}}{\sigma_0}\right)^m \frac{1}{m+1}$$

where Γ is the total volume and σ_{max} is the maximum bending stress in the beam.

(2) Three-point bending rectangular cross-section

$$B = \frac{\Gamma}{2l_0}\left(\frac{\sigma_{max}}{\sigma_0}\right)^m \frac{1}{(m+1)}$$

where Γ is the total volume of the beam and σ_{max} is the maximum bending stress.

(3) Three-point bending and triangular cross-section

$$B = \frac{8\Gamma}{9l_0}\left(\frac{\sigma_{max}}{\sigma_0}\right)^m \frac{1}{(m+1)(m+2)}$$

where Γ is the total volume of the beam and σ_{max} is the maximum bending stress.

These results can be used to compare the strengths of the different components and the loading conditions. The same probability of failure requires B to be equal for the different geometries.

APPENDIX 3

The Bundle Element Model

The load carrying capacity of the composite is given by contributions for the unbroken and broken fibers as

$$\bar{\sigma}\, f = \sigma_u P_s + \sigma_s(1 - P_s) \quad \text{(A3)}$$

where σ_u is the stress in the unbroken fibers, σ_s is the average sliding contribution from the broken fibers, and P_s is the survivor probability that is equal to the fraction of unbroken fibers.

The unit cell height is given as $2l_p^M$. Where l_p^M is the length of the longest fiber that could be pulled out and cause a reduction in the load carrying capacity. Axial equilibrium for a broken fiber gives

$$l_p^M = \frac{d}{4}\frac{\sigma_u}{\tau_s} \quad \text{(A4)}$$

where τ_s is the sliding stress at the fiber–matrix interface.

The nominal stress in the unbroken fibers is assumed to be so high in relation to the variation induced by the matrix cracks and the friction at the fiber matrix interface that the fiber stress can be assumed to be constant. The survivor probability is then given as

$$P_s = \exp\left[-2\frac{l_p^M}{l_0}\left(\frac{\sigma_u}{\sigma_0}\right)^m\right]. \quad \text{(A5)}$$

The average stress due to sliding is given as

$$\sigma_s = \frac{4\bar{l}_p}{d}\tau_s \quad \text{(A6)}$$

where $\bar{l}_p$ is the average pullout length. If the stress is approximately constant in the unbroken fibers

$$\bar{l}_p = \tfrac{1}{2}\bar{l}_p^M \quad \text{(A7)}$$

where $\bar{l}_p^M$ can be determined from the frequency of the Weibull distribution as

$$\bar{l}_p^M = \frac{1}{1 - P_s}\int_0^{\sigma_u} l_p^M \frac{\partial}{\partial \sigma_u}(-P_s)\, d\sigma_u \quad \text{(A8)}$$

Using equations (A4) and (A5) in (A8) gives with (A7)

$$\bar{l}_p = \frac{d}{8}\left[\frac{2l_0}{d}\right]^{1/(m+1)}\left(\frac{\sigma_u}{\tau_s}\right)^{m/(m+1)}\Gamma\left[\frac{m+2}{m+1}, \frac{d}{2l_0}\frac{\sigma_u^m}{\sigma_0^m}\tau_s\right] \quad \text{(A9)}$$

where γ is the incomplete gamma function. Using the upper bound $\gamma(\alpha, x) \leq \Gamma(\alpha)[1 - \exp(-x)]$ as an approximation for γ gives the final expression for the average stress

$$\bar{\sigma}_f = \sigma_c \exp(\alpha) - \frac{\tau_s}{2}\left[\frac{2l_0}{d}\right]^{1/(m+1)}\left[\frac{\sigma_0}{\tau_s}\right]^{1/(m+1)} \times \Gamma\left(\frac{m+2}{m+1}\right)[1 - \exp(-\alpha)]$$

where

$$\alpha = \frac{d}{2l_0}\frac{\sigma_c^{m+1}}{\sigma_0 m \tau_s}$$

For the parallel model the average strain is equal to the strain in an unbroken fiber. Hence

$$\varepsilon = \frac{\sigma_c}{E_f}$$

The highest load that the bundle can carry is given by the condition

$$\frac{\partial \bar{\sigma}}{\partial \sigma_c} = 0$$

that gives

$$\bar{\sigma}_c^{m+1} = \frac{2l_0\sigma_0^m\tau_s}{(m+1)d}\left[1 + \frac{m+1}{2}\left[\frac{d}{2l_0}\frac{\sigma_0}{\tau_s}\right]^{m/(m+1)}\left(\frac{\bar{\sigma}_u}{\sigma_0}\right)^m\right] \quad \text{(A10)}$$

For a fiber bundle with a limited number of fibers there is a statistical variation of the strength [17]. The variation is given by the normal distribution with the expectation value

$$\bar{\sigma}_{FB} = \sigma_u P_s$$

and standard deviation

$$\bar{\sigma}_{FB}^{\gamma} = \sigma_f\sqrt{\frac{(1-P_s)P_s}{n}}$$

where P_s is the survivor probability at the load maximum and n is the number of fibers in the bundle. This corresponds to a standard deviation

$$\bar{\sigma}_u^{\gamma} = \bar{\sigma}_u\sqrt{\frac{1/P_s - 1}{n}}$$

for the stress in the unbroken fibers at the load maximum. For convenience the normal distribution is approximated with a Weibull distribution that has the same standard deviation. Using the approximate relation suggested by Irwin [18]

$$M \approx 1.2\frac{\bar{\sigma}_u}{\bar{\sigma}_x} = \sqrt{\frac{1.44n}{1/P_s - 1}}.$$

APPENDIX 4

Stress Distribution in Beams with Two Elastic Moduli

Because of the matrix cracking which occurs in tension, the elastic moduli in tension and compression differed by 16%. Because of this difference when a rectangular beam is subjected to moment the neutral axis no longer coincides with the center. Repeating the assumption of classical beam theory it is simple to demonstrate that the maximum tensile stress σ_t is related to the stress σ_c of classical beam theory by the formula

$$\sigma_t = \sigma_c\frac{\sqrt{\frac{E_t}{E_c}} + 1}{2}$$

where E_c is the modulus of the uncracked portion, and E_t the modulus of the cracked portion. The position of the neutral layer moves and the volume subjected to tension is increased with the factor

$$\alpha = \frac{2}{\sqrt{\frac{E_t}{E_c}} + 1}$$

APPENDIX 5

Post Fracture Load-Deflection Curve in Bending

The moment-curvature relationship for post tensile fracture is estimated by assuming that local fracture occurs when the bending stress reaches a critical value of σ_c.

In the case of a beam with rectangular cross-section the current beam depth is h and the fractured region is $(h_0 - h)$ (Fig. 11).

The relationship between moment M and the current depth h is

$$M = \frac{bh^2}{6}\sigma_c \quad \text{(A11a)}$$

and the curvature is

$$\kappa = \frac{2\sigma_c}{Eh}. \quad \text{(A11b)}$$

The relationship between moment and curvature is obtained by eliminating h to give

$$M = \frac{2\sigma_c^2 b}{3E^2\kappa^2}. \quad \text{(A12)}$$

Similarly the relationships for the beam of triangular cross-section are

$$M = \frac{\sigma_c b h_0^2}{6}\frac{\tilde{h}^2(7 - 6\tilde{h})}{3 - \tilde{h}} \quad \text{(A13a)}$$

$$\kappa = \frac{3\sigma_c}{Eh_0}\frac{2 - \tilde{h}}{\tilde{h}(3 - \tilde{h})} \quad \text{(A13b)}$$

where

$$\tilde{h} = h/h_0.$$

When the relationship (A12) and (A13) are applied to the long beam geometries in three-point bending the load-displacement are those given in Fig. 8 from which it can be seen that the effect of damage growth is more pronounced for the beam with triangular cross-section. This result is also evident in the experimental results shown in Figs 5 and 10.

MATERIALS

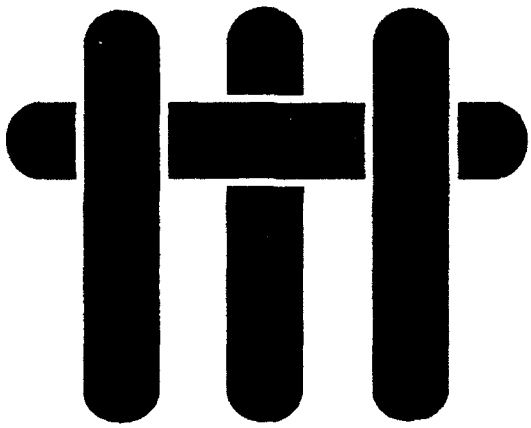

STOCHASTIC ASPECTS OF MATRIX CRACKING IN BRITTLE MATRIX COMPOSITES

by

S.M. Spearing* and F.W. Zok

Materials Department
College of Engineering
University of California
Santa Barbara, California 93106–5050

*Presently at BP Research Department
BP America Inc.
4440 Warrensville Cntr. Rd.
Cleveland, Ohio 44128-2837

Revised version December, 1992

7F:MS24(December 2, 1992)3:05 PM/mef

ABSTRACT

A computer simulation of multiple cracking in fiber-reinforced brittle matrix composites has been conducted, with emphasis on the role of the matrix flaw distribution. The simulations incorporate the effects of bridging fibers on the stress required for cracking. Both short and long (steady-state) flaws are considered. Furthermore, the effects of crack interactions (through the overlap of interface slip lengths) are incorporated. The influence of the crack distribution on the tensile response of such composites is also examined.

1. INTRODUCTION

The tensile stress-strain response of unidirectional fiber-reinforced brittle matrix composites is characterized by three regimes.[1-3] i) At low stresses, the response is linear elastic, with a modulus E_o given by the rule of mixtures. In this regime, there is no detectable microstructural damage. ii) At intermediate stresses, numerous matrix cracks are formed, leading to substantial reductions in the tangent modulus, E_t, relative to the initial elastic modulus. iii) At higher stresses, the matrix crack density saturates and, provided there is minimal fiber failure, E_t approaches $E_f f$, where E_f is the fiber modulus and f is the fiber volume fraction. Yet further loading leads to fiber bundle failure. Figure 1 shows such trends for a calcium alumino silicate (CAS) glass ceramic reinforced with 35% unidirectional Nicalon (SiC) fibers. In this case, the tangent modulus following crack saturation is below the contribution expected from the fibers, consistent with observations of multiple fiber failure in this composite.[1]

The *onset* of matrix cracking in brittle matrix composites is relatively well understood. This has been facilitated by the development of a mechanics framework that describes the influence of crack bridging on crack tip stress intensities[4,5] (or, equivalently, strain energy release rates[6-8]). In contrast, the *evolution* of multiple cracks is not well understood. This problem involves aspects of both mechanics and stochastics. The mechanics aspect refers to the *interactions* between neighboring cracks and their influence on the driving force for the propagation of yet additional cracks. This problem has previously been addressed in detail for the case of steady-state matrix flaws.[9] The stochastic aspect pertains to the role of the *distribution of matrix flaws*, which ultimately governs the spatial distribution of matrix cracks. The present article considers the role of the flaw distribution on both the evolution of matrix cracks and the tensile response of brittle matrix composites. This is accomplished through a computer simulation of multiple cracking.

The simulations performed in this study differ from those of other studies[10,11] in two ways. Firstly, they begin with the notion that the matrix *flaw* distribution (rather than the *strength*

distribution) is prescribed. The strength of the flaws is subsequently computed, taking into account the crack tip shielding effects associated with bridging fibers. Both "short" and "long" flaws are considered. Secondly, the interactions that occur between neighboring cracks (through the overlap of the interface slip zones[9]) are incorporated into the simulations.

The paper is organized in the following way. Section 2 summarizes the relevant mechanics associated with bridged cracks. Section 3 contains details of the simulations, as well as the results on the evolution of crack density with applied stress. These results are then used in Section 4 to compute the corresponding tensile stress-strain response. Section 5 provides remarks regarding the correspondence between experiment and theory.

2. MECHANICS OF BRIDGED CRACKS

The mechanics of cracks bridged by frictionally constrained fibers has been extensively studied. The notable contributions can be found in Refs. 4 to 8. An important aspect of the mechanics pertains to the notion of a steady-state: when the crack length, a, exceeds a critical value, a_o, the stress needed for propagation becomes *independent* of crack length. The critical crack length and the corresponding steady-state cracking stress are given by*

$$a_o = \gamma \Gamma_m (1-f) E/\sigma_o^2 \tag{1a}$$

and

$$\sigma_o = \left\{6E_f f^2 \tau E^2 \Gamma_m / E_m^2 (1-f) R\right\}^{1/3} \tag{1b}$$

* See Appendix for further discussion of the relevant mechanics.

where f is the fiber volume fraction, R is the fiber radius, τ is the interface sliding stress, Γ_m is the matrix toughness, E_m and E_f are the matrix and fiber moduli, E is the composite modulus (= $f E_f + (1 - f) E_m$) and γ is a numerical coefficient. In this regime, the cracking stress σ_c can be described simply by

$$\sigma_c/\sigma_o = 1 \qquad (a/a_o \geq 1) \tag{2a}$$

For cracks shorter than a_o, the variation in cracking stress with crack length can be described by an approximate relation of the form

$$\sigma_c/\sigma_o \approx (a/a_o)^{-n} \qquad (a/a_o \leq 1) \tag{2b}$$

where n is a numerical coefficient. Comparison of Eqn. 2(b) with rigorous numerical solutions for crack lengths in the range $0.1 < a/a_o < 1$ [4,5] indicates that $n \approx 1/8$, with the coefficient γ in Eqn. (1a) being set to 3.50 (see Fig. 2). It is of interest to note that the power on the crack length dependence for composites in this range of crack sizes is much smaller than that for monolithic materials (1/8 vs. 1/2). This result has important implications pertaining to the strength distribution, as described later. For yet shorter cracks ($a/a_o < 0.1$), the exponent n increases, approaching a value of 1/2 as $a/a_o \rightarrow 0$ [13]. The behavior of composites containing such short cracks is not considered in the present study.

As additional cracks are formed, the cracks interact with one another, reducing the driving force for the propagation of additional cracks. Such interactions occur when the crack spacing ℓ falls below 2d where d is the slip distance[9]

$$d = \sigma R E_m (1 - f)/2\tau E f \tag{3}$$

The strain energy release rate for interacting steady-state cracks has been evaluated elsewhere.[9] A summary of the pertinent results is presented in Fig. 3. The normalizing energy release rate $\mathcal{G}_o$ is the steady-state value for a single isolated crack[7]:

$$\mathcal{G}_o = \sigma^3 E_m^2 (1-f)^2 R / 6 E_f f^2 \tau E^2 \tag{4}$$

3. COMPUTER SIMULATION OF MULTIPLE CRACKING

The results of the previous section have been used to simulate the formation of multiple matrix cracks from various flaw size distributions. For this purpose, a one-dimensional array of volume elements, each of unit cross-sectional area, was constructed. Each element was assigned a flaw, such that the flaw size distribution was characterized by extreme value statistics, using:

$$F = \exp\left[- \frac{L}{\lambda d_o} \left(\frac{a_o}{a} \right)^{m/2} \right] \tag{5}$$

where F is the cumulative probability of flaws having size *smaller* than a in an elemental length, L, m is the shape parameter (or Weibull modulus) and a_o and λd_o are chosen as the reference crack size and element length, respectively, with λ being a dimensionless scaling factor and d_o the slip distance at the onset of cracking (given by Eqn. (3) with $\sigma = \sigma_o$). The flaw sizes were assigned to element locations according to a Monte Carlo process.

The simulation of matrix cracking proceeds in two parts. Firstly, flaws that are initially shorter than a_o are allowed to grow to a size a_o when $\sigma \geq \sigma_c$ (Eqn. 2a). Secondly, for each flaw of current size a_o, the distances to the two neighboring cracks are computed and $\mathcal{G}$ evaluated from the results of Fig. 3 (see Eqns. 34–38 of Ref. 9). If the condition for the propagation is satisfied ($\mathcal{G} \geq \Gamma_m (1-f)$, the location of the flaw is read into a second array containing the positions of propagated cracks. Once all the flaws have been inspected at a given stress level, the

stress is incremented and the process is repeated for the remaining, unpropagated flaws. At each stage, the distribution of crack spacing is calculated.

The simulations were based on a relatively long gauge length ($1000\, d_o$) and a high linear density of volume elements ($50/d_o$). This gives 50,000 volume elements in the gauge length, each occupying a length $L = d_o/50$. Relatively smooth size distributions were obtained by using 200 discrete flaw sizes. The elastic mismatch parameter, $\alpha = (1 - f)E_m/E_f f$, was set to $\alpha = 1$. The shape parameter m was assigned values of 4 and 10, which sensibly bounds the cases of practical interest. The scaling parameter λ was varied between 0.01 and 1000. These limits correspond to the extreme cases in which the vast majority of flaws are either smaller or larger than a_o. The flaw distributions are plotted on Fig. 4.

The results of the simulations are presented in Figs. 5 and 6. Figure 5 shows the crack spacing distributions at three levels of stress for $m = 4$ and $\lambda = 100$. Similar trends were observed for other values of m and λ. Figure 6 summarizes the trends in the average linear crack density (the inverse of crack spacing) with applied stress.

For cases where a significant number of initial flaws have a size greater than a_o ($\lambda \leq 0.1$), the development of crack density with stress is identical to that found by considering only steady-state cracks, as in our earlier work.[9] As the number of large flaws decreases (increasing λ), the initial jump in crack density at the matrix cracking stress diminishes. For very large values of λ, the curves become sigmoidal in shape, in accord with experimental measurements on glass ceramic matrix composites (Fig. 1).

It is also of interest to note that the *saturation* crack density appears to be relatively insensitive to λ and m (within ~ 10%). In addition, the stress required for crack saturation increases with increasing values of m and λ. It would appear then that the range of stress needed to complete the cracking process provides some measure of the flaw distribution.

4. STRESS-STRAIN CURVES

The results of the simulations were used to compute the tensile stress-strain curves. Prior to cracking ($\sigma/\sigma_o \leq 1$), the stress-strain relation is given simply by

$$\sigma/\sigma_o = \varepsilon/\varepsilon_o \tag{6}$$

where ε_o is the strain at the onset of matrix cracking (σ_o/E). Following cracking, the additional inelastic strain associated with the cracks is computed. In this regime, two different approaches were used to compute the strain. In the first, the fiber strain distribution was integrated along the entire length of the composite, taking into account the local variations in crack spacing. In the second, the cracks were replaced with a periodic arrangement of cracks with an equivalent average crack spacing, $\bar{\ell}$. The latter approach provides a simple analytical solution for the tensile strain in terms of the current crack spacing:

$$\varepsilon/\varepsilon_o = 1+\alpha d/\bar{\ell} \qquad \bar{\ell} \geq 2d \tag{7a}$$

$$\varepsilon/\varepsilon_o = 1+\alpha-\alpha\bar{\ell}/4d \qquad \bar{\ell} \leq 2d \tag{7b}$$

Both approaches neglect the additional *elastic* strain resulting from the presence of the cracks. Figure 7(a) shows a comparison of the stress-strain curves computed using the two approaches. The agreement is good, indicating that the approximate analytical solution (Eqn. 7) is adequate for further computations.

The stress-strain curves for three different flaw distributions, calculated using Eqn. (7), are shown in Fig. 7(b). The main difference between the curves is in their shape near $\sigma/\sigma_o = 1$. For small values of λ (corresponding to many large flaws), the composite exhibits a burst of strain at $\sigma/\sigma_o = 1$, a feature not generally observed experimentally. For large values of λ, the curves

appear smoother in this region, consistent with the experimental measurements. Figure 8 shows trends in the computed tangent modulus with stress. Once again, the shapes for relatively large values of λ are consistent with the experiments (compare with Fig. 1).

5. CONCLUDING REMARKS

A critical evaluation of the model predictions through comparisons with experimental measurements is presently not feasible. The difficulty lies in determining the parameters that characterize the flaw distributions in real composites. Nevertheless, the results of the model do provide qualitative insight into the general shape of measured stress-strain curves. Notably, the absence of a strain burst at $\sigma/\sigma_0 = 1$ indicates that most of the flaws leading to cracking are shorter than the critical value, a_0. For the CAS/SiC composite, this corresponds to a length $a_0 \approx 80\ \mu m$. Furthermore, the range of stresses over which cracks propagate provides a measure of the "average" flaw size relative to a_0: decreasing the average flaw size increases the stress range needed for cracking. Similar trends are predicted for increasing values of the shape parameter, m. It should be noted that the magnitude of these effects will be influenced by thermal residual stresses, as well as the onset of fiber failure, features yet to be incorporated in the model.

Finally, it is of interest to note the influence of the matrix flaw distributions on the strength distributions of fiber-reinforced composites. When all the flaws are larger than a_0, the strength is a deterministic quantity, independent of the flaw distribution. In cases where most of the flaws are shorter than a_0, the strength distribution remains remarkably narrow, even when the shape parameter m for the flaw distribution is low. This result is a manifestation of the weak crack length dependence of the cracking stress (Eqn. 2) compared with that for monolithic ceramics and glasses. It can be readily shown from the two dependencies ($a^{-1/2}$ and $a^{-1/8}$) that the effective Weibull modulus of the composite is *4 times* that of the monolithic matrix material for equivalent flaw populations. This feature may, in fact, account for the relative uniformity of strain-strain data for fiber-reinforced ceramic composites reported by various workers.[1-3]

ACKNOWLEDGMENTS

Funding for this work was supplied by the Defense Advanced Research Projects Agency through the University Research Initiative Program under Office of Naval Research Contract No. N–00014–86–K–0753.

APPENDIX

A variety of micromechanical models that have been developed to describe crack bridging by frictionally constrained fibers. These have led to solutions for either the crack tip energy release rate $\mathcal{G}$ [6-8] or the crack tip stress intensity K[4,5] in terms of the constituent properties. In general, the two loading parameters are related through

$$\mathcal{G} = K^2(1-\nu^2)/E \tag{A1}$$

allowing equivalence to be established between the different approaches. It has been recognized,[8,11] however, that such equivalence is not always achieved. Specifically, the steady-state stress intensity factor calculated in Refs. 4 and 5 gives an energy release rate (through Eqn. A1) which differs from that of the energy approaches[6-8] by a factor of $E_m(1-f)/E$. Thouless[12] proposed a modification to the traction law used in the stress intensity calculations,[4,5] incorporating the factor $E_m(1-f)/E$, such that the steady-state values of $\mathcal{G}$ for the two approaches are the same. In applying the numerical results[4,5] to the short crack regime in the present study (Eqn. 2), the modification introduced by Thouless was implicitly assumed. This approach gives consistent solutions for the steady-state $\mathcal{G}$ and the corresponding cracking stress in both the short and long crack regime as $a \rightarrow a_o$. Furthermore, it gives a value of a_o which differs from that given in Ref. 4 by the factor $E_m(1-f)/E$.

REFERENCES

[1] D. Beyerle, S.M. Spearing, F.W. Zok and A.G. Evans, *J. Am. Ceram. Soc.*, **75** (1992) 2719-25.

[2] R.Y. Kim and N. Pagano, *J. Am. Ceram. Soc.*, **74** (1991) 1082–90.

[3] A. Pryce and P. Smith, submitted to *J. Mater. Sci.* (1992).

[4] D.B. Marshall, B.N. Cox and A.G. Evans, *Acta Metall.*, **33** (1985) 2013–21.

[5] R.M. McMeeking and A.G. Evans, *Mech. of Mtls.*, **9**, (1990) 217.

[6] B. Budiansky, J.W. Hutchinson and A.G. Evans, *J. Mech. Phys. Solids*, **34** (1986) 164–89.

[7] J. Aveston, G.A. Cooper and A. Kelly, "The Properties of Fiber Composites," *IPC* (1971) 15–26.

[8] L.N. McCartney, *Proc. Roy. Soc., Series 4*, **409** (1987) 329–50.

[9] F.W. Zok and S.M. Spearing, *Acta Metall. Mater.*, **40** (1992) 2033-43.

[10] C. Cho, J.W. Holmes and J.R. Barber, *J. Am. Ceram. Soc.*, **75** (1992) 316–24.

[11] X.F. Yang and K.M. Knowles, *J. Am. Ceram. Soc.*, **75** (1992) 141–47.

[12] M.D. Thouless, *Acta Metall.*, **37** (1989) 2297–2304.

[13] B. N. Cox and D. B. Marshall, submitted to *Acta Metall. Mater.*, 1992.

FIGURE CAPTIONS

Fig. 1. Mechanical behavior of a unidirectional CAS/SiC composite: a) tensile stress-strain response, b) degradation in tangent modulus with applied stress, c) evolution of crack density and d) multiple matrix cracks following loading to failure.

Fig. 2. Trends in matrix cracking stress with crack length. (Numerical results adapted from Ref. 5)

Fig. 3. Strain energy release rate for interacting matrix cracks.

Fig. 4. Flaw distributions used for computer simulations: a) $m = 4$, b) $m = 10$.

Fig. 5. Histograms of crack spacing for various levels of applied stress ($m = 4, \lambda = 100$).

Fig. 6. Variations in the average crack density with stress for various values of λ: a) $m = 4$, b) $m = 10$.

Fig. 7. Computed tensile stress-strain curves
   a) A comparison of the results obtained from the two methods described in the text. The solid line shows prediction of Eqn. 7, assuming a periodic arrangement of cracks. The symbols correspond to calculations in which the fiber strain distribution was integrated along the entire length of the composite.
   b) Effects of the reference length parameter λ ($m = 4$).

Fig. 8. Effects of the reference length parameter λ on the degradation in the tangent modulus.

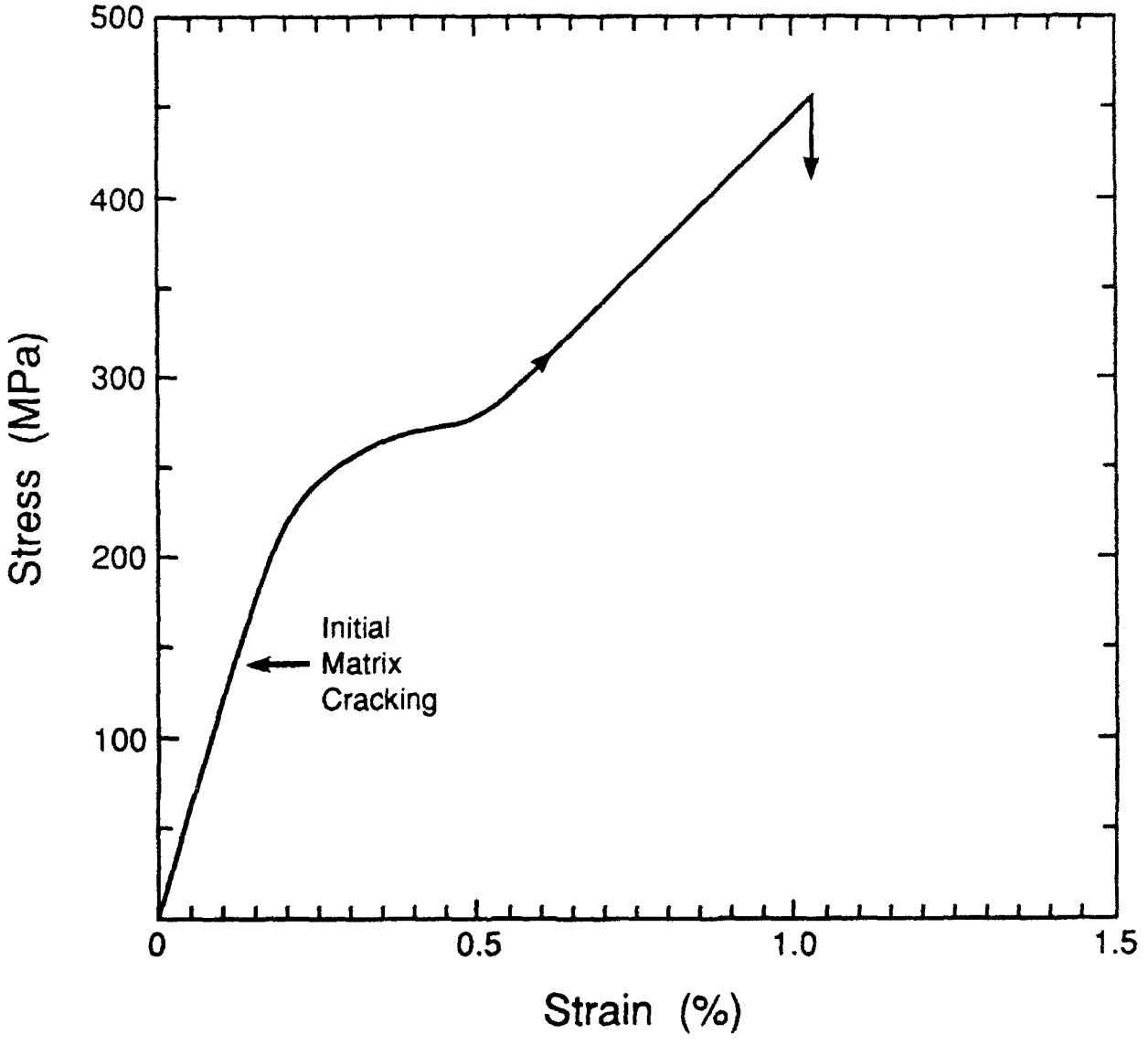
500
400
300
200
100
Stress (MPa)
Initial
Matrix
Cracking
0
0.5
1.0
1.5
Strain (%)

Fig. 1 (a)

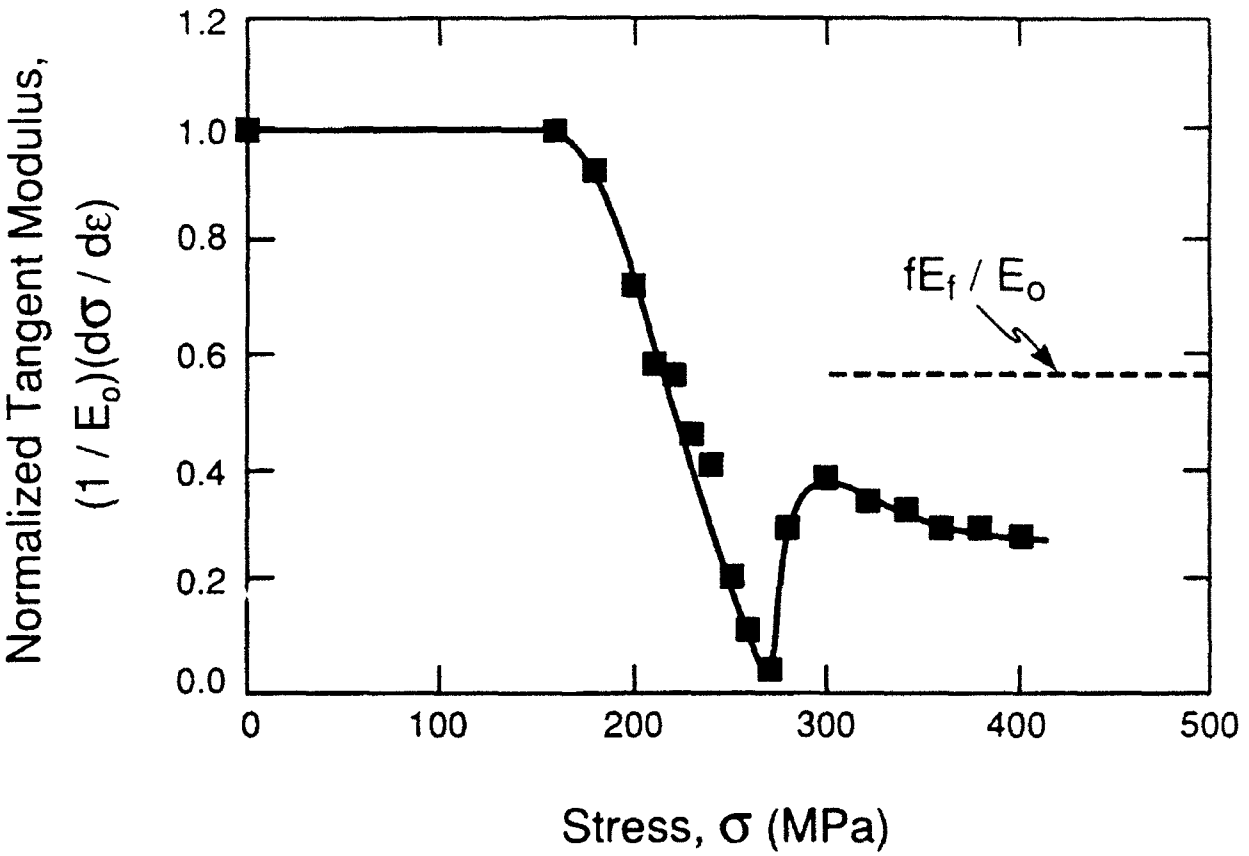

Fig. 1 (b)

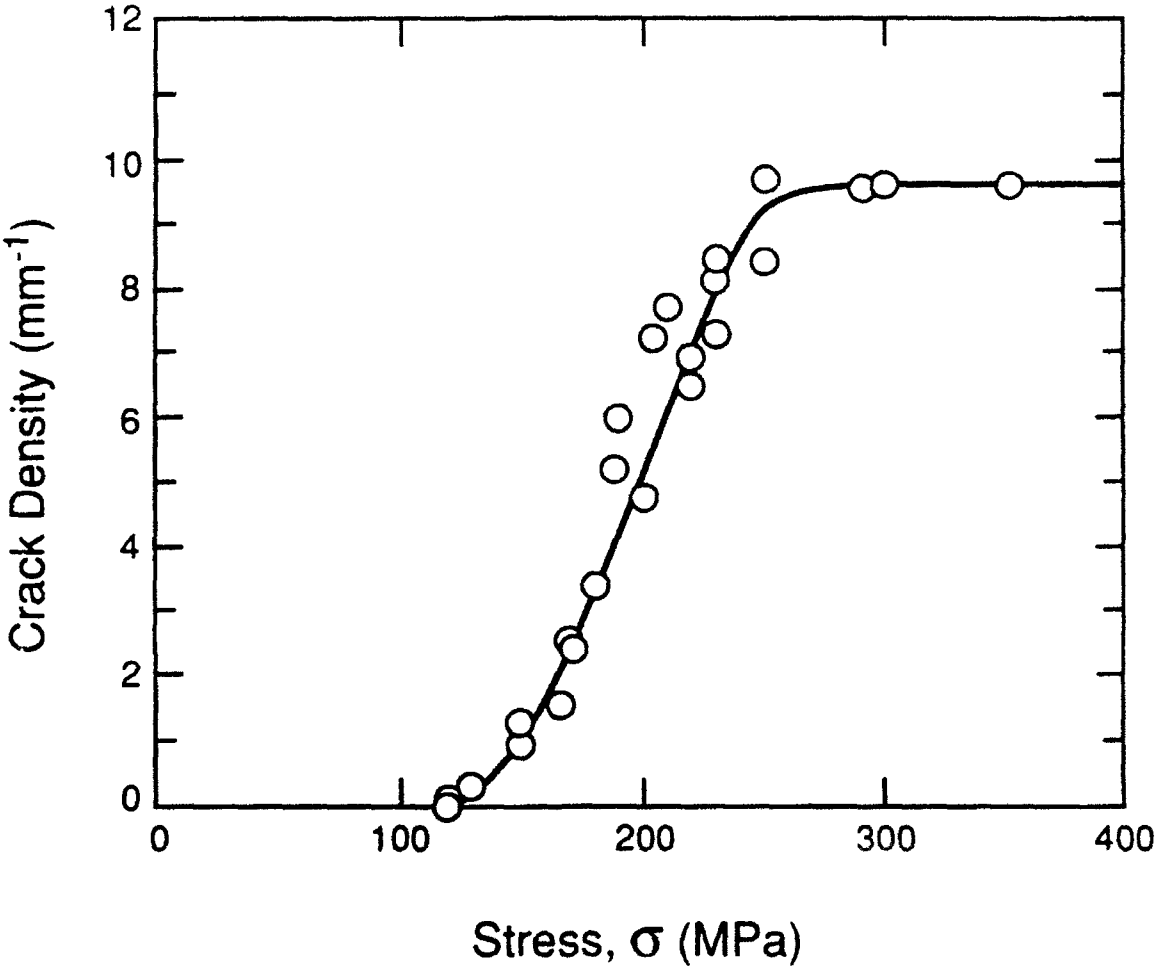

Fig. 1 (c)

Fig. 1 (d)

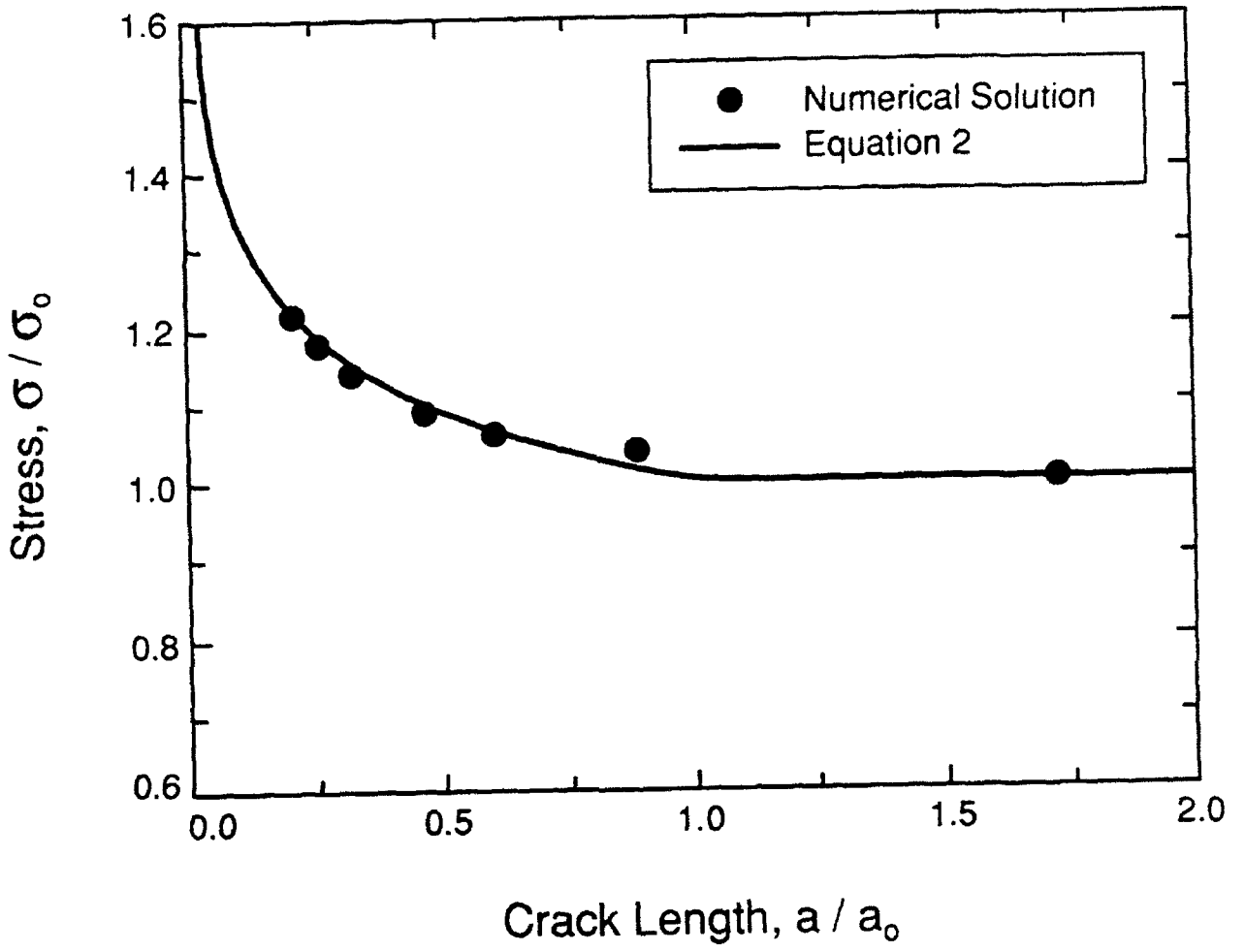
Numerical Solution
Equation 2
Stress, σ / σo
Crack Length, a / ao
1.6
1.4
1.2
1.0
0.8
0.6
0.0
0.5
1.0
1.5
2.0

Fig. 2

Fig. 3

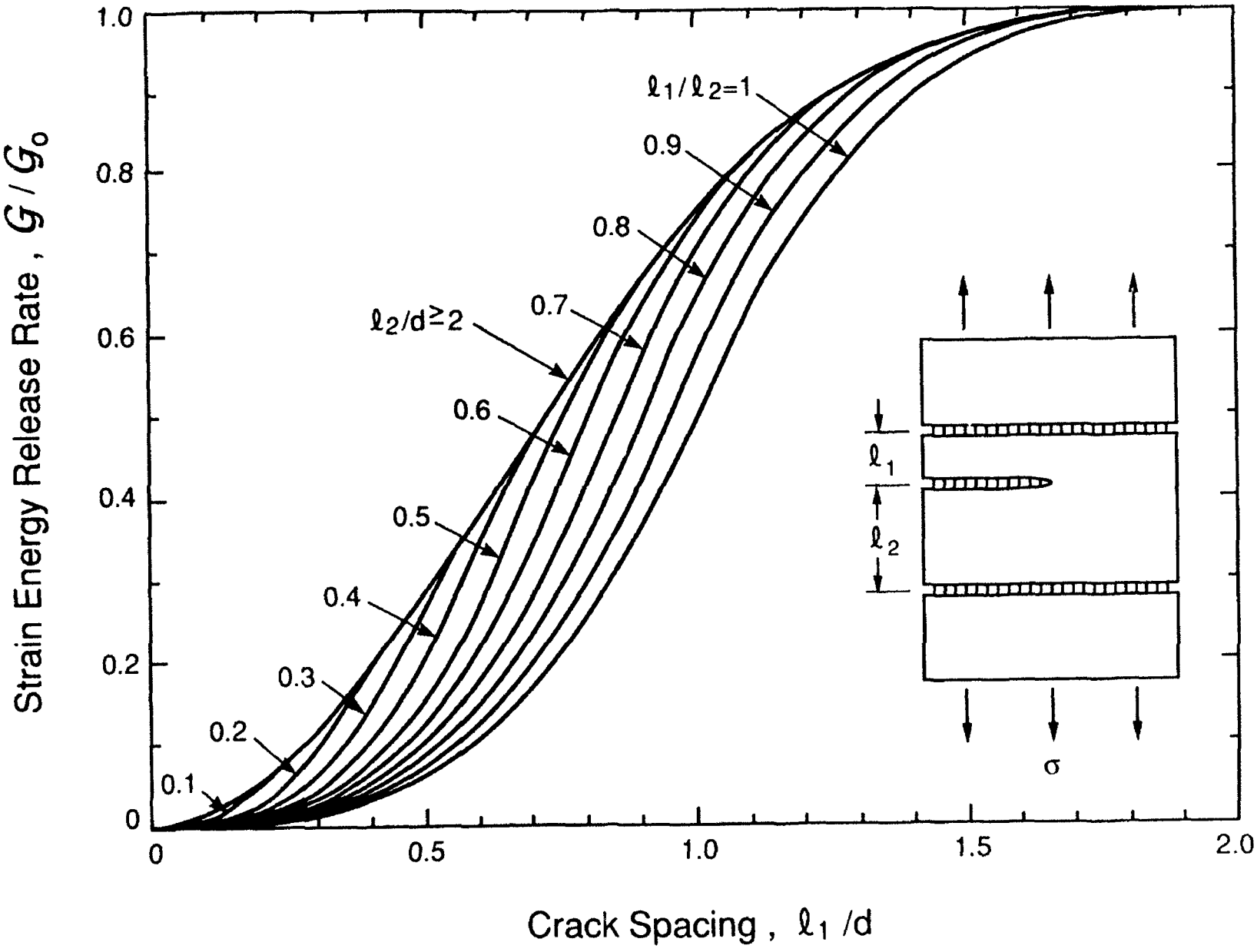

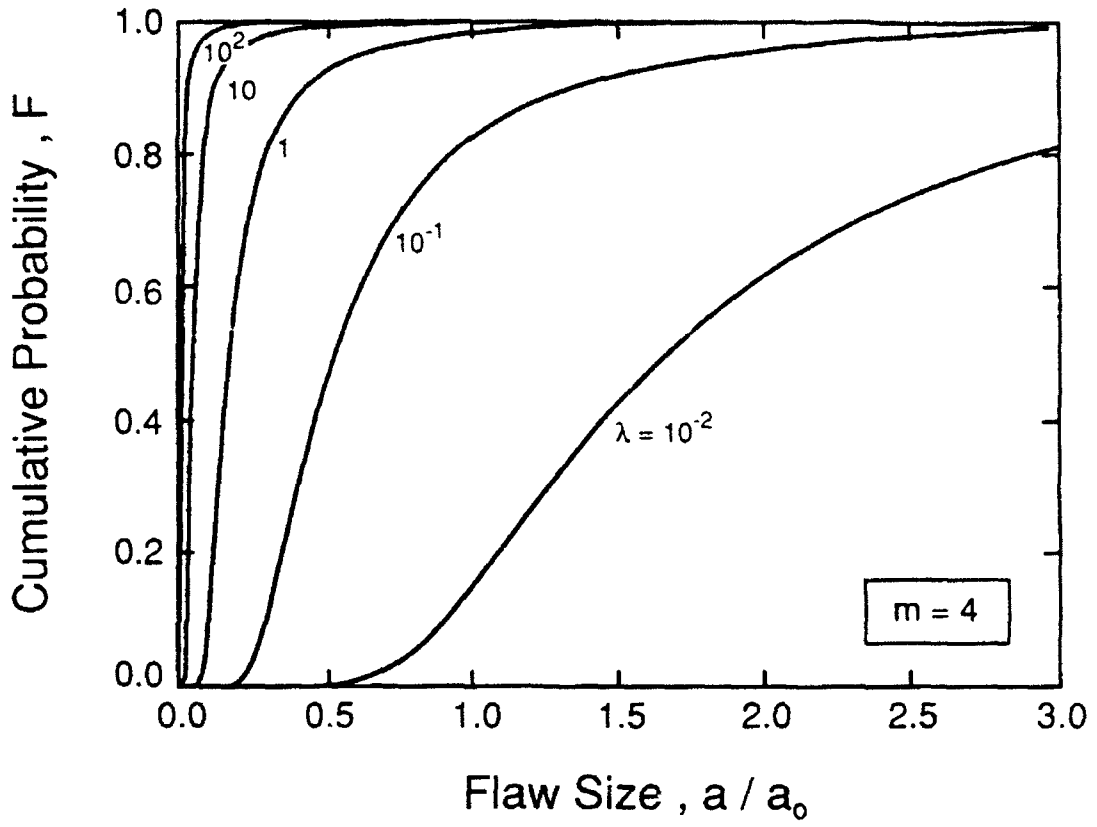
Cumulative Probability , F
1.0
0.8
0.6
0.4
0.2
0.0
0.0
0.5
1.0
1.5
2.0
2.5
3.0
Flaw Size , a / a$_o$
10^2
10
1
10^{-1}
$\lambda = 10^{-2}$
m = 4

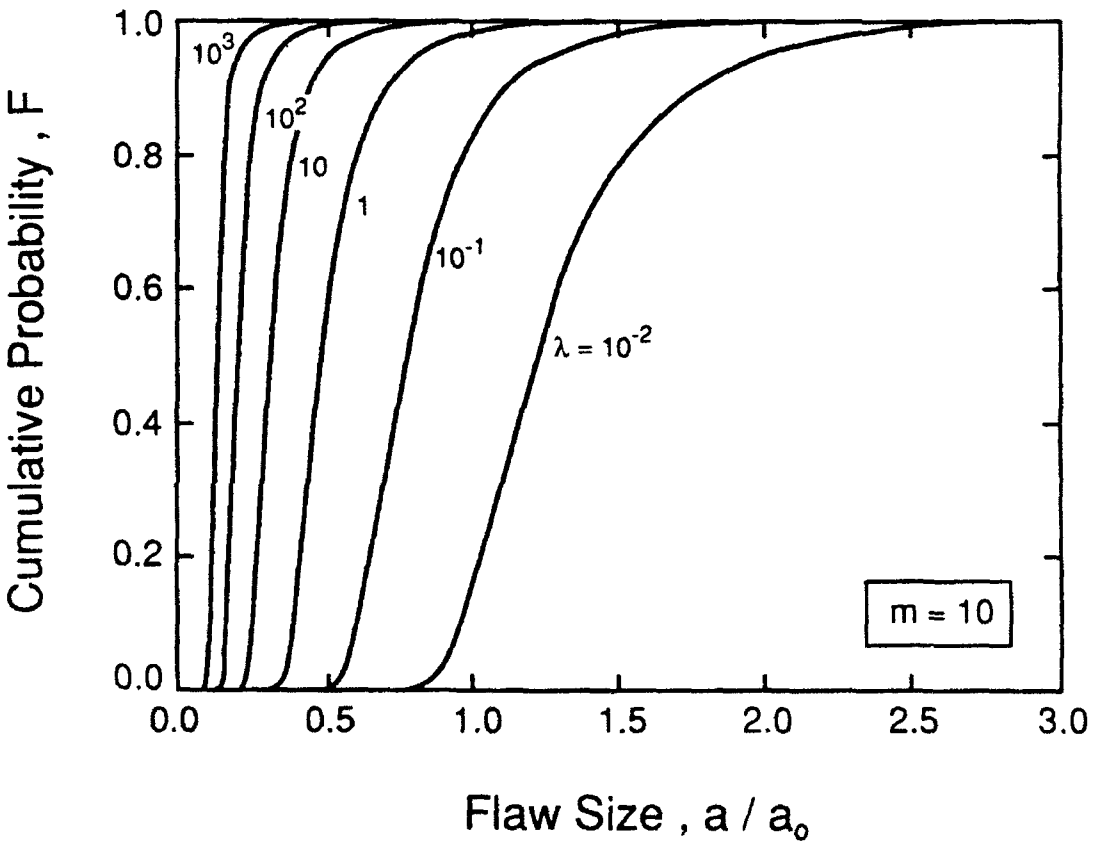
Cumulative Probability , F
1.0
0.8
0.6
0.4
0.2
0.0
0.0
0.5
1.0
1.5
2.0
2.5
3.0
Flaw Size , a / a$_o$
10^3
10^2
10
1
10^{-1}
$\lambda = 10^{-2}$
m = 10

Fig. 4

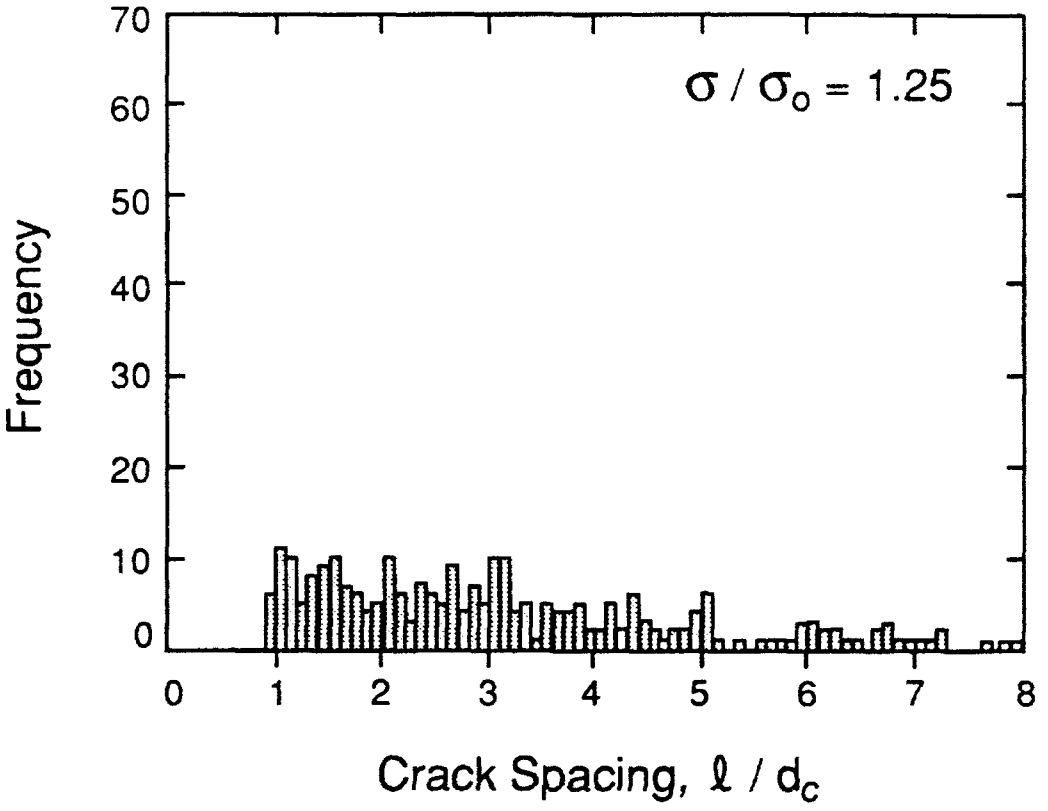
70
60
50
40
30
20
10
0
Frequency
σ / σo = 1.25
0
1
2
3
4
5
6
7
8
Crack Spacing, ℓ / dc

Fig. 5 (a)

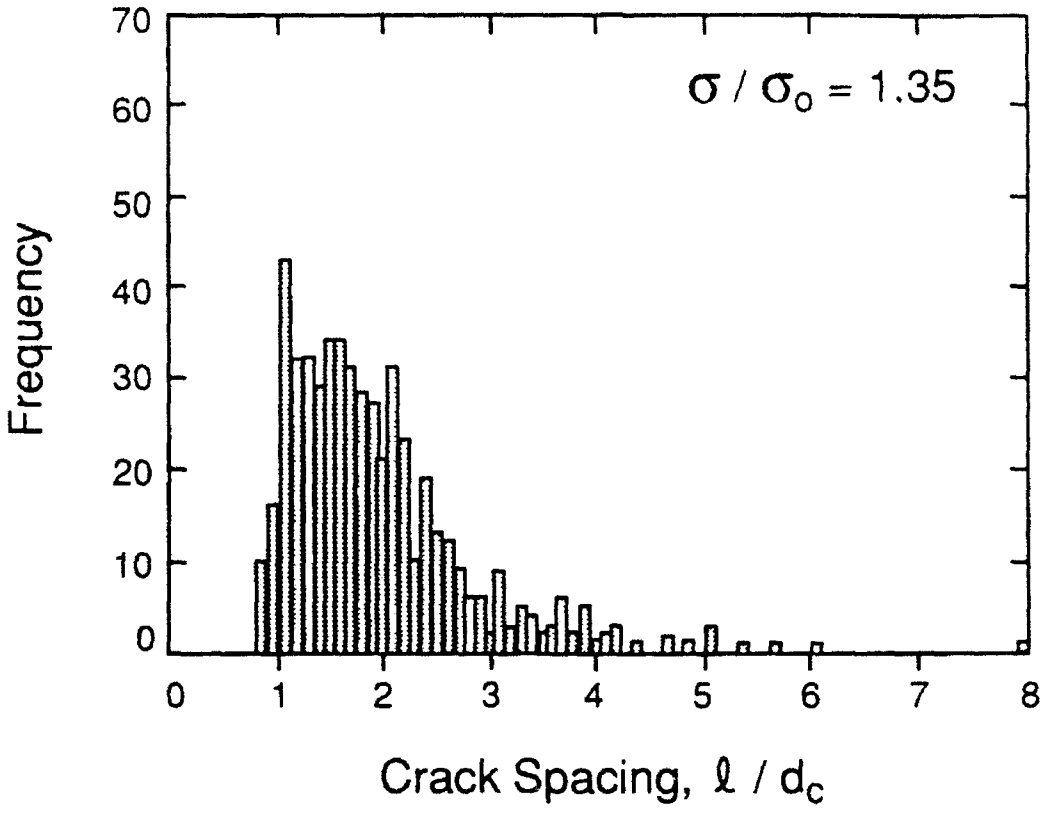
70
60
50
40
30
20
10
0
Frequency
σ / σo = 1.35
0
1
2
3
4
5
6
7
8
Crack Spacing, ℓ / dc

Fig. 5 (b)

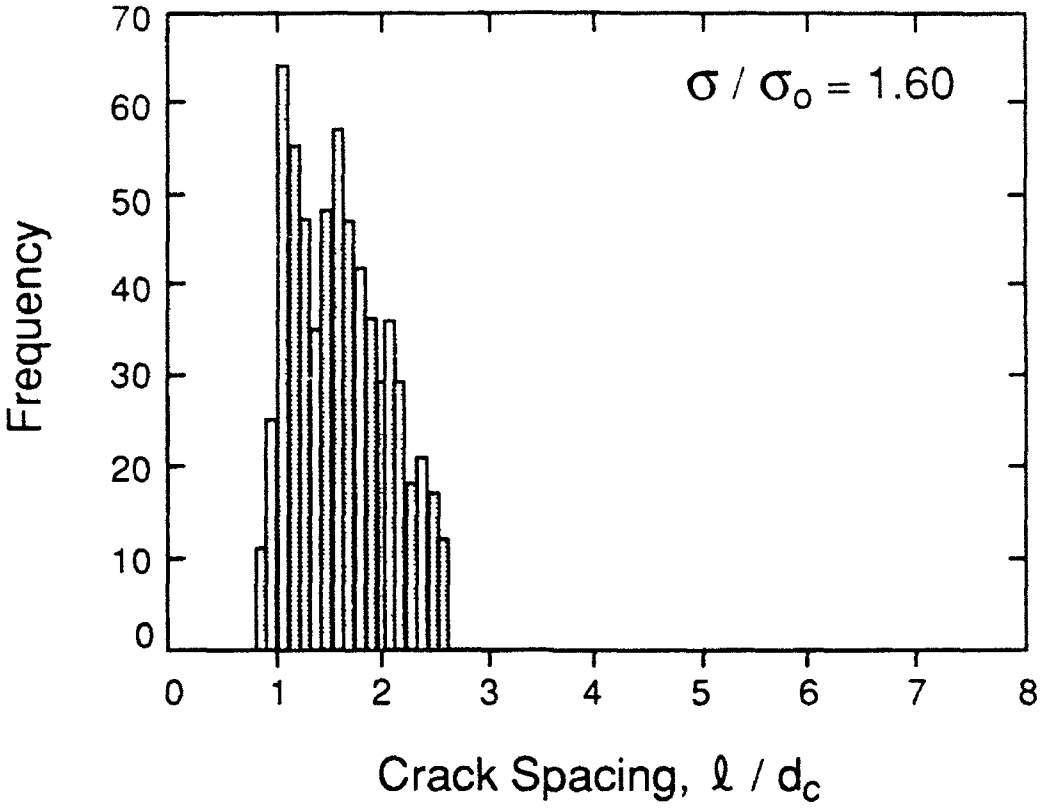

Fig. 5 (c)

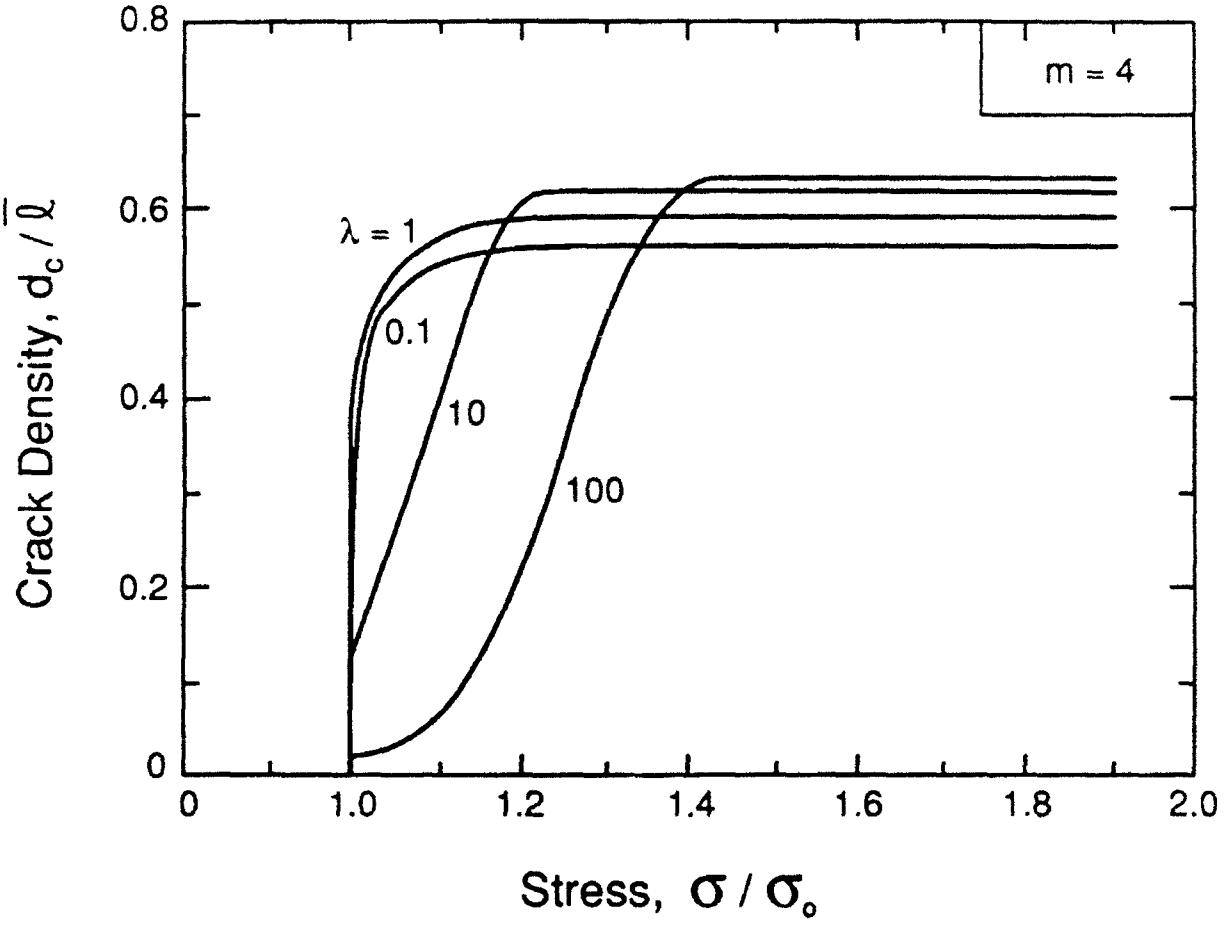
m = 4
λ = 1
0.1
10
100
Crack Density, $d_c / \bar{\ell}$
Stress, σ / σ_o
0.8
0.6
0.4
0.2
0
0
1.0
1.2
1.4
1.6
1.8
2.0

Fig. 6 (a)

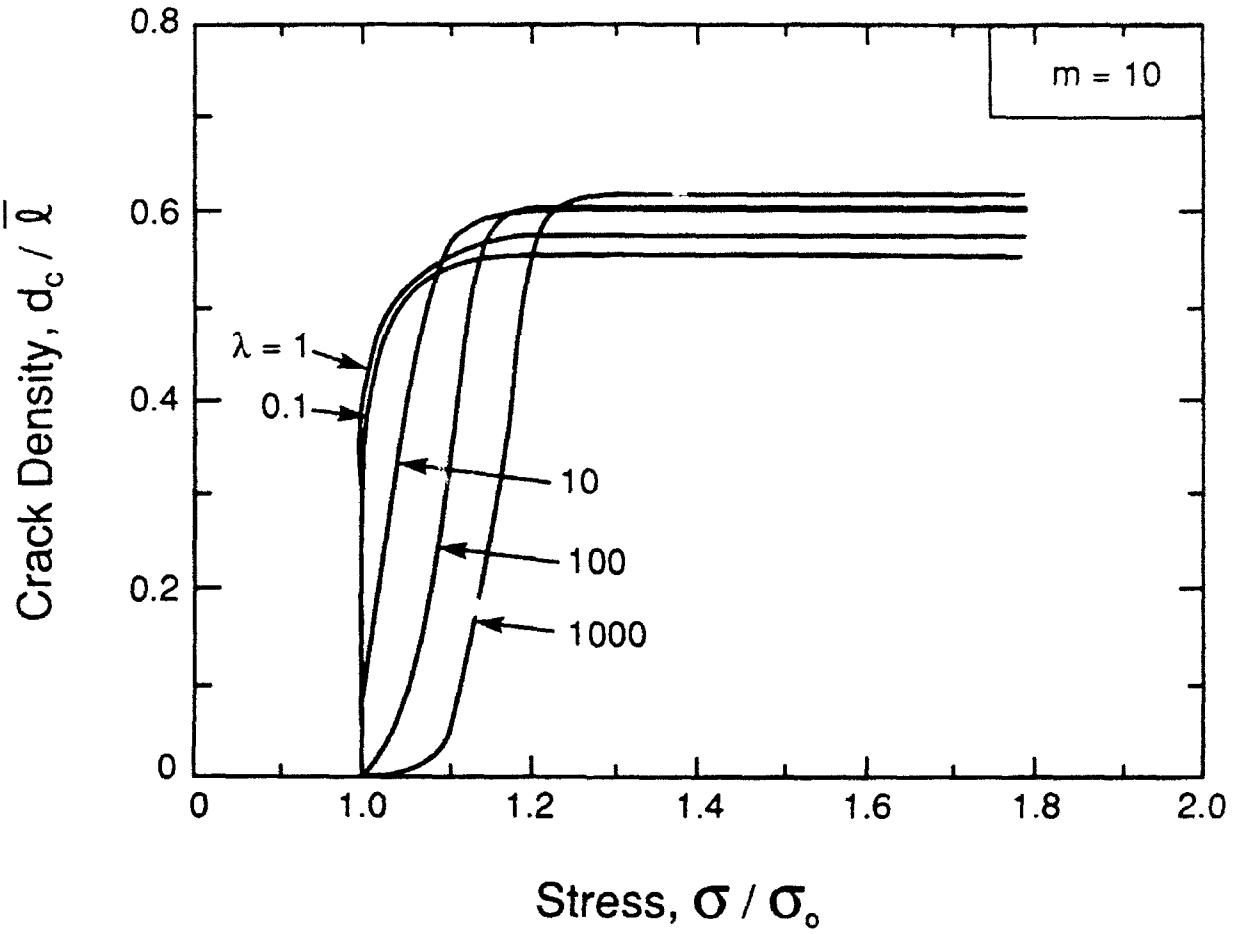

Fig. 6 (b)

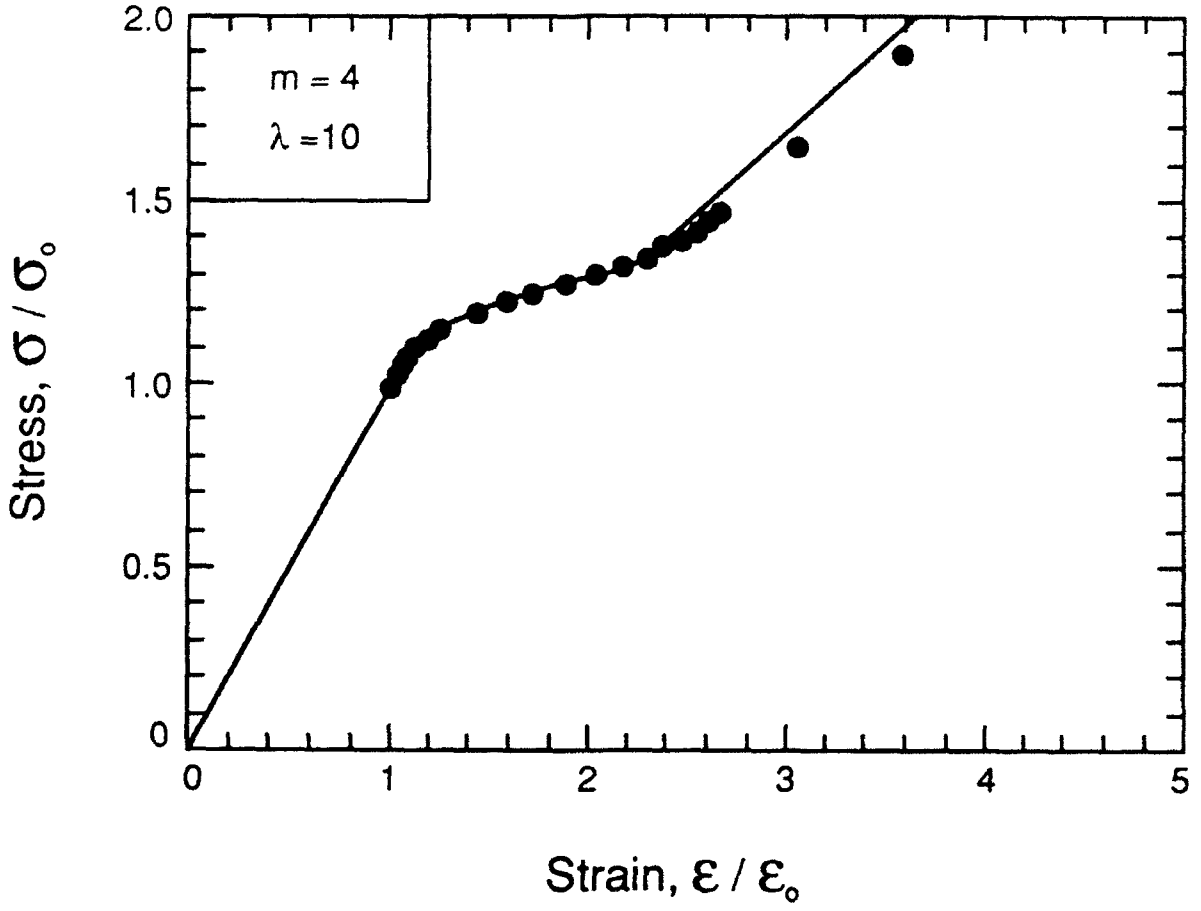

Fig. 7 (a)

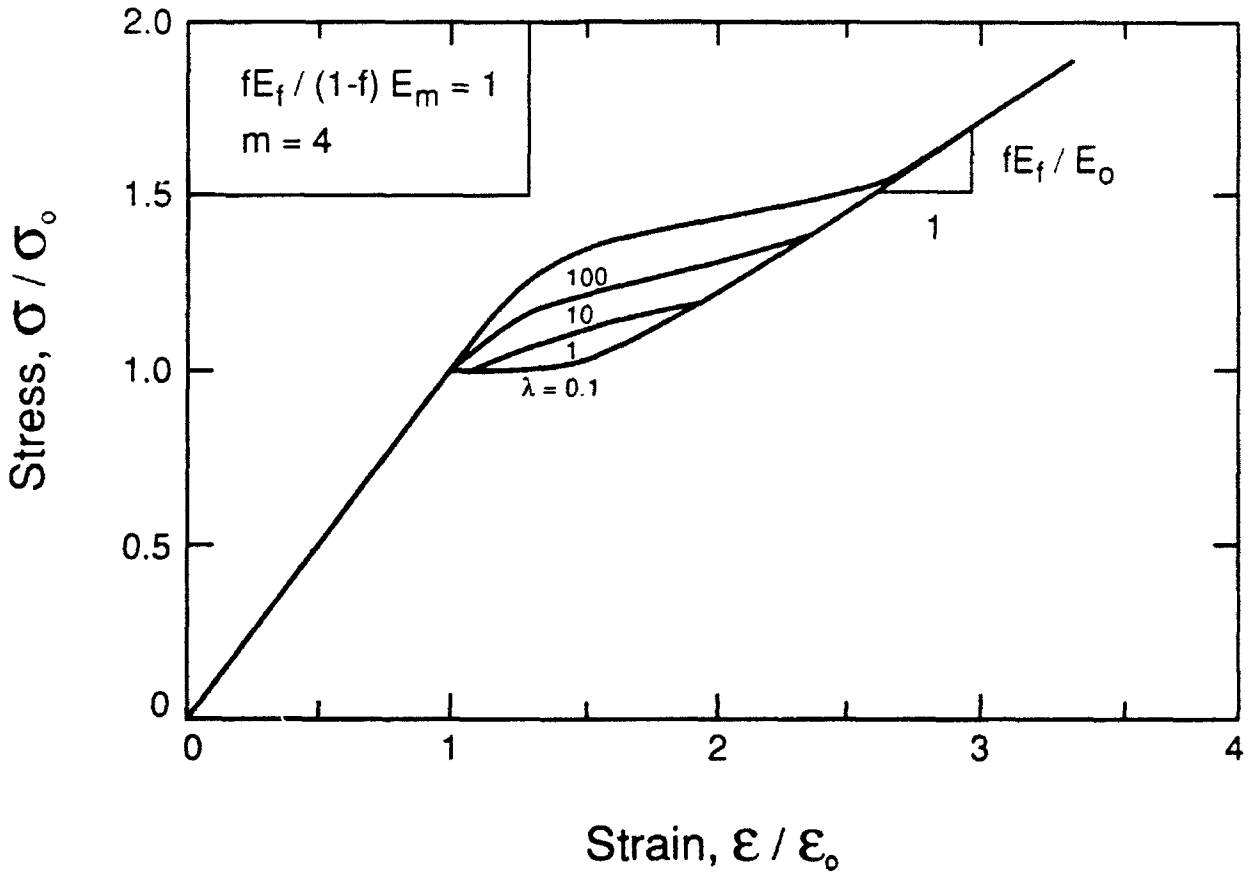
2.0
1.5
1.0
0.5
0
0
1
2
3
4
$fE_f / (1-f) E_m = 1$
$m = 4$
fE_f / E_o
1
100
10
1
$\lambda = 0.1$
Stress, σ / σ_o
Strain, $\varepsilon / \varepsilon_o$

Fig. 7 (b)

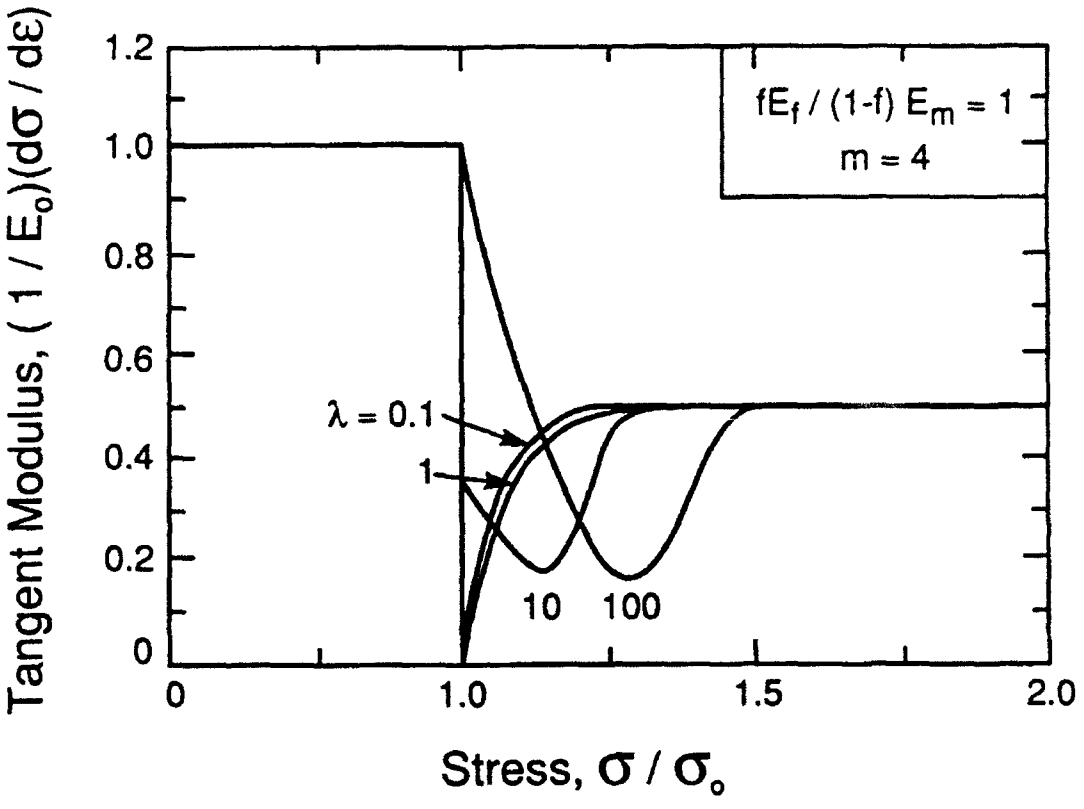
Tangent Modulus, (1 / E_o)(dσ / dε)
1.2
1.0
0.8
0.6
0.4
0.2
0
0
1.0
1.5
2.0
Stress, σ / $σ_o$
fE_f / (1-f) E_m = 1
m = 4
λ = 0.1
1
10
100

Fig. 8

MATERIALS

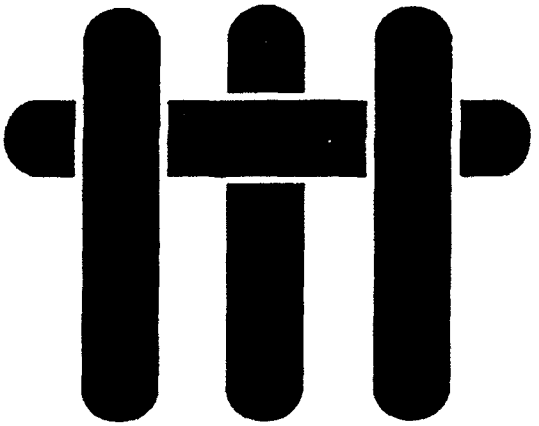

THE ROLE OF FIBER BRIDGING IN THE DELAMINATION RESISTANCE OF FIBER-REINFORCED COMPOSITES

by

S. M. Spearing and A. G. Evans
Materials Department
College of Engineering
University of California
Santa Barbara, California 93106

KJS-Evans-27•Tech Art•De-Dz•TA-Dim Rst 11/15/90•11:45 AM•3/29/91

ABSTRACT

Delamination cracks in composites may interact with misaligned or inclined fibers. Such interactions often lead to fiber bridging, which causes the nominal delamination resistance to increase as the crack extends. Substantial specimen geometry effects are also involved. An experimental investigation of the role of fiber bridging has been conducted for three different composites. The results are compared with fiber bridging models based on a softening traction law, leading to schemes for predicting trends in delamination resistance with specimen geometry and crack length. Implications for utilizing this effect to suppress the growth of delaminations are presented.

1. INTRODUCTION

Laminated brittle matrix composites reinforced with continuous fibers are prone to delamination cracking upon monotonic and fatigue loading.[1-6] The susceptibility to this mode of damage is the direct result of the extreme anisotropy in fracture resistance parallel and normal to the fiber orientation. Delamination cracking does not normally constitute an unstable failure mode for laminated composites. Nevertheless, such damage has several detrimental influences on the structural utility of the composite. The shear moduli and off-axis tensile moduli can be substantially reduced, leading to unacceptable structural deformations. Moreover, the compressive and shear strengths may be severely degraded. Approaches that suppress delamination cracking are thus of substantial concern for the structural application of these materials. Delamination cracking has been observed and discussed in both polymeric and ceramic matrix composites.[1-6] The most comprehensive assessments have been made for polymeric systems.[1,2]

Delamination cracking studies on polymeric systems have unequivocally identified the matrix fracture resistance as the dominant variable, leading to major research efforts on the use of higher toughness polymer matrices, such as PEEK.[7] This research has also provided a repertoire of test specimens capable of exploring delamination, subject to a range of mode mixities between pure opening (mode I) and pure shear (mode II).[1] It has generally been ascertained that the delamination resistance in mode I occurs subject to the lowest fracture resistance. Consequently, mode I tests address the most serious concerns regarding delamination. The emphasis of the present article is on the mode I delamination resistance, as measured using a standard double cantilever beam (DCB) specimen. Studies are conducted on both ceramic and polymer matrix composites, in order to contrast the relative roles of the matrix and the interfaces.

A substantive factor involved in the delamination crack growth resistance concerns the influence of the fibers. In general, delamination cracks have trajectories dominated by the matrix. However, some interaction with the fibers is inevitable, because of crack path instabilities and imperfect fiber alignments.[6,8,9] These interactions with fibers have the desirable effect of suppressing delamination.[9] However, such interactions also cause the delamination resistance to depend on specimen geometry, loading mixity, etc.[9,10] The resulting lack of uniqueness complicates the design of delamination resistant composites. The present study contributes to the development of a simple procedure that correlates the effects of geometry, loading and delamination plane.

2. SOME BASIC MECHANICS

2.1 Linear Elastic Behavior

The mode I strain energy release rate for an orthotropic DCB specimen is[11]

$$\mathcal{G} = \frac{P^2a^2}{bE_{11}I}\left[1 + \xi(\rho)\lambda^{1/4}(h/a)\right]^2 \qquad (1)$$

where P is the applied load, a is the crack length, h is half the specimen depth, b is the specimen width, I is the second moment of area of the arms of the DCB specimen:

$$I = bh^3/12$$

λ and ρ are measures of the elastic anisotropy

$$\lambda = E_{zz}/E_{11}$$

where E is Young's modulus, with the subscripts 22 and 11 referring to transverse and longitudinal, respectively, while

$$\rho = \frac{(E_{11}E_{22})^{1/2}}{2G_{12}} - (\upsilon_{12}\upsilon_{21})^{1/2}$$

where G is the shear modulus and ν is Poisson's ratio. The coefficient ξ has been evaluated numerically as[11]

$$\xi = 0.677 + 0.146(\rho - 1) - 0.0178(\rho - 1)^2 + 0.00242(\rho - 1)^3 \qquad (2)$$

For a significant number of test configurations and materials, the effects of shear deformations near the crack tip are negligible and Eqn. (1) simplifies to the beam theory solution,

$$\mathcal{G} = \frac{P^2a^2}{bE_{11}I} \qquad (3)$$

In some cases, measurement of the crack length is subject to experimental restrictions. Then, an alternative expression for $\mathcal{G}$ derived in terms of the crack mouth opening displacement, δ, is more convenient. The beam theory result is

$$\mathcal{G} = \frac{3P\delta}{2ab} \qquad (4)$$

which may also be modified to account for crack tip shear deformations.[11]

2.2 Non-Linear Behavior

A major source of non-linearity in the delamination cracking of laminated brittle matrix composites is governed by interactions between the crack and the fibers.[8,9,12] A general description of these effects can be provided by presuming that the fibers which interact with the delamination crack exert bridging tractions, p, that depend on the local crack opening, u.[10] Such tractions necessarily lead to resistance curve behavior, as well as effects of specimen geometry and loading mixity on the apparent fracture resistance, $\mathcal{G}_R$.[9,10] These features can be explicitly addressed by invoking a traction law, p(u). Consideration of the basic fiber bridging process (Appendix) suggests that a softening law is most relevant to delamination. The simplest form of such a law is,[10]

$$p = p_o(1 - u/u_o) \tag{5}$$

where p_o is the traction at $u = 0$ and u_o refers to the displacement at the end of the fiber bridging zone. A series of pertinent results has been derived using this law,[10] such that delamination is predicted to occur in accordance with a resistance $\mathcal{G}_R$ having the following characteristics. The mode I *steady-state* resistance is[10]

$$\mathcal{G}_{ss} = \Gamma_o + p_o u_o/2 \tag{6}$$

where Γ_o is the mode I *matrix fracture resistance*. The crack length upon attaining steady-state, a_{ss}, is given by,[10]

$$a_{ss} \propto \left(h^3 b E_{11}/12\right)^{1/4} \tag{7}$$

Both $\mathcal{G}_{ss}$ and a_{ss} provide a first order basis for comparing experiment with theory. In the range $0 < a < a_{ss}$, the resistance is given by,[10]

$$\mathcal{G}_R/\Gamma_o = (1/\alpha_3)^2\left[1 + 2\sqrt{3}\,\alpha_4\,(a/h)^2\,\mathcal{P}^{1/2}\right]^2 \tag{8}$$

where α_3 and α_4 are coefficients of order unity and $\mathcal{P} = p_o^2\,h/E_{11}\Gamma_o$. For the case $\Gamma_o << \mathcal{G}_R < \mathcal{G}_{ss}$, Eqn. (8) reduces to

$$\mathcal{G}_R E_{11}/p_o^2 h = 12\left(\alpha_4^2/\alpha_3^4\right)(a/h)^4 \tag{9}$$

which vividly demonstrates the strong influence of specimen geometry, h, and of fiber bridging, p_o.

3. EXPERIMENTAL

3.1 Materials

Two ceramic matrix composites were used, each with Nicalon fibers providing the reinforcement. A lithium alumino silicate (LAS) glass ceramic matrix material was provided by United Technologies.[13] A calcium alumino silicate (CAS–II) matrix material was provided by Corning.[14] Both composites were manufactured by hot pressing to obtain the laminate structure. A fiber volume fraction, $f \approx 0.4$ was achieved in both cases. All test specimens were cut from 150 mm x 130 mm plates. Unidirectional (0_{16}) laminates were employed, with a nominal ply thickness, 0.17 mm. In addition, a few tests were performed on a polymer matrix composite consisting of AS4 carbon fibers in a Poly(etheretherketone) thermoplastic matrix, comprised of (0_{16}) laminates, with a nominal ply thickness 0.125 mm.

3.2 Test Procedure

DCB specimens having dimensions 55 x 3 x 2.8 mm* were precracked at one end by cutting an initial notch with a wafering saw. The load was transferred to the specimen using hinges to avert extraneous bending moments. The load line displacement was monitored using a capacitance transducer. The tests were performed in displacement control. In all cases, the crack length was measured *in situ* using a travelling microscope. In the majority of tests, the propagation of (interlaminar) cracks between the original lamination layers was investigated. A few tests were also performed in which the crack extended in a (intralaminar) plane perpendicular to the laminate plies.

4. RESULTS

4.1 Ceramic Matrix Composites

A typical load/displacement plot for a DCB test on a ceramic matrix composite is reproduced in Fig. 1. In contrast to the assumptions of elastic beam theory, the load/displacement curve is significantly non-linear prior to first crack propagation. Unloading, after some crack propagation, reveals permanent deformation of the specimen. In addition, there is evidence of hysteresis in the loading/unloading behavior. Inspection of the crack reveals the presence of a few intact fibers bridging the crack over a substantial portion of its length (Fig. 2a, b, Fig. 3). This bridging behavior is probably responsible for the nonlinearity of the load/displacement curves. Insight can be gained by evaluating the apparent critical strain energy release rate using Eqns. (1)

---

* The limited quantity of these materials necessitated the use of small specimens.

and (4) (Fig. 4). The values obtained from the displacements using Eqn. (4) are lower, because of the effect of bridging fibers. The fracture resistance of the CAS matrix material is characterized by a steep rise for ~ 10 mm of crack growth, followed by a steady-state at $G_{ss} \approx 250\ Jm^{-2}$, with a fracture energy at crack growth initiation, $\Gamma_o \approx 20\ Jm^{-2}$, comparable to that obtained from mixed-mode tests on crossply laminates of glass LAS composites.[3] Observations of crack wake bridging suggest that the fibers remain intact in the region of rising fracture energy, while steady-state involves a bridging zone of constant length, with the bridging fibers having the characteristics sketched in Fig. 3.

A much greater rise of the apparent fracture resistance is observed for the LAS matrix material. The difference is attributed to variations in the fiber packing and the associated fiber misalignment, as elaborated below. To further examine the effect of fiber misalignment, CAS composites were loaded such that the cracks grew on intralaminar planes (Fig. 4). The marked increase in the resistance compared with that for interlaminar delamination confirms the importance of fiber alignment and placement relative to the crack plane.

To address effects of specimen geometry (since only sixteen-ply laminates were available), the DCB specimens were modified by bonding alumina layers to the top and bottom faces. The energy release rate was then evaluated from Eqn. (1), based on the second moment of area for the stiffened beam. The resistance determined for specimens of various flexural stiffnesses (Fig. 5) indicates that the steady-state resistance remains invariant, but the crack extension required to reach steady-state increases markedly with increase in the specimen stiffness. In the specimen having the highest stiffness, it was noted that initial crack pop-in to a length of ~ 8 mm occurred without interaction with the fibers. Consequently, the rising resistance only developed at lengths in excess of the pop-in length.

The crack opening profile was examined for a CAS specimen with an interlaminar crack. The specimen was wedged open at the crack mouth and the measurements taken using a scanning electron microscope. The measured profile (Fig. 6) is compared with that calculated using the assumptions of beam theory in conjunction with the following boundary conditions: zero opening and zero slope at the crack tip and a known opening displacement at the mouth. The correlation suggests that the bridging effect is only significant within ~ 10 mm of the crack tip.

4.2 Carbon Fiber-Peek Composite

Unidirectional carbons fiber/PEEK laminates with an overall thickness of 2.4 mm were used. The DCB specimen width was 6 mm. The resistance was calculated using Eqn. (1), accounting for the anisotropy and finite geometry of the specimens. A significant increase in resistance occurs with crack advance (Fig. 7).

5. ROLE OF FIBER BRIDGING

A comparison between experiment and theory, leading to an understanding of the resistance characteristics, can be conducted in accordance with the following steps. i) The steady-state bridging zone length a_{ss} is obtained from the fracture resistance data (Figs. 3, 6) based on the crack length at which steady-state commences. Consistency is addressed by comparing this value with a_{ss} predicted by the bridging model (Eqn. 7). ii) The opening at the end of the bridging zone, u_o, at a distance a_{ss} from the crack tip is calculated from beam theory, assuming that the bridging fibers have an insignificant effect on the beam profile (cf. Fig. 6). iii) With the premise that u_o is an explicit property of the fiber bridging process, the peak bridging traction p_o is evaluated by equating the measured steady-state toughness to that predicted by Eqn. (6). iv) Based on this p_o, the

full resistance curve is calculated using Eqn. (8) and compared with experiment. The parameters obtained for the three composites, using this approach, are summarized in Table I. Based on these parameters, a comparison is made (Fig. 4) between the measured resistance curves and the curves predicted using Eqn. (8). The correspondence is satisfactory and furthermore, the absolute magnitudes, as well as the ratios of p_0 among the materials appear reasonable, when compared with the simple model described in the Appendix.

Specimen geometry effects can be rationalized by using the fiber bridging parameters (Table I) and predicting the change in resistance with the stiffness of the arms of the DCB specimen. For this purpose, the second moment of area of the stiffened arms is used to determine that modified arm thickness h^* (as if the arms were made entirely of the composite material). This value is used in Eqn. (8) to predict the resistance. The predicted resistances are plotted on Fig. 8. For this purpose, the resistance for the highest stiffness specimen was only computed for crack length beyond pop-in, where fiber interactions were observed to commence. With this proviso, it is apparent that there is acceptable agreement with the experimental results.

6. CONCLUDING REMARKS

Experiments and models indicate that interlaminar fracture resistances obtained from DCB tests are sensitive to fiber bridging. Comparatively weak pull-out tractions result in resistances many times the fracture resistance for crack growth initiation. The shape of the resistance curve is influenced by the stiffness of the arms of the specimen relative to the bridging forces. This geometrical dependence leads to an overestimate of the resistance when bridging effects are not explicitly included in the analysis of the data.

Both LAS and CAS ceramic matrix composites exhibit an enhancement in resistance between 10 and 20 times that of the matrix material. Misaligned fibers bridging the crack account for this behavior. Should such fiber misalignment be eliminated, the fracture resistance would be limited to the initiation value of only 20 Jm^{-2}. Conversely, if misalignment could be guaranteed, or if through-thickness reinforcements were introduced, delamination could be largely avoided. A similar behavior obtains for a carbon fiber reinforced PEEK composite. In this case, the greater matrix toughness alleviates much of the concern regarding the role of fiber bridging. However, values for the delamination resistance cited in the literature are subject to error, when no allowance has been made for bridging fibers.

ACKNOWLEDGMENTS

Useful discussions with G. Bao and Z. Suo are gratefully acknowledged. The authors would like to thank Dr. C. Barlow for the provision of the PEEK material.

APPENDIX

Model for Bridging Functions in Mode I Delamination

From SEM observations (Fig. 2a–b), the following model appears to provide a reasonable description of ligament bridging. Following the idealization shown in Fig. 3, the bridging ligaments are considered to be short beams of retangular section, capable of deforming in shear and bending. The ligaments peel away from the crack faces, overcoming a fracture resistance, Γ_i. By symmetry, the curvature and the bending moment at the center of the beam is zero. The problem can, therefore, be simplified as consisting of two cantilever beams joined at the center, with dimensions shown in Fig. A1.

From Timoshenko and Goodier,[17] the end displacement, u/2, of the beam is given by

$$\frac{u}{2} = \frac{P\ell^2}{3EI} + \frac{Pt^2\ell}{2IG} \qquad \text{(A1)}$$

where P is the load, E is Young's modulus, G the shear modulus, ℓ the beam length, 2t the thickness and I the second moment of area. The compliance, C, is:

$$C \equiv \frac{u}{2P} = \frac{\ell^3}{3EI} + \frac{t^2\ell}{2IG} \qquad \text{(A2)}$$

The strain energy release rate, $\mathcal{G}$, is related to the compliance by

$$\mathcal{G} = \frac{P^2}{2W}\left(\frac{\partial C}{\partial \ell}\right) \tag{A3}$$

$$= \frac{P^2}{2W}\left(\frac{\ell^2}{EI} + \frac{t^2}{2IG}\right) \tag{A4}$$

where W is the beam width. For stable crack growth ($\mathcal{G} = \Gamma_i$), the cantilever length ℓ may be obtained from Eqn. (A4) as

$$\ell = \left\{\left(\frac{2W\Gamma_i}{P^2} - \frac{t^2}{2IG}\right)EI\right\}^{1/2} \tag{A5}$$

Substituting Eqn. (A5) into Eqn. (A1) gives the displacement relationship

$$u = \frac{2P}{3EI}\left\{\left(\frac{2W\Gamma_i}{P^2} - \frac{t^2}{2IG}\right)EI\right\}^{3/2} + \frac{Pt^2}{IG}\left\{\left(\frac{2W\Gamma_i}{P^2} - \frac{t^2}{2IG}\right)EI\right\}^{1/2} \tag{A6}$$

The predicted traction law obtained using the parameters for CAS given in Table II (Fig. A2) reveals softening, although not the simple linear softening assumed by Suo *et al.*[10] For comparison, the linear softening behavior that fits the experimental resistance curve data for CAS, obtained by assuming 80 discrete ligaments per mm^2 of crack, is superposed on Fig. A2. The general level of the traction is consistent with the simple model. No attempt has been made to incorporate either frictional sliding or ligament degradation, both of which are observed experimentally.

TABLE I

Fiber Bridging Parameters For Interlaminar Cracks

Matrix	a_{ss}(mm)*	u_0(μm)	p_0(MPa)
LAS	22	800	1.2
CAS	10	140	4
PEEK	4	90	11

*For a 16-ply laminate

TABLE II

Parameters Used For Ligament Model

t (3 fiber radii)	21 μm
w (6 fiber radii)	42 μm
E (local f = 0.5)	150 GPa
Γ_i	12 or 25 Jm^{-2}

REFERENCES

[1] J. M. Whitney, "Experimental Characterization of Delamination Fracture," in *Interlaminar Response of Composite Materials*, ed., N. J. Pagano, Elsevier 1989.

[2] S. Hashemi, A. K. Kinloch and J. G. Williams, "Mechanics and Mechanisms of Delamination in a Poly(ethersulphone) Fibre Composite," *Comp. Sci. Tech.*, 37 429–462 (1990).

[3] O. Sbaizero, P. G. Charalambides and A. G. Evans, "Delamination Cracking of Laminated Ceramic-Matrix Composites," *J. Am. Ceram. Soc.*, 73, 1936–40 (1990).

[4] H. Chai, "On the Correlation Between the Mode I Failure of Adhesive Joints and Laminated Composites," *Eng. Fract. Mech.*, 24, 413–431 (1986).

[5] A. G. Evans and D. B. Marshall, "The Mechanical Behavior of Ceramic Matrix Composites," *Acta Metall.*, Vol. 37, No. 10, 2567–2583 (1989).

[6] W. J. Johnson and P. D. Mangalgiri, "Investigation of Fiber Bridging in Double Cantilever Beam Specimens," *J. Comp; Technology and Research*, 9, 10–13 (1987).

[7] P. J. Hine, B. Brew, R. A. Duckett and I. M. Ward, "Failure Mechanism in Continuous Carbon Fibre Reinforced PEEK Composites," *Comp. Sci. Tech.*, 35, 31-51 (1989).

[8] R. Bordia, B. J. Dalgleish, P. G. Charalambides and A. G. Evans, *J. Am. Ceram. Soc.*, in press.

[9] G. Bao, B. Fan and A. G. Evans, *Mech. Mtls.*, in press.

[10] Z. Suo, G. Bao and B. Fan, "Delamination R-Curve Phenomena Due to Damage,", *J. Mech. Phys. Solids*, in press.

[11] G. Bao, S. Ho. B. Fan and Z. Suo, "Ort..otropy Rescaling and Fracture Specimens for Composites," *Intl. Jnl. Solids Structures*, in press.

[12] F. W. Zok and C. L. Hom, "Large Scale Bridging in Brittle Matrix Composites," *Acta Metall. Mater.*, 38 1895–1904 (1990).

[13] K. M. Prewo and J. J. Brennan, *Jnl. Mater. Sci.*, 17, 2371–2382 (1982).

[14] R. L. Stewart, K. Chyung, M. P. Taylor and R. F. Cooper, *Fracture Mechanism of Ceramics* (Ed. R. C. Bradt *et al.*) Plenum, NY, Vol. 7 (1986) p. 33.

[15] H. C. Cao, E. Bischoff, O. Sbaizero, M. Rühle, A. G. Evans, D. B. Marshall and J. J. Brennan, *J. Am. Ceram. Soc.*, 73 (1990) 1691–1699.

[16] D. Beyerle, S. M. Spearing and A. G. Evans, to be published.

[17] S. P. Timoshenko and J. N. Goodier, *Theory of Elasticity*, 3rd Edition, McGraw-Hill, 1970.

FIGURE CAPTIONS

Fig. 1. Load, displacement characteristics of a DCB interlaminar fracture test.

Fig. 2. a) Bridging ligaments near the crack tip in a CAS/Nicalon DCB specimen.
b) Bridging ligaments 6 mm behind the crack tip.

Fig. 3. A schematic of the bridging process.

Fig. 4. a) Comparison of nominal interlaminar mode I fracture resistance for LAS matrix composite determined using crack length and displacement measurements.
b) Nominal mode I fracture resistance for CAS on interlaminar and intralaminar planes, and for LAS on interlaminar planes. Also shown are the predicted curves.

Fig. 5. Nominal mode I fracture resistances for CAS specimens stiffened by bonding Al_2O_3 plates.

Fig. 6. Crack opening displacements measured as a function of distance from the crack tip. Also plotted is the elastic beam theory prediction.

Fig. 7. Nominal mode I, interlaminar fracture resistance data for unidirectional carbon fiber—PEEK DCB specimens.

Fig. 8. A comparison of the fracture resistance data from Fig. 5 with calculated curves (Eqn. 8).

Fig. A1. A cantilever beam used to model the elastic deformation of the bridging ligament.

Fig. A2. The traction, crack opening behavior predicted by the ligament model for two values of fracture energy, Γ_i. Also shown is the linear softening law used to correlate the resistance curve data.

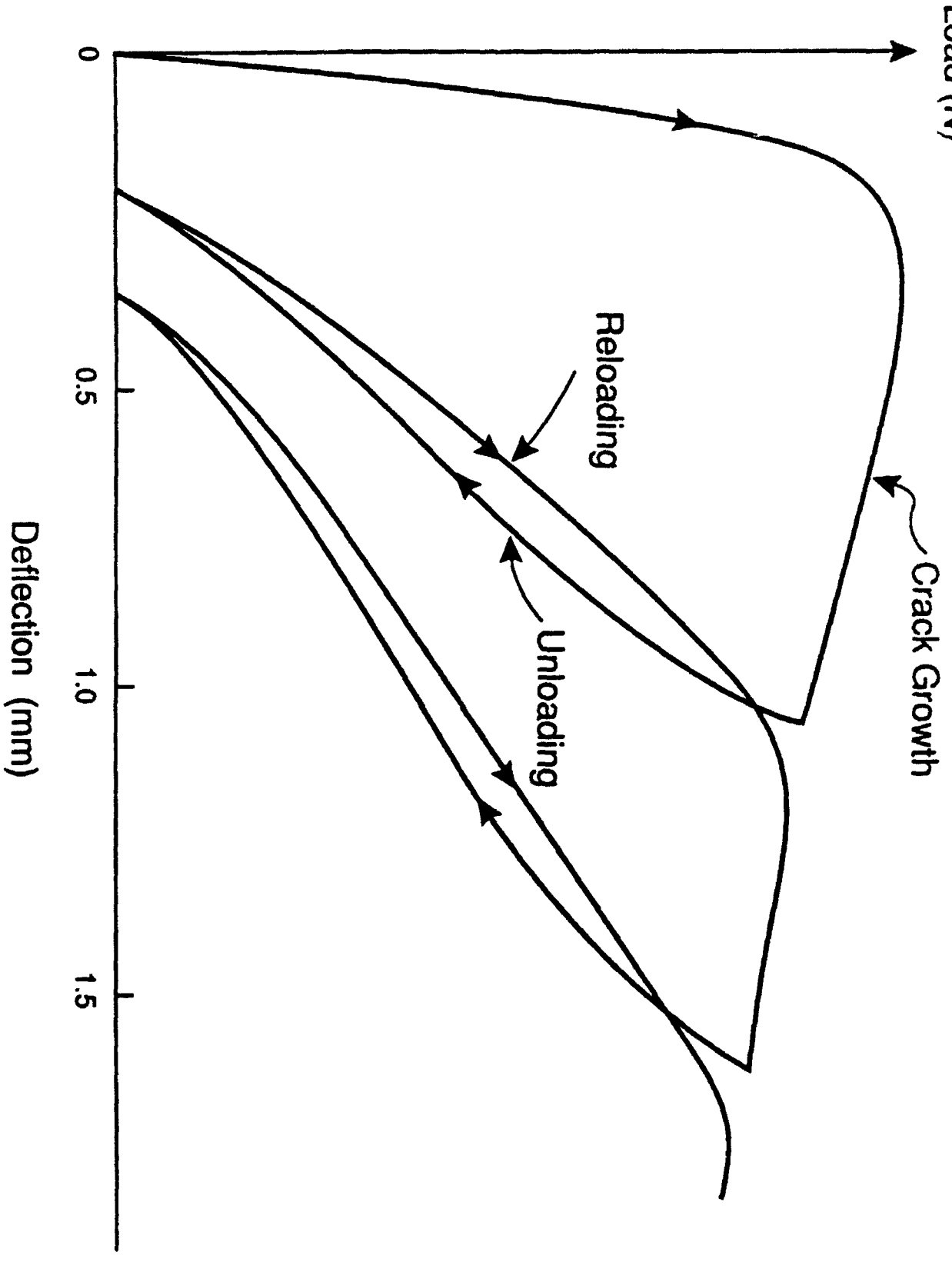
Load (N)
0
0.5
1.0
1.5
Deflection (mm)
Reloading
Unloading
Crack Growth

Fig. 1

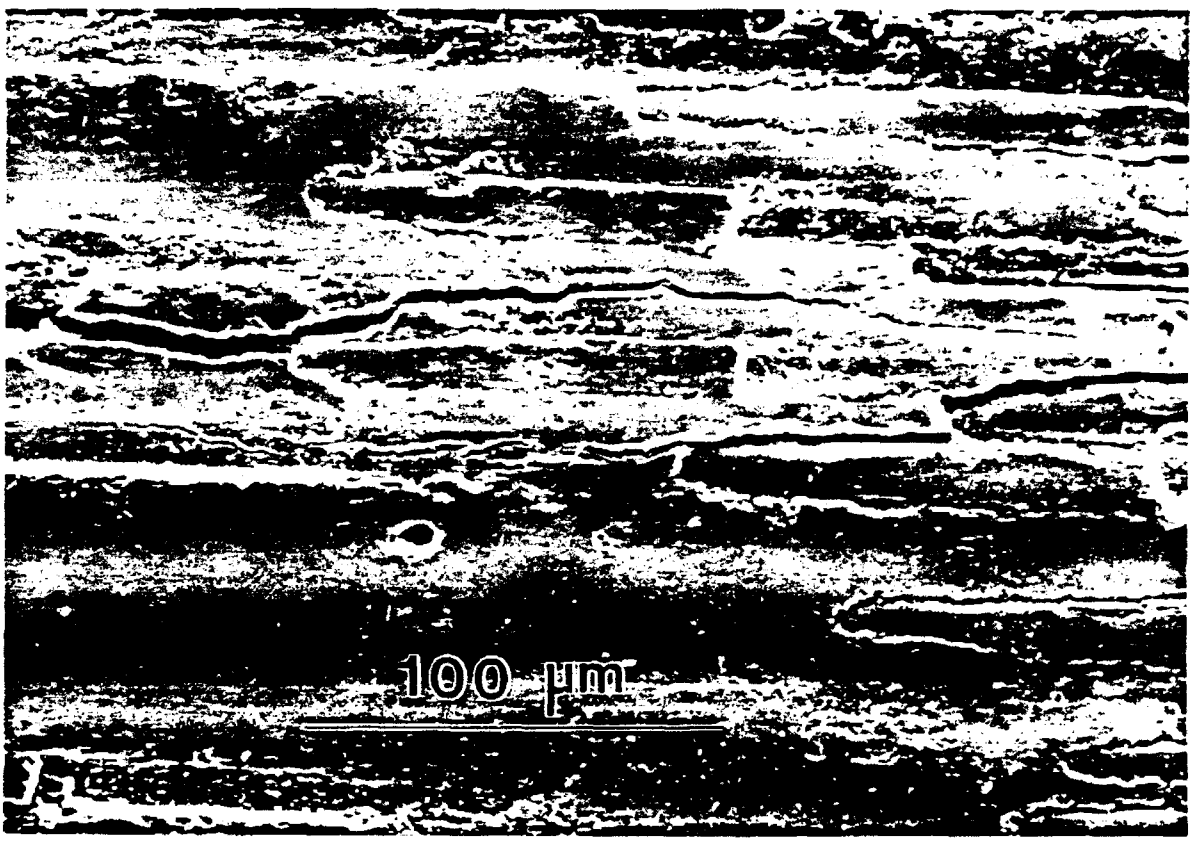

Fig. 2a

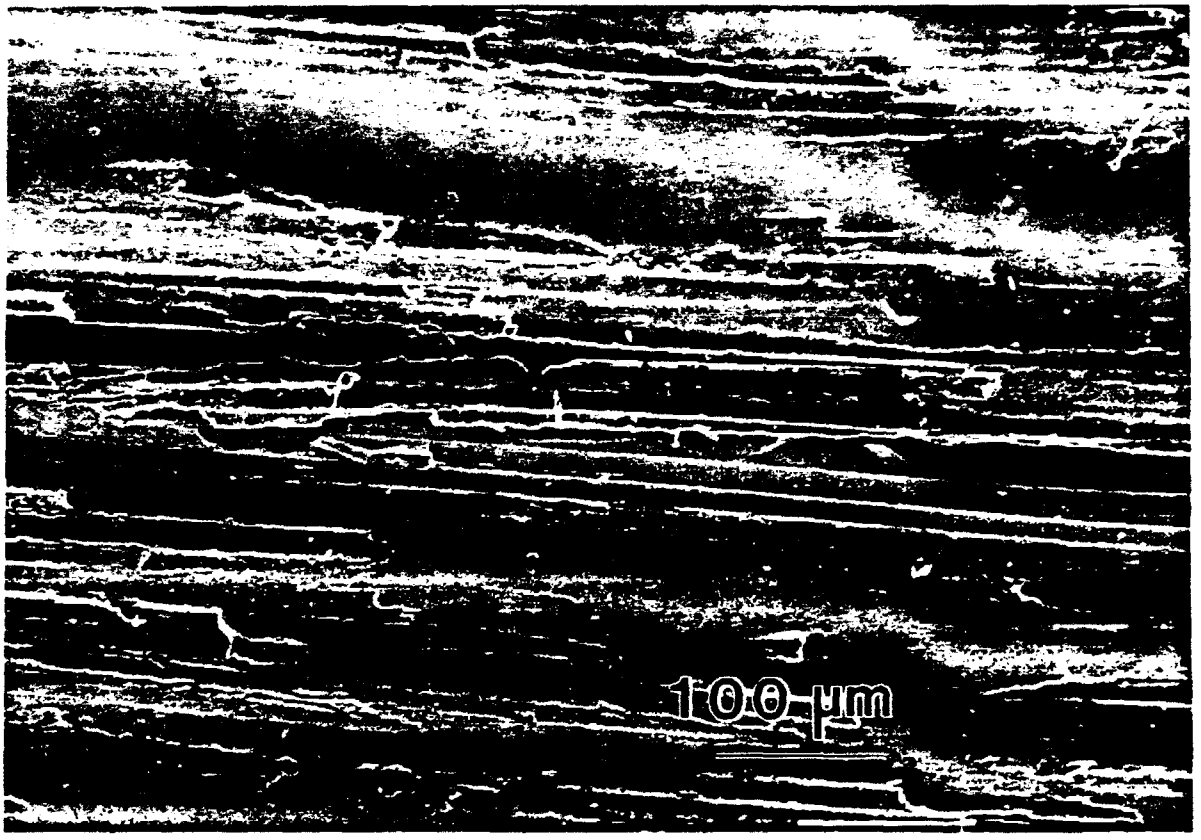

Fig. 2b

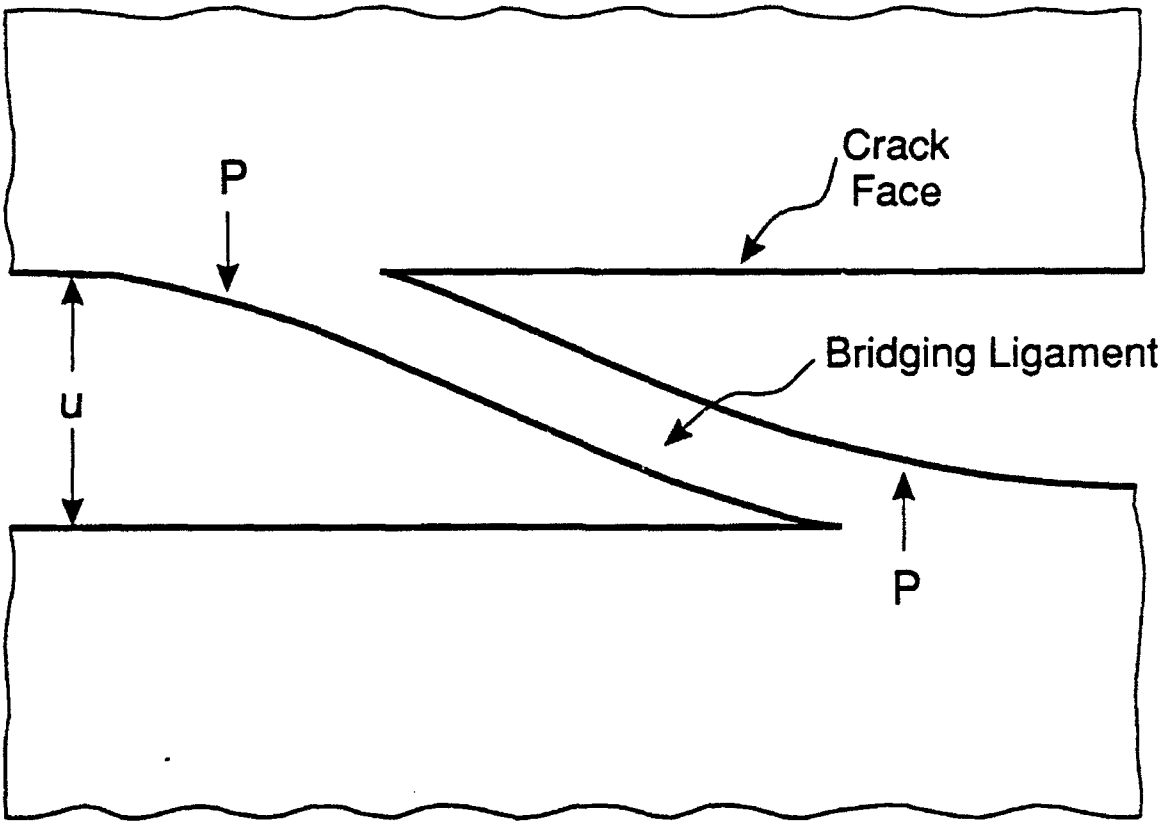

Fig. 3

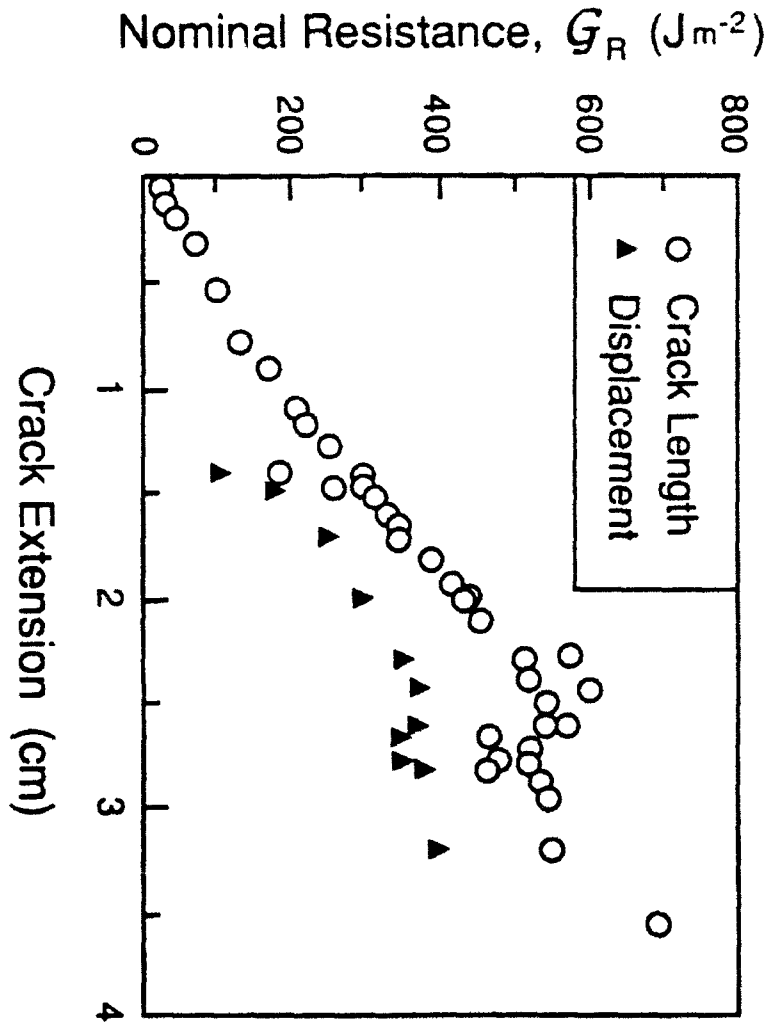

Spearing.URI/Evans-AI91-amk-016294-2

Fig. 4

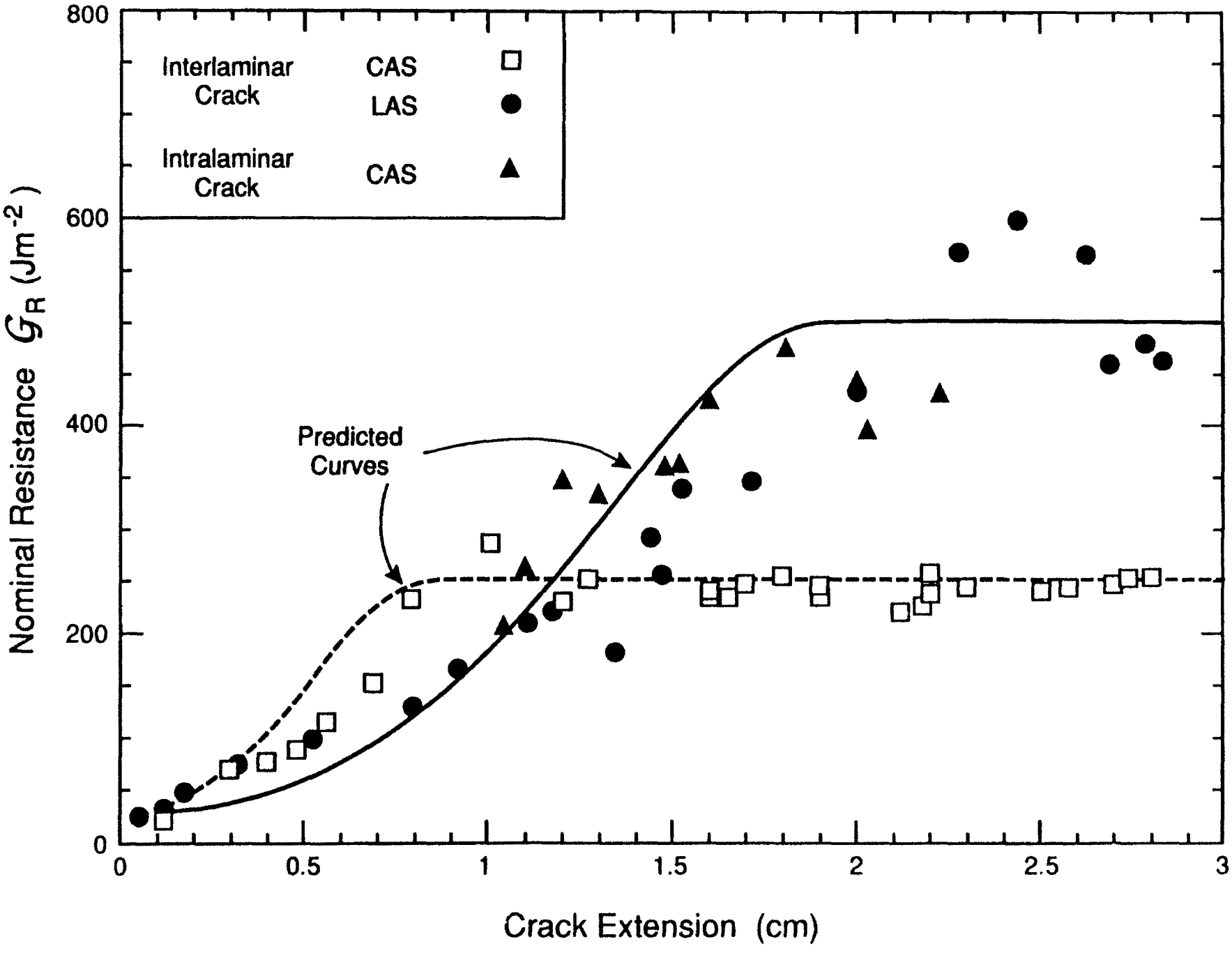
Interlaminar Crack
CAS
LAS
Intralaminar Crack
CAS
Predicted Curves
Nominal Resistance G_R (Jm^{-2})
Crack Extension (cm)
0
200
400
600
800
0
0.5
1
1.5
2
2.5
3

Fig. 5

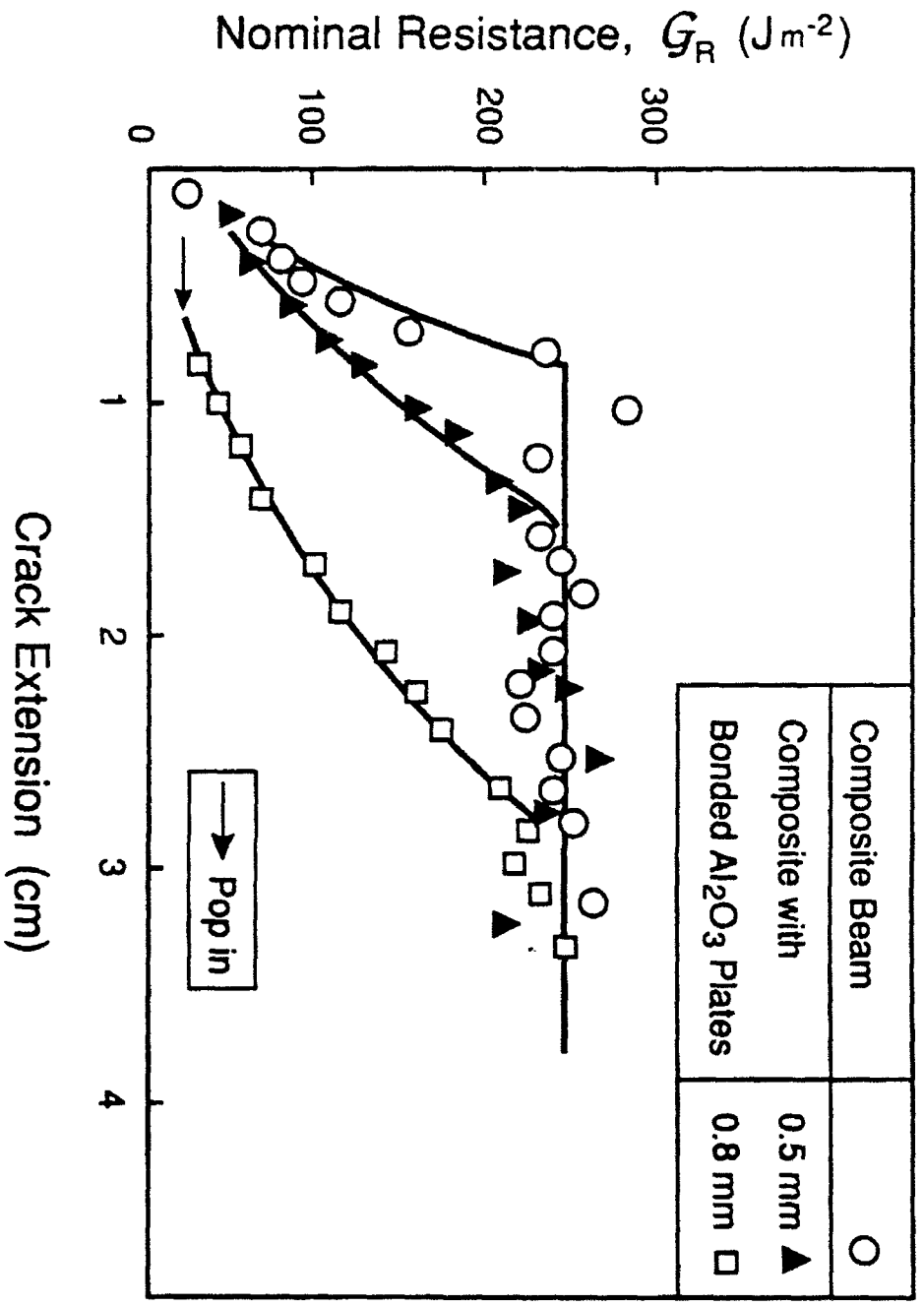
Nominal Resistance, $\mathcal{G}_R$ (J m^{-2})
0
100
200
300
Crack Extension (cm)
1
2
3
4
Pop in
Composite Beam
Composite with
Bonded Al_2O_3 Plates
0.5 mm ▲
0.8 mm □

Fig. 6

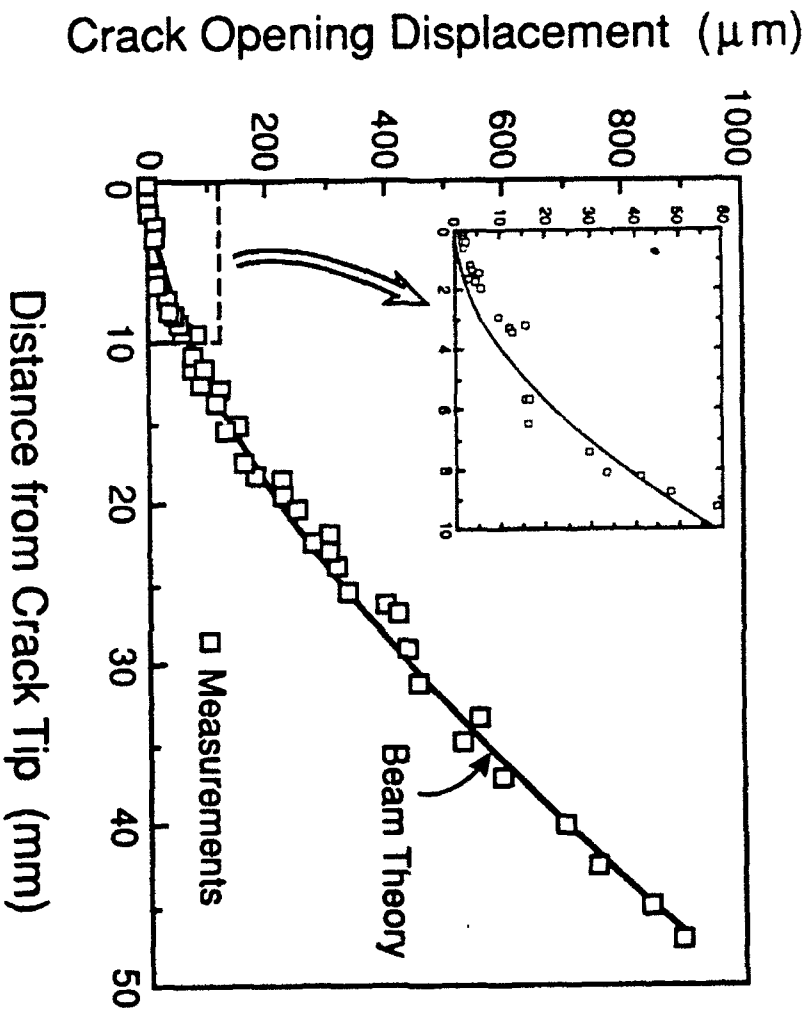
Crack Opening Displacement (μm)
0
200
400
600
800
1000
Distance from Crack Tip (mm)
0
10
20
30
40
50
Measurements
Beam Theory

Fig. 7

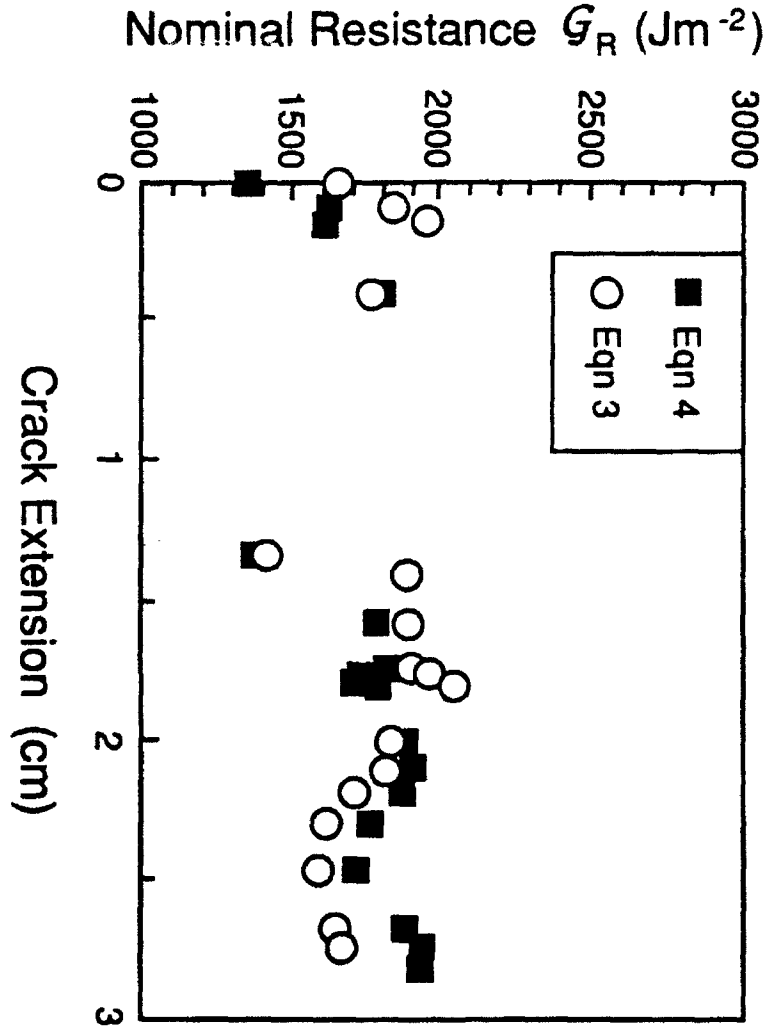
Nominal Resistance $\mathcal{G}_R$ (Jm^{-2})
1000
1500
2000
2500
3000
0
1
2
3
Crack Extension (cm)
Eqn 4
Eqn 3

Fig. 8

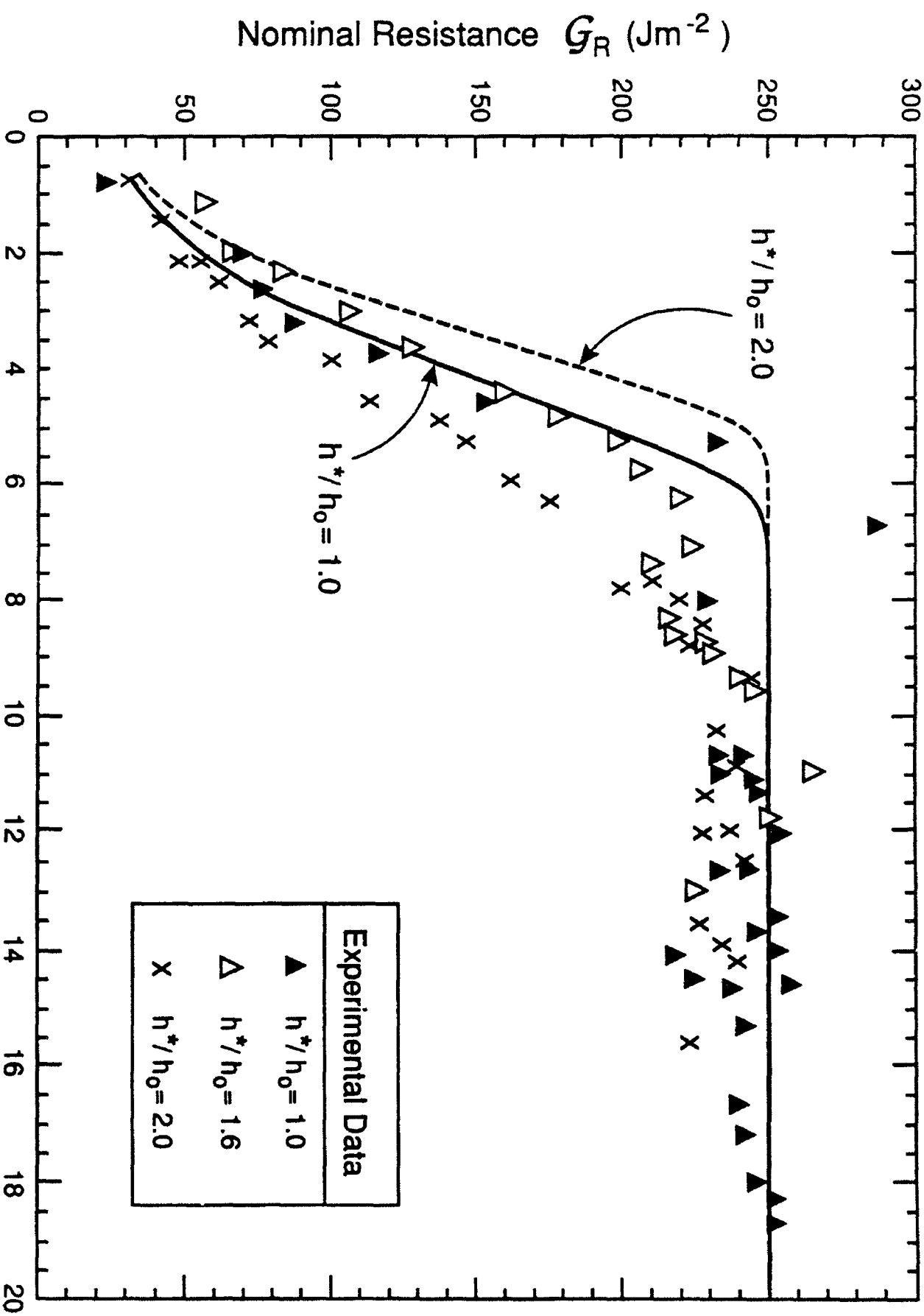
Nominal Resistance G_R (Jm^{-2})
Normalized Crack Extension Δa / h
h*/ h$_o$= 2.0
h*/ h$_o$= 1.0
Experimental Data
▲ h*/ h$_o$= 1.0
Δ h*/ h$_o$= 1.6
× h*/ h$_o$= 2.0

Fig. 9

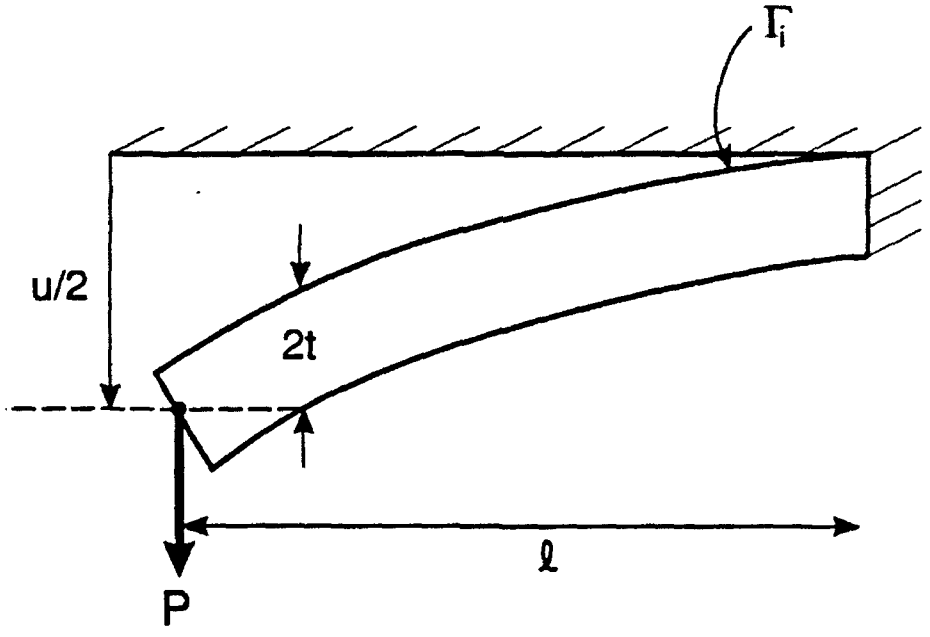

Fig. 10

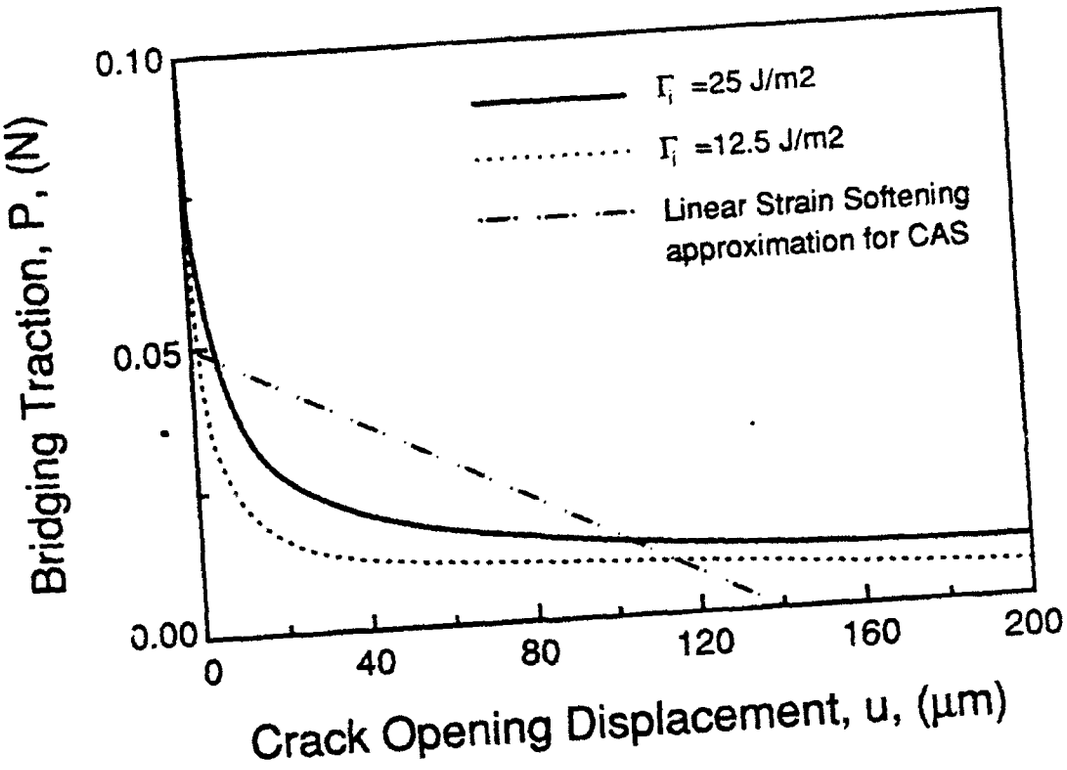
0.10
0.05
0.00
0
40
80
120
160
200
Bridging Traction, P, (N)
Crack Opening Displacement, u, (μm)
Γi =25 J/m2
Γi =12.5 J/m2
Linear Strain Softening
approximation for CAS

Fig. 11

MATERIALS

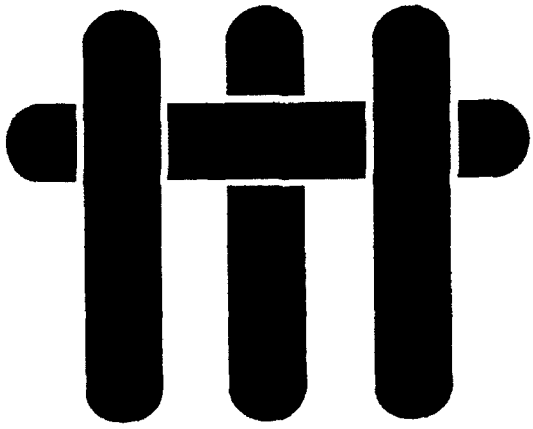

ON THE FLEXURAL PROPERTIES OF BRITTLE MULTILAYER MATERIALS

by

C.A. Folsom, F.W. Zok and F.F. Lange

Materials Department
College of Engineering
University of California
Santa Barbara, California 93106–5050

Submitted to the Journal of the American Ceramic Society, February 1993

7F:MS27(February 8, 1993)3:01 PM/mef

ABSTRACT

Multilayer systems comprised of brittle materials can exhibit substantially different behaviors under flexural and tensile loadings. The present article addresses the origins of such differences, with emphasis on the modeling of the *flexural* stress-strain response. Systems with both a deterministic tensile strength and a distribution in strengths (characterized by Weibull statistics) are considered. The model predictions show that both the ultimate strength and strain-to-failure in flexure exceed the corresponding values in uniaxial tension. In addition, systems comprised of alternating layers of two different materials are examined, and disparities in the flexural and tensile behaviors addressed.

1. INTRODUCTION

There has recently been considerable interest in the mechanical behavior of a wide range of multilayer systems. Some of these systems are man-made,[1,2] whereas others occur in nature (e.g., shells of mollusks[3,4]). The key feature that imparts good mechanical properties in these materials is the presence of crack-deflecting interfaces between layers: cracks that form in one layer are deflected along the interfaces with adjacent layers, preventing catastrophic failure.

Characterization of the mechanical properties of multilayer systems usually involves two types of tests: flexure and uniaxial tension. Flexure tests are frequently chosen because of limitations of small specimen volumes, and ease of both sample preparation and testing procedure. In selecting these tests, it is implicitly assumed that the measurements are characteristic of the *tensile* properties, particularly when all the layers in the system are brittle. However, it has become clear that layered materials exhibit rather different characteristics in the two tests. In particular, the nominal strain to failure measured in flexure can be substantially higher than that measured in uniaxial tension.[1,2] The purpose of the present article is to address the origins of such disparities.

It should be emphasized that neither test is necessarily "better" than the other in terms of characterizing mechanical properties: they are simply *different* from one another. The uniaxial tensile test simulates loading that leads to in-plane tensile stresses, whereas the flexure test simulates loading that involves stress gradients across the layers. Such gradients can arise through either mechanical loading, e.g., a plate, simply supported at discrete points on one side, with a uniformly distributed load on the other; or thermal loading, e.g., a plate with a temperature gradient across the plate. Consequently, it is necessary to understand the mechanics of failure in both cases.

Multilayer systems comprised of brittle layers can exhibit three types of behavior under flexural loading. The behavior is dictated by the properties of the interfaces

between the layers as well as the loading configuration. (i) When the layers are strongly bonded, the system behaves essentially as a monolithic ceramic: a crack in one layer can propagate readily into adjacent layers, with no beneficial effect of the interface. In this case, the flexural stress-strain response is linear elastic up to fracture (as it is in uniaxial tension). (ii) The second type of behavior involves sliding of the layers past one another prior to cracking. This occurs when the sliding resistance of the interface is low. The stress-strain response of such systems is characterized by a linear region with a *low* modulus, given approximately by E/N where E is the modulus of the ceramic and N is the number of layers. In principle, the sliding can be prevented by increasing the aspect ratio of the beam such that the in-plane shear stresses are minimized. (iii) The third, and most desirable, type of behavior occurs when the interface is sufficiently strong to prevent sliding, but its fracture resistance is sufficiently small to allow cracks to be deflected along the interfaces. In order to get crack deflection, the interface toughness, Γ_i, must be less than ~25% of the toughness of the ceramic, Γ_c[10]. The flexural stress-strain response of these systems is characterized by a linear elastic region with a modulus equivalent to that of the monolithic ceramic, followed by a step-like reduction in stress as the layers crack[1,6]. Systems that exhibit the latter characteristics are the focus of the present study.

This paper considers, theoretically, the flexural stress-strain response of three types of brittle, multilayer systems, all containing crack deflecting interfaces. In the first, all the layers are assumed to be the same and to have a deterministic tensile strength. This simple case demonstrates that the nominal failure strain in flexure is larger than that in tension. The flexural strength, however, remains the same as the tensile strength. In the second system, the strengths of the individual layers are assumed to follow a two-parameter Weibull distribution. In this case, both the strength and the strain to failure in flexure exceed the corresponding values for uniaxial tension. The third system is comprised of alternating layers of two different materials, both of which have a

deterministic tensile strength. This configuration is chosen to provide insight into the behavior of hybrid composites comprised of monolithic ceramics and fiber-reinforced composite layers.[2,5] A notable feature that emerges from these calculations is the difference in the critical volume fraction of reinforcement needed for strength enhancement: the critical value being lower in flexure than in tension. Comparisons between theoretical predictions and experimental measurements will be presented elsewhere.[6]

2. SYSTEMS WITH DETERMINISTIC STRENGTH

The flexural stress-strain response of a weakly-bonded multilayer material with a deterministic tensile strength σ_t is evaluated following Euler-Bernoulli beam theory.[7] The compressive strength of the material is assumed to be very much larger than the tensile strength and the material is taken to be linear elastic up to fracture. These characteristics are representative of many brittle solids, including ceramics. The loading is assumed to be pure bending. The results are presented in terms of nominal stresses and strains, calculated on the basis of the overall beam dimensions.

Upon initial loading, the system behaves like a monolithic solid in the sense that both the stress and the strain distributions across the beam are linear. The maximum values of tensile stress and tensile strain are thus given by[7]

$$\sigma = 6M/b(N_0 t)^2 \tag{1}$$

and

$$\varepsilon = \sigma/E = 6M/b(N_0 t)^2 E \tag{2}$$

where M is the applied bending moment, N_o is the number of layers, t is the thickness of each layer and b is the beam width. When σ reaches σ_t, the outermost layer (on the tensile side) breaks: the remaining layers are assumed to stay intact since the crack deflects along the interface with the second layer. The corresponding values of nominal stress and strain are simply

$$\sigma_1 = \sigma_t \tag{3}$$

and

$$\varepsilon_1 = \sigma_t/E \equiv \varepsilon_t \tag{4}$$

For the purpose of calculating the subsequent stress-strain response, it is assumed that the stress everywhere in the first layer is reduced to zero following cracking. In essence, the outer layer is removed from the composite, leaving $(N_o - 1)$ intact layers. As a result, the stress and strain distributions can be assumed to remain linear, with a shift in the neutral axis by a distance of t/2. The reduction in plate stiffness following the initial cracking event leads to a drop in the nominal stress to the value

$$\sigma_1' = \sigma_1\left(\frac{N_o - 1}{N_o}\right)^3 \tag{5}$$

In order to break the next layer, the plate must be loaded further until, once again, the stress in that layer reaches σ_t. The loading conditions required for this event are described by

$$\sigma_2 = \sigma_t\left(\frac{N_o - 1}{N_o}\right)^2 \tag{6}$$

and

$$\varepsilon_2 = \varepsilon_t\left(\frac{N_o - 1}{N_o}\right)^{-1} \tag{7}$$

Following the second cracking event, the load drops again, and the stress for further cracking calculated assuming that *both* cracked layers do not support any stress. Using this approach, the nominal stress, σ_i, and the nominal strain, ε_i, for cracking the i^{th} layer are

$$\frac{\sigma_i}{\sigma_t} = \left(\frac{N_i}{N_o}\right)^2 \tag{8}$$

and

$$\frac{\varepsilon_i}{\varepsilon_t} = \left(\frac{N_i}{N_o}\right)^{-1} \tag{9}$$

where N_i is the number of intact layers. Similarly, the nominal stress *after failure* of the i^{th} layer is

$$\sigma_i' = \sigma_t\left(\frac{(N_i - 1)^3}{N_o^2 N_i}\right) \tag{10}$$

The preceding results can be combined to describe two relevant curves: one is the locus of nominal stress and nominal strain values *at* each cracking event; the other is the locus of the corresponding values *following* each cracking event. The stress-strain curves oscillate between these loci in a saw-tooth fashion until all the layers have broken, as illustrated in Fig. 1. For comparison, the behavior corresponding to uniaxial tensile loading is also shown. The former locus is obtained by combining Eqns. (8) and (9), resulting in

$$\frac{\sigma_i}{\sigma_t} = \left(\frac{\varepsilon_i}{\varepsilon_t}\right)^{-2} \tag{11}$$

Note that this relationship does not depend on the number of layers. The latter locus is obtained from Eqns. (9) and (10), resulting in

$$\frac{\sigma_i'}{\sigma_t} = \left[1 - \frac{1}{N_o}\left(\frac{\varepsilon_i}{\varepsilon_t}\right)\right]^3 \left(\frac{\varepsilon_i}{\varepsilon_t}\right)^{-2} \tag{12}$$

In this case, the stress increases with increasing number of layers, N_o, as shown in Fig. 2. As N_o approaches ∞, the lower curve converges with the upper curve and the stress-strain curve becomes a smooth, monotonically decreasing function beyond the stress maximum. It should be noted that the flexural strength of these systems (defined by the maximum point in the nominal stress/nominal strain curve) is identical to the tensile strength. However, the nominal strain-to-failure can be substantially higher in flexure: by a factor of ~ 3–4 for large values of N_o.

3. ROLE OF FRACTURE STATISTICS

Many brittle materials, including ceramics, exhibit a distribution in strengths. This distribution can generally be described by the empirical Weibull function

$$P = 1 - \exp\frac{-V}{V_o}\left(\frac{\sigma}{\sigma_o}\right)^m \tag{13}$$

where P is the cumulative probability of failure at stresses up to σ, V is the sample volume, V_o and σ_o are the reference values of volume and stress, and m is the Weibull modulus. The approach developed in the previous section is used here to describe the flexural response of multilayer systems in which the strength of the layers follows such a distribution. For convenience, N_o is assumed to be large, allowing the stress gradients across individual layers to be neglected. To provide a basis for comparison, the results for uniaxial tensile loading are presented first. The latter results are not new: they are equivalent to those obtained in the theory of fiber bundle failure.

During uniaxial *tensile* loading, the stress in each intact layer is simply $E\varepsilon$, where ε is the remote tensile strain. The stress in the broken layers is assumed to be zero, as in the preceding section. Consequently, the variation in nominal stress with nominal strain can be written as

$$\frac{\sigma}{\sigma_o} = \frac{\varepsilon E(1-P)}{\sigma_o} = \left(\frac{\varepsilon E}{\sigma_o}\right)\exp\left[\frac{-V}{V_o}\left(\frac{\varepsilon E}{\sigma_o}\right)^m\right] \tag{14}$$

Typical tensile stress-strain curves, presented in the normalized form σ/σ_o vs $\varepsilon E/\sigma_o$, for several values of m are shown in Fig. 3(a). The tensile strength, $\bar{\sigma}_T$, is obtained by setting

$$\frac{d(\sigma/\sigma_o)}{d(\varepsilon E/\sigma_o)} = 0, \tag{15}$$

whereupon

$$\frac{\bar{\sigma}_T}{\sigma_o} = \frac{1}{(me\,V/V_o)^{1/m}} \tag{16}$$

Trends in $\bar{\sigma}_T/\sigma_o$ with m for $V/V_o = 1$ are presented in Fig. 4.

The corresponding results for *flexural* loading are more complicated and, as shown below, require numerical integration. The assumptions used in deriving the equations here are essentially the same as those outlined in Section 2, with one notable exception. Since the strength of the layers is assumed to follow a Weibull distribution, cracking does not necessarily occur sequentially through the layers in order of their positions. Consequently, the stress distribution across the beam does not remain linear, though the *strain* distribution does.

Evaluation of the nominal stress-strain behavior of such systems involves two steps. In the first, the applied bending moment, M, is equated to the moment induced by the stresses within the beam. This condition can be written as

$$M = \frac{b(N_o t)^2}{(\varepsilon_t - \varepsilon_c)^2} \int_{\varepsilon_c}^{\varepsilon_t} \sigma(\varepsilon)\cdot(\varepsilon - \varepsilon_c)\,d\varepsilon \tag{17}$$

where ε_c and ε_t are the maximum values of compressive and tensile strains, respectively. Furthermore, assuming the stress-strain relation $\sigma(\varepsilon)$ to be linear in the

compressive region ($\varepsilon < 0$) and to follow Eqn. (14) in the tensile region ($\varepsilon > 0$) allows Eqn. (17) to be re-written in the non-dimensional form

$$\frac{\sigma}{\sigma_o} = \frac{6}{(e_t - e_c)^2}\left[\int_{e_c}^{o} e(e - e_c)de + \int_{o}^{e_t} e(e - e_c)\exp\left[\frac{-V}{V_o}e^m\right]de\right], \tag{18}$$

where e is a normalized strain ($\varepsilon E/\sigma_o$), and the subscripts c and t represent compression and tension, respectively. In the second step, the sum of the forces acting parallel to the plate is set equal to zero, enforcing static equilibrium. This condition can be expressed as

$$\int_{e_c}^{o} e\,de + \int_{o}^{e_t} e\cdot\exp\left[-\left(\frac{V}{V_o}\right)e^m\right]de = 0 \tag{19}$$

Combining Eqns. (18) and (19) leads to the final result

$$\frac{\sigma}{\sigma_o} = \frac{2}{(e_t - e_c)^2}\left\{3\int_{o}^{e_t} e^2\cdot\exp\left[-\left(\frac{V}{V_o}\right)e^m\right]de - e_c^3\right\} \tag{20}$$

where

$$e_c = -\left[2\int_{o}^{e_t} e\cdot\exp\left[-\left(\frac{V}{V_o}\right)e^m\right]de\right]^{1/2} \tag{21}$$

The integrals in these equations have been solved using a numerical method. The resultant stress-strain curves for $V/V_o = 1$ and several values of m are plotted in Fig. 3(b). Comparison with the tensile curves indicates that the ultimate flexural

strength $\bar{\sigma}_F$, consistently exceeds the ultimate tensile strength, $\bar{\sigma}_T$,: the difference being largest for low values of m (Fig. 4). The influence of m on the strength ratio (flexural to tensile) is plotted in Fig. 5.

It is of interest to note that the trend in Fig. 5 is similar to that obtained when comparing the mean flexural strength of a *monolithic* ceramic with the corresponding mean tensile strength. In the latter case, the strength ratio is given by[8]

$$\frac{\hat{\sigma}_F}{\hat{\sigma}_T} = \left[c(m+1)\right]^{1/m} \tag{22}$$

where c is a numerical coefficient. When the specimen volumes are equivalent, c = 2. The trend predicted by Eqn. (22) is plotted on Fig. 5 as a dashed line. It appears to scale with the results for multilayer systems over the range of values of m considered here, suggesting that the present results can be described empirically by a function with a form similar to that of Eqn. (22). Indeed, when c is taken to be 0.75, Eqn. (22) provides a good approximation to the exact results, with an error $\leq 0.8\%$, over the range $3 \leq m \leq 20$. This comparison is presented in Fig. 5. It is also of interest to note that the strain-to-failure of the multilayer systems in flexural loading is substantially higher than that for tension for the entire range of values of m.

The origin of the disparity in the ultimate strengths in flexural and tensile loading can be understood by examining the stress and strain distributions across a flexural beam at various stages of loading. One such example, for m = 5, is presented in Fig. 6. Figure 6(a) shows the nominal stress-strain response and Figs. 6(b) and (c) show the corresponding strain and stress distributions at three load levels, represented by points A, B and C. Prior to extensive cracking (A), both the strain and stress distributions remain essentially linear and symmetric about the beam center, as expected for an elastic beam. When extensive cracking occurs, the strain distribution remains linear,

though the neutral axis shifts toward the compressive face. At the load maximum (point B in Fig. 6(a)), the stress distribution on the tensile side becomes highly non-linear: the shape of this distribution is identical to the *tensile* stress-strain curve shown in Fig. 3(a) (though with a part of the tail truncated). This similarity arises because the strain distribution is assumed to vary linearly across the beam. The maximum *local* tensile stress in the plate is thus equivalent to the ultimate tensile strength (0.59 σ_o for the present case), whereas the maximum compressive stress reaches significantly higher levels: 0.85 σ_o at the load maximum. Consequently, the maximum nominal stress supported by the beam is higher in flexure (0.80 σ_o) than in tension (0.59 σ_o). In essence, this difference can be attributed to the process of stress re-distribution following cracking in the flexure specimen, coupled with the high *compressive* strength of the constituent layers.

To provide insight into the relative magnitudes of these effects (one due to the stress re-distribution and the other to the tension-compression strength differential), it is useful to consider a hypothetical case where the *compressive* stress-strain response is the same as that for *tension* (Eqn. 14). This approach allows determination of the ratio of flexural to tensile strength when the only effect is the geometric one associated with stress re-distribution. (Clearly, this is an academic exercise since there are no real materials that exhibit such behavior.) The results of these calculations are plotted as the dotted line in Fig. 5. Apparently, the strength ratio (flexure/tension) is due largely to the stress re-distribution effect, though there is a noticeable contribution associated with the tension-compression strength differential.

4. BIMATERIAL SYSTEMS

The preceding analysis for single-phase systems is extended here to cases in which the beams consist of alternating layers of different phases: one being the 'matrix' phase

(material 1) and the other the 'reinforcing' phase (material 2). The motivation for this analysis stems from recent experimental studies on hybrid composites comprised of alternating layers of monolithic ceramics and fiber-reinforced sheets. The present analysis is limited to symmetric lay-ups in which the exterior layers are the 'matrix' phase. Each of the two phases is assumed to be linear elastic and to have a deterministic tensile strength. For simplicity, differences in elastic moduli between the two materials are neglected. (The elastic mismatch is accounted for in a companion paper [6].) Once again, cracks formed in one layer are assumed to be deflected along the interfaces with adjacent layers, allowing the layers to behave independently of one another. Furthermore, the tensile strength $\bar{\sigma}_2$ of the reinforcing layers is assumed to be larger than the tensile strength $\bar{\sigma}_1$ of the matrix layers. The behavior of plates comprised of an infinite number of layers is considered first, since a closed form expression for the stress-strain response can be readily derived.

The *tensile* stress-strain relationship of such bimaterial beams is a discontinuous linear function of strain in three intervals of strain. This relationship can be expressed in the non-dimensional form

$$\sigma/\varepsilon E = 1 \qquad \varepsilon/\bar{\varepsilon}_1 \le 1 \tag{23a}$$

$$\sigma/\varepsilon E = f \qquad 1 \le \varepsilon/\bar{\varepsilon}_1 \le \bar{\varepsilon}_2/\bar{\varepsilon}_1 \tag{23b}$$

$$\sigma/\varepsilon E = 0 \qquad \varepsilon/\bar{\varepsilon}_1 > \bar{\varepsilon}_2/\bar{\varepsilon}_1 \tag{23c}$$

where f is the volume fraction of the reinforcing phase, and $\bar{\varepsilon}_1$ and $\bar{\varepsilon}_2$ are the failure strains of materials 1 and 2, respectively. Due to the discontinuous nature of the tensile response, the nominal stress in flexure is also a discontinuous function of strain. The flexural response must be determined separately for each of the three intervals and then

combined in a piece-wise fashion to determine the overall response. In all cases, the flexural response is determined from static equilibrium (by setting the average longitudinal stress equal to zero) and setting the resultant bending moment equal to the applied moment.

The first interval is simply the trivial case where the body is linear elastic, whereupon the stress-strain relation becomes

$$\frac{\sigma}{\bar{\sigma}_1} = \frac{\varepsilon}{\bar{\varepsilon}_1} \qquad \frac{\varepsilon_t}{\bar{\varepsilon}_1} \le 1, \tag{24}$$

where ε_t is the maximum tensile strain in the beam.

For the second interval, the nominal stress-strain relation is

$$\frac{\sigma}{\bar{\sigma}_1} = \left(\frac{\left(1 - \left(\frac{\varepsilon_c}{\bar{\varepsilon}_1}\right)^3\right) + f\left[\left\{2\left(\frac{\varepsilon}{\bar{\varepsilon}_1}\right) + \left(\frac{\varepsilon_c}{\bar{\varepsilon}_1}\right)\right\}^3 - 1\right]}{2\left(\frac{\varepsilon}{\bar{\varepsilon}_1}\right)^2} \right) \qquad 1 \le \frac{\varepsilon_t}{\bar{\varepsilon}_1} \le \frac{\bar{\varepsilon}_2}{\bar{\varepsilon}_1}. \tag{25}$$

where ε_c is the maximum compressive strain and is related to the nominal strain ε by

$$\frac{\varepsilon_c}{\bar{\varepsilon}_1} = \frac{2f\left(\frac{\varepsilon}{\bar{\varepsilon}_1}\right) + \left[f^2 + 2f\left(2\left(\frac{\varepsilon}{\bar{\varepsilon}_1}\right)^2 - 1\right) + 1\right]^{1/2}}{(1-f)} \tag{26}$$

The expression for the third interval is

$$\frac{\sigma}{\bar{\sigma}_1} = \left(\frac{1 - \left(\frac{\varepsilon_c}{\bar{\varepsilon}_1}\right)^3 + f\left(\left(\frac{\varepsilon_2}{\bar{\varepsilon}_1}\right)^3 - 1\right)}{2\left(\frac{\varepsilon}{\bar{\varepsilon}_1}\right)^2} \right) \qquad \frac{\varepsilon_t}{\bar{\varepsilon}_1} \geq \frac{\bar{\varepsilon}_2}{\bar{\varepsilon}_1}. \tag{27}$$

where the maximum compressive strain is now given by

$$\frac{\varepsilon_c}{\bar{\varepsilon}_1} = -\left[f\left(\left(\frac{\bar{\varepsilon}_2}{\bar{\varepsilon}_1}\right)^2 - 1\right) + 1 \right]^{1/2} \tag{28}$$

It can readily be shown that, when f = 0, the results for intervals two and three (Eqns. 25 and 27) are identical, and agree with the results derived for single phase multilayered materials (Eqn. 11).

Similar calculations have also been carried out for plates containing *finite* numbers of layers. In this case, no simple closed form expression for the flexural stress-strain response can be obtained. The approach adopted here was to increase the nominal strain in small increments and, at each interval, evaluate the magnitude of the stresses in both phases. When the stresses reached the corresponding strengths (either $\bar{\sigma}_1$ or $\bar{\sigma}_2$), then those layers were discounted from subsequent calculations by simply setting their modulus equal to zero, as before. This procedure was repeated until all the layers had failed.

The resulting nominal stress-strain curves for the case where $\bar{\sigma}_2/\bar{\sigma}_1 = 3$ and $f = 0.1$ are plotted in Fig. 7(a). In this case, the ultimate strengths in tension and flexure are governed by the strength of the matrix phase (material 1), though the nominal flexural stress at strains beyond the load maximum is larger than that in tension. In general, the stress increases as the number of layers increases. It is also seen that the

result for beams containing 20 matrix layers (39 total layers) differ only slightly from the infinite layer solution.

The corresponding stress-strain curves for $f = 0.5$ are shown in Fig. 7(b). In this case, the ultimate strength is substantially larger than the stress required for the onset of matrix cracking. It is also apparent that the ultimate strength is greater in flexure than in tension and depends to some extent upon the number of layers.

The effects of reinforcement volume fraction f on the ultimate strengths in tension and flexure for the case where $\bar{\sigma}_2/\bar{\sigma}_1 = 3$ are shown in Fig. 8. At low values of f, there is no strength enhancement due to the presence of the reinforcements: once the matrix layers fail, the reinforcements are unable to support the additional load and thus the strength of the composite is dictated by that of the matrix. However, beyond a critical volume fraction, f_c, the strength increases with f, reaching a value of 3 when $f = 1$.

A notable feature in Fig. 8 is that the critical volume fraction for flexure is lower than that for tension. This critical volume fraction can be expressed solely in terms of the strength ratio, $\bar{\sigma}_1/\bar{\sigma}_2$. For tensile loading, the relationship is simply[9]

$$f_c = \bar{\sigma}_1/\bar{\sigma}_2 \tag{29}$$

For flexure, the critical value is found by setting the maximum nominal stress (given by the intersection of Eqns. (25) and (27)) equal to unity, resulting in

$$f_c = \frac{4\left(\frac{\bar{\sigma}_2}{\bar{\sigma}_1}\right)^2 + 13\left(\frac{\bar{\sigma}_2}{\bar{\sigma}_1}\right) + 7 + \left[8\left(\frac{\bar{\sigma}_2}{\bar{\sigma}_1}\right)^3 + 33\left(\frac{\bar{\sigma}_2}{\bar{\sigma}_1}\right)^2 + 22\left(\frac{\bar{\sigma}_2}{\bar{\sigma}_1}\right) + 1\right]^{1/2}}{8\left[\left(\frac{\bar{\sigma}_2}{\bar{\sigma}_1}\right) + 1\right]^3} \tag{30}$$

The results of Eqns. (29) and (30) are plotted against the strength ratio $\bar{\sigma}_2/\bar{\sigma}_1$ in Fig. 9, and show that the critical volume fraction in flexure is consistently about half of that required in tension.

5. CONCLUDING REMARKS

The main goal of this study has been to quantify the basic trends in the fracture behavior of brittle multilayered systems and address, specifically, the origin of differences between flexural and tensile properties. A simple theory based on the bending of beams has been developed to account for the progressive cracking through such systems and its effects on the nominal stress-strain response. A number of important features have been identified. Firstly, single phase multilayer beams with deterministic strengths, while not possessing greater strengths than the individual layers, do have the ability to withstand flexural load beyond the initial cracking event under displacement-controlled conditions. When the individual layers possess a statistical distribution of strengths (as expected for most brittle solids), both the strength and the failure strain are higher in flexure than in tension. In either case, multilayer systems are likely to be stronger than monolithic materials of the same dimensions, due simply to the fact that thin layers usually contain smaller flaws and hence possess greater mean strengths (i.e. the two dimensional analog to fibers). Secondly, further property improvements can be obtained by introducing reinforcing layers with a high strength and strain-to-failure (e.g. fiber composite). Such hybrid systems are expected to provide a high matrix cracking stress (relative to that of conventional unidirectional CMCs) in combination with a high strain-to-failure. Finally, the critical volume fraction required to strengthen layered ceramic systems under flexural loading is about one half the value corresponding to uniaxial tension. This result is important in designing composites for applications subject to stress gradients across the layers.

It should be noted the present theory is rather simplistic in the sense that the interfacial cracks are assumed to propagate to sufficiently long lengths such that the cracked layers are completely unloaded. In reality, the interfacial cracks are expected to propagate only a finite length along the beam: the average stress within each cracked layer could then be substantial. This is expected to increase the ultimate flexural strength in relation to the present model predictions. A more rigorous model is needed to incorporate such effects.

ACKNOWLEDGMENTS

Funding of this work was supplied by the DARPA University Research Initiative Program of UCSB under ONR contract N-0014-92-J-1808. In addition, one of the authors (C.A.F.) was supported through the Air Force Palace Knights Program.

REFERENCES

[1] W.J. Clegg, K. Kendall, N.McN. Alford, T.W. Burton and J.D. Birchall, "A Simple Way to Make Tough Ceramics, *Nature* [347], No. 6292, pp. 455–57, Oct. 4 (1991).

[2] C.A. Folsom, F.W. Zok, F.F. Lange and D.B. Marshall, "Mechanical Behavior of a Laminar Ceramic/Fiber-Reinforced Epoxy Composite," *J. Am. Ceram. Soc.*, **75 [11]** pp. 2969–75 (1992).

[3] J.D. Currey and A.J. Kohn, "Fracture in the Crossed-Lamellar Structure of Conus Shells," *J. Mater. Sci.*, **11**, pp. 1615–73 (1976).

[4] V.J. Laraia and A.H. Heuer, "Novel Composite Microstructure and Mechanical Behavior of Mollusk Shells," *J. Am. Ceram. Soc.*, **72 [11]** pp. 2177–79 (1989).

[5] C.A. Folsom, F.W. Zok and F.F. Lange, "Flexural Properties of Brittle Matrix Laminar Composites," Ceramic Engineering and Science Proceedings of the 16th Annual Conference on Composites and Advanced Ceramic Materials, J.B. Watchman Ed., American Ceramic Society (1992).

[6] C.A. Folsom, F.W. Zok and F.F. Lange, to be published.

[7] S Timoshenko, *Strength of Materials*, 3rd Ed. Princeton (1955) pp. 137–40.

[8] G.J. DeSalvo, "Theory and Structural Design Applications of Weibull Statistics," *WANL-TME-2688*, Westinghouse Electric Corp., Pittsburgh, PA, May 1970.

[9] A. Kelly and N.H. MacMillan, "Strong Solids," Clarendon Press, Oxford (1986).

[10] M.Y. He and J.W. Hutchinson, "Kinking of a Crack out of an Interface," *J. Appl. Mech.*, **56**, 270-78, (1989).

FIGURES

Fig. 1. Comparison of the tensile and flexural stress-strain curves of a system comprised of 8 brittle layers, each with a deterministic tensile strength, σ_t. The dashed lines are calculated from Eqns. (11) and (12), and show the bounds on the flexural stress-strain curve.

Fig. 2. The locus of points bounding the flexural stress-strain response of systems with finite numbers of layers. The solid curve represents the upper bound, and the dashed curves represent the lower bounds.

Fig. 3. Influence of the Weibull modulus, m, on (a) the tensile and (b) the flexural stress-strain response of multilayer systems.

Fig. 4. Trends in the ultimate strength with Weibull modulus for flexural and tensile loading.

Fig. 5. Influence of Weibull modulus on the ultimate strength ratio (flexure-to-tension).

Fig. 6. (a) The flexural stress-strain curves for m = 5, and (b) the corresponding strain and (c) stress distributions at three load levels, indicated by points A, B and C on the curve in (a).

Fig. 7. Comparisons of the tensile and flexural stress-strain curves for bimaterial systems: (a) f = 0.1, (b) f = 0.5. Note that the tensile curves do not depend on the number of layers, whereas the flexural curves do.

Fig. 8. Influence of reinforcement volume fracture on (a) the flexural and tensile ultimate strengths and (b) the strength ratio (flexure/tension).

Fig. 9. Influence of strength ratio $\bar{\sigma}_2/\bar{\sigma}_1$ on the critical reinforcement volume fractions for both flexural and tensile loading.

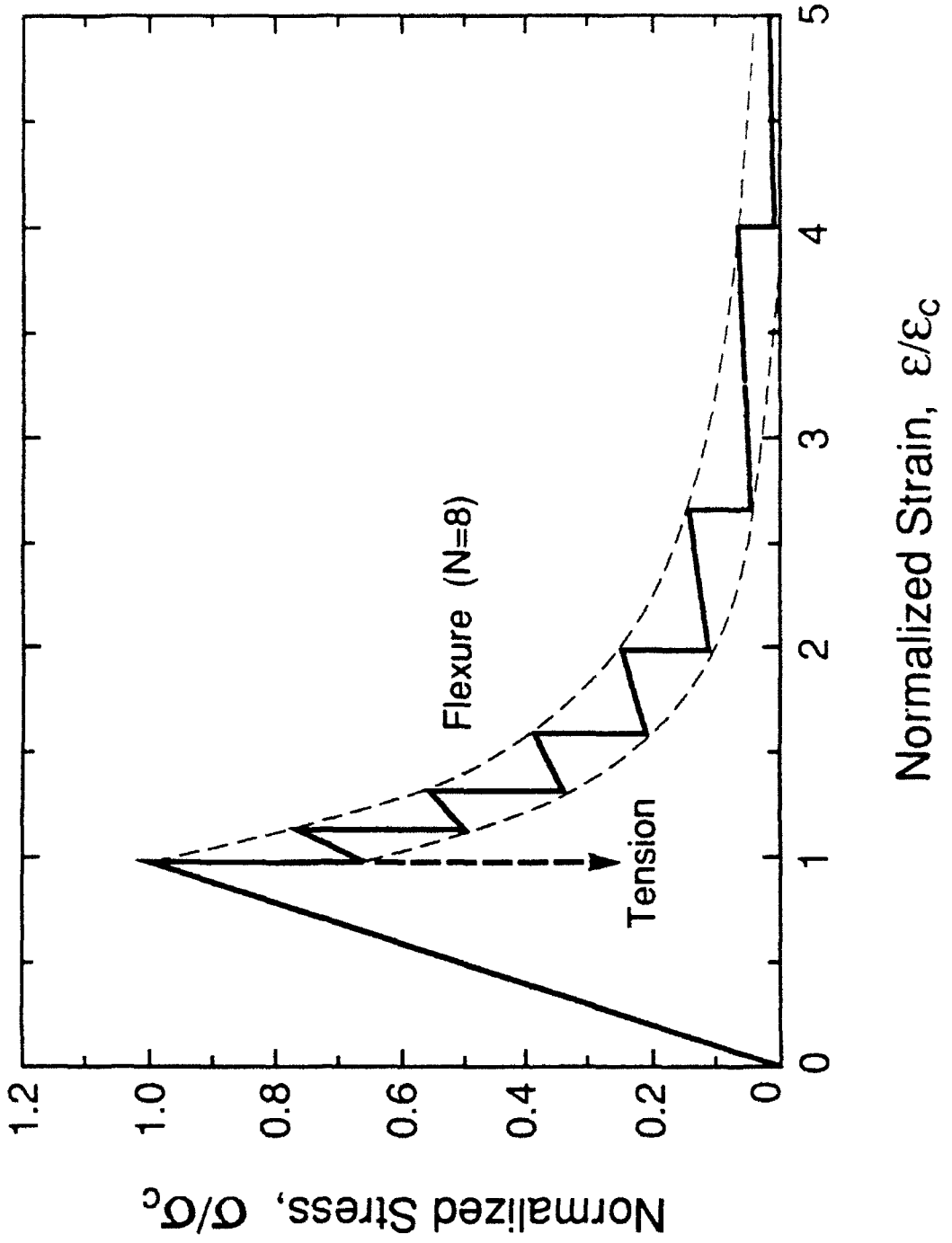
Normalized Stress, σ/σc
Normalized Strain, ε/εc
Flexure (N=8)
Tension
0
0.2
0.4
0.6
0.8
1.0
1.2
0
1
2
3
4
5

Fig. 1

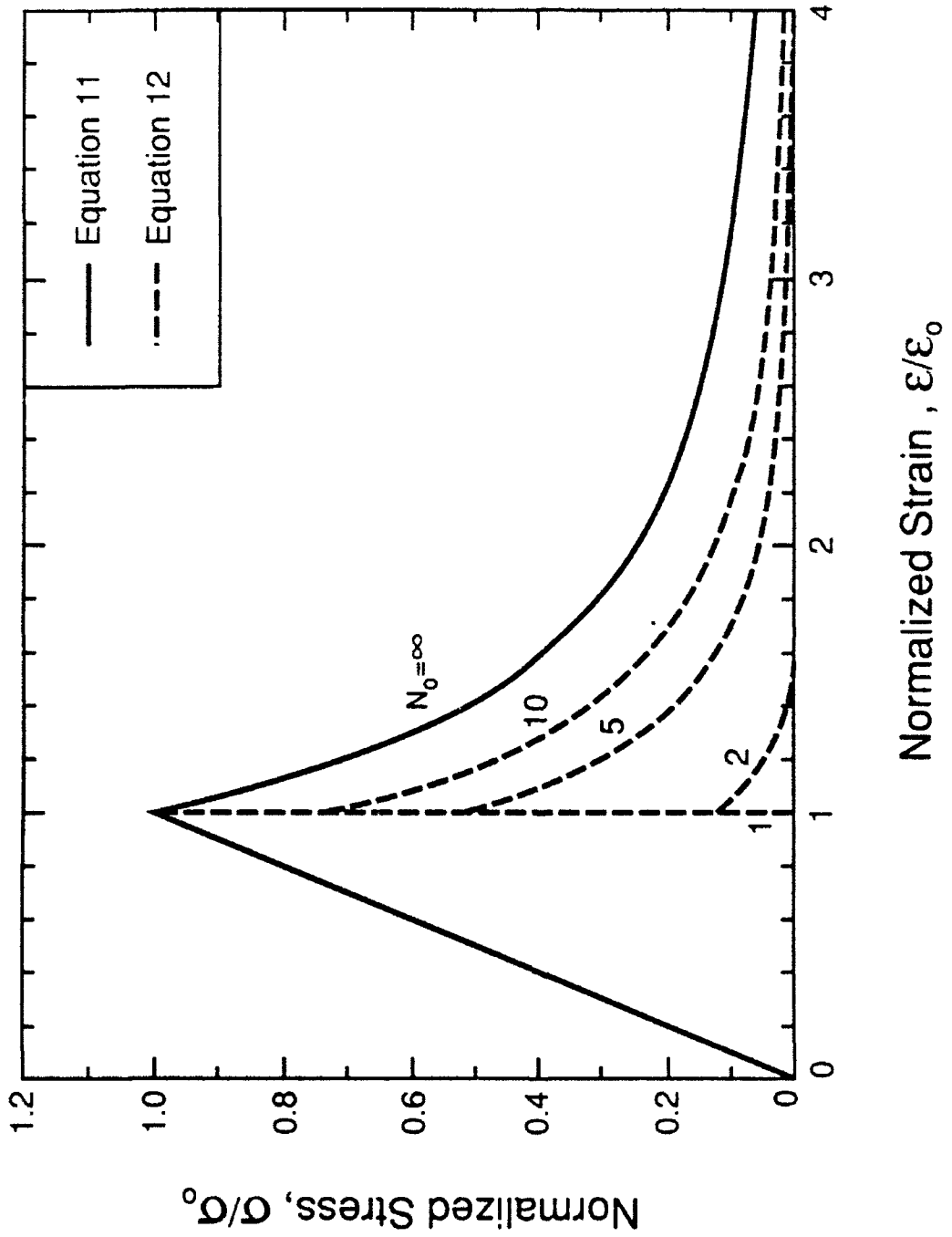
Equation 11
Equation 12
$N_o=\infty$
10
5
2
1
Normalized Stress, σ/σ_o
Normalized Strain, $\varepsilon/\varepsilon_o$
0
0.2
0.4
0.6
0.8
1.0
1.2
0
1
2
3
4

Fig. 2

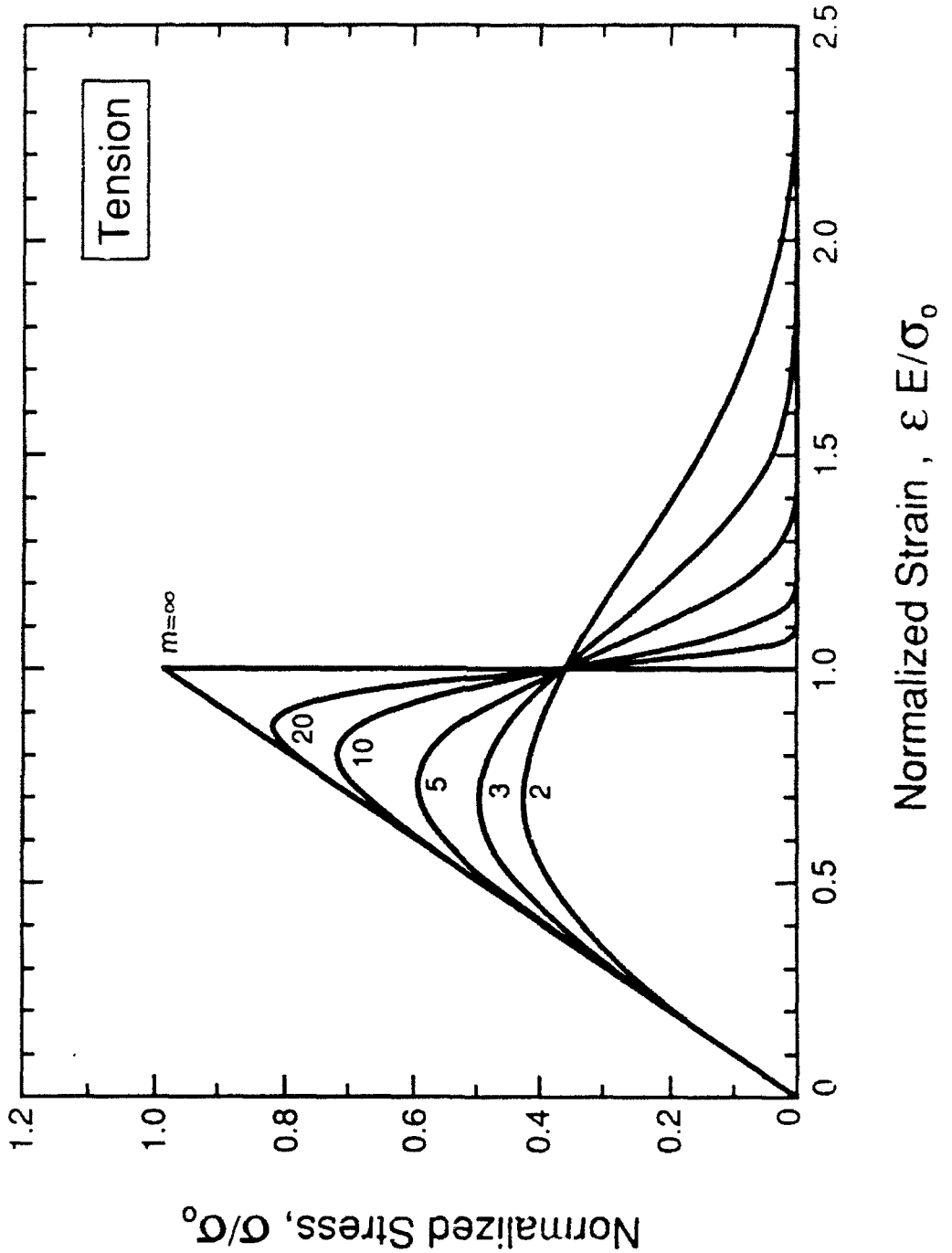
Tension
m=∞
20
10
5
3
2
Normalized Stress, σ/σ$_o$
Normalized Strain , ε E/σ$_o$
0
0.2
0.4
0.6
0.8
1.0
1.2
0.5
1.0
1.5
2.0
2.5

Fig. 3a

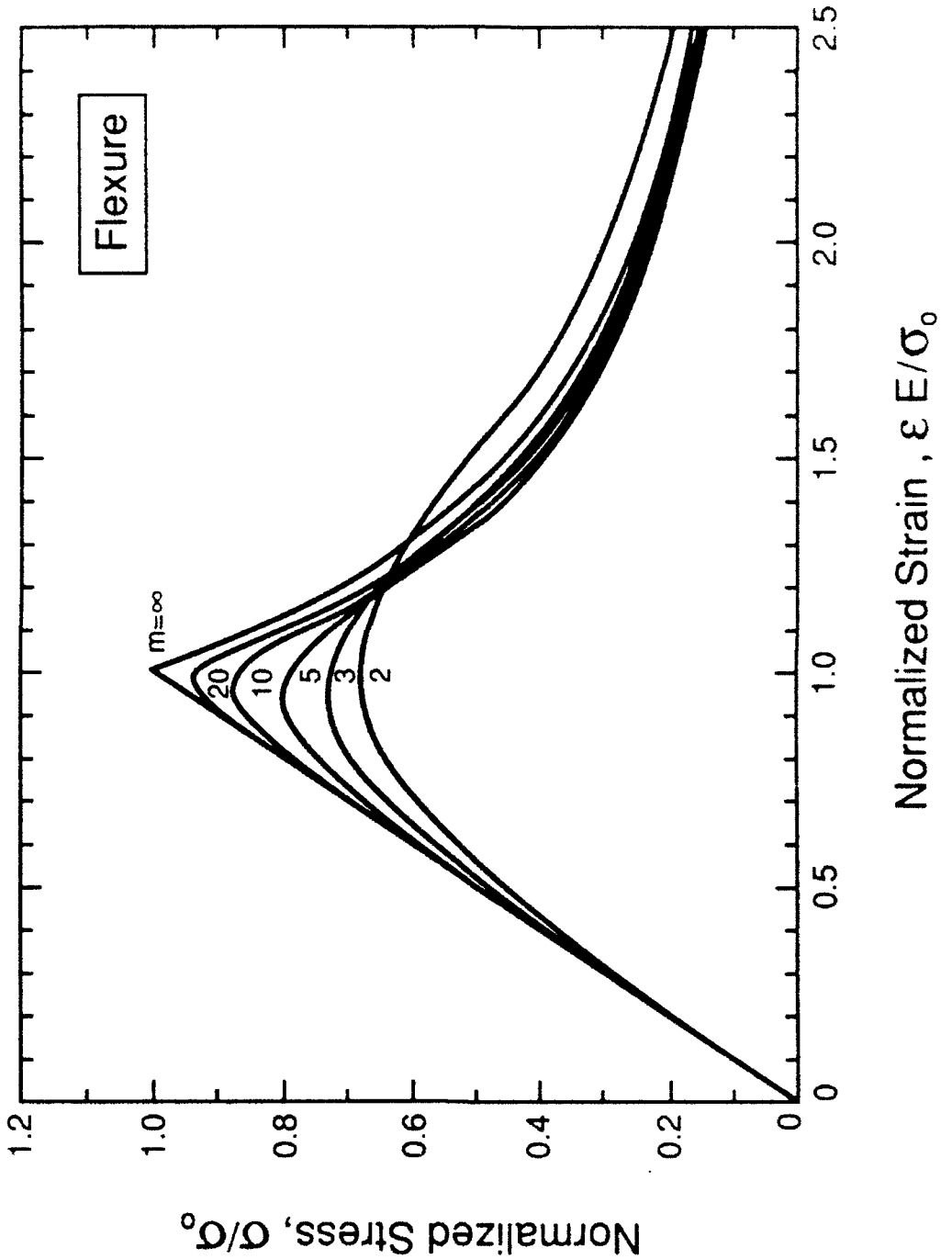
Flexure
m=∞
20
10
5
3
2
Normalized Stress, σ/σ$_o$
Normalized Strain , ε E/σ$_o$
0
0.2
0.4
0.6
0.8
1.0
1.2
0.5
1.0
1.5
2.0
2.5

Fig. 3b

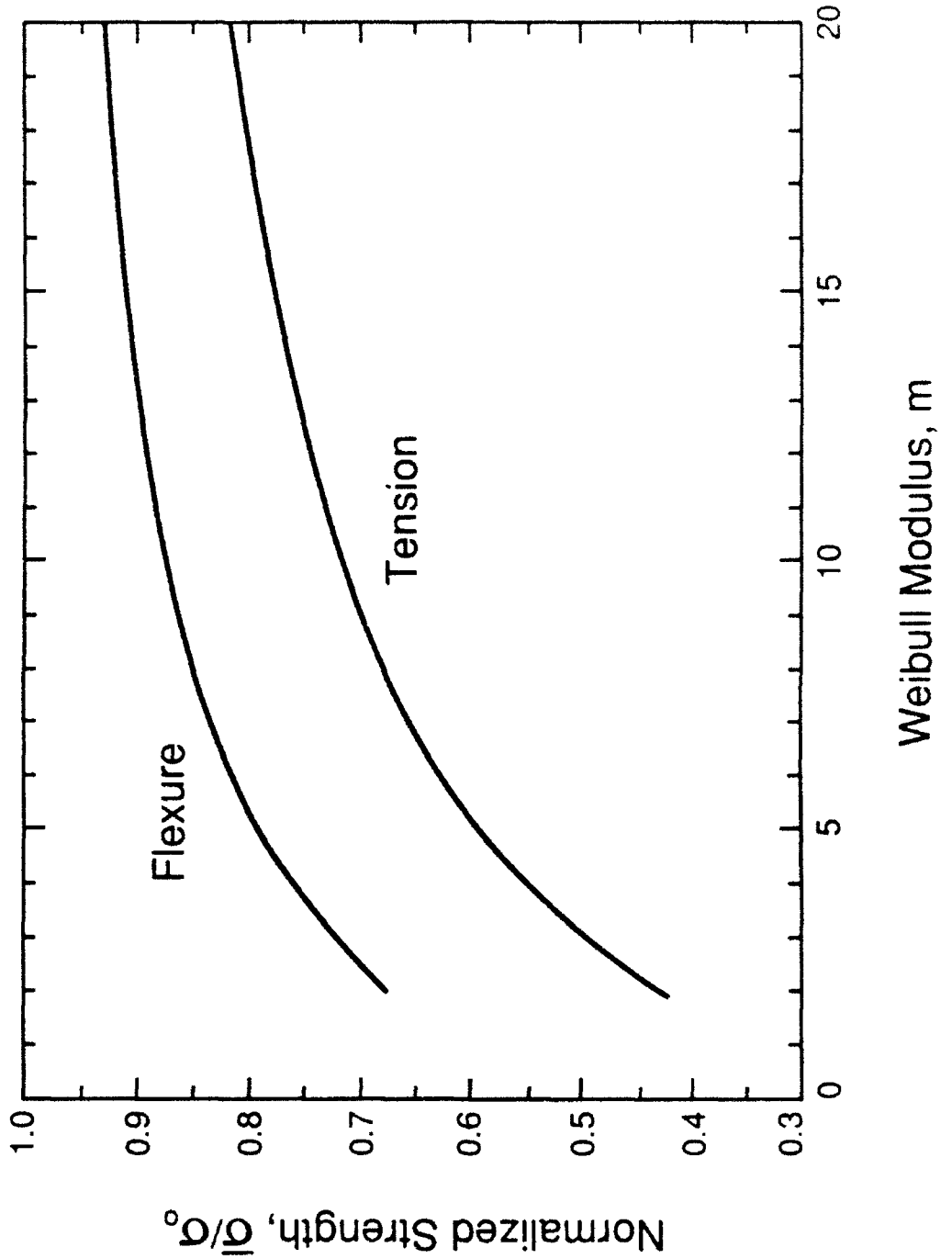
Normalized Strength, $\bar{\sigma}/\sigma_o$
1.0
0.9
0.8
0.7
0.6
0.5
0.4
0.3
Flexure
Tension
0
5
10
15
20
Weibull Modulus, m

Fig. 4

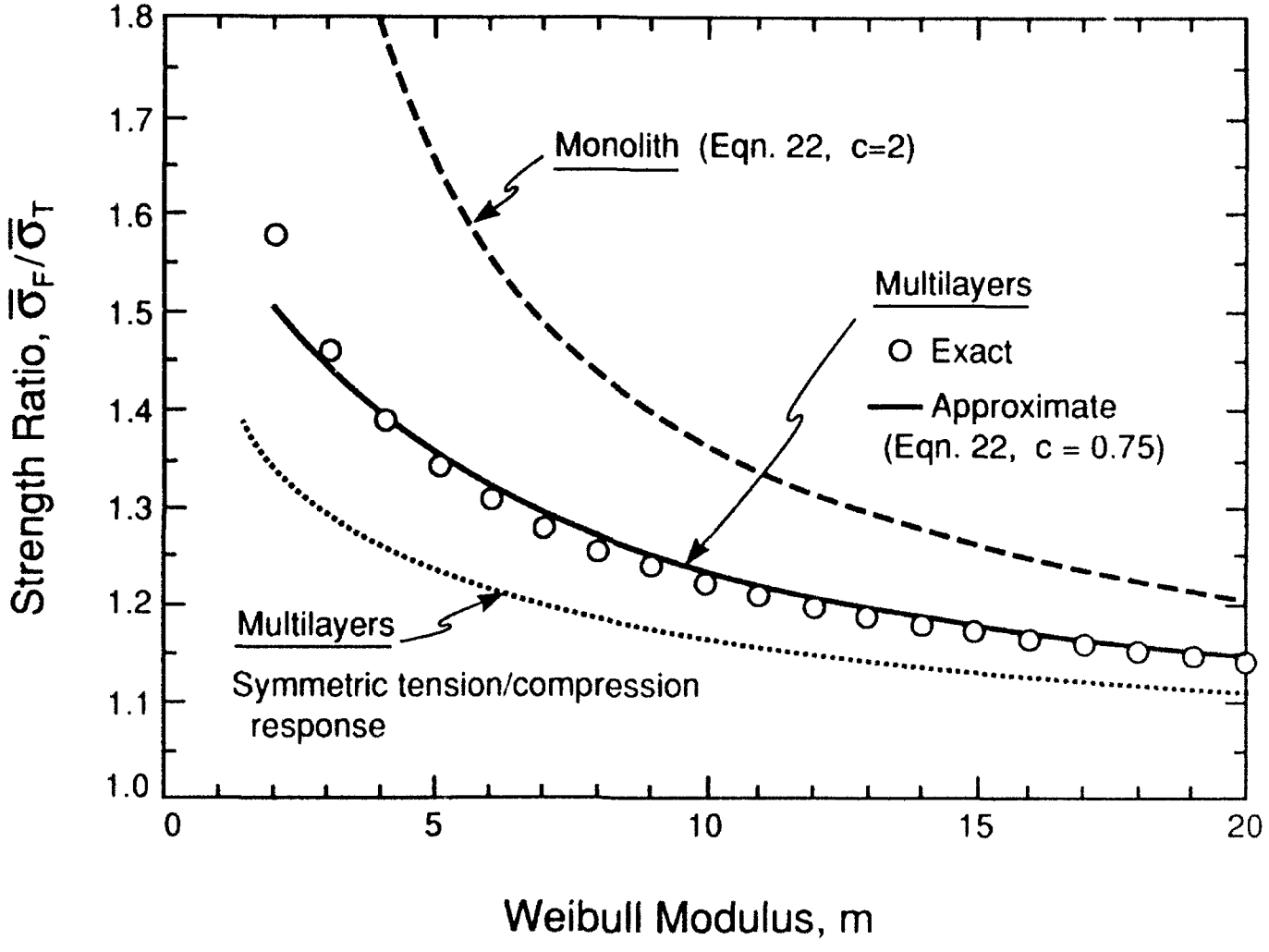
Strength Ratio, $\overline{\sigma}_F/\overline{\sigma}_T$
1.8
1.7
1.6
1.5
1.4
1.3
1.2
1.1
1.0
0
5
10
15
20
Weibull Modulus, m
Monolith (Eqn. 22, c=2)
Multilayers
O Exact
— Approximate
(Eqn. 22, c = 0.75)
Multilayers
Symmetric tension/compression
response

FIG. 5

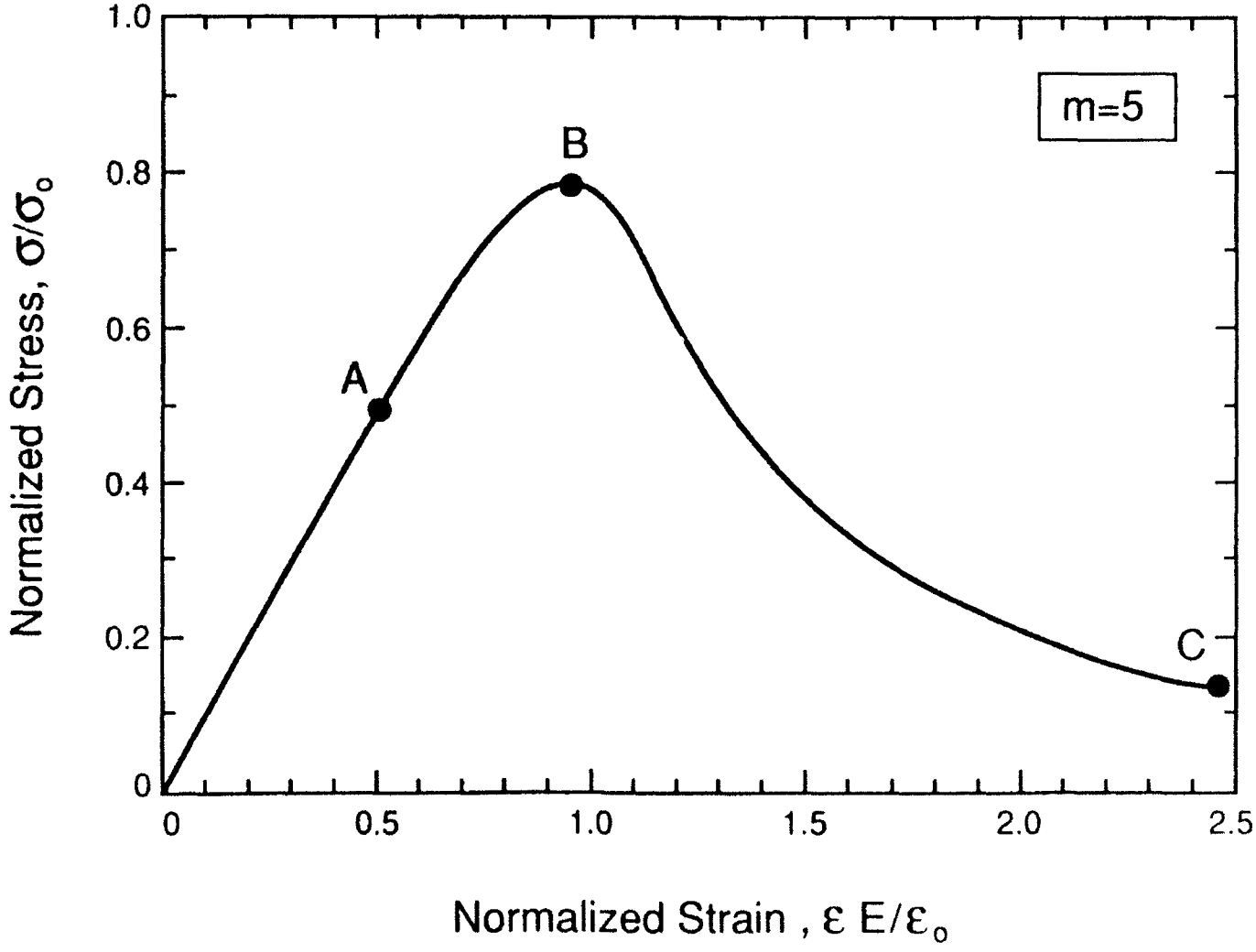
m=5
A
B
C
Normalized Stress, σ/σ₀
Normalized Strain , ε E/ε₀
0
0.2
0.4
0.6
0.8
1.0
0
0.5
1.0
1.5
2.0
2.5

Fig. 6a

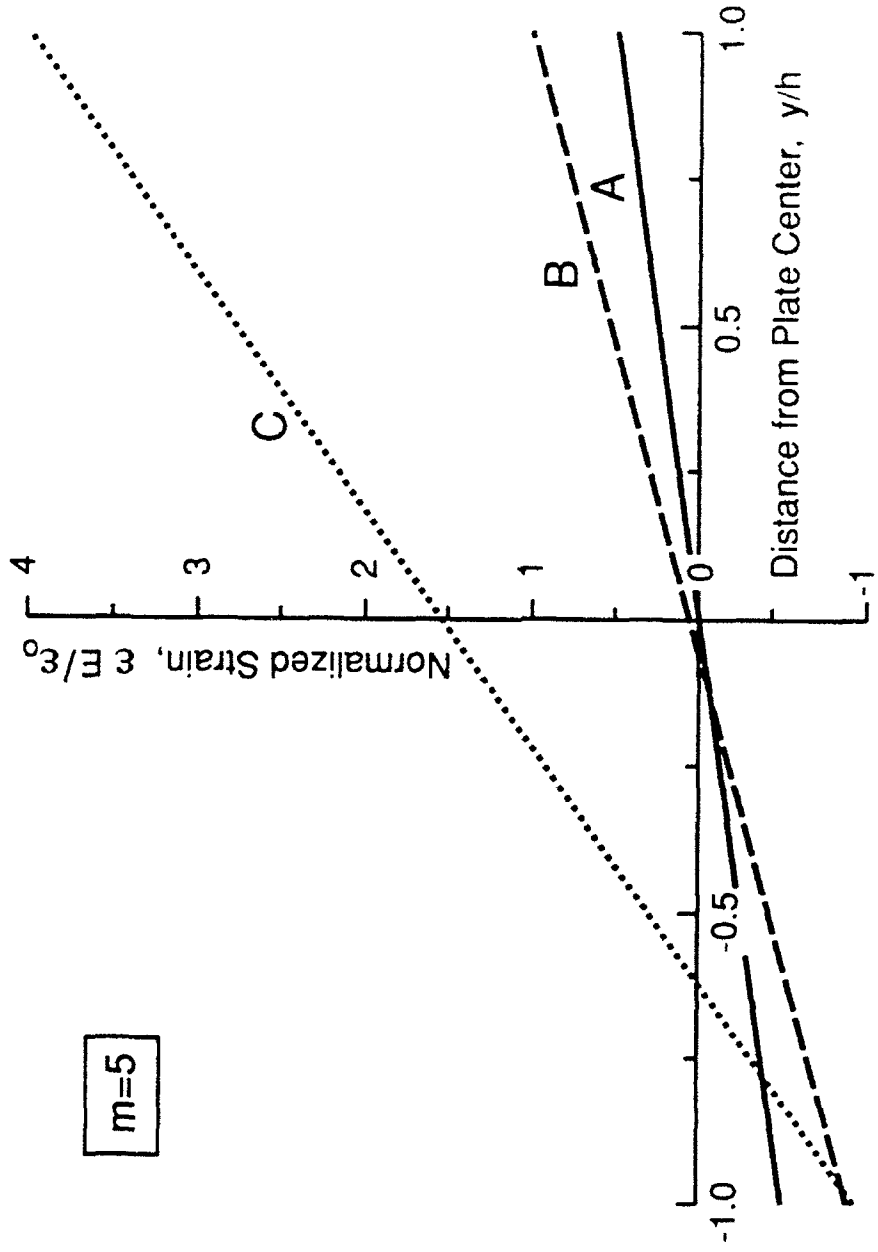
m=5
Normalized Strain, ε E/ε$_o$
4
3
2
1
0
-1
-1.0
-0.5
0.5
1.0
Distance from Plate Center, y/h
A
B
C

Fig. 6b

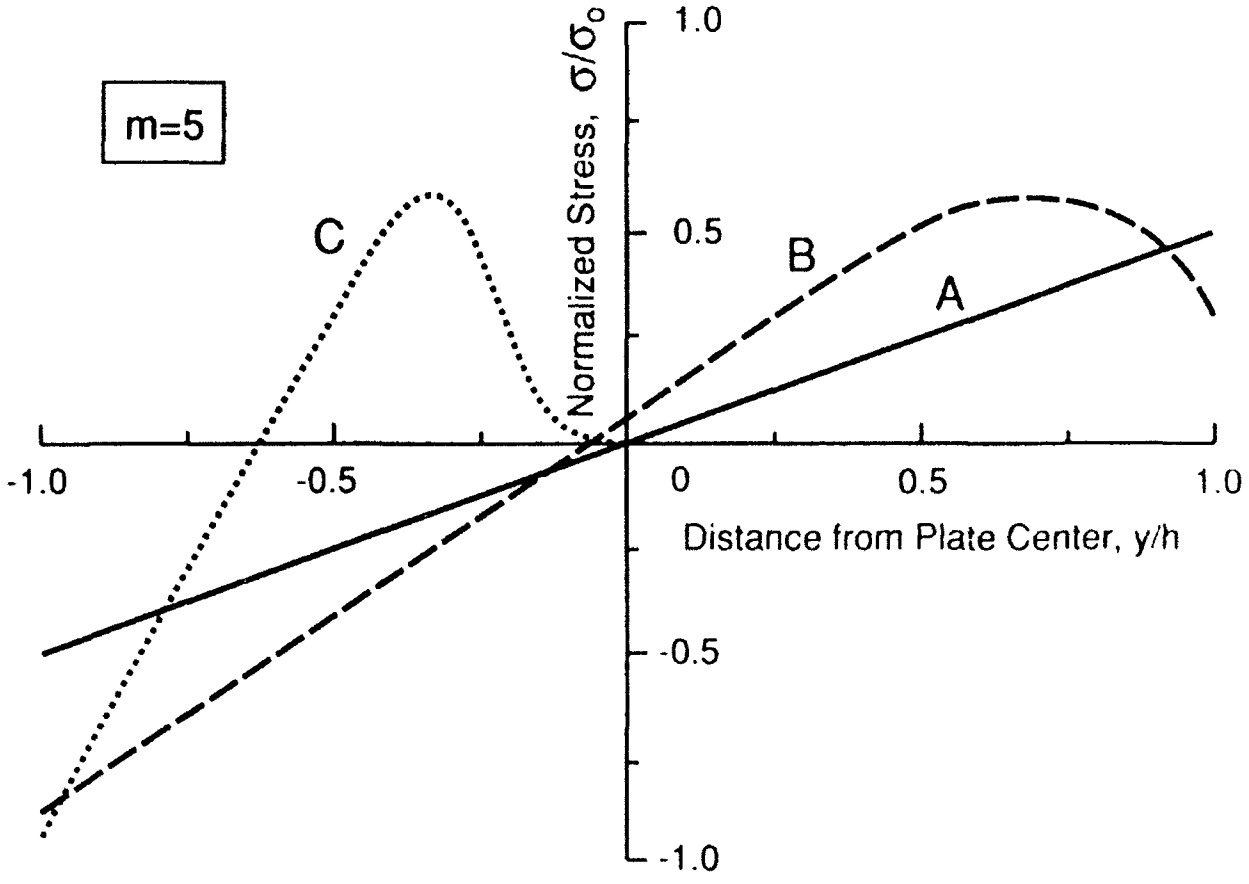
m=5
C
B
A
Normalized Stress, σ/σ_o
1.0
0.5
-0.5
-1.0
-1.0
-0.5
0
0.5
1.0
Distance from Plate Center, y/h

Fig. 6c

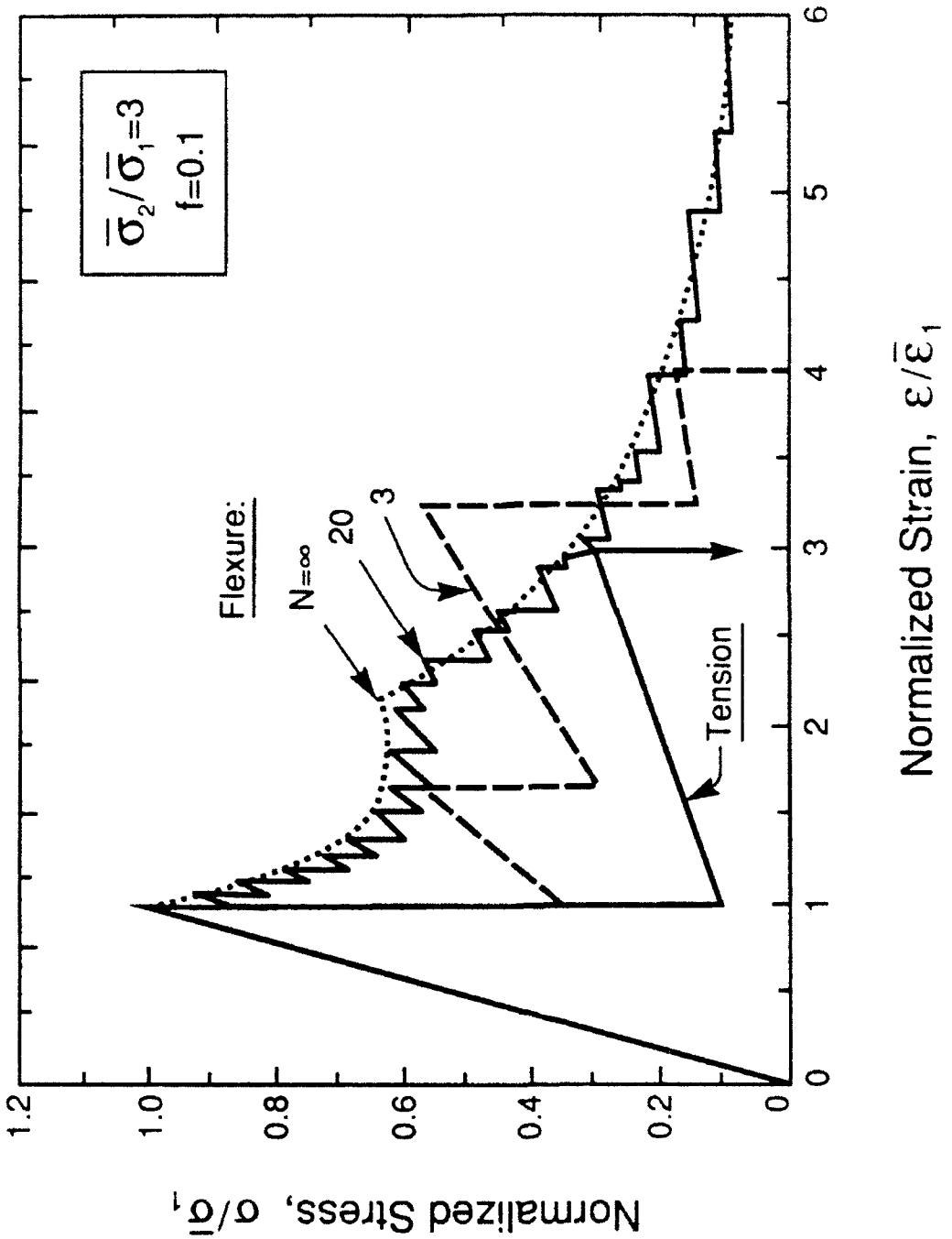
$\bar{\sigma}_2/\bar{\sigma}_1$=3
f=0.1
Flexure:
N=∞
20
3
Tension
Normalized Stress, $\sigma/\bar{\sigma}_1$
Normalized Strain, $\varepsilon/\bar{\varepsilon}_1$
0
0.2
0.4
0.6
0.8
1.0
1.2
1
2
3
4
5
6

Fig. 7a

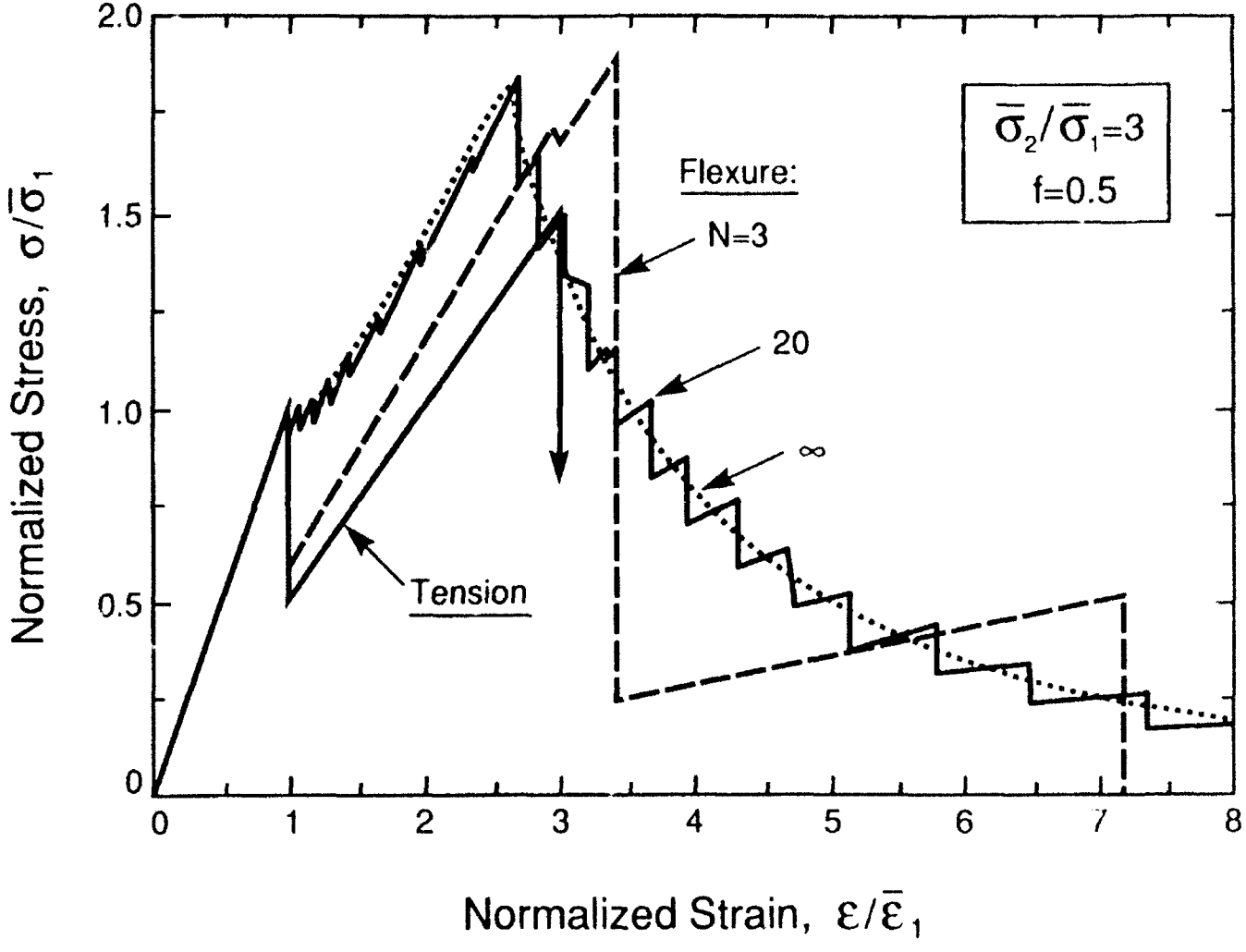
2.0
1.5
1.0
0.5
0
0
1
2
3
4
5
6
7
8
Normalized Stress, $\sigma/\bar{\sigma}_1$
Normalized Strain, $\varepsilon/\bar{\varepsilon}_1$
$\bar{\sigma}_2/\bar{\sigma}_1$=3
f=0.5
Flexure:
N=3
20
∞
Tension

Fig. 7b

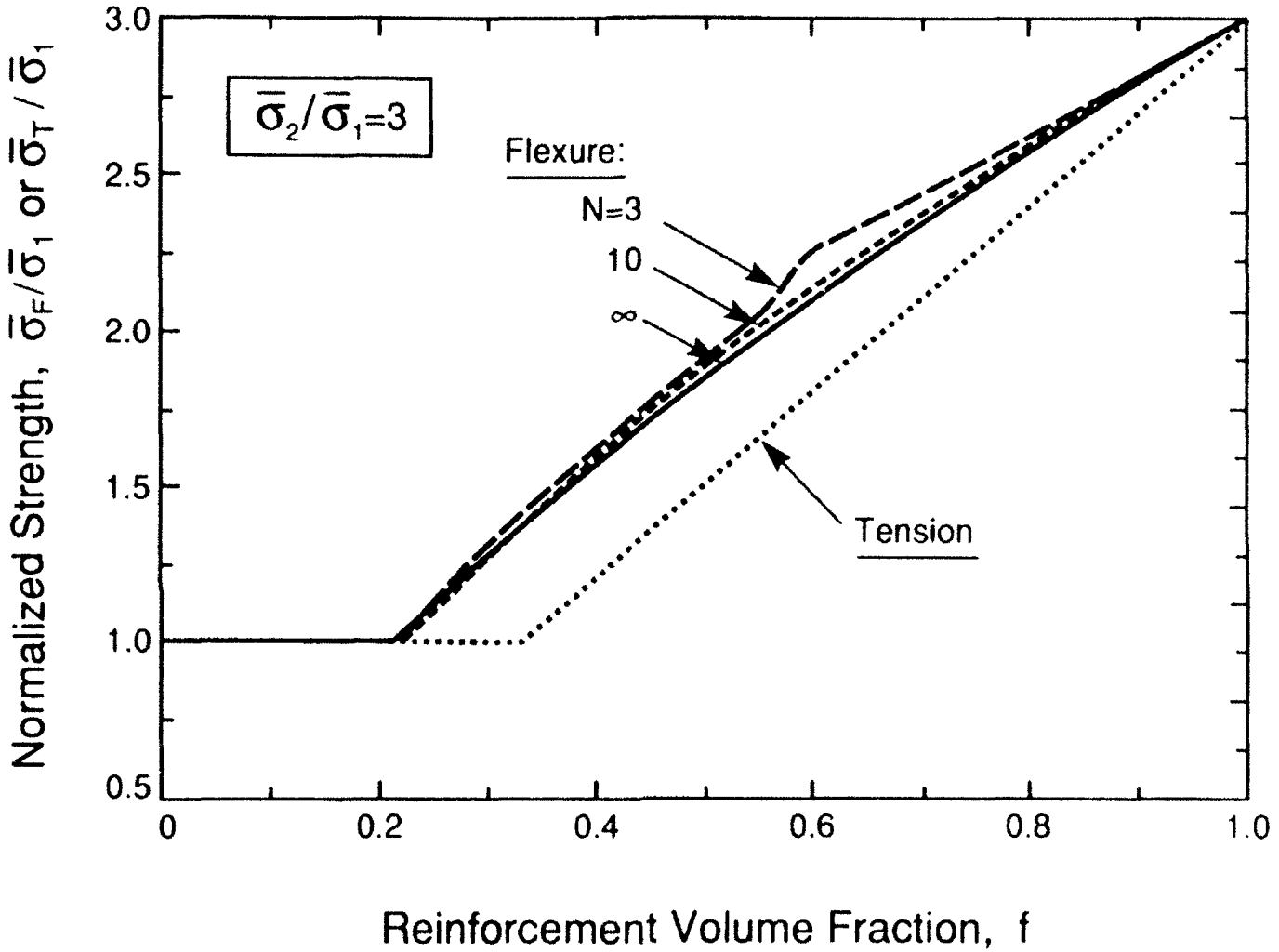
$\bar{\sigma}_2/\bar{\sigma}_1$=3
Flexure:
N=3
10
∞
Tension
Normalized Strength, $\bar{\sigma}_F/\bar{\sigma}_1$ or $\bar{\sigma}_T/\bar{\sigma}_1$
Reinforcement Volume Fraction, f
3.0
2.5
2.0
1.5
1.0
0.5
0
0.2
0.4
0.6
0.8
1.0

Fig. 8a

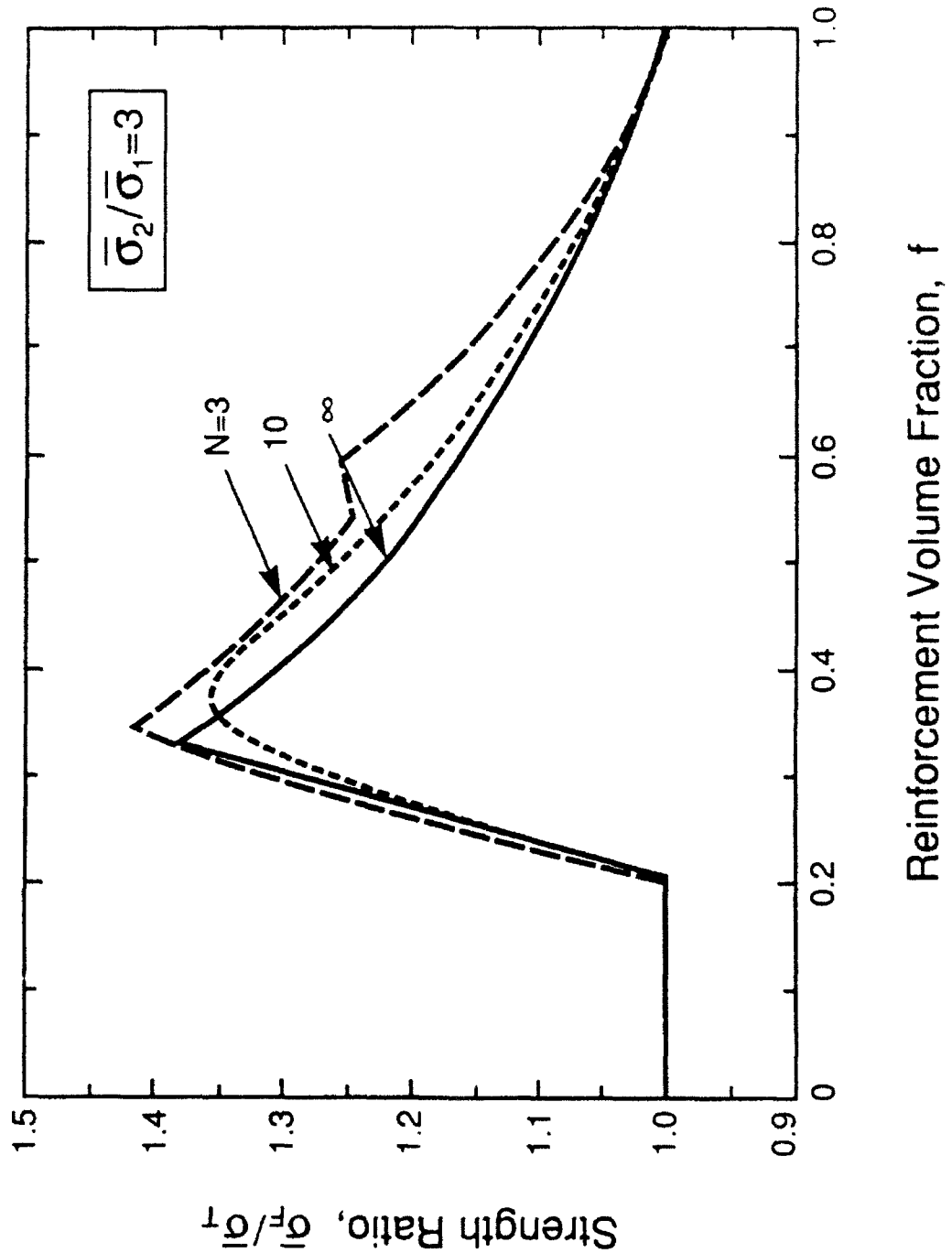
Strength Ratio, $\bar{\sigma}_f/\bar{\sigma}_t$
Reinforcement Volume Fraction, f
$\bar{\sigma}_2/\bar{\sigma}_1=3$
N=3
10
∞
1.5
1.4
1.3
1.2
1.1
1.0
0.9
0
0.2
0.4
0.6
0.8
1.0

Fig. 8b

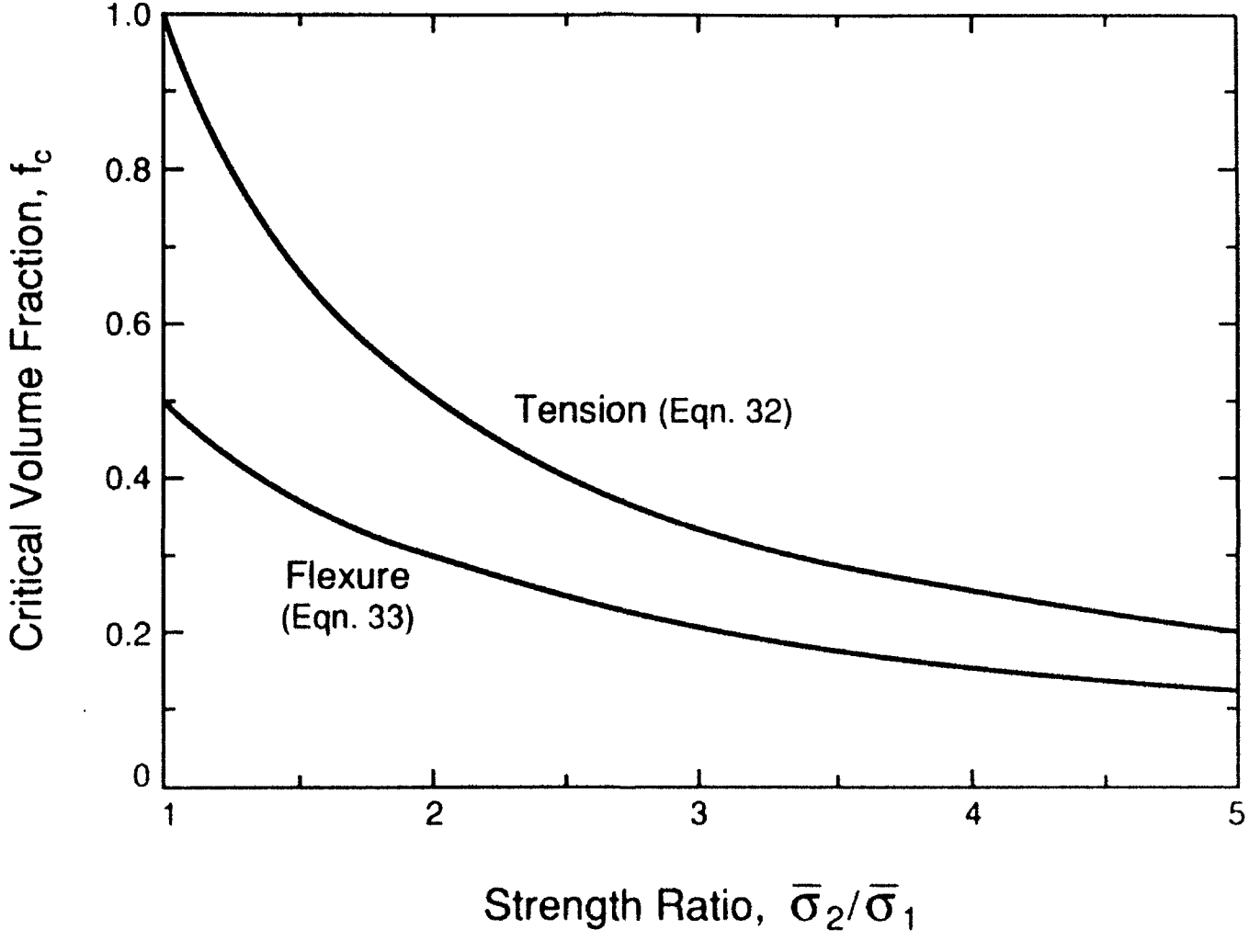
Critical Volume Fraction, f_c
1.0
0.8
0.6
0.4
0.2
0
Tension (Eqn. 32)
Flexure
(Eqn. 33)
1
2
3
4
5
Strength Ratio, $\bar{\sigma}_2/\bar{\sigma}_1$

Fig. 9

MATERIALS

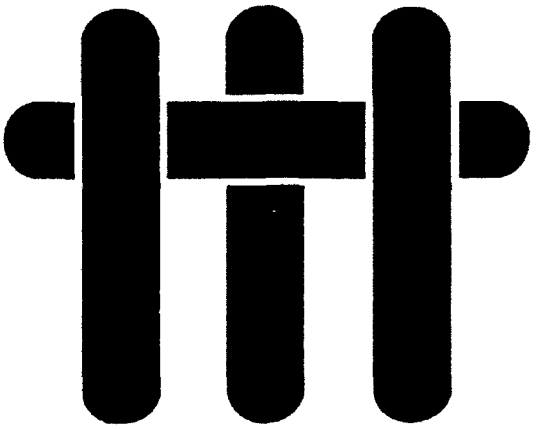

THE CREEP BEHAVIOR OF CAS/NICALON CONTINUOUS-FIBER COMPOSITES

by

C.H. Weber, J.P.A. Löfvander and A.G. Evans
Materials Department
College of Engineering
University of California
Santa Barbara, California 93106–5050

Submitted to the Journal of the American Ceramic Society.

ABSTRACT

Nicalon fibers are found to provide substantial axial creep strengthening of CAS at 1200°C. The axial creep is transient in nature, caused by a strength enhancement of the fibers, attributed to grain growth at elevated temperatures. This, in turn, results in reduced diffusional creep. The transverse creep properties are dominated by the matrix, resulting in considerable anistropy. This anisotropy leads to severe distortion when off-axis loading arises. Residual stresses develop upon unloading after creep, and cause superficial matrix cracking.

1. INTRODUCTION

Ceramic matrix composites are expected to have a key role in achieving the performance goals of the next generation of advanced aircraft. The intrinsic ceramic properties of high refractoriness, good oxidation resistance and low density have been motivating the development of these materials. Much of the recent effort has been expended in overcoming some of the key limitations of ceramic materials, particularly their notch sensitivity. This work has led to the development of ceramic matrix composites (CMCs), using fiber reinforcement as a means of controlling damage and redistributing stresses.[1-3] Critical to the success of this approach is the presence of a fiber coating that provides a "weak" interface.[4,5]

While the low temperature mechanical behavior of ceramic matrix composites is now reasonably well understood,[6-9] much remains to be addressed at high temperatures, where most of the performance benefit is to be obtained. The presence of reinforcing fibers can have additional advantages at such temperatures. In particular, if the fibers are more creep resistant than the matrix, a substantial creep strengthening should be achieved.[10-12] This is expected to be the case for glass ceramics reinforced with silicon carbide fibers. However, the actual creep strengthening will be influenced by several factors. For instance, it is presently unclear whether the presence of a "weak" interface obviates the strengthening effect by allowing debonding and relative sliding between fiber and matrix, at prematurely failed fibers. Furthermore, most currently used fibers are polycrystalline, and rely upon a fine grain size (< 1 μm) to achieve high strength. This fine grain size implies a susceptibility to creep and rupture,[13-15] both of which may limit the useful

temperature of the composite. Composite creep may also be influenced by high temperature microstructural changes occurring in the fibers.[16-18]

Another important factor governing composite behavior is the anisotropy. Unidirectional fiber reinforcement results in optimum creep strengthening in the fiber direction, but at the expense of a diminished transverse strength. In practice, the inferior out-of-plane properties may limit structural integrity. It therefore becomes imperative to understand this anisotropy in detail, in order to guide materials development and ensure reliable engineering design.

In this study, the creep behavior of the calcium aluminosilicate (CAS) system, unidirectionally reinforced with SiC (Nicalon[∞]) fibers, has been investigated.[19] In this material, the presence of a carbon layer at the fiber/matrix interface results in a strong dependence of mechanical properties on the extent of oxidation.[4] Consequently, in order to allow separation of the influence of mechanical loading and environment, creep tests are conducted in inert conditions. The responses to both axial and transverse loads are investigated, as needed to reveal the creep strengthening provided by the fibers, as well as the anisotropy in material response. The creep properties are correlated with changes in the microstructure occurring during the tests.

[∞] Nicalon®

2. EXPERIMENTAL PROCEDURES

2.1 Creep Tests

Creep tests were performed with a hydraulic testing machine in argon (≈ 0.1 MPa) within a furnace having a 2200°C temperature capability. The composites were tested in four-point flexure on beams measuring approximately 3 x 3.5 x 45 mm. A device was constructed which directly and continuously evaluates the (constant) curvature over the inner span by measurement of the displacement Δ (Fig. 1). The maximum tensile creep strain rate ε is then given rigorously by[20]

$$\varepsilon = h\Delta/\left(\Delta^2 + s^2\right) \qquad (1)$$

where h is the beam thickness and s the span. The device allows strain measurements accurate to within ∓0.01%, and a resolution of ∓0.0005%. Subsequent numerical treatment of the data then yields the corresponding strain rate behavior.

The stresses that develop in the composite relate to the applied moment through the longitudinal constitutive properties of the composite. Determining exact values for the stress during flexural creep is not straightforward. Procedures used in this study are described in Appendix I.

This test system was also adapted for compressive creep measurements. In this case, the outer two gauging rods (Fig. 1) contacted the top loading plate and the central gauging rod, attached to the LVDT, contacted a creep resistant SiC platen directly under the specimen. Deformation of the specimen was measured from the

relative displacement of the inner and outer gauging rods, from which the strain can be determined directly.

2.2 Characterisation Techniques

Specimens for scanning electron microscopy (SEM) were prepared using standard metallographic techniques. Carbon-coated samples were examined in JEOL SM 848 SEM in secondary mode. The microscope was equipped with a Tracor Northern TN 5500 analysis system.

For transmission electron microscopy (TEM) chracterization, samples prepared by ion milling were examined at 200kV in a JEOL 2000FX TEM equipped with a LINK eXL high take-off angle energy dispersive spectroscopy system. Computer simulations and indexing of selected area diffraction (SAD) patterns were facilitated by the Desktop Microsopist software package (Virtual Labs, Ukiah, CA 95482). TEM of the composite after creep was impeded by crumbling of the matrix during foil preparation. The following, alternative, procedure was thus used to obtain samples of fibers. Wafers, approximately 2.5 mm square and 300 μm thick, were cut using a slow speed diamond wafering blade, with the fiber orientation in the plane of the wafer. These wafers were then soaked in concentrated hydroflouric acid for about 3 minutes to remove most of the matrix, leaving the intact fibers behind. These fibers were then extracted using a tweezers, mounted on a copper grid and ion milled prior to TEM analysis.

3. MATERIAL

The composite investigated in the present study is a calcium-alumino-silicate (CAS) glass ceramic, unidirectionally reinforced with continuous (Nicalon) silicon carbide fibers.[19] These composites were produced by passing tows of fibers through a liquid slurry containing fine particles of the matrix in suspension. The tows were subsequently dried, stacked unidirectionally, and consolidated by hot-pressing. The resulting material comprises 16 plies, with an average fiber volume fraction ($f \approx 0.4$), although local variations are evident (Fig. 2). The composite is produced as a flat plate, with a glass-rich surface layer[8,19]. During testing, this layer constitutes the outer surface of the side faces and may protect the composite from attack by residual oxygen in the test environment.

TEM characterisation revealed that the CAS matrix consists of Anorthite with a grain size $\leq$ 1 μm. Substantial twinning (≈ 20 nm width) was evident throughout the matrix in the as-received state. Very fine (≈ 20 nm) precipitates, probably zirconia, were detected within the CAS grains. The fiber/matrix interface consisted of a 300Å thick carbon layer (Fig. 3a), identified by means of scanning EELS micrographs, recorded with the characteristic energy loss for carbon (Fig. 3b). SEM analysis revealed the presence of occasional brittle matrix cracks, perpendicular to the fiber/matrix interface. Electron diffraction analysis of the fibers revealed a characteristic ring pattern, representative of β-SiC with a very fine grain size. Dark-field imaging established a grain size, d ≈ 1-3 nm.

4. RESULTS

4.1 Creep Rates

Flexural creep experiments were conducted at 1200°C, between 50 to 150 MPa, with fibers oriented along the length of the sample, in order to obtain the *uniaxial* creep rates summarized in Fig. 4. The total (outer fiber) strains during testing were limited to ~ 1%. It is apparent that the strain-rate is fully transient, at all applied stresses, indicative of continuous creep strengthening (with accumulating strain).

To determine the effect of loading history on the creep rate, two tests were conducted at the same nominal stress, but with one periodically interrupted, (Fig. 5). To prevent recovery effects,[21] the sample was cooled rapidly during interruption. The strain was then measured from the beam curvature at room temperaure. The results demonstrate the history insensitivity of the composite creep.

Transverse *compressive* creep data obtained at 1200°C are presented in Fig. 6. In contrast to the axial response, the transverse behavior is characterized by a minimum, (apparent steady-state), deformation-rate, preceeded by an initial transient. The steady-state behavior can be characterised by a power-law, with a power law exponent, $m \approx 2.4$. A comparison of the axial and transverse creep-rate at 50 and 75 MPa (Fig. 7), provides direct evidence that creep strengthening is achieved using Nicalon fibers.

An alternative demonstration of the creep anisotropy is provided by the cross-sectional profiles of crept flexural samples (Fig. 8). The ratio λ of peak shear stress between the inner and outer loading points to peak tensile stress in the midspan is typically low (≤ 0.1)¶ , so that in isotropic beams the effect of shear

¶ $\lambda = 2(L - \ell)/h$, for elastic or linearly creeping fibers.

deformation can usually be neglected. However, the relatively poor creep strength of unidirectional fiber composites in shear results in shear deformations substantially higher than those caused by bending.

4.2 Observations

Scanning electron microscopy conducted on the crept samples provided information about microstructural damage upon transverse and axial loading. At small strains (≤1%), there was no apparent *matrix* damage: The absence of matrix cracks in axially loaded specimens, at the stress level used in these tests (maximum of 150 MPa), is consistent with earlier studies conducted at room temperature.[8] However, cracks *were* found in the glass-ceramic *coating*, on those sides that had been subject to compression during creep (Fig. 9). The occurrence of such cracks implies the presence of a *residual tension* after cooling and unloading (Appendix II). Cracking was more prevalent at higher loads.

At larger strains (1-5%) *transverse* damage was apparent in the matrix, manifest as voids that emanate from interface separations, at fiber segments perpendicular to the loading axis (Fig. 10). Additional damage was evident at the contact points between neighboring fibers, often associated with fiber fractures. At even larger deformations (≥5%) interface voids and cracks coalesced on a plane between the centers of neighboring fibers. This damage concentrated along well defined bands. Failure typically occurred along the principal shear stress plane.

TEM revealed significant *microstructural* changes in the fibers (Fig. 11). A well-defined outer shell formed within which substantial grain growth had occurred ($d \approx 10 - 15$ nm) and an inner core in which the grain size remained unaltered ($d \approx 1 - 3$ nm), (Fig. 12), consistent with other studies.[18] The extent of the

large grained regions increased with time at temperature. These regions were associated with enhanced levels of Fe, which may be a grain growth promoter[22], while similar observations in unincorporated fibers have suggested the non-stoichiometric nature of the fiber to be responsible.[18] More precise determinations of the kinetics of grain growth and shell evolution are in progress.

5. DISCUSSION

Information about the creep properties of the *matrix* can be obtained from the data obtained in transverse compression (Fig. 6). In the steady-state range the power law for the matrix should be the same as that for the composite [23,24](m = 2.4), in the absence of significant matrix damage. Furthermore, the reference stresses should be related by[23,24]

$$\sigma_{mo} = \beta(f,m)\sigma_{co} \qquad (2)$$

where σ_{mo} refers to the matrix and σ_{co} to the composite: β is a coeffecient that has been calculated for perfectly bonded interfaces[23,24], with f being the fiber volume fraction. For the present composite (with m = 2.4 and f = 0.4) the calculations give $\beta = 0.7$. Consequently, the data of Fig. 6 can be related to the matrix creep properties by means of a reference stress conversion, (given by Eq. 2 with $\beta = 0.7$), obtaining $\sigma_{mo} = 0.7$ MPa and $\dot{\varepsilon}_{mo} = 4.0\times10^{-11}$ s^{-1}. This conversion is strictly applicable only in steady-state and at small strains, prior to matrix damage.

The axial data are dominated by the fibers (Fig. 7). The lack of significant fiber fracture at small strains suggests that a 'rule-of-mixtures' law may be used to

interpret these data. The following procedure is used for this purpose. First, the matrix creep data is obtained from transverse compression, as described above. A beam analysis then yields the fraction of the moment borne by the fibers (Appendix I). This procedure reveals that, for t > 5 h, essentially all of the creep strength is associated with the fibers. Furthermore, the transient nature of the creep arises because of microstructural changes within the fibers (Figs. 11,12). The most important of these appears to be grain growth, which is expected to be time dependent. Consequently, by using *time* as an independant variable (rather than strain), it is found that the axial creep data can be uniquely correlated (Fig. 13). For t > 1 h, the associated constitutive law closely approaches the form

$$\dot{\varepsilon} / \dot{\varepsilon}_{co} = \eta(\sigma / \sigma_{co})^{n}(t / \tau)^{\alpha} \qquad (3)$$

with $n \approx 1$, $\eta = 1$§, $\tau = 5.5 \times 10^{-6}$ s and $\alpha \approx -0.9$ ($\sigma_{co} = 1$ MPa, $\dot{\varepsilon}_{co}=1/s$). Finally, the extent and magnitude of the grain growth is found to be consistent with the observed level of creep strengthening (Appendix III). This interpretation is also consistent with a stress exponent, n=1, characteristic of diffusional creep.[14]

The cracking of the coating on the compressive side of the flexural specimens after unloading is associated with the development of *residual tensile stresses* (Appendix II). Such cracking may be important in causing exposure of the fibers to environmental attack. The peak value of the residual stress is expected to be proportional to the magnitude of the applied stress during creep (Appendix II), consistent with the greater tendency for such cracking at larger stresses, as well as being dependant on the creep properties and volume fraction of fibers (see Fig. B1)

§ The *fiber* constitutive law is obtained by setting $\eta = f$.

For the present material, since the fibers carry most of the load during creep, the residual stresses approach $\approx 0.7\sigma_e$, where σ_e is the elastic stress. Cracking of the *coating* under these levels of residual tension is consistent with measurements made in other studies.[8]

6. CONCLUDING REMARKS

The present study has demonstrated the beneficial effect of fibers on the longitudinal creep behavior of calcium aluminosilicate (CAS) glass ceramics. Time-dependent microstructural changes in the fibers have been shown to result in long-term creep hardening of the composite. However, the transverse creep-rates are large and can cause extensive distortion with off-axis loadings. In addition, it has been demonstrated that residual stresses resulting from non-linear creep can damage the composite upon cooling and may degrade its subsequent structural integrity.

ACKNOWLEDGEMENTS

Thanks are expressed to Dr. Ken Chung of Corning Inc. for supplying the material and to Dr. Joachim Mayer of the Max-Planck Institute, Stuttgart, Germany for the scanning EELS image of the CAS/Nicalon interface

APPENDIX I
Stress Redistribution in a Creeping Beam

In a beam subject to elastic bending, the maximum tensile and compressive stresses, σ_e, are

$$\sigma_e = (3/2)\left\{P(L-\ell)/bh^2\right\} \tag{A1}$$

where L and ℓ are the length of the outer span and inner span, respectively, P the load and b the beam width. When the *entire body* is subject to power law (steady-state) creep, with the strain-rate, $\dot{\varepsilon}$, characterized by,

$$\dot{\varepsilon} = \dot{\varepsilon}_o(\sigma/\sigma_o)^n \tag{A2}$$

where σ_o is a reference stress, $\dot{\varepsilon}_o$ a reference strain-rate and n the power law exponent, the maximum stress $\hat{\sigma}$ in the flexural specimen is

$$\hat{\sigma}/\sigma_e = (2n+1)/3n \tag{A3}$$

The corresponding stress distribution is[25]

$$\frac{\sigma(y)}{\sigma_e} = \left(\frac{2n+1}{3n}\right)\left(\frac{2y}{h}\right)^{1/n} \tag{A4}$$

where y is the distance from the neutral axis.

In creeping *composite* beams, when the fibers have a higher creep strength than the matrix, account must be taken of the redistribution in moment from the matrix to the fibers. To address this phenomenon both matrix and fibers are assumed to follow power-law creep behavior, with power-law exponents m and n respectively, and material response is assumed equal in tension and compression. In the absence of fiber fracture, the strain-rate in the fibers and matrix are equal. Inserting this strain-rate equality into Eqs. (A2) and (A4), the following relationship is obtained.

$$\frac{\xi^n}{(1-\xi)^m} = \chi\left[\frac{f^n}{(1-f)^m}\right]\sigma_e^{m-n}\left(\frac{2m+1}{3m}\right)^m \Big/ \left(\frac{2n+1}{3n}\right)^n \qquad \text{(A5)}$$

The strain rate ratio, $\chi = [\dot{\varepsilon}_{mo}\sigma_{fo}^n / \dot{\varepsilon}_{fo}\sigma_{mo}^m]$, where the reference stress and strain-rate subscripts correspond to the matrix and fiber. This equation must be solved iteratively to obtain the fraction ξ of applied moment carried by the fibers. Inserting ξ into Eq. (A4) maximum stress in the matrix and fibers during creep is obtained as

$$\frac{\hat{\sigma}_m}{\sigma_e} = \left(\frac{2m+1}{3m}\right)\frac{(1-\xi)}{(1-f)} \qquad \text{(A6)}$$

and

$$\frac{\hat{\sigma}_f}{\sigma_e} = \left(\frac{2m+1}{3m}\right)\frac{\xi}{(1-f)} \qquad \text{(A7)}$$

respectively. The equivalent result for the composite is

$$\frac{\hat{\sigma}_c}{\sigma_e} = \left(\frac{2n+1}{3n}\right)\xi + \left(\frac{2m+1}{3m}\right)(1-\xi) \qquad \text{(A8)}$$

For CAS/Nicalon, the strain rate ratio, χ, is time dependant because of the creep hardening behaviour of the fibers. Provided most of the load is carried by the fibers, this time dependance may be obtained from the axial data, and expressed as

$$\dot{\varepsilon}_{fo} = f\dot{\varepsilon}_{co}\varphi(t/\tau) \qquad \text{(A9)}$$

where $\varphi(t/\tau)$ is a function of time (σ_{fo} = 1 MPa, n = 1). Values for $\dot{\varepsilon}_{fo}$ obtained from Fig. 13 are used to determine the variation in χ throughout the test. For t > 1 h the time dependance of χ can be described by $\varphi(t/\tau) = (t/\tau)^{\alpha}$, (Eq. 3). Trends in ξ and $\hat{\sigma}/\sigma_e$ during the test can then be computed using data relevant for CAS/Nicalon: Plots for accumulated test times of 1 - 70 h (corresponding to strain rate ratios of order 1.6×10^{-10} - 6.5×10^{-9}) and $f \approx 0.4$ show that, except during the early stages of creep, most (>90%) of the load is indeed carried by the fibers (Fig. A1), thus supporting the validity of the assumption made in Eq. A9. Consequently, as $\hat{\sigma} \approx \sigma_e$, the elastic formula (Eq. A1) is used to evaluate the stress presented in the figures.

APPENDIX II
Residual Stresses

Creep resistant fibers cause the matrix stress levels to approach zero. Cooling followed elastic unloading causes the matrix stress to change by an amount $\Delta\sigma_m$, dictated by the relative moduli of the matrix and the fiber:

$$\Delta\sigma_m = \sigma_e\left[(1-f)+\frac{E_f}{E_m}f\right]^{-1} \qquad \text{(B1)}$$

Conseqently, residual tensile stresses may ocur in those regions of the matrix initially subjected to compression. The magnitude of the residual stress depends on the relative creep behavior of fiber and matrix. Typical result are plotted in Fig. B1.

APPENDIX III
Creep Properties of Fibers

Fine-grained polycrystalline ceramics often creep in accordance with a steady-state law,[14]

$$\dot{\varepsilon} / \dot{\varepsilon}_o = (\sigma / \sigma_o)^n \left(\Omega^{2/3} / d\right)^\beta \qquad \text{(C1)}$$

where Ω is the atomic volume, d is the grain size and β a coeffecient in the range 2-3 and n is in the range 1-2.

Based on the present microstructural observations (Fig. 11) the fiber is treated as two concentric cylinders, the outer defined by a grain size d_f and the inner by a grain size d_i. The thickness of the outer cylinder is represented by, $\zeta = t/R$, (Fig. 12). The load distribution between the large and fine grained regions is determined from the 'rule-of-mixtures' using Eq. C1. Then the overall creep rate is

$$\dot{\varepsilon} / \dot{\varepsilon}_o = (\sigma / \sigma_o)^n \left(\Omega^{2/3} / d^*\right)^\beta \qquad \text{(C2)}$$

where $d^* = [(1-\zeta)^2 d_i + \zeta(2-\zeta) d_f]$. By inserting the measured value for $d_i = 2$ nm and $d_f = 15$ nm and noting that $\zeta \approx 0.4$ after 2 h at 1200°C[18], Eq. (C2) predicts a creep strengthening of about an order of magnitude. This strengthening level is consistent with the measurements summarised in Fig. 13.

REFERENCES

[1] A.G. Evans & D.B. Marshall, The Mechanical Behavior of Ceramic Matrix Composites, Overview No. 85, *Acta Metall.*, **37** 2657-83 (1989).

[2] G. Bao & Z. Suo, Remarks on Crack-Bridging Concepts, to be published.

[3] S. Ho & Z. Suo, Notch Brittle-to-Ductile Transition in Metal and Ceramic Matrix Composites, to be published.

[4] M.D. Thouless, O. Sbaizero, L.S. Sigl & A.G. Evans, Effect of Interface Mechanical Properties on Pullout in a SiC-Fiber-Reinforced Lithium Aluminium Silicate Glass Ceramic, *J. Am. Ceram. Soc.*, **72** 525-32 (1989).

[5] H.C. Cao, E. Bischoff, O. Spaizero, M. Rühle & A.G. Evans, Effect of Interfaces on the Properties of Fiber-Reinforced Ceramics, *J. Am. Ceram. Soc.*, **73** 1691-99 (1990).

[6] O. Sbaizero, P.G. Charalambides & A.G. Evans, Delamination Cracking in a Laminated Ceramic-Matrix Composite, *J. Am. Ceram. Soc.*, **73** 1936-40 (1990).

[7] S.M. Spearing & F.W. Zok, Stochastic Aspects of Matrix Cracking in Brittle Matrix Composites, *Acta. Metall. et Mater.*, in press.

[8] D. Beyerle, S.M. Spearing, F. Zok & A.G. Evans, Damage and Failure in Unidirectional Ceramic-Matrix Composite, *J. Am. Ceram. Soc.*, **75** 2719-25 (1992).

[9] A.G. Evans & F.W. Zok, Cracking and Fatigue in Fiber-Reinforced Metal and Ceramic Matrix Composites, to be published.

[10] A. Kelly & K.N. Street, Creep of Discontinuous Fiber Composites II. Theory for the Steady-State, *J. Mech. Phys. Solids*, **14** 177-86 (1966).

[11] M. McLean, Creep Deformation of Metal-Matrix Composites, *Comp. Sci. & Tech.*, **23** 37-52 (1985).

[12] D.W. Petrasek, D.L. McDaniels, L.J. Westfall and J.R. Stephens, Fiber-Reinforced Superalloy Composites Provide an Added Performance Edge, *Met. Progress*, **130** 27-31 (1986).

[13] G. Simon & A. R. Bunsell, Creep Behavior & Structural Characterisation at High Temperatures of Nicalon SiC Fibers, *J. Mat. Sci.*, **19** 3658-70 (1984).

[14] A. G. Evans & T.G. Langdon, Structural Ceramics, *Prog. in Mat. Sci.*, **21** 171-442 (1976).

[15] A.H. Heuer, R.M. Cannon & N.J. Tighe, Plastic Deformation in Fine Grained Ceramics, Ultrafine-Grain Ceramics, Eds. J.J. Burke, N.L. Reed & V. Weiss, Syracuse Univ. Press, 1970, 339-65.

[16] S.M. Johnson, R.D. Brittain, R.H. Lamoreaux & D.J. Rowcliffe, Degradation Mechanisms of Silicon Carbide Fibers, *J. Am. Ceram. Soc.*, **71** C-132 - C-135 (1988).

[17] R. Chaim, A.H. Heuer & R.T. Chen, Microstructural & Microchemical Characterization of Silicon Carbide & Silicon Carbonitride Ceramic Fibers Produced From Polymer Precursors, *J. Am. Ceram. Soc.*, **71** 960-69 (1988).

[18] T. Mah, N.L. Hecht, D.E. McCullum, J.R. Hoenigman, H.M. Kim, A.P. Katz and H.A. Lipsitt, Thermal Stability of SiC Fibers (Nicalon®), *J. Mat. Sci.*, **19** 1191-201 (1984).

[19] K. Chyung, Corning Inc., private correspondence.

[20] C.H. Weber, J.P.A. Löfvander, J.Y. Yang, C.G. Levi and A.G. Evans, in Advanced Metal Matrix Composites for Elevated Temperatures, *ASM Conf. Proc.*, 69-77 (1991).

[21] J.W. Holmes & J.W. Jones, Creep Recovery Behavior of Nicalon Calcium-Aluminosilicate Composites, *submitted to J. Am. Ceram. Soc.*

[22] J.P.A. Löfvander, J.Y. Yang, C.G. Levi & R. Mehrabian, Microstructural Development of MoSi2 Fiber Composites Prepared by Slurry Processing Methods, *Advanced Metal Matrix Composites For Elevated Temperatures*, Ed. M.N. Cungor, E.J. Lavernia & S.G. Fishman, ASM Intl., 1-10 (1991).

[23] G. Bao, J. W. Hutchinson and R.M. McMeeking, Particle Reinforcement of Ductile Phases Against Plastic Flow and Creep, *Acta Metall. et Mater.*, **8** 1871-82 (1991).

[24] S. Schmauder and R.M. McMeeking, to be published.

[25] S. Timoshenko, *Strength of Materials, Part II, 3d ed.*, Van Nostrand-Reinhold, Princeton, (1956) 527.

FIGURE CAPTIONS

Fig. 1. Schematic of apparatus used for a) flexural creep assessment, b) transverse compressive creep measurements.

Fig. 2. Overview of the fiber distribution.

Fig. 3. a) TEM bright field micrograph of interfacial layer of carbon. b) EELS spectrum verifies that the layer is predominantly carbon.

Fig. 4. Axial creep characteristics of the composite at 1200°C.

Fig. 5. Effects of periodic unloading on axial creep curves.

Fig. 6. Transverse compressive creep curves at 1200°C.

Fig. 7. A comparison of axial and transverse creep rates at two equivalent stress levels

Fig. 8. The profile of a flexural specimen after testing at 1250°C and 50 MPa.

Fig. 9. Surface cracks evident on the compressive face of flexural specimens after testing.

Fig. 10. Scanning electron micrograph of matrix and interface damage found upon transverse compression testing.

Fig. 11. Transmission electron micrograph of Nicalon fiber after creep testing at 1200°C for 50 h.

Fig. 12. Schematic of grain growth behavior in Nicalon fibers at 1200°C.

Fig. 13. Normalised plot of axial creep behavior. $\sigma_{co}/\dot{\varepsilon}_{co} = 1$ MPa/s.

Fig. A1. Maximum composite stress and fraction of applied moment carried by matrix at different times during creep. Dashed line is approximate.

Fig. B1. Maximum residual tension in matrix at different times during creep. Dashed line is approximate.

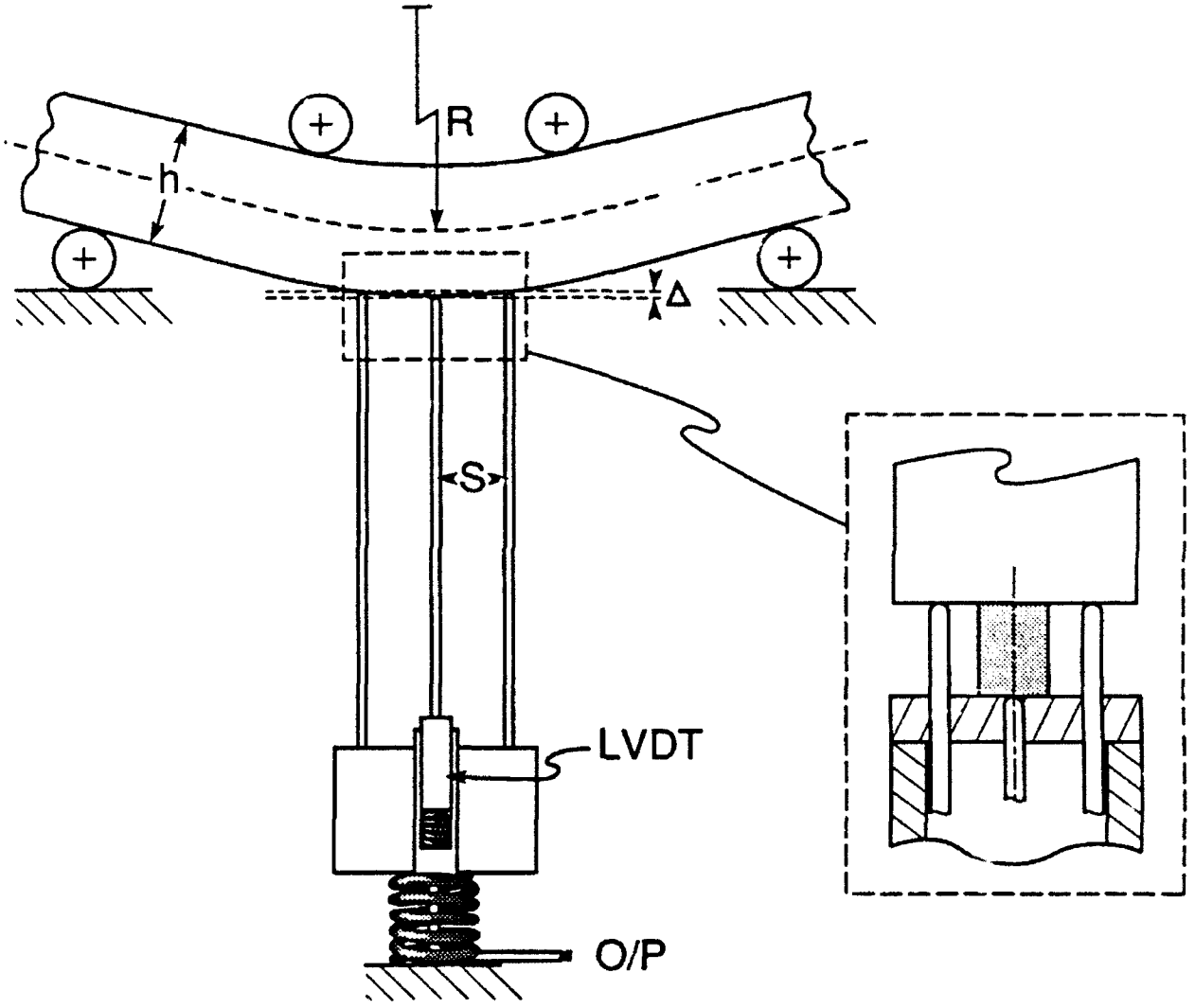

Fig. 1

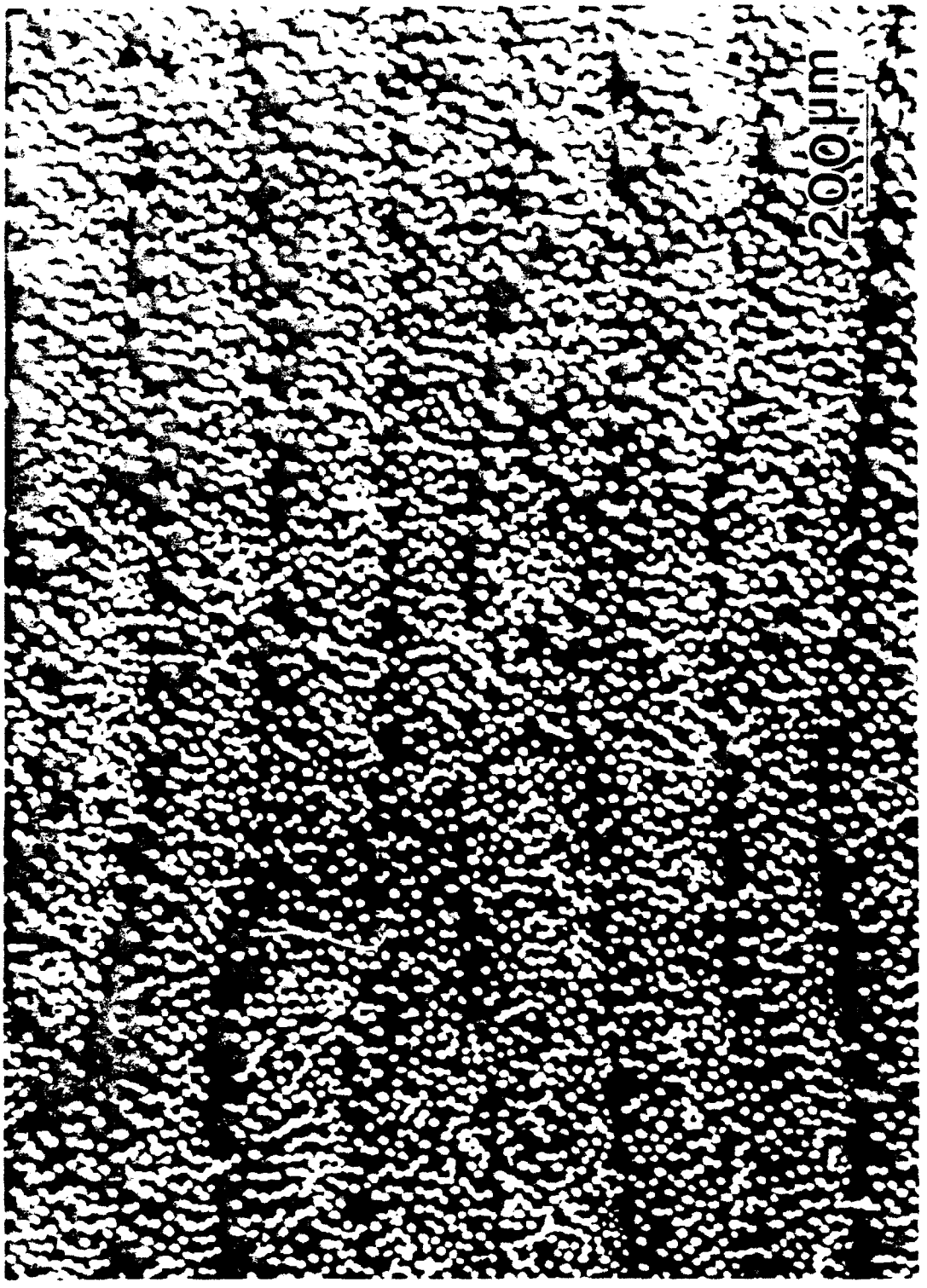

Fig. 2

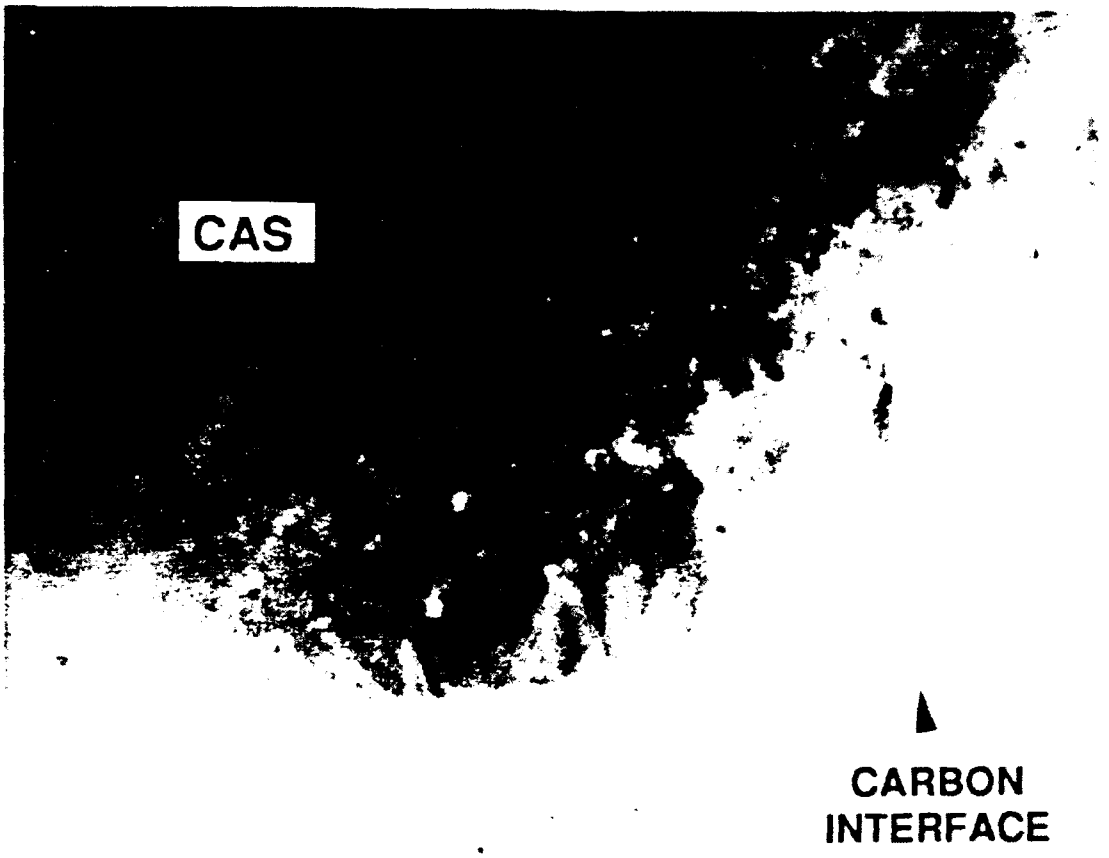

Fig. 3a

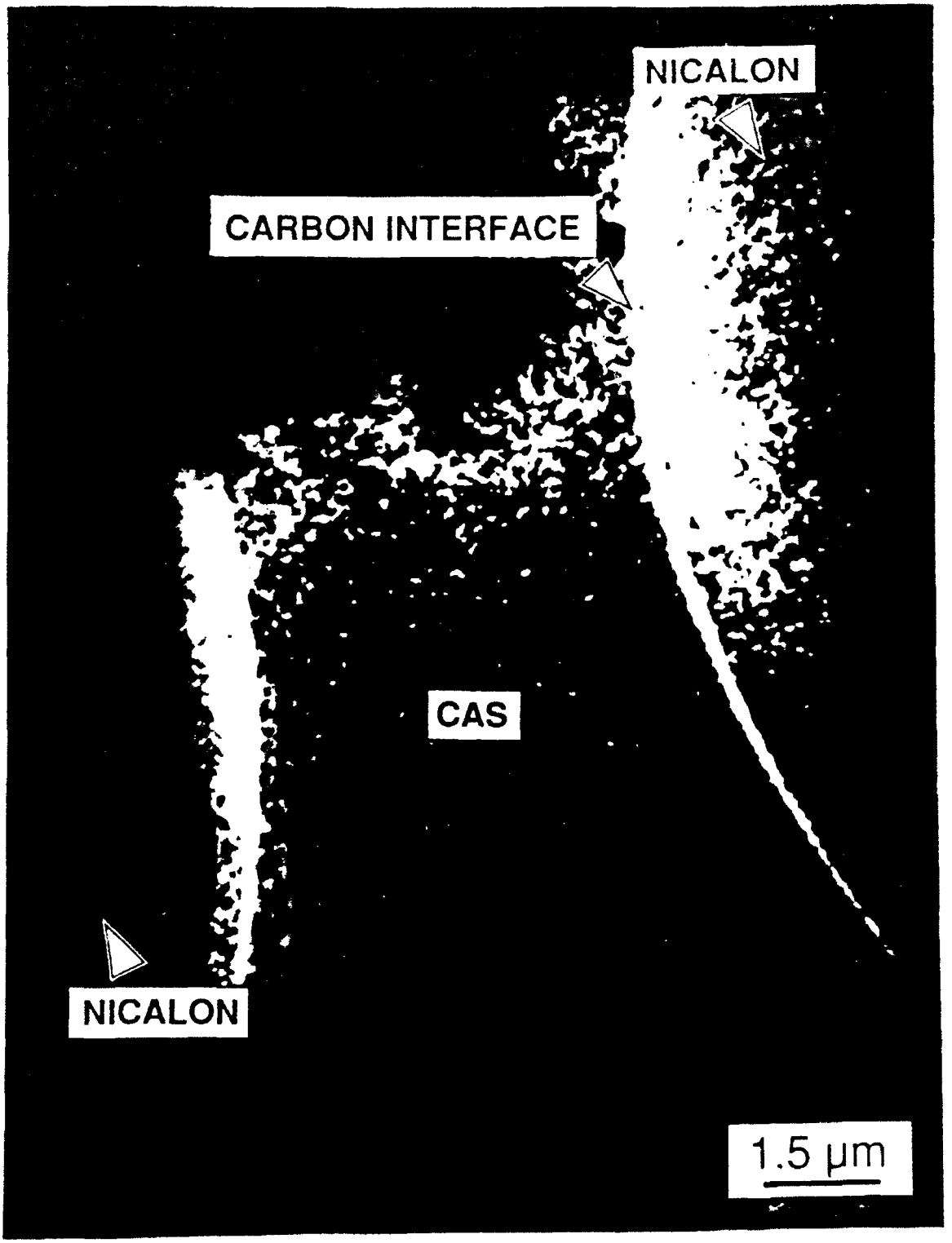

Fig. 3b

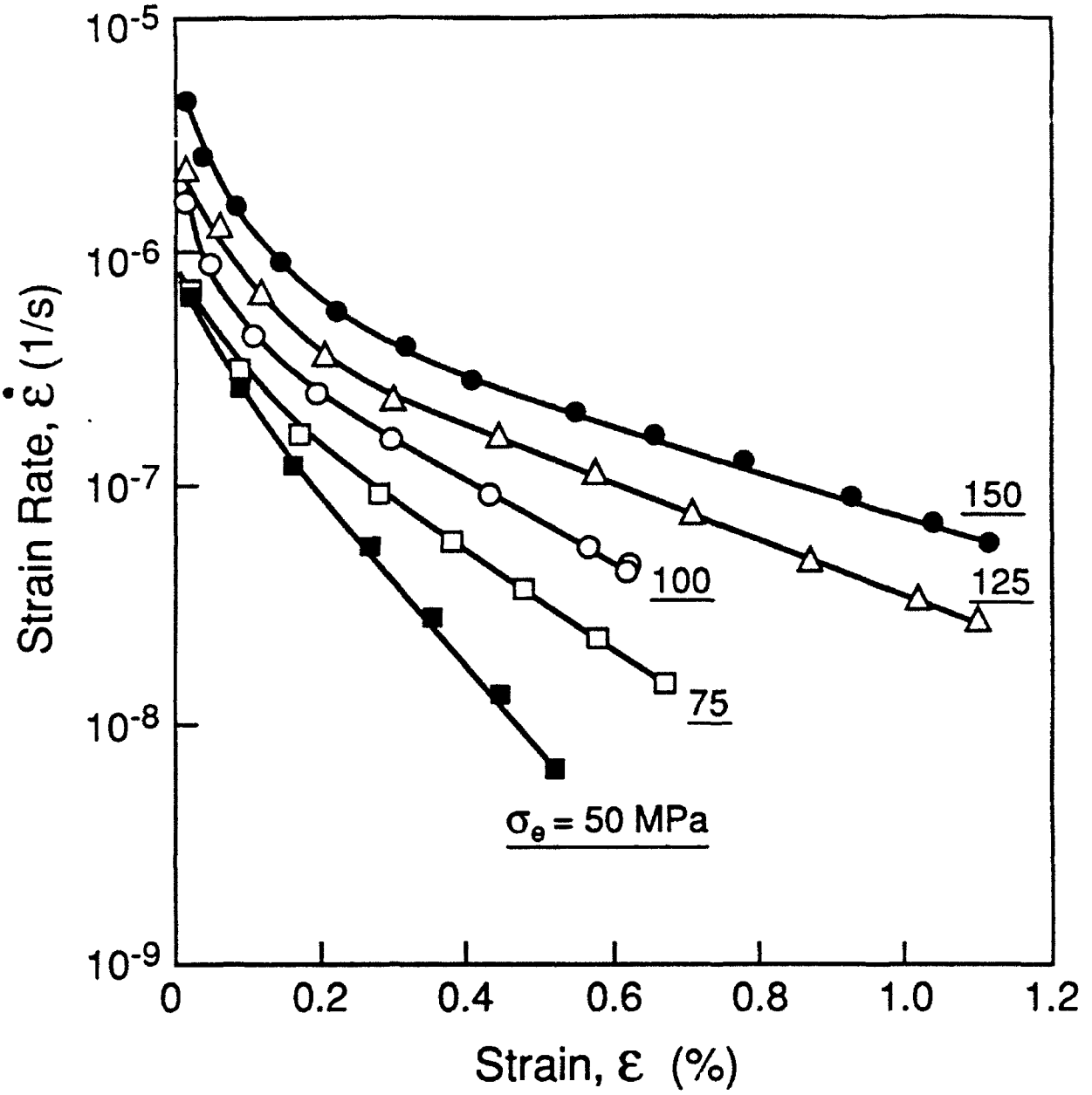
10^{-5}
10^{-6}
10^{-7}
10^{-8}
10^{-9}
Strain Rate, $\dot{\varepsilon}$ (1/s)
0
0.2
0.4
0.6
0.8
1.0
1.2
Strain, ε (%)
150
125
100
75
σ_e = 50 MPa

Fig. 4

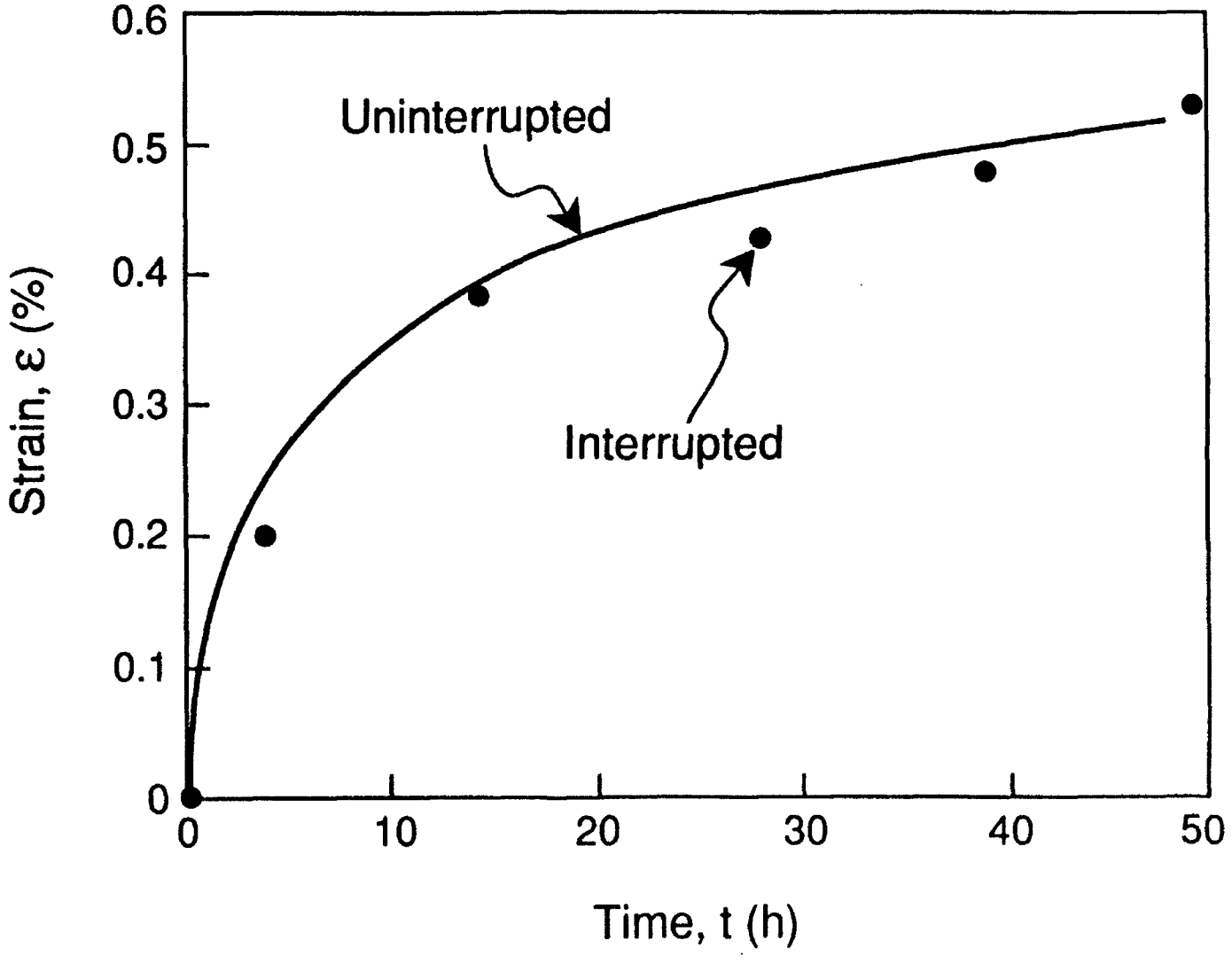
0.6
0.5
0.4
0.3
0.2
0.1
0
Strain, ε (%)
Uninterrupted
Interrupted
0
10
20
30
40
50
Time, t (h)

Fig. 5

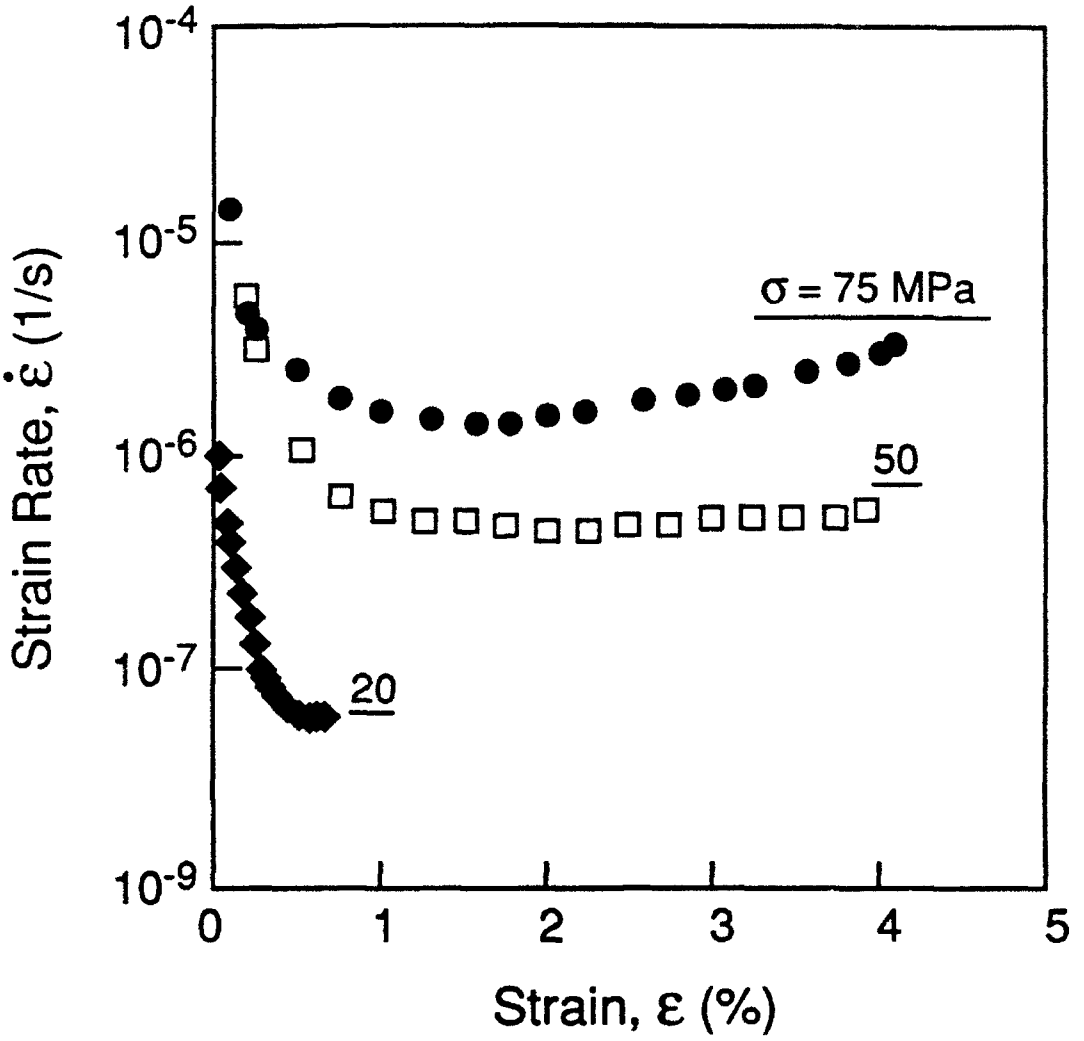
10-4
10-5
10-6
10-7
10-9
Strain Rate, ε̇ (1/s)
σ = 75 MPa
50
20
0
1
2
3
4
5
Strain, ε (%)

Fig. 6

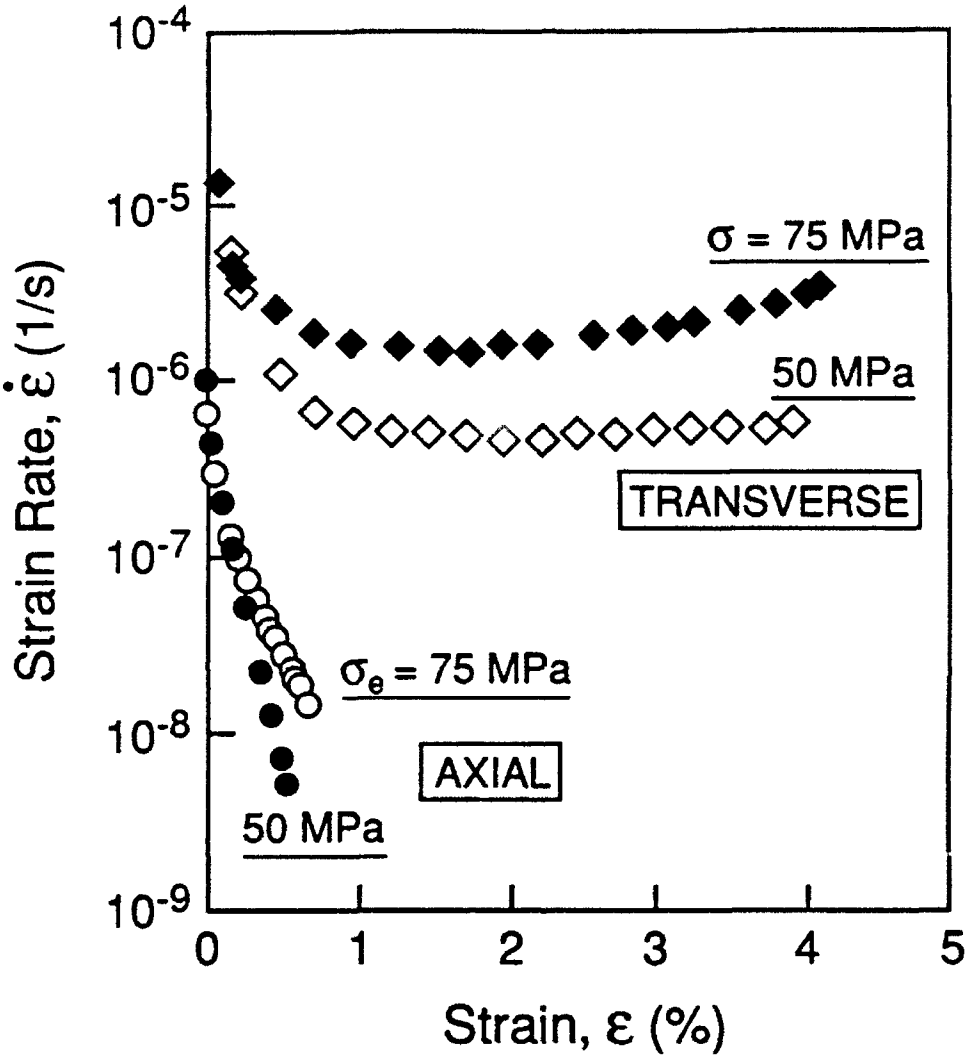
Strain Rate, ε̇ (1/s)
10-4
10-5
10-6
10-7
10-8
10-9
σ = 75 MPa
50 MPa
TRANSVERSE
σe = 75 MPa
AXIAL
50 MPa
0
1
2
3
4
5
Strain, ε (%)

Fig. 7

Fig. 8

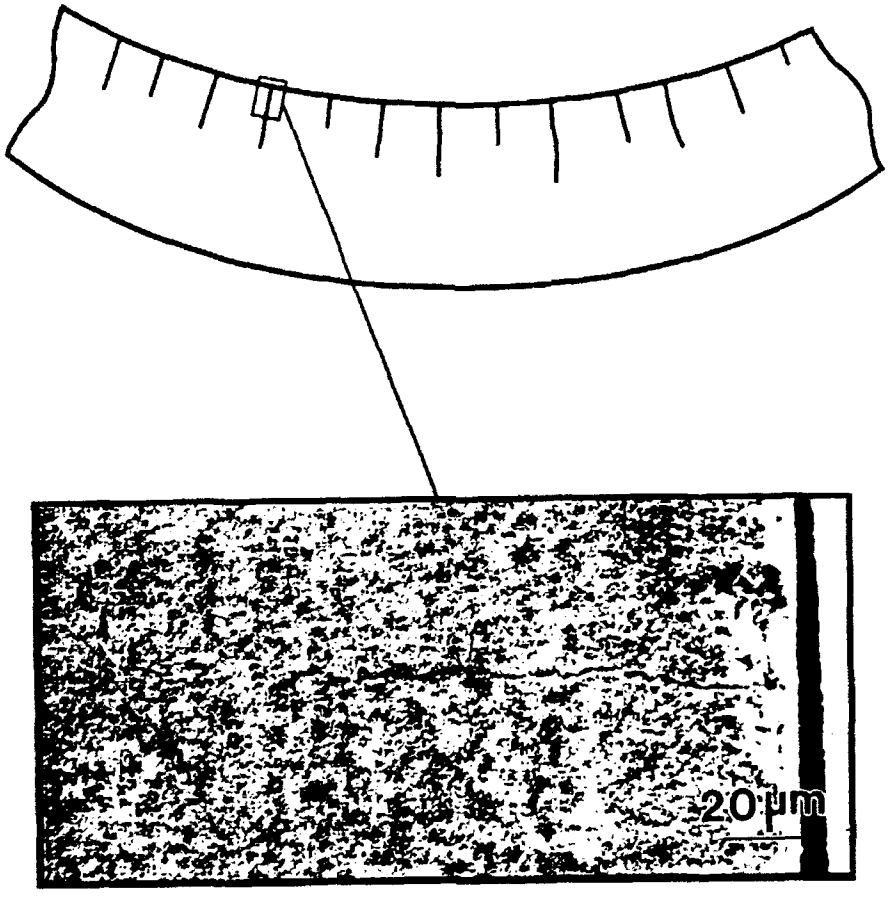

Fig. 9

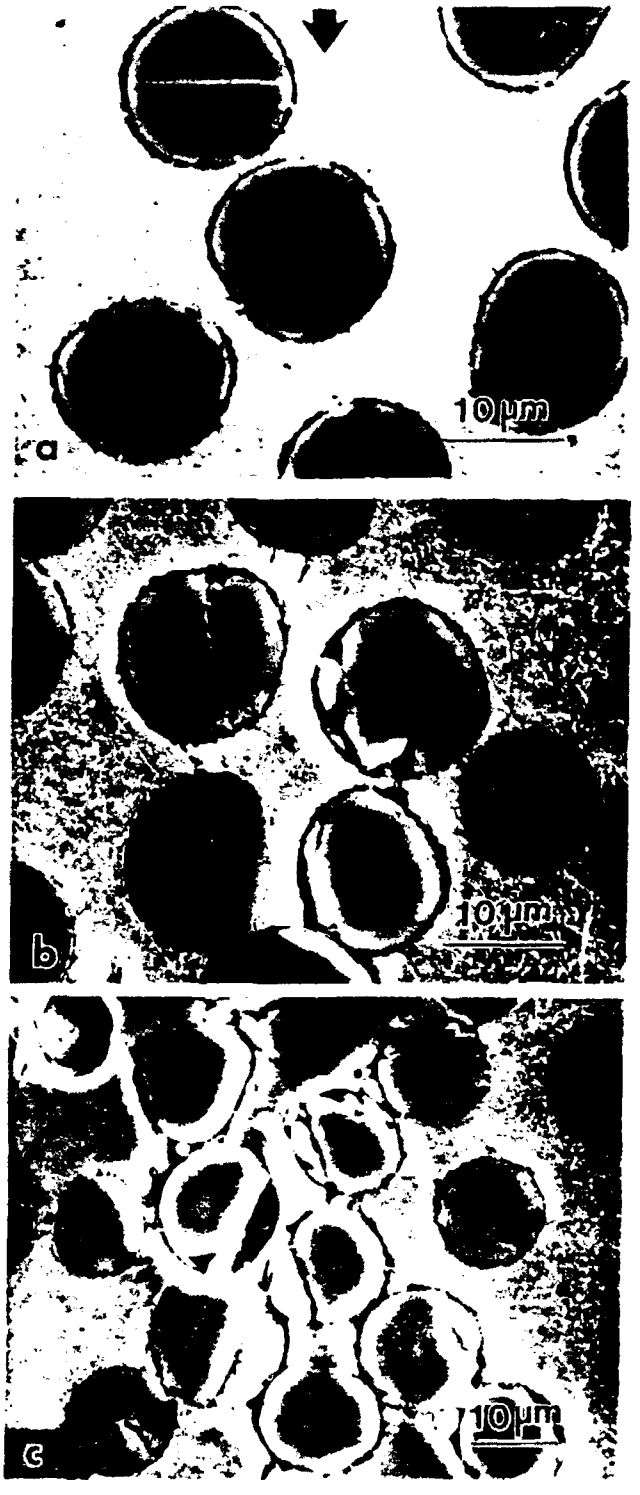

Fig. 10

Fig. 11

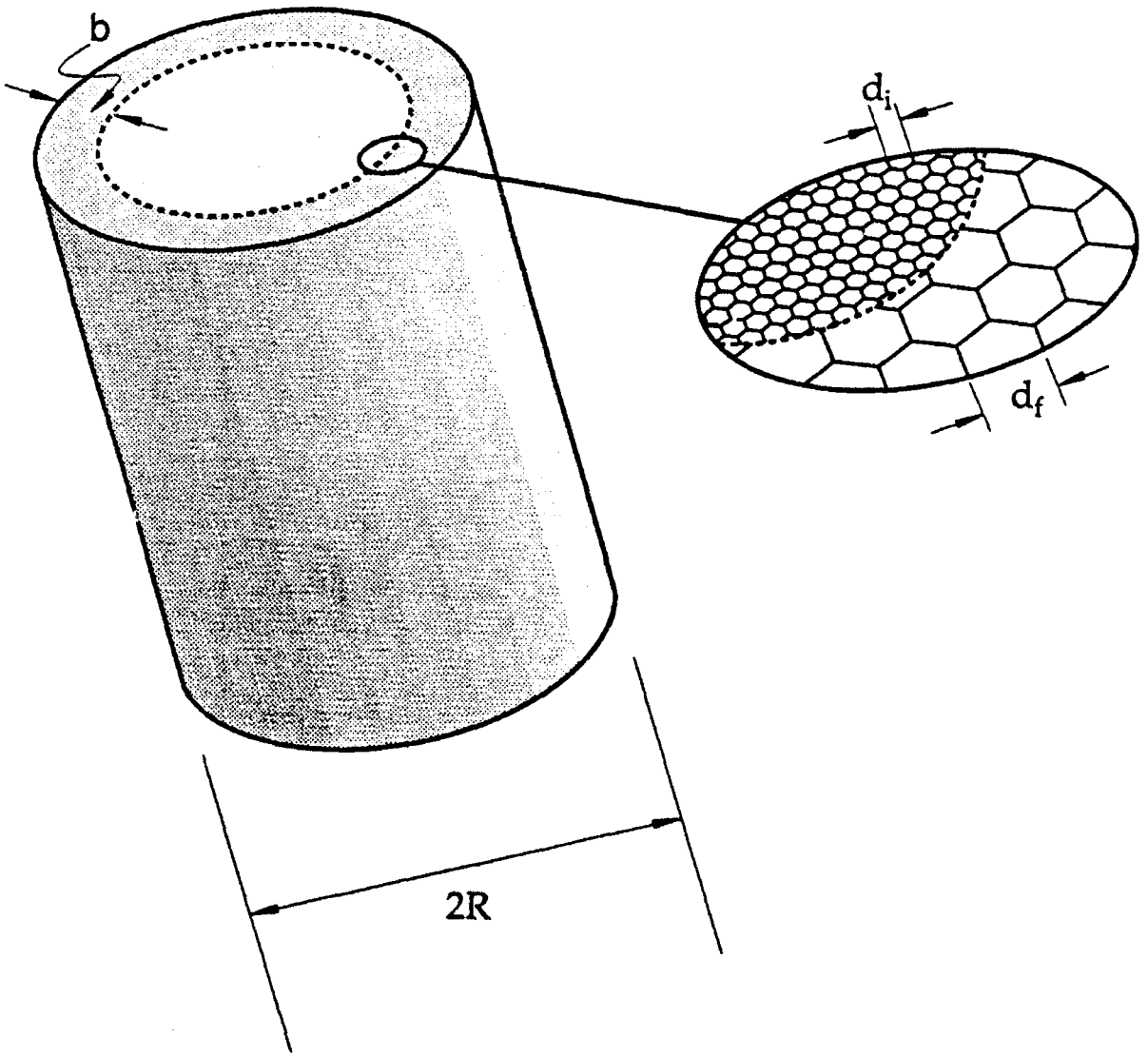

Fig. 12

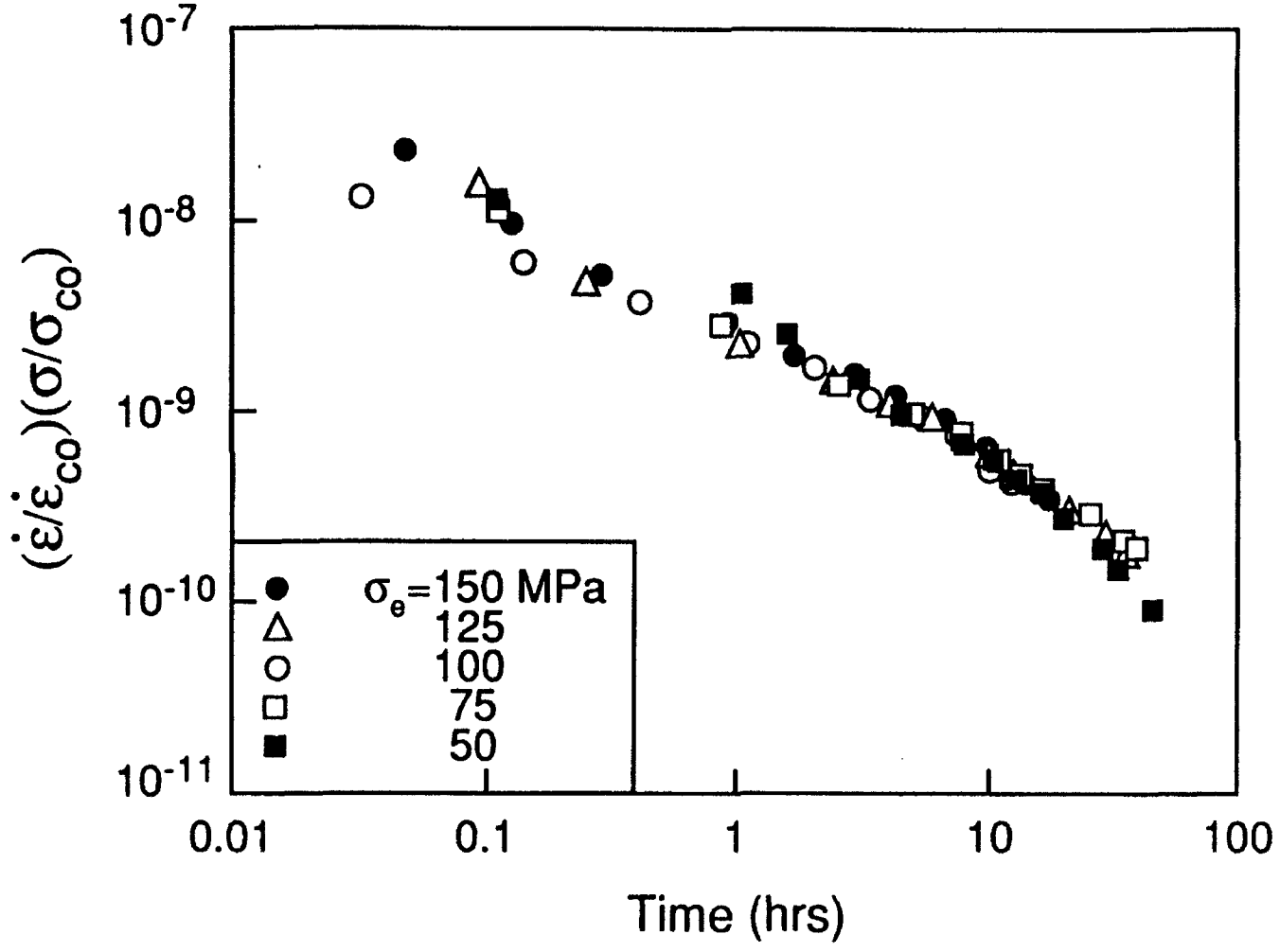
10^{-7}
10^{-8}
10^{-9}
10^{-10}
10^{-11}
$(\dot{\varepsilon}/\dot{\varepsilon}_{co})(\sigma/\sigma_{co})$
σ_e=150 MPa
125
100
75
50
0.01
0.1
1
10
100
Time (hrs)

Fig. 12

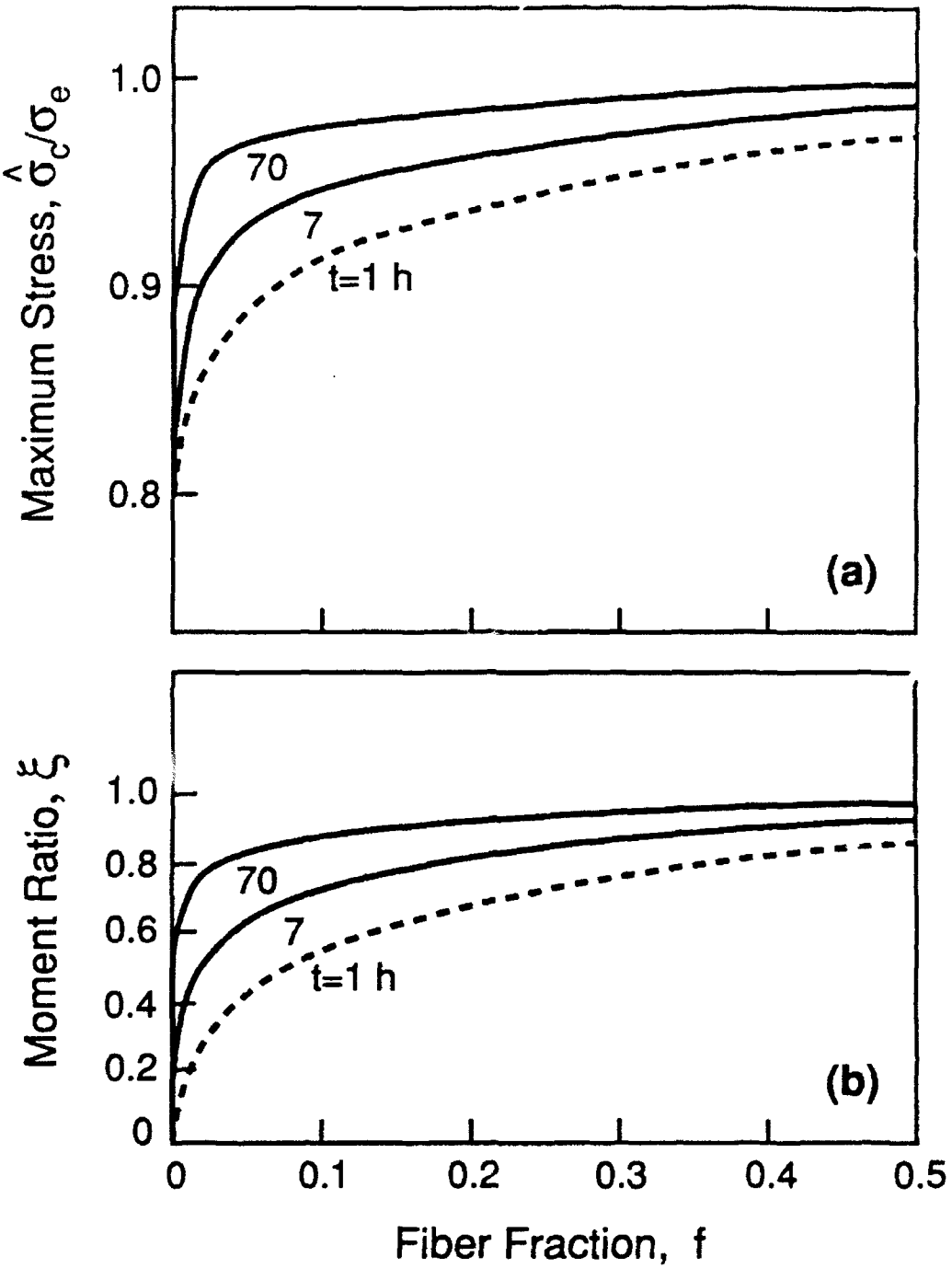
Maximum Stress, $\hat{\sigma}_c/\sigma_e$
1.0
0.9
0.8
70
7
t=1 h
(a)
Moment Ratio, ξ
1.0
0.8
0.6
0.4
0.2
0
70
7
t=1 h
(b)
0
0.1
0.2
0.3
0.4
0.5
Fiber Fraction, f

Fig. A1

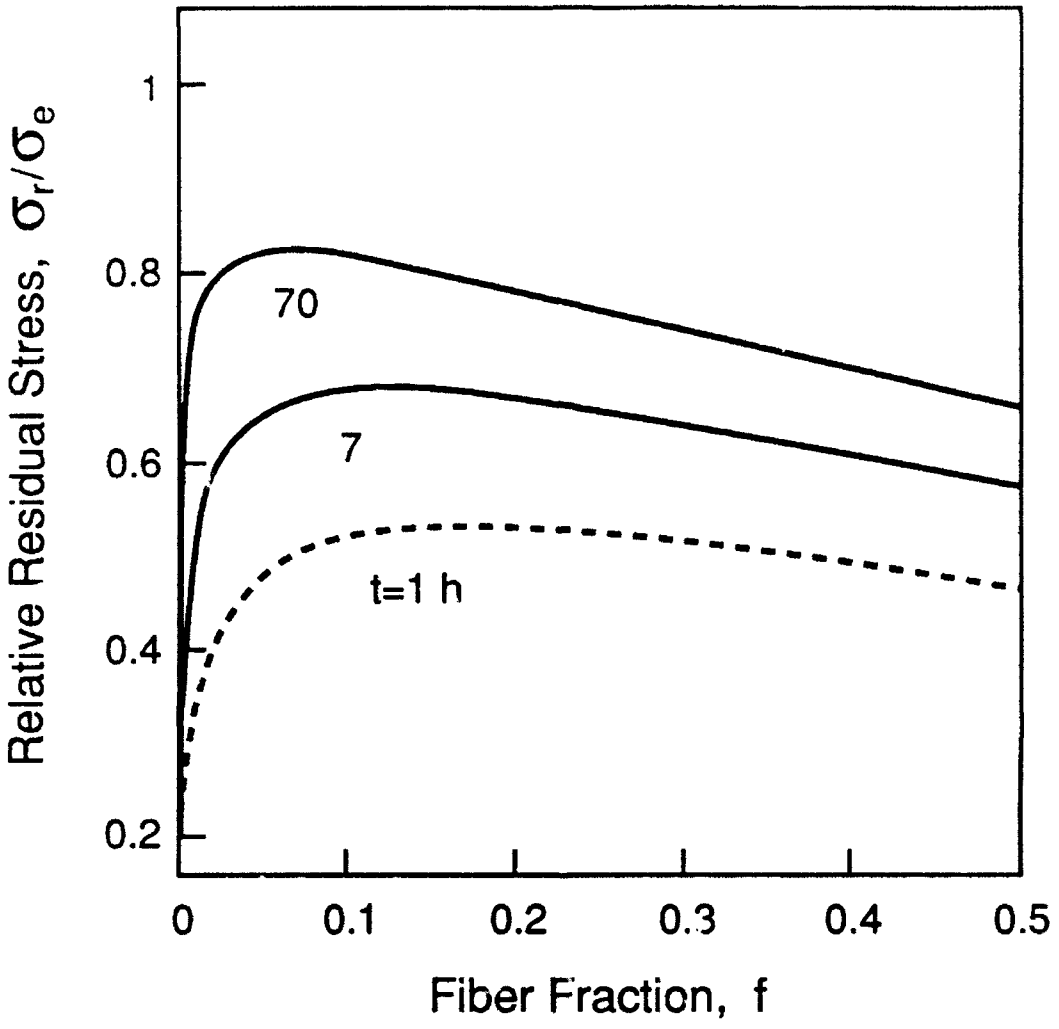
Relative Residual Stress, σ_r/σ_e
1
0.8
0.6
0.4
0.2
70
7
t=1 h
0
0.1
0.2
0.3
0.4
0.5
Fiber Fraction, f

Fig. B1

MATERIALS

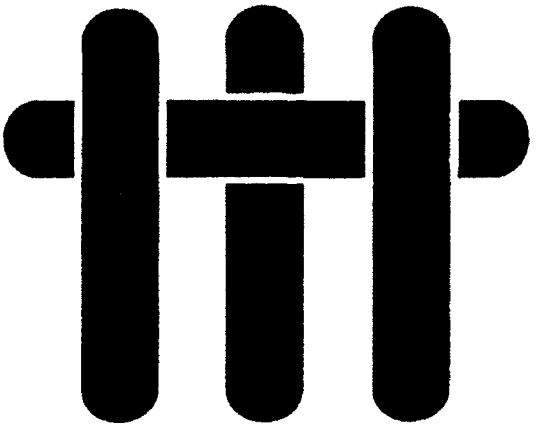

STRESS CORROSION CRACKING IN A UNIDIRECTIONAL CERAMIC-MATRIX COMPOSITE

by

S. M. Spearing, F. W. Zok and A. G. Evans
Materials Department
College of Engineering
University of California
Santa Barbara, California 93106–5050

Submitted to the Journal of American Ceramic Society, April 1993

ABSTRACT

A study of matrix cracking in a unidirectional ceramic matrix composite under static loading conditions has been conducted. The evolution of crack density with time has been measured using both flexure and uniaxial tension tests. *Sub-critical cracking* has been observed at stresses below that required to develop matrix cracks in short duration, monotonic loading tests. Furthermore, a relatively high final crack density has been observed following extended periods (~10^6 s) under static load. A fracture mechanics analysis applicable to sub-critical crack growth has been developed and used successfully to model the evolution of matrix cracking with time and applied stress. The model incorporates the properties of the matrix, fibers and the interfaces, as well as the residual stress and the initial flaw distribution in the matrix.

1. INTRODUCTION

Unidirectional metal (MMC), intermetallic (IMC) and ceramic matrix composites (CMC) have been observed to undergo multiple matrix cracking during either monotonic or cyclic tensile loading[1-8]. All of these matrices are susceptible to either cycle or time dependent crack growth associated with either fatigue (MMC and IMC) or stress corrosion (CMC). Multiple cracking reduces the stiffness of the material, contributes to the inelastic strain and results in permanent deformations upon unloading[3,4].

The development of multiple matrix cracks upon *monotonic* loading has been extensively investigated on CMCs by analytical and experimental means[1,3,4,9-13]. It has also been found that significant degradation of the mechanical properties of CMCs occur upon cyclic loading[14-16]. However, the time-dependent behavior under static load has not been addressed. The aim of this paper is to present an experimental investigation of such behavior, in conjunction with the mechanics needed to predict matrix crack growth. The paper builds upon previous experimental studies of the SiC/CAS system[3,4] and associated modelling[3,4,10-12].

2. EXPERIMENTAL PROCEDURES

2.1 Mechanical Tests

All experiments were conducted on a unidirectional laminate of Nicalon/CAS material provided by Corning[17]. Relevant material properties are summarized in Table I. Tensile specimens were prepared by diamond machining coupons having dimensions 150 x 3 x 2.8 mm, followed by polishing. Similar procedures were used to prepare flexural specimens having dimensions 50 x 3 x 2.8 mm, with the fibers oriented along the beam axis.

Tensile tests were conducted in a servohydraulic machine, at constant load. For such tests, aluminum tabs were bonded to the specimen ends to ensure even load transfer from the hydraulic grips and also to avoid crushing of the specimen. Surface replicas were periodically made using a cellulose acetate tape. The replicas were subsequently examined in an optical microscope to determine the crack density. The flexure tests were conducted in four-point bending with inner and outer spans of 20 and 40 mm, respectively. The apparatus was situated within an optical microscope, allowing *in situ* observations to be made of the cracking process on the tensile face of the beam‡. A thermometer and humidity gauge were placed near the specimens during the tests. The temperature was consistently in the range 15 to 20°C and the relative humidity varied from 60 to 80%.

After the onset of matrix cracking, the stress distribution in a flexural beam becomes non-linear. Analysis of the errors associated with the non-linearity (Appendix) indicates that the stress on the tensile face is within ~10% of the *nominal* value calculated on the basis of linear-elasticity. In the subsequent presentation, only the *nominal* stress corresponding to each flexure test is reported. The following results validate that stress re-distribution does not influence the important trends in the damage evolution process.

2.2 Crack Density Measurements

Previous experience with unidirectional CMCs (including CAS/SiC) indicates that, during tensile loading, matrix cracks develop into more-or-less periodic arrays, with a characteristic crack spacing[3,4]. The cracks generally span a significant fraction of the specimen width and are bridged by fibers. One such example is shown in Fig. 1. Because of the periodic nature of the cracks, the average crack spacing can be related to changes in the composite modulus and the permanent strain following unloading using

‡ No particular effort was made to control the test environment.

relatively simple models based on shear lag[3,4]. This experience suggests that the relevant measure of damage in such composites is the *linear* crack density, measured parallel to the fiber direction[‡]. This approach was adopted in the present study. In all cases, the crack density was measured along a 20 mm gauge length parallel to the tensile axis. At the outset of each test, only one gauge length was examined. After longer durations (~ 30 minutes), measurements were made along three separate gauge lengths parallel to one another.

In making such measurements, two complicating features were encountered. In some instances, cracks were seen to bifurcate. Invariably, one of the branches arrested after propagating ~ 10-30 μm, whereas the other continued to propagate large distances. An example is indicated on Fig. 1. In other instances, cracks propagating in one direction arrested when they reached other cracks which were on nearly the same plane, but propagating in the opposite direction. In such cases, both sets of cracks arrested after propagating ~ 10-30 μm past one another. An example is again indicated on Fig. 1. These artefacts were excluded from the present crack density measurements. This was accomplished by counting only those cracks that traversed more than ~ 40 μm on both sides of the gauge line.

3. EXPERIMENTAL RESULTS

In situ observations of the flexure specimens indicated that matrix cracks evolve over time at constant load. Two types of cracking were observed (designated Type I and Type II) . At *low stresses* and *short times*, Type I cracking occurred. In this case, cracks appeared suddenly and grew rapidly across the specimen width. There was no

‡ The linear crack density is equivalent to the *inverse* of the average crack spacing.

evidence that visible cracks were subject to detectable growth*. This observation suggests that sub-critical* growth occurs at very short cracks which are invisible in the optical microscope. At larger lengths, the cracks propagated under sub-critical conditions at a sufficiently high velocity that they could not be followed in the optical microscope. Type I behavior coincides with low crack densities.

Type II behavior, at higher stresses or long times, involves the extension of existing, long cracks, between other closely-spaced cracks. One such example is shown in Fig. 2. This behavior arises at high crack density. This observation suggests that the cracks "shield" each other, thereby reducing the driving force for further growth, as shown schematically in Fig. 3.

In situ measurements of the crack density, ρ, in the flexure specimens revealed strong effects of the applied stress (Fig. 4(a)). This contrasts with the behavior of monolithic ceramics, for which time-dependent effects are only apparent at stresses close to the instantaneous failure stress. Two features of the damage evolution process are noteworthy: (i) At stresses below the matrix cracking stress measured in short duration, monotonic tests (~150 MPa), no cracks were visible initially. However, appreciable cracking subsequently occurred over a period of ~ 10^6 s. Indeed, the final crack density, ρ_f, measured at ~ 125 MPa reached a significant fraction of the *saturation* crack density, ρ_s*, found in short duration, monotonic tests ($\rho_f \approx 1/2\ \rho_s$)[4]. (ii) At either long times or high stress, ρ tends toward a constant value ($\rho \approx 12.5$ cracks/mm). This level is *higher* than ρ_s.

Measurements of crack density made from surface replicas of the tensile specimens are shown in Fig. 4(b). One of these tests was conducted at a stress close to

---

* Detectable crack growth is defined as the condition wherein the crack velocity is sufficiently low to allow crack growth to be followed in the microscope. In contrast, *sub-critical* crack growth refers *only* to conditions wherein the crack tip energy release rate is below the composite toughness. High crack growth rates (~ 10^{-3} m/s) have been measured in monolithic glass-ceramics under sub-critical conditions[18]. Such behavior would not result in detectable growth.

* $\rho_s \approx 10$ cracks/mm.

the initial matrix cracking stress (150 MPa) and the other at a higher stress (200 MPa). The results show trends similar to those found in flexure at comparable stress levels. The slight discrepancies may be attributed to differences in the stress states in the two types of tests, as well as variations in the testing environment (temperature and relative humidity). An assessment of the effects of flexure on matrix damage is given in the Appendix.

4. DAMAGE MECHANICS

The experimental observations affirm the existence of appreciable effects of time on matrix cracking. The modelling approach used to rationalize the experimental results has the following features*. (i) Crack growth in the matrix is governed by the crack tip energy release rate, $\mathcal{G}_{tip}$, in association with a stress corrosion law. (ii) Bridging of the crack by fibers occurs, subject to a sliding stress, τ. The magnitude of τ can change as a result of environmental interactions. However, in the following analysis, τ is assumed to be constant along the debonded interface. (iii) Fiber bridging is subject to two regimes. When the cracks are *short*, the tip energy release rate increases with crack length. When the cracks are *long*, the tip energy release rate is *independent* of crack length. (iv) Once the cracks became closely spaced, the slip lengths of neighboring cracks overlap, reducing the driving force for additional crack growth. Much of the relevant mechanics has been derived elsewhere[9-13]. In this section, adaptations of the existing mechanics suitable for sub-critical crack growth are presented.

*These features are suggested by the present consensus regarding the mechanisms of stress corrosion in ceramics[19].

4.1 Energy Release Rates

The effects of bridging fibers on the crack tip energy release rate $\mathcal{G}_{tip}$ or stress intensity K_{tip} for *single, isolated* cracks have been extensively analyzed[9-13]. Here, the numerical results of McMeeking and Evans[13] are presented and adapted to the problem of sub-critical crack growth. The trends in energy release rate with crack length (from Fig. 6 of Ref. 13) are shown in Fig. 5. These results are found to be well-approximated by two analytical expressions‡. When $2\xi\sigma_t R/\tau a \leq \gamma$,

$$\frac{\mathcal{G}_{tip} E}{\sigma^2 \pi a\left(1-\nu^2\right)} = \frac{1}{25}\left(\frac{2\xi\sigma_t R}{\tau a}\right)^{2/3} \tag{1a}$$

and, when $2\xi\sigma_t R/\tau a > \gamma$

$$\frac{\mathcal{G}_{tip} E}{\sigma^2 \pi a\left(1-\nu^2\right)} = \frac{1}{12\pi}\left(\frac{2\xi\sigma_t R}{\tau a}\right) \tag{1b}$$

where R is the fiber radius; 2a is the crack length; E is the longitudinal composite modulus,

$$E = f E_f + (1\text{-}f) E_m \tag{2}$$

with E_m and E_f being the moduli of the matrix and the fibers; ν is Poisson's ratio, assumed to be the same for the matrix and the fibers; γ is a numerical coefficient

$$\gamma = (12\pi/25)^3 \approx 3.43 \tag{3}$$

---

‡ These features are suggested by the mechanisms of stress corrosion found in monolithic ceramics[19].

σ_t is the stress (applied plus residual),

$$\sigma_t = \sigma + q\,E/E_m \tag{4}$$

with q being the residual axial stress in the matrix; and ξ characterizes the elastic properties.

$$\xi = \frac{(1-f)^2 E_m^2}{f^2 E E_f (1-\nu^2)} \tag{5}$$

The expressions (1) and (2) are accurate to within 5% over the range $0 \le 2\xi\,\sigma R/\tau a \le 20$ (Fig. 5)‡.

For subsequent analysis, Eqns. (1a) and (1b) are re-written in terms of two fixed quantities, independent of stress and crack length. The first is the *steady state matrix cracking stress in the absence of residual stress*, σ_o. *This stress is obtained by setting* $\mathcal{G}_{tip}$ equal to the composite toughness,

$$\Gamma = \Gamma_m (1-f) \tag{6}$$

with Γ_m being the matrix toughness, whereupon[9,11]

$$\sigma_o = \left(\frac{6 E_f f^2 E^2 \tau \Gamma_m}{E_m^2 (1-f) R} \right)^{1/3}. \tag{7}$$

---

‡ Note that the result of Eqn. (1a) corresponds to the short crack regime wherein the tip energy release rate increases with crack length. In contrast, the result of Eqn. (1b) corresponds to the steady-state regime wherein $\mathcal{G}_{tip}$ is independent of crack length.

This is the stress required to propagate a steady-state crack under monotonic tensile loading (in the absence of sub-critical behavior). The other quantity is the crack length, a_o, at which steady state conditions are attained at $\sigma = \sigma_o$. This length is obtained by equating the expressions for $\mathcal{G}_{tip}$ in Eqns. (1a) and (1b), yielding

$$a_o = \frac{2\xi R(\sigma_o + q E/E_m)}{\gamma \tau} . \tag{8}$$

Upon combining Eqns. (7) and (8) with Eqns. (1) and (2), the final results are:

$$\frac{\mathcal{G}_{tip}}{\Gamma_m (1-f)} = \left(\frac{\sigma_t}{\sigma_o}\right)^{8/3} \left(\frac{a}{a_o}\right)^{1/3} \qquad \left[\frac{a}{a_o} \le \frac{\sigma_t}{\sigma_o}\right] \tag{9a}$$

and

$$\frac{\mathcal{G}_{tip}}{\Gamma_m (1-f)} = \left(\frac{\sigma_t}{\sigma_o}\right)^{3} \qquad \left[\frac{a}{a_o} > \frac{\sigma_t}{\sigma_o}\right]. \tag{9b}$$

The predicted trends in energy release rate, $\mathcal{G}_{tip}/\Gamma_m$ (1-f), with crack length, a/a_o, for various values of stress, σ_t/σ_o, are presented in Fig. 6. Also shown by the dashed line is the boundary between the short crack and long crack regimes. These results predict three types of behavior, depending on the level of stress. (i) When $\sigma_t = \sigma_o$, the energy release rate initially increases with crack length, but reaches a steady state value equivalent to the composite toughness (Γ_m (1-f)) at a crack length $a = a_o$. (ii) When $\sigma_t > \sigma_o$, the energy release rate reaches the toughness at a crack length, $a/a_o = (\sigma/\sigma_o)^{-8}$. Crack growth beyond this point occurs subject to a constant energy release rate, equivalent to the toughness. The steady state conditions predicted by Eqn. (9b) are never attained. (iii) When $\sigma_t < \sigma_o$, the energy release rate reaches its

steady-state value, $(\sigma_t/\sigma_o)^3$, at a crack length, $a/a_o = \sigma/\sigma_o$. In this regime, the energy release rate never reaches the toughness. Consequently, the cracks extend *only under sub-critical conditions.*

When *multiple* matrix cracks occur and interact, an important quantity in the mechanics is the slip length, d, between matrix and fiber, given by[9,12],

$$d/R = 2E f \tau/(\sigma + qE/E_m) E_m (1-f) \tag{10}$$

When the slip zones between neighboring cracks overlap, $\mathcal{G}_{tip}$ for long cracks falls below the steady state value, $\mathcal{G}_o$, for a single, isolated crack, given by

$$\mathcal{G}_o = \frac{(\sigma + qE/E_m)^3 E_m^2 (1-f)^2 R}{6\tau f^2 E_f E^2} . \tag{11}$$

The relationship between $\mathcal{G}_{tip}$ and $\mathcal{G}_o$ is dictated by the spacing, ℓ, between neighboring cracks relative to d[12], and can be expressed as

$$\frac{\mathcal{G}_{tip}}{\mathcal{G}_o} = 1 \qquad \left[\frac{\ell}{d} \geq 2\right] \tag{12a}$$

$$\frac{\mathcal{G}_{tip}}{\mathcal{G}_o} = 1 - 4\left(1 - \frac{\ell}{2d}\right)^3 \qquad \left[1 \leq \frac{\ell}{d} \leq 2\right] \tag{12b}$$

$$\frac{\mathcal{G}_{tip}}{\mathcal{G}_o} = 4\left(\frac{\ell}{2d}\right)^3 \qquad \left[0 \leq \frac{\ell}{d} \leq 1\right]. \tag{12c}$$

Once again it is convenient to re-express these results in terms of two fixed quantities: the steady state matrix cracking stress, σ_o (defined in Eqn. 7), and the slip length, d_o, at $\sigma = \sigma_o$:

$$d_o/R = \frac{(\sigma_o + qE/E_m)E_m(1-f)}{2Ef\tau} . \qquad (13)$$

Combining Eqn. (9) with (4) and (10) yields the results

$$\frac{\mathcal{G}_{tip}}{\Gamma_m(1-f)} = \left(\frac{\sigma_t}{\sigma_o}\right)^3 \qquad \left[\frac{\ell}{d_o} \geq 2\frac{\sigma_t}{\sigma_o}\right] \qquad (14a)$$

$$\frac{\mathcal{G}_{tip}}{\Gamma_m(1-f)} = \left(\frac{\sigma_t}{\sigma_o}\right)^3\left[1-4\left(1-\frac{\ell}{2d_o}\frac{\sigma_o}{\sigma_t}\right)^3\right] \qquad \left[\frac{\sigma_t}{\sigma_o} \leq \frac{\ell}{d_o} \leq 2\frac{\sigma_t}{\sigma_o}\right] \qquad (14b)$$

$$\frac{\mathcal{G}_{tip}}{\Gamma_m(1-f)} = 4\left(\frac{\ell}{2d_o}\right)^3 \qquad \left[0 \leq \frac{\ell}{d_o} \leq \frac{\sigma_t}{\sigma_o}\right] . \qquad (14c)$$

The predicted trends in energy release rate, $\mathcal{G}_{tip}/\Gamma_m$ (1-f), with crack spacing, ℓ/d_o, for several values of stress, σ_t/σ_o, are shown in Fig. 7. These results also predict three types of behavior, depending on the level of stress. (i) When $\sigma_t < \sigma_o$, the energy release rate is independent of spacing, provided that $\ell/d_o > 2\,\sigma_t/\sigma_o$. In this regime, the slip lengths of adjacent crack do no overlap. When the crack spacing is in the range, $\sigma_t/\sigma_o \leq \ell/d_o \leq 2\,\sigma_t/\sigma_o$, the energy release rate decreases with decreasing ℓ at a rate that depends on the stress. Once the crack spacing reaches $\ell/d_o \leq \sigma_t/\sigma_o$, the energy release rate decreases with decreasing ℓ at a rate *independent* of stress. (ii) When the stress is in the range, $1 \leq \sigma_t/\sigma_o \leq 2^{1/3}$, the crack spacing immediately drops to

$$\frac{\ell}{d_o} = 2\frac{\sigma_t}{\sigma_o}\left\{1-\left[\frac{1}{4}\left(1-\left(\frac{\sigma_o}{\sigma_t}\right)^3\right)\right]^{1/3}\right\}. \qquad (15)$$

Further reductions in spacing lead to a decrease in $\mathcal{G}_{tip}$, first at a rate dependent on stress (over the range $\sigma_t/\sigma_o \le \ell/d_o \le 2\,\sigma_t/\sigma_o$), then at rate independent of stress (over the range $0 \le \ell/d_o \le \sigma_t/\sigma_o$). (iii) Finally, when the stress $\sigma_t/\sigma_o \ge 2^{1/3}$, the crack spacing diminishes to $\ell/d_o = 2^{1/3}$. Further reductions in crack spacing lead to a drop in $\mathcal{G}_{tip}$ independent of stress.

4.2 Crack Growth

The preceding energy release rates $\mathcal{G}_{tip}$ can be used in conjunction with a crack growth criterion to predict crack evolution. As noted above, stress corrosion is considered to be the mechanism that causes time-dependent matrix cracking. Consequently, crack growth can be described by the commonly-used power law,

$$\frac{da}{dt} = \dot{a}_o\left(K_{tip}/K_m\right)^n \equiv \dot{a}_o\left(\mathcal{G}_{tip}/\Gamma_m(1-f)\right)^{n/2} \qquad (16)$$

where $\dot{a}_o$ is a reference velocity, n is the power law exponent and K_m is the critical stress intensity factor for the matrix. For aluminosilicate glass ceramics[18], stress corrosion is caused by moisture and the power law exponent is, $n \approx 50$.

To provide a basis for further modeling, it is instructive to re-state the key experimental observations. The process of crack evolution exhibits three regimes. (i) At low stresses and small crack densities (Type I), damage evolution is governed by short, non-interacting cracks, with $\mathcal{G}_{tip}$ given by Eqn. (9). In this regime, because n is large, the behavior is dominated by stress corrosion occurring when the cracks are small and

invisible. (ii) At either high stresses or long times (Type II), multiple cracks are already present, and further crack growth occurs under steady-state conditions (independent of crack length), with $\mathcal{G}_{tip}$ given by Eqn. (14). Then, the new cracks should be continually visible and grow at a discernible, near-constant velocity across the specimen. (iii) An intermediate regime must exist which combines features of type I and II behaviors. The behavior in this regime is inherently difficult to analyze and is not considered in this study. Instead, interpolation between type I and type II could be used.

4.2.1 Short Cracks (Type I)

For short, non-interacting cracks, the time t_i required to grow a matrix crack of initial length a_i is evaluated by integrating the growth law (Eqn. (16)) between appropriate limits, yielding the result

$$t_i = \frac{1}{\dot{a}_o}\int_{a_i/a_o}^{a_f/a_o}\left(\frac{\Gamma_m(1-f)}{\mathcal{G}_{tip}}\right)^{n/2} d(a/a_o) \tag{17}$$

where a_f is an upper limit on the crack length, described below. Two cases are considered, defined by the level of stress. In the first, $\sigma_t/\sigma_o \geq 1$. In this regime, the appropriate upper limit on the integral is the crack length at which $\mathcal{G}_{tip}$ reaches the composite toughness. Beyond this point, the crack grows catastrophically. As noted earlier, this limit is, $a_f/a_o = (\sigma/\sigma_o)^{-8}$. Combining this result with Eqns. (9a) and (17) gives

$$\begin{aligned} t_i &= \frac{1}{\dot{a}_o}\left(\frac{\sigma_t}{\sigma_o}\right)^{-4n/3}\int_{a_i/a_o}^{(\sigma_t/\sigma_o)^{-8}}\left(\frac{a}{a_o}\right)^{-n/6} d\left(\frac{a}{a_o}\right) \\ &= \frac{1}{\dot{a}_o}\left(\frac{\sigma_t}{\sigma_o}\right)^{-4n/3}\left(\frac{6}{6-n}\right)\left[\left(\frac{\sigma_t}{\sigma_o}\right)^{-8(1-n/6)} - \left(\frac{a_i}{a_o}\right)^{(1-n/6)}\right]. \end{aligned} \tag{18}$$

For the material of present interest, n is large and thus $(\sigma/\sigma_o)^{-8(1-n/6)} << (a_i/a_o)^{(1-n/6)}$. Consequently, Eqn. (18) reduces to

$$t_i \approx \frac{1}{\dot{a}_o}\left(\frac{\sigma_t}{\sigma_o}\right)^{-4n/3}\left(\frac{6}{n-6}\right)\left(\frac{a_i}{a_o}\right)^{(1-n/6)} \tag{19}$$

The second regime is defined by $\sigma/\sigma_o < 1$. In this case, $\mathcal{G}_{tip}$ initially increases with crack length according to Eqn. (6), but then reaches a steady state level given by Eqn. (9b), at a crack length $a/a_o = \sigma/\sigma_o$. It is therefore convenient to separate the integral in Eqn. (15) into two parts. One is for condition wherein $\mathcal{G}_{tip}$ increases with a, and the other for $\mathcal{G}_{tip}$ independent of a. The result is

$$\begin{aligned} t_i &= \frac{1}{\dot{a}_o}\left\{\left(\frac{\sigma}{\sigma_o}\right)^{-8/3}\int_{a_i/a_o}^{\sigma/\sigma_o}\left(\frac{a}{a_o}\right)^{-2/n} d\left(\frac{a}{a_o}\right) + \left(\frac{\sigma_t}{\sigma_o}\right)^{-3/n}\int_{\sigma/\sigma_o}^{a_f/a_o} d\left(\frac{a}{a_o}\right)\right\} \\ &= \frac{1}{\dot{a}_o}\left\{\left(\frac{\sigma_t}{\sigma_o}\right)^{-4n/3}\left(\frac{6}{6-n}\right)\left[\left(\frac{\sigma_t}{\sigma_o}\right)^{(1-n/6)} - \left(\frac{a_i}{a_o}\right)^{(1-n/6)}\right] + \left(\frac{\sigma_t}{\sigma_o}\right)^{-3n/2}\left(\frac{a_f}{a_o} - \frac{\sigma_t}{\sigma_o}\right)\right\} \end{aligned} \tag{20}$$

where a_f is on the order of the specimen width.

Once again, because n is large, $(\sigma/\sigma_o)^{(1-n/6)} << (a_i/a_o)^{(1-n/6)}$. Furthermore, the experimental observations suggest that, once steady state conditions have been attained, the time required to grow the crack across the specimen width is relatively small. As a result, the last term in Eqn. (20) is neglected. With these approximations, Eqn. (20) reduces to

$$t_i \approx \frac{1}{\dot{a}_o}\left(\frac{\sigma_t}{\sigma_o}\right)^{-4n/3}\left(\frac{6}{n-6}\right)\left(\frac{a_i}{a_o}\right)^{(1-n/6)} \tag{21}$$

which is equivalent to the result in Eqn. (19). Consequently, the distinction between the two regimes is neglected in the subsequent analysis.

A representation for the matrix flaw distribution is now needed in order to predict damage evolution. For this purpose, an extreme value matrix flaw size distribution is assumed, given by

$$F = 1 - \exp\left[-\frac{V}{V_*}\left(\frac{a_*}{a_i}\right)^{\alpha} \right] \tag{22}$$

where F is the fraction of flaws having size greater than a_i in a volume V, α is the shape parameter, and a_* and V_* are scale parameters. Consequently, if η_v is the total number of flaws per unit volume, the number η having size $a \geq a_i$ is

$$\eta = \eta_v \left[1 - \exp\left[-\frac{V}{V_*}\left(\frac{a_*}{a_i}\right)^{\alpha} \right] \right] \tag{23}$$

Assuming that only the largest flaws in the distribution evolve into *visible* matrix cracks, Eqn. (23) reduces to

$$\eta \approx \eta_v \left(V/V_*\right)\left(a_*/a_i\right)^{\alpha} \tag{24}$$

Combining this distribution with Eqn. (21) gives the number of flaws, η_s, that have developed into steady state cracks within a time, t:

$$\eta_s \approx \eta_v \left(\frac{V}{V_*}\right)\left(\frac{a_*}{a_o}\right)^{\alpha}\left(\frac{n-6}{6}\right)^{6\alpha/(n-6)}\left(t\dot{a}_o\right)^{6\alpha/(n-6)}\left(\frac{\sigma_t}{\sigma_o}\right)^{8n\alpha/(n-6)}$$

$$\equiv \lambda\left(t\dot{a}_o\right)^{y}\left(\frac{\sigma_t}{\sigma_o}\right)^{x} \tag{25}$$

where

$$x \equiv \frac{8n\alpha}{n-6}, \tag{26a}$$

and $$y \equiv \frac{6\alpha}{n-6} \tag{26b}$$

while λ contains all of the parameters characterizing the flaw distribution. Furthermore, the linear density of cracks ρ measured parallel to the tensile axis, is related to η_s through

$$\rho = A \cdot \eta_s \tag{27}$$

where A is the cross-sectional area of the composite.

Equations (25) and (27) suggest that the evolution of crack density can be described by a generic law of the form

$$\rho = \lambda' t^{y} \sigma^{x} \tag{28}$$

where λ' embodies all the relevant material properties. However, many of the properties contributing to λ' are poorly characterized. Consequently, it is expedient to

use Eqn. (28) to fit data at one stress level and then *predict* crack growth rates at other stress levels.

4.2.2 Long Cracks

The evolution of crack density in the regime characterized by high stresses and high crack densities has been computed in a similar fashion. In this case, the governing relations for $\mathcal{G}_{tip}$ are given by Eqn. (14). Since the energy release rates are crack length *independent*, the crack density is computed by combining Eqn. (14) with Eqn. (16) and numerically integrating. Some predicted changes in crack density with time for a range of stresses are plotted on Fig. 8. In general, interpolation between these curves and the short crack results is needed to establish the overall behavior. An approach for such interpolation has not yet been established. However, it is important to note that, regardless of the initial state, the crack density eventually evolves with time in a manner *independent* of stress. This behavior arises because the strain energy release rates for multiple cracks converge to a single curve at high crack densities (Fig. 7), corresponding to the regime of closely-spaced cracks where Eqn. (14c) operates.

4.3. Comparison with Experiment

The approach used to compare experiment to theory involved two steps. (i) One set of experimental results was fitted to the model, in order to evaluate the unknown constants, (ii) By using the *same constants* the model was used to *predict* the behavior for other testing conditions. Comparisons of the constants inferred in this manner with values expected from corresponding phenomena occurring in monolithic material assess the consistency of the models. This procedure was applied separately to the low and high stress regimes.

The model was used to examine the data shown in Fig. 3(a). In the low stress regime (Type I), Eqn. (28) was fitted to the data at 120 MPa, using a stress corrosion exponent, $n = 50$[18] (Fig. 9). The best fit line corresponds to a value of the shape parameter, $\alpha = 1.5$. The value of α inferred from this comparison corresponds to a Weibull modulus*, $m \approx 3$. Values in this range are reasonable for ceramic matrix composites. Using the same constants, the model was used to *predict* the crack densities at other stress levels (Fig. 9). Evidently, the model predictions are in reasonable agreement with the experimental results for stresses $\sigma \leq 150$ MPa and for crack densities $\rho \lesssim 6$ mm. This model thus appears to provide a satisfactory description of damage evolution at low stresses and low crack densities.

The model predictions for type II behavior at high stresses and high crack densities was assessed by using the *same stress corrosion exponent* ($n = 50$). The curves were fitted to the measured crack density at 250 MPa after 10 s (9.7/mm), and then used to predict the behavior at other stresses and times. These predictions appear to be consistent with the data at stresses $\sigma \geq 180$ MPa at crack densities $\rho > 8$/mm.

5. CONCLUDING REMARKS

Matrix cracks have been shown to develop in a time-dependent manner in a unidirectional Nicalon fiber/CAS matrix composite. The phenomenon has been rationalized by a stress corrosion mechanism operating in the matrix. This process results in crack growth at stresses below that found in short duration monotonic tests. Furthermore, for most stress levels, the crack density ultimately evolves with time in a manner independent of the stress, and reaches values higher than those found in

*The shape parameter, α on flaw size (Eqn. 22) is half that for the tensile strength, via the Griffith relationship.

monotonic tests. Both of these observations have implications for the use of these materials in structural applications. The behavior of the composite contrasts with that of monolithic ceramics for which stress corrosion only occurs at stresses within a few percent of the failure stress. It is anticipated that ceramic matrix composites will be subjected to *localized* stresses well above the matrix cracking stress, in which case it will prove necessary to account for the effect of stress corrosion in the design process.

A fracture mechanics analysis has been used successfully to model the development of multiple matrix cracks with time and applied stress. The model has been developed separately for the regimes dominated by either non-interacting short cracks or interacting steady-state cracks. The approach is consistent with existing models for matrix cracking under monotonic loading conditions. However, a method for interpolating between the two regimes has yet to be developed.

ACKNOWLEDGMENTS

This work was supported by the Defense Advanced Research Projects Agency through the University Research Initiative under ONR contract N-0014-92-J-1808. The authors would like to thank Dr. K. Chyung for supplying the test material.

TABLE I

Properties of Unidirectional CAS/SiC Composite[4,20]

Property	Value
Fiber Radius, R (μm)	7.5
Fiber Volume Fraction, f	0.37*
Matrix Modulus, E_m (GPa)	97*
Fiber Modulus, E_f (GPa)	200
Thermal Expansion Coefficient of Matrix, α_m (K^{-1})	5×10^{-6}
Thermal Expansion Coefficient of Fibers, α_f (K^{-1})	4×10^{-6}
Sliding Stress, τ (MPa)	10 - 30
Residual Stress, q (MPa)	89
Matrix Fracture Energy, Γ_m (J/m^2)	25
Matrix Cracking Stress, $\sigma_o - q\,E/E_m$ (MPa)	130 - 150
Ultimate Tensile Strength, σ_u (MPa)	450
Ultimate Strain, ε_u	1.0%

* K. Chyung, Corning Labs

APPENDIX: An Assessment of the Effect of Flexure

During flexural loading of unidirectional CMCs, matrix cracks develop along the tensile face of the beam, leading to non-linearity in the stress-strain response. As a result, the nominal stress calculated from Euler-Bernoulli beam theory, assuming the material to be linear elastic, overestimates the true stress acting along the tensile face. The following analysis provides an estimate of the effects of such non-linearity on the maximum tensile stress in a flexural beam, both at the onset of loading and after an extended period under load.

The initial stress distribution (upon loading) is calculated assuming that: (i) the *compressive* stress-strain response of the composite is linear, with a modulus given by the rule of mixtures; (ii) the tensile response is that measured in a short-term uniaxial tensile test (Fig. A1), and (iii) the strain distribution across the beam remains linear. The analysis involves two steps. In the first, the sum of the forces acting parallel to the fiber direction is set equal to zero, enforcing static equilibrium. This condition can be expressed as

$$-\int_{\varepsilon_c}^{0} E\varepsilon\, d\varepsilon + \int_{0}^{\varepsilon_T} \sigma_T(\varepsilon)\, d\varepsilon = 0 \qquad \text{(A1)}$$

where $\sigma_T(\varepsilon)$ is the tensile stress-strain relation, and ε_c and ε_T are the maximum compressive and tensile strains, respectively. Solving the first integral in (A1) and re-arranging gives

$$\varepsilon_c = -\left[\frac{2}{E}\int_{0}^{\varepsilon_T} \sigma_T(\varepsilon)\, d\varepsilon\right]^{1/2}. \qquad \text{(A2)}$$

This equation relates ε_c to ε_T. In the second step, the applied bending moment, M, is equated to the moment supported by the beam. This condition can be written as

$$M = \frac{BD^2}{(\varepsilon_T - \varepsilon_c)^2}\left[\int_{\varepsilon_c}^{0} E\varepsilon(\varepsilon - \varepsilon_c)d\varepsilon + \int_{0}^{\varepsilon_T} \sigma_T(\varepsilon)(\varepsilon - \varepsilon_c)d\varepsilon\right] \quad \text{(A3)}$$

where B is the beam depth and D the height. The nominal stress, σ_{nom}, calculated on the assumption of linear elasticity, is related to M through

$$\sigma_{nom} = 6M/BD^2. \quad \text{(A4)}$$

Combining Eqns. (A3) and (A4) leads to the result

$$\sigma_{nom} = \frac{1}{(\varepsilon_T - \varepsilon_c)^2}\left[E\varepsilon_c^3 + 6\int_{0}^{\varepsilon_T} \sigma_T(\varepsilon)(\varepsilon - \varepsilon_c)d\varepsilon\right] \quad \text{(A5)}$$

To proceed further, an expression for $\sigma_T(\varepsilon)$ is required. For this purpose, the measured tensile stress-strain curve is fit by a polynominal of the form

$$\sigma_T(\varepsilon) = a\varepsilon + b\varepsilon^2 + c\varepsilon^3 + d\varepsilon^4 \quad \text{(A6)}$$

where the coefficients a, b, c and d are

$a = 1.4 \times 10^5$ MPa

$b = -1.12 \times 10^7$ MPa

$c = -3.89 \times 10^9$ MPa

$d = 5.51 \times 10^{11}$ MPa

This polynominal provides a good description of the experimental curve over the relevant range of stresses ($0 \leq \sigma_T \leq 300$ MPa), as shown in Fig. A1.

Equations (A2), (A5) and (A6) have been combined to determine the relation between the stress σ_T on the tensile face and the nominal applied stress, σ_{nom}. The results are presented in Fig. A2. Below the first matrix cracking stress (150 MPa), the two quantities are equal, since the composite is linear-elastic in both tension and compression. At higher nominal stresses, the true stress deviates from the nominal value, the difference increasing with increasing σ_{nom}. At the highest stress used in the present study (σ_{nom} = 250 MPa), the difference is ~11%.

Under sustained loading, additional matrix cracks are developed, leading to further stress re-distribution across the beam. A rigorous analysis of this problem is not presently feasible. However, it is instructive to consider a limiting case in which the stresses in the matrix on the tensile side of the beam are reduced to zero, such that the fibers support all the stress. In this case, the tensile response of the composite can be taken to be

$$\sigma_T(\varepsilon) \approx E_T \varepsilon \tag{A7}$$

where E_T is an effective (reduced) tensile modulus. A conservative estimate of E_T is σ_u/ε_u, where σ_u is the ultimate tensile strength and ε_u the corresponding tensile strain. This relation is plotted as the dashed line in Fig. A1. In this case, Eqns. (A2) and (A5) reduce to the simple analytical result

$$\sigma_T / \sigma_{nom} = \left(1+\sqrt{\sigma_u / E\varepsilon_u}\right)/2. \tag{A8}$$

Using the experimentally measured values σ_u = 450 MPa and ε_u = 1.0% gives σ_T/σ_{nom} = 0.80. This result is plotted on Fig. A2. At most, there is a 20% reduction in the stress below the elastic value.

REFERENCES

[1] R.Y. Kim and N. Pagano, "Crack Initiation in Unidirectional Brittle Matrix Composites," *J. Am. Ceram. Soc.*, **74** [5], 1082-90 (1991).

[2] H.C. Cao, E. Bischoff, O. Sbaizero, M. Ruhle, A.G. Evans D.B. Marshall and J.J. Brennan, "Effect of Interfaces on the Properties of Fiber-Reinforced Ceramics" *J. Amer. Ceram., Soc.*, **73** (6), 1691-99 (1990).

[3] A. Pryce and P. Smith, "Modelling the Stress Strain Behaviour of Unidirectional Ceramic Matrix Composite Laminates" submitted to *J. Mater. Sci.*, (1991).

[4] D.S. Beyerle, S.M. Spearing, F.W. Zok and A.G. Evans, "Damage and Degradation of a Ceramic Matrix Composite," *J. Am. Ceram. Soc.*, **75** [10], 2719-25 (1992).

[5] A.G. Evans and D.B. Marshall, "The Mechanical Behavior of Ceramic Matrix Composites," *Acta Metall.*, **37** [10], 2567-83 (1989).

[6] D.M. Harmon and C.R. Saff "Damage Initiation and Growth in Fiber Reinforced Metal Matrix Composites" Metal Matrix Composites: Testing, Analysis and Failure Modes, ASTM STP 1032, W. S. Johnson, Editor, ASTM, Philadelphia, (1989).

[7] G. Rosenkranz, V. Gerold, K. Kromp, D. Stockel, L. Tillmann "Fatigue Behavior of Metallic Fibre-Reinforced Materials: A Study of Steel Fiber-Reinforced Silver, Part 2 Failure Mechanisms and High Cycle Fatigue Life" *J. Mat. Sci.*, **17**, 277-289 (1982).

[8] S.M. Jeng, C.J. Yang, J-M. Yang, D.G. Rosenthal and J. Goebel, "Mechanical Behavior and Failure Mechanisms of SCS6-Ti_3Al Composites" Mat. Res. Soc. Symp. Proc. **194**, 277-84 (1990).

[9] J. Aveston, G.A. Cooper and A. Kelly, "Single and Multiple Fracture in the Properties of Fiber Composites," *The Properties of Fiber Composites, IPC*, (1971).

[10] D.B. Marshall, B.N. Cox and A.G. Evans, "The Mechanics of Matrix Cracking in Brittle Matrix Fiber Composites," *Acta Metall.*, **33** [11], 2013-21 (1985).

[11] B. Budiansky, J.W. Hutchinson and A.G. Evans, "Matrix Fracture in Fiber-Reinforced Ceramics," *J. Mech. Phys. Solids*, **34** [2], 164-189 (1986).

[12] F.W. Zok and S.M. Spearing, "Matrix Crack Spacing in Brittle Matrix Composites," *Acta Metall. Mater.*, **40** [8], 2033-2043 (1992).

[13] R.M. McMeeking and A.G. Evans, "Matrix Fatigue Cracking in Fiber Reinforced Metal Matrix Composites," *Mech. Mater.*, **9**, 217 (1990).

[14] L.M. Butkus, L.P. Zawada and G.A. Hartman, "Fatigue Testing of Ceramic Matrix Composites at Room and Elevated Temperatures Matrix Composites," *J. Cyclic Deformation, Fracture and Nondestructive Evaluation of Advanced Materials, ASTM STP XXXX* (1990).

[15] T.J. Kotil, J.W. Holmes and M. Cominou, "Origin of Hysteresis Observed During Fatigue of Ceramic-Matrix Composites," *J. Am. Ceram. Soc.*, **73** [7], 1879-83 (1990).

[16] K.M. Prewo, "Fatigue and Stress rupture of Silicon Carbide Fibre-Reinforced Glass-Ceramics," *J. Mater. Sci.*, **22**, 2695-2701 (1987).

[17] K. Chyung, U.S. Patent 4,615,987 (7 Oct., 1986).

[18] B. Pletka and S.M. Wiederhorn, "Subcritical Crack Growth in Glass Ceramics," *Fracture Mechanics of Ceramics* (Ed. R.C. Bradt *et al.*) Plenum, NY, 745-59 (1983).

[19] S. Suresh, "Fatigue of Materials", *Cambridge Solid State Science Series*, Cambridge Univ. Press (1991).

[20] T.J. Mackin and F.W. Zok, *J. Amer. Ceram. Soc.*, **75**, (1993).

FIGURE CAPTIONS

Fig. 1 An optical micrograph showing matrix cracks in the CAS/SiC composite following a short duration, monotonic tensile test. The arrow labeled "A" indicates an example of a crack that had bifurcated and arrested. Arrow "B" indicates a crack that arrested as it approached another crack on nearly the same plane.

Fig. 2 (a) Micrograph of matrix cracks upon initial loading of a flexure specimen to 175 MPa. (b) Micrograph of the same region after 3 days at the same level of stress. Note the additional growth of matrix cracks in (b) (indicated by arrows).

Fig. 3 Schematic diagram showing the type of cracks observed either at high stress or long time, and the expected variation in energy release rate as the cracks interact.

Fig. 4 Evolution of crack density with time under static load: (a) flexure tests, (b) uniaxial tension tests. For comparison, the results of (b) have been superimposed onto (a) using dashed lines.

Fig. 5 Trends in crack tip energy release rate with crack length (adapted from [13]).

Fig. 6 Variation in energy release rate for single, isolated crack with crack length.

Fig. 7 Effects of crack spacing and stress on the steady state energy release rate.

Fig. 8 Predicted trends in crack density evolution, assuming existing long (steady-state) cracks based on Eqn. (9).

Fig. 9 Comparison of damage evolution predictions with experimental measurements.

Fig. A1 Tensile stress-strain response of the CAS/SiC composite.

Fig. A2 Variation in the stress, σ_T, acting along the tensile face of a flexure specimen with the nominal stress, σ_{nom}.

Fig. 1

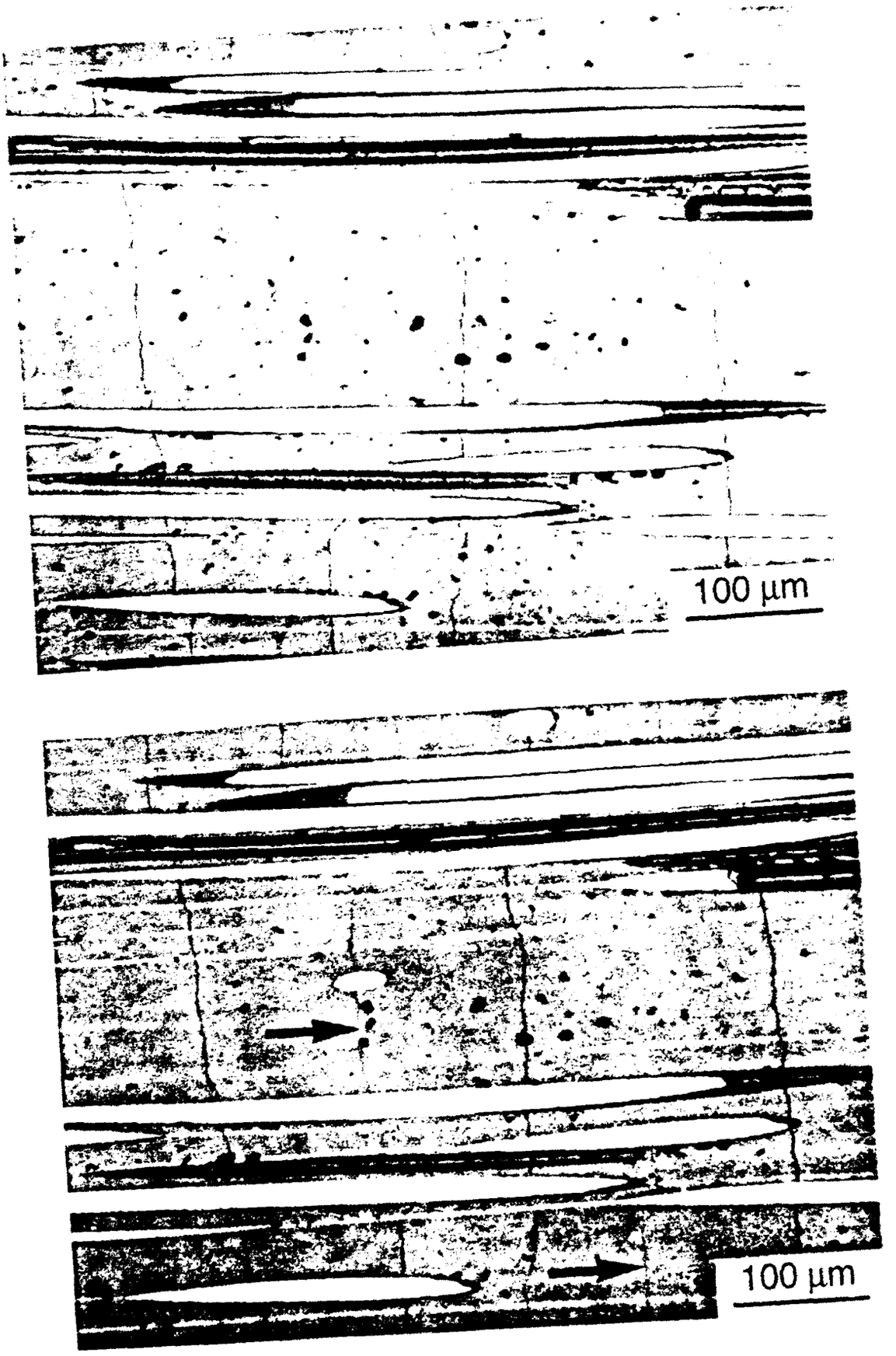

Fig. 2

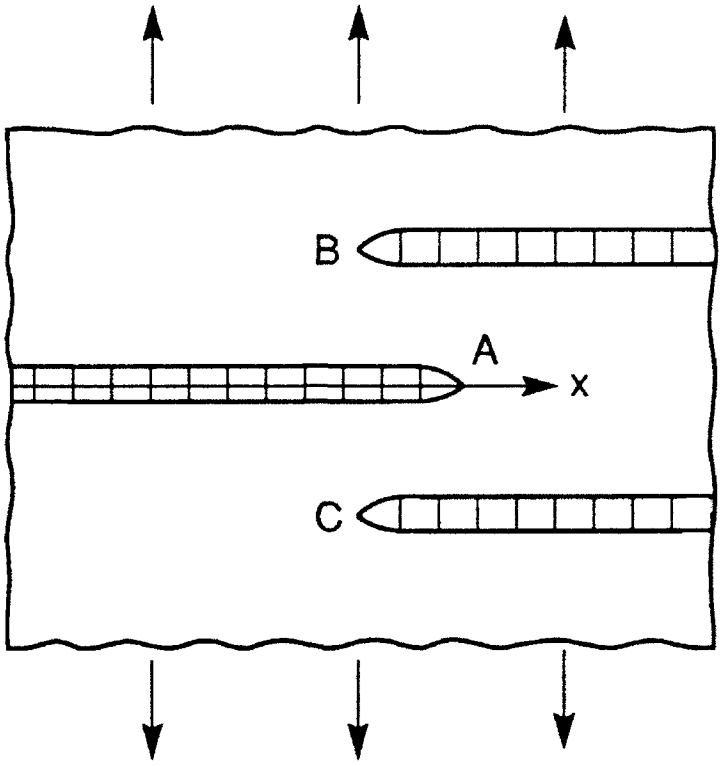

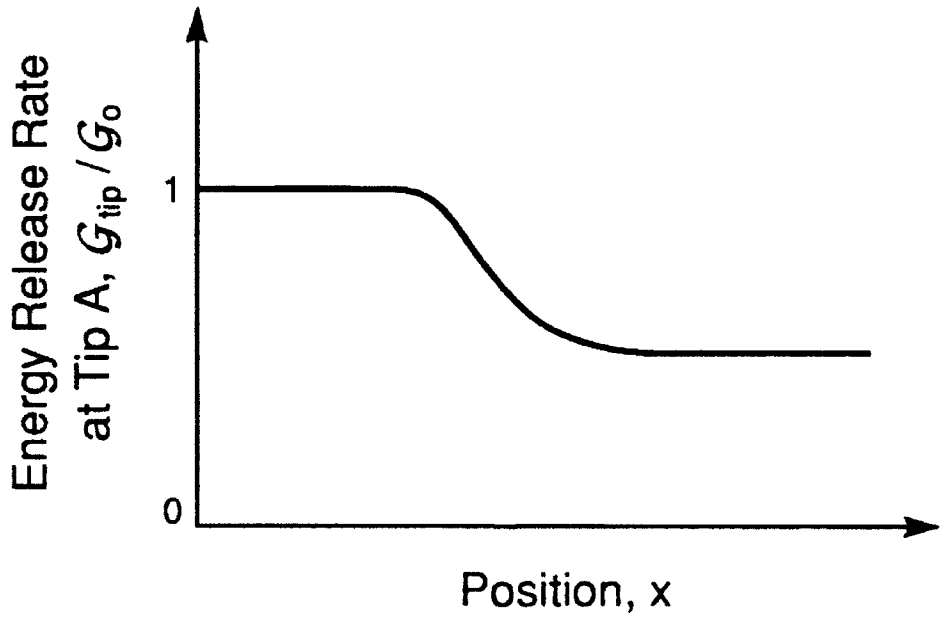

Fig. 3

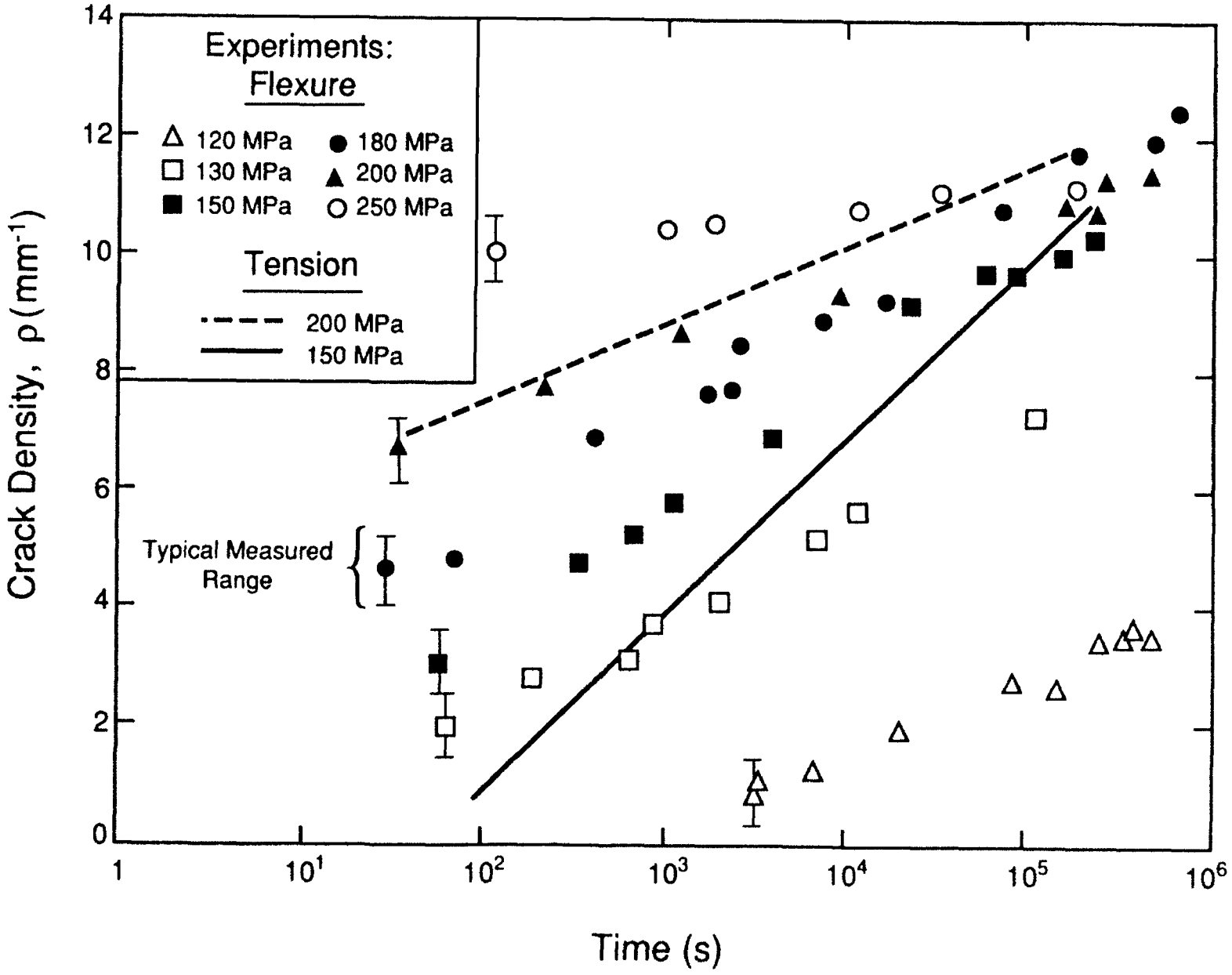
Experiments:
Flexure
120 MPa
130 MPa
150 MPa
180 MPa
200 MPa
250 MPa
Tension
200 MPa
150 MPa
Typical Measured Range
Crack Density, ρ (mm⁻¹)
Time (s)
0
2
4
6
8
10
12
14
1
10¹
10²
10³
10⁴
10⁵
10⁶

Fig. 4(a)

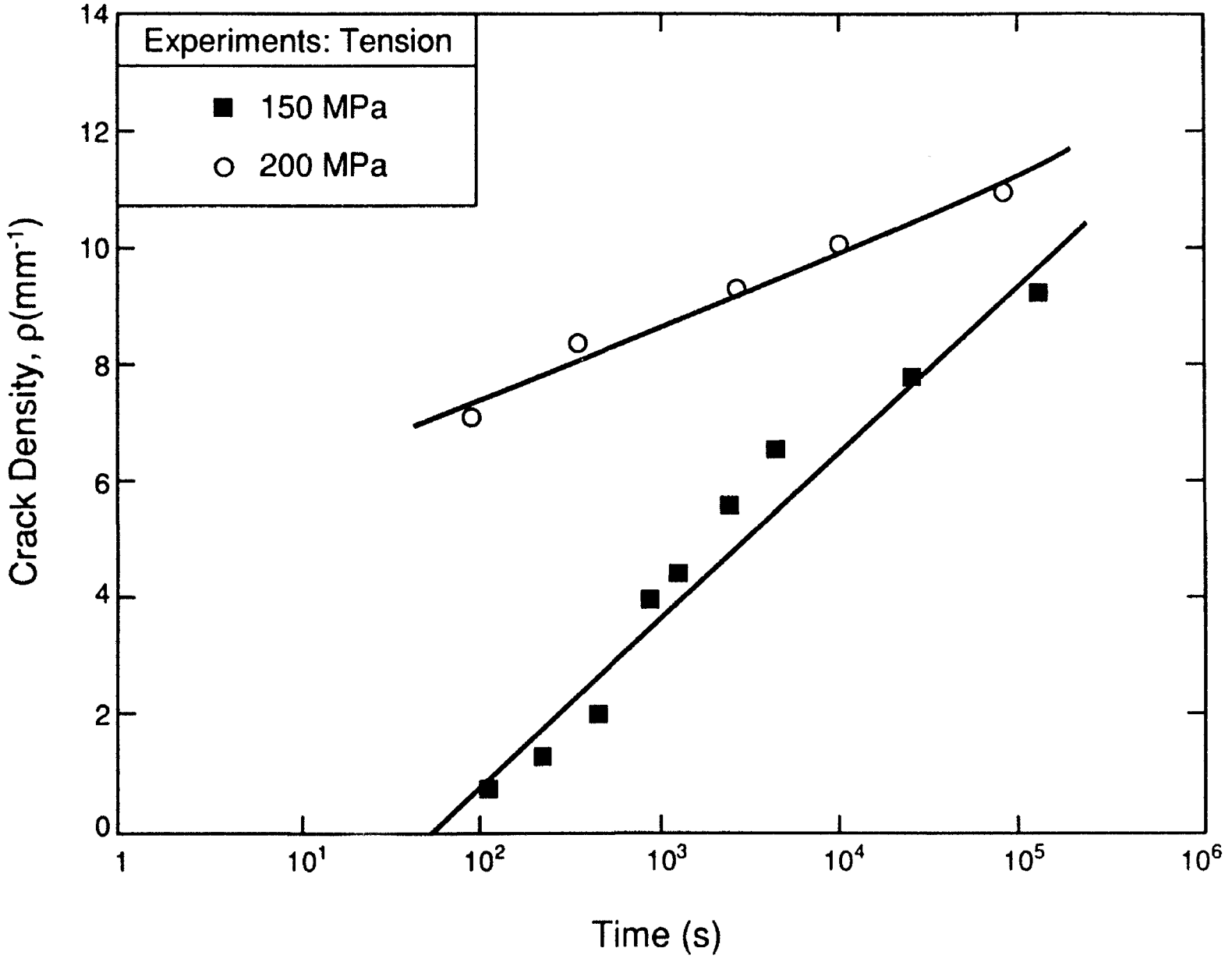
Experiments: Tension
150 MPa
200 MPa
Crack Density, ρ(mm⁻¹)
Time (s)
0
2
4
6
8
10
12
14
1
10¹
10²
10³
10⁴
10⁵
10⁶

Fig. 4(b)

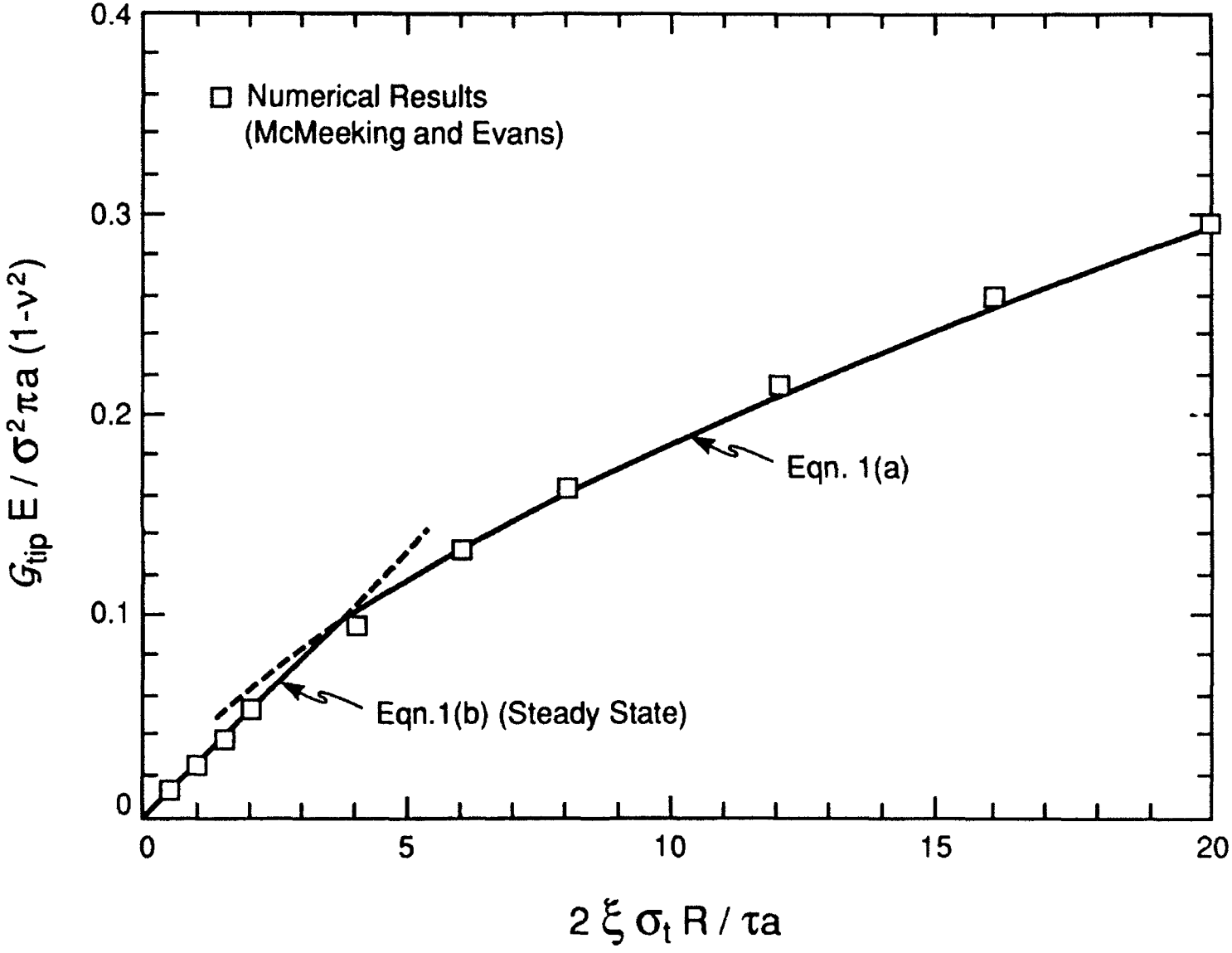
0.4
0.3
0.2
0.1
0
0
5
10
15
20
Numerical Results
(McMeeking and Evans)
Eqn. 1(a)
Eqn.1(b) (Steady State)
$\mathcal{G}_{tip} E / \sigma^2 \pi a (1-\nu^2)$
$2 \xi \sigma_t R / \tau a$

Fig. 5

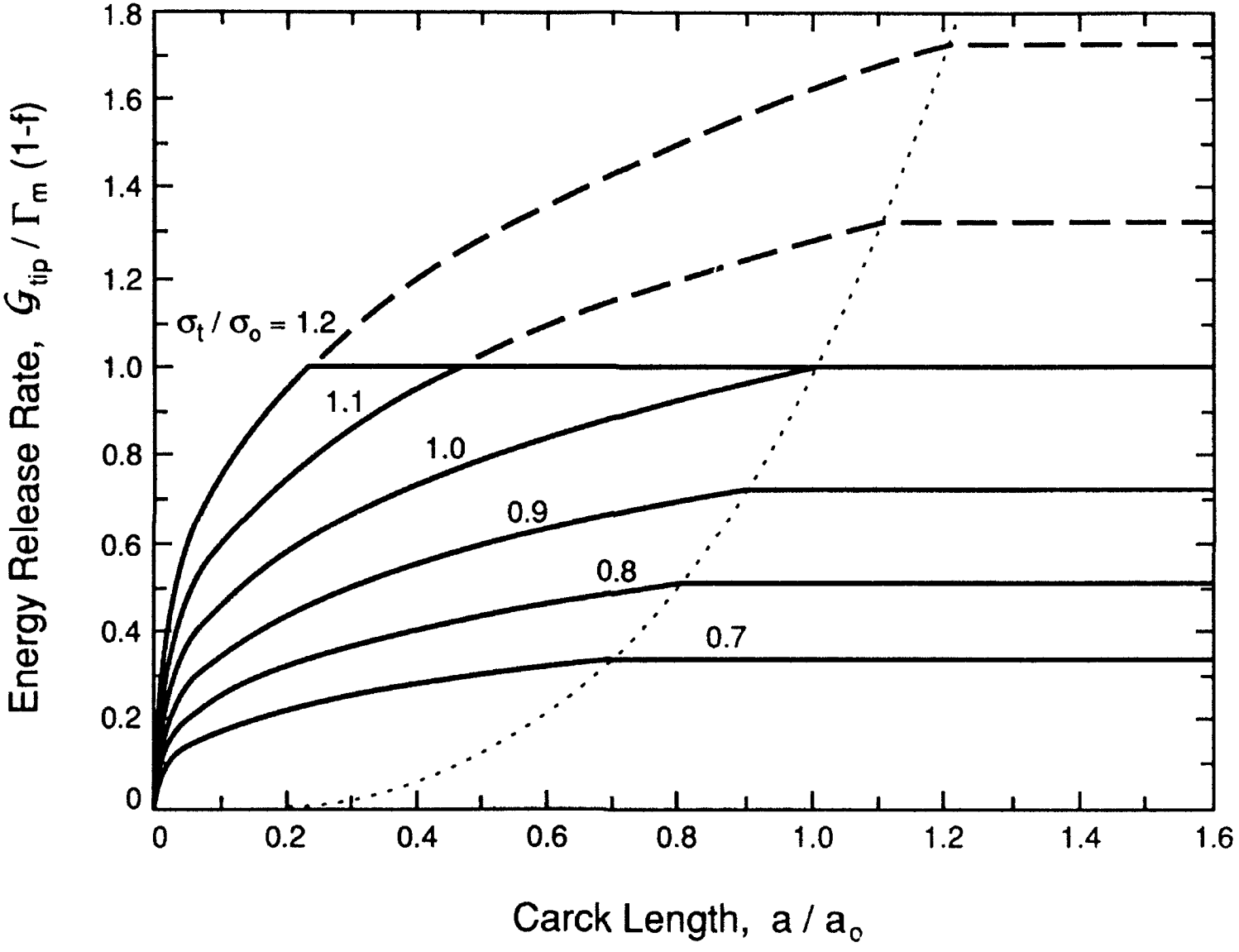
Energy Release Rate, $\mathcal{G}_{tip} / \Gamma_m (1-f)$
Carck Length, a / a_o
$\sigma_t / \sigma_o = 1.2$
1.1
1.0
0.9
0.8
0.7
0
0.2
0.4
0.6
0.8
1.0
1.2
1.4
1.6
1.8

FIG. 6

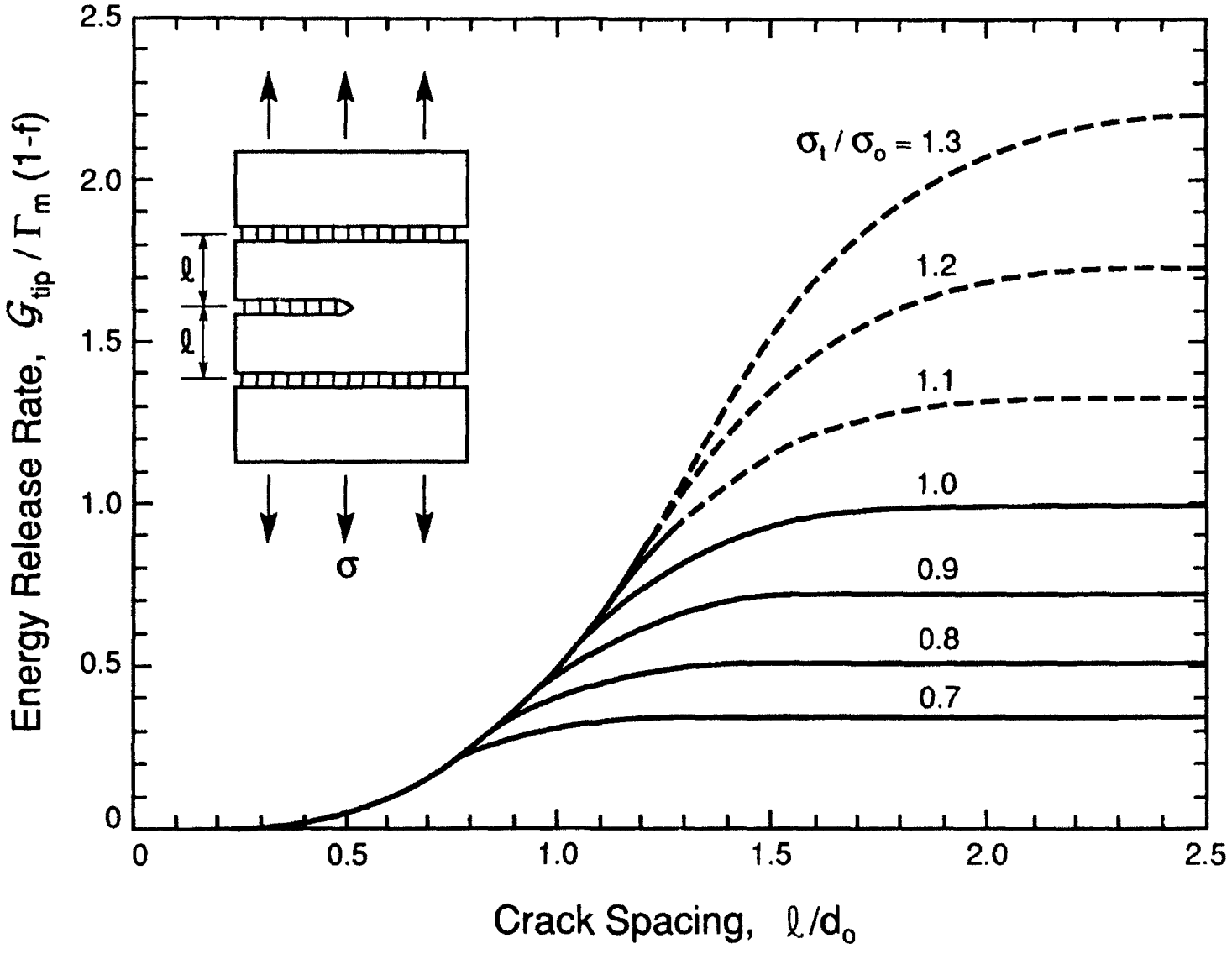
Energy Release Rate, $\mathcal{G}_{tip} / \Gamma_m (1-f)$
Crack Spacing, ℓ / d_o
$\sigma_1 / \sigma_o = 1.3$
1.2
1.1
1.0
0.9
0.8
0.7
ℓ
ℓ
σ
0
0.5
1.0
1.5
2.0
2.5

Fig. 7

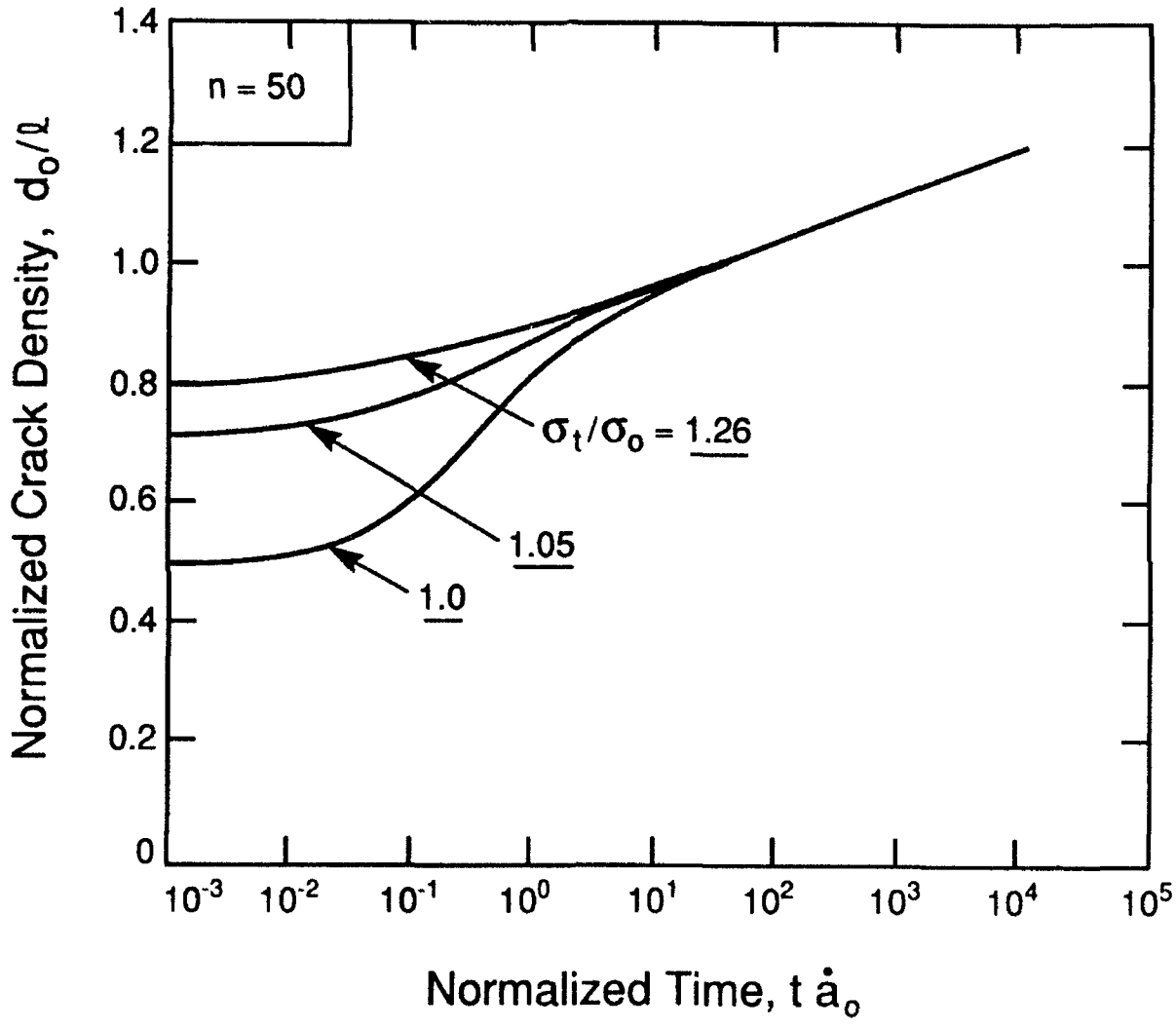
n = 50
1.4
1.2
1.0
0.8
0.6
0.4
0.2
0
Normalized Crack Density, d_o/ℓ
σ_t/σ_o = 1.26
1.05
1.0
10^{-3} 10^{-2} 10^{-1} 10^{0} 10^{1} 10^{2} 10^{3} 10^{4} 10^{5}
Normalized Time, $t\,\dot{a}_o$

Fig. 8

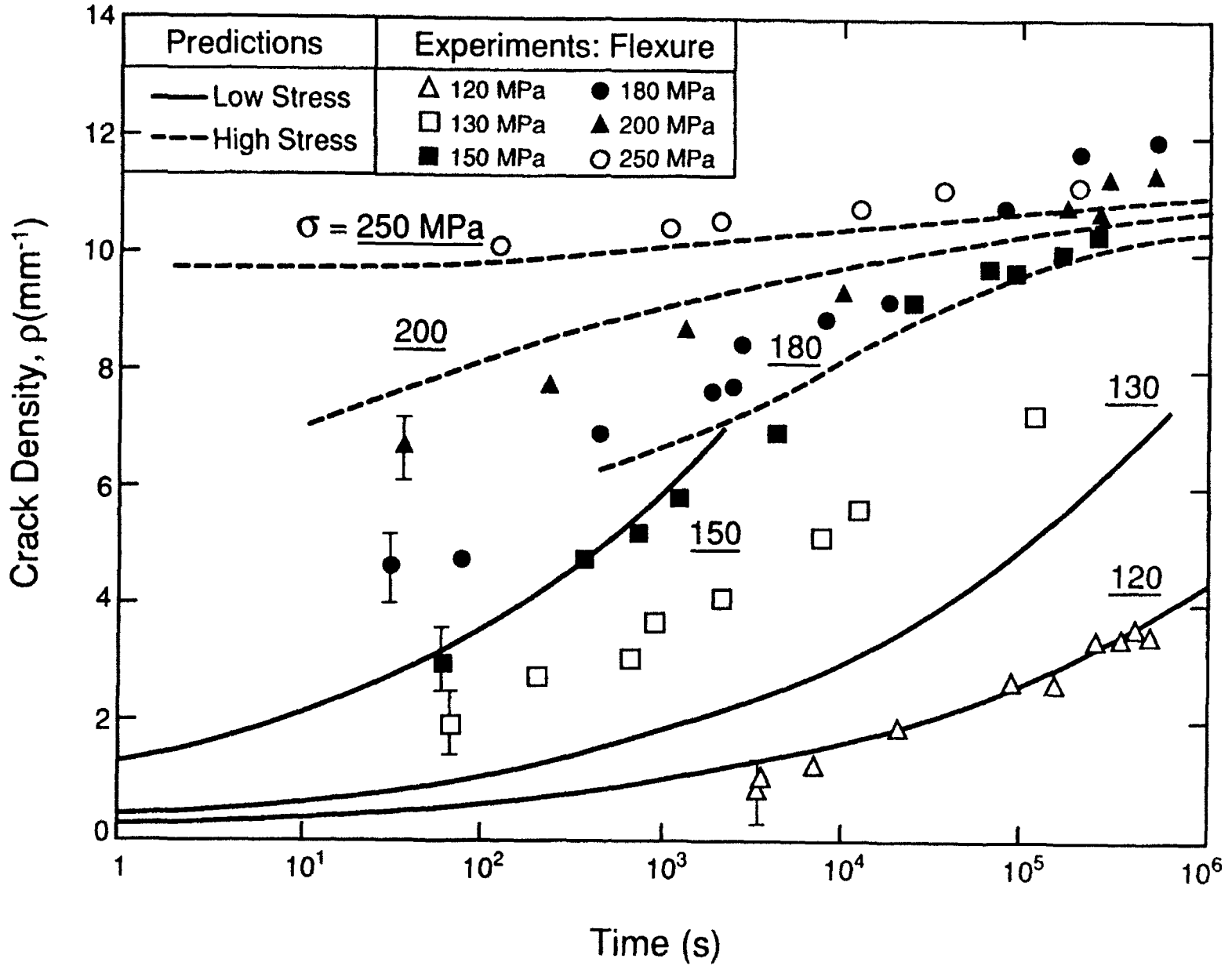
Predictions
Low Stress
High Stress
Experiments: Flexure
120 MPa
130 MPa
150 MPa
180 MPa
200 MPa
250 MPa
σ = 250 MPa
200
180
130
150
120
Crack Density, ρ(mm⁻¹)
Time (s)
0
2
4
6
8
10
12
14
1
10¹
10²
10³
10⁴
10⁵
10⁶

FIG. 9

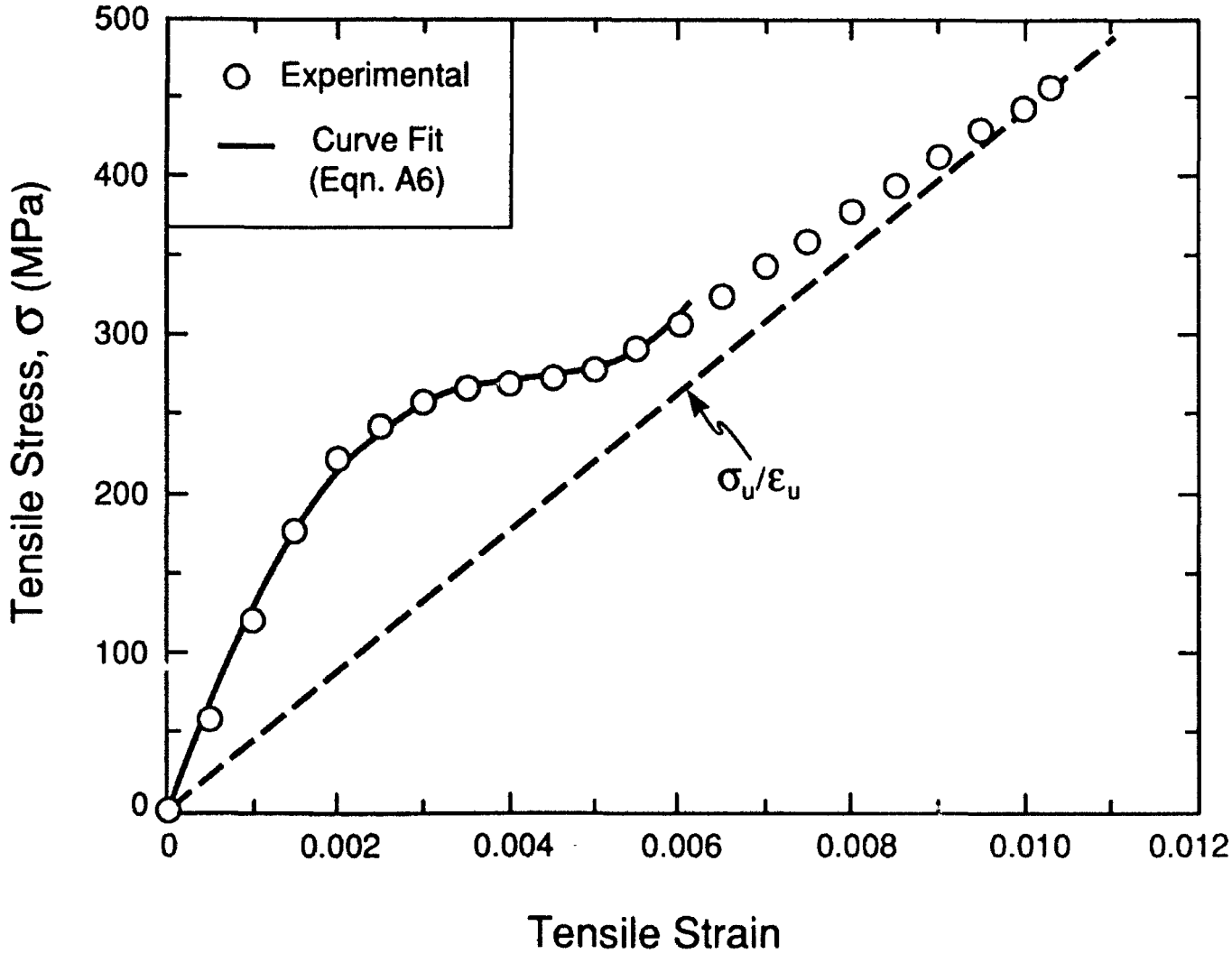
Experimental
Curve Fit
(Eqn. A6)
σ_u/ε_u
Tensile Stress, σ (MPa)
Tensile Strain
0
100
200
300
400
500
0
0.002
0.004
0.006
0.008
0.010
0.012

Fig. A1

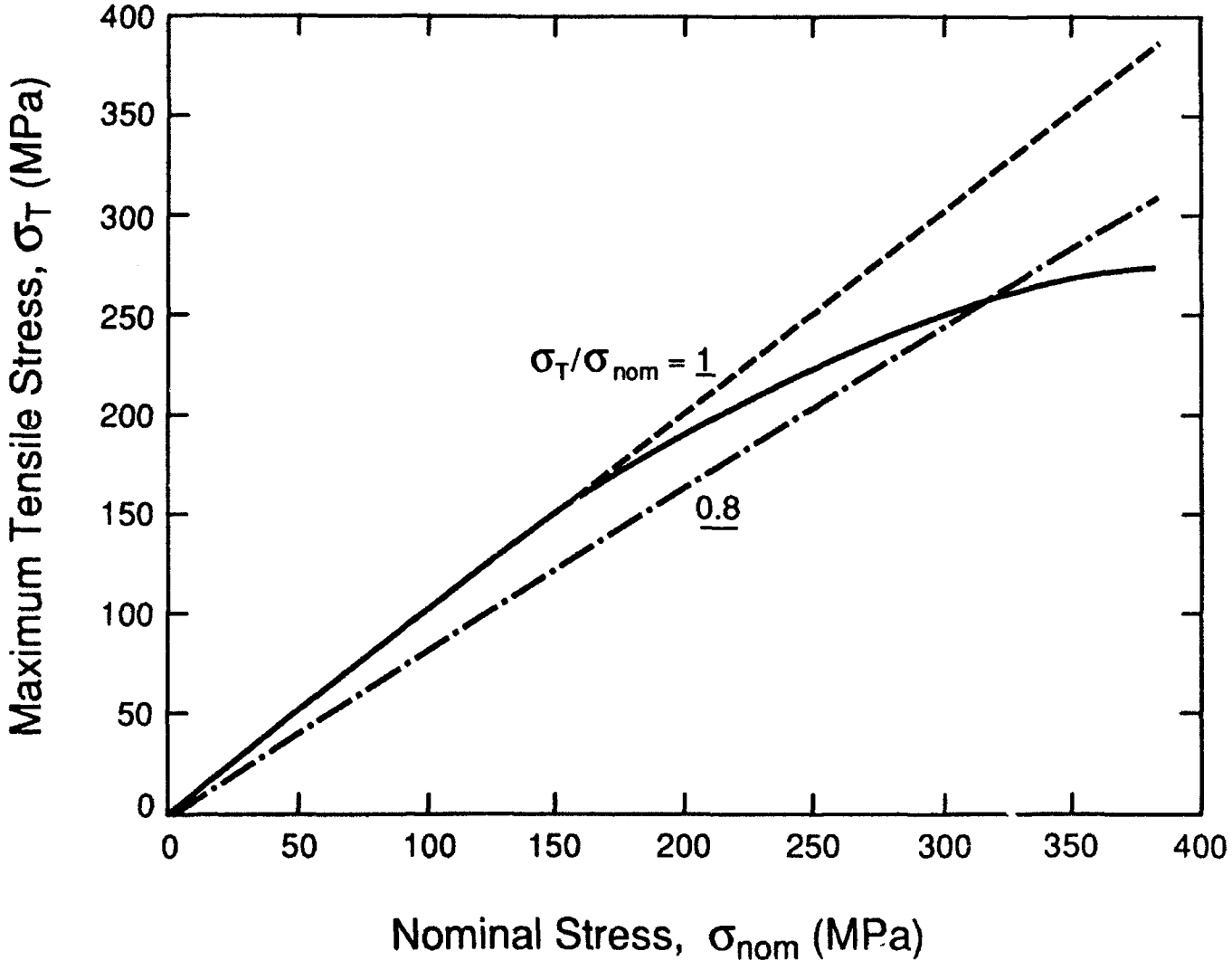
Maximum Tensile Stress, σ_T (MPa)
400
350
300
250
200
150
100
50
0
0
50
100
150
200
250
300
350
400
$\sigma_T/\sigma_{nom} = 1$
0.8
Nominal Stress, σ_{nom} (MPa)

Fig. A2

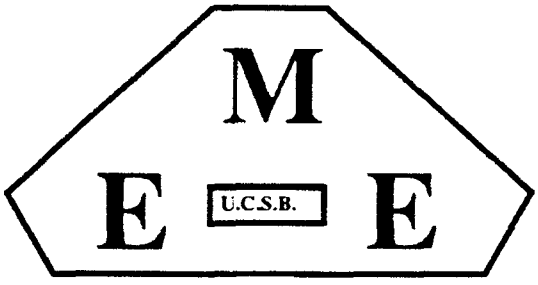

MECHANICAL AND ENVIRONMENTAL
ENGINEERING DEPARTMENT

MATERIALS

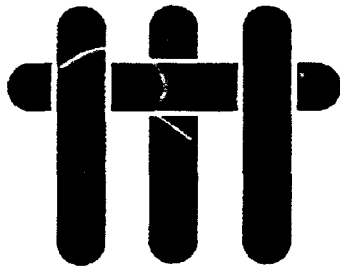

TENSILE AND FLEXURAL ULTIMATE STRENGTH OF FIBER-REINFORCED CERAMIC-MATRIX COMPOSITES

by

François HILD[1*] Jean-Marc DOMERGUE[2**]
Frederick A. LECKIE[1] Anthony G. EVANS[2]

[1]Department of Mechanical and Environmental Engineering and [2]Materials Department
College of Engineering, University of California, Santa Barbara, California 93106, U.S.A.

* Now at Laboratoire de Mécanique et Technologie, E.N.S. Cachan
61, avenue du Président Wilson, F-94235 Cachan Cedex, France
** Now at S.E.P, Les 5 chemins, Le Haillan, F-33160 Saint Médard en Jalles, France

KJS-Evans-26•Tw-Z•TA-Unf Eq 92/03/03•11:28 AM•4/28/92

TENSILE AND FLEXURAL ULTIMATE STRENGTH OF FIBER-REINFORCED CERAMIC-MATRIX COMPOSITES

François HILD
Jean-Marc DOMERGUE
Frederick A. LECKIE
Anthony G. EVANS

Abstract: A constitutive equation has been derived for fiber reinforced ceramic–matrix composites, based on fiber breakage and distributed fiber pull–out. Length dependent and length independent regimes, governed by the size of the specimen, are differentiated. The constitutive equation is used to predict the ultimate strength of fiber reinforced ceramic–matrix composites subjected to tensile and flexural loadings.

1. INTRODUCTION

The stress-strain behavior of ceramic-matrix composites (CMCs) is non-linear, provided that the interfaces slide with low shear resistance, τ . The loading of such composites results in two *independent* damage mechanisms: fiber failure and matrix cracking. The latter results in a diminished secant modulus $\bar{E}$, as well as a permanent strain, ε_p [Pryce and Smith; Beyerle *et al.*]. Furthermore, the fibers are subject to global load sharing, whereby the load transmitted from each failed fiber is shared equally among the intact fibers. Some aspects of the associated fiber failure stochastics have already been addressed [Curtin, 1991 a, b]. Two key parameters have been identified: a) a characteristic *length*

$$\delta_c^{m+1} = \left[S_o L_o^{1/m} R/\tau\right]^m \tag{1}$$

where m is the shape parameter, S_o is a stress scale parameter and L_o a reference length; b) a characteristic *strength*

$$S_c^{m+1} = L_o S_o^m \tau/R \tag{2}$$

When the gauge length, L, is large compared with δ_c, the fibers are capable of *multiple failures* within the gauge section. Consequently, the ultimate strength S_u is predicted to be gauge length independent, and given by [Curtin, 1991 a, b],

$$S_u \equiv f S_c \left[2/(m+2)\right]^{1/(m+1)} \left[(m+1)/(m+2)\right] \tag{3}$$

where f is the fiber volume fraction along the loading direction. Validation of Eqn. (3) has been provided for several CMCs, subject to global load sharing (small $\tau / f S_c$)

[Heredia *et al., 1991;* Beyerle *et al., 1991*]. Deviation from Eqn. (3) would be expected both for short gauge lengths, $L \lesssim \delta_c$, and when the stress on the composites is non-uniform. *These effects are analyzed in this paper.* The analytic approach has the same fundamental features established by others [Curtin, 1991 a, b]. However, the formulae are rederived to enable the solution to be presented in a form that facilitates analysis of composite failure subject to *complex situations*, such as non-uniform states of stress.

2. THE BASIC STOCHASTIC MODEL

A composite with a saturation density of matrix cracks is considered, spacing L_m, within a unit cell of length L_R (Fig. 1a). The length L_R is the *recovery* length and refers to the longest fiber that can be pulled out and cause a reduction in the load carrying capacity. The recovery length is thus related to the maximum stress in the fiber by

$$L_R = RT/\tau \tag{4}$$

where the reference stress T is the fiber stress in the plane of the matrix crack. Generally, $L_m << L_R$ and the stress field in intact fibers have the form illustrated in Fig. 1b. Consequently, the local stress in the fiber [Cox, 1952; Kelly, 1973] is ($0 \lesssim x \lesssim L_m/2$):

$$\sigma_F(T, x) = T - 2\tau x/R \tag{5}$$

If the fibers exhibit a statistical variation of strength that obeys a two-parameter law [Weibull, 1939], then the probability that a fiber would break anywhere within the characteristic length L_R at or below a reference stress T is given by

$$P_F(T) = 1 - \exp\left[-\left(\frac{1}{L_0}\right)\int_{-L_R/2}^{L_R/2}\left\{\frac{\sigma_F(T,x)}{S_0}\right\}^m dx\right] \quad (6)$$

Consequently, from Eqns. (5) and (6),

$$P_F(T) = 1 - \exp\left[-\frac{L_R}{(m+1)L_m}\left(\frac{T}{S_c}\right)^{m+1}\left\{1-\left(1-\frac{\tau L_m}{RT}\right)^{m+1}\right\}\right] \quad (7)$$

Often, $\tau L_m/RT << 1$, so that Eqn. (4) can be simplified to

$$P_F(T) \cong 1 - \exp\left[-\left(\frac{T}{S_c}\right)^{m+1}\right] \quad (8)$$

The cumulative failure probability is thus *independent* of the total length of the composite.

The average stress $\bar{\sigma}$ applied to the composite is related to the reference stress T by

$$\bar{\sigma} = fT\left[1 - P_F(T)\right] + f\sigma_p(T) \quad (9)$$

where σ_p (T) denotes that component of the stress provided by *failed fibers* as they pull out from the matrix. For global load sharing, the pull-out stress is given by

$$\sigma_p(T) = \int_0^T \frac{dP_F}{d\sigma}\bar{\sigma}_b(\sigma)d\sigma \quad (10)$$

where $\bar{\sigma}_b$ (σ) denotes the average stress at x = 0 when a fiber breaks at location x = t, and at the reference stress level σ

$$\bar{\sigma}_b(\sigma) = \int_{-L_R/2}^{L_R/2} \sigma_b(t) f(t, \sigma) dt \tag{11}$$

where $f(t, \sigma)$ is the probability density of failure locations. When the load is assumed to be constant over the entire recovery length, $f(t, \sigma) = 1/L_R$, the average pull-out stress (at reference stress σ) reduces to

$$\bar{\sigma}_b(\sigma) = \left(\frac{1}{L_R}\right) \int_{-L_R/2}^{L_R/2} \sigma_b(t) dt \tag{12}$$

For $t < 0$

$$\sigma_b(t) = -2\tau t/R$$

and for $t > 0$

$$\sigma_b(t) = 2\tau t/R$$

Provided that the composite length $L > L_R$, the average pull-out stress, at reference stress level σ, is

$$\bar{\sigma}_b(\sigma) = \sigma/2 \tag{13}$$

Then, the external stress takes the form

$$\bar{\sigma} = fT\left[1 - P_F(T)\right] + \frac{fS_c}{2}\gamma\left[\frac{m+2}{m+1}; \left(\frac{T}{S_c}\right)^{m+1}\right] \tag{14}$$

where $\gamma[.\,;.]$ represents the incomplete gamma function.

If pull-out were neglected, the following formulae would apply,

$$\bar{\sigma} = fT\left[1 - P_F(T)\right] \tag{15}$$

and

$$fT = \frac{\bar{\sigma}}{1 - P_F(T)} \tag{16}$$

This latter expression is analogous to the concept of effective stress in the framework of Continuum Damage Mechanics [Kachanov, 1958; Rabotnov, 1963; Lemaitre and Chaboche, 1990], when the damage variable, D, is described as the percentage of broken fibers [Krajcinovic and Silva, 1982; Hult and Travnicek, 1983; Hild et al., 1991] in a cell of length L_R.

The ultimate tensile strength of the composite is defined by the condition

$$d\bar{\sigma}/d\bar{\varepsilon} = 0$$

or

$$d\bar{\sigma}/dT = 0 \tag{17}$$

because the reference stress T is proportional to the average strain on the composite

$$\bar{\varepsilon} \;=\; \frac{2}{L_m}\int_0^{L_m/2}\frac{\sigma_F(T,x)}{E_f}\,dx \;\equiv\; T/E_f \tag{18}$$

where E_f denotes the Young's modulus of the *unbroken* fibers. The ultimate strength arises when

$$\frac{T}{S_c} \;=\; \left(\frac{2}{m+1}\right)^{1/(m+1)} \tag{19}$$

at a recovery length

$$\frac{L_R}{\delta_c} \;=\; \left(\frac{2}{m+1}\right)^{1/(m+1)} \tag{20}$$

Since, $\delta_c = L_o(S_o/S_c)^m$, the number of defects N which cause failure at a stress, $T = S_c$, in a fiber of length δ_c is given by [Curtin, 1991a, b]

$$N \;=\; \frac{\delta_c}{L_0}\left(\frac{S_c}{S_0}\right)^m \;=\; 1 \tag{21}$$

Consequently, the ultimate tensile strength becomes

$$S_u \;=\; fS_c\left\{\left(\frac{2}{m+1}\right)^{1/(m+1)}\exp\left(-\frac{2}{m+1}\right)+\frac{1}{2}\gamma\left[\frac{m+2}{m+1};\frac{m+2}{m+1}\right]\right\} \tag{22}$$

The ultimate tensile strength is *independent* of the total length of the composite [Curtin, 1991a, b], and the relevant scaling stress is the characteristic stress S_c. Equation (22) can be rewritten using a series expansion

$$S_u = f S_c F(m) \tag{23}$$

where

$$F(m) = \left(\frac{2}{m+1}\right)^{1/(m+1)}\left[1+\sum_{n\geq 1}\frac{(-1)^n}{n!}\,\frac{2+n(m+1)}{11+n(m+1)}\,\frac{2^{n-1}}{(m+1)^n}\right]$$

The function F increases as m increases (Fig. 2a) and tends asymptotically to unity. However, the ultimate tensile strength when normalized by explicit fiber properties decreases‡ as m increases (Fig. 2b). Consequently, a larger scatter leads to higher ultimate tensile strength. An approximate expression for the ultimate tensile strength can be obtained by reducing the function F to its first order (n = 1):

$$S_u \equiv f S_c\left[\frac{2}{m+1}\right]^{1/(m+1)}\left[\frac{m^2+2m-1}{(m+2)(m+1)}\right] \tag{24}$$

This result has essentially the same dependence on m as Eqn. (3), which was also derived by using an approximation [Curtin, 1991].

From a continuum damage mechanics perspective, it is useful to relate the average stress $\bar{\sigma}$ and strain $\bar{\varepsilon}$, given by:

‡ In the two figures, the values taken for the material parameters are those used by Jansson and Leckie [1991].

$$\bar{\sigma} = f E_F \bar{\varepsilon}\left[1 - P_F(E_F \bar{\varepsilon})\right] + f\frac{S_c}{2}\gamma\left[\frac{m+2}{m+1}; \left(\frac{E_F \bar{\varepsilon}}{\sigma_c}\right)^{m+1}\right] \tag{25a}$$

or

$$\bar{\sigma}/f S_c = \left(E_f \bar{\varepsilon}/S_c\right)\left[1 + \sum_{n\geq 1}\frac{(-1)^n}{2n!}\frac{2+n(m+1)}{1+n(m+1)}\left(E_f \bar{\varepsilon}/S_c\right)^{n(m+1)}\right] \tag{25b}$$

In general, thermal residual stresses due to processing cause an *additional* contribution to the strain associated with the displacements that arise upon matrix cracking (Pryce and Smith, Beyerle *et al.*).

The preceding basic results will now be used to derive solutions for two *new* problems: i) short specimens with $L \lesssim L_R$ and ii) flexural loading.

3. SHORT SPECIMENS

3.1 Stochastic Solutions

When the recovery length L_R becomes greater than the total length of the composite L, the previous results no longer apply, and the cumulative failure probability becomes length *dependent*,

$$P_F(T) \equiv 1 - \exp\left[-\frac{L}{L_0}\left(\frac{T}{S_0}\right)^m\right] \tag{26}$$

The corresponding average pull-out stress at stress level T is given by

$$\bar{\sigma}_b = \tau L/2R \tag{27}$$

The external stress takes the form

$$\bar{\sigma} = fT\left[1 - P_F(T)\right] + \frac{fS_c}{2}\gamma\left[\frac{m+2}{m+1}; \left(\frac{L}{\delta_c}\right)^{m+1}\right] + f\sigma_p^* \tag{28a}$$

where the stress σ_p^* corresponds to the revised contribution from pull-out

$$\sigma_p^* = \frac{\tau L}{2R}\left\{\exp\left[-\left(\frac{L}{\delta_c}\right)^{m+1}\right] - \exp\left[-\frac{L}{L_0}\left(\frac{T}{S_0}\right)^m\right]\right\} \tag{28b}$$

The external stress is now *explicitly* dependent upon the total length of the composite, L. The ultimate tensile strength is solution of the follcwing equation,

$$1 - m\frac{L}{\delta_c}\left(\frac{T}{S_c}\right)^m + \frac{m}{2}\left(\frac{L}{\delta_c}\right)^2\left(\frac{T}{S_c}\right)^{m-1} = 0 \tag{29}$$

A closed form solution for Eqn. (29) does not exist, but a typical result is plotted on Fig. 4. When $L = L_R$, the solution is

$$\left(\frac{T}{S_c}\right) = \left(\frac{2}{m}\right)^{1/(m+1)} \tag{30}$$

such that

$$\left(\frac{L_R}{\delta_c}\right) = \left(\frac{2}{m}\right)^{1/(m+1)} \tag{31}$$

Furthermore, as $L \to 0$, S_u tends to the ultimate tensile strength obtained by neglecting the contribution associated with distributed fiber pull-out (Fig. 3),

$$S_u(L) \cong f S_0 \left(\frac{L_0}{mL} \right)^{1/m} \exp\left(- \frac{1}{m} \right) = S_b \tag{32}$$

where S_b denotes the classical fiber bundle strength. In this case, the length dependence has the desired form for a fiber bundle. Similar results have been independently derived by Curtin [1992].

The solutions for short and long gauge lengths *intersect* in the region where

$$\left(\frac{2}{m+1} \right)^{1/(m+1)} \leq \frac{L}{\delta_c} \leq \left(\frac{2}{m} \right)^{1/(m+1)} \tag{33}$$

The length at the intersection is a transition length, L^* (S_u is length dependent when $L \leq L^*$ and length independent when $L \geq L^*$). In terms of normalized quantities (L/δ_c and T/S_c), L^* only depends on m (Fig. 4): Note how the actual intersection L^*/δ_c compares with the two bounds given in Eqn. (33).

3.2 Comparison with Experiment

Comparison of the above stochastics will be made with three different experimental results for CMCs. i) Experiments on LAS matrix composites reinforced by SiC (Nicalon) fibers provide the general information summarized on Table I [Prewo, 1986]. For each specimen, the transition length L^* is small (< 3L), suggesting use of the *gauge length independent* solution. The corresponding predictions are given on Table I. It is apparent that the agreement between experiment and prediction is quite good, especially for

τ = 3 MPa. ii) Experiments performed on two carbon matrix composites (material A and C) reinforced by SiC (Nicalon) fibers [Heredia et al., 1991]) are summarized in Table II. Again, the predictions agree well with experiments. iii) Experiment on a CAS matrix reinforced by SiC (Nicalon) fibers provide the data summarized in Table III [Beyerle et al., 1991]. Corresponding to these experimental data, the transition length, L^* (0.85 mm) is again small compared with the total length of the composite. In this case, the predicted ultimate tensile strength S_u = 485 MPa, is somewhat larger than the measured value, S_u = 430 MPa. The discrepancy is not understood.

4. THE FLEXURAL STRENGTH

Expressions for the *flexural strength* are derived from the regime where there is *no length dependence*. The tensile side of the specimen is considered to have a stress/strain curve represented by Eqn. (25). Consequently, strains associated with matrix cracking are neglected. On the compressive side, it is assumed that the behavior is elastic and characterized by the Young's modulus of the composite $\bar{E}$. The strain is given by [Timoshenko and Goodier, 1970]

$$\bar{\varepsilon} = \mathcal{R} z \tag{34}$$

where $\mathcal{R}$ denotes the curvature, and z the height ordinate (Fig. 5). Consequently, from Eqn. (25),

$$\Sigma = Z\left[1 + \sum_{n\geq 1} \frac{(-1)^n}{2n!} \frac{2 + n(m+1)}{1 + n(m+1)} Z^{n(m+1)}\right] \tag{35}$$

where

$$Z = E_f R Z / S_c ; \quad \Sigma = \bar{\sigma} / f S_c$$

Force balance dictates the position of the neutral axis, h, (Fig. 5), such that

$$h_1/h = \left[1 + \sqrt{\frac{g(m)}{1 - D_1}} \right]^{-1} \tag{36}$$

where

$$g(m) = 1 + \sum_{n \geq 1} \frac{(-1)^n}{n!} \left[\frac{1}{1 + n(m+1)} \right] \left[2/(m+1) \right]^n$$

and D_1 is a damage variable reflecting the difference in Young's modulus in tension and compression

$$D_1 = 1 - f E_f / \bar{E} \tag{37}$$

The flexural strength is derived by evaluating the stress at the tensile surface and equating to Eqn. (23) to give

$$S_u = f S_c H(m, D_1) \tag{38}$$

where

$$H(m, D_1) = 2 \left(\frac{h_1}{h} \right)^2 \left(\frac{2}{m+1} \right)^{1/(m+1)} \left[\frac{1}{1 - D_1} \left\{ \frac{h}{h_1} - 1 \right\}^3 + G(m) \right]$$

and

$$G(m) = 1 + 3\sum_{n\geq 1}\frac{(-1)^n}{n!}\frac{2+n(m+1)}{[1+n(m+1)][3+n(m+1)]}\left[\frac{2^{n-1}}{(m+1)^n}\right]$$

The flexural strength again scales with the characteristic strength, S_c, and the fiber volume fraction f, because the length independent failure regime is assumed to operate in the tensile part of the beam. However, for short specimens, shear failure is more likely than tensile failure and the present analysis is not valid.

The flexural strength is also explicitly dependent upon the damage variable, D_1, and the Weibull modulus, m (Fig. 6). As $m \rightarrow \infty$, the ratio of the flexural strength to the ultimate tensile strength tends to the Young's modulus difference between tension and compression, $2/(1 + \sqrt{1 - D_1})$. As also evident in tension, the higher the scatter in fiber failure strength, the higher the normalized flexural strength. Furthermore, the higher the damage variable, D_1, (i.e., the lower the ratio of the Young's modulus in tension to that in compression), the higher the normalized flexural strength.

Flexural results for the same materials described above, summarized in Table IV, indicate reasonable agreement between experimental and predicted values. However, the SiC/CAS composite failed in shear. Apparently, tensile failure would have occurred at similar stress if a longer specimen had been used. The relatively low flexural strength predicted in the case of the SiC/C (C) composite is consistent with a similar underestimation of the ultimate tensile strength. Indeed, by using the *experimental* value of the ultimate tensile strength, the predicted flexural strength (430 MPa) is much closer to the experimental value.

5. CONCLUDING REMARKS

Expressions for the ultimate strength in tension and flexure have been derived in the framework of global load sharing and single fiber pull-out, in terms of the two main characterizing parameters δ_c and S_c. A characteristic *length*, δ_c, provides a dimension that differentiates long and short specimens and establishes two different regimes: A length dependent ultimate strength for short specimens ($L \lesssim \delta_c$) and a length independent ultimate strength for long specimens ($L \gtrsim \delta_c$). The characteristic *strength*, S_c, allows scaling of the ultimate tensile strength and flexural strength, provided that the specimens are *long*. For short specimens, the bundle strength, S_b gives a good measure of the ultimate tensile strength, independently of the interfacial shear stress τ. The Weibull modulus, m, gives a measure of the fraction D of broken fibers in an elementary cell at the ultimate: for large specimens $D = 1 - \exp[2/(m+1)]$. Furthermore, the associated scatter *enhances* the ultimate strength of the composite.

In flexure, a parameter, D_1, has been defined that measures the loss of stiffness of the tensile side. This effect, coupled with the degradation associated with fiber breakage and pull-out, causes the normalized flexural strength to increase. Beyond the ultimate, a new phenomenon takes place: localized fiber pull-out, wherein one matrix crack becomes predominant. At this stage, there is a loss of uniqueness and localization may occur [Hild et al., 1991] accompanied by a substantial load drop.

TABLE I

Results and Predictions For LAS Matrix Composite

τ = 2–3 MPa R = 8 μm

L = 25 mm L_0 = 25 mm

EXPERIMENTAL RESULTS

Sample #	f	m	S_0 (MPa)	S_u(MPa)
2369 (p)	0.46	3.8	1740	758
2369 (c)	0.46	2.7	1740	664
2376 (p)	0.44	3.9	1615	670
2376 (c)	0.44	3.1	1632	680

PREDICTIONS

Sample #	L^* (mm) (τ = 2 MPa)	L^* (mm) (τ = 3 MPa)	S_u (MPa) (τ = 2 MPa)	S_u (MPa) (τ = 3 MPa)
2369 (p)	7.8	5.6	695	755
2369 (c)	8.7	6.5	710	792
2376 (p)	7.3	5.3	625	680
2376 (c)	7.8	5.7	635	700

TABLE II

Results and Predictions For Carbon-Matrix Composites

EXPERIMENTAL RESULTS

L = 25 mm L_0 = 25 mm R = 6.5 μm

Material	f	S_0 (MPa)	m	τ	S_u (MPa)
A	0.2	1165	4.5	10	290
C	0.2	1140	4.5	14	345

PREDICTIONS

Material	L^* (mm)	S_u (MPa)
A	1.43	300
C	1.08	315

* This volume fraction corresponds to the fiber volume fraction in the longitudinal direction.

TABLE III

Experimental Results For CAS Matrix Composite

S_0 = 1050 MPa	L_0 = 10 mm	m = 3.6
τ = 15 MPa	R = 7.5 μm	f = 0.37
	L = 10 mm	
	S_u = 430 MPa	

TABLE IV

Flexural Experiments and Predictions

Material	S_u (MPa)	
	Experiment	Prediction
SiC/CAS	620	635
SiC/LAS	1050	1080
SiC/C (A)	435	435
SiC/C (C)	455	395

REFERENCES

Beyerle, D.S., Spearing, S.M., Zok, F.W. and Evans, A.G., 1991. "Damage, Degradation and Failure in a Unidirectional Ceramic-Matrix Composite," *J. Am. Ceram. Soc.*, in press.

Cao, H.C., Bischoff, E., Sbaizero, O., Rühle, M. and Evans, A.G., 1990. "Effect of Interfaces on the Properties of Fiber-Reinforced Ceramics," *J. Am. Ceram. Soc.*, **73** [6], 1691–1699.

Cao, H.C. and Thouless, M.D., 1990. "Tensile Tests of Ceramic-Matrix Composites: Theory and Experiment, *J. Am. Ceram. Soc.*, **73** [7] 2091–2094.

Cox, H.L., 1952. "The Elasticity and the Strength of Paper and Other Fibrous Materials," *Br. J. Appl. Phys.*, Vol. 3, 72–79.

Curtin, W.A., 1991a. "Exact Theory of Fiber Fragmentation in Single–Filament Composite," *J. Mat. Sci.*, **26**, 5239–5253.

Curtin, W.A., 1991b. "Theory of Mechanical Properties of Ceramic Matrix Composites," *J. Am. Ceram. Soc.*, **74** 11, 2837–2845.

Curtin, W.A., 1992, to be published.

Henstenburg, R.B. and Phoenix, S.L., 1989. "Interfacial Shear Strength Using Single-Filament-Composite Test. Part II: A Probability Model and Monte Carlo Simulations," *Polym. Comp.* **10** [5] 389–406.

Heredia, F.E., Spearing, S.M., Evans, A.G., Mosher, P. and Curtin, W.A., 1991. "Mechanical Properties of Carbon Matrix Composites Reinforced with Nicalon Fibers," *J. Am. Ceram. Soc.*, in press.

Hild, F., Larsson, P.-L. and Leckie, F., 1991. "Localization Due to Damage in Fiber Reinforced Composites," *Int. J. Solids Struct., in press.*

Hult, J. and Travnicek, L., 1983. "Carrying Capacity of Fiber Bundles with Varying Strength and Stiffness," *Journal de Mécanique Théorique et Appliquée*, **2** [2], 643–657.

Jansson, S. and Leckie, F.A., 1991. "The Mechanics of Failure of Silicon Carbide Fiber–Reinforced Glass–Matrix Composites," *Acta Metall., accepted.*

Kachanov, L.M., 1958. "Time of the Rupture Process under Creep Conditions," *Izv. Akad. Nauk. S.S.R. Odt. Tekh. Nauk.*, **8**, 26–31.

Kelly, A., 1973. *Strong Solids*, 2nd edn, Oxford University Press, Chapter 5.

Krajcinovic, D. and Silva, M.A.G. (1982). "Statistical Aspects of the Continuous Damage Theory," *Int. J. Solids Structures*, **18** [7], 551–562.

Lemaitre, J. and Chaboche, J.-L., 1990. *Mechanics of Solid Materials*, Cambridge University Press. Cambridge.

McMeeking, R.M. and Evans, A.G., 1990. "Matrix Fatigue Cracking in Fiber Composites," *Mech. of Mtls.* **9**, 217-227.

Oh, H.L. and Finnie, I., 1970. "On the Location of Fracture in Brittle Solids-I Due to Static Loading," *Int. J. Frac. Mech.*, **6** 3, 287–300.

Prewo, K.M., 1986. "Tension and Flexural Strength of Silicon Carbide Fibre-Reinforced Glass Ceramics," *J. Mat. Sci.*, **21**, 3590–3600.

Pryce, A.W. and Smith, P.A., 1991. "Modelling the Stress/Strain Behaviour of Unidirectional Ceramic Matrix Composite Laminates," *J. Mater. Sci.*, submitted.

Rabotnov, Y.N., 1963. "On the Equations of State for Creep," *Progress in Applied Mechanics*, Prager Anniversary Vol., McMillan, New-York, 307.

Schwartz, S., Lee, S. and Mosher, P., 1991. "Properties of Silicon Carbide Fiber Reinforced Carbon Composite," *15th Annual Conference on Composite Materials and Structures, ACerS*, Cocoa Beach, FL, January 16-18, 1991.

Sutcu, M., 1989. "Weibull Statistics Applied to Fiber Failure in Ceramic Composites and Work of Fracture," *Acta Metall.*, **37** [2] 651–661.

Thouless, M.D. and Evans, A.G., 1988. "Effects of Pull-Out on the Mechanical Properties of Ceramic-Matrix Composites," *Acta Metall*, **36** [3], 517–522.

Thouless, M.D., Sbaizero, O., Sigl, L.S. and Evans, A.G., 1989. "Effect of Interface Mechanical Properties on Pullout in a SiC-Fiber-Reinforced Lithium Aluminum Silicate Glass-Ceramic," *J. Am. Ceram. Soc.*, **72** [4], 525–532.

Timoshenko, S.P. and Goodier, J.N., 1970. *Theory of Elasticity*, 3rd edition, McGraw-Hill.

Weibull, W., 1939. "A Statistical Theory of the Strength of Materials," *Ingeniörsvetenskapakademiens*, Handlingar Nr 151.

FIGURE CAPTIONS

Fig. 1. a) Depiction of the recovery length L_R when the density of matrix cracks reaches saturation.

b) Fiber stress field $\sigma_f(T\ x)$ along a length L_R for a reference stress, T, when the fibers are intact.

c) Stress in the fiber when the fiber fails. Also shown is a visualization of the pull-out stress σ_b when the matrix crack is located at $x = 0$ and fibers break at different locations t.

Fig. 2. a) Non-dimensional ultimate strength, F, as a function of Weibull modulus m.

b) Ultimate tensile strength S_u, normalized by $f\ S_0$, as a function of Weibull modulus [when $S_0 = 1500$ MPa, $\tau = 5$ MPa, and $L_0 = 25$ mm].

Fig. 3. Ultimate tensile strength as a function of the normalized total length of the composite. A comparison is made with a fiber bundle prediction.

Fig. 4. Comparison between the upper and lower bounds for the transition between short and long specimen behaviors with the actual intersection point, as a function of the Weibull modulus m.

Fig. 5. Definition of the beam geometry in the case of flexure.

Fig. 6. Normalized flexural strength against Weibull modulus m, for three different values of the parameter D_1 (0.1, 0.2 and 0.3).

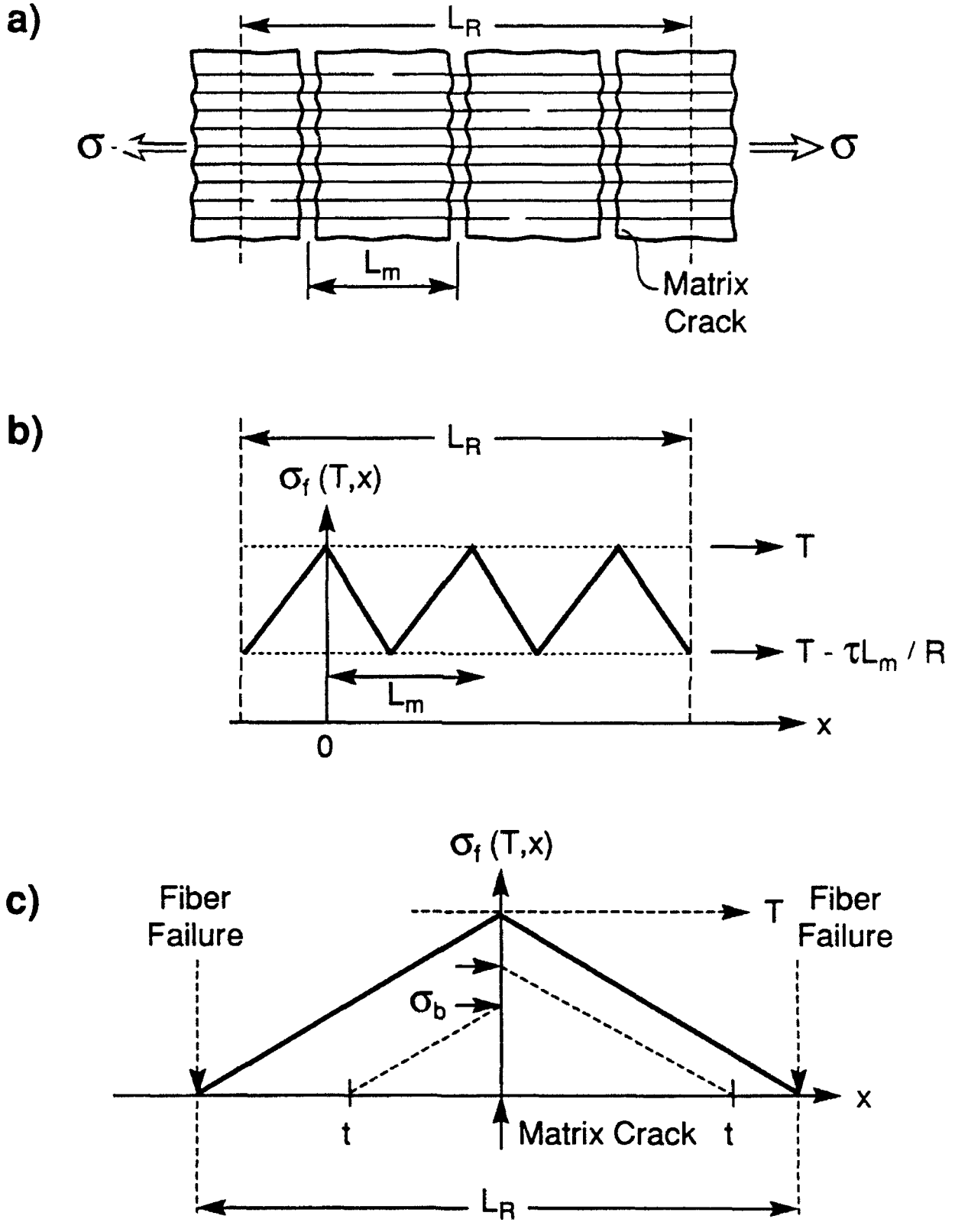
a)
L_R
σ
σ
L_m
Matrix
Crack
b)
L_R
σ_f (T,x)
T
T - τL_m / R
L_m
x
0
c)
σ_f (T,x)
Fiber
Failure
T
Fiber
Failure
σ_b
x
t
Matrix Crack
t
L_R

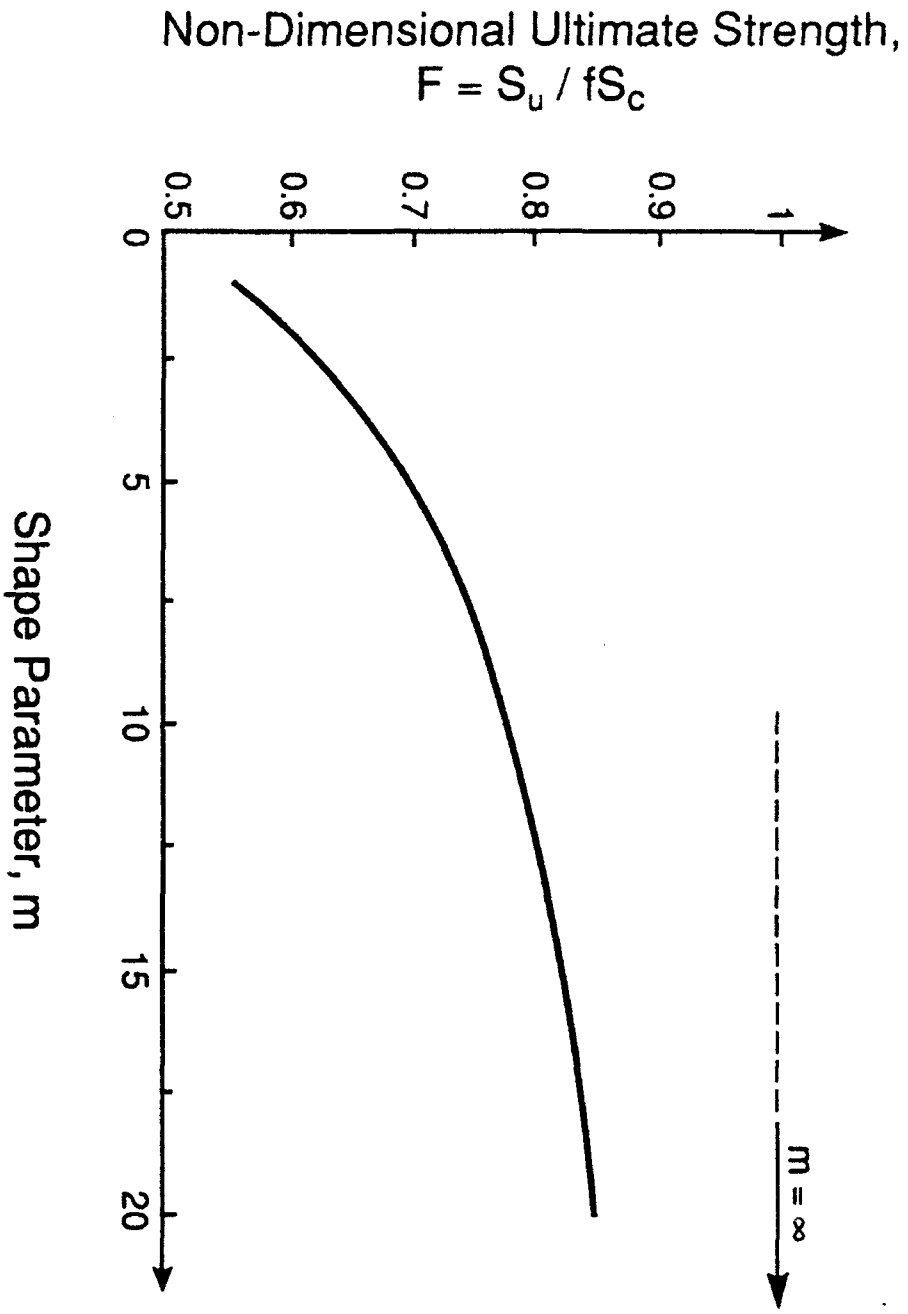

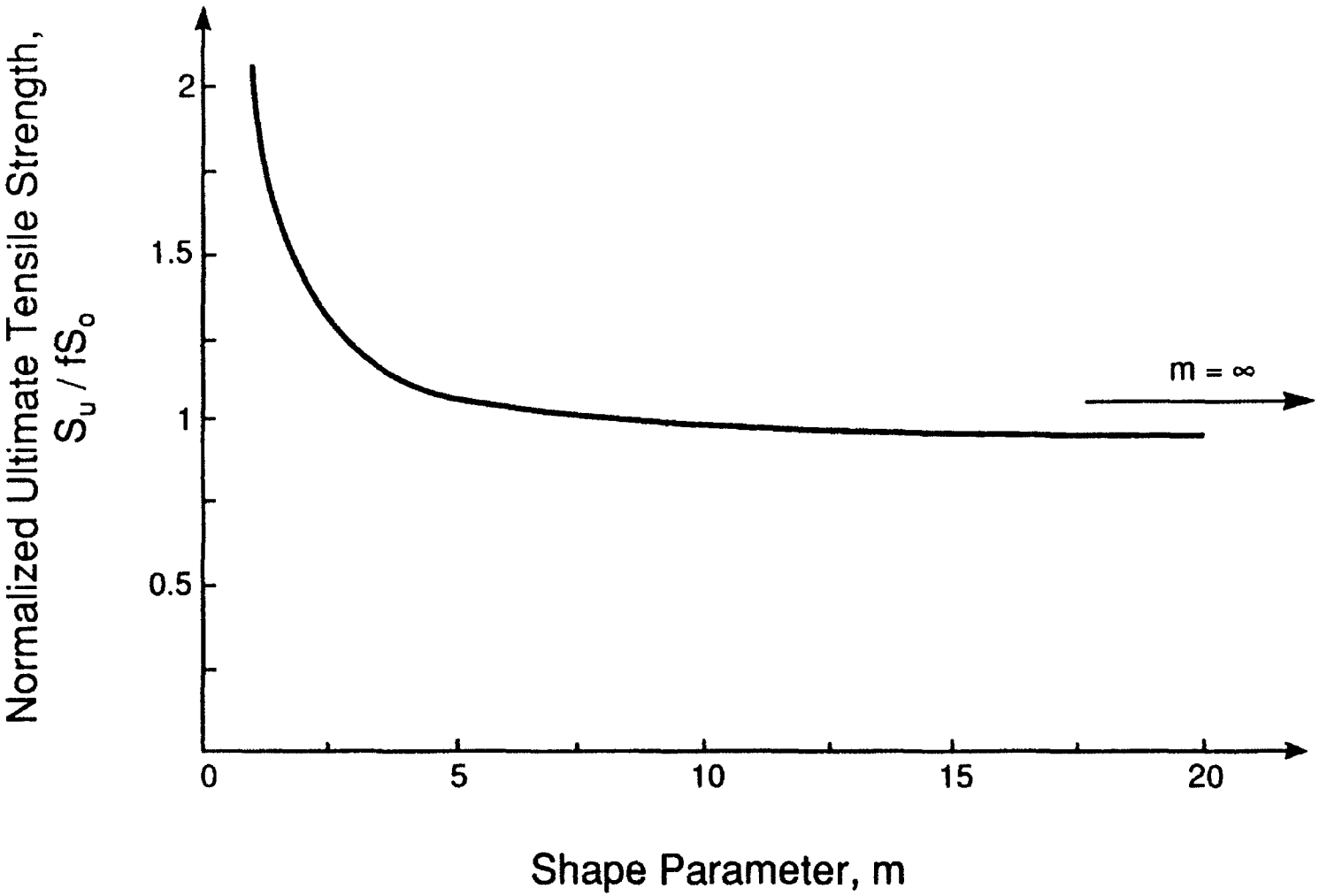
Normalized Ultimate Tensile Strength,
S_u / fS_o
2
1.5
1
0.5
0
5
10
15
20
m = ∞
Shape Parameter, m

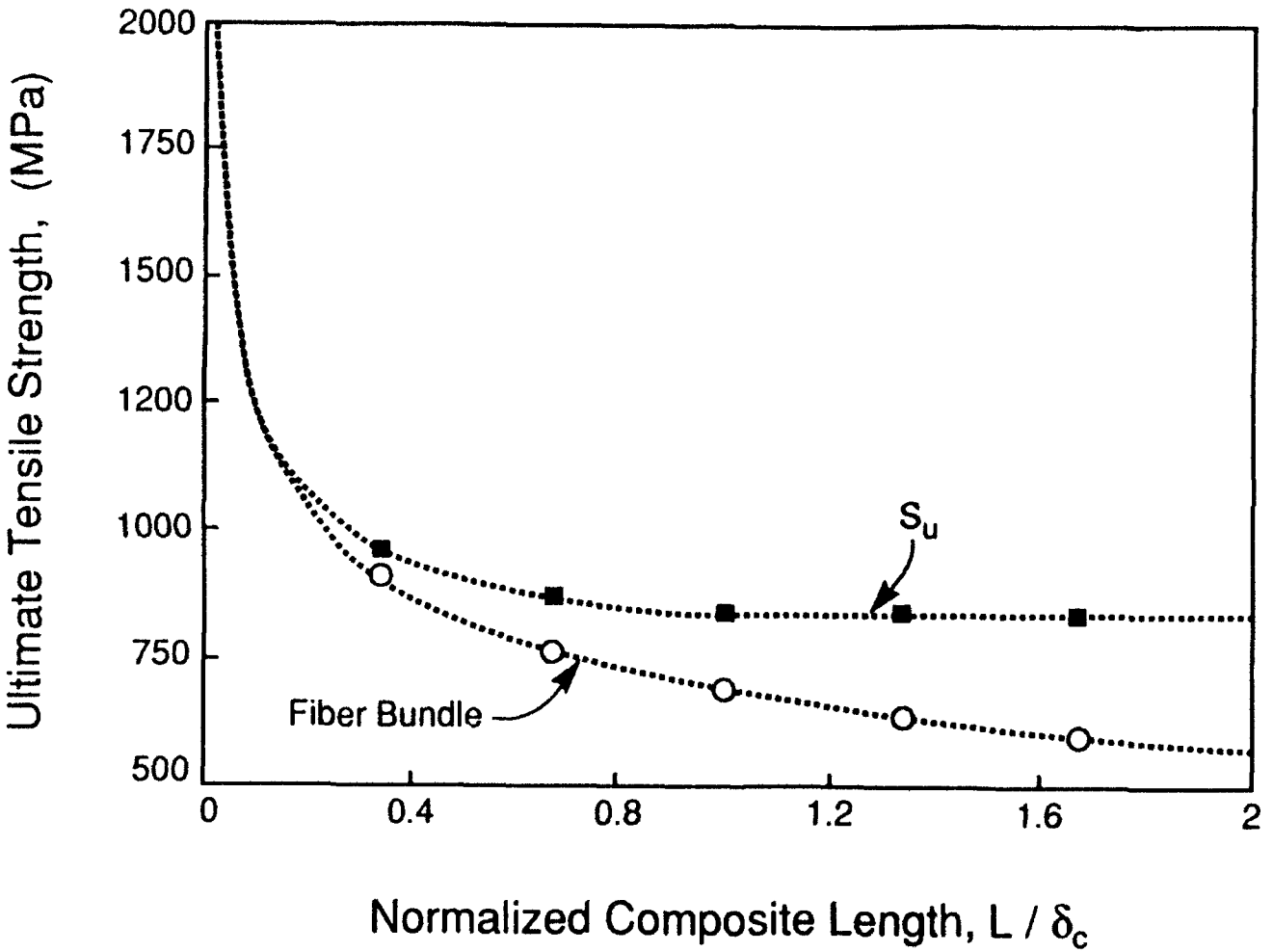
Ultimate Tensile Strength, (MPa)
2000
1750
1500
1200
1000
750
500
0
0.4
0.8
1.2
1.6
2
S_u
Fiber Bundle
Normalized Composite Length, L / δ_c

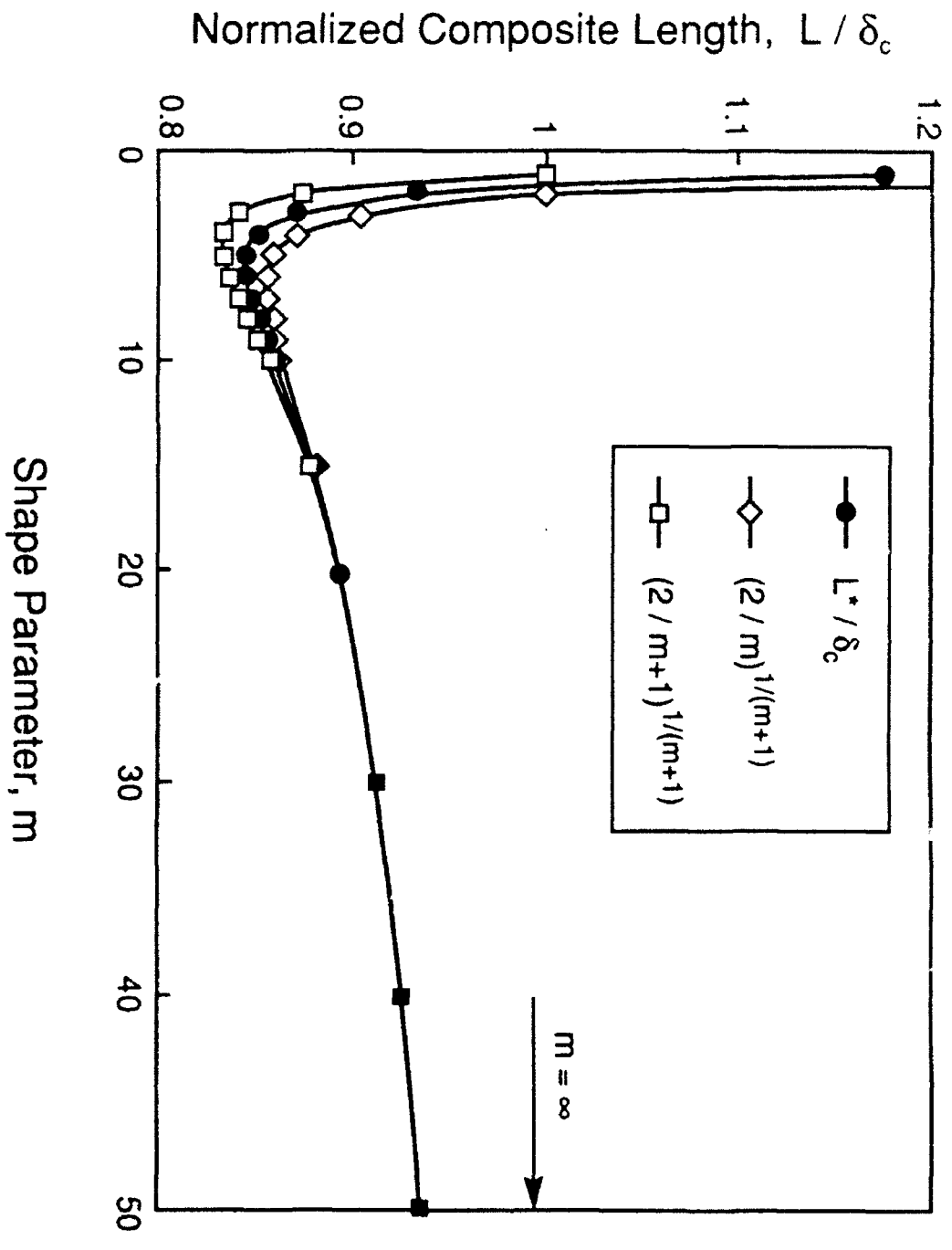

M
h
h1
h2
z
M
x

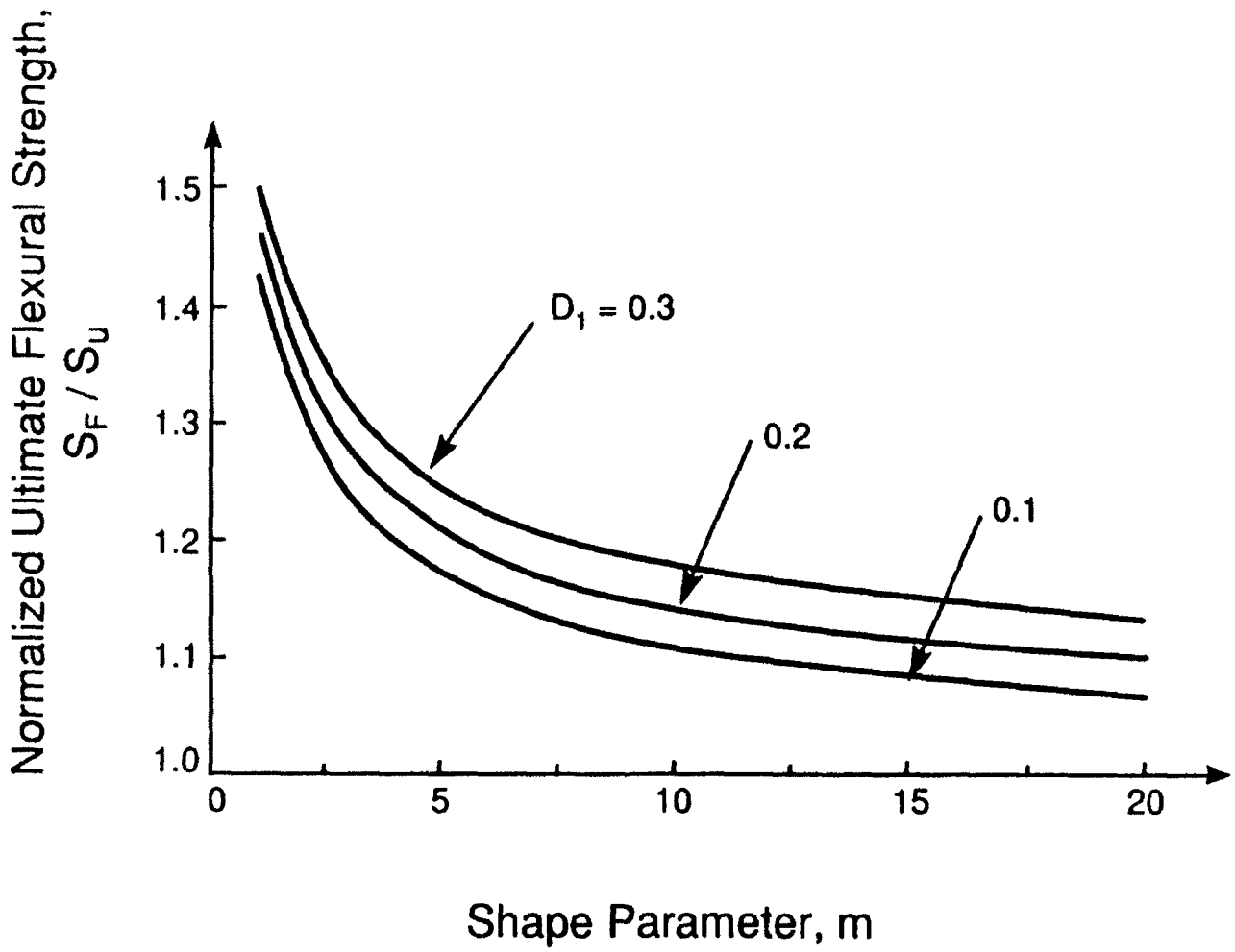
Normalized Ultimate Flexural Strength,
S_F / S_u
1.5
1.4
1.3
1.2
1.1
1.0
0
5
10
15
20
$D_1 = 0.3$
0.2
0.1
Shape Parameter, m

Submitted to J. Am. Ceram. Soc., 1992
Revised version

M A T E R I A L S

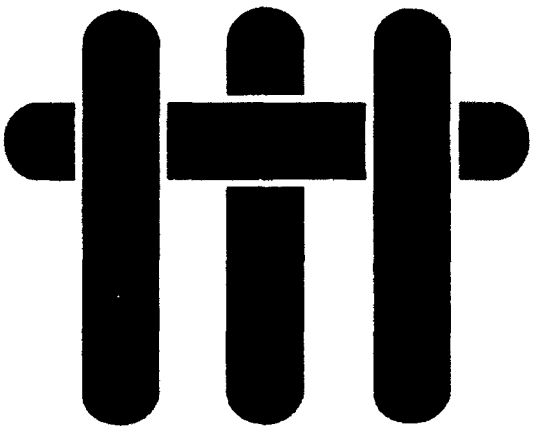

THE FRACTURE RESISTANCE CHARACTERISTICS OF A METAL TOUGHENED CERAMIC

by

B.D. Flinn, C.S. Lo, F.W. Zok and A.G. Evans
Materials and Mechanical Engineering Departments
College of Engineering
University of California
Santa Barbara, California 93106–5050

KJS-Evans-23•Mf-Mt•TA-Mtl Tgh Crm 91/11/05•10:00 AM•6/30/92

ABSTRACT

The fracture characteristics of an Al_2O_3/Al composite are examined. Measurements of resistance curves and work of rupture are compared with predictions of a micromechanical model, incorporating the effects of crack bridging by the Al reinforcements. The bridging traction law is assumed to follow linear softening behavior, characterized by a peak stress, σ_c, and a critical stretch-to-failure, u_c. The values of σ_c and u_c inferred from such comparisons are found to be broadly consistent with independent measurements of stretch-to-failure, along with the measured flow characteristics of the Al reinforcement. The importance of large-scale bridging on the fracture resistance behavior of this class of composite is also demonstrated through both the experiments and the simulations.

1. INTRODUCTION

The toughening of ceramics and intermetallics by ductile reinforcements has been comprehensively studied,[1-16] and has encompassed the range of materials indicated on Table I. Three key factors regarding such toughening have emerged from these studies as being in need of clarification and further understanding: i) The partitioning of the plastic dissipation accompanying crack growth between bridging metal ligaments and a process zone; ii) Control of interface debonding and associated relationships with the dissipation occurring within the bridging ligaments; iii) The incidence and importance of large-scale bridging (LSB)[17] and the resulting relationships between resistance curves, basic constituent properties and the macroscopic load/deflection response of the composite. This article addresses aspects of each of these issues through experiments and analysis on Al_2O_3 toughened with an Al/Mg alloy.

Experimental evidence presented for WC/Co[9] and Al_2O_3/Al[2] has indicated that both bridging and non-linear process zones can accompany crack growth and contribute to the crack growth resistance. Trends in these two contributions with microstructure are predicted to be very different.[9] Consequently, it is important to understand and model the separate contributions. Calculations indicate that the dissipation is dominated by the plastically stretching ligaments,[18] provided that the crack surface tractions induced by the ligaments are relatively small compared with the flow strength of the composite material within the process zone. The explicit requirement for ligament dominance is given by the inequality:

$$f\sigma_b \lesssim 3\sigma_f \qquad (1)$$

where f is the volume fraction of the *ductile* material, σ_b is the average crack surface traction generated by the intact metal ligaments and σ_f is a measure of the flow

strength of the composite. For Al_2O_3/Al alloy composites with typical values of metal concentration ($f \approx 0.2$), σ_b scales with the uniaxial yield strength of the alloy,[15] σ_o, and is relatively low (~ 100 MPa), whereas σ_f, which is dominated by the elasticity of the matrix,[9] is considerably larger (> 500 MPa). Consequently, Eqn. (1) predicts that the dissipation should occur *exclusively* in the bridging ligaments. This material system should thus provide a good experimental test of the crack growth predictions based on bridging.

The Al_2O_3/Al interface is "strong,"[19] but can experience ductile debonding in constrained regions. It should thus be possible in this system to examine the *influence of controlled debonding* on the fracture resistance. Furthermore, such debonding is expected to result in large-scale bridging. Consequently, this material also provides an experimental model for testing and validating the LSB analyses[20,21] now available for predicting effects of specimen geometry on the nominal fracture resistance.

When fracture resistance is dominated by plastically deforming ligaments, the stress/stretch function associated with these ligaments σ_b (u) is the key composite property. A major objective of the present study is the determination of σ_b (u) and its rationalization in terms of the properties of the Al alloy reinforcements, as well as the interface debonding. In general, it has been found that a linear softening traction law has applicability to ductile phase toughened materials,[22] governed by,

$$\sigma_b \approx \sigma_c(1 - u/u_c) \tag{2}$$

where u is the crack opening displacement, and σ_c and u_c are constants to be determined either by experiment or by calculation. Furthermore, σ_c should be a multiple of the uniaxial yield strength of the reinforcements σ_o. This formulation has lead to the following explicit results for the crack growth resistance under small-scale bridging (SSB) conditions: i) a steady-state toughness Γ_{ss} given by,[21]

$$\Gamma_{ss} = \Gamma_m(1-f) + \sigma_c u_c f/2 \quad (3)$$

where Γ_m is the matrix fracture energy; and ii) a resistance prior to steady-state Γ_R, given by,[21]

$$\Gamma_R(\Delta a) \approx \Gamma_m(1-f) + \sigma_c f u_c \left[1.6\ell - 0.1\ell^2 + 0.53\ell^3\right]/4 \quad (4)$$

where $\ell = \Delta a/L_s$, with Δa being the crack extension and L_s the crack growth at the onset of steady-state,

$$L_s = 0.37 E u_c/\sigma_c \quad (5)$$

where E is Young's modulus for the composite. However, as already noted, when large-scale bridging occurs, the nominal resistance may deviate substantially from the SSB predictions. This issue will be a major focus of the present study.

2. MATERIALS

Composites used in this investigation were fabricated using the method developed by Lange *et al.*[23] In this method, the architecture of the metal is determined by the choice of a pyrolyzable precursor. The precursor (a polymer fiber felt) is packed with a high-purity alumina* slurry by pressure infiltration. After drying, the green body is slowly heated to burn out the precursor and then sintered at 1550°C for 30 min., leaving an interconnected network of channels. The as-sintered Al_2O_3 structure is visible on the

* Sumitomo AKP-50

channel walls. This sintering schedule produces a fine-grained (~ 4 μm) ceramic preform, with a relative density ≥ 99% (exclusive of the channels) (Fig. 1a). The preform is then infiltrated with molten Al/4 wt.% Mg alloy, by squeeze casting, to produce the composite. The alloy had been heated to 780°C and squeeze cast at a pressure of 170 MPa. The composite billets were typically ~ 30 mm in diameter and ~ 5 mm thick. Microstructural examination of the composite revealed a relatively uniform network of randomly oriented cylindrical aluminum fibers, ~ 19 μm in diameter. The metal volume fraction, measured by quantitative metallography, was $f = 0.28$ (Fig. 1b).

The Al channels were devoid of porosity and were bonded to the Al_2O_3 matrix. The Al_2O_3 grain boundaries appeared devoid of grain boundary phases, as ascertained in the transmission electron microscope (TEM) using dark field, through focus and the EDS X-ray technique. Bright field TEM indicated no detectable segregation and no interphase formation at the metal/ceramic interface. The aluminum alloy was single phase with magnesium in solid solution.

3. MEASUREMENTS AND OBSERVATIONS

3.1 Mechanical Testing Procedures

Mechanical test specimens were cut from the composites, surface ground with diamond impregnated wheels and notches cut using thin (150 μm) diamond blades. Polished surfaces for crack length measurements were prepared using standard metallographic techniques. Two types of mechanical test were performed to obtain the fracture resistance curves and the work of rupture. *Resistance curve* measurements were made upon polished, notched flexure beams (3.6 mm x 3.6 mm x 20 mm), in accordance with ASTM standards.[24] Specimens were prepared with notch depths of 0.5, 1.0 and 1.5 mm, representing notch depth to specimen height ratios, a_o/W, of 0.14, 0.28 and 0.42. Two flexure test procedures were used: 1) *in situ* inside a scanning electron

microscope, and 2) within a stiff servohydraulic test frame* using a traveling optical microscope to measure crack lengths. Tests were conducted at a displacement rate of 0.2 μm/s.

The steady-state fracture properties were characterized using *work-of-rupture* tests.[25,26] This test involved measurement of the work required to stably propagate a crack across a chevron-notched flexure specimen. To ensure stable crack propagation, the specimen width was twice the specimen height ("double-width specimens").[25,26] Furthermore, a short pre-crack (~ 100 μm) was introduced at the notch using a Vickers indentor with a load of 200 N. Corresponding tests were conducted on fully dense Al_2O_3 specimens, to allow the toughness enhancement attributable to the metal reinforcements to be evaluated.

The flow properties of the bulk Al/Mg alloy were measured from dog-bone tensile specimens machined from squeeze cast ingots. Hardness measurements were also made with a nanoindentor on both the bulk Al-Mg alloy and the reinforcements within the composite, in order to compare their flow properties.

3.2 Fracture Observations

In situ and post fracture observations conducted in the SEM provided insight into the crack growth mechanism, as well as the plastic stretching of the Al ligaments. Observations performed *in situ*, shown at four different crack openings in Fig. 2, confirm the existence of a plastic stretching mechanism. Investigation of the resultant fracture surfaces by SEM revealed primarily transgranular cleavage of the Al_2O_3 and extensive plastic deformation of the Al. The stretch to failure of ~ 60 ligaments was measured using stereo measurements on SEM micrographs. The Al ligament orientation was found to have a strong effect on both the debonding behavior and the plastic

* MTS Model 810

stretch to failure. Ligaments aligned perpendicular to the crack plane (Fig. 3) exhibited debonding, on the order of the fiber diameter, 2R, and a large plastic stretch to failure: $u_c/R \approx 3.5$. Inclined ligaments partially debonded (around that segment of the interface experiencing normal tension, Fig. 4a), and failed at a relatively small plastic stretch. Ligaments parallel to the crack plane often debonded completely and experienced negligible plastic deformation (Fig. 4b). A summary of plastic stretch measurements (Fig. 5) indicates a mean value, $\overline{u_c/R} = 2.9$, with a standard deviation of $\pm$ 0.9.

Closer examination of the debonded surfaces provided insight into the debond mechanism and the role of matrix microstructure. The Al_2O_3 side of the debonded interface (Fig. 6a) reveals the presence of a network of Al. The network cell size is similar to that of the matrix grains and the cell centers are frequently situated at triple grain junctions on the Al_2O_3 surface. The debonded metal exhibited a corresponding, distorted, dimpled surface (Fig. 6b). These observations indicate that debonding occurred by a ductile process involving void nucleation at triple grain junctions or the matrix surface, followed by plastic void growth and coalescence *within the metal*, near the interface. This mechanism of interfacial fracture is consistent with earlier studies which indicate that the Al_2O_3/Al interface is "strong."[19]

The effect of matrix microstructure on debonding was explored by heat treating some of the Al_2O_3 compacts at 1600°C for 30 h, to induce substantial grain growth in some regions* and thus reduce the number of triple grain junctions at the channel surfaces. After infiltration and fracture, the debonding in these regions was found to be negligible (Fig. 7), whereas the debonding in the fine-grained region was essentially the same as that in the original fine-grained composite (c.f. Fig. 3). The plastic stretch of the reinforcements in the coarse-grained region was correspondingly lower $u_c/R \approx 1$.

---

* These heat treatments produced a bimodal distribution of grain sizes: a result of abnormal grain growth.

3.3 Properties of Al Alloy

Tensile stress-strain curves for the bulk Al-Mg alloy (Fig. 8) indicated a yield strength of ~ 70 MPa and an ultimate tensile strength of ~ 180 MPa. The reduction in area was approximately 20%. Nanoindentation results at a load of 5mN indicated similar hardness levels for the bulk aluminum alloy (1.1 ± 0.1 GPa) and for the reinforcements in the composite (1.3 ± 0.2 GPa). The relatively large values of hardness (compared to the uniaxial yield strength) reflect the indentation size effect that occurs in the nanometer range.[28]

3.4 Fracture Resistance

The resistance curves for the composite (Fig. 9) have three characteristic features: i) an initial fracture resistance, $K_o \approx 3$ MPa$\sqrt{m}$, similar to the fracture toughness of the matrix, ii) an intermediate region wherein the fracture resistance increases gradually, and iii) a final region in which the resistance increases rapidly. The latter region commences at smaller crack extensions for specimens with deeper notches. Such behavior is characteristic of large-scale bridging (LSB).[17]

The work of rupture of the composite was, $W_R = 400 \pm 50$ Jm^{-2} and that of the fully dense Al_2O_3‡ was $W_R = 25 \pm 5$ Jm^{-2}. The toughness enhancement ΔW_R attributed to the metal reinforcements, re-expressed in the non-dimensional form,[1,15]

$$\chi = \Delta W_R / f \sigma_o R \qquad (6a)$$

becomes

$$\chi = 2.0 \pm 0.3. \qquad (6b)$$

‡ Processed similarly and having comparable grain size.

The steady-state fracture resistance K_{ss} of the composite can then be calculated using

$$K_{ss} \approx \sqrt{EW_R} \tag{7}$$

where E is the composite Young's modulus. Taking E = 300 GPa, Eqn. (7) gives the result $K_{ss} \approx 11\ MPa\sqrt{m}$, significantly less than the nominal LSB fracture resistance measured at large crack extensions (Fig. 9).

4. MODELING

4.1 Bridging Tractions

The traction function $\sigma_b(u)$ for the ductile Al ligaments was obtained using two methods. In the first, the function was assumed to obey a linear softening law (Eqn. 2). Selection of the peak stress parameter, σ_c, and the stretch-to-failure, u_c, was based on the following procedure: i) The stretch-to-failure was made to coincide closely with the SEM measurements ($u_c/R = 2$); ii) The maximum stress was then selected such that the computed R- curve (described in Section 4.2) for one of the specimen geometries was in good agreement with the experimental data. *This fit specifies both σ_c and u_c in Eqn. (2);* iii) The R-curves for the other geometries were computed and compared with the experiments. As an additional consistency check, the area under the normalized $\sigma_b(u)$ curve was evaluated and compared with the value of χ obtained from the work-of-rupture tests (Eqn. 6b).

In the second method, the traction function was computed using a geometric necking model[29] by assuming cylindrical bridging ligaments oriented perpendicular to the crack plane (Appendix). The shape of the ligaments during deformation was taken to be a paraboloid of revolution, with the nominal stress computed from Bridgman's

solution[30] for a necking bar. This calculation requires a flow law for the Al ligaments applicable at the large plastic strains that occur during rupture. The commonly used Ramberg-Osgood law typically overestimates the flow stress at large strains, because hardening is limited by the development of a stable dislocation cell structure.[31] Consequently, a more appropriate flow law at large strains is,[32]

$$\sigma = \sigma_s\left[1 - me^{-n\varepsilon_p}\right] \tag{8}$$

where σ_s is the saturation strength, with m and n being coefficients that reflect the hardening. A fit of Eqn. (8) to the data from Fig. 8 gives the parameters σ_s = 300 MPa, m = 0.75 and n = 5.8. The stress/stretch relationships for various debond lengths and their influence on the toughness enhancement, predicted using Eqn. (8) in the geometric necking model (Appendix), are shown in Fig. 10.

4.2 Fracture Resistance

A cohesive crack model with linear softening has been used (Eqn. 2) and solved by an integral equation method.[20,21] The relevant geometric parameters are shown in Fig. 11. The model considers a matrix crack of length a, growing from a notch of length a_0 in a flexure specimen of width w. The bridging tractions are denoted $f\sigma_b(x)$, where x is the distance from the tensile face of the beam. The applied load is represented by the stress, $\sigma_a(x)$, that would exist on the fracture plane in the absence of the crack, represented by,

$$\sigma_a(x) = 6M(1 - 2x/w)/w^2 b \tag{9}$$

where b is the specimen depth and M is the bending moment. The net tractions p(u) acting on the crack face are assumed to follow a linear softening law of the form

$$p(u) = f\sigma_c(1 - u/u_c) \tag{10}$$

Thereafter, the crack opening profile can be related to the applied load by an integral equation,[20,21] which leads to an expression for the stress intensity factor at the crack tip,

$$K_{tip} = \frac{2}{\sqrt{\pi a}}\int_0^a \frac{H(x/a, a/w)}{\sqrt{1-(x/a)^2}}\left[\sigma_a(x) - p(u(x))\right]dx \tag{11}$$

where H is a weight function defined in Refs. 20 and 21. Using the criterion for matrix crack propagation, $K_{tip} = K_0$ (the matrix toughness), the crack growth resistance has been simulated by solving the integral equation for K_{tip}, as elaborated below.

4.3 Comparison Between Theory And Experiment

Initially, the experimentally measured resistance curve for a notch depth, $a_0/w = 0.28$, was compared with predictions for a range of σ_c/σ_0. Coincidence was obtained for $\sigma_c/\sigma_0 = 2.12$ (Fig. 9). Further comparisons for other notch geometries ($a_0/w = 0.14$ and 0.42), made using *the same value of* σ_c/σ_0, indicate good agreement over the entire range of crack extension (Fig. 9). In addition, the steady-state toughness enhancement *calculated* from the linear softening traction law ($\chi = 2.1$) is in accord with the value *measured* from the work of rupture tests ($\chi = 2.0 \pm 0.3$). The consistency between the various measurements and predictions provides confidence in the utility of the linear softening traction law, as well as the key material parameters, σ_c and u_c.

A discrepancy that arises from the comparison between measurement and calculation is concerned with the predictions of the geometric necking model. The model predicts a peak stress and a toughness enhancement consistently higher than those found by experiment for debond lengths that give the appropriate range of u_c/R

(Fig. 10). Notably, the peak stress should not be lower than the (unconstrained) ultimate tensile strength of the Al alloy ($\sigma_c \approx 2.6\ \sigma_o$). Yet, a lower value of the peak stress is inferred from the resistance curves ($\sigma_c \approx 2.1\ \sigma_o$). The discrepancy is believed to be attributable to the random orientation of the ligaments, which significantly lowers the limit load.[32] This effect, in turn, reduces the steady-state toughness enhancement associated with the metal reinforcements.

5. CONCLUSION

The close comparison between theory and experiment revealed by the present study has several implications. The primary mechanism of toughening by ductile reinforcements can now be confidently attributed to plastic dissipation by stretching between the crack surfaces. Consequently, the important microstructural variables can be defined and evaluated, especially the requirement for controlled debonding.

The importance of large-scale bridging in metal/ceramic composites has been vividly demonstrated. A major implication of LSB is that the very large specimens required to satisfy semi-infinite specimen geometry assumptions are impractical and would hinder the development of new materials. Furthermore, it is anticipated that applications for these composites will be in small, complex components, for which the fracture resistance measured from semi-infinite specimens would be of little use. The approach outlined here demonstrates a practical alternative wherein determination of the stress/stretch relationship of the ductile reinforcements from tests conducted on small, simple specimens combined with computer modeling allows the prediction of fracture resistance behavior of *finite sized components*.

Finally, it is apparent that a traction law applicable to composites reinforced with *randomly oriented* metal channels cannot be simulated using simple geometric models of necking ligaments. Experimental evaluation of this law is preferred.

TABLE I

Ductile Reinforcement Toughened Ceramics and Intermetallics

MATRIX	REINFORCEMENT	REFERENCES
Al_2O_3	Al	1–4
B_4C	Al	5
WC	Co	6–9
TiAl	Nb	10
$MoSi_2$	Nb	11,12
NiAl	Mo, Cr	13
AlN	Al	14

APPENDIX

The effect of debond length on the stress/stretch relationship for a bridging ligament is estimated using the geometric model described by Mataga.[29] Here, the ligaments are taken to be cylindrical in shape and oriented perpendicular to the crack plane. Debonding is assumed to occur instantaneously (at u = 0), such that the debond length, d, remains fixed during stretching. The profile of the ligament is assumed to be described by a paraboloid of revolution. The minimum ligament diameter, 2r, and the local radius of curvature are then evaluated in terms of the crack opening displacement by requiring the volume of the ligament to remain constant. This leads to an expression for the crack opening in terms of the current ligament geometry,

$$u/R = 2(d/R)\left[(1 - 4\rho/3 + 8\rho^2/15)^{-1} - 1\right] \tag{A1}$$

where

$$\rho = 1 - r/R \tag{A2}$$

The nominal stress depends on the current load bearing area of the ligament (as manifest in the parameter ρ), the work hardening behavior of the metal and the plastic constraint resulting from the ligament profile. Utilizing Bridgman's solution[30] for the average nominal stress in a necking bar leads to the result,

$$\sigma/\sigma_o = (1-\rho^2)\left[1 + h^2/R^2\rho(1-\rho)\right]\ell n\left[1 + \rho(1-\rho)R^2/h^2\right] \tag{A3}$$

where 2h is the current "gauge length" of the ligament,

$$2h = 2d + u, \tag{A4}$$

Combining these results with the flow law for the Al alloy (Eqn. 8 in the text) gives the $\sigma_b(u)$ predictions plotted on Fig. 10a.

REFERENCES

[1] B.D. Flinn, M. Rühle and A.G. Evans, "Toughening in Composites of Al_2O_3 Reinforced with Al," *Acta Metall.*, **37**, 3001–06 (1989).

[2] B.D. Flinn, F.W. Zok, F.F. Lange and A.G. Evans, "Processing and Properties of Al_2O_3 Reinforced with Al Alloys," *Mat. Sci. Eng.*, **A144**, 153–57 (1991).

[3] M.S. Newkirk, A.W. Urqhart and H.R. Zwicker, "Formation of Lanxide™ Ceramic Composite Materials," *J. Mater. Res.*, **1**, 81 (1986).

[4] M.K. Aghajanian, N.H. MacMillan, C.R. Kennedy, S.J. Luszez and R. Roy, "Properties of Microstructure of Lanxide™ Al_2O_3-Al Ceramic Composite Materials," *J. Mater. Sci.*, **24**, 658–670 (1989).

[5] M. Yasrebi, G.H. Kim, K.E. Gunnison, M. Sarikaya and I.A. Aksay, "Biomimetic Processing of Ceramics and Ceramic-Metal Composites," pp. 625–35 in *MRS Symposium Proceedings*, vol. 180, Materials Research Society, Pittsburgh, PA, 1990.

[6] L.S. Sigl and H.E. Exner, "Experimental Study of the Mechanics of Fracture in WC-Co Alloys," *Met. Trans.*, **18A**, 1299–1308 (1987).

[7] L.S. Sigl and H.F. Fischmeister, "On the Fracture Toughness of Cemented Carbides," *Acta Metall.*, **36**, 887–97 (1988).

[8] L.S. Sigl, P.A. Mataga, B.J. Dalgleish, R.M. McMeeking and A.G. Evans, "On the Toughness of Brittle Materials Reinforced with a Ductile Phase," *Acta Metall.*, **36**, 945 (1988).

[9] D.B. Marshall, W.S. Morris, B.N. Cox and M.S. Dadkhah, "Toughening Mechanisms in Cemented Carbides," *J. Am. Ceram. Soc.*, **73** 2938–43 (1990).

[10] C.K. Elliott, G.R. Odette, G.E. Lucas and J.W. Sheckherd, "Toughening Mechanisms in Intermetallic γ-TiAl Alloys Containing Ductile Phases," *Mat. Res. Soc. Symp. Proc.*, **120**, 95 (1988).

[11] T.C. Lu, A.G. Evans, R.J. Hecht and R. Mehrabian, "Toughening of $MoSi_2$ with a Ductile (Niobium) Reinforcement," *Acta Metall. Mater.*, **35**, 1853–62 (1991).

[12] D.H. Carter and P.L. Martin, "Ta and Nb Reinforced $MoSi_2$," pp. 131–38 in *MRS Symposium Proceedings*, vol. 194, Materials Research Society, Pittsburgh, PA, 1990.

[13] P.R. Subramanian, M.G. Mendiratta, D.B. Miracle and D.M. Dimiduk, "Microstructure and Mechanical Properties of NiSl + Mo *In Situ* Eutectic Composites," pp. 147–54 in *MRS Symposium Proceedings*, vol. 194, Materials Research Society, Pittsburgh, PA, 1990.

[14] C. Troy and W.D. Scott, "Ceramic-Metal Composites Produced by Melt Infiltration," *J. Am. Ceram. Soc.*, **73**, 97–101 (1990).

[15] M.F. Ashby, F.J. Blunt and M. Bannister, "Flow Characteristics of Highly Constrained Metal Wires," *Acta Metall.*, **37**, 1947–57 (1989).

[16] V.D. Krstic, P.S. Nicholson and R.G. Hoagland, "Toughening of Glasses by Metallic Particles," *J. Am. Ceram. Soc.*, **64**, 499, (1981).

[17] F.W. Zok and C.L. Hom, "Large Scale Bridging in Brittle Matrix Composites," *Acta Metall. Mater.*, **38**, 1895–1904 (1990).

[18] V. Tvergaard and J.W. Hutchinson, "Relation Between Crack Growth Resistance and Fracture Process Parameters in Elastic/Plastic Solids, *J. Mech. Phys. Solids*, (1992) in press.

[19] B.J. Dalgleish, K.P. Trumble and A.G. Evans, "The Strength and Fracture of Alumina Bonded to Aluminum Alloys," *Acta Metall.*, **37**, 7, 1923 (1988).

[20] B.N. Cox, "Stable and Unstable Solutions for Bridged Cracks in Various Specimens," *Acta Metall. Mater.*, **39**, 1189–1201 (1991).

[21] B.N. Cox and C.S. Lo, "Load Ratio, Notch, and Scale Effects for Bridged Cracks in Fibrous Composites," *Acta Metall. Mater.*, **40**, 69–80 (1992).

[22] G. Bao and C.Y. Hui, "Effects of Interface Debonding on the Toughness of Ductile-Particle Reinforced Ceramics," *Intl. Jnl. Solids Structures*, **26**, 631–42, (1990).

[23] F.F. Lange, B.V. Velamakanni and A.G. Evans, "Method for Processing Metal-Reinforced Ceramic Composites," *J. Am. Ceram. Soc.*, **73**, 388–93 (1988).

[24] ASTM E399–83, "Plane Strain Fracture Toughness Testing of Metallic Materials," *Annual Book of ASTM Standards*, ASTM, Philadelphia (1988).

[25] H.G. Tattersall and G. Tappin, "The Work of Fracture and Its Measurement in Metals, Ceramics and Other Materials," *J. Mater. Sci.*, **1**, 296–301 (1966).

[26] J.I. Bluhm, "Slice Synthesis of a Three-Dimensional 'Work of Fracture' Specimen," *Eng. Fract. Mech.*, **7**, 593–604 (1975).

[27] A.G. Varias, Z. Suo and C.F. Shih, "Ductile Failure of a Constrained Metal Foil," *J. Mech. Phys. Solids*, **39**, 963 (1991).

[28] D. Tabor, "Indentation Hardness and Its Measurement: Some Cautionary Comments," *ASTM STP 889*, P.J. Blau and B.R. Lawn, Eds., American Society for Testing Materials, Philadelphia, 1986, pp. 129–59.

[29] P.A. Mataga, "Deformation of Crack-Bridging Ductile Reinforcements in Tough Brittle Materials," *Acta Metall.*, **37**, 3349–59 (1989).

[30] P.W. Bridgman, *Studies in Large Plastic Flow and Fracture*, McGraw-Hill, NY (1952).

[31] G.E. Dieter, *Mechanical Metallurgy*, McGraw-Hill, 1976.

[32] J. Chakrabarty, *Theory of Plasticity*, McGraw-Hill, 1987.

FIGURE CAPTIONS

Fig. 1. a) Ceramic perform, prior to metal infiltration.
b) Composite microstructure, after metal infiltration.

Fig. 2. Bridging Al ligaments in the composite at four different crack openings. Micrographs taken *in situ* under load.

Fig. 3. a) Composite fracture surface in area where fibers are aligned perpendicular to fracture surface.
b) High angle (85°) tilt view illustrating plastic stretching of ligaments.

Fig. 4. Composite fracture surface in area where fibers are (a) inclined with respect to crack plane, and (b) aligned parallel to the crack plane.

Fig. 5. Cumulative distribution of plastic stretch to failure of Al ligaments.

Fig. 6. a) View of debonded Al_2O_3 surface, with cell-like Al network centered around triple-grain junctions.
b) View of debonded Al surface, with ductile dimples corresponding to the Al_2O_3 grain size.

Fig. 7. Fracture surface of composite produced from large-grained Al_2O_3 preform. Note the absence of debonding and the reduction in plastic stretch.

Fig. 8. True stress/strain curves from experimental data and calculated using the Voce law.[31]

Fig. 9. Comparison of measured and computed fracture resistance curves for three notch depths, a_0/w.

Fig. 10. a) Linear softening stress/stretch relationships used in modeling of resistance curves and predictions of the geometric necking model for various debond lengths.
b) Comparison of steady-state toughness enhancement from the geometric model and the experimental measurements.

Fig. 11. Schematic representation of specimen geometry.

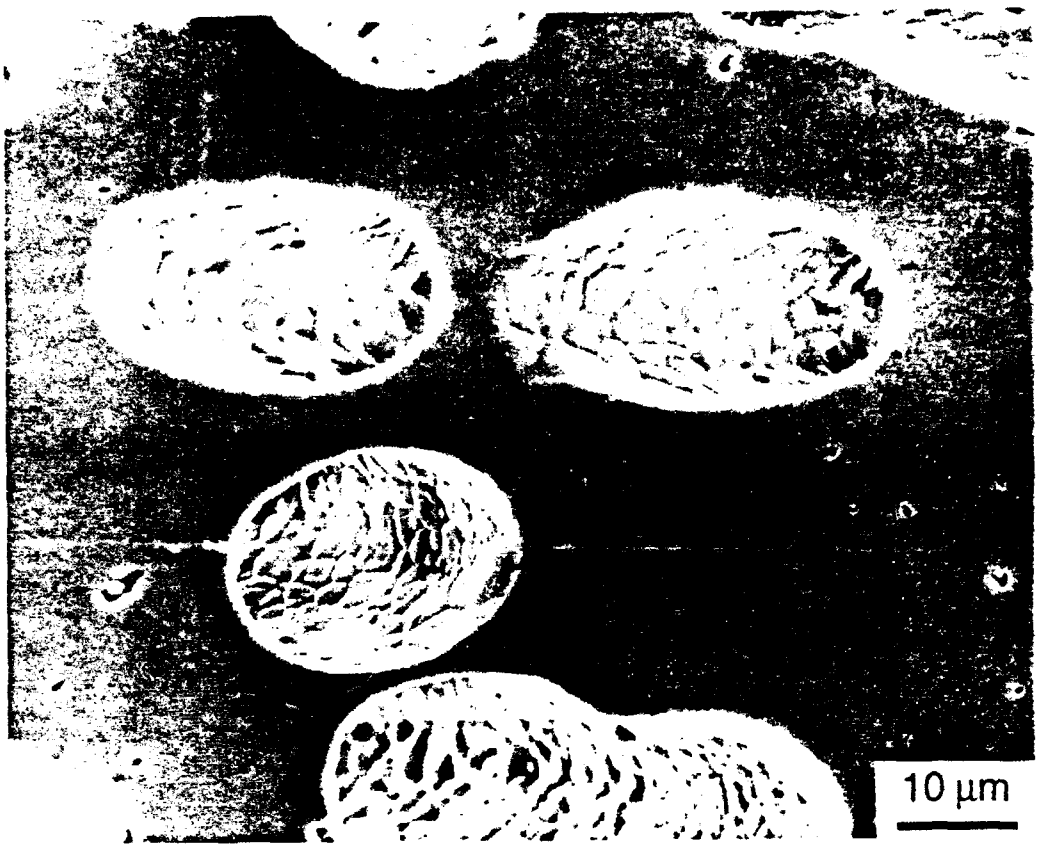

Fig. 1 (a)

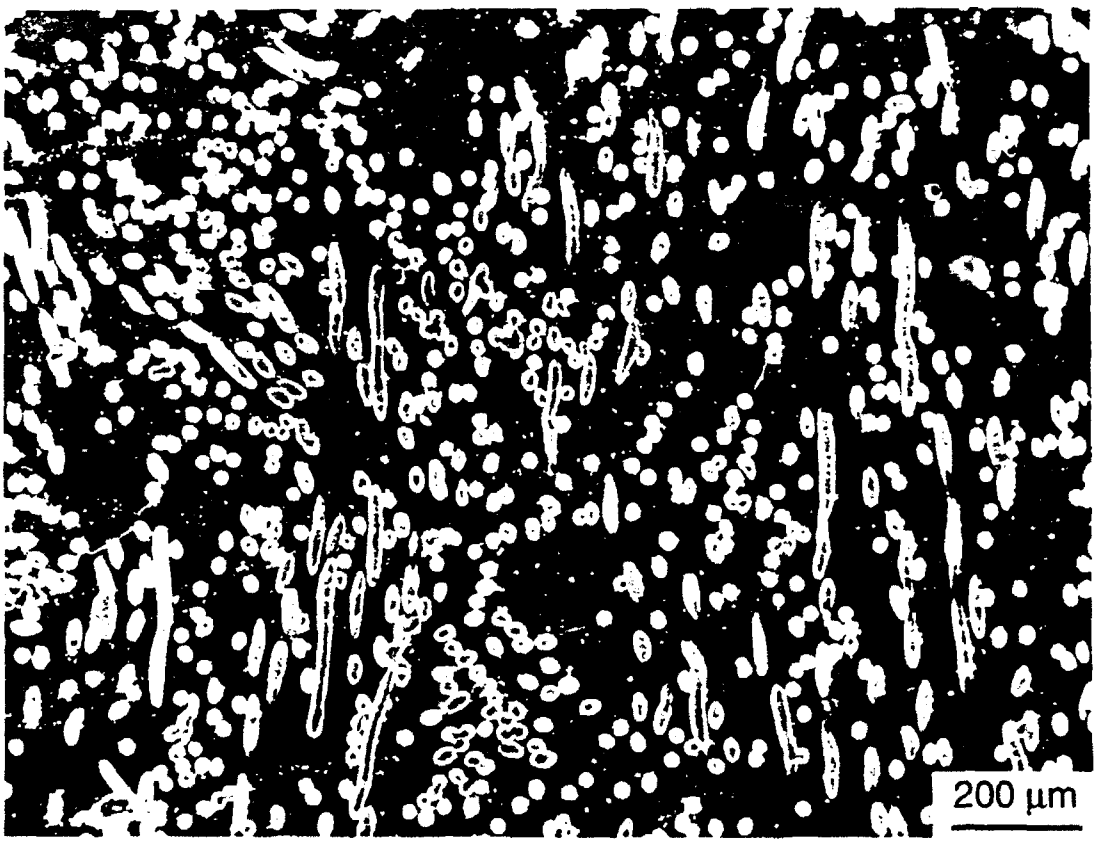

Fig. 1 (b)

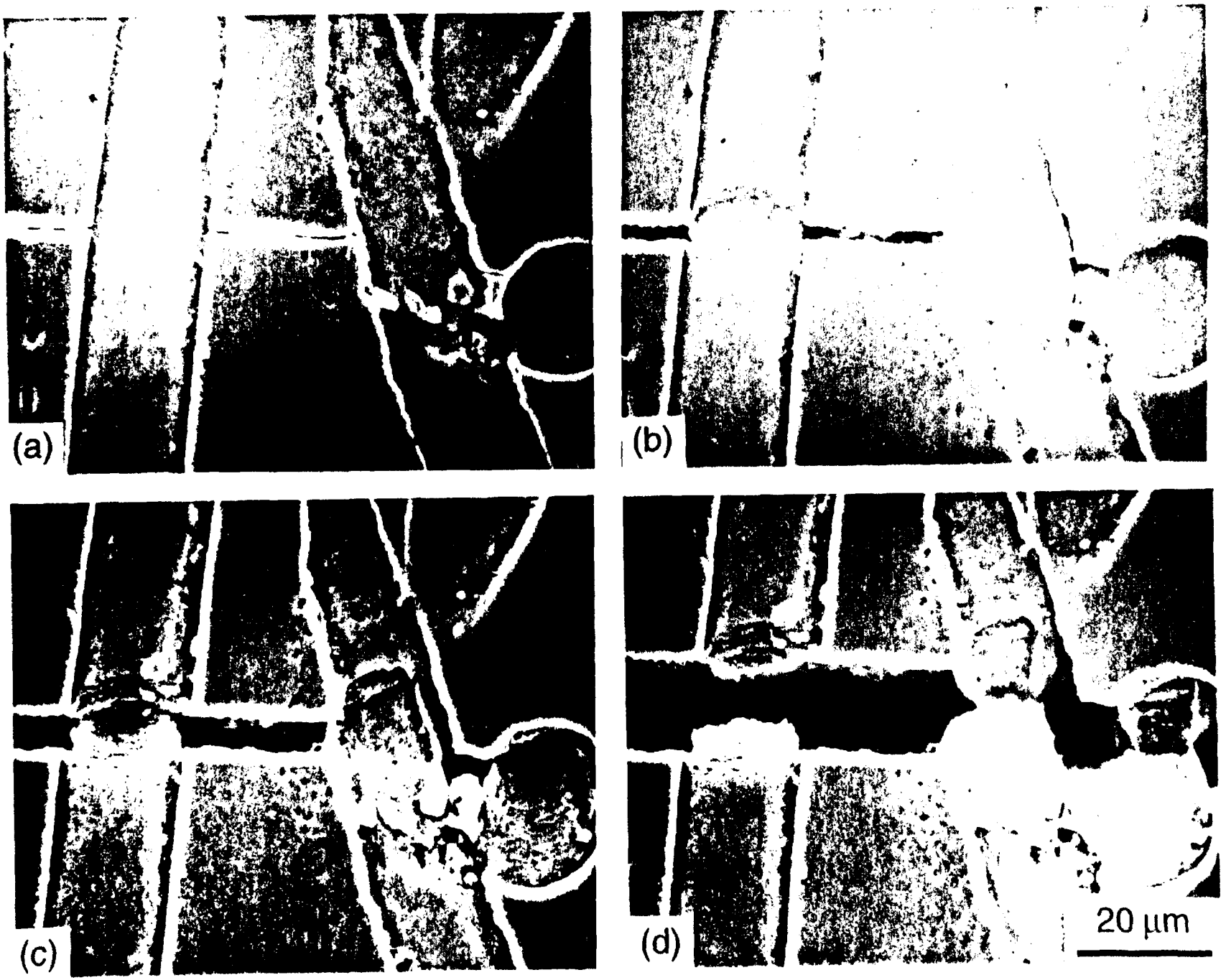

Fig. 2

Fig. 3 (a)

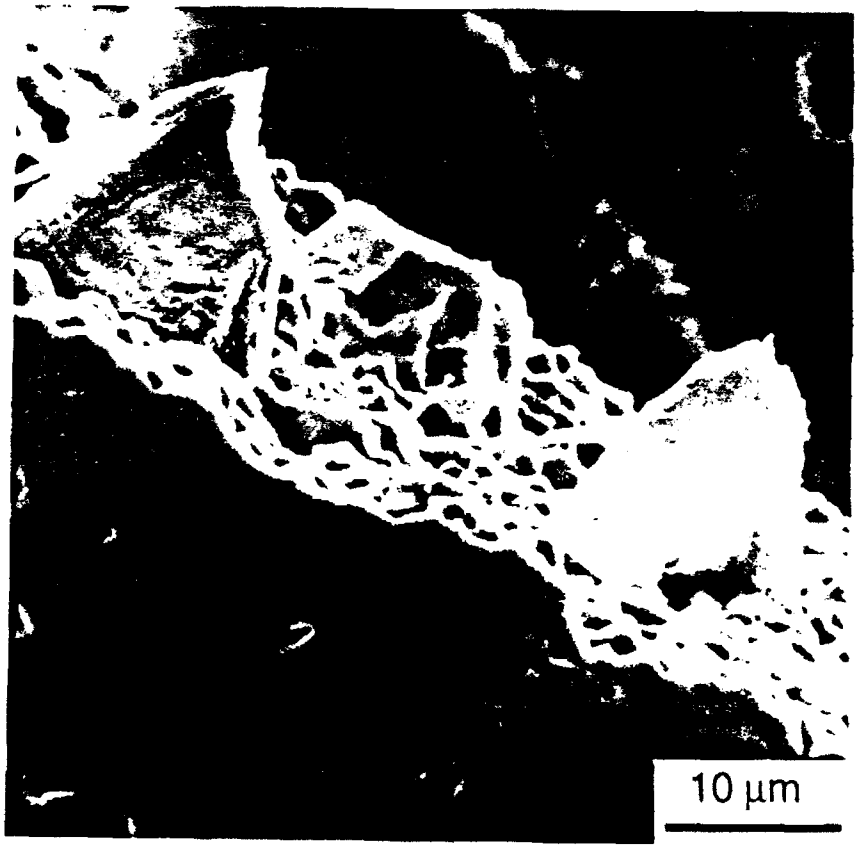

Fig. 3 (b)

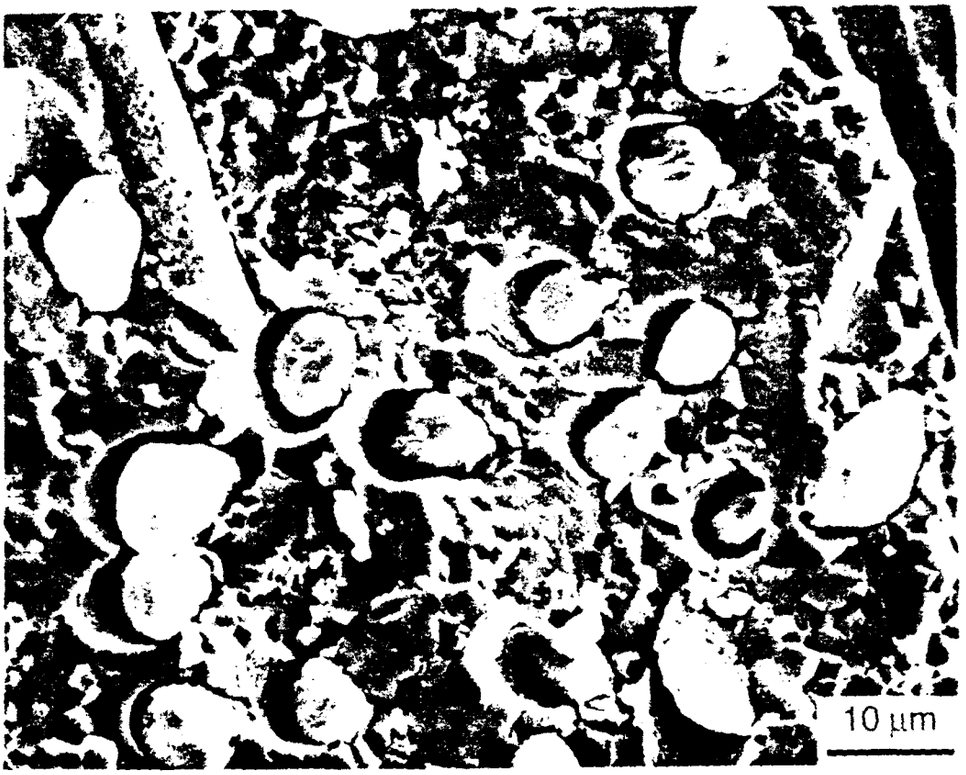

Fig. 4 (a)

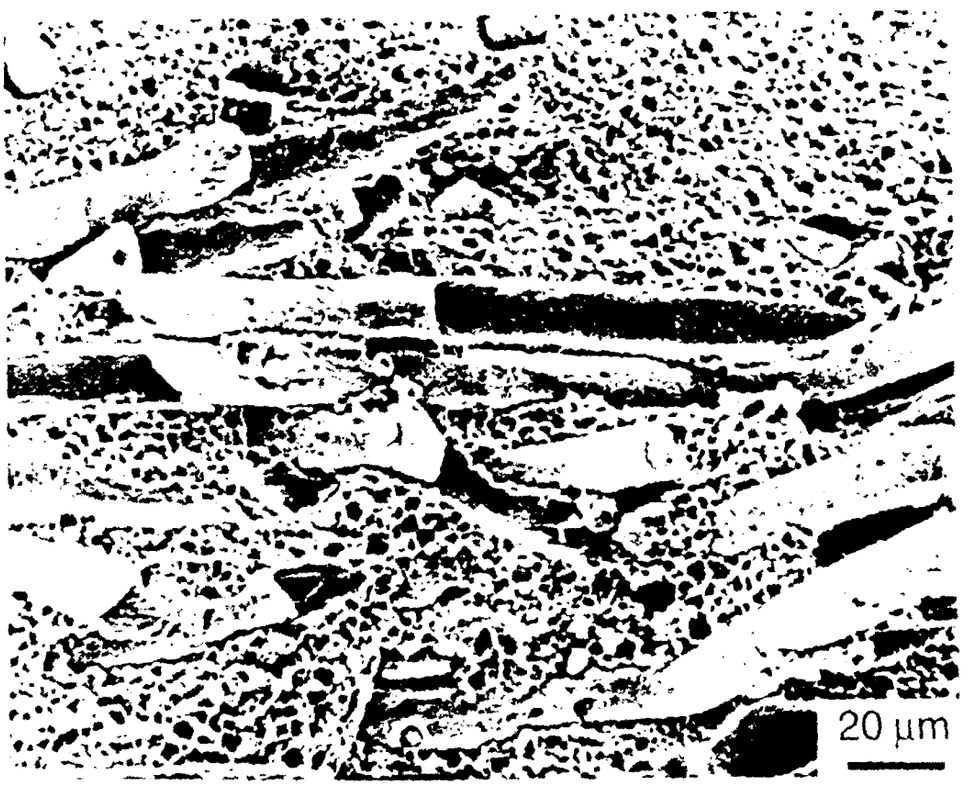

Fig. 4 (b)

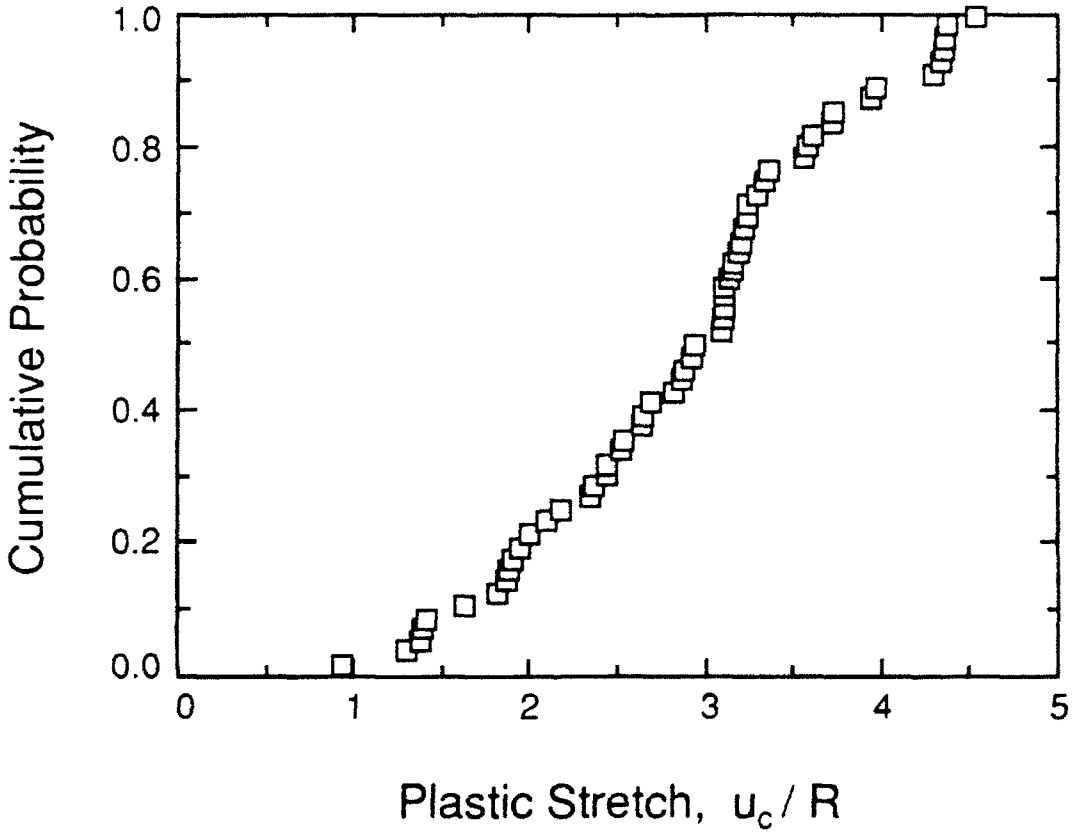
Cumulative Probability
1.0
0.8
0.6
0.4
0.2
0.0
0
1
2
3
4
5
Plastic Stretch, u_c / R

Fig. 5

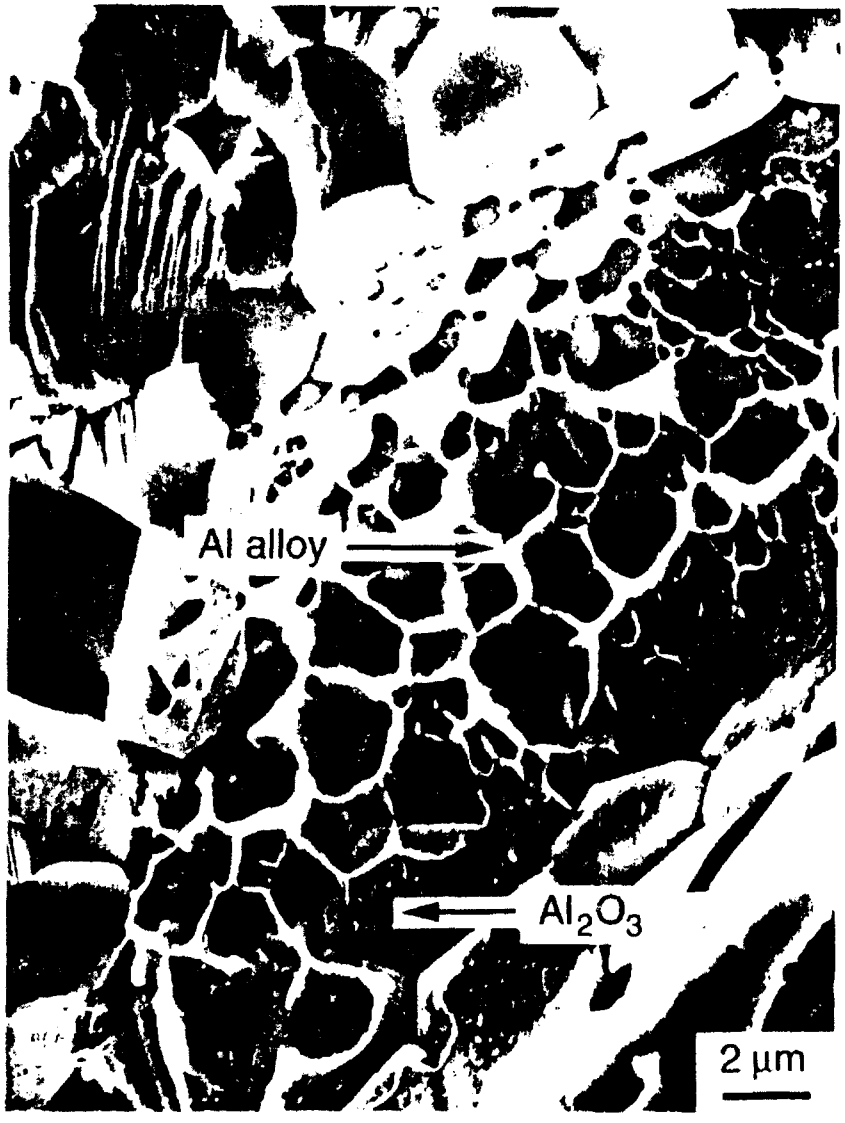

Fig. 6 (a)

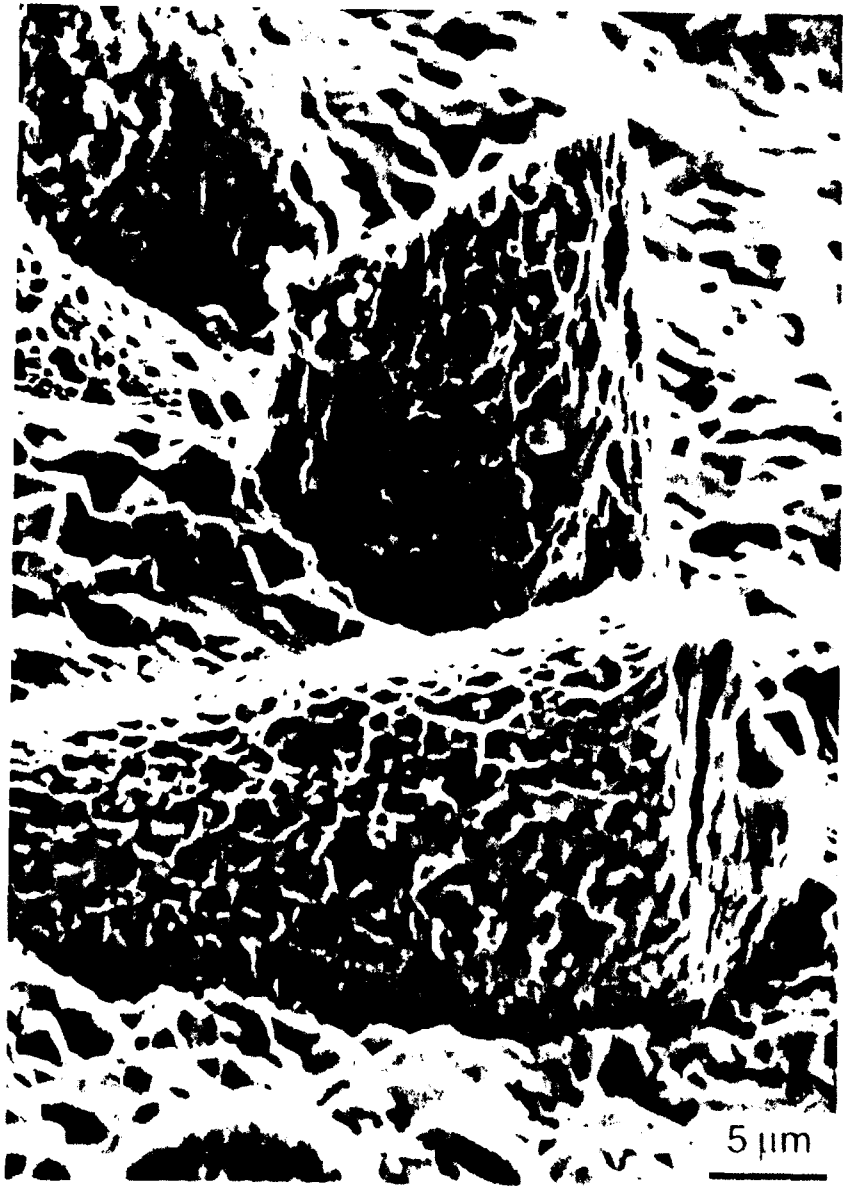

Fig. 6 (b)

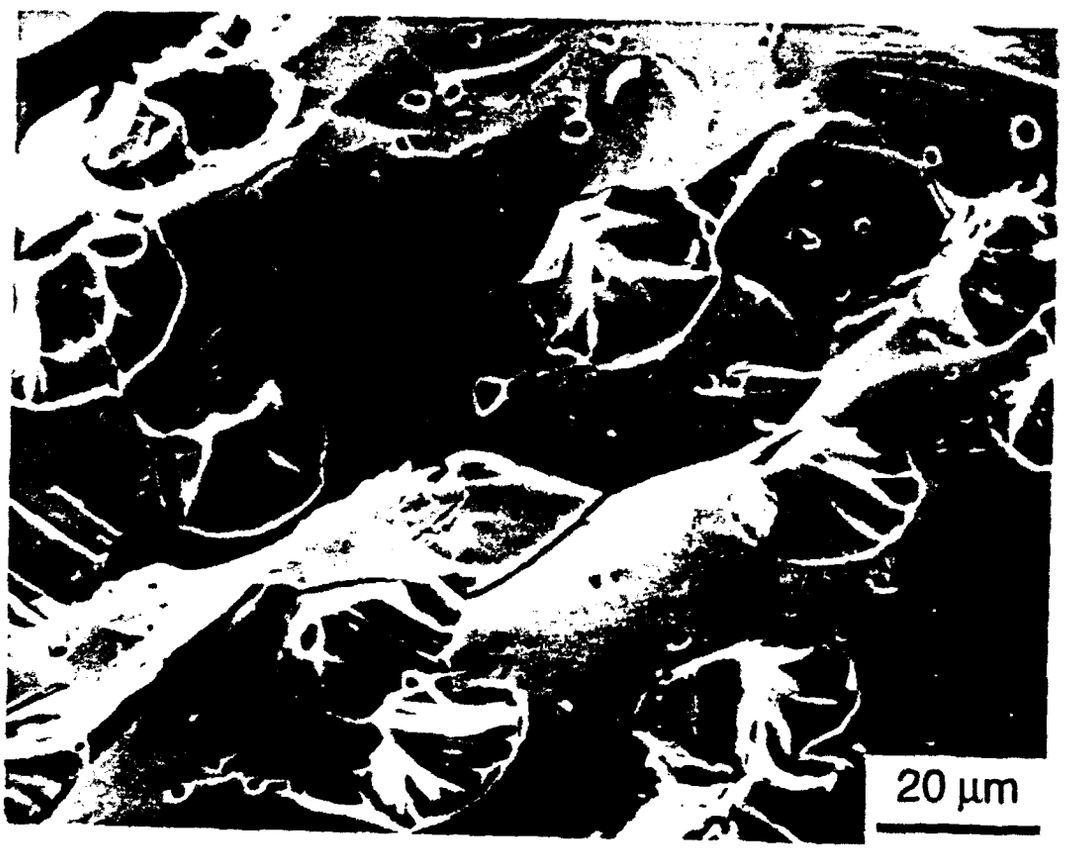

Fig. 7

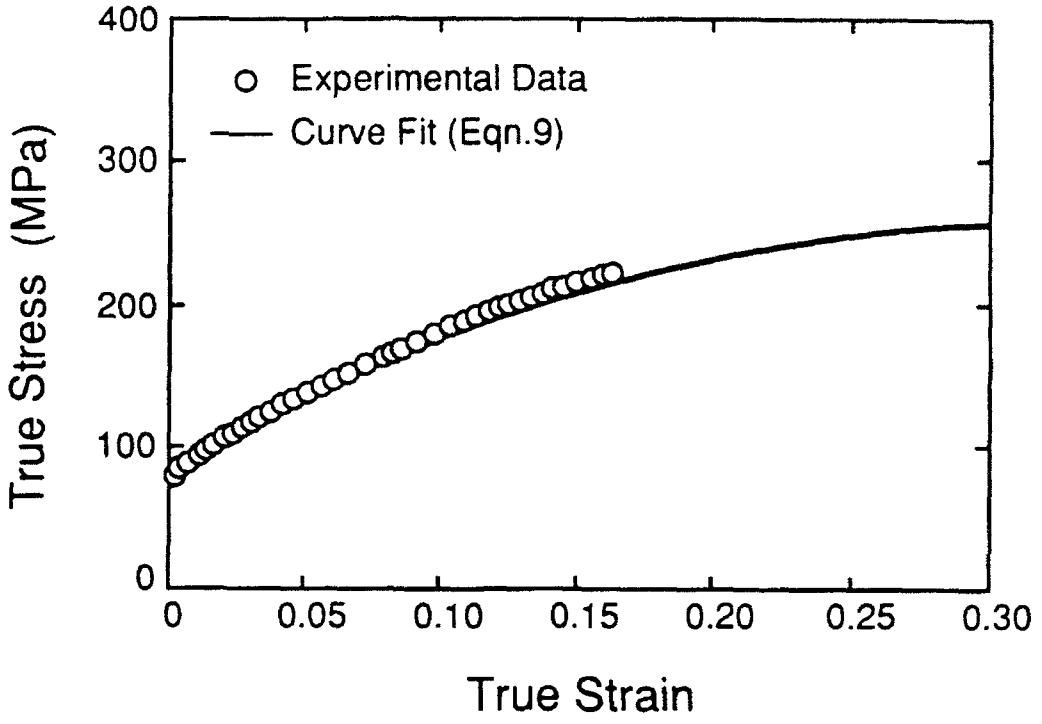
400
300
200
100
0
True Stress (MPa)
Experimental Data
Curve Fit (Eqn.9)
0
0.05
0.10
0.15
0.20
0.25
0.30
True Strain

Figure 8

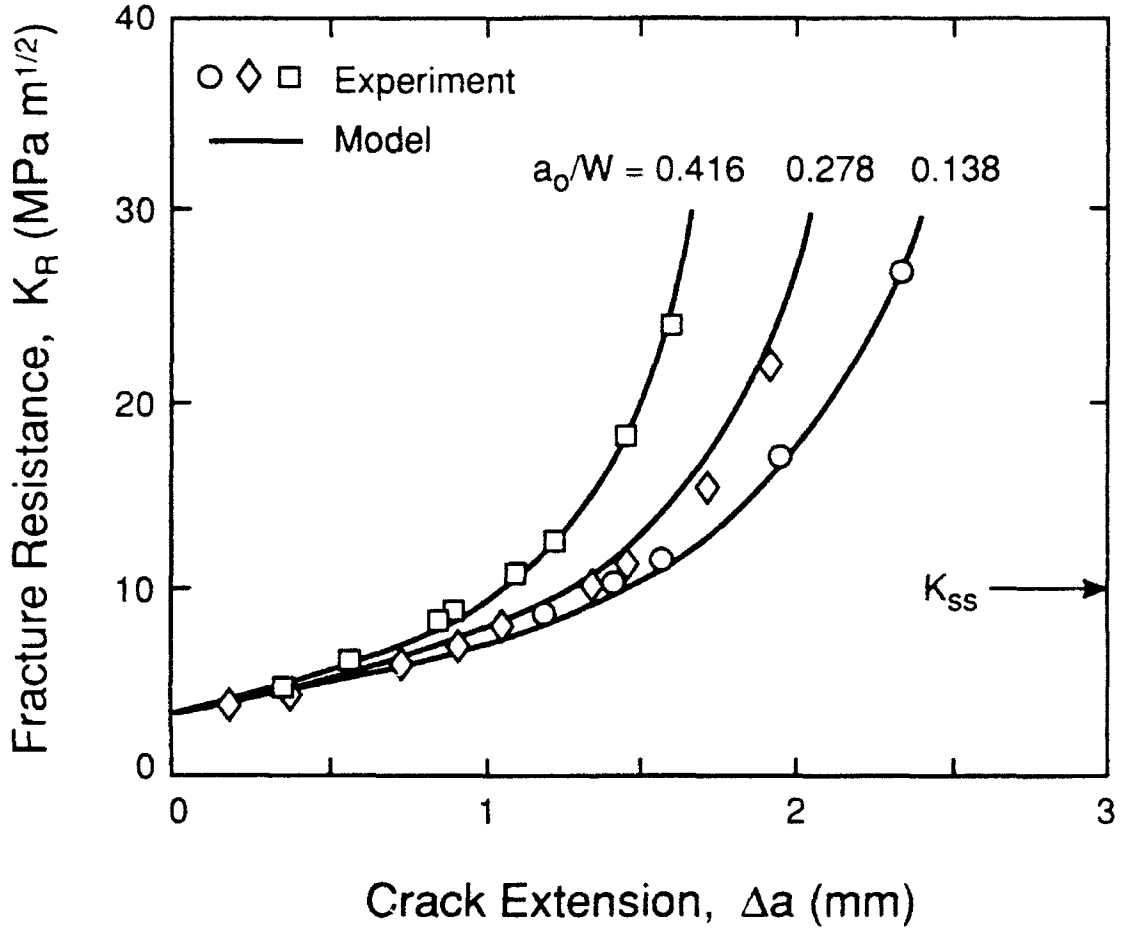
Fracture Resistance, K_R (MPa $m^{1/2}$)
Crack Extension, Δa (mm)
Experiment
Model
a_o/W = 0.416 0.278 0.138
K_{ss}
0
10
20
30
40
0
1
2
3

Fig. 9

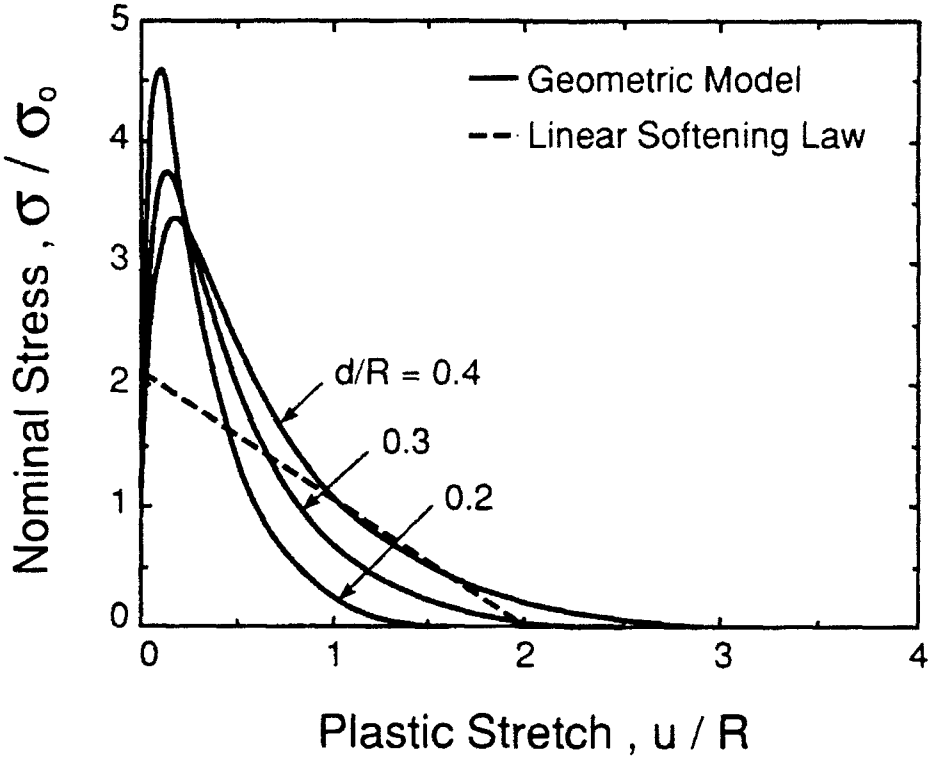

Fig. 10 (a)

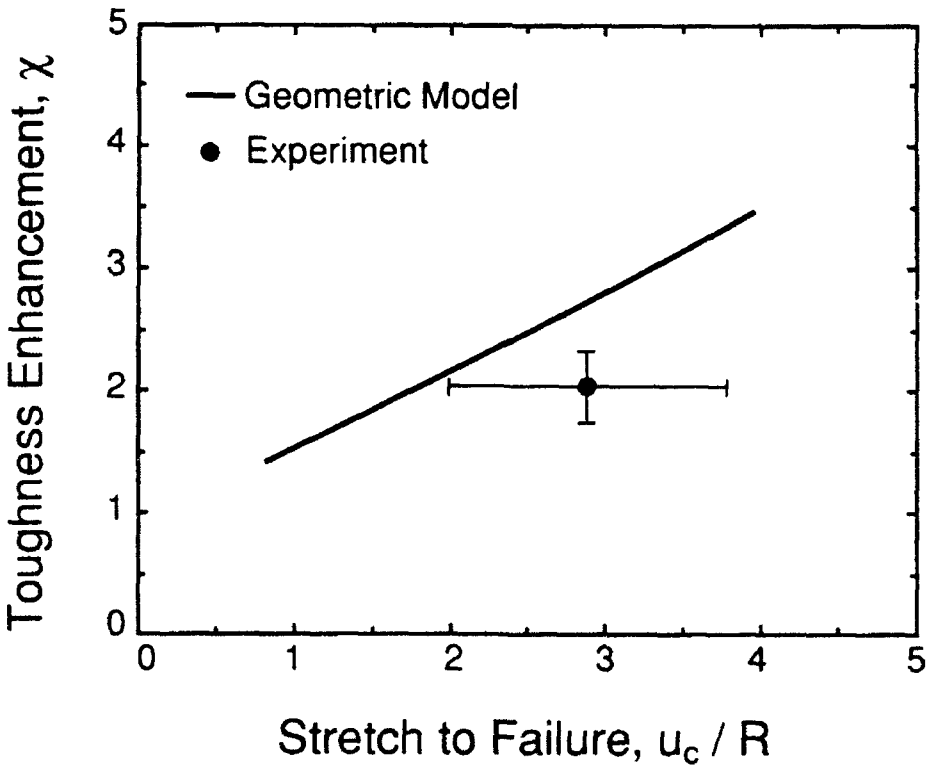

Fig. 10 (b)

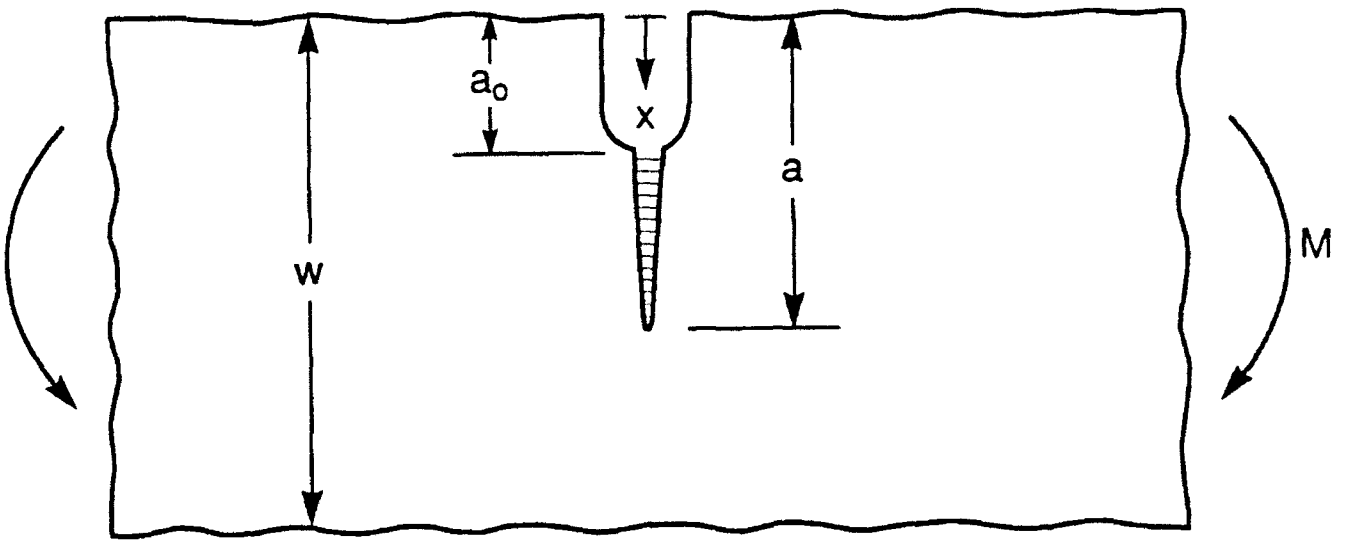

Fig. 11

MATERIALS

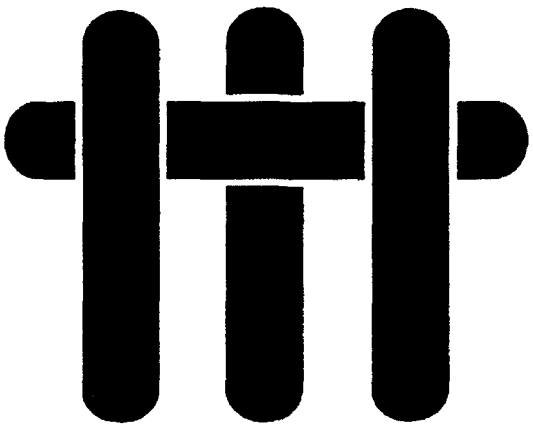

ON THE STRENGTH OF DUCTILE PARTICLE REINFORCED BRITTLE MATRIX COMPOSITES

G. Bao[†] and F. Zok[*]

[†]Department of Mechanical Engineering, The Johns Hopkins University
Baltimore, MD 21218

[*]Materials Department, University of California
Santa Barbara, CA 93106

February, 1993

7F:MS26(February 12, 1993)/9:20 AM/mef

ABSTRACT

The present study examines the strength characteristics of brittle materials reinforced with ductile metal particles. The strength enhancement in such materials is derived from a process of crack bridging by the particles. The study focuses primarily on the role of the bridging traction law: the relation between the crack surface traction and the crack opening displacement. Two types of bridging traction laws are considered: one exhibits linear softening, and the other is rectilinear. The results are expressed in terms of two non-dimensional parameters that account for the effects of the flaw size and a variety of material properties, including the elastic modulus, the matrix toughness, and the parameters characterizing the traction law. It is shown that such composites can be substantially more flaw tolerant than monolithic ceramics. This flaw tolerance is manifested as a narrowing of the strength distribution for a prescribed flaw size distribution. Finally, the role of the interface debond length is examined. A geometric necking model is used to derive the relevant bridging traction law which, in turn, is used to evaluate the composite fracture properties. It is shown that there exists *optimal* debond lengths at which the composite strength is maximized. In contrast, the steady state toughness increases monotonically with debond length. The implications of these results on the design of composite microstructures are briefly described.

1. INTRODUCTION

Ductile particles can substantially *toughen* a brittle material [1-5]. During crack extension the particles bridge the crack and thus reduce the stress intensity at the crack tip (Fig. 1(a)). As a result, the *strength* of the composite may exceed the strength of the matrix. The composite strength depends on various factors, including the matrix toughness, the initial flaw size, the crack surface tractions exerted by the particles, and the specimen geometry. In this study, emphasis is placed on the effects of the *bridging traction law*: the relationship between the crack surface traction, σ, and the crack opening displacement, δ.

The bridging traction law appropriate to ductile particles can be determined either through a micromechanical analysis [6-8], or by experimental measurement [4]. Two typical σ–δ relations for ductile reinforcements are shown schematically in Fig. 2: one corresponds to systems with relatively strong interfaces (a), and the other to systems with relatively weak interfaces (b) [4]. For modeling purposes, the curve in (a) can be approximated by a linear softening law and the curve in (b) by a rectilinear law, as indicated by the dashed lines. The approximations can be formally written as

$$\sigma/\sigma_o = \chi = \begin{cases} 1, & 0 \le \delta/\delta_o < 1 \\ 0, & \delta/\delta_o > 1 \end{cases} \tag{1a}$$

for the rectilinear law, and

$$\sigma/\sigma_o = \chi = \begin{cases} 1-\delta/\delta_o, & 0 \le \delta/\delta_o \le 1 \\ 0, & \delta/\delta_o \ge 1 \end{cases} \tag{1b}$$

for the linear softening law. Here σ_o is the maximum surface traction exerted by the particles: it is a function of the yield stress and volume fraction of particles, and the interface debond length. Furthermore, δ_o is the crack opening displacement at which the tractions fall to zero: it, too, is a function of the interface debond length, as well as the ductility and size of the particles. It is of interest to note that there are only two parameters that characterize these laws (σ_o and δ_o), making the laws amenable to modeling studies of the type described below.

The resistance to crack growth $\mathcal{G}_\mathcal{R}$ in this class of composite, obtained using the J-integral, can be expressed as

$$\mathcal{G}_\mathcal{R} = \Gamma_o + \sigma_o\delta_o \int_o^{\delta_t/\delta_o} \chi(s)ds \tag{2}$$

where Γ_o is the matrix toughness and δ_t is the crack opening displacement at the notch root (Fig. 1(a)). The initial (unbridged) crack starts to grow when $\mathcal{G}_\mathcal{R}$ reaches Γ_o. As it grows, a bridging zone develops in its wake, causing an increase in the resistance to further growth (Fig. 1(b)). Once δ_t reaches δ_o, particles begin to rupture at the notch root. Particle rupture continues with crack extension until a steady-state bridging zone length is obtained. The corresponding steady-state fracture resistance, Γ_s, is evaluated by setting $\delta_t = \delta_o$ in Eqn. (2), yielding the results:

$$\Gamma_s = \Gamma_o + \sigma_o\delta_o . \tag{3a}$$

for the rectilinear law, and

$$\Gamma_s = \Gamma_o + \sigma_o\delta_o/2. \tag{3b}$$

for the linear softening law.

Although Γ_s is a characteristic fracture property of the composite, it cannot be used directly to evaluate the composite *strength* since the conditions for crack instability are often met before steady state conditions are attained. Indeed, when the initial flaw size is small compared to the steady state bridging zone length, the strength enhancement attributable to the particles is negligible even though the toughness enhancement may be substantial. The main objective of the present article is to examine theoretically the relations between the traction law appropriate to ductile reinforcements and the strength and reliability of such composites, incorporating the effects of finite crack sizes. For simplicity, attention is focused on the rectilinear and linear softening traction laws.

The remainder of the paper is divided into four parts. Section 2 provides background on the mechanics of cracks bridged by ductile particles. In Section 3, the trends in composite strength with flaw size and the various materials properties (including elastic modulus, matrix toughness and the parameters characterizing the traction law) are presented. Section 4 focuses on the issue of reliability. Here the results of Section 3 are combined with a statistical description of the flaw size distribution in order to examine the changes in the strength distributions that arise from crack bridging. The role of interface debonding is examined in Section 5. For this purpose, a geometric necking model is used to derive the traction law for a prescribed debond length, which, in combination with the calculations of Section 3, are used to predict variations in strength with debond length. Finally, Section 6 provides remarks on some of the limitations and implications of the present results for the design of composite microstructures.

2. BASIC MECHANICS

Consider a mode I, plane strain center crack in a large composite body subject to a remote uniform tension, $\bar{\sigma}$, as depicted in Fig. 3. The length of the initial unbridged crack is $2a_o$and the total crack length is 2a.

2.1 Small Scale Bridging (SSB)

When the bridging zone length L is much smaller than both the crack length and the in-plane specimen dimensions, the problem is one of small-scale bridging (SSB). The crack can then be taken as semi-infinite, such that the effect of the applied load and specimen geometry can be represented by the applied stress intensity K or energy release rate $\mathcal{G}$: the interplay between crack bridging and finite geometry can be neglected. In this case, the curves characterizing the increase in fracture resistance with crack extension (so-called R-curves) are material properties. A comprehensive series of SSB solutions for $\mathcal{G}_{\mathcal{R}}$ and L in composites with rectilinear and linear softening bridging laws have been documented elsewhere [10].

Under SSB conditions, the composite strength S is attained when $\mathcal{G}_{\mathcal{R}}$ reaches its steady state value, Γ_s, whereupon the strength is given by the usual relation

$$S = \left[\frac{\bar{E}\Gamma_s}{\pi a_o}\right]^{1/2} \tag{4}$$

where $\bar{E}$ is the plane strain modulus of the composite and the crack length at fracture is taken to be equal to the initial flaw size, a_o. Combining Eqns. (3) and (4) leads to expressions for the normalized strengths

$$\frac{S}{\sigma_o} = \left[\frac{1+\lambda}{\pi\alpha}\right]^{1/2} \tag{5a}$$

for the rectilinear law, and

$$\frac{S}{\sigma_o} = \left[\frac{\frac{1}{2}+\lambda}{\pi\alpha}\right]^{1/2} \tag{5b}$$

for the linear softening law, where α and λ are the non-dimensional parameters

$$\alpha = \frac{\sigma_o a_o}{\delta_o \bar{E}}, \quad \lambda = \frac{\Gamma_o}{\sigma_o \delta_o} \tag{6}$$

Alternatively, these results can be expressed in terms of the *matrix* strength, S_o,

$$S_o = \left[\frac{\bar{E}\Gamma_o}{\pi a_o}\right]^{1/2} \tag{7}$$

assuming that the flaw size and elastic properties of the matrix are the same as those of the composite. Combining Eqns. (4) and (7) yields the result

$$\frac{S}{S_o} = \sqrt{\frac{\Gamma_s}{\Gamma_o}} \tag{8}$$

for both the rectilinear and the linear softening traction laws.

The non-dimensional parameters α and λ have the following physical meaning. The parameter α is a normalized flaw size: the normalizing parameter, $\delta_o \bar{E}/\sigma_o$, is a material length scale that is proportional to the steady state bridging zone length. Using order of magnitude estimates of the various material properties ($\delta_o \sim 10$ to $100\,\mu m$, $\bar{E} \sim 100$ GPa and $\sigma \sim$ 10-100 MPa) gives values of $\delta_o \bar{E}/\sigma_o$ that

range between ~1 and 100 mm. Consequently, for virtually all problems of practical interest, α lies in the range $0 < \alpha < 1$. The other parameter, λ, is a normalized matrix toughness: the normalizing parameter, $\sigma_o\delta_o$, is proportional to the energy dissipated through plastic deformation of the ductile particles. Alternatively, the inverse, $1/\lambda$, can be viewed as a measure of the toughness enhancement attributable to the particles, since the enhancement in steady-state toughness is

$$(\Gamma_s - \Gamma_o)/\Gamma_o = \eta/\lambda \tag{15}$$

where η is of order unity ($\eta = 1$ for the rectilinear law and $\eta = 1/2$ for the linear softening law). Using the values quoted above, $\sigma_o\delta_o$ lies between 10^2 and 10^4 Jm^{-2}. Furthermore, the toughness of most glasses and ceramics is $\Gamma_o \sim 10$ to 100 Jm^{-2}, putting λ in the range $\sim 0 < \lambda < 1$.

2.2 Large Scale Bridging (LSB)

When the bridging zone length is comparable to either the crack length or the in-plane specimen dimensions, the reduction in stress intensity due to the bridging particles is a function of the applied stress intensity as well as the specimen geometry and size [12]. In this regime, *the fracture resistance curve is not a material property*. However, it will become clear shortly that the resistance curve is not essential in deriving the composite strength, and thus the shortcomings of such curves in this regime are not a major concern.

Using a stress intensity approach, the relation between the applied stress and the current crack length for the crack configuration shown in Fig. 3 can be expressed as [11]

$$\bar{\sigma}\sqrt{\pi a} = \sqrt{\bar{E}\Gamma_o} + 2\sqrt{\frac{a}{\pi}}\int_{\ell}^{a}\frac{\sigma(x)}{\sqrt{a^2-x^2}}\,dx \tag{9}$$

where $\sigma(x)$ is the stress distribution in the bridging zone, x is the distance from the crack center, and 2ℓ is the length of the unbridged portion of the crack. Prior to particle rupture, 2ℓ is equivalent to the initial flaw size, $2a_o$; following particle rupture $\ell < a_o$. For convenience, the traction law is inverted and written in the generic form

$$\delta/\delta_o = \psi(\sigma/\sigma_o) \tag{10}$$

where ψ is a continuous or piece-wise continuous function of σ/σ_o. The displacement δ consists of two components: one due to the remote tension and another due to the bridging stress [11]. When summed together, the total displacement is

$$\delta = \frac{4}{\bar{E}}\bar{\sigma}\sqrt{a^2-x^2} - \frac{4}{\pi\bar{E}}\int_{\ell}^{a}\sigma(s)\ell n\left|\frac{\sqrt{a^2-x^2}+\sqrt{a^2-s^2}}{\sqrt{a^2-x^2}-\sqrt{a^2-s^2}}\right|ds \,. \tag{11}$$

Combining Eqns. (9) to (11) and introducing appropriate normalizations yields the governing equation for the bridging traction distribution

$$\psi(\phi(\bar{x})) + 4\alpha\frac{a}{a_o}\int_{\ell/a}^{1}\phi(t)\Omega(\bar{x},t)dt = 4\sqrt{\frac{\alpha\lambda}{\pi}}\sqrt{\frac{a}{a_o}}\sqrt{1-\bar{x}^2}\,, \qquad a_o/a \le \bar{x} \le 1 \tag{12a}$$

where $\bar{x}$ is the normalized position in the bridging zone ($\bar{x} = x/a$); ϕ is the normalized bridging traction distribution:

$$\phi(\bar{x}) = \frac{\sigma(\bar{x})}{\sigma_o}; \tag{12b}$$

and Ω is a singular kernel,

$$\Omega(\bar{x},t) = \frac{1}{\pi}\ell n\left|\frac{\sqrt{1-\bar{x}^2}+\sqrt{1-t^2}}{\sqrt{1-\bar{x}^2}-\sqrt{1-t^2}}\right| - \frac{2}{\pi}\frac{\sqrt{1-\bar{x}^2}}{\sqrt{1-t^2}}. \tag{12c}$$

Equation (12) is solved either analytically or numerically (depending on the nature of the traction law) and the resulting traction distribution $\phi(\bar{x})$ inserted into the non-dimensional form of Eqn. (9):

$$\frac{\bar{\sigma}}{\sigma_o} = \sqrt{\frac{\lambda}{\pi\alpha}}\sqrt{\frac{a_o}{a}} + \frac{2}{\pi}\int_{\ell/a}^{1}\frac{\phi(t)}{\sqrt{1-t^2}}\,dt \tag{13}$$

to obtain the remote stress corresponding to each value of crack length. The composite strength, S, is then identified from the maximum point on the $\bar{\sigma}/\sigma_o$ versus a/a_o curve.

It will be shown momentarily that the composite strength can be attained either before or upon the onset of particle rupture, depending on the nature of the traction law and the values of the parameters α and λ. When the strength is attained *prior to* particle rupture (as it always is for the linear softening law), the lower limits on the integrals in Eqns. (12) and (13) are replaced by a_o/a. When the strength is attained at the onset of particle rupture (as it *sometimes* is for the rectilinear law), the variation in ℓ with the crack length, a, must be evaluated in order to solve these integrals. This is accomplished by setting $\delta = \delta_o$ at $x = \ell$ in Eqn. (11).

3. COMPOSITE STRENGTH

3.1 Rectilinear Traction Law

Substituting the rectilinear bridging traction law (Eqn. 1(a)) into Eqn. (13) and integrating yields the stress-crack length relation:

$$\frac{\bar{\sigma}}{\sigma_o} = \sqrt{\frac{\lambda}{\pi\alpha}}\sqrt{\frac{a_o}{a}} + \frac{2}{\pi}\cos^{-1}(a_o/a) \tag{14}$$

over the range $1 < a/a_o < a_c/a_o$, where a_c is the crack length at which particle rupture begins (i.e., δ_t reaches δ_o). In this regime, the maximum value of $\bar{\sigma}/\sigma_0$ occurs at a crack length, a_f, obtained by setting

$$\frac{d(\bar{\sigma}/\sigma_o)}{d(a/a_o)} = -\frac{1}{2a_f\sqrt{\pi}}\sqrt{\frac{\lambda}{\alpha}}\sqrt{\frac{a_o}{a_f}} + \frac{2a_o}{\pi a_f^2}\frac{1}{\sqrt{1-(a_o/a_f)^2}} = 0 \tag{15}$$

The solution to Eqn. (15) is

$$a_f/a_o = \left[\sqrt{(8\alpha/\pi\lambda)^2 + 1} - 8\alpha/\pi\lambda\right]^{-1}. \tag{16}$$

Substituting this result into Eqn. (14) gives the strength of the composite, i.e. $\bar{\sigma} = S$. It should be emphasized that this result is valid only when the stress maximum is attained *prior* to particle rupture i.e. $a_f \leq a_c$.

In the other regime ($a_c < a_f$), the maximum stress is attained *at the onset* of particle rupture. The value of a_c is obtained be setting $\delta = \delta_o$ at $x = a_o$ in Eqn. (11), resulting in

$$\delta_o = \frac{4}{\bar{E}}\bar{\sigma}a_c\sqrt{1-(a_o/a_c)^2} - \frac{4\sigma_o a_c}{\pi\bar{E}}\int_{a_o/a_c}^{1} \ell n\left|\frac{\sqrt{1-(a_o/a_c)^2}+\sqrt{1-t^2}}{\sqrt{1-(a_o/a_c)^2}-\sqrt{1-t^2}}\right| dt \quad . \tag{17}$$

The integral in Eqn. (17) can be worked out in a closed form

$$\int_{a_o/a_c}^{1} \ell n\left|\frac{\sqrt{1-(a_o/a_c)^2}+\sqrt{1-t^2}}{\sqrt{1-(a_o/a_c)^2}-\sqrt{1-t^2}}\right| dt = 2\sqrt{1-(a_o/a_c)^2}\left(\frac{\pi}{2}-\sin^{-1}\frac{a_o}{a_c}\right) - 2\frac{a_o}{a_c}\ell n\frac{a_o}{a_c} \tag{18}$$

which, in combination with Eqn. (17), leads to the result

$$4\alpha\frac{a}{a_o}\left[\frac{\bar{\sigma}}{\sigma_o}\sqrt{1-(a_o/a_c)^2} - \frac{2}{\pi}\sqrt{1-(a_o/a_c)^2}\left(\frac{\pi}{2}-\sin^{-1}\frac{a_o}{a_c}\right) - \frac{2}{\pi}\frac{a_o}{a_c}\ell n\frac{a_o}{a_c}\right] = 1 \quad . \tag{19}$$

Inserting Eqn. (14) into Eqn. (19) and using the identity $\cos^{-1}\gamma = \pi/2 - \sin^{-1}\gamma$, gives

$$4\sqrt{\frac{\lambda\alpha}{\pi}}\sqrt{\frac{a_c}{a_o}-\frac{a_o}{a_c}} - \frac{8\alpha}{\pi}\ell n\frac{a_o}{a_c} = 1 \quad . \tag{20}$$

This equation defines a_c/a_o in terms of only two parameters: α and λ. The strength is then obtained by solving for a_c/a_o and substituting the result into Eqn. (14).

Three stress-crack length curves showing the effects of particle rupture are presented in Fig. 4(a). The effects of the parameters α and λ on the critical condition wherein $a_f = a_c$ (obtained from Eqns. (16) and (20)) are presented in Fig. 4(b). Evidently, the stress maximum is attained prior to particle rupture only when the initial flaw size is small: $\alpha \leq 0.10$ to 0.15. This result is relatively insensitive to λ over the relevant range of λ.

The preceding results for the composite strength can be conveniently summarized in the form

$$\frac{S}{\sigma_o} = \sqrt{\frac{\lambda\beta}{\pi\alpha}} + \frac{2}{\pi}\cos^{-1}\beta \tag{21}$$

where

$$\beta = \begin{cases} a_o/a_f, \text{ if } a_f \le a_c \\ a_o/a_c, \text{ if } a_f > a_c. \end{cases} \tag{22}$$

For composites of this type, λ is typically much smaller than unity. Consequently, a first order estimate of the composite strength can be obtained by setting $\lambda = 0$. In this limit, $a_f \to \infty$, whereas a_c remains finite; thus the second condition in Eqn. (20) applies. Combining Eqns. (20) and (21) yields the simple analytical result

$$\frac{S}{\sigma_o} = \frac{2}{\pi}\cos^{-1}\left(e^{-\pi/8\alpha}\right). \tag{23}$$

The relevant results are presented in Fig. 5. The trends in strength, S/σ_o, with flaw size, α, are shown in Fig. 5(a) for values of λ ranging from 0 to 0.5. (The curve corresponding to $\lambda = 0$ is computed using Eqn. (23)). The same results are presented in an alternate form in Fig. 5(b). Here the composite strength is normalized by the matrix strength, S_o, and plotted against the square root of the normalized toughness: $(\Gamma_s/\Gamma_o)^{1/2}$. The latter normalizations are selected so that the prediction of the SSB solution ($\alpha = \infty$) is linear and exhibits a slope of unity (Eqn. (8)). The remaining curves correspond to values of α ranging from 0.05 to 2.

In the regime $\alpha \lesssim 0.5$ (which is relevant to most composites of interest), the SSB solution strongly overestimates the composite strength, demonstrating the need to account for the LSB effects. Evidently, S/S_o varies almost linearly with $(\Gamma_s/\Gamma_o)^{1/2}$ for all values of α. However, the degree of strength enhancement (characterized by the ratio S/S_o) is considerably smaller than $(\Gamma_s/\Gamma_o)^{1/2}$ for small values of α.

3.2 Linear Softening Traction Law

The effects of bridging on the composite strength for the linear softening traction law have been evaluated following the approach outlined in the preceding section. Two salient differences exist. Firstly, there is no analytical expression for the composite strength for the linear softening law. The relevant solution for the stress - crack length relation over the range $0 \le a/a_o \le a_c/a_o$ can be written as

$$\frac{\bar{\sigma}}{\sigma_o} = \sqrt{\frac{\lambda}{\pi\alpha}}\sqrt{\frac{a_o}{a}} + \frac{2}{\pi}\int_{a_o/a}^{1} \frac{\phi(t)}{\sqrt{1-t^2}}\, dt \qquad (24)$$

(This result is equivalent to Eqn. (13) with the lower limit on the integral replaced by a_o/a.) Here the integral must be solved numerically since no analytical solution exists. Secondly, the maximum stress is *always* attained prior to particle rupture, i.e. no finite values of α and λ satisfy the equality $a_f = a_c$. As a result, it is unnecessary to calculate the stress - crack length relation for the regime in which $a/a_c > 1$: Eqn. (24) can be used in all cases. Three stress - crack length curves for this traction law are shown in Fig. 6. The composite strength is obtained by identifying the maximum points on a family of such curves, each corresponding to a specified combination of α and λ.

The trends in the strength ratio, S/σ_o, with flaw size, α, and the strength ratio, S/S_o, with toughness, $(\Gamma_s/\Gamma_o)^{1/2}$ are shown in Fig. 7. Qualitatively, the curves exhibit features similar to those corresponding to the rectilinear traction law (Fig. 5). The main difference between the two is that the linear softening law leads to lower strengths for small values of α coupled with large values of λ. In the limit of SSB, ($\alpha >> 1$), the strength depends only on the toughness ratio, Γ_s/Γ_o, not on the form of the traction law.

The curves in Fig. 7 can be well represented by the fitting formula

$$\frac{S}{\sigma_o} = \left(1+\frac{\lambda}{\sqrt[3]{\alpha}}\right)\left[1-\exp\left(-\sqrt{\frac{0.64}{\pi\alpha}}\right)\right]. \tag{25}$$

When the results are normalized by the matrix strength, S_o, Eqn. (25) becomes

$$\frac{S}{S_o} = \sqrt{\frac{\pi\alpha}{\lambda}}\left(1+\frac{\lambda}{\sqrt[3]{\alpha}}\right)\left[1-\exp\left(-\sqrt{\frac{0.64}{\pi\alpha}}\right)\right]. \tag{26}$$

The error in Eqns. (25) and (26) over the practical range of $0.02 \le \lambda \le 0.2$ and $0 < \alpha < 1$ is less than 5%.

4. RELIABILITY

In addition to improving the strength and toughness of ceramics, ductile particles can, in some instances, improve the reliability of the materials. Reliability here refers to the sensitivity of the strength to the flaw size, rather than the strength itself. One manifestation of this sensitivity is the breadth of the strength distribution that corresponds to a prescribed flaw size distribution: materials whose

strengths are sensitive to flaw size tend to exhibit broader strength distributions. In this context, most monolithic ceramics are *unreliable* since their strengths are sensitive to flaw size, i.e. strength scales with $a_o^{-1/2}$. Consequently, flaws introduced during processing or in service can substantially degrade their strength. In contrast, materials that exhibit R-curve behavior tend to exhibit narrower strength distributions[16,17], an attractive feature for the design of structural components.

To demonstrate the degree of flaw sensitivity of ductile particle reinforced ceramics, the results of Fig. 5(a) (S/σ_o vs. α) have been re-plotted in Fig. 8(a) using logarithmic coordinates. For monolithic ceramics that do not exhibit R-curve behavior, such plots are linear with a slope of -1/2. In contrast, for the composites, there are three regimes of behavior, governed mainly by the value of α. (i) When the flaws are very small ($\alpha \lesssim 0.01$), the strength is essentially dictated by the *matrix* toughness and is given by

$$\frac{S}{\sigma_o} = \left(\frac{\lambda}{\pi\alpha}\right)^{1/2} \tag{27}$$

In this regime, the relation between log S/σ_o and log α is linear with a slope of -1/2, as it is for monolithic ceramics. This trend is shown by the dotted lines on the left side of Fig. 8(a). (ii) For very large flaws ($\alpha \gtrsim 1$), the relationship is again linear, only now it is dictated by the steady state *composite* toughness. In this case, the strength is obtained from the SSB solution (Eqn. (5a)). This trend is shown by the dashed lines on the right side of Fig. 8(a). (iii) In the intermediate regime (particularly around $0.03 \lesssim \alpha \lesssim 0.3$), the sensitivity of strength to the flaw size is substantially lower, as manifest in the reduction in the slope of these curves.

One parameter that can be used to characterize the degree of flaw sensitivity of such composites is the slope, $-d[\log (S/\sigma_o)]/d[\log \alpha]$. This parameter can vary

between 0 and 1/2, with 0 corresponding to the most desirable behavior (i.e. flaw *insensitive*) and 1/2 to the least desirable (i.e. flaw *sensitive*). Fig. 8(b) shows the variation in this parameter with flaw size for the results of Fig. 8(a). The figure shows how the flaw sensitivity approaches 1/2 for very short and very long cracks, but drops to substantially lower values for intermediate crack sizes. With the intermediate regime, the composites would be expected to be significantly more reliable than monolithic ceramics.

The results of Figs. 5 and 7 can also be used to describe the strength distribution corresponding to a prescribed flaw size distribution. In monolithic ceramics, a convenient empirical description of the flaw size distribution is given by the Weibull function

$$P = 1 - \exp\frac{-V}{V_o}\left(\frac{a_o}{a}\right)^{m/2} \tag{28}$$

where P is the cumulative probability of flaws having size greater than a in an elemental volume, V, m is the Weibull modulus, and V_o and a_o are the reference values of volume and flaw size, respectively. The corresponding strength distribution is obtained by relating the crack size to the strength via the Griffith equation. For ductile particle reinforced ceramics, Eqn. 28 can be re-expressed in terms of the normalized flaw size, α, whereupon

$$P = 1 - \exp\frac{-V}{V_o}\left(\frac{\alpha_o}{\alpha}\right)^{m/2} \tag{29}$$

where α_o is the reference flaw size, a_o, normalized by $\delta_o \bar{E}/\sigma_o$. Equation 29 can then be combined with the results of the type shown in Fig. 5 to obtain the strength distribution for a prescribed flaw distribution (characterized by α_o and m).

An illustrative example for m = 5 and α_o = 0.03 is shown in Fig. 9. Here the dotted and dashed lines correspond to the limiting cases described for Fig. 8. In essence, the dotted lines represent the trends expected for the matrix itself: the relationship is linear with a slope of 2.303 m. Similarly, the dashed lines can be viewed as being representative of the behavior of a monolithic ceramic with a toughness equivalent to the steady state composite toughness. This relationship is also linear with a shape of 2.303 m, though it is shifted to higher values of strength. The figure indicates that the main role of the crack bridging is to increase the strength of the largest flaws, reducing the failure probability at low stresses relative to that of the matrix. As a result, the strength distribution is narrowed.

5. EFFECT OF INTERFACE DEBONDING

The preceding sections have described the effects of the traction law, characterized by the parameters σ_o and δ_o, on the composite strength, without consideration of the microstructural origins of these parameters. It has been recognized, however, that the properties of the particle-matrix interface play a key role in determining the values of these parameters [1,6,8]. Specifically, *strong* interfaces result in minimal interface debonding during crack growth. Consequently, the particles are subjected to a large plastic constraint, leading to an elevation in the peak stress, σ_o, coupled with a reduction in the limiting separation, δ_o. Conversely, weak interfaces lead to large debond lengths which in turn reduce σ_o and increase δ_o. In addition, the steady state toughness generally increases with increasing debond length*. The purpose of the present section is to examine the

*It is recognized that when the interfaces are extremely weak, the particles completely debond from the matrix and no toughness enhancement is obtained. This limiting case is not considered in the present study.

effects of interface debonding on the strength of such composites. It will become evident that there exist *optimal* values of debond length that maximize composite strength.

Here the traction law is computed using a geometric necking model similar to the one initially developed by Mataga [7]. It is assumed that the particles are short circular cylinders oriented perpendicular to the crack plane. The shape of the ligaments during deformation is taken to be a paraboloid of revolution, and the nominal stress computed from Bridgman's solution for a necking bar [15]. Details of the model are presented in the Appendix. The corresponding traction law is then approximated by the linear softening traction law, wherein the bridging parameters σ_o and δ_o are given by

$$\delta_o/R = F_1(\ell/R) = 4.256\,\ell/R \tag{30a}$$

and

$$\frac{\sigma_o}{f\sigma_y} = F_2(\ell/R) = 1.487\sqrt{\frac{1+\ell/R}{2\ell/R}} - 2.044\frac{\ell}{R}\left(1-\frac{\ell}{R}\right)^2. \tag{30b}$$

where ℓ is the interface debond length, R is the particle radius, f is the volume fraction of particles and σ_y is the yield stress of the particles. The effects of the normalized debond length, ℓ/R, on the bridging parameters σ_o and δ_o are shown in Fig. 10. An example of the traction law for $\ell/R = 0.5$ and the corresponding linear approximation are shown in Fig. 11.

The steady state toughness is obtained by substituting Eqn. (30) into Eqn. (3b), whereupon

$$\frac{\Gamma_s}{\Gamma_o} = 1 + \left\{\frac{F_2\,F_1}{2}\right\}\left\{\frac{t\,\sigma_y\,R}{\Gamma_o}\right\} \tag{31}$$

Furthermore, the normalized flaw size is obtained by combining Eqns. (7), (12b) and (30), resulting in

$$\alpha = \left\{\frac{F_2}{\pi F_1}\right\}\left\{\frac{\Gamma_o}{S_o R}\right\}\left\{\frac{f\sigma_y}{S_o}\right\} \tag{32}$$

The results of Eqns (31) and (32) are then combined with the results of Fig. 7(b) to get the composite strength.

The variations in composite strength, S/S_o, and steady-state toughness, Γ_s/Γ_o, with debond length, ℓ/R, are plotted in Fig. 11. The relevant material parameters were selected to be $S_o/f\sigma_y = 1$, and $\Gamma_o/f\sigma_y R = 0.1$ and 0.2. The curves show that the steady state toughness increases monotonically with debond length, whereas the strength is maximized at an intermediate value. The reduction in strength beyond the maximum is attributable to the loss in plastic constraint associated with increased debonding.

6. CONCLUDING REMARKS

The design of composite microstructures for structural applications requires consideration of a variety of composite properties, including fracture resistance, strength and reliability. To date, most studies on metal-reinforced ceramics have focused on the effects of crack bridging on *fracture resistance*. It is clear that substantial improvements in fracture resistance can be obtained with modest additions of ductile particles. Furthermore, the important relationships between fracture resistance and the parameters characterizing the bridging traction law (σ_o and δ_o) have been well established[1-7]. The results of the present study show the relevant trends in composite *strength* with the bridging law parameters, using two

bridging laws that are appropriate to ductile particles. The effects of the initial flaw size and the various composite properties (e.g. Γ_o, σ_o, δ_o, $\bar{E}$) on composite strength can be incorporated into two non-dimensional parameters: α and λ. Furthermore, the composites can, in some instances, be considerably more flaw tolerant than monolithic ceramics, resulting in narrower strength distributions. As a result, the composites may be good candidates for applications in which flaws are likely to be introduced during service (e.g. surface abrasion and impact).

The results for composite strength have also been combined with a geometric necking model to evaluate the role of the interface debond length on the composite strength and toughness. The steady state toughness increases monotonically with debond length, whereas the strength is maximized at an intermediate value of debond length. Such calculations could be used in the design of composites with prescribed combinations of fracture properties, i.e. strength and toughness.

Two cautionary notes regarding the use of the present results should be made. The first pertains to the assumption that the bridging tractions associated with the particles can be smeared out over the crack faces. This assumption is valid only when both the initial flaw size and the degree of crack growth through the composite are large in relation to the spacing between the particles. Otherwise, an alternate, more detailed approach is needed to model the process of crack bridging. Secondly, in comparing the strength of the composite with that of the matrix, it has been assumed that the flaw populations in the two are the same. However, composite materials are generally more difficult to process than monolithic ceramics; consequently, there is a tendency for producing larger flaws within the composites. Such effects need to be considered in comparing the strength characteristics of the composites with those of the matrix.

ACKNOWLEDGMENTS

Funding for this work was supplied by the DARPA University Research Initiative Program of UCSB under ONR contract N-0014-86-K-0753, and by NSF through a Research Initiation Award MSS-9210250 (GB).

REFERENCES

1. M.F. Ashby, F.J. Blunt and M. Bannister, "Flow Characteristics of Highly Constrained Metal Wires", *Acta Metall.* **37**, 1847 (1989).

2. H.C. Cao, B.J. Dalgleish, H.E. Deve, C. Elliott, A.G. Evans, R. Mehrabian and G.R. Odette, *Acta Metall.* **37**, 2969 (1989).

3. H.E. Deve, A.G. Evans, G.R. Odette, R. Mehrabian, M.L. Emiliani and R.J. Hecht, *Acta Metall. mater.* **38**, 1491 (1990).

4. M. Bannister and M.F. Ashby, *Acta Metall. mater.* **39**, 2575 (1991).

5. M. Bannister, H. Shercliff, G. Bao, F. Zok and M.F. Ashby, "Toughening in Brittle Systems by Ductile Bridging Ligaments", *Acta Metall. mater.*, (1992), in press.

6. L.S. Sigl, P.A. Mataga, B.J. Dalgleish, R.M. McMeeking and A.G. Evans, *Acta Metall.* **36**, 945 (1988).

7. P.A. Mataga, *Acta Metall.* **37**, 3349 (1989).

8. G. Bao and C.Y. Hui, *Int. J. Solids Structures*, **26**, 631 (1990).

9. F. Erdogan and P.F. Joseph, *J. Am. Ceram. Soc.*, **72**, 262 (1989).

10. G. Bao and Z. Suo, "Remarks on Crack-Bridging Concepts", to appear in *Applied Mechanics Review*, 1992.

11. H. Tada, P.C. Paris and G.R. Irwin, *The Stress Analysis of Cracks Handbook.* Del Research, St. Louis, MO, (1985).

12. F.W. Zok and C.L. Hom, "Large Scale Bridging in Brittle Matrix Composites" Acta *Metall. mater.*, **38**, 1895 (1990).

13. M.P. Harmer, H.M. Chan and G.A. Miller, *J. Am. Ceram. Soc.*, **75**, 1715 (1992).

14. K. Niihara, *J. Ceram. Soc. Jpn.*, **99**, 974 (1991).

15. P.W. Bridgman, *Studies in Large Plastic Flow and Fracture*, McGraw-Hill, NY, pp. 9-32 (1952).

16. K. Kendall, N. McN. Alford, S.R. Tan and J.D. Birchall, *J. Mater. Res.*, **1**, 120 (1986).

17. R.F. Cook and D.R. Clarke, *Acta Metall.*, **36**, 555 (1988).

APPENDIX

Here details of the geometric necking model are presented. The flow behavior of the particles is assumed to obey the power hardening law

$$\sigma_f / \sigma_y = (\varepsilon / \varepsilon_y)^n \tag{A1}$$

where σ_f is the flow stress, n is the hardening exponent, and σ_y and ε_y are the yield stress and yield strain, respectively. Assuming the shape of the cylinders to be a paraboloid of revolution, the relationship between the bridging traction σ and the crack opening δ can be written as [7]

$$\sigma = f\sigma_y(1-\rho)^2[-\ell n(1-\rho)]^n\left(\frac{2}{\varepsilon_y}\right)^n\left[1+\left(\frac{\ell}{R}\right)^2\frac{\omega^2(\rho)}{\rho(1-\rho)}\right]\ell n\left[1+\left(\frac{R}{\ell}\right)^2\frac{\rho(1-\rho)}{\omega^2(\rho)}\right], \tag{A2}$$

$$\delta = 2\ell[\omega(\rho)-1], \tag{A3}$$

with $$\omega(\rho) = \left[1-\frac{4}{3}\rho+\frac{8}{15}\rho^2\right]^{-1} \tag{A4}$$

where f is the volume fraction of particles, ℓ is the interface debond length, R is the particle radius, and ρ is a non-dimensional parameter in the range $0 \le \rho < 1$.

The traction law defined by Eqns. (A2) to (A4) has been evaluated for debond lengths in the range $0 \le \ell/R \le 0.5$, using $n = 0.25$ and $\varepsilon_y = 0.003$. The resulting curves were subsequently approximated by the linear softening traction law, with σ_o taken as the peak value of σ, and δ_o taken as

$$\delta_o = 2w/\sigma_o \tag{A5}$$

where w is the area under the σ vs. δ curve. One example of a traction law obtained using the geometric model and the corresponding linear approximations is shown in Fig. 11. The bridging parameters σ_o and δ_o so obtained are plotted against the debond length, ℓ/R, in Fig. 10. The curves have then been approximated by the expressions in Eqn. (30).

FIGURE CAPTIONS

Fig. 1 Schematic diagrams showing (a) crack bridging by ductile particles, and (b) the corresponding fracture resistance curve.

Fig. 2 Schematic representations of the bridging traction laws and the linear approximations.

Fig. 3 A bridged mode I crack in an infinite body.

Fig. 4 (a) Trends in applied stress with crack extension for a composite with a rectilinear traction law. (b) The combinations of α and λ for which $a_f = a_c$.

Fig. 5 (a) Effect of the initial flaw size, α, on the composite strength (rectilinear traction law). (b) The results of (a) re-plotted to show the relationship between strength and steady state toughness. Note that the SSB solution provides a good approximation when α is large (≥ 1), but strongly overestimates the results when α is small.

Fig. 6 Trends in applied stress with crack extension for a composite with a linear softening traction law. (Note that $\bar{\sigma}/\sigma_0$ reaches its maximum before the onset of particle rupture).

Fig. 7 (a) Effect of the initial flaw size, α, on the composite strength (linear softening traction law). (b) The results of Fig. 7(a) re-plotted to show the relationship between strength and steady state toughness.

Fig. 8 The results of Fig. 5(a) plotted in logarithmic coordinates. The dotted lines are the predictions of Eqn. (27) and the dashed lines of Eqn. (5a). (b) Variation in flaw sensitivity with flaw size for the two curves shown in (a).

Fig. 9 Effects of crack bridging on the composite strength distribution.

Fig. 10 Effects of debond length on the bridging parameters. The symbols represent the results of the linear softening approximations; the lines are given by Eqn (30).

Fig. 11 A comparison of the traction law computed from the geometric necking model (Appendix) and the corresponding linear approximation. ($\ell/R = 0.5$).

Fig. 12 Effects of debond length, ℓ/R, on the composite strength and steady state toughness.

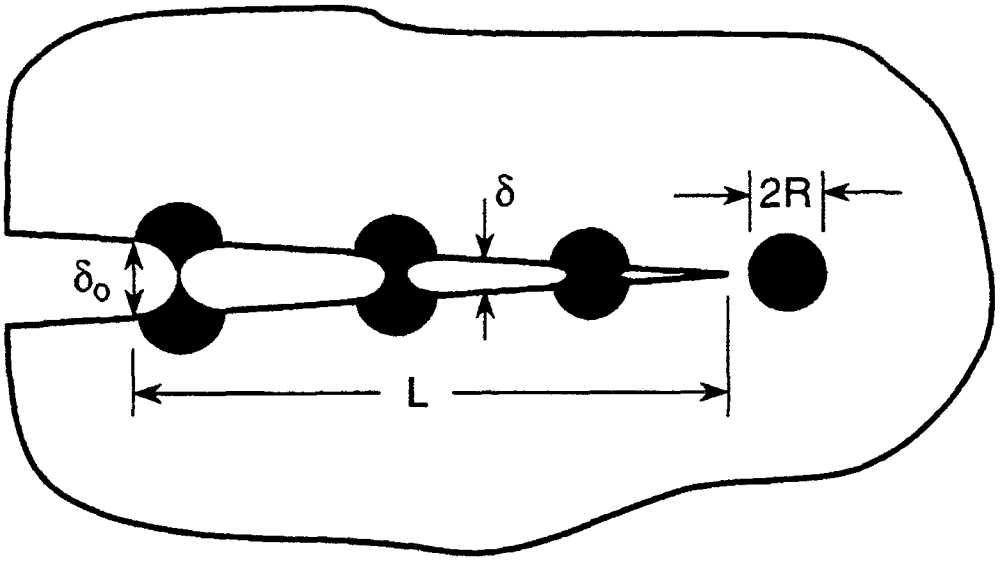
δ
2R
δo
L

(a)

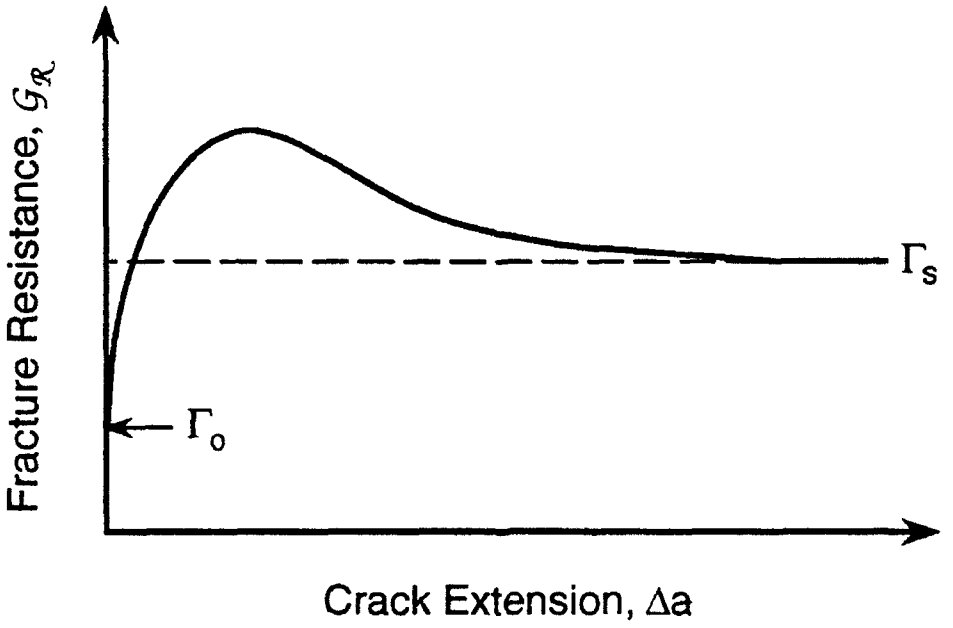
Fracture Resistance, $\mathcal{G}_{\mathcal{R}}$
Γ_s
Γ_o
Crack Extension, Δa

(b)

Fig. 1

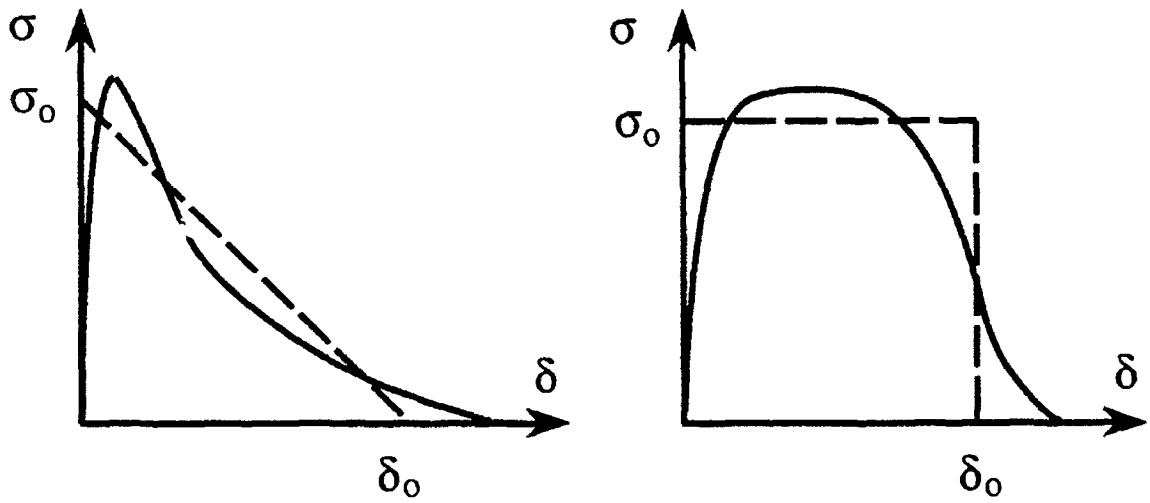

Fig. 2

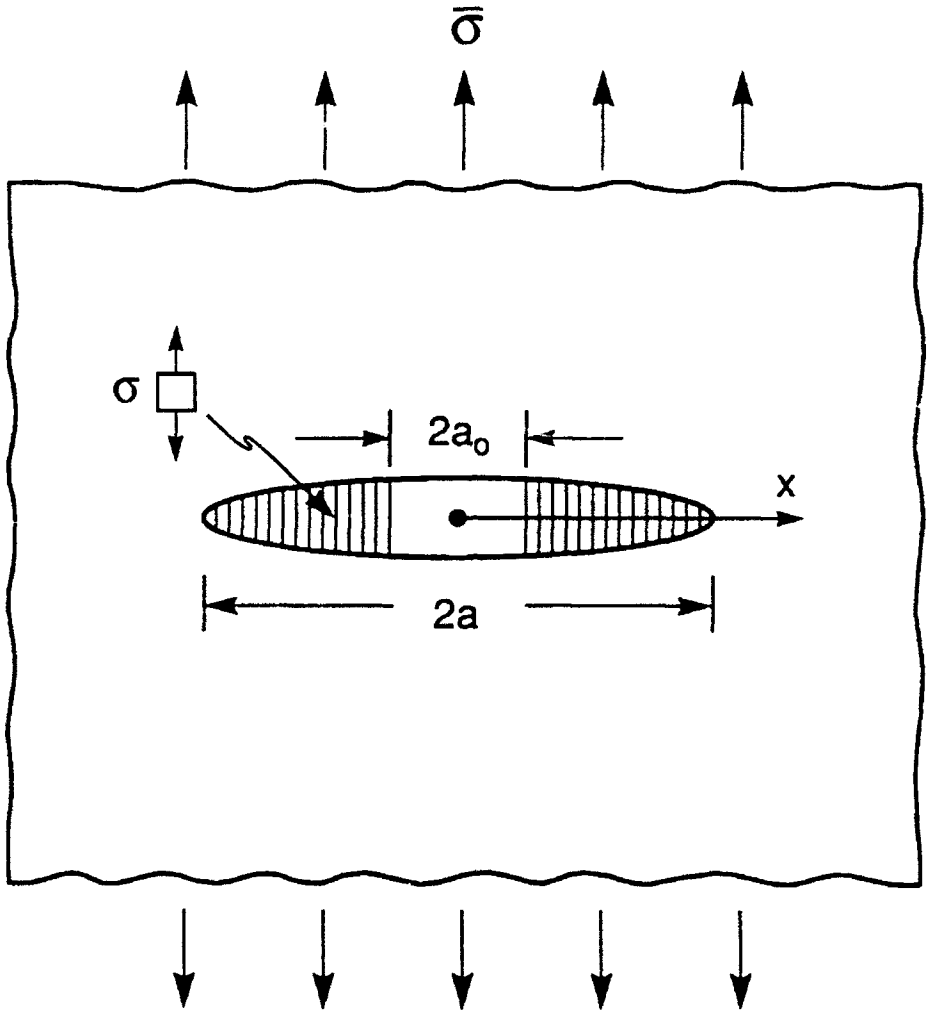

Fig. 3

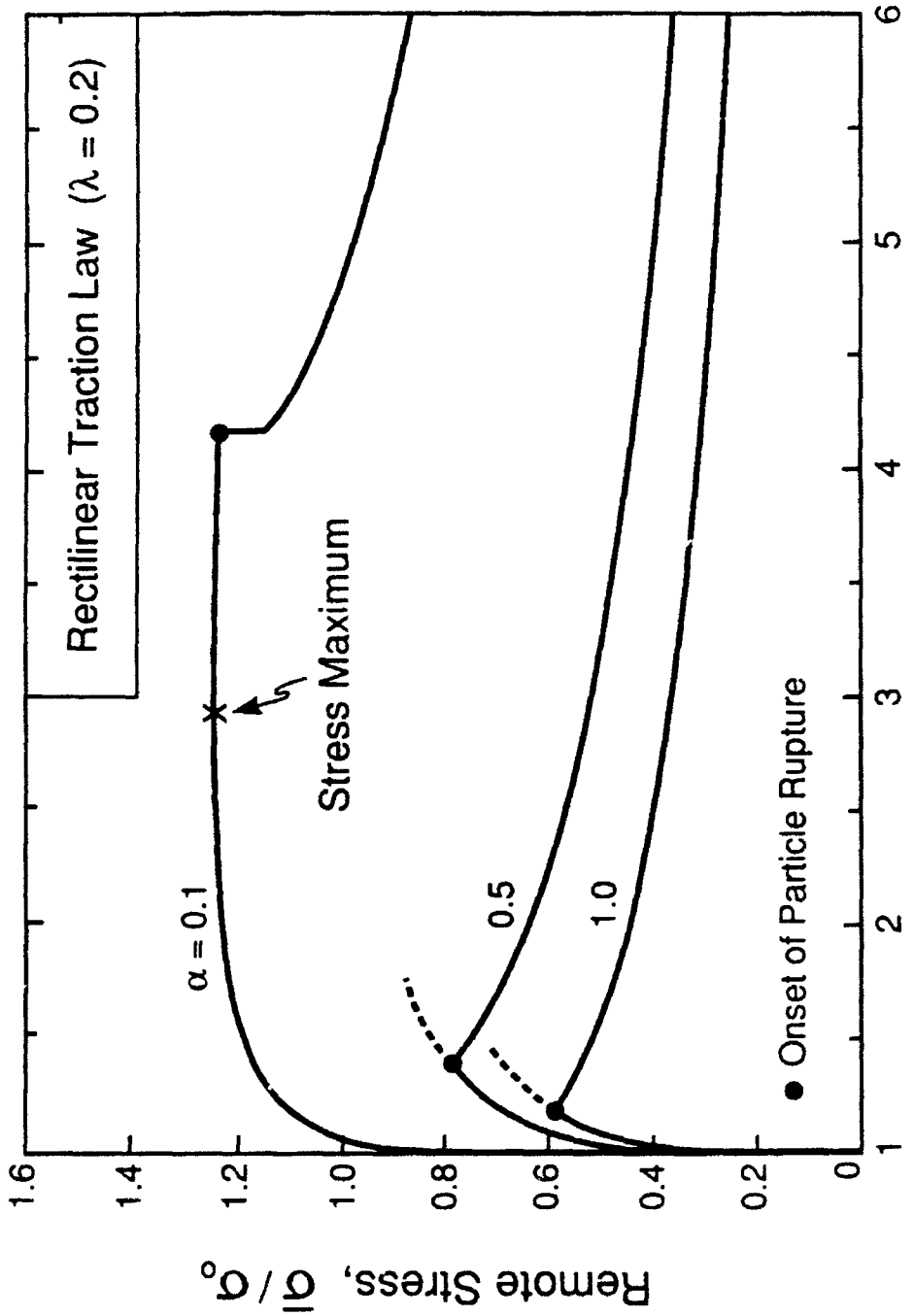
Rectilinear Traction Law (λ = 0.2)
Stress Maximum
α = 0.1
0.5
1.0
● Onset of Particle Rupture
Remote Stress, σ̄ / σ_o
Crack Length, a/a_o
1.6
1.4
1.2
1.0
0.8
0.6
0.4
0.2
0
1
2
3
4
5
6

Fig. 4(a)

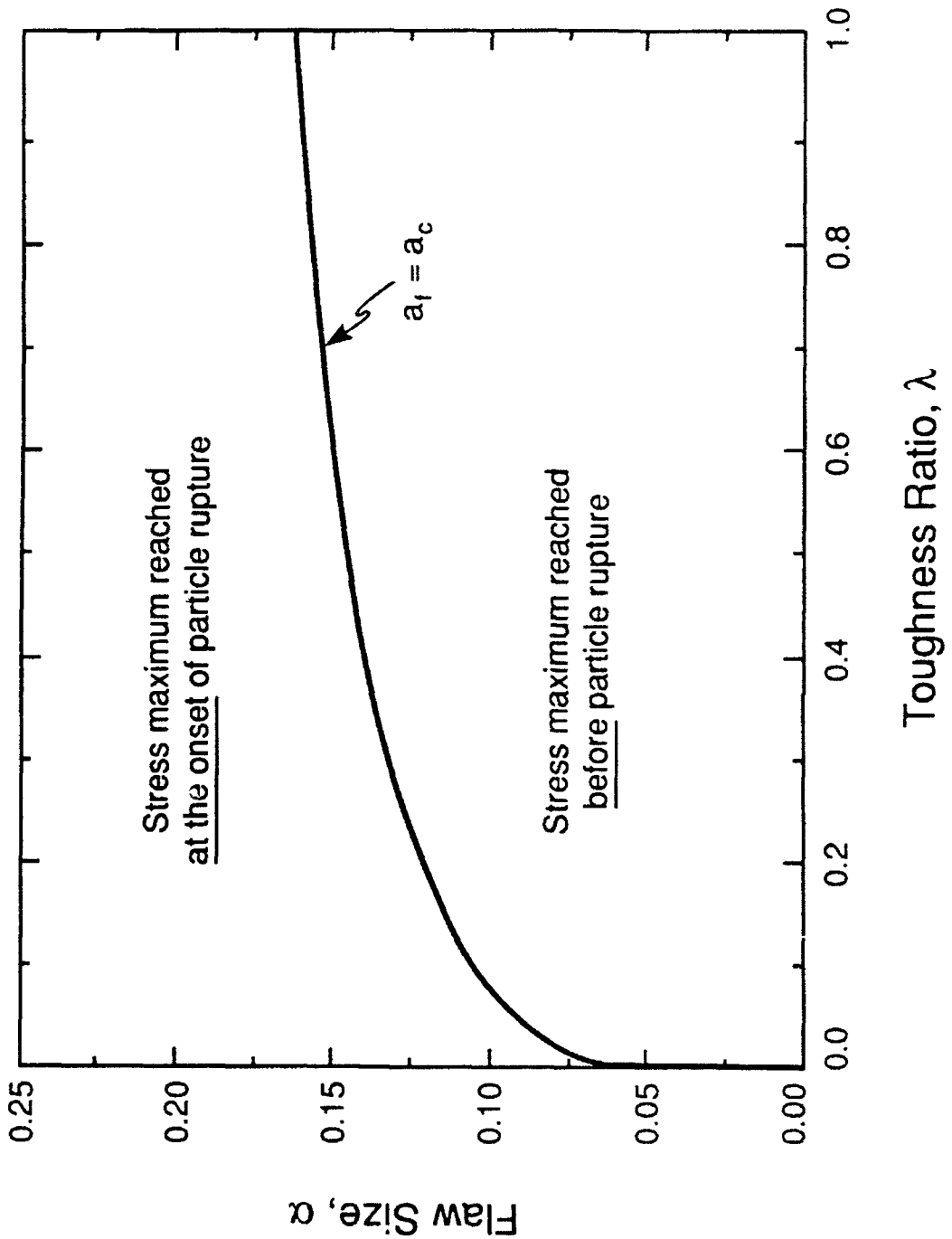
Flaw Size, α
0.25
0.20
0.15
0.10
0.05
0.00
0.0
0.2
0.4
0.6
0.8
1.0
Toughness Ratio, λ
$a_f = a_c$
Stress maximum reached
at the onset of particle rupture
Stress maximum reached
before particle rupture

Fig. 4(b)

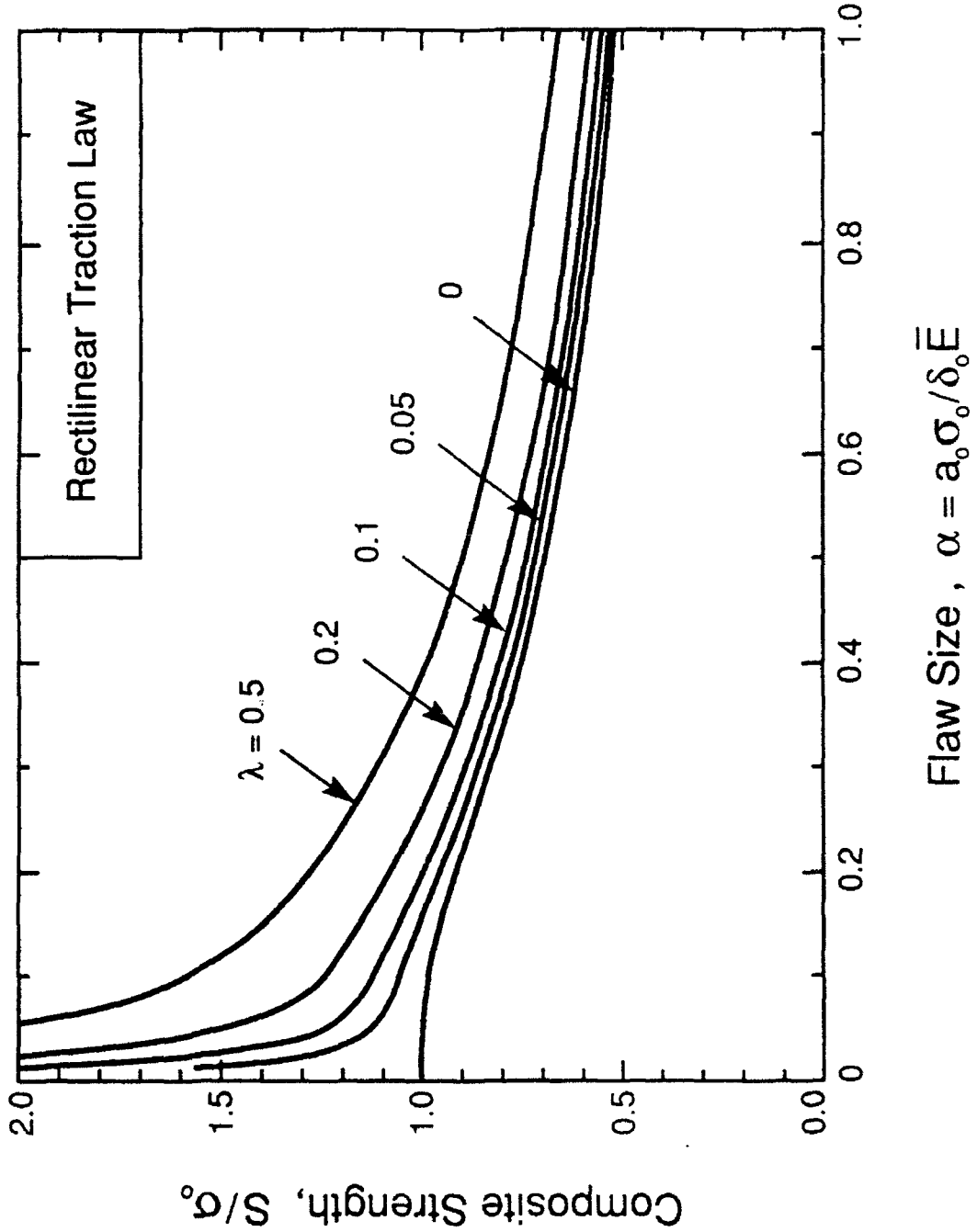
Rectilinear Traction Law
λ = 0.5
0.2
0.1
0.05
0
Composite Strength, S/σ₀
Flaw Size , α = a₀σ₀/δ₀Ē
2.0
1.5
1.0
0.5
0.0
0
0.2
0.4
0.6
0.8
1.0

Fig. 5(a)

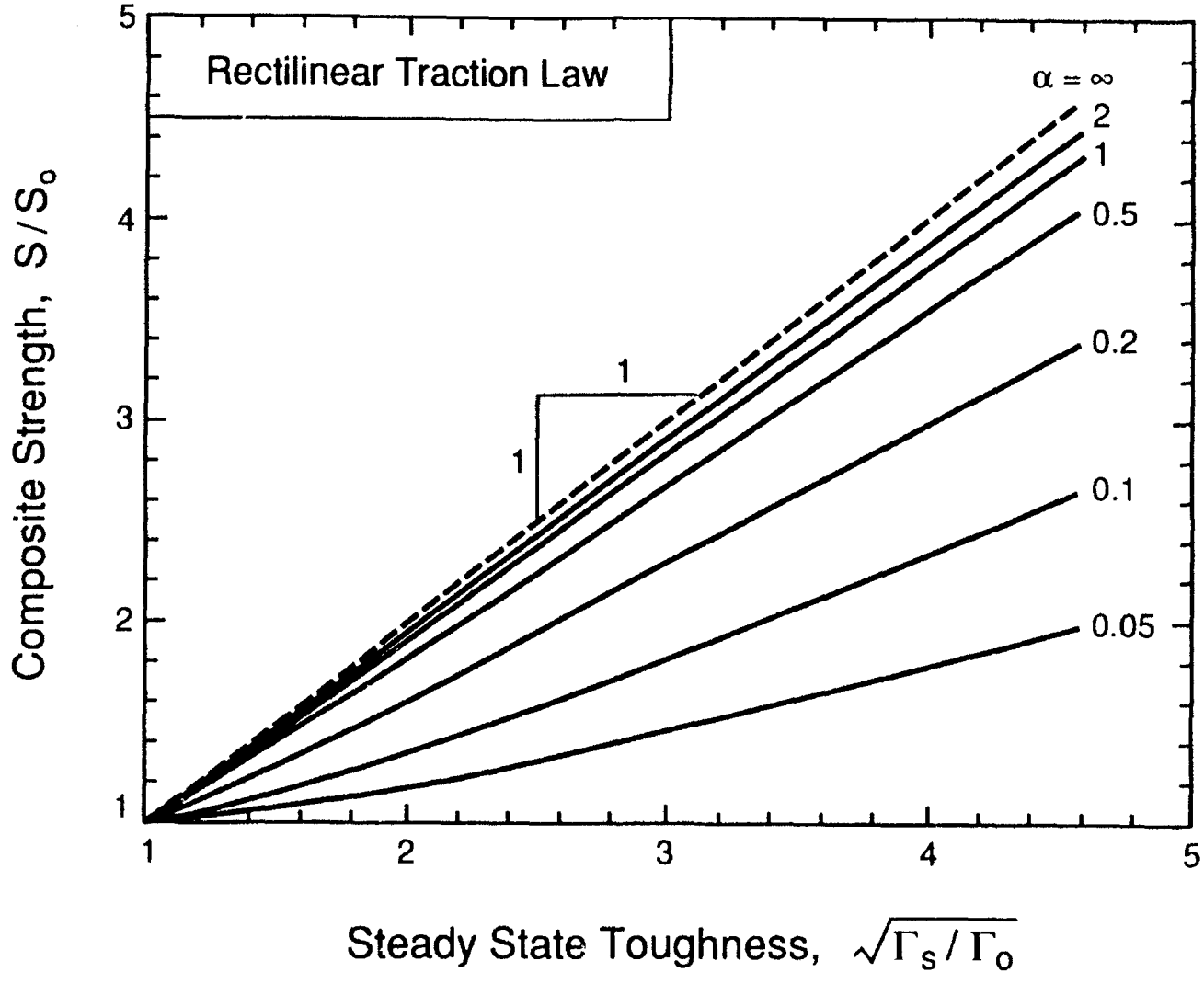
Rectilinear Traction Law
α = ∞
2
1
0.5
0.2
0.1
0.05
1
1
Composite Strength, S/S₀
Steady State Toughness, √(Γs/Γo)
1
2
3
4
5

Fig. 5(b)

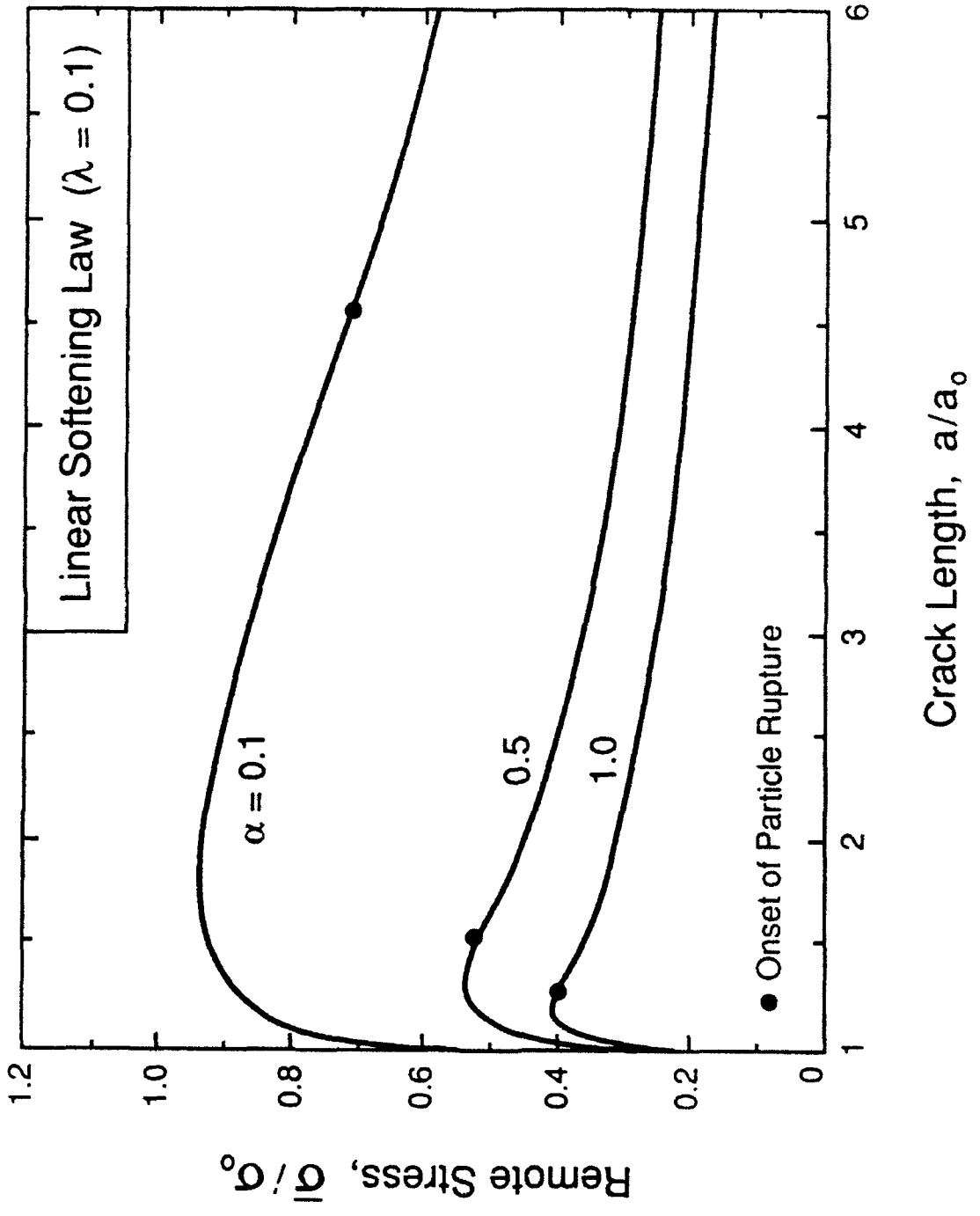
Linear Softening Law ($\lambda = 0.1$)
$\alpha = 0.1$
0.5
1.0
● Onset of Particle Rupture
Remote Stress, $\bar{\sigma} / \sigma_o$
Crack Length, a/a_o
0
0.2
0.4
0.6
0.8
1.0
1.2
1
2
3
4
5
6

Fig. 6

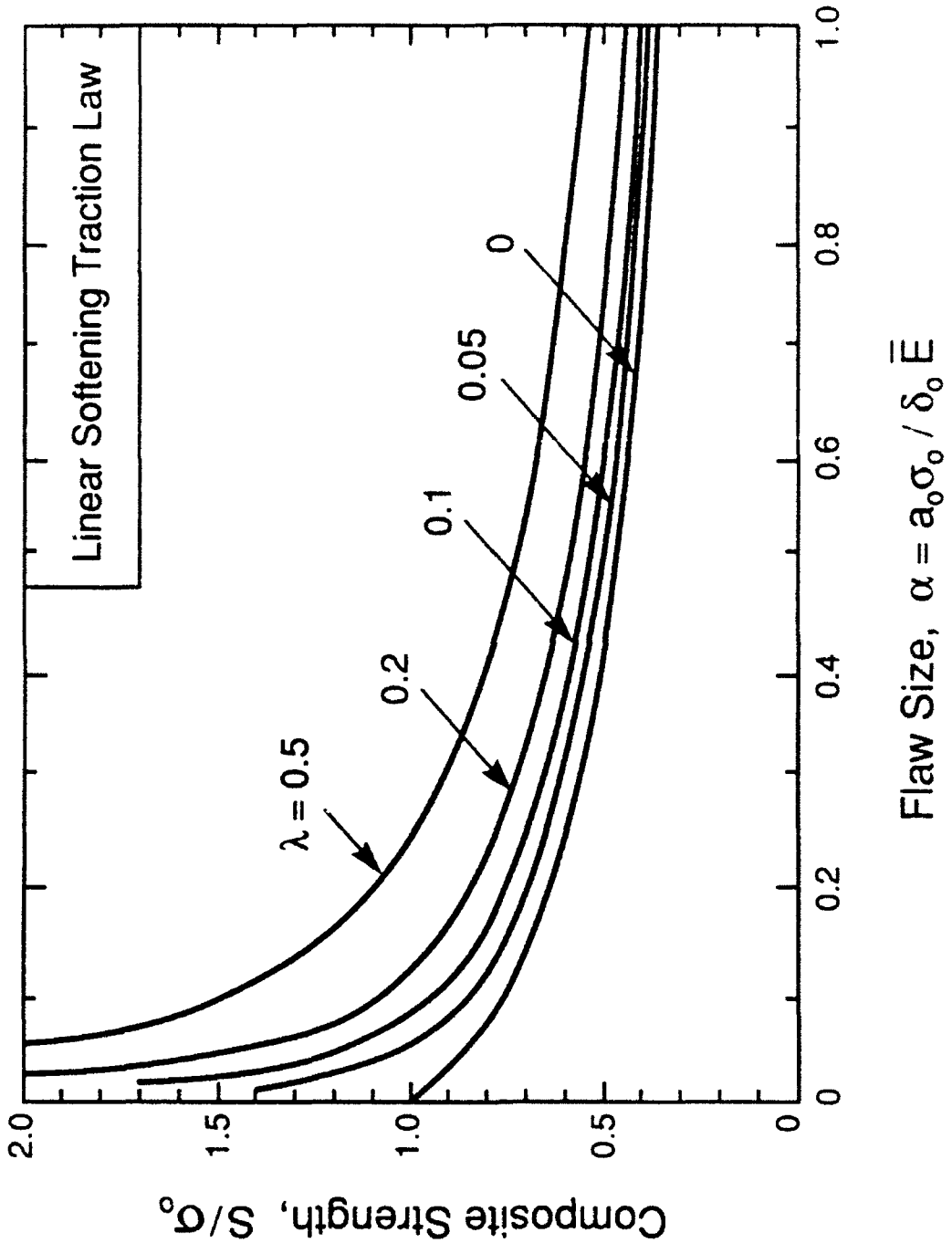
Linear Softening Traction Law
λ = 0.5
0.2
0.1
0.05
0
Composite Strength, S/σ₀
Flaw Size, α = a₀σ₀ / δ₀ Ē
0
0.5
1.0
1.5
2.0
0.2
0.4
0.6
0.8
1.0

Fig. 7(a)

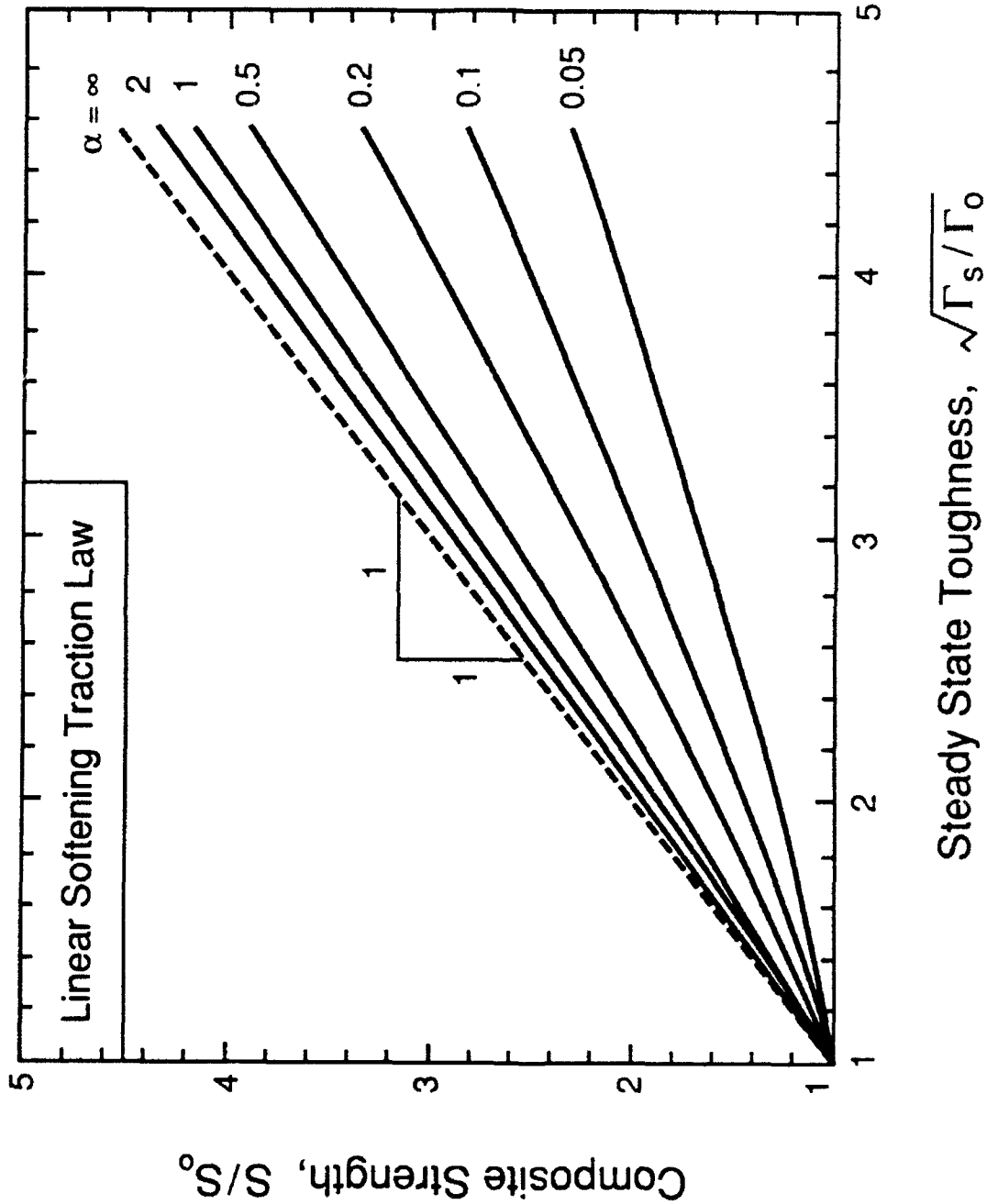
Linear Softening Traction Law
α = ∞
2
1
0.5
0.2
0.1
0.05
1
1
Composite Strength, S/S$_o$
Steady State Toughness, $\sqrt{\Gamma_s / \Gamma_o}$
1
2
3
4
5

Fig. 7(b)

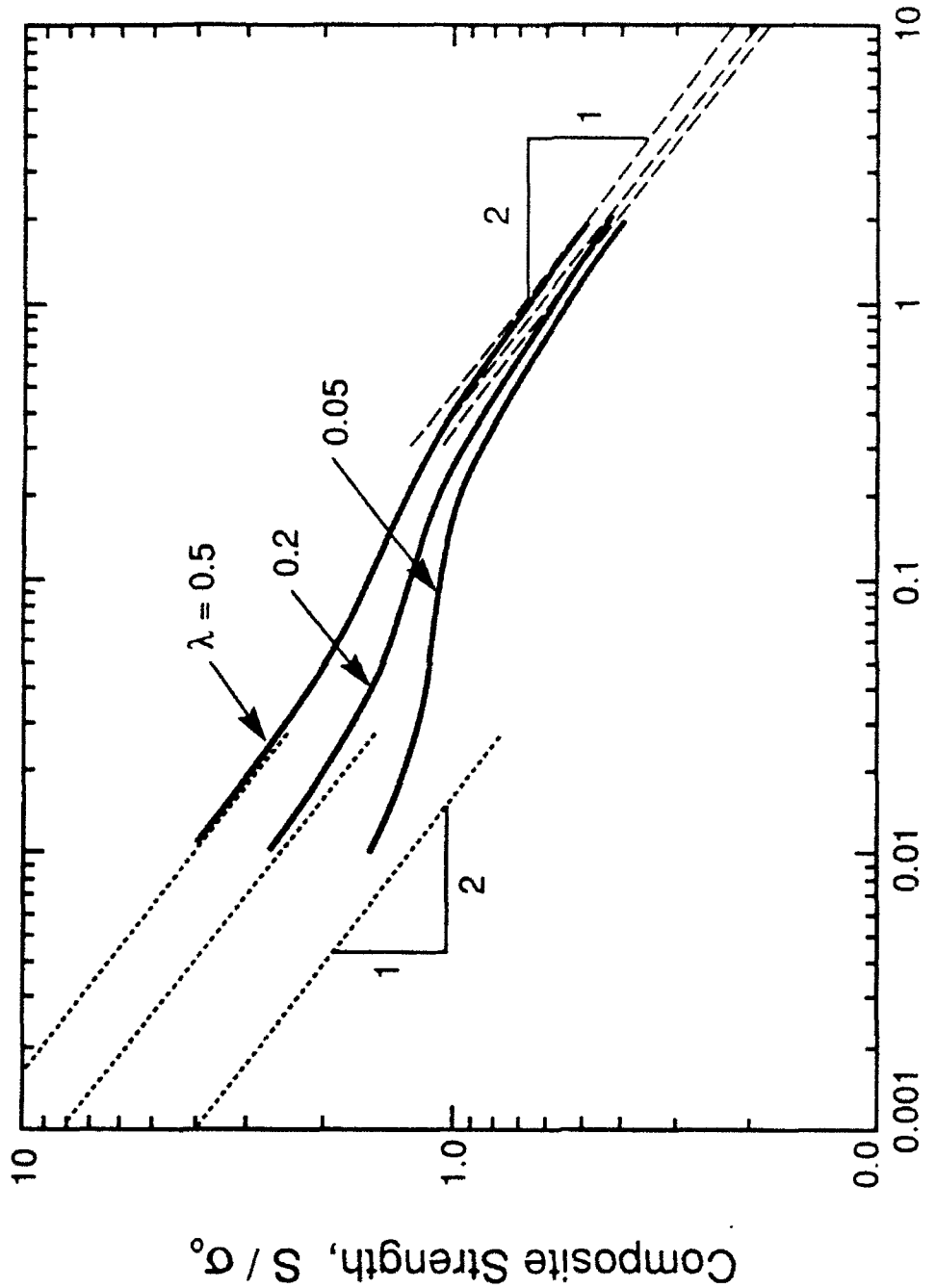
Composite Strength, S / σ₀
Flaw Size, α
λ = 0.5
0.2
0.05
1
2
1
2
10
1.0
0.0
0.001
0.01
0.1
1
10

Fig. 8(a)

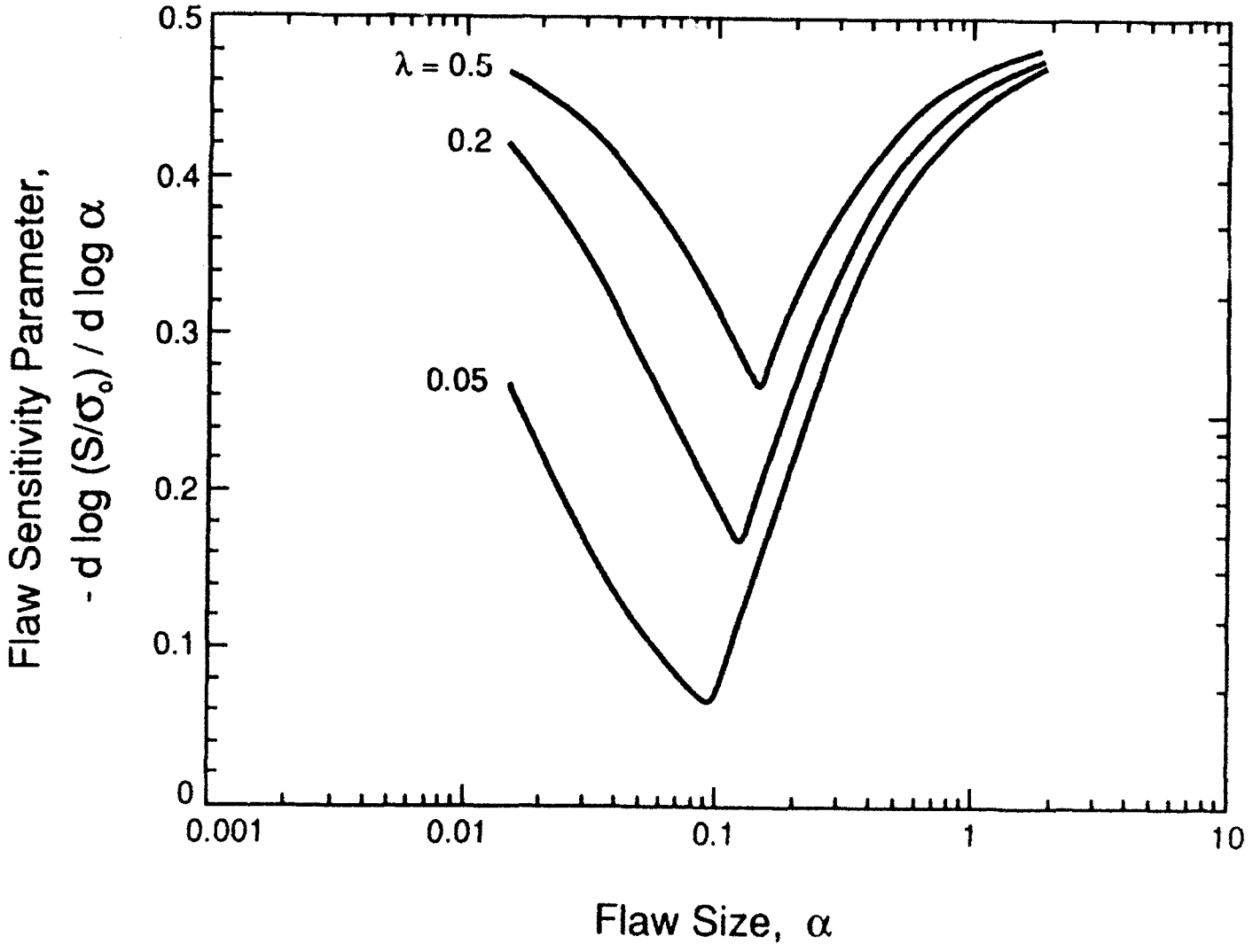
Flaw Sensitivity Parameter,
- d log (S/σo) / d log α
0.5
0.4
0.3
0.2
0.1
0
λ = 0.5
0.2
0.05
0.001
0.01
0.1
1
10
Flaw Size, α

FIG. 8(b)

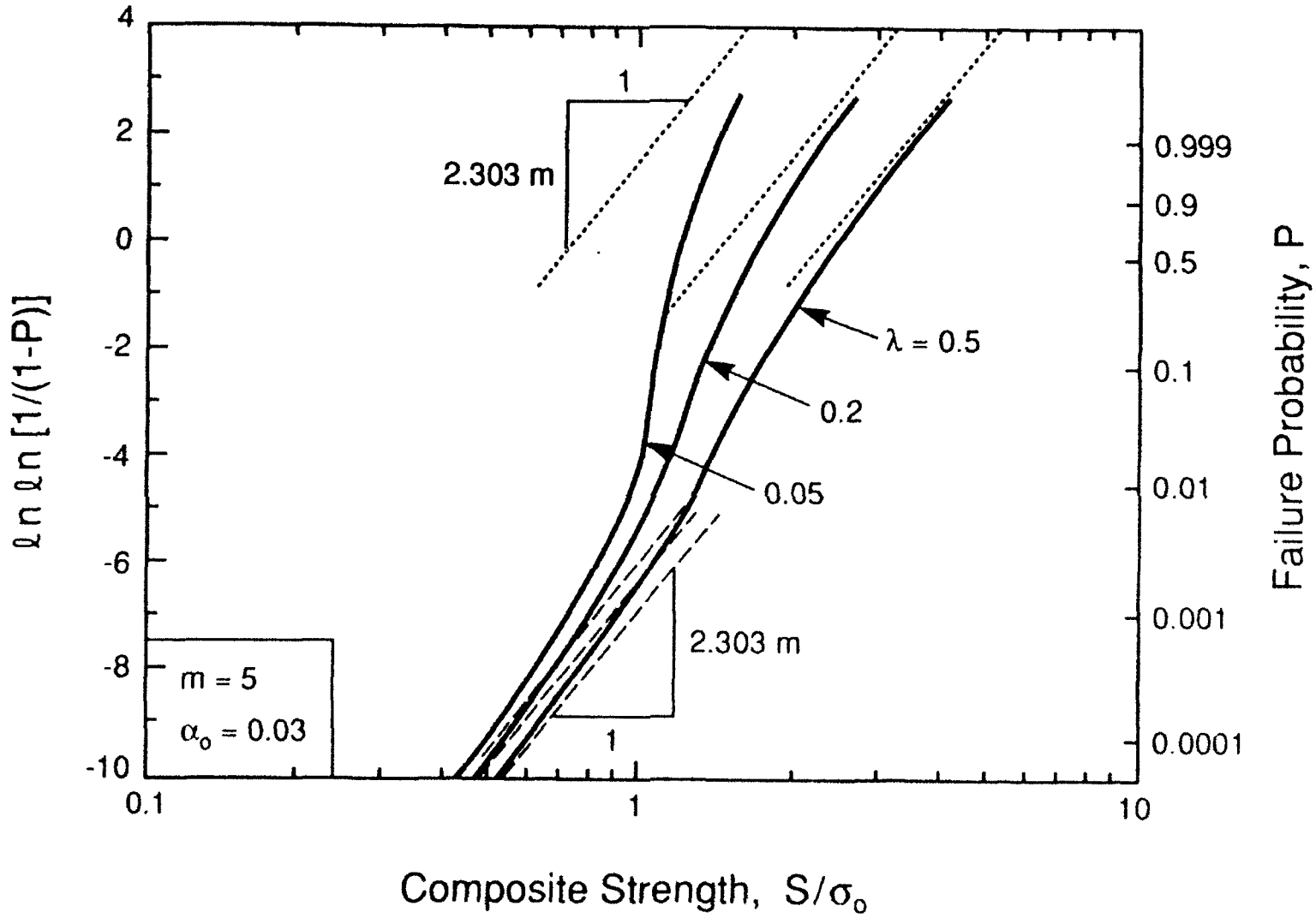
4
2
0
-2
-4
-6
-8
-10
0.1
1
10
1
2.303 m
2.303 m
1
λ = 0.5
0.2
0.05
m = 5
α_o = 0.03
0.999
0.9
0.5
0.1
0.01
0.001
0.0001
Failure Probability, P
ℓn ℓn [1/(1-P)]
Composite Strength, S/σ_o

FIG. 9

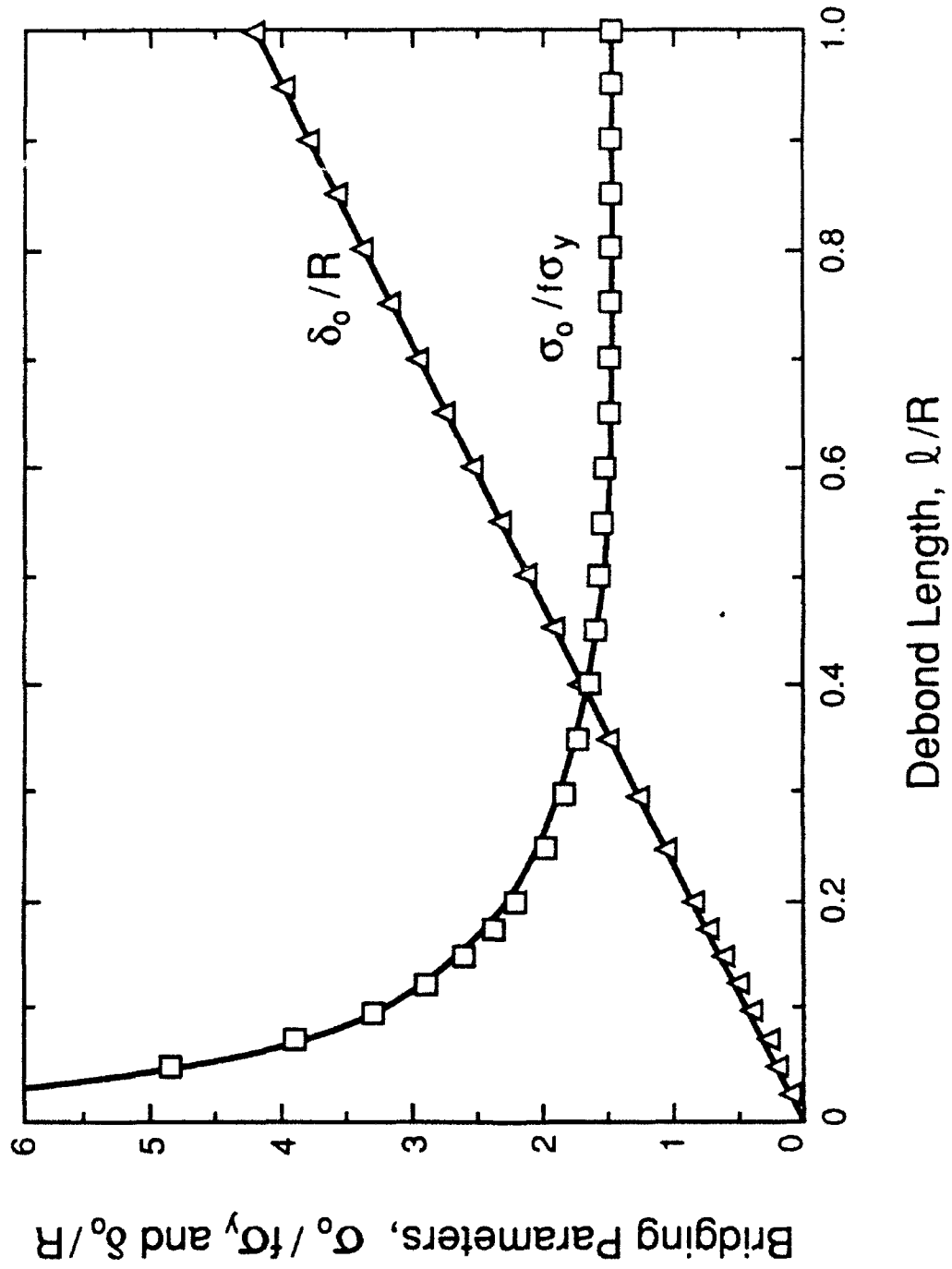
Bridging Parameters, $\sigma_o / f\sigma_y$ and δ_o / R
Debond Length, ℓ / R
δ_o / R
$\sigma_o / f\sigma_y$
0
1
2
3
4
5
6
0
0.2
0.4
0.6
0.8
1.0

Fig. 10

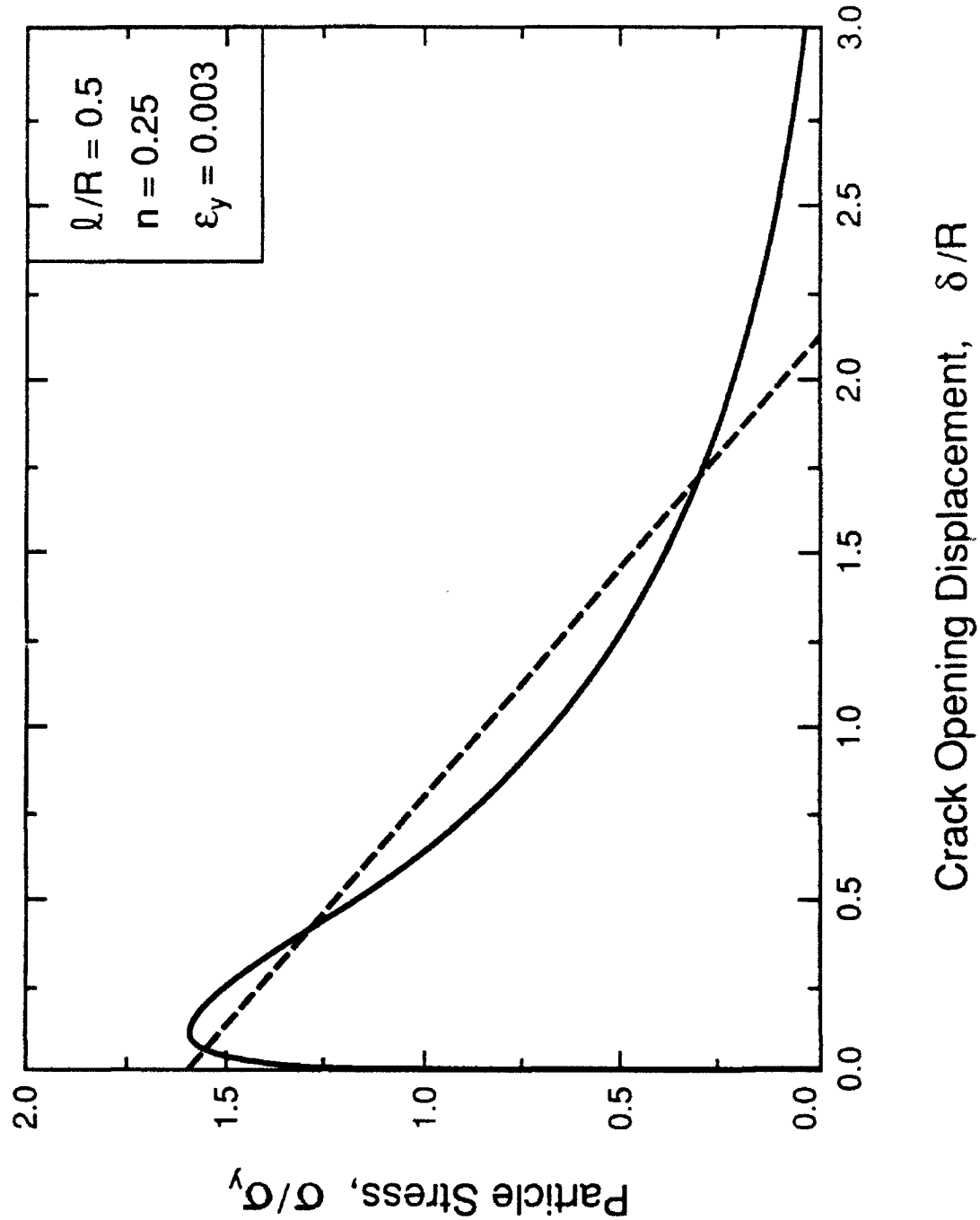
ℓ/R = 0.5
n = 0.25
ε_y = 0.003
Particle Stress, σ/σ$_y$
Crack Opening Displacement, δ/R
0.0
0.5
1.0
1.5
2.0
2.5
3.0

Fig. 11

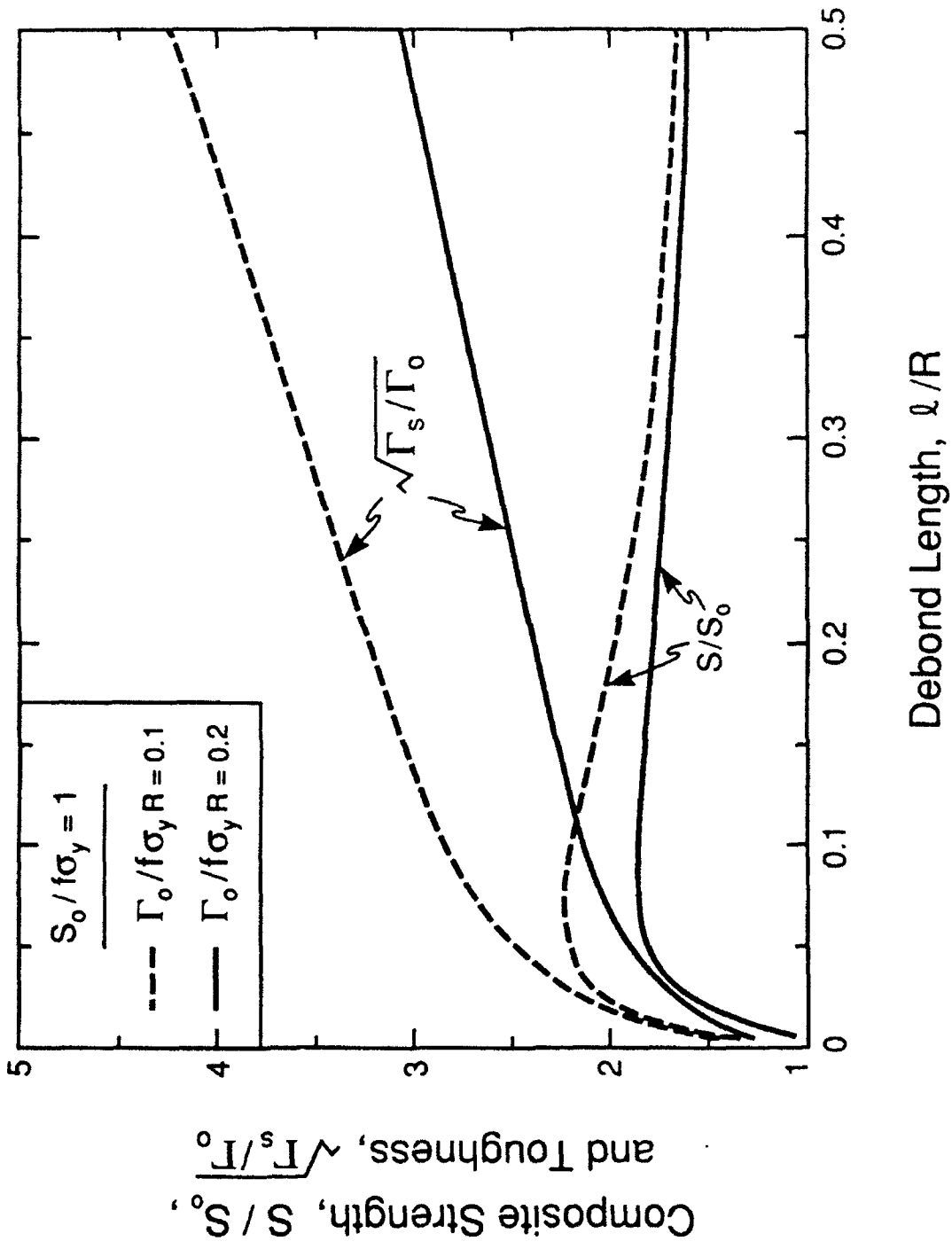
Composite Strength, S / S$_o$,
and Toughness, $\sqrt{\Gamma_s/\Gamma_o}$
Debond Length, ℓ/R
$S_o / f\sigma_y = 1$
$\Gamma_o/f\sigma_y R = 0.1$
$\Gamma_o/f\sigma_y R = 0.2$
$\sqrt{\Gamma_s/\Gamma_o}$
S/S_o
0
0.1
0.2
0.3
0.4
0.5
1
2
3
4
5

Fig. 12

MATERIALS

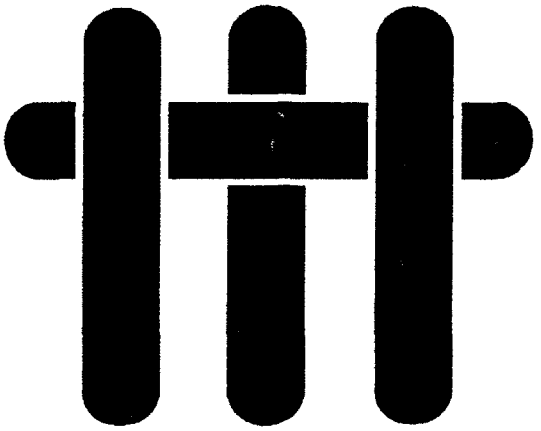

SiC/CAS: A NOTCH INSENSITIVE CERAMIC MATRIX COMPOSITE

by

Carl M. Cady, Thomas J. Mackin, and Anthony G. Evans*

*High Performance Composites Center
Materials Department
College of Engineering
University of California, Santa Barbara
Santa Barbara, California 93106–5050

KJS 5/13/93

ABSTRACT

Tension experiments performed on a 0/90 laminated SiC/CAS composite at room temperature establish that this material is notch insensitive. Multiple matrix cracking is determined to be the stress redistribution mechanism. This mechanism is found to provide a particularly efficient means for creating local inelastic strains, which eliminate stress concentrations.

1. INTRODUCTION

One of the most important attributes of ceramic matrix composites (CMCs) is the existence of mechanisms that redistribute stress at strain concentration sites, such as notches and holes.[1-5] These mechanisms involve matrix cracking as well as fiber pull-out and bridging. The basic stress redistribution phenomena are manifest as three classes of behavior (Fig. 1), each associated with different contributions of matrix cracking and fiber pull-out.[2,6] Class I behavior, dominated by fiber bridging and pull-out, has been extensively documented and characterized through the development of large scale bridging models[1,5,7,8] (LSBM). Class III systems redistribute stress by shear band formation. This phenomenon has also been analyzed[9,10] and related to the in-plane shear strength of the material. Class II behavior has received least attention, and yet, appears to be the most effective means of stress redistribution.[4] The underlying phenomenon is the occurrence of multiple matrix cracks, with minimal accompanying fiber failure. The intent of the present article is to study matrix cracking and stress redistribution around strain concentration sites in a class II system. Moreover, it has been proposed that continuum damage mechanics (CDM) may be useful for characterizing stress redistribution in such materials.[2,12] The present results may provide perspective on the potential for CDM as an analysis procedure.

The material of choice is a Nicalon™ silicon carbide fiber in a calcium alumino silicate glass ceramic matrix (SiC/CAS) material.[13] The material is in the form of a 0/90 laminate. The tensile characteristics and the constituent properties are described elsewhere[11,14,15] (Fig 2). In this material, the matrix crack spacing in the 0° plies changes with stress[11,14] (Fig. 3) in a manner that fundamentally governs stress redistribution.

2. EXPERIMENTAL APPROACH

2.1 Material

Plates of the SiC/CAS composite were provided by Corning.[13] The material was laid up in a 0/90 laminate structure with a nominal fiber volume fraction, $f \approx 0.36$, and a fiber fraction aligned in each of the two principle axes, $f_1 \approx 0.18$. The laminate structure consisted of 16 alternating 0°, 90° layers with a double 90° center layer. The structure was densified by a hot pressing technique. After densification, the total thickness of the composite was ~ 3 mm. Optical microscopy established that the average thickness of each ply to be ≈ 180 μm.

2.2. Test Procedures

Tensile specimens with a variety of holes and notches, located at both the center and the edges (Fig. 4), were cut from the plates by diamond machining. The ratio of the notch length to the sample width (a_o/b) was varied between 0.25 and 0.75. The specimens were then polished to remove surface irregularities and to reveal the first underlying fiber layer in the composite. Tensile tests were performed on these specimens, by using gripping and alignment procedures described in other articles.[10,11]

The tensile tests were carried out on a servohydraulic load frame. Strain gages were used to measure localized strains at the notch tip and in the far field. In some cases, the specimens were monotonically loaded to failure, in order to document the influence of the notch on the ultimate tensile strength (UTS), designated S^*. In other cases, the tests were interrupted at various fractions of the UTS, whereupon several measurements and observations

were made concerning matrix crack accumulation, as well as stress redistribution.

Matrix crack measurements were accomplished by using a surface replica technique that duplicated the topography of the specimen surface. Stress redistribution was assessed using thermoelastic measurements, by means of a technique involving stress pattern analysis through thermal emission (SPATE).[4] In this technique, temperature gradients produced by cycling the stress between 1.5 and 40 MPa at 10 Hz are measured and related to the first stress invariant, σ_{kk}.

Some tensile experiments were performed with sequential, repeated load cycling, subject to full unloading and reloading. The properties of the interface and the misfit strain were obtained from the associated hysteresis loops and the permanent strain.[15,16,17,18] Finally, measurements of fiber pull-out were made using scanning electron microscopy (SEM) on the failure plane.

3. RESULTS

3.1 Monotonic Loading

Stress/strain curves obtained from edge-notched specimens revealed appreciable non-linearity before failure (Fig. 2b). This non-linearity also coincided with an increase in compliance. The ultimate tensile strength (UTS) data are presented in terms of the ratio of the notched UTS, designated S*, to the unnotched UTS, designated S. This ratio is plotted as a function of the relative notch width, a_o/b. The results are summarized in Fig. 4. It is evident from these results that the 0/90 SiC/CAS material exhibits *notch*

insensitive behavior.[1] In fact, there is evidence that some notch *strengthening* may be occurring.

3.2 Damage Observations

Measurements of matrix cracks (Fig. 5) taken from samples tested to failure, as well as from the replicas, indicate a relatively high crack density close to the notch root. Generally, cracks first appear at the notch root (Fig. 6). Then, as the load increases, the density of cracks increases. Thereafter, some of the cracks extend throughout the cross section. Eventually, the saturation crack spacing is approached near the notch root. The final average crack spacing decreased as the ratio a_o/b increased, such that the crack density in the specimen with $a_o/b = 0.75$ most closely resembled that found in an unnotched tensile specimen after testing.

SPATE measurements revealed an initial stress concentration at the notch root (Fig. 7), which diminished as matrix cracks appeared. These measurements relate to the matrix cracks, which generate a compliance gradient,[4] that lowers the stress concentration, as well as redistributing the stress across the remaining section. A comparison of SPATE line scans with acetate replicas taken at the same damage level (Fig. 8) provides striking evidence of the effect of multiple matrix cracking.

The fiber pull-out measurements and the hysteresis loop data (Figs. 9 and 10) can be used to provide information about the interface sliding stress, τ, and the residual stress, q.[11,14,16-18] The sliding stress obtained from these measurements (τ = 20 MPa) is in reasonably good agreement with the values previously reported for this material.[11,14] However, the permanent strains suggest a residual stress, q = 30 MPa, somewhat lower than that found previously.[11,14] This difference reflects changes in processing conditions.

4. DISCUSSION

All of the above results indicate that the 0/90, SiC/CAS behaves as a *notch insensitive* material in tension at room temperature. The most direct evidence is given by the trend in the UTS with notch size (Fig. 4). Confirmatory evidence is provided by the crack density distribution, as well as the SPATE results.

The crack density within the 0° plies may be approximately related to the σ_{yy} stress in those plies, in accordance with the curve shown in Fig. 3. Notably, the crack density measured around the notch (Fig. 6) may be used with Fig. 3 to estimate the σ_{yy} stress distribution. The results (Fig. 11) confirm that the stress concentration is small prior to failure.

The SPATE measurements (Fig. 7) reflect the influence of the matrix cracks on the elastic stiffness of the material around the notch.[4] The gradient in stiffness caused by these cracks allows the σ_{kk} stress to redistribute and eventually become uniform across the net section. Thus, the change in the SPATE line scans with peak load provide an excellent qualitative picture of how the tensile stresses are being redistributed across the net section. However, as yet, they cannot be used to accurately measure the magnitude of those stresses.

5. CONCLUSION

Some simple experiments have been performed which vividly demonstrate that a 0/90 SiC/CAS composite is notch insensitive in tension at room temperature. The behavior is related to the inelastic strains (Fig. 2) that

arise from matrix cracking (Fig. 3), which redistribute stress around notches. The matrix cracking mechanism appears to be particularly efficient for this purpose, because stress concentrations can be completely eliminated, even though the ductility is small, < 1% (Fig. 2). Since the matrix crack density is relatively high at strain concentration sites, it should be possible to develop a mechanism-based CDM approach[12] which could be used to predict redistribution effects. The available matrix cracking models,[17,18,19] combined with the constituent properties should be suitable for this purpose.

ACKNOWLEDGEMENTS

This work was supported by the Defense Advanced Research Projects Agency through the University Research Initiative under Office of Naval Research Contract No. N–00014–86–K–0753. Thanks go to Corning Glass Works, especially Kenneth Chyang, for providing the material. Special thanks to Jean Marc Domergue and Emmanuel Vagaggini for useful discussions.

REFERENCES

[1] G. Bao and Z. Suo, "Remarks on Crack Bridging Concepts," *Applied Mech. Rev.*, **45[8]**, 355–66, 1992.

[2] A.G. Evans, F. Zok and T.J. Mackin, "The Mechanical Performance of Ceramic Matrix Composites," *Solid State Physics*, to be published.

[3] S. Mall, D.E. Bullock and J.J. Pernot, "Tensile Fracture Behavior of Fiber Reinforced Ceramic Matrix Composite with Hole," to be published.

[4] T.J. Mackin, T.E. Purcell, M.Y. He and A.G. Evans, "Notch Sensitivity and Stress Redistribution in CMCs," to be published.

[5] Z. Suo, S. Ho and X. Gong, "Notch Brittle to Ductile Transition Due to Localized Inelastic Band," *J. Matl. Eng. Tech.*, in press.

[6] A.G. Evans, "The Mechanical Properties of Reinforced Ceramics, Metal and Intermetallic Matrix Composites," *Mat. Sci. Eng.* **A143**, 63, 1991.

[7] B.N. Cox and C.S. Lo, "Load Ratio, Notch and Scale Effects for Bridged Cracks in Fiberous Composites," *Acta Metall. Mater.*, **40**, 69, 1992.

[8] B.N. Cox and D.B. Marshall, "Crack Bridging in the Fatigue of Fibrous Composites," *Fatigue and Fracture of Engineering Materials*, **14**, 847, 1991.

[9] H.S. Chan, M.Y. He, and J.W. Hutchinson, "Cracking and Stress Redistribution in Ceramic Layered Composites," *Mater. Sci. Eng.*, in press.

[10] F.E. Heredia, S.M. Spearing, M.Y. He, T.J. Mackin and A.G. Evans, "Notch Effects in Carbon Matrix Composites," *J. Amer. Ceram. Soc.*, in press.

[11] D. Beyerle, S.M. Spearing and A.G. Evans, "Damage Mechanisms and the Mechanical Properties of a Laminated 0/90 Ceramic/Matrix Composite," *J. Amer. Ceram. Soc.*, **12**, 3321, 1992.

[12] D. Hayhurst, F.A. Leckie and A.G. Evans, "Component Design-Based Model for Deformation and Rupture of Tough Fibre-Reinforced Ceramic Matrix Composites," *Proc. Roy. Soc.*, London, **A434**, 369, 1991.

[13] K. Chyung, U. S. Patent 4, 615, 987 (7 October, 1986).

[14] D. Beyerle, S.M. Spearing, F.W. Zok and A.G. Evans, "Damage and Failure in Unidirectional Ceramic-Matrix Composites," *J. Amer. Ceram. Soc.*, **[10]** 2719, 1992.

[15] T.J. Kotil, J.W. Holmes and M. Comninou, "Origin of Hysteresis Observed During Fatigue of Ceramic-Matrix Composites," *J. Am Ceram. Soc.*, **73**[7], 1879–83, 1990.

[16] A.W. Pryce and P. Smith, "Modelling the Stress/Strain Behaviour of Unidirectional Ceramic Matrix Composite Luminates," *J. Mater. Sci.*, **27**, 2695–2704, 1992.

[17] A.G. Evans, J.M. Domergue and E. Vagaggini, "Methodology for Relating the Tensile Constitutive Behavior of Ceramic Matrix Composites to Constituent Properties," *J. Amer. Ceram. Soc.*, in press.

[18] E. Vagaggini, J.M. Domergue and A.G. Evans, "Relationships Between Macroscopic Performance of Ceramic Matrix Composites and Constituent Properties: I: Theory and Methodology," *J. Amer. Ceram. Soc.*, in press.

[19] J.W. Hutchinson and H. Jensen, "Models of Fiber Debonding and Pullout in a Brittle Composite with Friction," *Mech. Mtls.*, **9**, 139–63, 1990.

FIGURE CAPTIONS

Fig. 1. The mechanisms of fiber pull-out and matrix cracking that lead to stress redistribution in CMCs are identified with 3 classes of behavior.

Fig. 2. Tensile stress-strain curve for 0/90 laminated SiC/CAS composite indicating unload-reload hysteresis loops, (a) schematic, (b) experimental results.

Fig. 3. The trend in crack density with stress for the 0° plies with applied stress for 0/90 SiC/CAS.

Fig. 4. Effect of notch size on relative UTS, indicating that SiC/CAS is notch insensitive in tension at room temperature. The inset shows a schematic of the test specimen.

Fig. 5. A replica showing the matrix cracks that occur between two edge notches .

Fig. 6. The crack density as a function of distance from the notch at differing levels of net section stress, for a specimen with edge notches, $a_o/b = 0.5$.

Fig. 7. Typical results of SPATE measurements: (a) full-field temperature distributions before and after matrix cracking (b) Line scans through the notches at various damaging loads shows the effect of applied stress on the distribution of σ_{kk} between the notches after loading to 0.7 UTS.

Fig. 8. A comparison of SPATE images at several loads with the replicas taken at the same loads. The replicas record the crack density at each damage level, while SPATE images reveal the hydrostatic stress distribution.

Fig. 9. Fiber pull-out distribution measured from the failure plane

Fig. 10. Hysteresis loop data presented as a function of the peak stress with the predicted line for $\tau = 20$ MPa indicated.

Fig. 11. Estimate of the distribution of σ_{yy} stresses between the notches based upon crack density measurements (Fig. 3). Results shown for two levels of net section stress.

Class I

Matrix Cracking + Fiber Failure

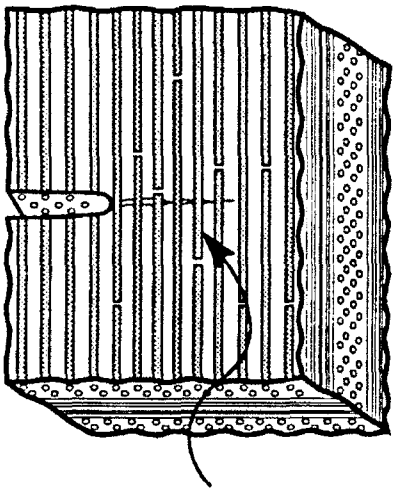

Pull-Out Tractions
Redistribute Stress

Class II

Matrix Cracking: No Fiber Failure

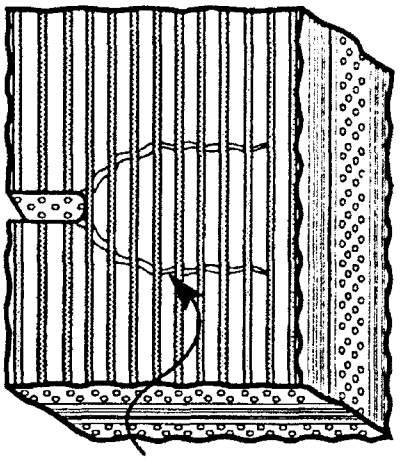

Matrix Cracks
Redistribute Stress

Class III

Shear Damage By Matrix Cracking

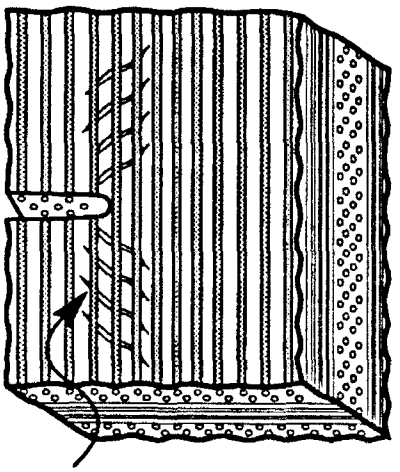

Shear Damage Zone
Redistributes Stress

Figure 1

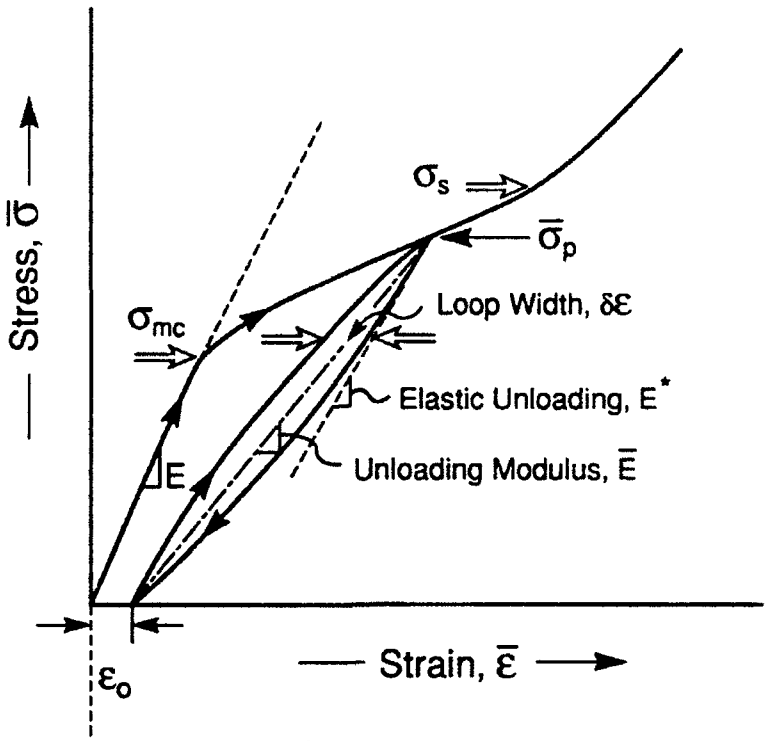

a) Schematic

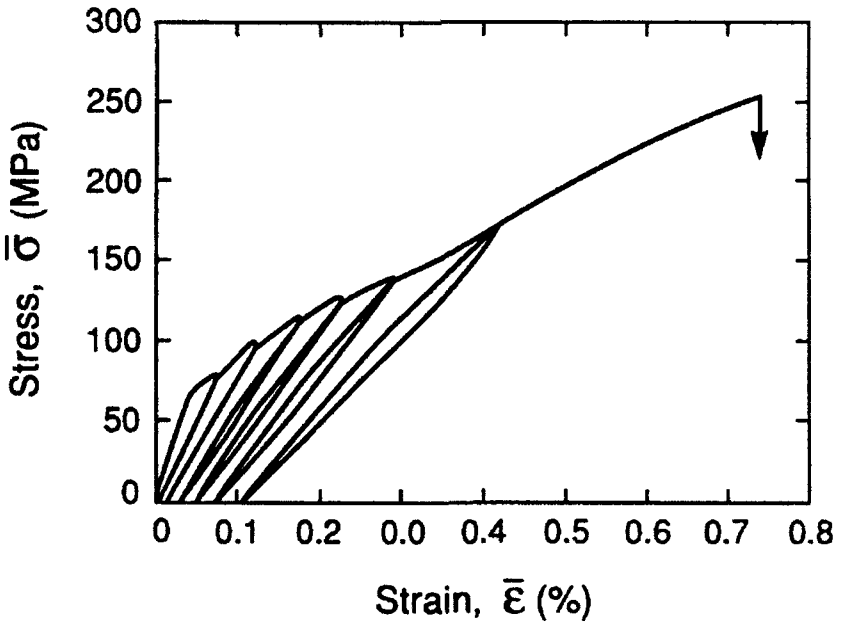

b) Experimental Results, 0/90 SiC/CAS

Cady Evans.URI-4/93-amk-D1#1091-8

Figure 2

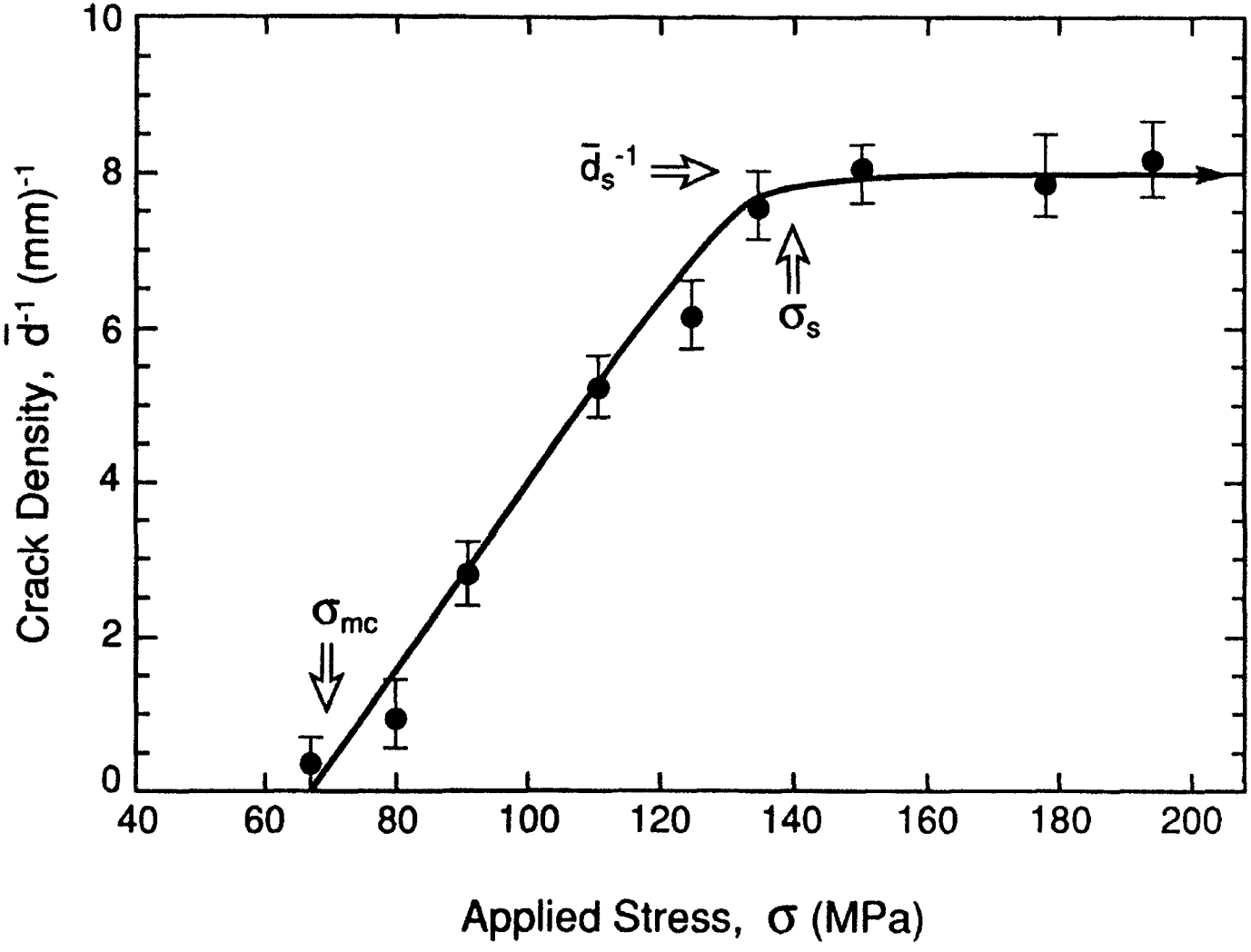

Fig. 3

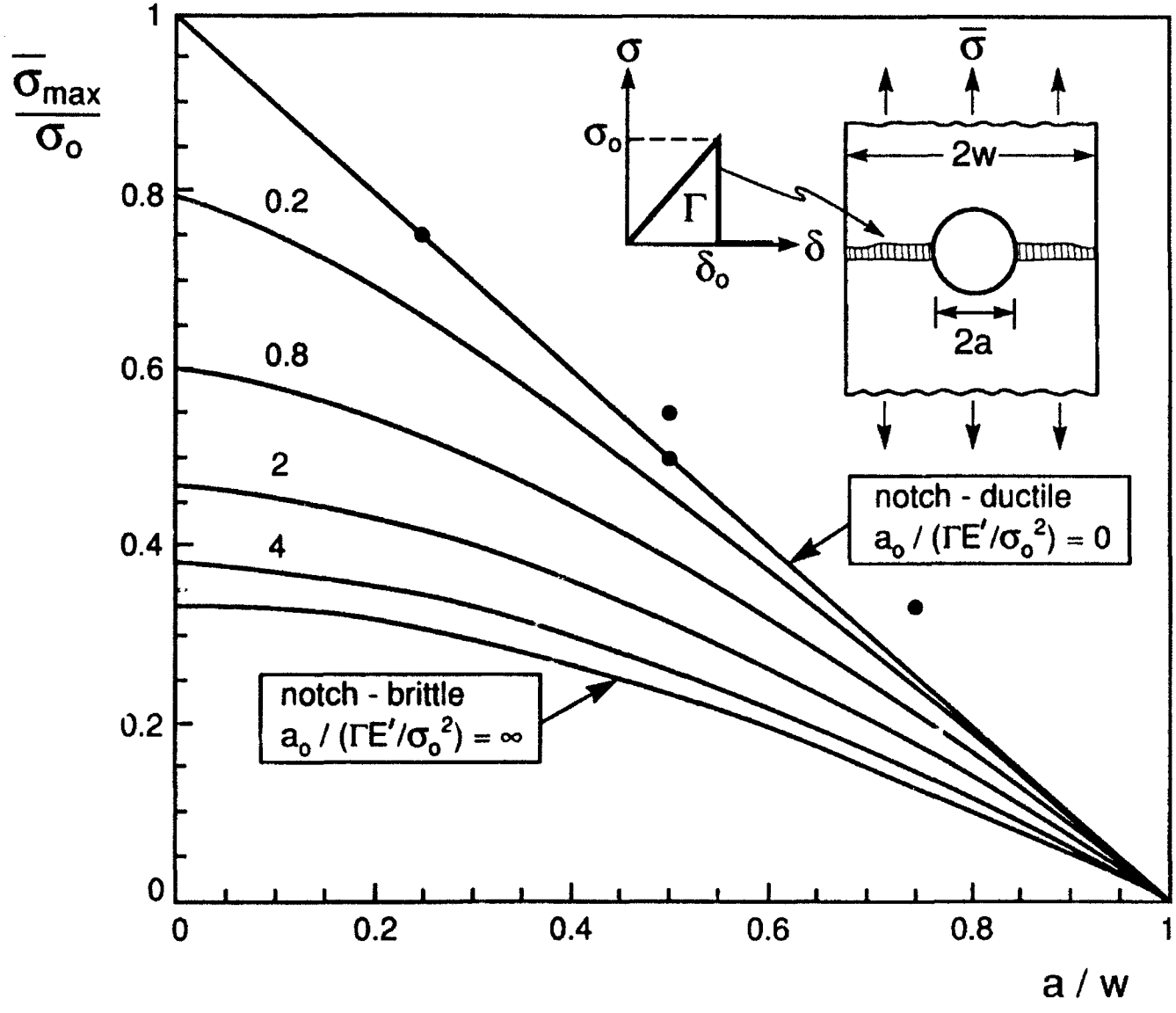

Fig. 4

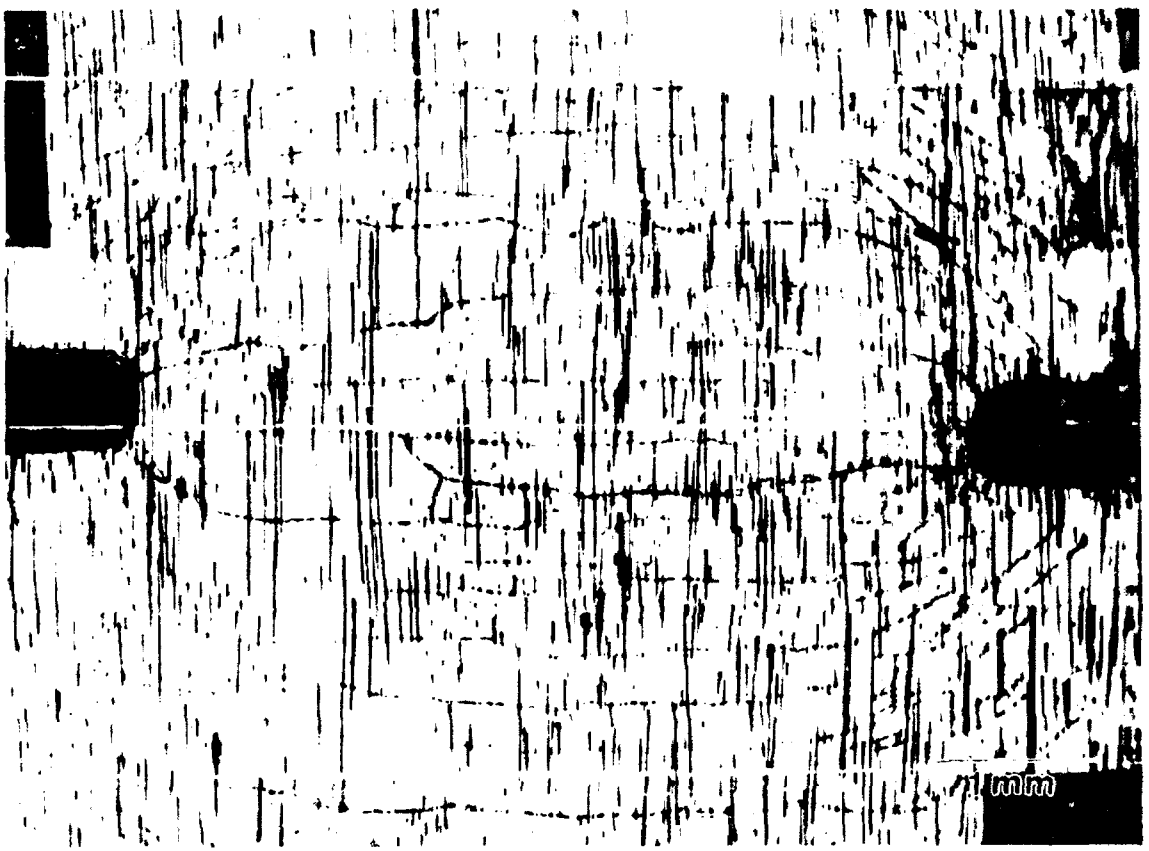

Figure 5

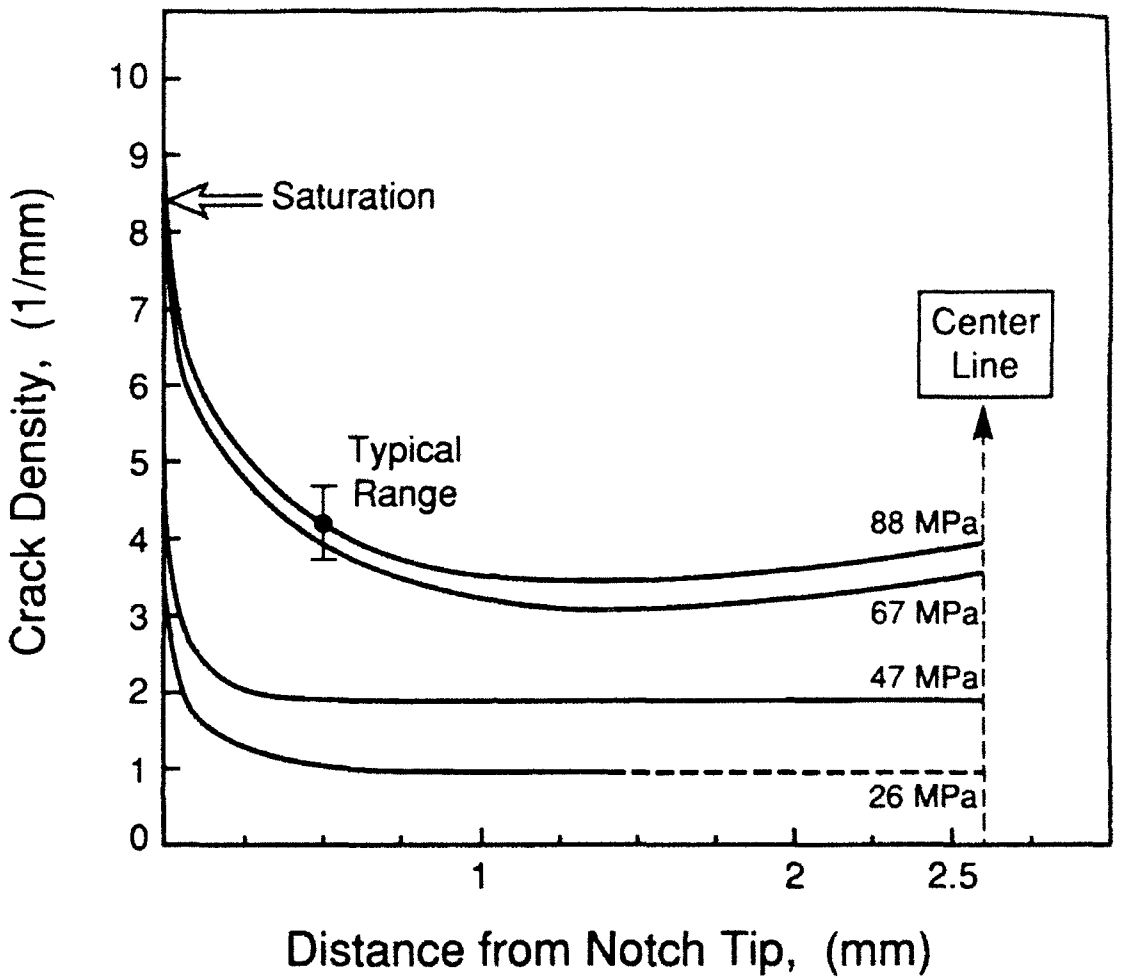
Crack Density, (1/mm)
10
9
8
7
6
5
4
3
2
1
0
Saturation
Typical
Range
Center
Line
88 MPa
67 MPa
47 MPa
26 MPa
1
2
2.5
Distance from Notch Tip, (mm)

Fig. 6

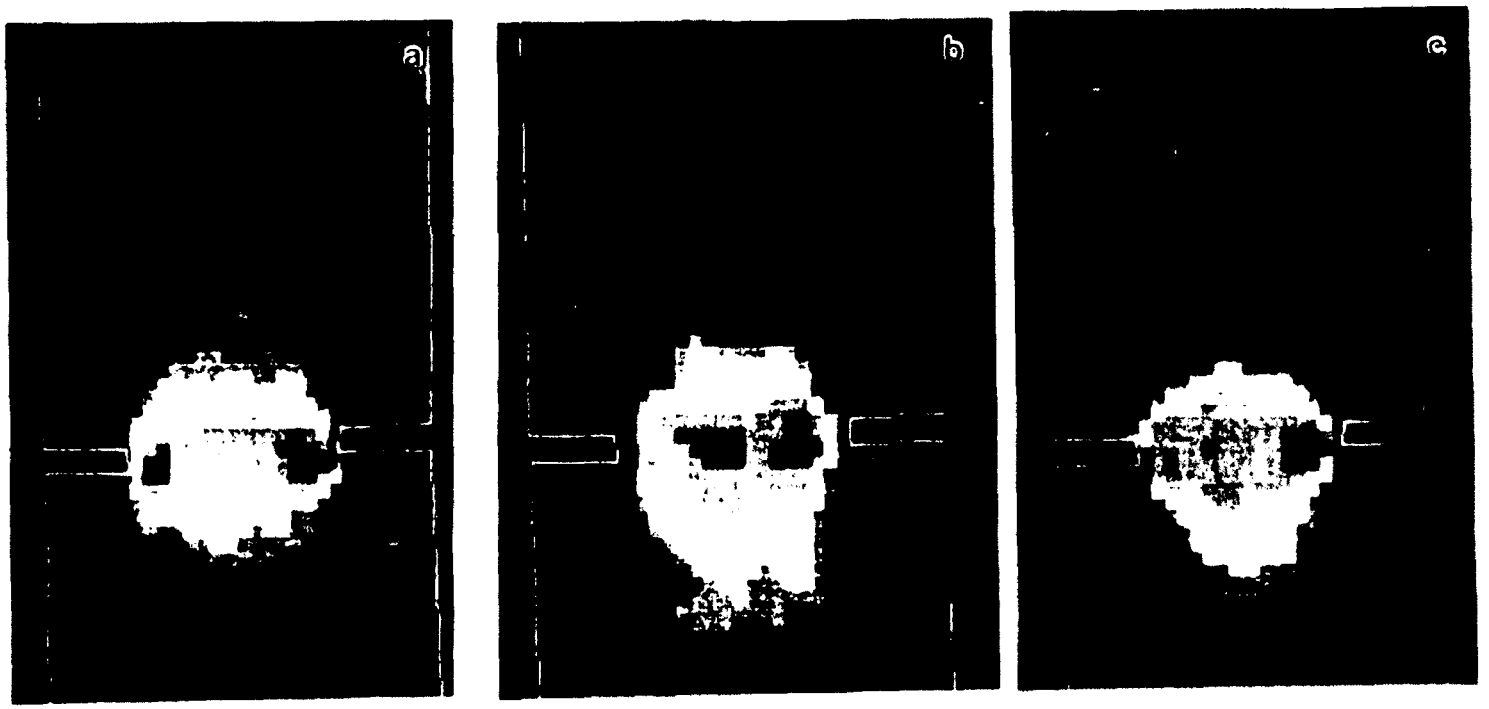

Figure 7a

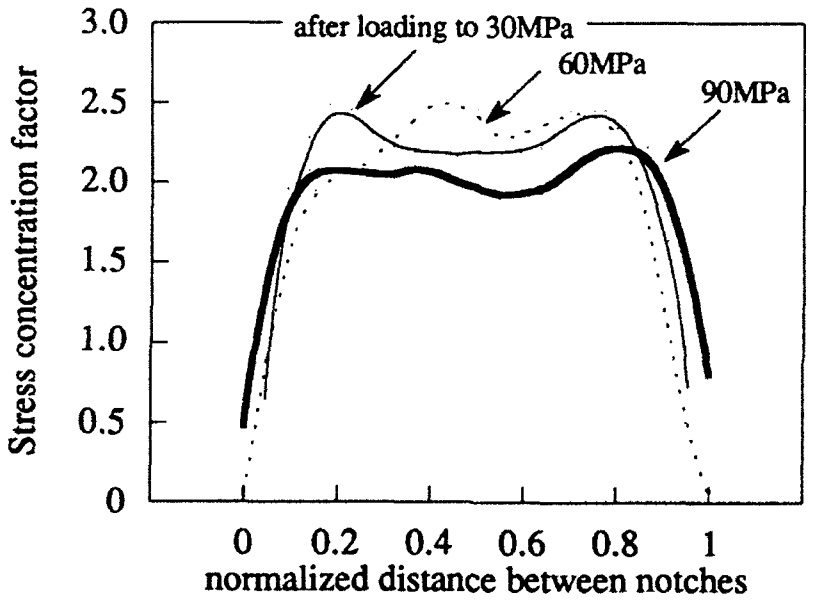
3.0
2.5
2.0
1.5
1.0
0.5
0
Stress concentration factor
after loading to 30MPa
60MPa
90MPa
0
0.2
0.4
0.6
0.8
1
normalized distance between notches

Figure 7b

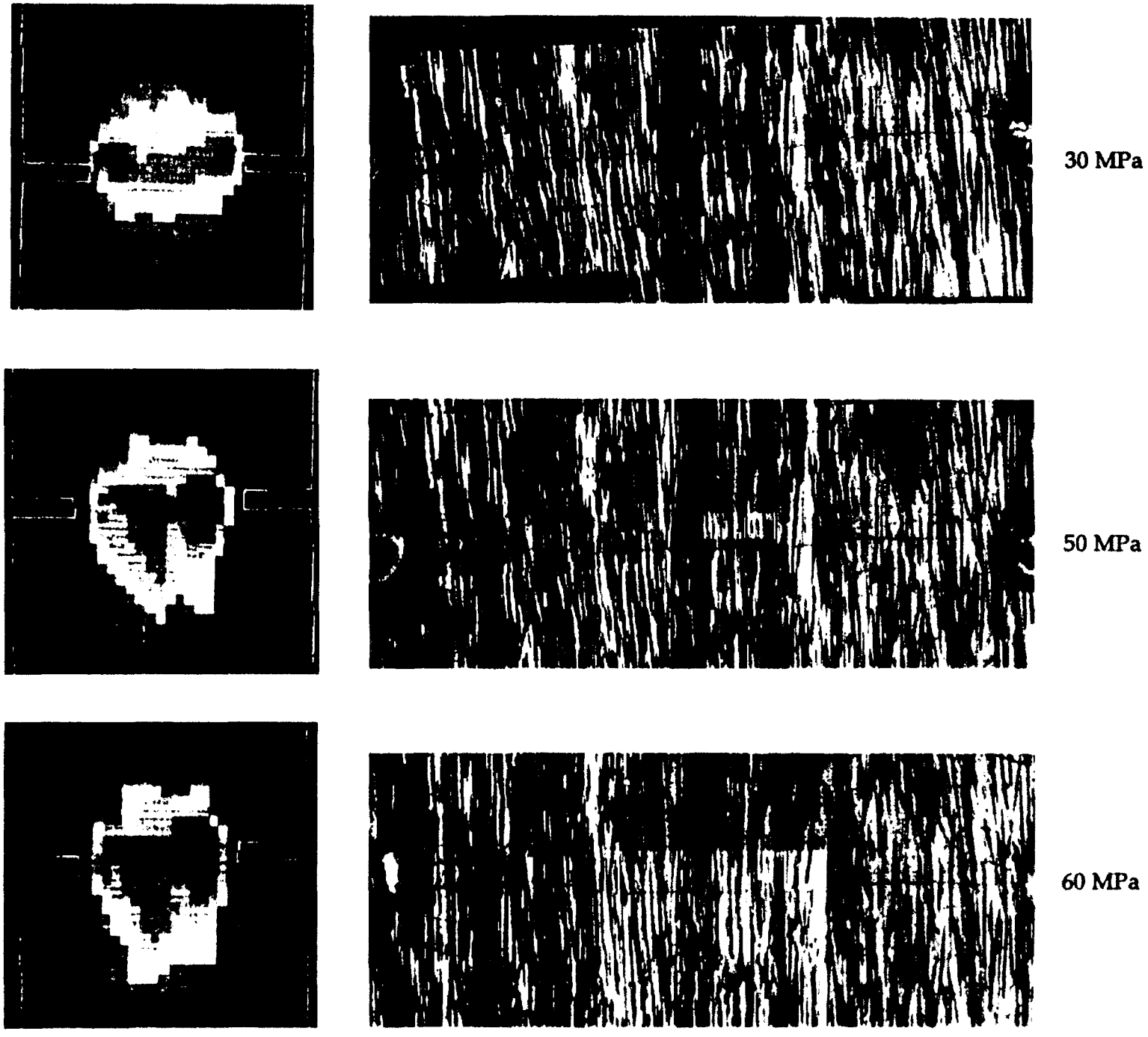

Figure 8

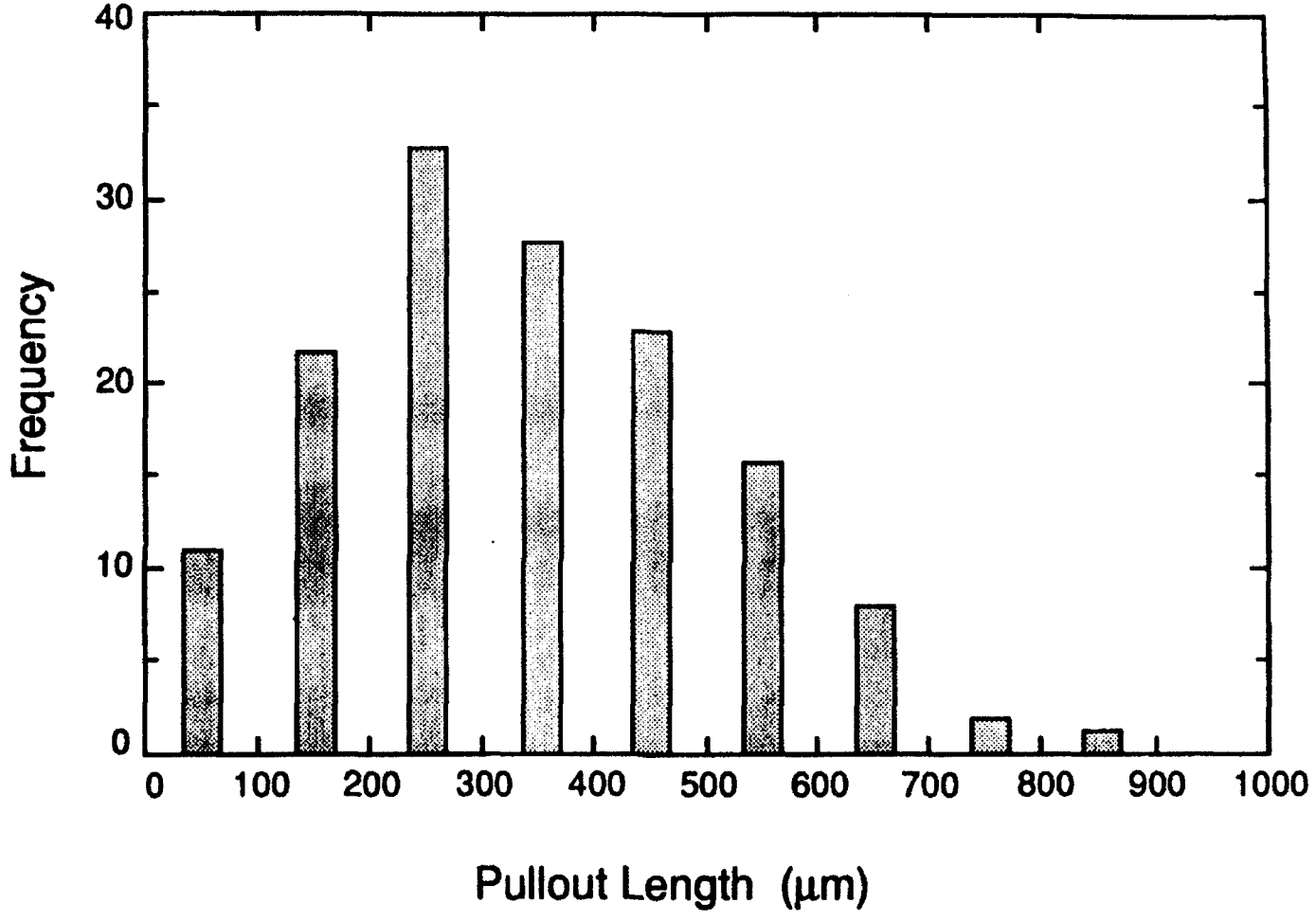
40
30
20
10
0
Frequency
0
100
200
300
400
500
600
700
800
900
1000
Pullout Length (μm)

Fig. 9

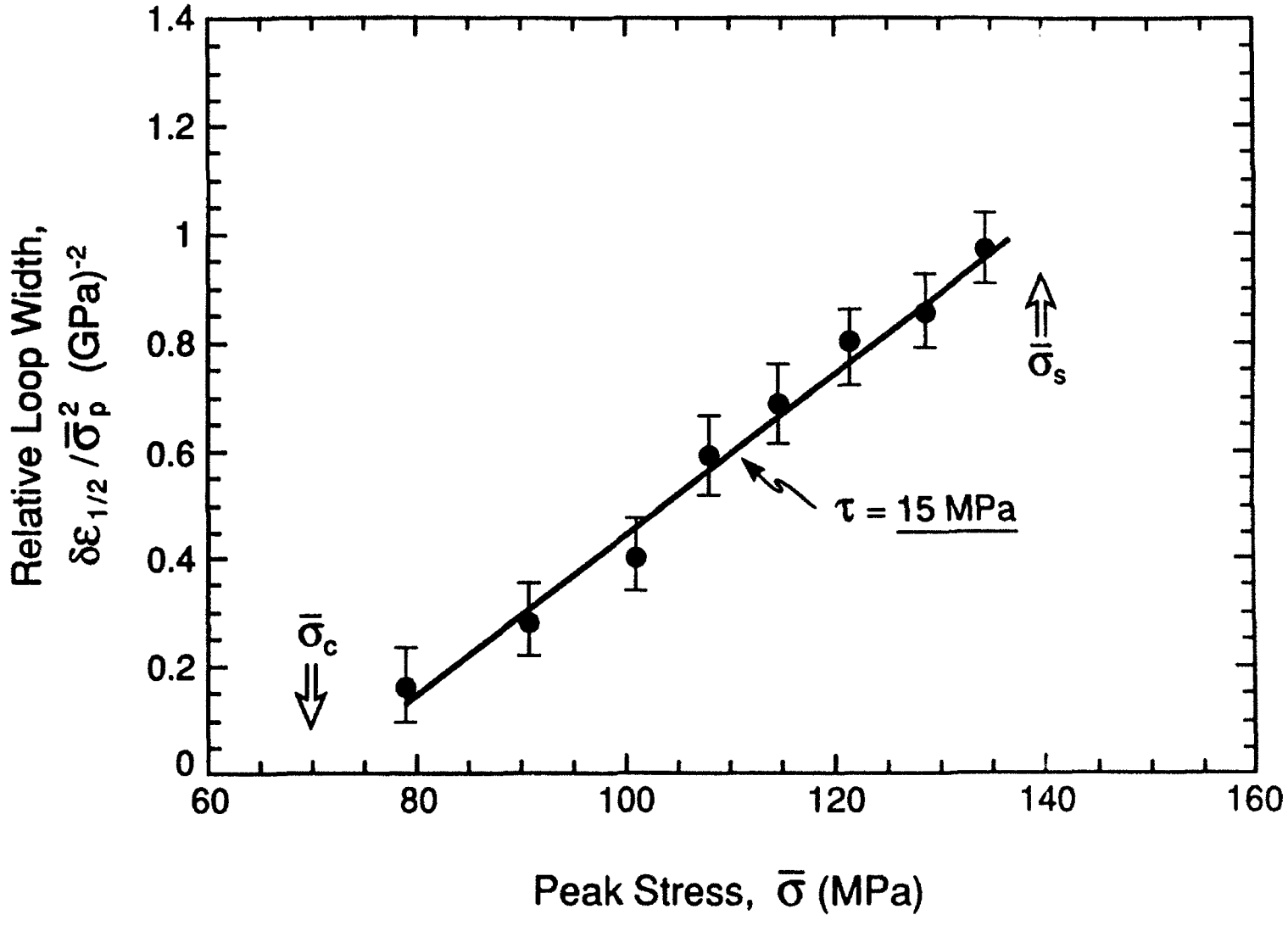
Relative Loop Width,
$\delta\varepsilon_{1/2}/\bar{\sigma}_p^2$ (GPa)$^{-2}$
1.4
1.2
1
0.8
0.6
0.4
0.2
0
60
80
100
120
140
160
$\bar{\sigma}_c$
$\bar{\sigma}_s$
τ = 15 MPa
Peak Stress, $\bar{\sigma}$ (MPa)

Fig. 10

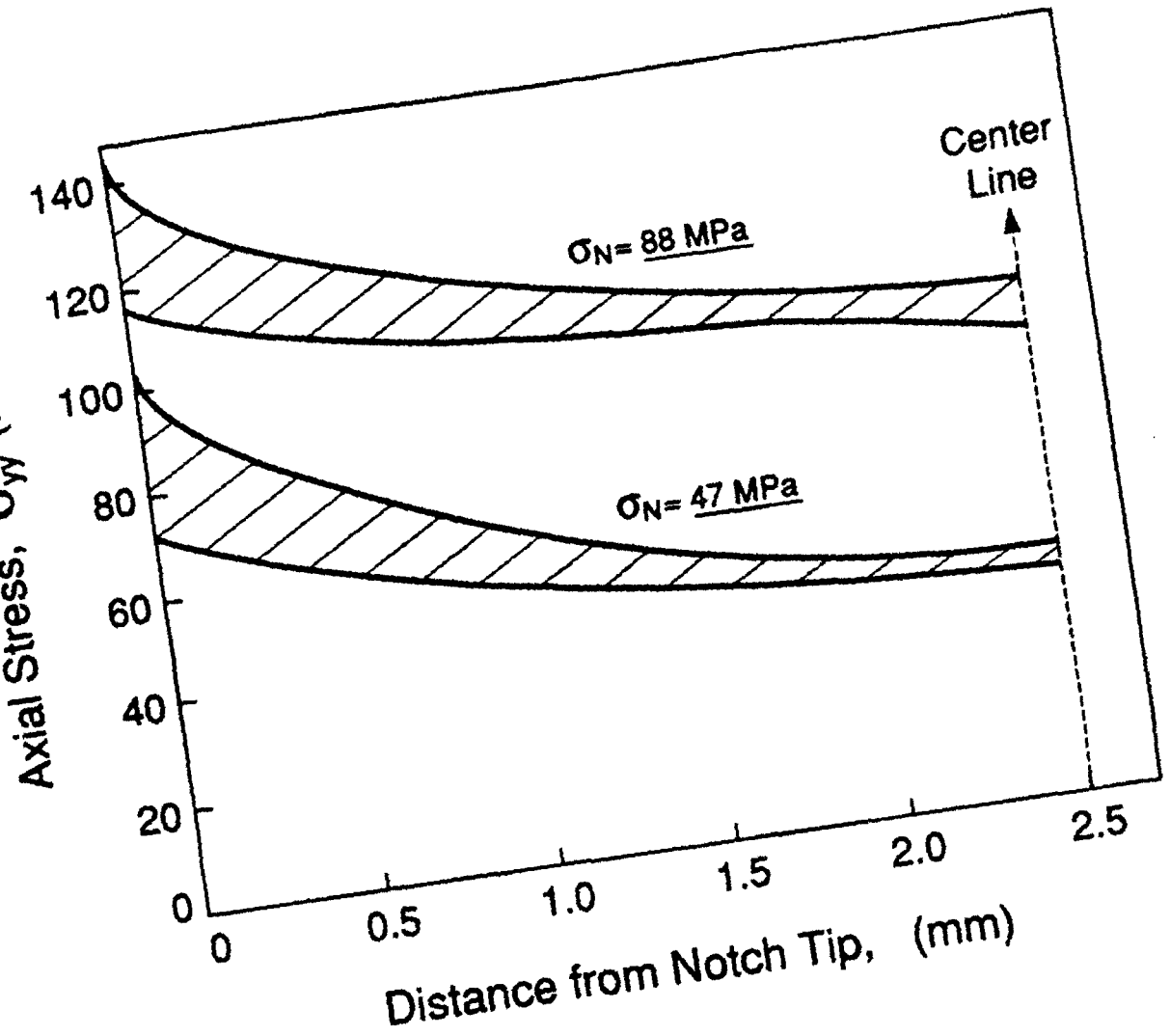
Center
Line
σ_N= 88 MPa
σ_N= 47 MPa
140
120
100
80
60
40
20
0
Axial Stress, σ_{yy} (MPa)
0
0.5
1.0
1.5
2.0
2.5
Distance from Notch Tip, (mm)

Figure 11

MATERIALS

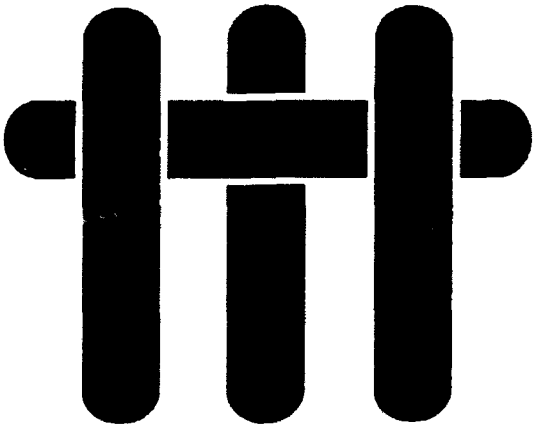

Notch Sensitivity and Stress Redistribution in CMC'S

Thomas J. Mackin,* Thomas E. Purcell,† Ming Y. He* and Anthony G. Evans*

*High Performance Composites Center
Materials Department
College of Engineering
The University of California at Santa Barbara
Santa Barbara, CA 93106-5050

†Pratt and Whitney
United Technologies
17900 Beeline Highway
Jupiter, Fl 33478

ABSTRACT

Fiber reinforced ceramic matrix composites depend upon inelastic mechanisms to diffuse stress concentrations associated with holes, notches and cracks. These mechanisms consist of fiber debonding and pullout, multiple matrix cracking and shear band formation. In order to understand these effects, experiments have been conducted on several double-edge-notched CMC's that exhibit different stress redistribution mechanisms. Stresses have been measured and mechanisms identified by using a combination of methods including: x-ray imaging, edge-replication and thermoelastic analysis. Multiple matrix cracking was found to be the most effective mechanism.

1. INTRODUCTION

One of the major attributes of fiber reinforced ceramic matrix composites (CMC's) is the existence of inelastic mechanisms that allow stress redistribution around strain concentration sites such as notches, holes, attachments, etc.[1-4] These mechanisms, analogous to plasticity in metals, involve combinations of matrix cracking and fiber pull-out.[1,6-10] In the presence of notches and holes, three damage phenomena have been found, based on matrix cracking and fiber pull-out (Fig 1). Others may, of course, exist. The operative damage class depends on the magnitudes of non-dimensional parameters which combine interface, fiber, and matrix properties.[1,7,8,10] The intent of the present article is to provide an experimental assessment of stress redistribution effects around notches in CMC's that exhibit these damage phenomena.

CMC's exhibit a variety of tensile (Fig 2a) and shear (Fig 2b) stress/strain curves,[1,10,14] with varying amounts of inelastic strain prior to failure. One purpose of the present study is to attempt to relate features of the inelastic strain measured in tensile and shear tests to the stress redistribution behavior. This would be achieved through an understanding of the inelastic mechanisms and their role in governing the dominant mode of damage (Fig 1).

The importance of stress redistribution is manifest in the notch sensitivity, which is a key factor affecting the practical utility of a structural material. [11,12] Notches and holes are a source of strain concentration. The corresponding stress concentration depends upon the material response. One limit obtains for elastic materials. In such materials, the stress concentrations are severe, resulting in extreme notch sensitivity. When inelastic mechanisms operate, the stresses redistribute in regions of large strain concentration and reduce the notch sensitivity. In some cases, the stress concentration can be completely eliminated, resulting in a notch insensitive material.[3,13] More generally, the behaviors can be presented on a notch sensitivity diagram[11,12] (Fig. 3). In this diagram, the ordinate is a measure of the tensile strength normalized by the un-notched strength, while the abscissa is the notch/hole size ($2a_0$) relative to the plate width (2b). Each line represents a measure of the inelastic displacement permitted by the material near the notch tip, prior to failure. This measure is given by the ratio of the notch length to the length of the inelastic zone.[11]

Related stress redistribution mechanisms are known to occur in polymer matrix composites (PMC's), particularly upon cyclic loading. [13-21] Studies on

PMCs have established a precedent for a test methodology[15-21] that can be used to monitor damage in CMCs and thereby measure effects on the stress distribution. The methods include the use of Moiré interferometry to measure strain distributions, thermoelastic measurements to assess stress distributions,[15-19] x-ray imaging with dye penetration to highlight damage, and replication methods to examine matrix cracking.[15-21] All of these methods may be augmented by conventional optical and scanning electron microscopy. In the present study, a combination of these methods is used to study stress redistribution in three CMCs: SiC/CAS, C/C and SiC/SiC.

The experimental procedure given principal emphasis is the thermoelastic emission method, which provides a measure of the stress distribution.[15-19,22-25] A brief synopsis of this method is given in the next section, prior to a description of the experiments and their analysis.

2. STRESS ANALYSIS BY THERMOELASTIC EMISSION

Stress Pattern Analysis from Thermoelastic Emission (SPATE) is a technique that relates instantaneous changes in the hydrostatic stress at any location in a material to instantaneous changes in local temperature.[22-25] The method has been used extensively to evaluate stress distributions in monolithic metals and polymer matrix composites.[15-19] The underlying phenomenon concerns the temperature change that occurs when an elastic body is subjected to hydrostatic deformation under adiabatic conditions. The fundamental thermodynamic relation for the temperature change $\dot{T}$ and its dependence on the hydrostatic stress rate $\dot{\sigma}$, is given by (see Appendix):[22-29]

$$\dot{\sigma} = -K_m\beta\left[1 + \frac{\rho_0 C_v}{K_m\beta^2 T_0}\right]\dot{T} \qquad (1)$$

where K_m is the isothermal bulk modulus, C_v is the specific heat at constant volume, β is the bulk thermal expansion coefficient, ρ_0 is the density, and T_0 is the mean temperature.

The sum in parentheses is dominated by the second term, resulting in the approximation,

$$\dot{\sigma}_{kk} \approx -\frac{\rho_0 C_v}{\beta T_0}\dot{T} \tag{2}$$

Typically, the material constants are combined to define a thermoelastic 'constant,' κ given by,

$$\kappa = \frac{\beta}{\rho_0 C_v} \tag{3}$$

In the SPATE method a sinusoidal stress input is used, which creates a thermal response at both the first and second harmonics . For materials, such as CMC's, the modulus is a weak function of temperature. Upon applying a cyclic hydrostatic stress amplitude, $\Delta\sigma_{kk}$, the temperature change, ΔT, at the first harmonic, is given by,[20-25]

$$\Delta T = \kappa T_0 \Delta\sigma \sin(\omega t) \tag{4}$$

where ω is the frequency and t is time. A key feature of the SPATE procedure is that the spatial variation in temperature, T(x,y), relates to the hydrostatic stress distribution. $\Delta\sigma(x,y)$.[††] Moreover, when matrix damage occurs, the properties which influence κ, (namely ρ_0, C_v, and β) are unchanged and eqn (4) still applies.

For typical values of the strain range, the temperature changes expected for CMC's are, at most, $\approx 0.1°C$. Very sensitive measurements are thus required. Furthermore, to satisfy the adiabatic assumption, the thermometry must be in thermal equilibrium with the test specimen.

[††] For a composite, the material constants that relate stress and temperature involve combinations of the properties of the fiber and the matrix, leading to anisotropy in the thermoelastic 'constant', κ. The magnitude can be obtained either by calibration or calculation. [22,23]

To satisfy these requirements, recent experimental techniques use the principal of black body radiation and infrared thermometry, wherein the photon flux is measured by a detector sensitive to infrared radiation.*[22,23] In practice, the detector response is the sum of the emitted photons and the background. Improvements in signal to noise are made by averaging the sample many times at a given location. This is accomplished by locking the detector data acquisition onto the frequency of the applied cyclic strain. A commercial system which embodies these concepts† has been used to measure the photon flux emitted from the test specimens. The system consists of a mercury doped CdTe detector affixed to a liquid nitrogen cooled dewar. The detector is housed within a camera body to reduce the effect of spurious radiation. A collimator and lenses at the inlet to the camera body focus the emitted IR onto the detector. The collimated infrared issues from a location on the specimen of either 200 or 400 micron diameter at a working distance of 25cm, and can detect temperature differences as small as 0.001°C. Before testing, specimens are coated with a thin layer of commercial flat black paint to provide uniform emission from the sample surface. Background IR is reduced by placing a flat black card behind the specimen.

The experiments are conducted by applying a 10Hz, uniaxial cyclic load, creating a 10Hz fluctuation in the thermoelastic response. The frequency is chosen to minimize the effects of thermal conduction from the measurement zone during the measurement time, thereby creating adiabatic conditions.[22,23] The maximum load is usually chosen to correspond to a stress less than the elastic limit, while the minimum is chosen to ensure specimen alignment. A lock-in amplifier controls the data acquisition system by locking the detector output to the frequency of the applied load. The phase lag is automatically adjusted by locking into the peak signal difference at the test frequency. Locking into the applied cyclic load performs two basic functions: It correlates the thermal signal to the applied stress, and it eliminates the effect of absolute temperature changes that may be occurring in the specimen.

---

* Typical IR detectors have a band gap of ~ 0.1eV, corresponding to photon wavelengths <14 microns.

† SPATE 9000 IR imaging system by Ometron

3. EXPERIMENTAL PROCEDURES

Double edge-notched test coupons were fabricated from panels of 0/90 composites: C/C, SiC/SiC and SiC/CAS. These materials and their properties are described elsewhere and summarized in figure 3. Notches were cut into the sides by using a diamond blade, resulting in a nominal notch root radius of 50 microns, and having relative notch depths, $a_0/b = 0.5$. Aluminum tabs were bonded onto the ends of the test coupons for gripping purposes. The specimens were aligned and clamped using hydraulic grips. A strain gage was attached at a location remote from the reduced section, in order to allow monitoring of the far field strain. The strain gage was connected to a dynamic strain amplifier, the output of which was used to calibrate the thermal emission.

Each test was interrupted at various points along the stress-strain history in order to assess the stress distribution, as well as the development of damage around the notches. Stress redistribution was quantified using the thermoelastic emission procedures described above. Damage was characterized using both radiographic procedures and acetate tape replicas. The radiographs were obtained as follows: While under load, a zinc iodide penetrant was dispersed onto the specimen. The specimens were then unloaded, removed from the grips, and placed into an x-ray system. The penetrant enters into the damaged region and provides absorption contrast for an x-ray image of the damaged region.

Acetate replicas were obtained while the load was maintained in order to hold the matrix cracks open. Sections of replication tape were cut and held over the notch root region, and a small amount of acetone applied above the tape. The replicas were dried, removed and examined using optical microscopy.

4. RESULTS

4.1 SPATE Calibration

Before proceeding with measurements, a SPATE calibration experiment was conducted on an edge notched steel specimen. A low resolution full field scan (Fig 4) combined with line scans demonstrates the thermal response. For purposes of analysis, the temperature field is calibrated to the strain gage response in the far field by comparing thermoelastic and strain gage signals and adjusting the SPATE output accordingly. Several items are notable: (i) The specimen was not perfectly aligned, resulting in bending stresses. This is evident

from the slope of the line scans through the far field. (ii) Fluctuations in the far field signal (10% of the signal) arise from polishing scratches, variations in surface emissivity, and thermal fluctuations in the background. (iii) Edge effects appear on scans made in the vicinity of the notch and at the sample edges. The consequence is that a finite edge region, approximately 400μm in width, cannot be analyzed. The edge effect arises for two reasons: First, when scanning near an edge, the detector spot is partially off the specimen. Second, as the specimen is cyclically loaded, the edges of the notch move relative to the detector.

Stress concentration factors are derived from the temperature measurements by comparing the temperatures at the notch root with the temperature in the far-field, which relates directly to the known far field stress. For this purpose, it is recalled that the SPATE signals relate to the hydrostatic stress. Finite element solutions (Fig 5) reveal that the stresses are virtually uniaxial[††] within one notch width of the root. Furthermore, measurements made in this location are unaffected by the edge effect. Consequently, it is straightforward to relate the temperature measured in this region to the far field temperature in order to evaluate the concentration of σ_{yy} stress near the notch. The experimental values of σ_{yy} measured at this location are superposed onto the finite element results (Fig 5). Upon noting that the spot size is 400μm, it is apparent that the SPATE measurement gives satisfactory estimates of the stress concentration.

4.2 CMC Measurements

Measurements made on the notched C/C material provide a sequence of SPATE images (Fig 6a), obtained at several prior peak load levels. These are accompanied by radiographic images of the same specimens, (Fig 6b). This material develops shear bands perpendicular to the notch which are comprised of multiple matrix cracks in a manner characteristic of a Class III system (Fig 1). Both SPATE and radiographic images illustrate this effect. The low resolution SPATE scan (Fig 6c) reveals a dramatic elongation in the notch root field, coincident with the development of the shear bands. Such bands form in this composite because of its relatively low shear strength (Fig 2b). A sequence of line scans connecting the notches (Fig 7) establish that there is a reduction in the

[††] $\sigma_{xx} = 0$

magnitude of the notch root temperature as the shear bands extend. Furthermore, there is a decrease in the temperature gradient, consistent with stress redistribution across the net section. The results are further quantified by plotting a measure of the stress concentration factor (SCF) as a function of shear band length (Fig 8). This SCF is defined as the ratio of the temperature along the notch plane, measured 400μm from the notch root, to the far field temperature. As noted above, the stress at this location near the notch should be largely uniaxial. Consequently, this ratio of temperatures is a measure of the σ_{yy} stress concentration ahead of the notch. It is evident that this SCF diminishes as the shear band length increases, consistent with finite element calculations [2] (fig 9).

A similar series of experiments conducted on the SiC/CAS material revealed different characteristics (figs 10-11). The SPATE images (fig 10) indicate that the zone of highest temperature moves away from the notch root toward the specimen center as the peak load increases. Moreover, at the highest load, SPATE scans (fig 11) show that the temperature is essentially uniform within the net section, with only random fluctuations remaining. These observations imply that the stresses are uniform and equal to the net section stress. Such observations are consistent with the notch insensitive behavior found for this material (fig 2). Surface replicas revealed a multiplicity of matrix cracks emanating from the notch (fig 10). There was no evidence of shear bands in this material. This evidence classifies the SiC/CAS material as a class II composite, in which stress redistribution is achieved through the inelastic deformation provided by multiple matrix cracks.

SPATE images and line scans obtained for the SiC/SiC material(Figs 12 and 13) show some stress redistribution. However, a stress concentration persists throughout. The damage mechanism operating in this material is presently unknown. Whichever mechanism operates, it is clearly less effective in stress redistribution than the shear band and multiple matrix cracking mechanisms that occur in the C/C and SiC/CAS composites, respectively.

5. ANALYSIS AND INTERPRETATION

The combination of SPATE measurements with x-ray and replicated images indicate that matrix cracking damage, occurring as either shear bands or multiple matrix cracks, modify the stress around notches. To further understand the implications of the SPATE results, it is recalled that the measurements are

made at small stress levels, following the introduction of damage at larger stresses. Consequently, the damage must influence the stress/strain laws applicable at small strains. Unloading/reloading measurements conducted in both tension and shear have indicated that the unloading modulus diminishes as a consequence of matrix crack damage (Fig 14). The damaged material would be located primarily ahead of the notch in the SiC/CAS composite, but normal to the notch, within the shear bands, in the C/C composite. The diminished modulus is regarded as the phenomenon that causes the stresses inferred from the SPATE measurements to differ from the elastic solution . It is proposed that the damage creates a gradient in the elastic modulus, such that the stresses near the notch are reduced, as sketched in Fig 15. Moreover, results for stress redistribution in materials subject to shear bands (Fig 9) indicate features comparable to the measurements performed on the C/C composite. A more detailed understanding of stress redistribution would require that SPATE measurements be made over a range of superposed mean stresses, thereby illuminating the non-linear stress-strain behavior in the damaged regions. Such measurements would provide constitutive relations that could be used in stress redistribution calculations.

SUMMARY

SPATE measurements, in conjunction with x-ray and replica observations, indicate the existence of damage mechanisms that result in local gradients in elastic modulus. These gradients in modulus cause stress redistribution. The magnitudes of these effects at small strains have been established from SPATE measurements. These measurements have also revealed differing stress redistribution behavior for each of the three composite systems, associated with different damage mechanisms. The damage mechanisms themselves, have been described elsewhere.[1-5] While the present study affirms that damage mechanisms occur, which change the local properties of the composite, [30-32] quantitative assessment of stress redistribution requires further research. Most importantly, the stress redistribution which arises at peak loads will be more extensive than that found at small strain by the SPATE measurement, because of the additional contributions to the inelastic strain caused by sliding at the fiber/matrix interface.

APPENDIX

The Thermoelastic Phenomenon

Thermoelasticity describes the relationship between applied stress and temperature in an elastic body. The thermal and mechanical state is given by the first law of thermodynamics[28]

$$dU = dQ + PdV \tag{A1}$$

where the change in internal energy, dU, is related to the heat conduction, dQ, and the work performed on the body, PdV. Upon combining the first and second laws,[28]

$$\dot{U} = T\dot{S} + V\sigma_{ij}\dot{\varepsilon}_{ij} \tag{A2}$$

The dilatational† and deviatoric strain-rates are related, respectively, to the corresponding stress rates by[26-28]

$$\dot{e} = \frac{\dot{\sigma}}{K_m} + \beta\dot{T} \tag{A3}$$

and

$$\dot{e}_{ij} = \frac{\dot{s}_{ij}}{2G_m} \tag{A4}$$

where K_m is the adiabatic bulk modulus, G_m is the adiabatic shear modulus, and β is the coefficient of thermal expansion,. By using the Helmholtz free energy

$$F = U - TS \tag{A5}$$

the time derivative is

$$\dot{F} = \dot{U} - T\dot{S} - S\dot{T} \tag{A6}$$

---

† For convenience the subscript kk is omitted on both the dilatational stress and strain.

Upon combining (A2) and (A6)

$$\dot{F} = V(\sigma\dot{e} + s_{ij}\dot{e}_{ij}) - S\dot{T} \tag{A7}$$

Also, the total differential is

$$dF = V(\sigma de + s_{ij}de_{ij}) - SdT \tag{A8}$$

Assuming that strain and temperature are the independent variables, both the free energy and entropy are expressed as functions of these variables,

$$F = F(e,e_{ij},T) \tag{A9}$$
$$S = S(e,e_{ij},T) \tag{A10}$$

From elasticity,

$$\sigma = K_m e - K_m \beta T \tag{A11a}$$

and

$$e_{ij} = \frac{s_{ij}}{2G_m} \tag{A11b}$$

Equations (A9) through (A11), in conjunction with (A8) can be used to derive a functional relationship between changes in stress and changes in temperature. The total differential of the Helmholtz free energy and the entropy (from A9 and A10) is given by

$$dF = \frac{\partial F}{\partial e}de + \frac{\partial F}{\partial e_{ij}}de_{ij} + \frac{\partial F}{\partial T}dT \tag{A12}$$

and

$$dS = \frac{\partial S}{\partial e}de + \frac{\partial S}{\partial e_{ij}}de_{ij} + \frac{\partial S}{\partial T}dT \tag{A13}$$

Comparing (A12) and (A8), the partial derivatives of the Helmholtz free energy are

$$\frac{\partial F}{\partial e} = V\sigma \qquad \frac{\partial F}{\partial e_{ij}} = Vs_{ij} \qquad \text{and} \quad \frac{\partial F}{\partial T} = -S \tag{A14}$$

These relationships can be used to determine the partial derivatives of the entropy. Using the fact that F is a perfect differential and[26-29]

$$S = -\frac{\partial F}{\partial T}$$

the partials of S can be determined as follows:

$$\frac{\partial S}{\partial e} = -\frac{\partial\, \partial F}{\partial e \partial T} = -\frac{\partial\, \partial F}{\partial T\, \partial e} \tag{A15}$$

However, from relations (A14), by assuming constant volume (small strain), and elastic constants independent of temperature,

$$\frac{\partial F}{\partial e} = V\sigma \tag{A16}$$

such that,

$$\frac{\partial S}{\partial e} = -V\frac{\partial \sigma}{\partial T} \tag{A17}$$

Using (A11a) as the functional form of σ, the partial with respect to temperature is

$$\frac{\partial \sigma}{\partial T} = -K_m\beta \tag{A18}$$

leading to

$$\frac{\partial S}{\partial e} = K_m\beta V \tag{A19}$$

In a similar manner,

$$\frac{\partial S}{\partial e_{ij}} = -V\frac{\partial s_{ij}}{\partial T} = 0 \qquad \text{(A20)}$$

The differential of heat is related to the specific heat at constant volume, and temperature through[27]

$$dQ = \rho_0 V C_v dT \qquad \text{(A21)}$$

and with entropy defined as[28]

$$TdS = dQ \qquad \text{(A22)}$$

then,

$$\frac{\partial S}{\partial T} = \frac{\rho_0 V C_v}{T} \qquad \text{(A23)}$$

Using (A19, A20 and A23) in (A13) gives an expression for the total differential of the entropy in terms of the independent variables

$$dS = \frac{\rho_0 V C_v}{T} dT + K_m \beta V de \qquad \text{(A24)}$$

Multiplying by T, and taking the time rate of change of the differentials gives

$$T\dot{S} = \rho_0 V C_v \dot{T} + K_m \beta V T \dot{e} \qquad \text{(A25)}$$

Under adiabatic conditions, since $T\dot{S} = \dot{Q} = 0$, equation (A25) reduces to an expression for the dilatational strain rate as a function of temperature,

$$\dot{e} = -\frac{\rho_0 C_v}{K_m \beta T}\dot{T} \qquad \text{(A26)}$$

Using (A3) in (A26) gives an expression for the hydrostatic stress (eqn 1)

$$\dot{\sigma} = - K_m\beta\left(1 + \frac{\rho_0 C_v}{K_m\beta^2 T}\right)\dot{T}$$

This equation relates temperature changes in an elastic body to changes in the hydrostatic stress. The second term in brackets is much larger than the first, resulting in a simpler approximation that, typically, differs in value by less than 0.6%, (eqn 2)

$$\dot{\sigma} \approx - \frac{\rho_0 C_v}{\beta T}\dot{T}$$

The important assumptions that lead to this equation are: (i) a reversible process, (ii) adiabatic conditions, (iii) e, e_{ij} and T are independent variables, (iv) constant volume (small strains), and (v) the elastic constants do not change with temperature.

ACKNOWLEDGEMENTS

This research was sponsored by DARPA through the University Research Initiative program under ONR contract N-00014086-K-0753. Special thanks to the technical support staff at Pratt and Whitney, West Palm Beach, including Scott Stevens, Gene Leiske and Duwayne Brodnicky; the engineering staff: Jennifer Heine and Barrie Peters; and the management: Brad Cowles and Doug Nethaway.

LIST OF FIGURES

Figure 9. Stress redistribution along the notch plane by shear bands having a shear strength, t = 50MPa.

Figure 10. SPATE images (a,b, c) and corresponding surface replicas (d, e, f) taken following loading of the SiC/CAS composite. These images show stress redistribution due to multiple matrix cracking.

Figure 11. SPATE line scans extracted from the full field scans shown in Figure 10 graphically illustrate stress redistribution across the net section.

Figure 12. SPATE images obtained for the SiC/SiC material.

Figure 13. Overlay of line scans connecting the notches (a) as-received specimen, (b) after loading to 160MPa.

Figure 14. The unloading modulus decreases with increasing matrix crack density.. (Data from SiC/CAS and SiC/SiC courtesy of Jean-Marc Domergue).

Figure 15. A gradient in a materials' modulus results in stress redistribution.

REFERENCES

1. A. G. Evans, F. W. Zok and T. J. Mackin, " The Mechanical Performance of Ceramic-Matrix Composites," to be published.

2. F. E. Heredia, S. M. Spearing, M. Y. He, T. J. Mackin, A. G. Evans, P. Mosher, and P. Bronsted, "Notch Effects in Carbon Matrix Composites," J. Amer Cer Soc, in press.

3. C. Cady, T. J. Mackin and A. G. Evans, "Stress Redistribution and Notch Insensitivity in a Ceramic Matrix Composite," J. Amer Cer Soc, to be published.

4. S. Mall, D. E. Bullock and J. J. Pernot, "Tensile Fracture Behavior of Fiber Reinforced Ceramic Matrix Composites with Holes," to be published.

5. A. G. Evans, "The Mechanical Performance of Reinforced Ceramic, Metal and Intermetallic Matrix Composites," Mat Sci and Eng., A 143, pp. 63-76, 1991.

6. J. W. Hutchinson and H. M. Jensen, "Models of Fiber Debonding and Pullout in Brittle Composites with Friction," Mechs of Materials, 9, 139-63, 1990.

7. D. B. Marshall, "Analysis of Fiber Debonding and Sliding Experiments in Brittle Matrix Composites," Acta Metall. Mater. Vol 40, No. 3, pp. 427-441, 1992.

8. M. D. Thouless, O. Szaibero, L. S. Sigl, and A. G. Evans, J Amer Cer Soc, 72, pp. 525-532, 1989.

9. W. A. Curtin, "Theory of Mechanical Properties of Ceramic Matrix Composites," J Am. Ceram Soc., 74, pp. 2837-45, 1991.

10. A. G. Evans, J. M Domerque and E. Vagaggini, "A Methodology for Relating Macroscopic Behavior of Ceramic Matrix Composites to Constitutive Properties," J Amer Cer Soc, to be published.

11. G. Bao and Z. Suo, "Remarks on Crack-Bridging Concepts," in Micromechanical Modelling of Quasi-Brittle Materials Behavior, edited by V. V. Li, Appl Mech. Rev., Vol 45, No. 8., pp. 355-365, August, 1992.

12. Z. Suo, S. Ho and X. Gong, "Notch Ductile-to Brittle Transition Due to Localized Inelastic Band," J. Mat. Engr. Tech., in press.

13. S. M. Spearing, P. W. R. Beaumont, and M. F. Ashby, "Fatigue Damage Mechanics of Notched Graphite-Epoxy Laminates," in Composite Materials: Fatigue and Fracture, ASTM STP 1110, edited by T. K. O'Brien, pp. 596-616, 1991.

14. P Bronsted, F. E. Heredia and A. G. Evans, "The In-Plane Shear Properties of 2-D Ceramic Matrix Composites," J. Amer Cer Soc, in press

15. W. W. Stinchcomb and C. E. Bakis, "Fatigue Behavior of Composite Laminates," Fatigue of Composite Materials, Edited by K. L. Reifsnider, Elsevier Science Publishers B.V., pp. 105-180, 1990.

16. K. L. Reifsnider and C. E. Bakis, "Adiabatic Thermography of Composite Materials," Characterization of Advanced Materials, Edited by W. Altergott and E. Henneke, Plenum Press, New York, pp. 65-76, 1991.

17. K. L. Reifsnider, W. W. Stinchcomb, C. E. Bakis, and R. Y. Yih, " The Mechanics of Micro-Damage in Notched Composite Laminates," Damage Mechanics in Composites - AD-Vol. 12, Edited by A. S. D. Wang and G. K. Haritos, ASM, New York, pp. 65-72, 1987.

18. C. E. Bakis, R. A. Simonds, L. W. Vick, and W. W. Stinchcomb, "Matrix Toughness, Long-Term Behavior, and Damage Tolerance of Notched Graphite Fiber-Reinforced Composite Materials, " ASTM STP 1059, pp. 349-370, 1990.

19. C. E. Bakis and K. L. Reifsnider, "Nondestructive Evaluation of Fiber Composite Laminates by Thermoelastic Emission," Review of Progress in Quantitative Nondestructive Evaluation, Vol. 7B, Edited by D. O. Thompson and D. E. Chimend, Plenum Publishing Corp., pp. 1109-1116, 1988.

20. C. E. Bakis, H. R. Yih, W. W. Stinchcomb, and K. L. Reifsnider, "Damage Initiation and Growth in Notched Laminates Under Reversed Cyclic Loading," ASTM STP 1012, pp. 66-83, 1989.

21. R. A. Simonds, C. E. Bakis, and W. W. Stinchcomb, "Effects of Matrix Toughness on Fatigue Response of Graphite Fiber Composite Laminates, ASTM STP 1012, pp. 5-18, 1989.

22. N. F. Enke, "Thermographic Stress Analysis of Isotropic Materials," Ph. D. Thesis, Department of Engineering Mechanics, The University of Wisconsin-Madison, 1989.

23. Thermoelastic Stress Analysis, N. Harwood and W. M. Cummings, Adam Hilger, IOP publishing, 1991.

24. A. K. Wong, J. G. Sparrow, and S. A. Dunn, "On The Revised Theory of the Thermoelastic Effect," J. Phys. Chem. Solids Vol. 49, No. 4, pp. 395-400, 1988.

25. A. K. Wong, R. Jones and J. G. Sparrow, "Thermoelastic Constant of Thermoelastic Parameter?" Phys. Chem. Solids Vol. 48, No. 8, pp. 749-753, 1987.

26. B. Budiansky and R. J. O'Connell, "Bulk Thermoelastic Attenuation of Composite Materials," J. Geophysical Research, Vol. 88, No. B12, pp. 10,343-10,348, December 10, 1983.

27. B. Budiansky, "Thermal and Thermoelastic Properties of Isotropic Composites," J. Comp. Materials, Vol. 4, pp. 286-295, July 1970.

28. Heat and Thermodynamics, M. W. Zymansky, 5th Edition, McGraw-Hill, 1968.

29. Equilibrium Statistical Mechanics, E. A. Jackson, Prentice-Hall International Series in Engineering of the Physical Sciences, 1968.

30. D. Zhang and B. I. Sandor, "Thermographic Analysis of Stress Concentrations in a Composite," Experimental Mechanics, pp. 121-125, June 1989.

31. D. Zhang, N. F. Enke, and B. I. Sandor, "Thermographic Stress Analysis of Composite Materials," accepted for publication in Experimental Mechanics, June 1989.

32. R. Jones, M. Heller, D. Lombardo, S. Dunn, J. Paul and D. Saunders, "Thermoelastic Assessment of Damage Growth in Composites," Composite Structures, 12, pp. 291-314, 1989.

Class I

Matrix Cracking + Fiber Failure

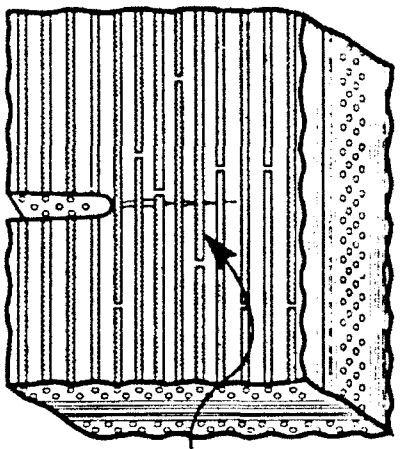

Pull-Out Tractions
Redistribute Stress

Class II

Matrix Cracking: No Fiber Failure

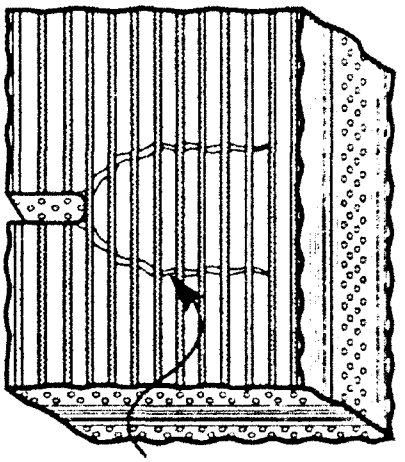

Matrix Cracks
Redistribute Stress

Class III

Shear Damage By Matrix Cracking

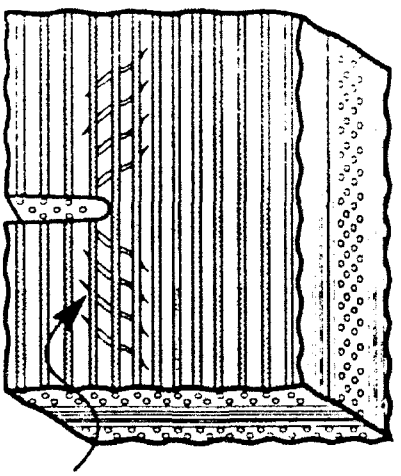

Shear Damage Zone
Redistributes Stress

Figure 1

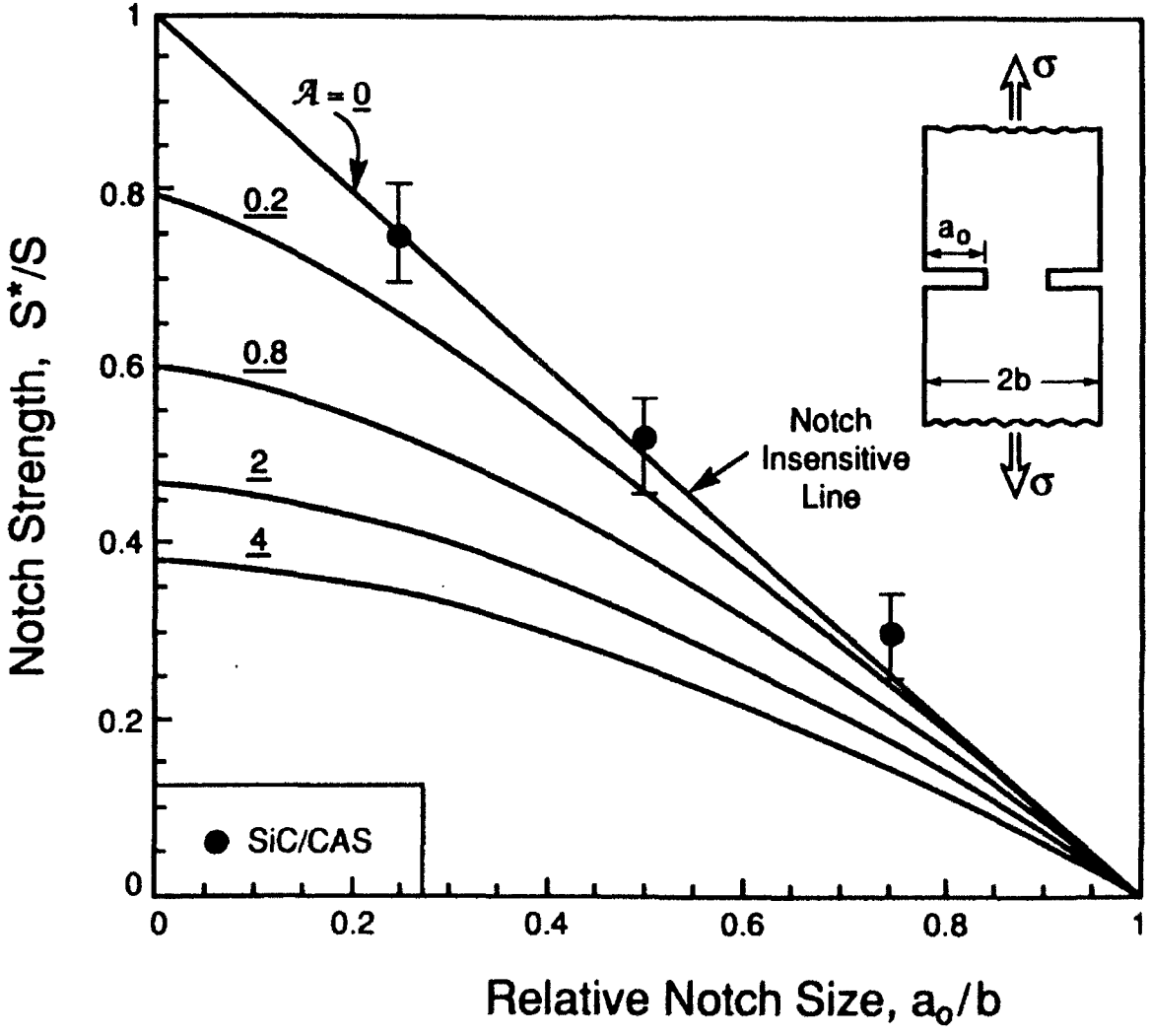

Figure 2

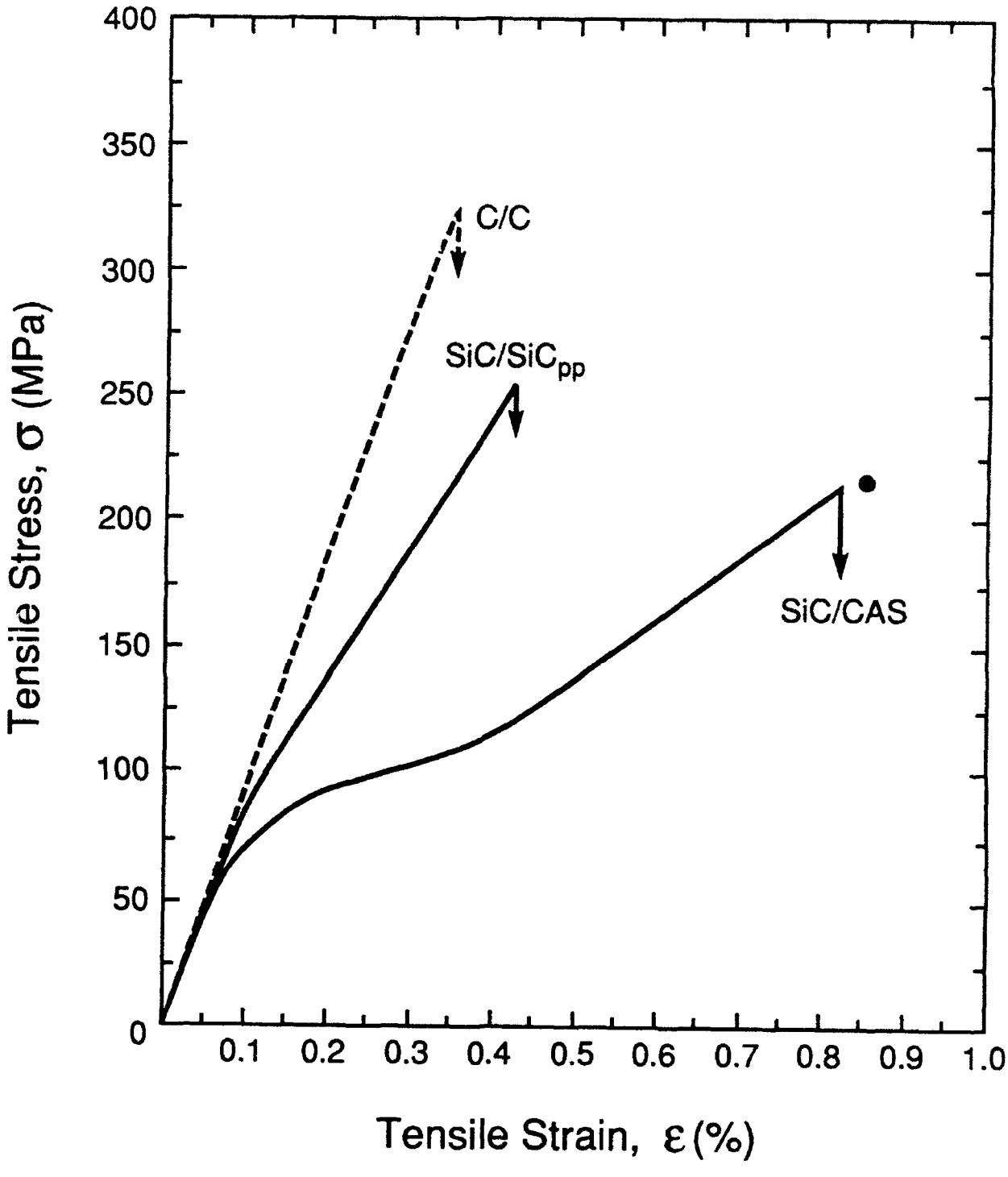
400
350
300
250
200
150
100
50
0
Tensile Stress, σ (MPa)
C/C
SiC/SiCpp
SiC/CAS
0.1
0.2
0.3
0.4
0.5
0.6
0.7
0.8
0.9
1.0
Tensile Strain, ε (%)

Figure 3a

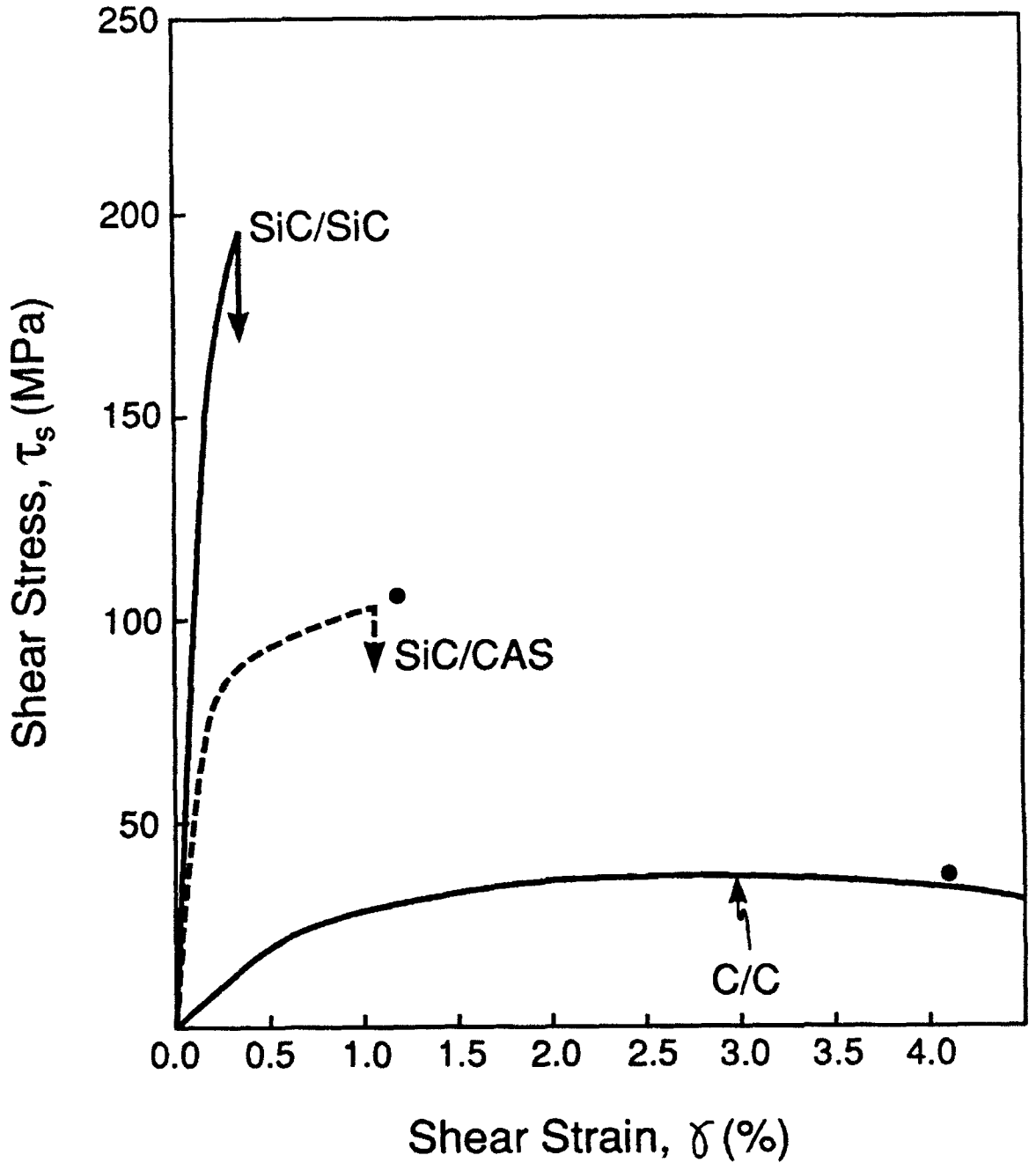
250
200
150
100
50
SiC/SiC
SiC/CAS
C/C
Shear Stress, τ_s (MPa)
0.0
0.5
1.0
1.5
2.0
2.5
3.0
3.5
4.0
Shear Strain, γ (%)

Figure 3b

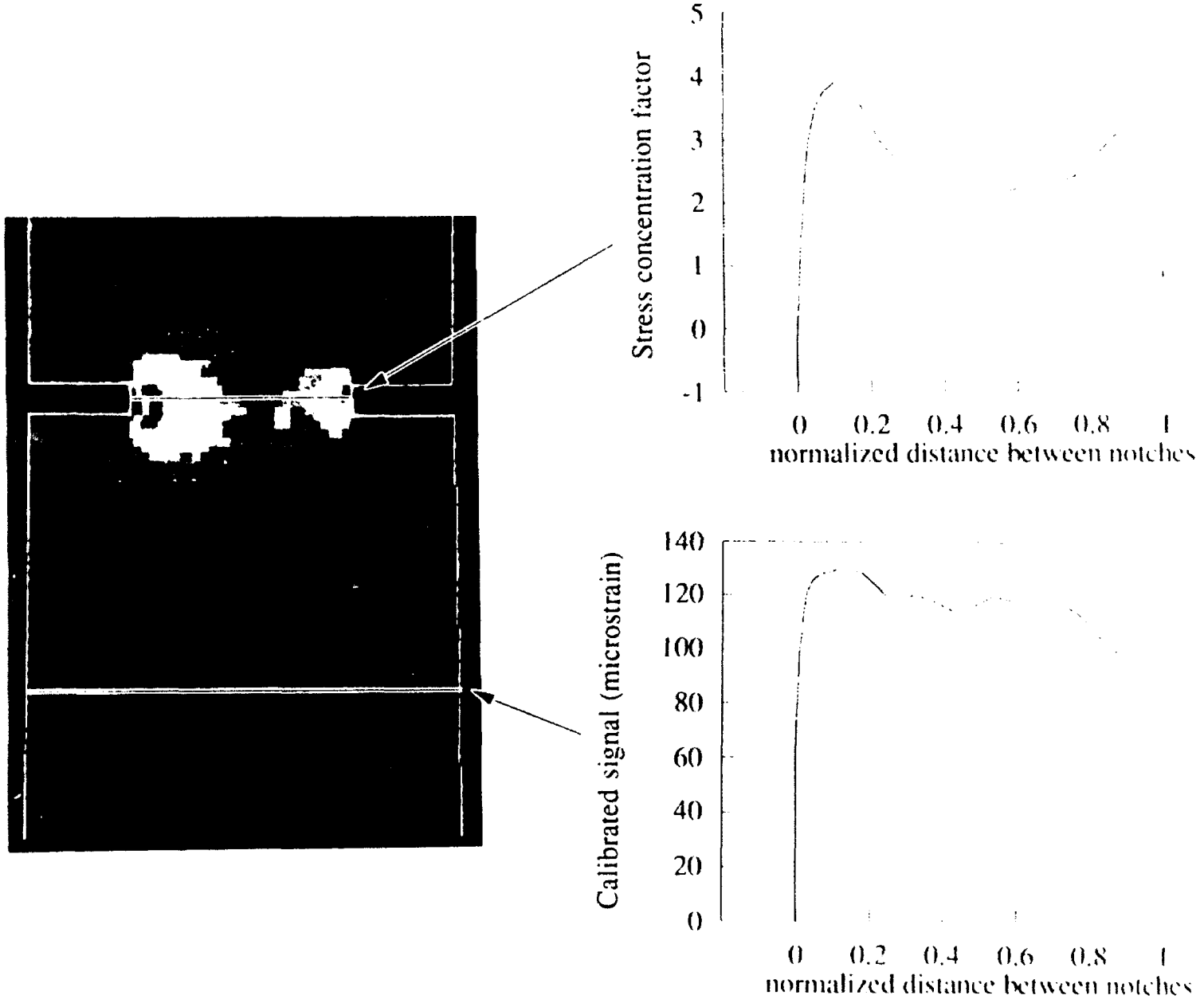
Stress concentration factor
5
4
3
2
1
0
-1
0
0.2
0.4
0.6
0.8
1
normalized distance between notches
Calibrated signal (microstrain)
140
120
100
80
60
40
20
0
0
0.2
0.4
0.6
0.8
1
normalized distance between notches

Figure 4

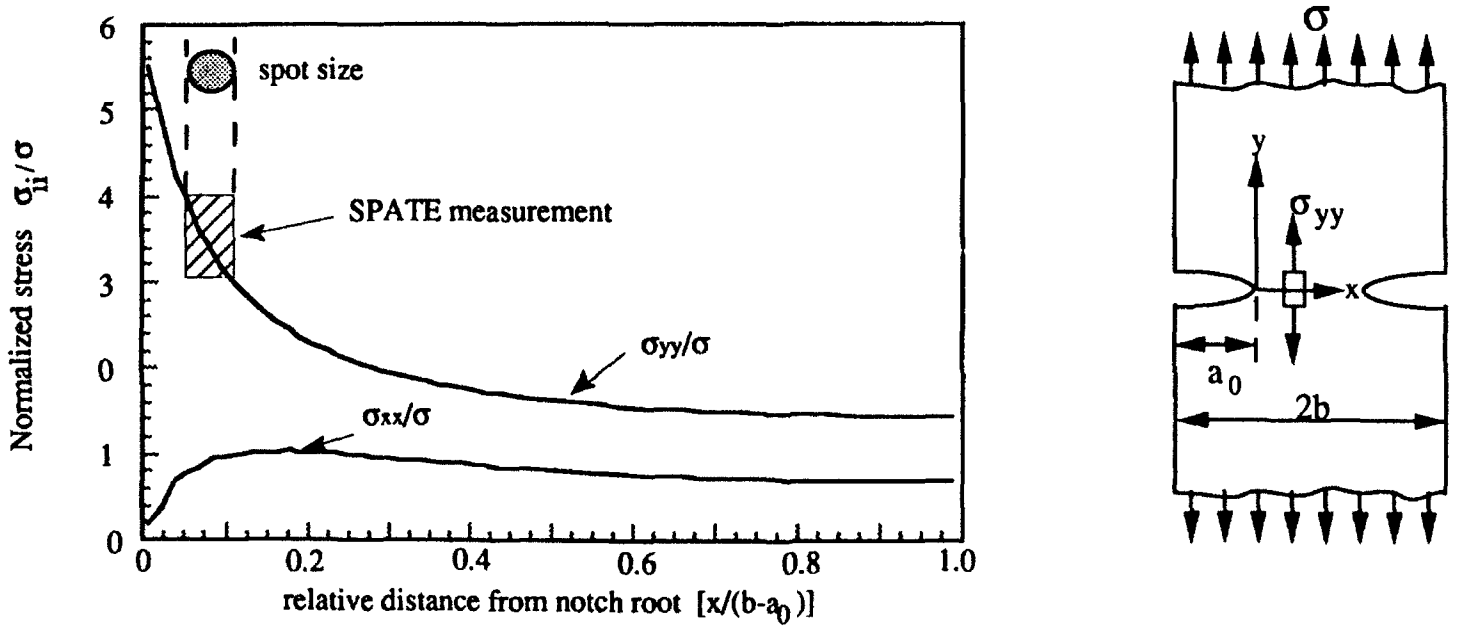
Normalized stress σ_{ii}/σ
6
5
4
3
0
1
0
spot size
SPATE measurement
σ_{yy}/σ
σ_{xx}/σ
0
0.2
0.4
0.6
0.8
1.0
relative distance from notch root $[x/(b-a_0)]$
σ
y
σ_{yy}
x
a_0
2b

Figure 5

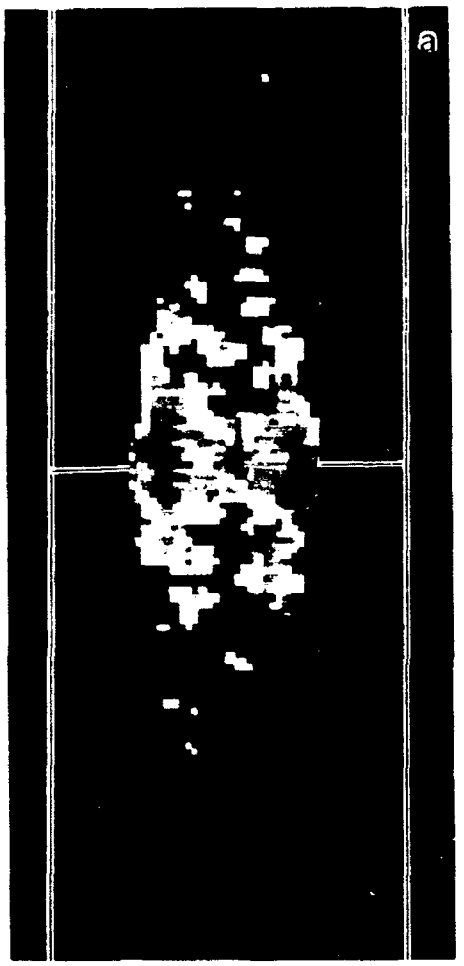

Figure 6

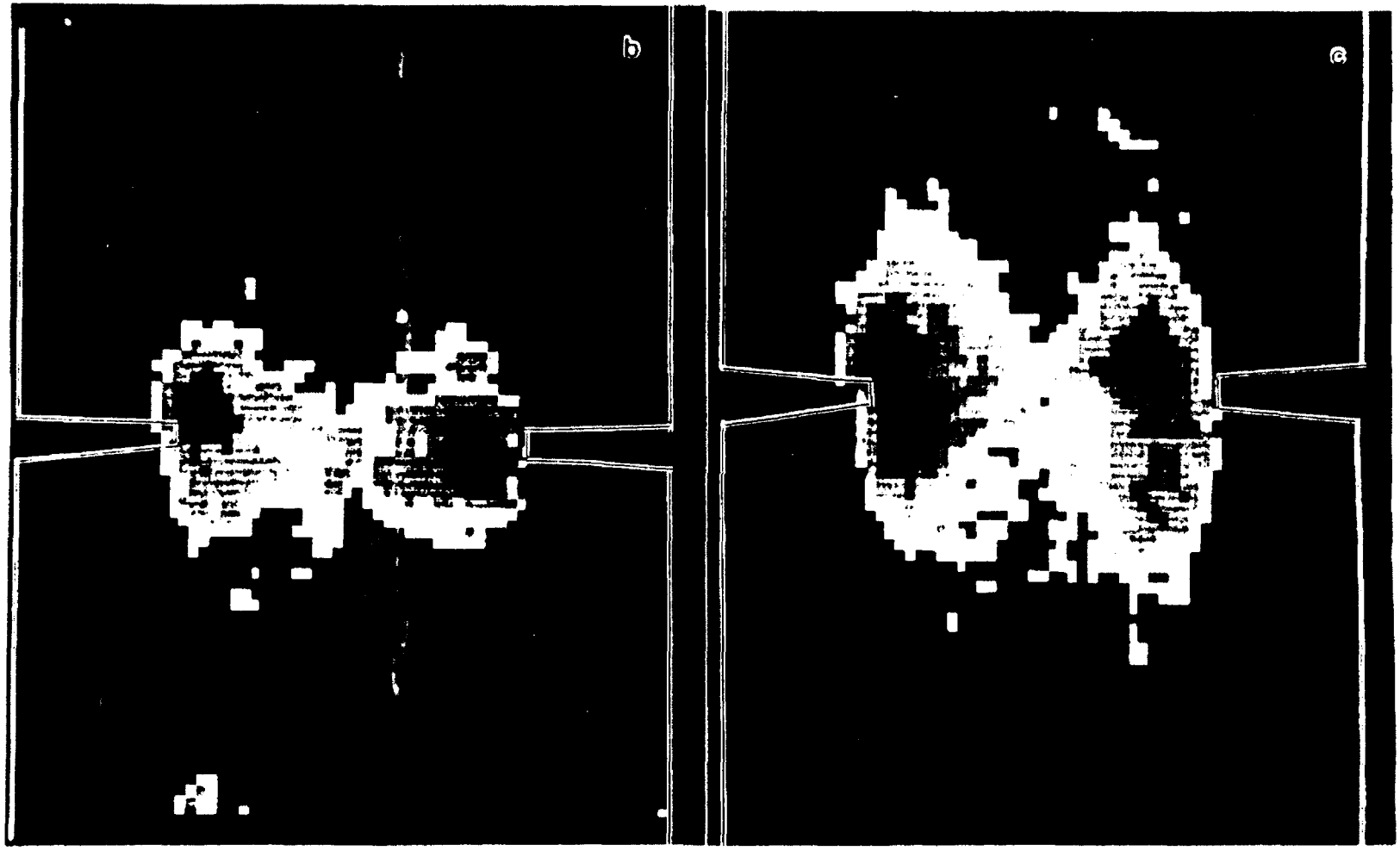

Figure 6

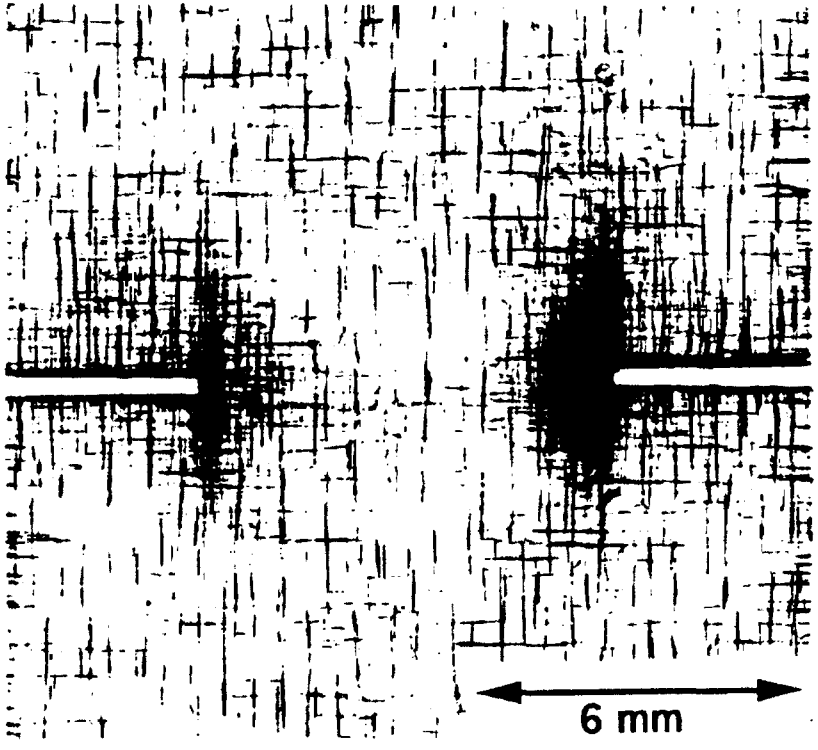

Figure 6d

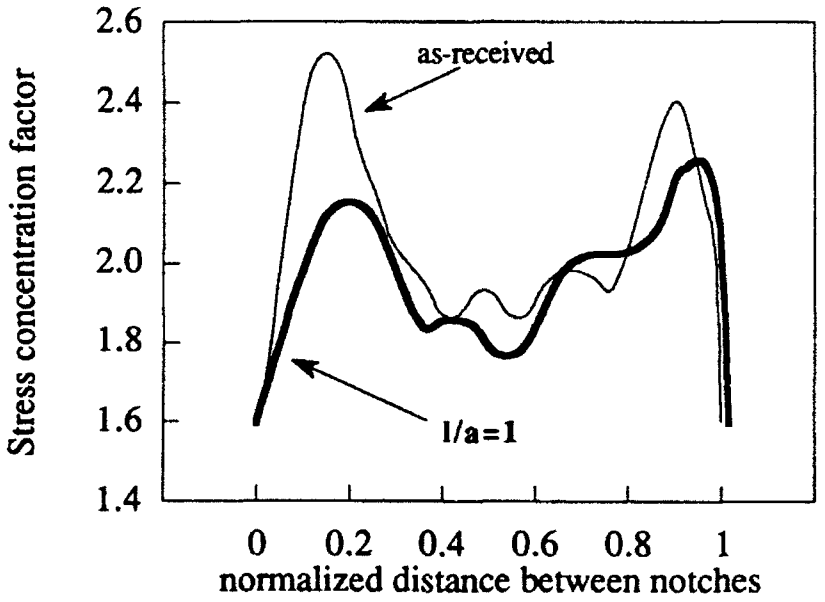
Stress concentration factor
2.6
2.4
2.2
2.0
1.8
1.6
1.4
as-received
l/a=1
0
0.2
0.4
0.6
0.8
1
normalized distance between notches

Figure 7

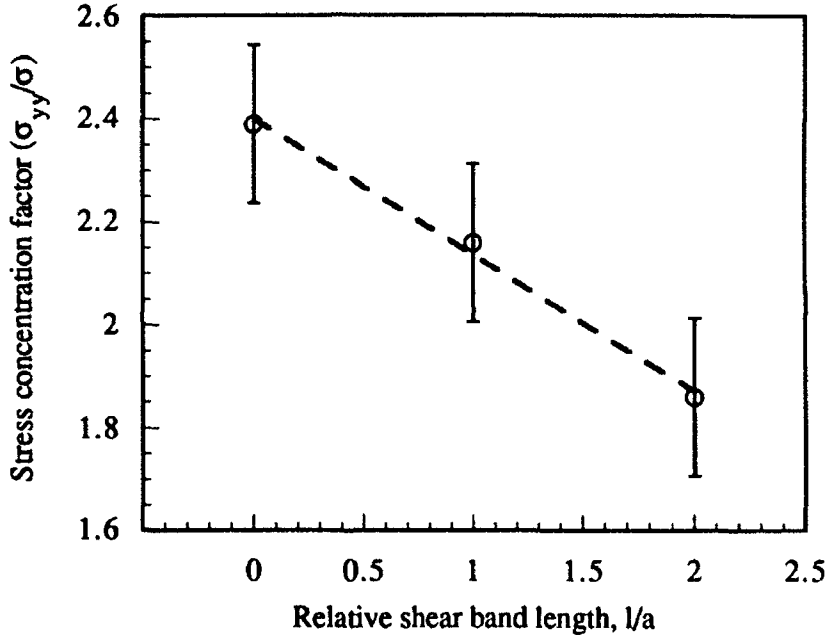
Stress concentration factor (σ_{yy}/σ)
2.6
2.4
2.2
2
1.8
1.6
0
0.5
1
1.5
2
2.5
Relative shear band length, l/a

Figure 8

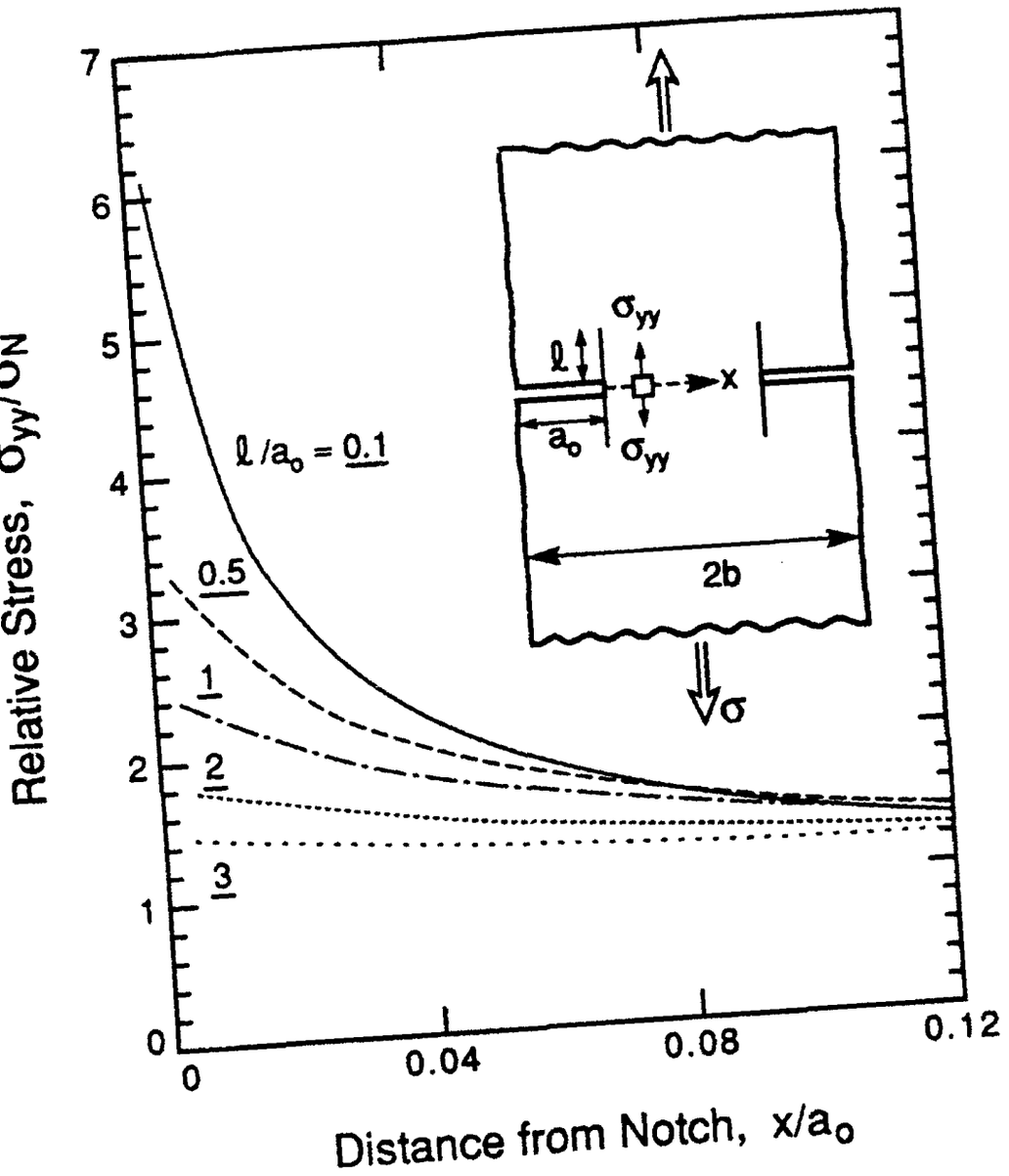
Relative Stress, σ_{yy}/σ_N
Distance from Notch, x/a_o
$\ell/a_o = 0.1$
0.5
1
2
3
σ_{yy}
ℓ
x
a_o
σ_{yy}
2b
σ
0
0.04
0.08
0.12
1
2
3
4
5
6
7

Figure 9

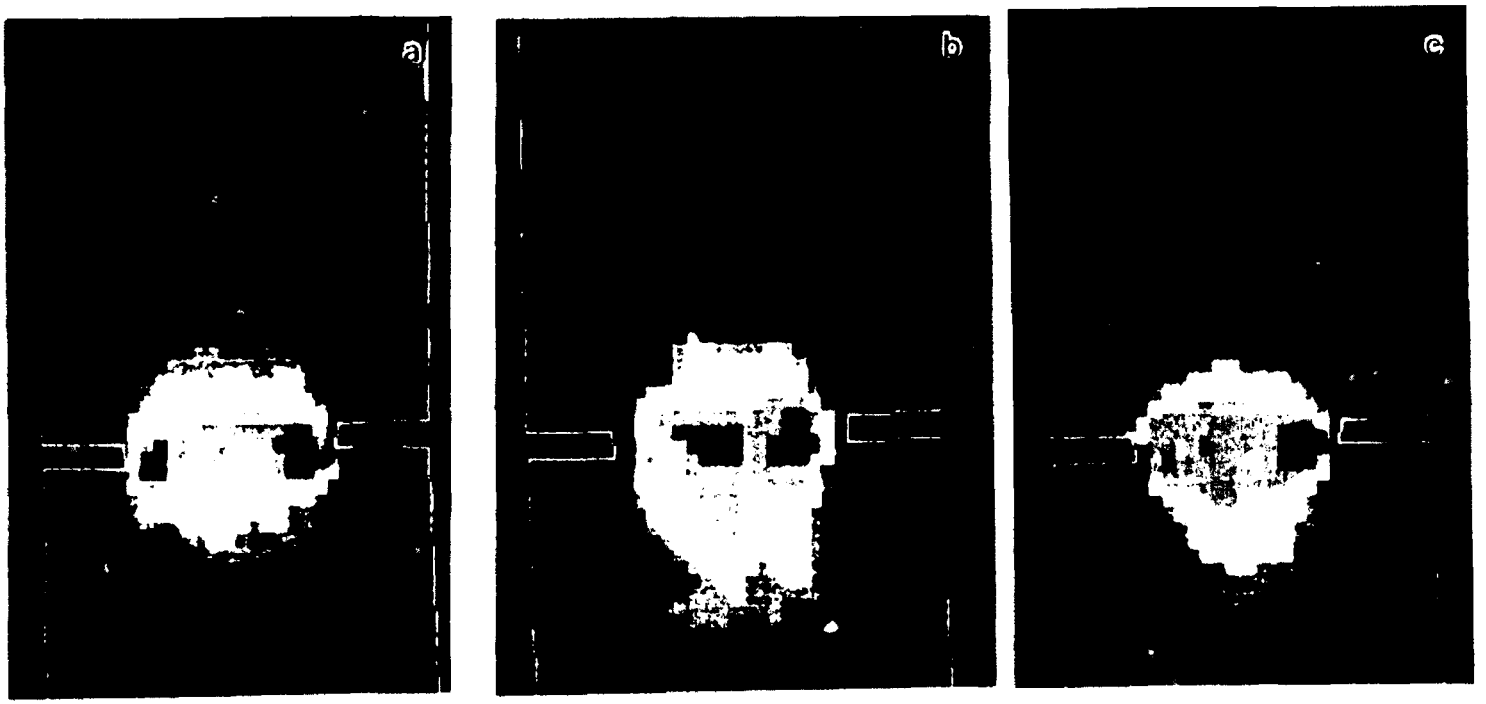

Figure 10

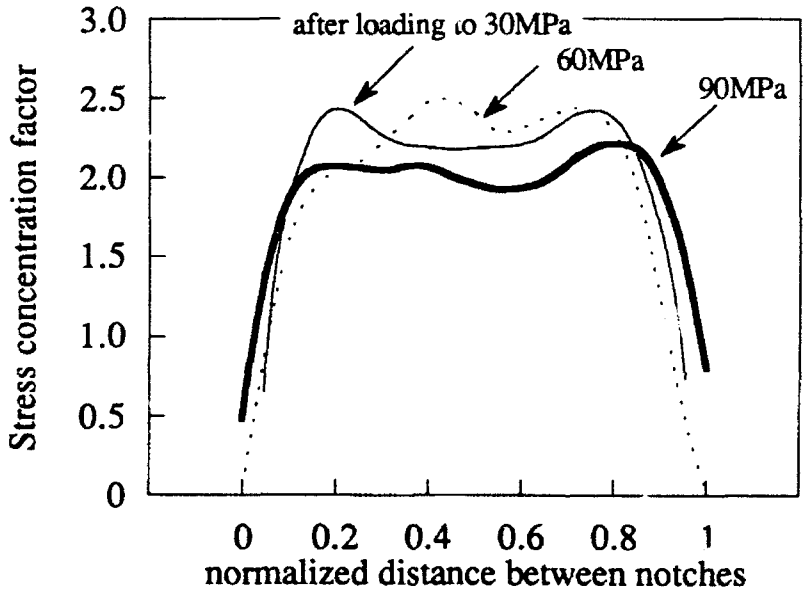
after loading to 30MPa
60MPa
90MPa
Stress concentration factor
3.0
2.5
2.0
1.5
1.0
0.5
0
0
0.2
0.4
0.6
0.8
1
normalized distance between notches

Figure 11

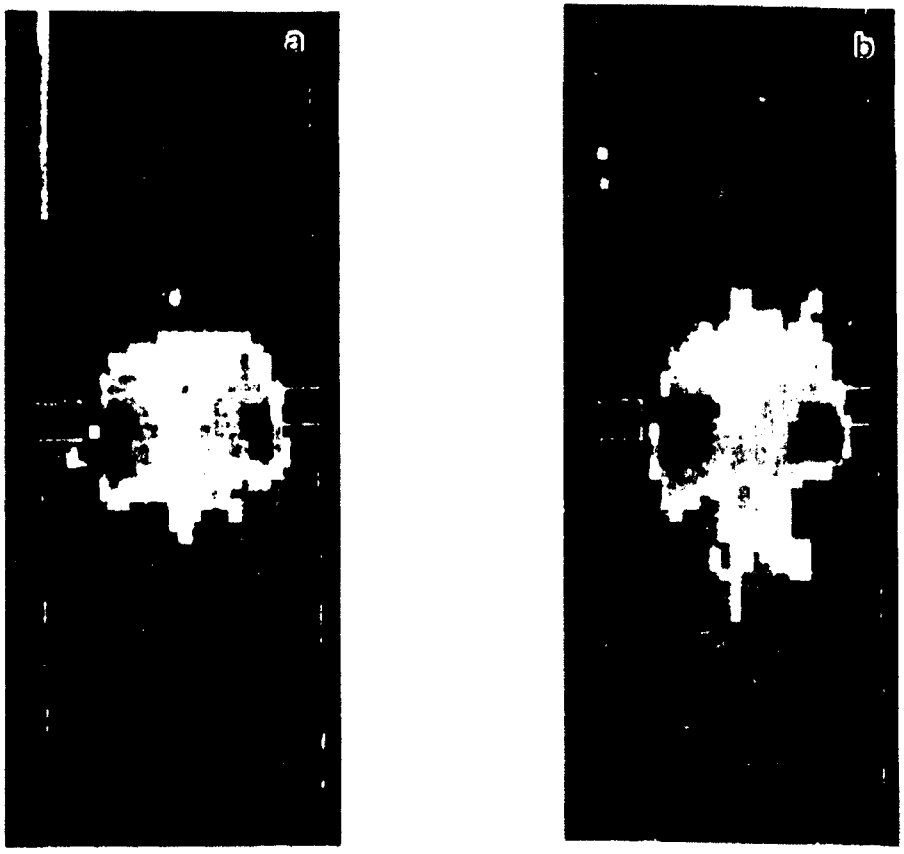

Figure 12

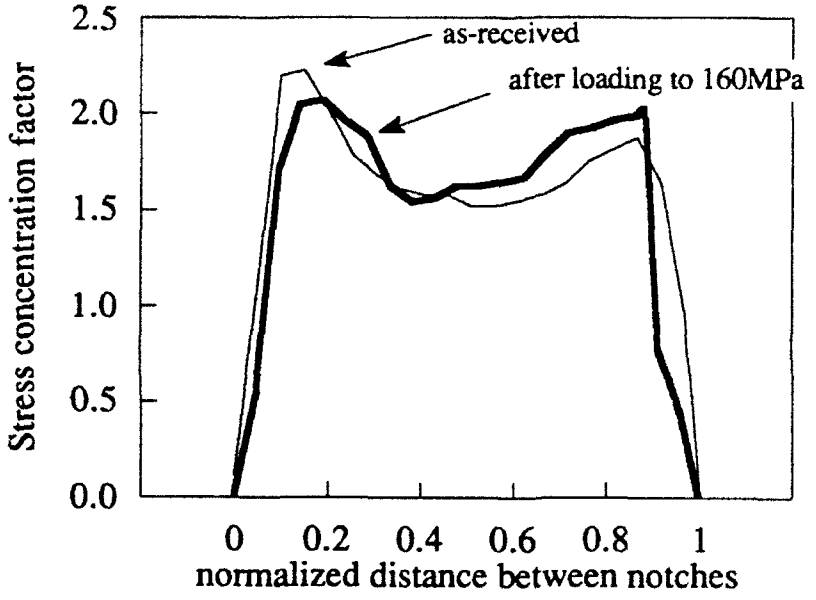
2.5
2.0
1.5
1.0
0.5
0.0
Stress concentration factor
as-received
after loading to 160MPa
0
0.2
0.4
0.6
0.8
1
normalized distance between notches

Figure 13

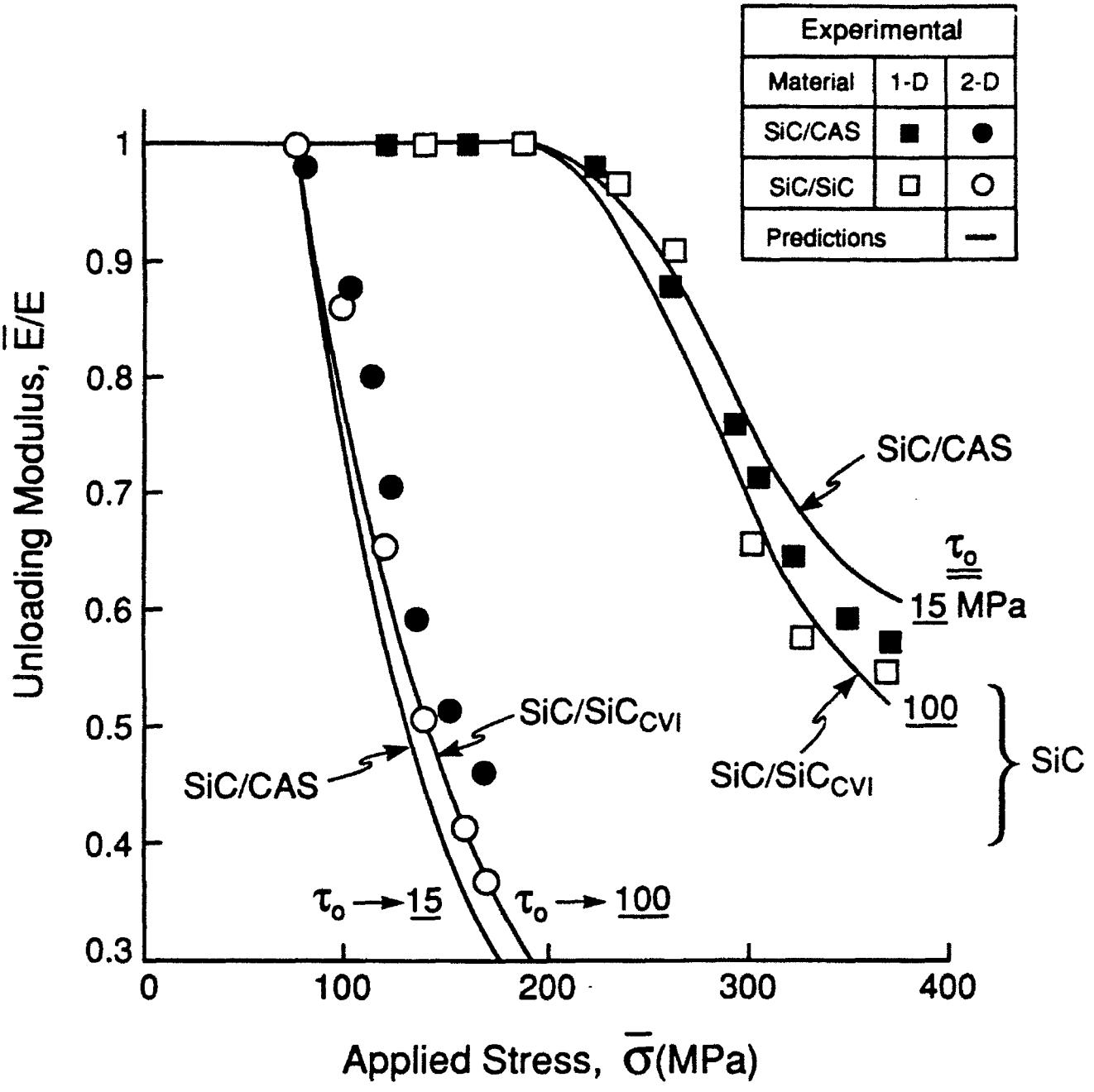
Experimental
Material
1-D
2-D
SiC/CAS
SiC/SiC
Predictions
Unloading Modulus, $\bar{E}/E$
1
0.9
0.8
0.7
0.6
0.5
0.4
0.3
0
100
200
300
400
Applied Stress, $\bar{\sigma}$(MPa)
SiC/CAS
τ_o = 15 MPa
100
SiC/SiC$_{CVI}$
SiC
SiC/CAS
SiC/SiC$_{CVI}$
$\tau_o \rightarrow$ 15
$\tau_o \rightarrow$ 100

Figure 14

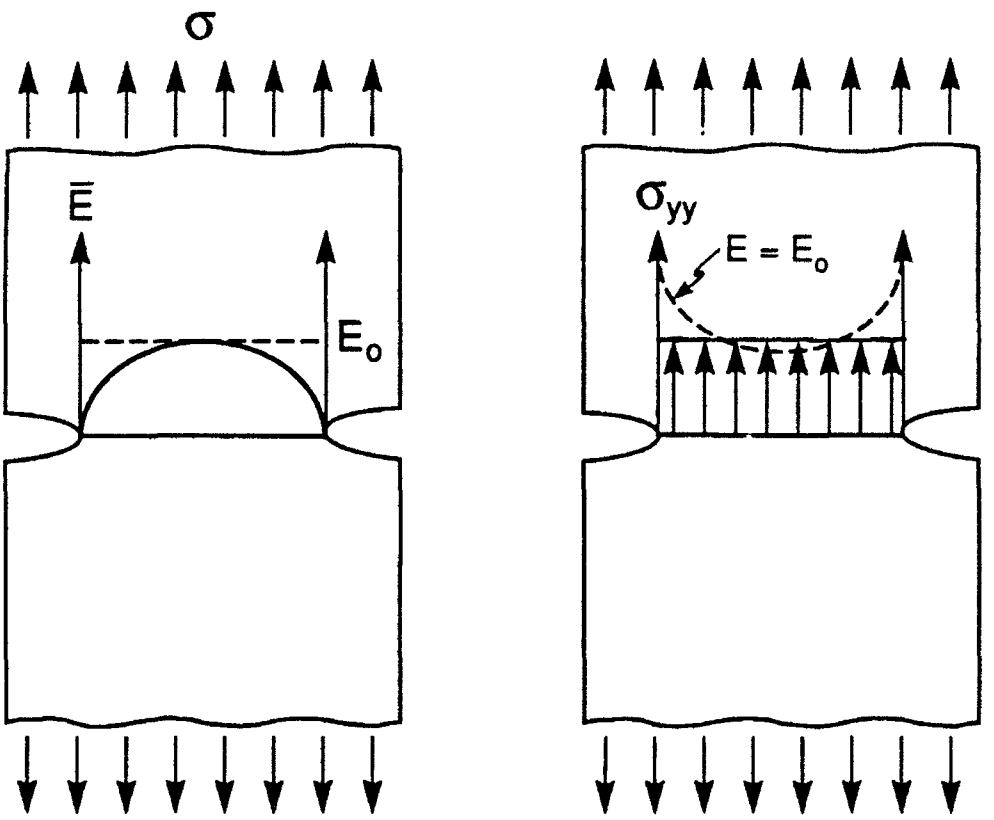

Figure 15